Cardiac Flow Analysis Using Magnetic Resonance Imaging

by

Kelvin K. L. Wong

B.Eng (Hons), Nanyang Technological University, 2001
Master Appl. I.T., The University of Sydney, 2003

Thesis submitted for the degree of

Doctor of Philosophy

in

School of Electrical and Electronic Engineering,
Faculty of Engineering, Computer and Mathematical Sciences
The University of Adelaide

August, 2009

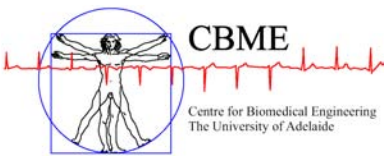

Contents

Abstract

Many types of cardiac abnormality have an implication on blood flow. However, most present-day diagnostic modalities analyse myocardial structures and not the cardiac flow within to detect heart defects *in vivo*. Currently, various imaging modalities, such as echocardiography, single photon emission computed tomography (SPECT), positron emission tomography (PET), X-ray computed tomography (CT), and cardiac magnetic resonance imaging (CMRI) provide a non-invasive approach for scanning humans with heart abnormalities, and are utilised in the management of cardiac patients. There is a need to develop a visualisation system for analysing flow of blood within the human heart. Motional properties of blood can be measured against normal controls and patients with cardiac abnormalities in order to discover underlying cause of these flow phenomena. This can potentially extend medical knowledge of the defects and their hemodynamic behaviour.

We characterise motion patterns of blood in the human heart and analyse the flow properties, by means of tracking, using a series of time dependent magnetic resonance images. An indication of flow vortices can be provided by numerical computation of vorticity values within the defined region of blood flow. The global estimation of parametric motion flow fields over the whole image provides useful information on the presence of vortices within the heart chamber that can be used to assess cardiac functions. In this study, the crucial strategies for this approach are implemented, and the achievable diagnostic results and quality of assessment are investigated. The developmental stages of the framework and system design of each component for cardiac diagnosis are detailed in this thesis. The key objectives of the research and development for this diagnostic system are implemented herein:

1. Realisation of a non-invasive technique to compute flow features within cardiac structures. System evaluation and velocity calibration of the flow tracker are incorporated in the study. Verification of calculated flow in time-resolved cardiac vessels is performed by error analysis using flow fields constructed by velocity-encoded magnetic resonance imaging velocimetry.

2. Measurement of cardiac vorticities in heart chambers is performed for investigation of flow phenomena. We examine the time-dependent behaviour of cardiac

flow structures in the heart. The variation of flow patterns that are associated with myocardial wall deformations and pressure changes is analysed.

3. Realisation of a statistical framework for examining variations of flow due to myocardial defects in the heart. The quantification of flow will offer the potential to complement diagnostic methods that analyse cardiac defects and evaluate patient condition after surgical intervention.

As an alternative to established medical imaging-based diagnostic techniques such as chest X-rays, and pulsed or continuous wave Doppler ultrasound scans for cardiac diagnosis, we develop a magnetic resonance imaging based approach and perform flow quantification to analyse the heart, *vis-à-vis* blood movement in chambers based on a measured flow field. This framework offers potential for non-invasive flow visualisation in cardiac structures. We validate this methodology specifically for analysing flow characteristics within a human heart case study. We also demonstrate the potential for non-invasive assessment of cardiac abnormality for a pathological case of the heart.

Statement of Originality

This work contains no material that has been accepted for the award of any other degree or diploma in any university or other tertiary institution and, to the best of my knowledge and belief, contains no material previously published or written by another person, except where due reference has been made in the text.

I give consent to this copy of the thesis, when deposited in the University Library, being available for loan, photocopying, and dissemination through the library digital thesis collection, subject to the provisions of the Copyright Act 1968.

I also give permission for the digital version of my thesis to be made available on the web, via the University's digital research repository, the Library catalogue, the Australasian Digital Thesis Program (ADTP) and also through web search engines, unless permission has been granted by the University to restrict access for a period of time.

Signed

Date

Acknowledgments

My supervisors during the course of the PhD study are Professors Jagannath Mazumdar, Derek Abbott, Richard Malcolm Kelso, Stephen Grant Worthley, and Prasthanthan Sanders. Apart from them, a great number of people have collaborated to make this thesis possible. Their support, encouragement, and exchange of ideas have been mind enriching and paved the way for a fruitful research during my study at the University of Adelaide.

Supervision and Mentorship

I would like to convey my warmest appreciation to **Prof Jagannath Mazumdar** for encouraging me to broaden my range of knowledge in medical imaging, biomechanics, and flow visualisation. His advice has motivated me to effectively integrate them into a successful research thesis that I present here. He has also assisted me in establishing important working relationships with medical experts and paved the ways for research collaboration with professional bodies. For his practical contribution, moral support and ever lasting friendship, I owe him a great depth of gratitude.

I am deeply indebted to **Prof Derek Abbott** for his support in my mental and career development. He has imparted to me his invaluable experience and knowledge that has allowed me to develop a unique philosophy of excelling in research. Apart from his patient guidance throughout these years, he has also strengthened my motivation to be knowledgeable in the field of computer tomography and medical image visualisation. Therefore, I also acknowledge him to be an important person to have influenced and groomed my research career.

Special appreciation is extended to **Assoc Prof Richard M. Kelso** from the School of Mechanical Engineering for imparting his knowledge in fluid mechanics, as well as image velocimetry, which are utilised in the development of the techniques used in this study. I sincerely thank his generous contribution of time in my education. He has taught me the important concepts used in flow visualisation methods and groomed me to be a confident and motivated researcher. I look up to him as the best teacher in fluid mechanics.

I have the pleasure of working in the Cardiovascular Research Centre (CRC) and Faculty of Health Science that is based at the Royal Adelaide Hospital and the University of Adelaide. **Prof Prashanthan Sanders** and **Prof Stephen G. Worthley** in the School of Medicine have supervised and supported me in the technical and instrumental portions of this thesis, particularly in magnetic resonance imaging. I thank them sincerely for providing me with a fertile environment to crystallise ideas and transforming them into successful outcomes.

Financial Support

I gratefully acknowledge that my scholarship was personally funded by **Prof Derek Abbott** and partly by the Cardiovascular Research Centre (CRC). In additional, the funding for the purchase of software, textbooks and equipment during the course of my work was provided by **Prof Derek Abbott** and **Prof Stephen G. Worthley**. Travel funding to conferences was contributed by Prof Abbott and the School of Electrical & Electronic Engineering.

Commercialisation

I also convey appreciation to **Dr Matthew Chong** from the Adelaide Research and Innovation Pty Ltd for his useful advice in relation to technology transfer and intellectual property rights. He has assisted me in commercialisation of the software deliverable from my research.

Proof Reading and Discussion

It is also a great pleasure to express my gratitude to **Professor Derek Abbott** and **Dr Peter Cooke** at the School of Electrical & Electronic Engineering, as well as **Assoc Prof Richard M. Kelso** for proof reading this thesis. Their advice in scientific writing and referencing has been tremendously helpful.

I thank **Dr Pawel Kuklik** at the Faculty of Health Science and School of Medicine for his encouragement and interest in this work. He has streamlined the discussion of important concepts used in my research. I am delighted to acknowledge **Dr Mathias Baumert** for checking the technical accuracy of my publications and this thesis.

MRI Scanning and Data

The assistance during the scanning of test subjects that is rendered by **Dr Payman Molaee** and **Mr Angelo Carbone** at the Faculty of Health Science and School of Medicine has been invaluable. The supply of magnetic resonance images by the Royal Adelaide Hospital is appreciated. I also thank them for imparting to me their knowledge of medical imaging.

Software Development and Programming

Appreciation is extended to my colleague **Mr Shaoming Zhu** for his assistance in programming the statistical library package of the medical image processing software that is used in my work, and also to **Ms Yumay Chen** for her input in data preparation during program testing. Thanks are also due to **Mr Ishwor Gurung** for his patient help in debugging during the development of graphical user interface for the subsequent version of the software. The advice given by my colleagues **Mr Withawat Withayachumnankul**, **Ms Shaghik Atakaramians** and **Ms Gretel Png**, during the typesetting of my thesis in Latex, is gratefully acknowledged.

Emotional and Mental Support

Special appreciation goes out to the rest of my colleagues in the Centre for Biomedical Engineering for their friendship and emotional support during my study in Adelaide.

Finally, and most importantly, I would like to thank my parents for their support during my PhD study. If not for their kind encouragement and concern during the occasions when I was facing difficulties, I may not have been able to complete all the work presented in this thesis.

Conventions

1. **Typesetting:** This thesis is typeset using the LaTeX2e software. TeXnicCenter 1 Beta 6.31 (Firenze) was used as an interface to LaTeX. Processed plots and images were generated using Matlab 7.0 (Mathsworks Inc.). Adobe Illustrator (Adobe Systems Incorporated) was used to produce schematic diagrams and other drawings. Medflovan medical image processing software was developed using C++ programming language—Borland C++ Builder Version 6.0 (Borland Software Corporation). The OpenGL library (Silicon Graphics, Inc) is the application programming interface for plotting colour contour and vector flow maps.

2. **Spelling:** Australian English spelling has been adopted throughout, as defined by the Macquarie English Dictionary (A. Delbridge, Ed., Macquarie Library, North Ryde, NSW, Australia, 2001).

3. **Referencing:** Harvard style is used for referencing and citation in this thesis.

Awards

Young Investigator Award

Title: Blood flow assessment in the aortic heart valve based on magnetic resonance images using optical flow analysis

Authors: Kelvin K. L. Wong, Pawel Kuklik, Richard M. Kelso, Stephen G. Worthley, Prashanthan Sanders, Jagannath Mazumdar & Derek Abbott

Conference: XVth International Conference on Mechanics in Medicine and Biology (15th ICMMB), Singapore, 6-8th Dec 2006.

Publication: Proceedings of the XVth International Conference on Mechanics in Medicine and Biology, ISBN 1-930746-05-9, Volume 15, pages 74-76, 2006.

Outstanding Paper Award

Title: Flow imaging and validation of MR fluid motion tracking

Authors: Kelvin K. L. Wong, Richard M. Kelso, Stephen G. Worthley, Prashanthan Sanders, Jagannath Mazumdar & Derek Abbott

Conference: 13th International Conference on Biomedical Engineering (ICBME 2008), Singapore, 3-6th Dec 2008.

Publication: Proceedings of the International Federation for Medical and Biological Engineering and the 13th International Conference on Biomedical Engineering, ISBN 1680-0737, Volume 23, pages 569-573, 2008.

Publications

Journals

WONG-K. K. L., KELSO-R. M., WORTHLEY-S. G., SANDERS-P., MAZUMDAR-J., AND ABBOTT-D. (2009). Noninvasive cardiac flow assessment using high speed magnetic resonance fluid motion tracking, *PLoS ONE*, **4**(5), Article No. e5688.

WONG-K. K. L., KELSO-R. M., WORTHLEY-S. G., SANDERS-P., MAZUMDAR-J., AND ABBOTT-D. (2009). Medical imaging and processing methods for cardiac flow reconstruction, *Journal of Mechanics in Medicine and Biology*, **9**(1), pp. 1–20.

WONG-K. K. L., KELSO-R. M., WORTHLEY-S. G., SANDERS-P., MAZUMDAR-J., AND ABBOTT-D. (2009). Cardiac flow analysis applied to phase contrast magnetic resonance imaging of the heart, *Annals of Biomedical Engineering, doi: 10.1007/s10439-009-9709-y*.

WONG-K. K. L., KELSO-R. M., WORTHLEY-S. G., SANDERS-P., MAZUMDAR-J., AND ABBOTT-D. (2009). Theory and validation of magnetic resonance fluid motion estimation using intensity flow data, *PLoS ONE*, **4**(3), Article No. e4747.

WONG-K. K. L., MAZUMDAR-J., PINCOMBE-B., WORTHLEY-S. G., SANDERS-P., AND ABBOTT-D. (2006). Theoretical modeling of micro-scale biological phenomena in human coronary arteries, *Medical & Biological Engineering & Computing*, **44**(11), pp. 971–982.

IKBALA-M., CHAKRAVARTYA-S., WONG-K. K. L., MAZUMDAR-J., AND MANDAL-P. K. (2008). Unsteady response of non-Newtonian blood flow through a stenosed artery in magnetic field, *Journal of Computational and Applied Mathematics, doi:10.1016/j.cam.2008.11.010*.

Conferences

WONG-K. K. L., KELSO-R. M., WORTHLEY-S. G., SANDERS-P., MAZUMDAR-J., AND ABBOTT-D. (September 2009). A novel measurement system for cardiac flow analysis applied to phase contrast magnetic resonance imaging of the heart, *Proceedings of the World Congress on Medical Physics and Biomedical Engineering*, Munich, Germany.

WONG-K. K. L., KELSO-R. M., WORTHLEY-S. G., SANDERS-P., MAZUMDAR-J., AND ABBOTT-D. (2008). Cardiac flow characterisation based on statistical analysis of vorticity maps, *Proceedings of the SPIE Microelectronics, MEMS, and Nanotechnology (Complex Systems II)*, Melbourne, Australia, **7270**, Article No. 72700W.

WONG-K. K. L., KELSO-R. M., WORTHLEY-S. G., SANDERS-P., MAZUMDAR-J., AND ABBOTT-D. (2008). Flow imaging and validation of MR fluid motion tracking, *Proceedings of the*

International Federation for Medical and Biological Engineering and the 13th International Conference on Biomedical Engineering (ICBME 2008), Singapore, **23**, pp. 569–573.

WONG-K. K. L., KELSO-R. M., WORTHLEY-S. G., AND ABBOTT-D. (2008). The effect of noise and sampling size on vorticity measurements in rotating fluids, *Proceedings of the International Conference on Experimental Mechanics (ICEM 2008),* Nanjing, China.

WONG-K. K. L., KELSO-R. M., WORTHLEY-S. G., SANDERS-P., MAZUMDAR-J., AND ABBOTT-D. (2008). MR fluid motion tracking of blood flow in right atrium of patient with atrial septal defect, *Proceedings of the 5th International Conference on Information Technology and Applications in Biomedicine (ITAB 2008),* Shenzhen, China, **1253**, Article No. 1253.

WONG-K. K. L., KELSO-R. M., WORTHLEY-S. G., SANDERS-P., MAZUMDAR-J., AND ABBOTT-D. (2007). Flow in left atrium using MR fluid motion estimation, *Proceedings of the SPIE Microelectronics, MEMS, and Nanotechnology (Complex Systems II),* Canberra, Australia, **6802**, Article No. 68021H.

WONG-K. K. L., MOLAEE-P., KUKLIK-P., KELSO-R. M., WORTHLEY-S. G., SANDERS-P., MAZUMDAR-J., AND ABBOTT-D. (2007). Motion estimation of vortical blood flow within the right atrium in a patient with atrial septal defect, *Proceedings of the IEEE/ICME International Conference on Complex Medical Engineering (CME 2007),* Beijing, China, pp. 862–869.

WONG-K. K. L., KUKLIK-P., KELSO-R. M., WORTHLEY-S. G., SANDERS-P., MAZUMDAR-J., AND ABBOTT-D. (2006). Blood flow assessment in a heart with septal defect based on optical flow analysis of magnetic resonance images, *Proceedings of the SPIE Biomedical Applications of Micro- and Nanoengineering III ,* Adelaide, Australia, **6416**, Article No. 64160L.

WONG-K. K. L., KUKLIK-P., KELSO-R. M., WORTHLEY-S. G., SANDERS-P., MAZUMDAR-J., AND ABBOTT-D. (2006). Blood flow assessment in the aortic heart valve based on magnetic resonance images using optical flow analysis, *Proceedings of the XVth International Conference on Mechanics in Medicine and Biology (15th ICMMB),* Singapore, **15**, pp. 74–76.

WONG-K. K. L., MAZUMDAR-J., AND ABBOTT-D. (2005). A study of the relationship between geometrical variation of atherosclerotic arteries and flow resistance, *Proceedings of the International Federation for Medical and Biological Engineering and the 12th International Conference on Biomedical Engineering (12th ICBME 2005),* Singapore, **12**, Article No. 3A5–01.

List of Symbols

Notation	Description
B_0	Static magnetic field
B_1	Magnetic field at right angles to B_0
M_z	Net magnetisation in longitudinal alignment with B_0
μ_m	Nuclear magnetic moment in an applied magnetic field B_0
ΔE	Energy difference between the two spin states
g	Lande g-factor
$\hbar$	Bohr magneton constant
E	Energy of a RF photon
h	Plank's constant
ν	Frequency of a RF photon
x, y, z	Image plane coordinate system
t	Time of first exposure
δt	Exposure time delay
p	Orientation index of image set
I	Image intensity field of first exposure
J	Image intensity field of second exposure
ϵ	Higher order terms
$\vec{v}$	Motion of a point feature in space
∇I	Intensity spatial gradient
Ω	Interrogation spatial region
τ_D	User specified threshold
$\vec{w}$	Optical flow interrogation window size
$\vec{d}$	Intensity image displacement
L	Level number of the image pyramid
n_x	Image width
n_y	Image height
M	Number of rows
N	Number of columns

Notation	Description
$\omega(r)$	Angular velocity of vortex
$v_\theta(r)$	Tangential velocity of vortex
Γ	Circulation of vortex
a	Characteristic core radius
r	Radius from vortex core
θ	Angle of vortex rotation
W	Pyramidal optical flow sampling window size
W_v	Velocity inteerogation window size
E_{contour}	Energy function of active contour
E_{int}	Internal energy function of active contour
E_{ext}	External energy function of active contour
F_{int}	Internal force of active contour
F_{ext}	External force of active contour
α	Tension of active contour deformation
β	Rigidity of active contour deformation
P	Potential associated with the external forces
X, Y, Z	Image plane grid system
T	Image time grid
v^{Axial}	Two-dimensional velocity grid in axial orientation
v^{Sagittal}	Two-dimensional velocity grid in sagittal orientation
v^{Coronal}	Two-dimensional velocity grid in coronal orientation
V	Three-dimensional velocity grid system
V_R	Resultant vector magnitude
ω	Vorticity of fluid
ω_{Abs}	Magnitude value of vorticity
ω_{Dir}	Polarised value of vorticity
ω_N	Ratio of ω_{Dir} to ω_{Abs}
Φ	Shear strain rate of fluid
Ψ	Normal strain rate of fluid
μ	Mean of histogram
m	Median of histogram
$\overline{\omega}_\mu$	Mean of vorticity map

Notation	Description
$\overline{\omega}_m$	Median of vorticity map
$\overline{\sigma}_\mu$	Standard deviation from mean of vorticity map
$\overline{\sigma}_m$	Standard deviation from median of vorticity map
$\langle\overline{\omega}_\mu\rangle$	Temporal average of $\overline{\omega}_\mu$ values
$\langle\overline{\omega}_m\rangle$	Temporal average of $\overline{\omega}_m$ values
$\langle\overline{\sigma}_\mu\rangle$	Temporal average of $\overline{\sigma}_\mu$ values
$\langle\overline{\sigma}_m\rangle$	Temporal average of $\overline{\sigma}_m$ values
ρ	Reliability of measurement
γ	Ratio of true vorticity grid variance to a measured one
Λ_s	Vorticity grid of resolution s
Δ	Normalised error function of two vorticity grids
p_s	Pixel spacing
t_s	Trigger time interval
S	Slice thickness
p_k	Percentage of pixels in segmented flow map
A	Percentage area of region
c_j	Data cluster centroid with label j
G_j	Data cluster group based on c_j
D	Discrimination of spatial separation during data clustering
n_t	Time frame index

Abbreviations

A-P	Anterior-Posterior	36
F-H	Foot-Head	36
2C	2-chamber	32
3C	3-chamber	32
4C	4-chamber	32
SA	Short axis	32
LVOT	Left ventricular outflow tract view	32
HLA	Horizontal long axis	32
ROI	Region of interest	6, 89, 288
CW	Clockwise	162, 229
CCW	Counter-clockwise	162, 229
RA	Right atrium	32, 205
LA	Left atrium, Long axis	32, 205
RV	Right ventricle	32
LV	Left ventricle	32
AS	Anterior septum	32
IS	Inferior septum	32
SD	Septal defect	11
ASD	Atrial septal defect	204, 213
ASO	Atrial septal occlusion	204, 205, 211
FOV	Field of view	59, 60
OF	Optical flow	324
CFD	Computational fluid dynamics	8
ECG	Electrocardiogram	6, 31, 56, 148, 161
CT	Computed tomography	xi, 10, 204, 210
PET	Positron emission tomography	xi, 204
SPECT	Single photon emission computed tomography	xi, 204
NMR	Nuclear magnetic resonance	24, 26
MRI	Magnetic resonance imaging	38, 238, 255
CMRI	Cardiac magnetic resonance imaging	xi, 204
PCMRI	Phase contrast magnetic resonance imaging	3

MRIV	Magnetic resonance image velocimetry	5, 13, 15
MRV	Magnetic resonance velocimetry	5
MRA	Magnetic resonance angiography	245
FID	Free induction decay	28
T1W	T_1 weighted	29
T2W	T_2 weighted	29
TE	Echo time	29
TR	Repetition time	29
PDW	Proton density weighted	29
SSFP	Steady state free precession	29, 219, 245, 284
GCFP	Global coherent free precession	245
SNR	Signal-to-noise ratio	6
RF	Radio frequency	24, 26
VENC	Velocity encoding	5, 35, 219
PIV	Particle image velocimetry	5, 15, 243, 323
API	Application Programming Interface	252
MIP	Medical image processing	251
IIL	Intel imaging library	252
IPP	Intel integrated performance primitives	252
DICOM	Digital imaging and communications in medicine	60, 190
True FISP	Fast imaging with steady-state free precession	29, 284
MEDFLOVAN	Medical flow visualisation and analysis	255

List of Figures

List of Tables

Chapter 1

Introduction

MAGNETIC resonance imaging (MRI) was first introduced in the 1970s for visualisation of structure and function of a human body. Since then, development for cardiac imaging that is based on this technology has reached a stage whereby magnetic resonance encoding of blood velocity can provide a clear overview of circulation within a heart. However, long scan time and offline processing of flow information renders the system inappropriate for clinical diagnostics.

We see the solution using a different perspective wherein a magnetic resonance image velocimetry system may not necessarily require time-consuming encoding of velocity information onto an image. Since magnetic resonating blood appears differently depending on its flow behaviour, application of motion tracking on registered magnetic resonance signals from blood in the heart can allow us to develop a unique velocimetry system.

This thesis introduces cardiac flow as an important tool for cardiac diagnostics and establishes the basis for development of an MRI-based velocimetry system. It concentrates on the research, development, and application of decoding velocity data from magnetic resonance images for cardiac flow reconstruction. Utilisation of blood flow information for quantifying heart abnormality is suggested and the significance of cardiac flow research is implicitly linked to these applications. The development of a flow visualisation and quantification system outlined in this thesis has potential impact for future cardiac flow imaging.

1.1 Motivation for Flow Imaging in Cardiac Assessment

Cardiovascular diseases remain a major single cause of mortality in developed nations despite improvements in clinical therapies. For example, based on a 2007 and 2008 statistical update in the United States (Rosamond *et al.* 2007, Rosamond *et al.* 2008), ischaemic heart failure due to the rupture of plaque (Helft *et al.* 2001) and occlusion of coronary arteries (Worthley *et al.* 2002) makes up 52% of cases, and diseases of arteries another 4%. Stroke forms 17% of mortality and heart failures contributes to 6% of deaths. Congenital cardiovascular defects, such as septal abnormalities (Overell *et al.* 2000), form 0.5% of cases. Various screening methods for cardiovascular diseases exist in the medical community (Sanchez and Khalil 2005). The development of modern technology in medical imaging has improved the methods for detection of heart abnormalities in recent decades. Some of the common techniques for detecting cardiac defects utilise the electrocardiogram, echocardiography, and chest radiography. Other diagnostic techniques that are based on medical imaging include cardiac magnetic resonance imaging and computed tomographic scans.

Cardiac examination and management of patients remains the key priority in the treatment of heart defects; however, the need for concise insight into a given defect is desired for diagnosis. For example, cardiac examination can be based on assessment of myocardial viability from magnetic resonance images (MRI) (Lauerma *et al.* 2000, Edelman 2004, Shan *et al.* 2004) or electrocardiograms for assessing abnormal electrical activity within the heart in the treatment of cardiac arrhythmia (Podrid and Kowey 2001, Malik and Camm 2004). A good cardiac diagnostics system will have the ability to provide information about the heart that can be utilised for effective analysis depending on the nature of the diagnosis. The high rate of mortality due to cardiovascular diseases in developed countries gives rise to a growing requirement in the market for diagnostic tools and therapeutic devices dedicated to the treatment of cardiovascular diseases. Appropriate and timely intervention by cardiologists can reduce mortality from heart diseases. Selection of medical treatment and methods of intervention, particularly in borderline cases, is important and appropriate diagnostic tools will augment medical expertise in terms of disease or cardiovascular defect classification.

We propose that it will be of clinical interest to apply flow analysis within the heart in order to examine cardiovascular heart diseases. For example, it is widely appreciated that flow characteristics in the left atrium are important for monitoring heart activity.

Blood shearing in turbulent flow induces platelet activation and contributes to thrombus formation (Smith *et al.* 1972, Stein and Sabbah 1974, Chen *et al.* 2003, Spieker *et al.* 2004, Liu *et al.* 2008). In other cases, blood clots are formed in the setting of blood stagnation and pooling within a non-contractile atrium of a heart with a condition such as atrial fibrillation. Consequently, a high incidence of left atrial thrombus results in higher risk of stroke in such patients (Eggers *et al.* 1999). Fluid-induced stresses also initiates the growth of atherosclerotic lesions (Chandran *et al.* 2006a). Therefore, blood flow that leads to the induction of plate activation can lead to blood clots and stroke, so cardiac patients may require lifelong therapies.

The study of cardiac blood flow can provide qualitative insights into normal and pathological physiology as well as cardiovascular functions (Powell *et al.* 2000, Kilner *et al.* 2000, Mark *et al.* 2007, Ghista and Ng 2007, Ghista 2008). Studies have shown that flow information can be used as an index of cardiac health (Vasan *et al.* 1999, Zile and Brutsaert 2002, Hasegawa *et al.* 2003, Gharib *et al.* 2006). This motivates the need for cardiac flow measurement and visualisation systems in practice. Flow visualisation within the human heart augments the percipience and experience of cardiologists and can assist in the understanding of the genesis and progression of cardiac abnormalities. Quantitative prediction or diagnosis of cardiac failures is of importance for clinical applications. Medical organisations will be able to assess the degree of a cardiac abnormality in the heart so that appropriate medical action can be taken.

Current methodologies, based on nuclear signals and pertaining to phase sensitive flow, enable velocity fields to be encoded within cine magnetic resonance images that are then post-processed (Hartiala *et al.* 1993, Stahlberg *et al.* 1995). The concept of contrasting the phases of imaged nuclear spins, during MRI measurement intervals, gives this system its commonly accepted terminology: phase contrast magnetic resonance imaging (PCMRI). It is essentially a technology that enables flow visualisation in cardiac structures by means of subtraction of flow-sensitised data from reference volumes during the processing stage (Gatehouse *et al.* 2005). However, because of inherent limitations, such as undesirable measurement duration and sub-optimal temporal resolution, time-resolved three-dimensional data acquisition has been mainly limited to the study of the heart in a research environment and not so much for clinical applications. Other complications exist at the present time; for example, respiration artefacts should be minimised as much as possible, while achieving a tolerable total scan time for patients (Mark *et al.* 2007).

Although phase contrast MRI scanning can perform flow visualisation in the human heart, data on flow abnormalities obtained by it becomes impractical for use in clinical evaluation due to long scanning and off-line processing. Therefore, there is a need for a dedicated protocol with quicker scan and low processing time. This means shortening scan time and resources during MR imaging, which may come at the expense of more post-processing for the assessment of cardiac blood flow. There is a need to balance the efficiency of flow imaging without compromising its accuracy to an unrealistic extent. Such a technology development may then facilitate the prognosis or diagnosis of cardiac abnormalities.

Blood flow visualisation can reveal vital information in the cardiac chambers and arteries. For example, streamline tracing of blood measured using phase contrast MRI can give users an indication of flow patterns within the heart. Interesting phenomena, such as vortices in the heart's ventricular chambers and aorta, have been studied previously (Kilner 1998, Brandt *et al.* 2001, Fyrenius *et al.* 2001, Uterhinninghofen *et al.* 2006). There are studies to understand the flow-related mechanisms of heart valve experimentally based on mock-up circulatory flow test rig (Bellhouse and Bellhouse 1969, Shi 2001, Shi *et al.* 2003) and non-invasive phase contrast magnetic resonance imaging (Dall'Armellina *et al.* 2007). The development of flow and velocity profile through tricuspid aortic valve at the root of the aorta and also into the ascending aorta has been investigated based on numerical or experimental modelling (Yearwood and Chandran 1982, Chandran *et al.* 1983, Chandran 1993) or using velocity-encoded MRI (Varaprasathan *et al.* 2002, Morbiducci *et al.* 2009). The quantification of flow characteristics within the heart and arteries provides vital information to cardiologists, who are interested in a range of problems from the hemodynamics of blood to biological phenomena in the heart. The scales and coherence of the vortex structures can be examined, and their existence can ultimately be linked to the operation of a number of cardiac structures influencing flow in the heart.

Cardiac flow analysis systems have the potential to be used as diagnostic devices for the assessment of heart disease and practical tools for physiological analysis. The *in vivo* acquisition of hemodynamical data has been investigated previously with accurate presentation of its vortical blood motion in cardiac chambers (Kilner *et al.* 2000). Variation in flow vorticity field is suggested to be a sensitive indicator of heart abnormalities, and verification studies have been carried out (Kerwin *et al.* 2004). There are

potential applications for identifying risks after heart valve implant as well as determining the degree of atrial and ventricular septal defects using cardiac flow analysis. Our approach is to measure flow and quantify its characteristics using outputs from steady-state free precession MR imaging protocol (Markl and Pelc 2004, Li *et al.* 2004), making it attractive to future clinical practice.

1.2 Review of Current Technologies

We examine some of the well-established velocimetry systems that exist to generate accurate time-resolved vector fields of up to three spatial dimensions. It is interesting to highlight that such flow tracking can be classified as optical-, magnetic resonance- and ultrasonic- image velocimetry. More importantly, we are interested to look at in-plane flow field generation using the different types of imaging systems. Particle image velocimetry (PIV) can serve as a validation tool for verifying magnetic resonance imaging velocimetry (MRIV). For example, two-dimensional phase contrast flow measurement (Markl *et al.* 2003) has been verified against experimental methods using PIV (Elkins *et al.* 2004) previously. On the other hand, phase contrast MRI of cardiac flow has been compared against that of ultrasonic imaging in various studies (Jung *et al.* 2004, Seitz *et al.* 2006).

Of the three types of velocimetry systems, only the optical-based one is unable to be deployed for cardiac flow imaging. Incompatibility of the tissue and blood medium creates a barrier in optical signal transmission even though the wavelength of laser transmission can be resolved to nano-magnitudes for registering high-resolution motion. In addition, the lack of optical-compatible feature trackers in blood and the necessity for introducing biologically incompatible track particles into the flow render the velocimetry system unsafe for cardiac flow imaging in humans. Therefore, we only review magnetic resonance- and ultrasonic- imaging systems in this section.[1]

1.2.1 Velocity-Encoded Magnetic Resonance Imaging

Velocity-encoded (VENC) phase contrast MRI allows three-dimensional MR velocity mapping based on the intrinsic sensitivity of MRI to flow, and enables the acquisition of spatially registered functional information simultaneously with morphological

[1] A more detailed coverage of optical image velocimetry using PIV can be found in Appendix G.

information (Mark *et al.* 2007). Three-dimensional MRI based velocity mapping operates by registering three separate flow-sensitive volumes in the x, y and z orientations of the scan. The flow velocities may be computed by determining the shift of phase pertaining to the collection of imaged blood proton spins and reconstructing the flow vectors in advanced visualisation packages. This concept has varying terminologies in literature, the most common being phase contrast MRI (Morbiducci *et al.* 2009), while some studies label it as phase-velocity MRI (Powell *et al.* 2000). In general, such MRI based techniques form a class of approach known as magnetic resonance velocimetry (MRV), sometimes also called magnetic resonance image velocimetry (MRIV). These techniques have been very commonly used for producing visualisation and investigation of flows even within non-organic structures (Elkins *et al.* 2004, Raguin *et al.* 2005).

The superiority of magnetic resonance imaging over other imaging modalities is the capability of generating up to three-dimensional velocity profiles that can reflect the dynamics of blood flow more accurately and with quantifiable details. Apart from such localised measurements that can provide interactive visualisation in cardiovascular flow (Yamashita *et al.* 2007), phase contrast MRI has also been utilised in global flow measurements such as determination of flow volumes in arterial structures, and in particular, blood ejection volumes in the ascending aorta (Maier *et al.* 1989, Powell *et al.* 2000, Lotz *et al.* 2002) as well as arterial wall shear stress (Oyre *et al.* 1997, Oyre *et al.* 1998, Wahle *et al.* 2006). It has been widely documented that phase contrast MRI is an established flow-imaging scheme for cardiovascular examination of human subjects and compares well with ultrasound technology (Maier *et al.* 1989).

Further development of phase contrast MRI to produce multi-slice cine images involves an electrocardiogram (ECG) synchronised time-resolved framework to allow assessment of blood-flow characteristics with high spatial and temporal resolution of a cardiovascular region of interest (ROI) (Herold *et al.* 2006, Yamashita *et al.* 2007). Sometimes there may be poor quality image registration due to poor respiratory control during scanning. Usually a ghosting artefact (Mark *et al.* 2007, Wigstrom *et al.* 1996, Bogren *et al.* 2004) appears on the images. Other issues, such as limited signal-to-noise ratio (SNR) control (Markl *et al.* 2004), affect the imaging sensitivity of the scanning modality. Nevertheless, recent development of navigator-gated time-resolved cine phase contrast MRI can control image distortion and ghosting effects due to the respiration of patients during image acquisition (Mark *et al.* 2007).

1.2.2 Colour Doppler Sonography

Doppler ultrasound, as its name implies, is based on Doppler shift caused by blood scatter movement and is a widely accepted technique for visualisation of blood flow patterns. Ultrasound technology can be used to determine blood flow velocity *in vivo* (Mudry *et al.* 2003). This class of approach is known as Doppler echocardiography. Medical ultrasound works by generating high frequency electrical pulses and using piezoelectric elements of a transducer to convert them into mechanical vibrations. The emission of ultra-frequency sound and detection of sound waves from the resulting echoes is performed by transducers. After conversion into electrical signals, processing is carried out to decipher blood flow velocities (Wolbarst 1999). The Doppler ultrasound output is usually represented as a two-dimensional image.

For extracting accurate flow information using ultrasound, especially when measuring blood velocities close to the wall, the time-dependent reflections are controlled by suppressing the excitations of high amplitude and low frequency rebounds (Brands *et al.* 1995). Analysis of the flow field obtained by ultrasound methods enables useful results in cardiac examination (Hatle and Angelsen 1982). Ultrasound technology can be used to diagnose cardiovascular diseases such as atrial septal defects (Webb and Gatzoulis 2006) and ambiguous calcific left main stenoses (Teo *et al.* 2004). Assessment of velocity waveforms of cardiac flow can be achieved using Doppler echocardiography (Mielke and Benda 2002, Chaoui *et al.* 2002, Freedom *et al.* 2003).

Real-time blood motion imaging using colour sonograms can be realised (Harrison *et al.* 2007). The two-dimensional colour-Doppler flow imaging can provide a spatial visualisation of cardiac flow (Vandenberg *et al.* 1988). For this medical imaging modality, the speckle pattern from the blood flow signal is preserved, enhanced, and visualised (Loevstakken *et al.* 2004, Kasai *et al.* 1985). In this technique, a high frame rate is necessary for acquiring speckle pattern motion due to the rapid decorrelation of the speckle pattern from blood flow. In addition, good spatial resolution of the speckle pattern is essential.

A significant limitation of ultrasound imaging is that the Doppler shift is only sensitive to the velocity component in the orientation of the ultrasonic beam. However, clinical examination can be achieved with low cost and produces real-time flow visualisation. In addition, ultrasound systems can be highly portable (Tang *et al.* 2007). This makes Doppler sonography more clinically attractive to use than magnetic resonance imaging (MRI). Despite these system advantages, a flow projection onto a plane for an accurate

slice assessment of the cardiac flow is difficult to perform. Based on this aspect, it is inferior to velocity-coded MRI which can reconstruct accurate temporal flow grids of up to three spatial dimensions (Fyrenius *et al.* 2001).

1.2.3 Other Cardiovascular Flow Measurement Techniques

It may be meaningful to highlight here, briefly, a few systems that are more appropriate for cardiovascular components like the arterial flow rather than chamber flow within the human heart.

Velocity mapping can be achieved using fluorescent flow velocity tracers. We examine the use of optical-based technology on arterioles (approximately 0.5 μm in diameter). For this technique, nano-particles usually in the form of fluorescently labelled blood platelets can be used as motion trackers (Tangelder *et al.* 1986). The displacement of the track particles during a measurement interval gives the velocity of the blood containing the illuminated tracer. Triggering sequences of illumination by referencing ECG and using a preset delay, velocity profiles can be determined in the systolic and diastolic phases. Computerised correlation of concomitant images of the tracer can then be used to determine the velocity profiles of the arterial flow.

Other methods include the Fick principle (Fritts and Cournand 1958, Rasmussen and Linzell 1963, Fishman 2000), indicator dilution (Eich *et al.* 1959, Clough *et al.* 2000, Geogiev *et al.* 2006), and radionuclide scintigraphy (Klausner *et al.* 1977, Thomas *et al.* 2003). However, these techniques are limited by sub-optimal accuracy, insufficient anatomical resolution, and surgical invasiveness. Modern medical imaging modalities, such as phase contrast magnetic resonance imaging, have been used to compare with the performance of these methods (Powell *et al.* 2000).

1.3 Cardiac Flow Visualisation Based on Computer Simulation

It may be worthwhile to examine flow quantification using simulated data. Although numerically derived data may not be reliable for clinical utility, the purpose of this section is to help us gain an understating of the quantification and post-processing methods involved to analyse flow, rather than the flow simulation techniques.

Computational Fluid Dynamics (CFD) is commonly used for modelling blood flow in cardiac mechanical devices (Ng and Zhou 1999, Ng and Zhou 2000, Arvand *et al.* 2004, Xia *et al.* 2005, Chandran *et al.* 2006b, Govindarajan *et al.* 2009). It can be used for describing flow dynamics in the heart during cardiac functions (Lemmon and Yoganathan 2000, Watanabe *et al.* 2004, Xiong *et al.* 2008, Schenkel *et al.* 2009) or under specific circumstances when a biomechanical component has been introduced into the heart of a cardiac patient (Kiris *et al.* 1997, Cheng *et al.* 2006). However, there is inherent error when assessing fluid dynamics with the aid of computer models. The advantage of VENC MRI over CFD lies in its ability to measure the actual flow. In the absence of flow measurement capabilities, there is a push to develop CFD to examine blood flow patterns in cardiac structures. In most CFD and MRI combined flow analyses, phase contrast MRI is still required to obtain velocities for boundary conditions (Zhao *et al.* 2003). Most flow outputs based on CFD platform uses vector plot, streamline tracing or pressure gradients mapping to qualitatively analyse flow (Anderson 1995, Singh and Li 2007, Xiong *et al.* 2008). In addition, wall shear stresses (Cheng *et al.* 2004, Ikbala *et al.* 2008, Goubergrits *et al.* 2008) and oscillatory shear index (Xiong and Chong 2007, Xiong and Chong 2008) for the arterial flow can also be used during flow analysis.

Cardiac wall motion reconstruction from image scans can be in conjunction with CFD to produce flow visualisation. Retrieval of myocardial information based on imaging modalities, such as ultrasound (Lange *et al.* 1996, Galderisi *et al.* 2007), CT (Weng *et al.* 1997, Eusemanna *et al.* 2000), cardiac magnetic resonance imaging (Winter *et al.* 2008), and tagged MRI (Moser *et al.* 2001), has been performed. Efforts have been made to use ultrasound data for motion analysis, which include the intensity-based optical flow method (Behar *et al.* 2004). However, implementation of myocardial wall reconstruction based on ultrasound and echocardiography is limited by local area distortion and poor resolution. Myocardial wall tracking performed based on tagged MRI images applies onto the arterial or cardiac walls (Jasjit 2000, Sühling *et al.* 2003, Cohen 1991) and not on the blood flow itself. Spatial and time-dimensional modelling of heart can be achieved via dynamic spatial reconstruction based on cine MRI (Zhukov *et al.* 2002, Schenkel *et al.* 2009) or Electron Beam CT (Lin and Robb 2000). Invasive techniques that involve localisation of an electrode (catheter) into the human heart collect data points from within the heart chamber to produce three-dimensional surface reconstruction (Kuklik *et al.* 2004, John *et al.* 2008). Other methods for invasive acquisition of the cardiac chamber geometry such as sonomicrometry are able to perform precise,

high-resolution recording of distances between ultrasonic crystals, which are strategically positioned at various positions of the heart, during each phase of the cardiac cycle (Goetz *et al.* 2005).

A combined CFD and medical imaging methodology can be developed to simulate blood flow in heart chambers (Saber *et al.* 2001, Merrifield *et al.* 2004). The framework employs computed tomographic (CT) scans of a human heart to obtain geometric data, which are then used for the CFD simulations, with specific application in the present study of flow through heart structures. Computational modelling of the ventricle can be accomplished using time-resolved anatomical slices of the ventricular geometry and imposition of inflow/outflow conditions at orifices notionally representing the mitral and aortic valves. The predicted flow structure evolution and physiologically relevant flow characteristics may be examined and compared with existing information. Three-dimensional reconstruction methodology based on CT scans allows us to achieve higher physiological accuracy of modelling. The measurement tool effectively extracts wall profile of the cardiac structures *in vivo*. Then we can duplicate the flow characteristics on the computational fluid dynamics simulation platform to observe the blood flow during cardiac operation.

Comparison of CFD modelling and phase contrast MRI in studies of arterial flow has demonstrated good qualitative and quantitative agreements under some limitations (Long *et al.* 2002, Zhao *et al.* 2003). Although CFD combined with MRI has been used for flow mapping extensively, it is more of a computational tool rather than a measurement system in this framework.

The study of flow in the heart and arteries based on CFD is of research interest for hemodynamics studies in cardiac structures when experimental measurement data is not readily available. However, even though numerical simulation based on geometrical and flow-related boundary conditions can predict the fluid flow field to a certain degree of accuracy, the expensive computational resource and time used in processing deems it inappropriate for real-time flow examination. The flow visualisation and quantification techniques in CDF can be applied on our experimental flow measurements in this thesis. We have utilised the vector and streamline plots, and vorticity field generation for our qualitative flow analyses.

1.4 Applications and Motivation of This Study

1.4.1 Assessment of Myocardial Abnormalities

A septal defect (SD) may be detected in the adult by physical examination, electrocardiogram, chest radiograph, echocardiography, or MRI scans (Webb and Gatzoulis 2006). Functional medical imaging is able to provide an alternative method for measurement and quantification of the blood flow rotation (defined as vorticity) in the heart of a patient diagnosed with SD. The usual surgical treatment would be septal occlusion (Duncan *et al.* 2008). Rate of blood rotation is related to pressure within the heart chamber, and can be used to assess the degree of septal defect before and after septal occluder insertion. Such a method is particularly useful for evaluating the risk inflicted on patients diagnosed with such cardiovascular diseases before and after surgical intervention, and therefore has high clinical benefit to medical doctors in parallel to examining the physical septal defect.

1.4.2 Assessment of Bio-Prosthetic Heart Valve Implants

The shortcomings in existing modelling and testing of bio-prosthetic heart valves is highlighted by the recently reported cases of post-market failure consisting of thromboembolism, in leaflet escape due to strut fracture (Gerosa *et al.* 2004). Strict regulatory *in vitro* evaluation must be performed on prosthetic heart valves, prior to passing the clinical standards before release to the market. While the structural integrity of the prosthetic heart valve is important, its mechanical design is also critical. For example, an optimal heart valve design can satisfy the criteria of a smooth washout and minimal leaflet stress (Ghista *et al.* 1978). Computational or experimental simulation may be used to examine the heart valves structurally in a non-invasive manner, where parameters such as wall shear stress (Engelmayr *et al.* 2008), as well as volumetric deformation and local tissue strains (Kim *et al.* 2008, Kortsmit *et al.* 2009) can be used for analysis. We propose that MRI-based flow imaging technique can be introduced for evaluating blood flow from MR images of natural heart valves in a human heart. In the case of a mechanically simulated environment (Paulis *et al.* 2005), we note that this is possible provided that the testing rig is compatible with magnetic resonance imaging. The global estimation of flow velocity vector fields over the whole image provides useful information on flow phenomena within the pathology that is vital for understanding the operation of the valve leaflets (Kini *et al.* 2000). This application offers potential

for non-invasive flow visualisation of *in vivo* natural and prosthetic heart valves in a beating heart that changes its spatial position with time.

1.4.3 Examination of Cardiac Functionalities

Using measured data, we can develop a procedure for evaluating arterial flow; in particular, the quantification of the (1) variation of blood velocity with respect to time through the artery, (2) cross-sectional blood flow profile across the artery, and (3) rotational characteristics (vorticity) of flow through the artery. It is of interest to examine blood flow spiralling along the aorta of the heart (Gatehouse *et al.* 2005, Frydrychowicza *et al.* 2006), in proximal femoral arteries (Frydrychowicz *et al.* 2007) or in intracranial arteries (Yamashita *et al.* 2007). It has been shown that blood has unique flow characteristics that determine the structure of the plaque growth in atherosclerotic arteries (Worthley *et al.* 2002, Wong *et al.* 2006). Flow information can be used for clinical diagnosis of atherosclerosis. The use of MRI scanning abrogates the limitations of using other techniques to assess blood flow as the opacity of the arteries does not affect results.

1.4.4 Assessment of Cardiac Behaviour during Heart Exercise

The analysis of healthy hearts to define typical blood flow both qualitatively and quantitatively is an important endeavour. Analyses of cardiac output can then give information about abnormalities in heart function in patient populations (Hambrecht *et al.* 1995). These analyses can be used to give a further indication of functional changes that occur with regular exercise from trainee to elite athlete. In addition, elite athletes from various sporting fields can be compared. For example comparing recovery rates after a maximal effort may be different between strength- and endurance-trained athletes (Otsuki *et al.* 2007), such as sprinters and weight lifters versus marathon runners and cyclists.

In terms of assessment of cardiac behavioural change and activity during exercise and resting times, as well as exercises based on different sports specialisation, an electrocardiogram recording and a cardiointervalogram evaluation can monitor cardiac activity during physical exercises (Zobkov 2002, Curfman and Hillis 2003). In most studies, heart rate, stroke volume and cardiac output are typical indicators for cardiac responses during recovery from exercise (Takahashi and Miyamoto 1998, Vanyushin *et al.*

2000, Morise 2004). A robust method, rather than simple heart rate and blood pressure, for evaluating heart function may be a useful tool for assessment of athletes during competition and during the recovery phase. We propose that the rate of blood swirl within heart chambers of athletes and a set of controls may be quantified to relate the degree of rotational flow to heart rate. In addition, the variation in heart beat rate influencing blood flow patterns in the heart may be characterised.

1.5 Outline of Approach

There are important and challenging issues in developing a system for diagnosis of cardiac defects based on flow information that is measured. The multidisciplinary approach adopted here highlights a unique combination of machine vision and concepts from particle image velocimetry, image segmentation, and computer visualisation. Since optical flow algorithms are implemented in our approach, we term this motion-based flow estimation method as a *fluid motion estimation scheme* (Cuzol *et al.* 2007); and because MRI is used, we classify the technique as a class of magnetic resonance image velocimetry (MRIV).

The application of machine vision algorithms to process medical images offers the potential for velocity measurement to become a commonly accessible and technically viable technology. The determination of flow velocities may be based on the intensity shifts of the pixels using the optical flow algorithm. The assessment of flow is accurate provided that a good time resolution is present. However, the number of phases per cardiac cycle will be dependent on the capabilities and specifications of the particular medical imaging device used.

Our proposed technique is specific for characterising blood flow movement in cardiac structures. The global estimation of a parametric motion field over the whole image provides useful information on non-laminar flow quantification within various pathologies. The cardio dynamics information that is based on flow analysis and visualisation of blood offers potential for the detection and quantification of heart valve failure, septal defects, as well as myocardial malfunctioning.

We can also analyse flow by constructing MRI slices from the axial, sagittal and coronal scans into a three-dimensional stack grid. For the examination of arteries, multiple axial planes angled at different sectioning along the arterial axis are imaged and fused together with coronal planes along the same longitudinal axis (Wong *et al.* 2006). The

construction of the planes results in a three-dimensional scaffold from which the arterial or cardiac chamber may be segmented and meshed into a three-dimensional structural surface. The flow fields within a surface enclosure or vessel may be simulated by computational fluid dynamics of blood. Therefore, a three-dimensional cardiac structure reconstructed from the two-dimensional MRI slices may provide the platform on which the fluid mechanics of blood may be verified numerically.

The optical flow technique (Horn and Schunck 1981, Barron *et al.* 1994, Bouguet 2000) can be extended to perform motion prediction based on MR signals and is useful for evaluating blood flow properties in heart chambers. Therefore, optical flow evaluation of MR images is able to provide flow field measurement. The global estimation of velocity vector fields across the whole image provides useful information on vorticity, which defines the vortices within regions of a relevant pathology. This type of approach has been used in imaging and computer vision previously for motion analysis of rigid structures, but we modify and apply it to compute fluid motion based on temporal signals from MR images, and hence have pioneered the method of MRI based fluid motion estimation (Wong *et al.* 2009e). Alternatively, another name for this developed framework is *MR fluid motion tracking*[2].

Although the particle image velocimetry system utilises the cross-correlation of particle windows in the optically captured image to compute the localised direction of flow, the motion estimation scheme can also be used for such optical-based experimental flow studies (Ruhnau *et al.* 2005, Corpetti *et al.* 2006, Cuzol *et al.* 2007). Parametric flow fields generated by the optical flow algorithms used in these studies compared favourably with results obtained from the well-established computational component used in particle image velocimetry. In contrast to predicting fluid motion based on illuminated nano-track particles in optically compatible vessels, the *MR fluid motion tracking* approach tracks MR signals produced by asynchronously aligned nuclear spins within opaque structures and provides motion fields of up to one vector per pixel.

The velocity-encoding MRI approach extracts MR signals produced by nuclear spins within a fluid, determines the phase shift of the transverse magnetisation during movement of the spin ensemble from the stationary spins, and encodes this information as

[2]We apply the term *MR fluid* particularly to a bio-fluid medium, such as blood, which experiences magnetic resonance (MR). Motion tracking refers to estimation of this fluid movement. Application of motion tracking on registered MR signals from blood in the heart allows us to develop this unique velocimetry system. The technical details of *MR fluid motion tracking* can be referenced in Chapter 3 and the application of this flow imaging technique can be found in Chapter 8 of this thesis.

pixel intensity onto an image. Since the phase shift is directly proportional to the velocity of the fluid, deciphering velocity components from the intensity images pertaining to the in-plane horizontal and vertical orientations, and reconstructing them, provides motion fields of up to one vector per pixel.

For MRI-based techniques, we are able to image through the heart, whereas PIV is optical-based, and therefore flow imaging within opaque cardiac structures is impossible. Particle image velocimetry can serve as a validation tool in verifying magnetic resonance imaging velocimetry (MRIV). For example, two-dimensional phase contrast flow measurement (Markl *et al.* 2003) has been verified against experimental methods using PIV (Elkins *et al.* 2004) previously. We validate the fluid motion estimation algorithm against analytical results based on a Lamb-Oseen vortex[3] (Saffman 1992, Meunier *et al.* 2005, Cariteau and Flór 2006) as well as performing system validation of the framework using phase contrast imaging in the subsequent chapters of this thesis.

The implementation of hierarchical motion estimation (Bergen *et al.* 1992) on the magnetic resonance images of heart can generate a two-dimensional velocity field of its chamber flow. The global estimation of velocity vector fields within a region of interest provides non-laminar flow quantification within the heart chamber. Such estimation of blood patterns can be used to give an indication of cardiac flow abnormality. The technique may also be introduced for evaluating blood flow from magnetic resonance images of arterial flow channels to provide information on myocardial ischemia and infarction. The study of vorticity, shear and normal strain distributions, computed from the velocity field, can be used to provide insight into the behaviour of the flow. The global estimation of vorticity fields provides useful data such as formation and evolution of vortices within heart chambers. One feature of our developed system is the computation and presentation of these properties temporally in two dimensions. The operations can also be performed for multiple image slices simultaneously.

Reconstruction of two-dimensional velocity images based on the axial, sagittal, and coronal orientations can be performed. This allows construction of a three-dimensional velocity field plot (Wong *et al.* 2009b) when the orthogonal velocity component data to the in-plane velocity field is not available. The estimated velocity field is used to

[3]The Lamb-Oseen vortex is a model of a line vortex such that its angular velocities decays from its core to the radius limited by a computational domain due to fluid viscosity. This vortex is named after Horace Lamb (University of Adelaide) and Carl Wilhelm Oseen (Uppsala University) who developed it. The Lamb-Oseen vortex is used in this thesis to provide a theoretical model for computational testing of our proposed tracking framework.

represent the movement of blood, within a volume of interest, in real-time. Blood intensity fields that are obtained from MRI scan sequences can be applied to the flow analysis. Our system works using intensity-based images, and therefore it is more convenient for clinical use as compared to three-dimensional phase contrast imaging.

The proposed research will carry out a comprehensive investigation and can involve further development of the following new methodologies/technologies:

1. Three-dimensional geometrical reconstructions of MRI slice sets from three or more planes at different orientations. This can create a surface or volume reconstruction of three-dimensional cardiac pathologies from two-dimensional imaging potentially.

2. Construction of a volumetric flow image grid based on scaffolds of planar flow images. This can be used to predict three-dimensional flow patterns in cardiac pathology. Streamline tracing can be incorporated to enhance flow visualisation.

3. Improved segmentation techniques for three-dimensional cardiac structures based on combined active contouring and optical flow analysis using volumetric mesh contours.

The fundamental principles of implementation and key development features are laid out in Chapter 5 and Appendix A, which can be used to build upon the current version of two-dimensional flow field mapping and visualisation into a three-dimensional one.

At this stage, the developed system in our study meets a currently unmet requirement of the medical imaging service industry by providing a non-invasive and fast method for analysing blood flow that can be used for a number of purposes such as an investigative or prognostic tool for patients at risk of abnormalities of the heart. It can also measure blood flow through artificial cardiac devices *in vivo* at a magnetic strength of not more than 3 Tesla (Martin and Sandler 2007).

1.6 Overview of Research Strategy and Implementation

Each stage of research is compiled into a chapter in this thesis and therefore, each chapter that is presented in this study represents a key research component of the project. A full understanding of the developmental stages of this project can be carried out

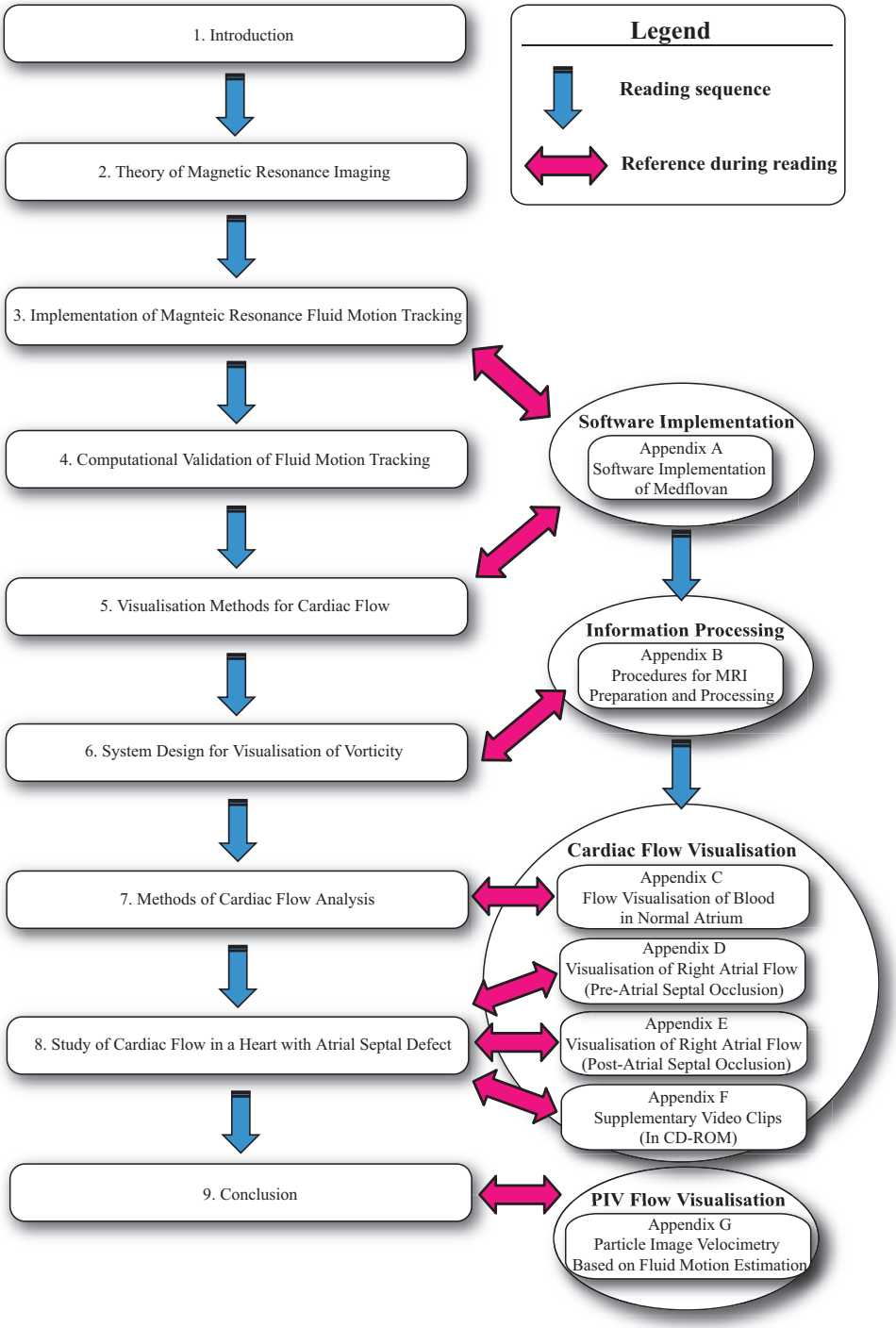

Figure 1.1. Overview of the thesis structure. The thesis presents the entire study comprising of concept generation, implementation, validation, and application of our developed system. The major technical contributions of the thesis may be divided into MRI velocimetry reconstruction and cardiac flow analysis. Motion estimation algorithms and velocity reconstruction schemes lay the groundwork for flow visualisation and analysis. The work is extended to vorticity visualisation applied to the blood pool within the human heart chamber, and used for cardiac investigation of patients with heart defects. Finally, a conclusion summarises the entire research and development work.

by referencing the chapters. All of the chapters mentioned in this thesis, as shown in the flow chart in Figure 1.1, have been designed to sufficiently cover the concepts for development of MRI velocimetry.

At the very preliminary stage, an overview of project is described in detail to allow an understanding of the problem definition and lay the blue prints for the development of a solution. This also gives a brief insight into the limitations of existing systems specialised in imaging blood flow in the heart. We also outline some concepts related to the development of a solution that is unique and applicable to current work in the industry. In the first stage of development, we examine the fundamentals of nuclear magnetic resonance, as the MRI machine is the driving technology for the development of *MR fluid motion tracking* system in our project.

Nuclear characteristics of materials under magnetic resonance are explained in Chapter 2. The multi-resolution motion tracking system that is described with mathematical details of optical flow algorithms in Chapter 3, forms another important building block that we will harness for our system. It is also important to validate this primary system using specially designed methods of verification that we outline in Chapter 4. Parallel to these important components, we also examine segmentation of cardiac chambers to extract a region of interest on which MR fluid motion estimation of blood flow will be based. This semi-automatic segmentation system is mentioned in Chapter 5.

The system integration of *MR fluid motion tracking* and cardiac chamber segmentation, and coupling vorticity estimation algorithm, forms a visualisation framework for rotational flow in the human heart. Chapter 6 presents a flow analysis methodology that is devised to characterise flow behaviour. We give a summary of the technology development and its application in Chapter 8 using experimentation of MR fluid motion tacking on the right atria of patients diagnosed with cardiac abnormalities such as ASD. Modelling and visualising myocardial structure as well as cardiac flow fields is implemented using a technique whose operating features are outlined in Chapter 3 to 7. The research plan involves a systematic development of our software named Medflovan, followed by execution of data retrieval and processing, right down to flow visualisation and analysis. More details of this medical image processing tool are mentioned in Appendix A. Systematic process implementation of the investigation is detailed in Appendix B. The concise set of flow maps pertaining to the human atria can be referenced using Appendices C, D and E. Some sections in the thesis are better supported with interactive documentation and user guide by referencing video clips listed

in Appendix F. The parametric flow mapping based on particle images can be achieved by fluid motion estimation and velocity fields generated using the hierarchical optical flow technique[4] that is outlined in Chapter 3 are presented.

Finally, a conclusion on the advantages of this study and a summary of our original contributions to the field is made. We also examine possible alternative solutions to refining the tracking system and future developments of the project. As can be observed, the top-down implementation of system for cardiac vorticity investigation using strategically designed stages of research enables not only a clear overview of the design steps, but also allows the reader to have a more detailed understanding of the problems associated with existing technology in achieving the proposed objectives.

1.7 Statement of Original Contributions

This thesis suggests several significant contributions to the development of cardiac flow analysis. We shall examine how it may serve to extend technologies and contribute to useful knowledge in this area.

1.7.1 Original Contributions to Medical Imaging

Our exploitation of intensity-based mapping from magnetic resonance imaging data to perform cardiac flow tracking is novel, as there is currently no way to computationally predict flow velocities from these images without encoding of velocity information. The technology lies in the use of commonly used equipment, the MRI machine based on SSFP MR imaging technique (Plein *et al.* 2001, Merrifield *et al.* 2001), to generate a series of images in spatial as well as temporal dimensions, and post-processing them to measure MR fluid flow in real time. Certainly, individual components of the system (e.g. use of the optical flow algorithm on magnetic resonance images) are not new, but the unique combination of these techniques, and the adaptation of multi-resolution motion tracking used in our study is the key novelty (Chapter 3).

Other alternative solutions lie in the use of phase contrast MR imaging, coupled with well-established flow field visualisation methods to analyse fluid flow (Chapters 5 and

[4]The optical flow technique that utilises the pyramidal implementation of various image resolution is a class of computational approach known as the multi-resolution motion estimation. Other variations of the multi-scale motion tracking terminology can be constructed by attaching descriptions, such as 'hierarchical', 'variational', 'coarse to over-fine' and 'pyramidal', to the term 'optical flow'.

7). However, velocity-encoding based on phase shifts in nuclear signals usually take longer scan duration than typical MR imaging. As there are few investigations to computationally measure blood flow using steady-state free precession (SSFP) magnetic resonance images, the system arising from our study provides a solution to a currently unmet need. Such a strategy can transfer most of the processing time, by reducing the scan sequence, to the flow prediction and visualisation in post-processing stages.

Our suggested means of examining the heart is to utilise normal and standard MRI protocol, however; extracting information from image scans offline with focus on localised flow characterisation. We estimate blood motion within the endocardium using computational techniques and post-process the velocity data to obtain flow derivatives such as vorticity for characterising cardiac circulation abnormality (Chapters 8). We also develop clinical scan procedures and offline processing stages using a flow diagram (Appendix B) to guide the effective study of atrial septal defect patients. Based on our original approach, we are able to characterise vortices in heart chambers and establish a relationship between atrial vorticity and a septal defect. The developed system has the potential to be used as a prognostic and investigative tool for assessment of cardiac abnormalities, and to be conducted in parallel to examining steady-state free precession magnetic resonance images. (Chapter 9). Of course, this framework can be translated for studying other cardiac abnormality as well but it is beyond the scope of this work to consider further future applications.

1.7.2 Contribution to Medical Science and Knowledge

In our study, we observe that a large vortex exists in each of the right and left atria of heart using both phase contrast magnetic resonance imaging and *MR fluid motion tracking* techniques. Patients that are diagnosed with atrial septal defect (ASD) have a right atrium that is enlarged due to a left-to-right shunt of blood through the defective septum. In a case study, we choose to base our analysis on the right atrium where a larger region of MR signal features can be measured (Chapter 8). From our flow results, we are able to document the presence of vortices that vary in strength depending on the cardiac condition of the patient. Our study demonstrates that after atrial septal occlusion, the speed of blood rotation increases.

The implementation of flow imaging within the right atrium of a patient diagnosed with atrial septal defect demonstrates a good indication of difference in the vortices

pre- and post-surgical intervention. A hypothesis for slower blood flow rotation, in the absence of atrial septal occlusion (ASO), is the reduction in the velocity of circulation due to the larger chamber that is the result of left-to-right shunting of blood. Once the septal occluder is inserted at the site of the defect, the chamber is restored to a more normal size and a higher vorticity of blood flow occurs. At the moment, there is a lack of study on the concise investigation of abnormal flow behaviour due to atrial septal defects and an application to perform flow diagnosis on the atrium of a patient with such a problem. As such, our study is original and its contribution serves to advance the development of future cardiac diagnostic tools. Our study opens up the possibility of applying the same investigation techniques on other types of cardiac abnormalities, which can be a variant of the developed frame of methods that we propose in this thesis.

Chapter 2

Theory of Magnetic Resonance Imaging

THIS chapter reviews the fundamental theory underlying nuclear magnetic resonance; from the examination of hydrogen proton spins, through to the development of magnetic resonance imaging machines that are able to provide two-dimensional image slices of the human body at any angle and orientation.

Recent decades have seen a plethora of significant advances in magnetic resonance imaging with relevant applications for medical imaging of the heart. However, there has been a lack of proper qualitative explanation of some observed phenomena such as gray-scale intensity variation of the imaged cardiac blood. Therefore, this chapter sets the scene for the further development of MR fluid motion estimation by providing the theoretical explanation for signals of contrasting intensity due to asynchronous proton spins in dynamic fluid and how they arise.

Various magnetic resonance imaging protocols, concepts and terminologies are covered in appropriately organised sections to ease misconceptions or misinterpretations of the terms used in subsequent chapters of this thesis.

2.1 Introduction

We examine the mechanics of magnetic resonance imaging abbreviated as MRI and document the definitions of terminologies and underlying related theories. The motivation behind this chapter is to enable understanding of outputs delivered by this imaging modality. Cardiac imaging and flow tracking using motion estimation is the key focus of the research undertaken, and the critical issue would be to understand the type and nature of signal features to track. Therefore, the theoretical investigation ranges from explaining the effects of magnetic field on hydrogen nuclei to the alignment of spins on registration of nuclear signals of a living body during MRI scanning (Fujio *et al.* 1995a, Fujio *et al.* 1995b).

2.2 Theory of Nuclear Magnetic Resonance Imaging

We examine nuclear magnetic resonance (NMR) imaging at a basic level to aid clarity of the quantum mechanical concepts. An organic structure positioned within the centre of an external magnetic field becomes itself partially magnetised with a magnitude of comparatively lower order. The assemblage of hydrogen nuclei (protons) in the water molecules within the body can be perturbed with radio frequency radiation (Mudry *et al.* 2003). The nuclear spins then realign with the magnetic field and emit radio frequency (RF) waves during this longitudinal relaxation period (Phillips 1984). The duration of the nuclei realignment and emission of RF signals can then be represented by MR images that we use for examination. Since the emission rate of RF waves is dependent on the type of material that contains the nuclei, different intensities of pixels representing the tissues can distinguish various anatomical structures. Thus, the concepts and terminologies that govern nuclear magnetic resonance will be discussed in detail, particularly in the context of cardiac magnetic resonance imaging.

2.2.1 Quantum Mechanics of Magnetic Resonance

The understanding of nuclear magnetic resonance is important in the use of this medical imaging modality, and therefore, it is important to give an outline of the quantum mechanical effect during the imaging of a human body.

Magnetic Moments of Nuclei

A charged particle possessing spin states will induce a magnetic field and therefore possesses its own magnetic dipole moment (Horowitz 1994). The atomic nucleus that comprises an uneven number of protons and neutrons possesses an inherent angular momentum spin that results in a magnetic field. In Figure 2.1[5], the magnetic moment is represented by the arrow vector around which the nucleus spins. The hydrogen nucleus, chemically represented as ^1H, has a single proton that is quantum mechanically affected during magnetic resonance (Phillips 1984). Therefore, terminologies used in this thesis for the individual nucleus and proton are inter-changeable. The hydrogen nuclei are commonly found in water, which can form up to 80% of the human body (Frisch *et al.* 1998), and are also present in lipids as well. Although other elements are also used in magnetic resonance imaging, it is mainly the hydrogen proton that is utilised.

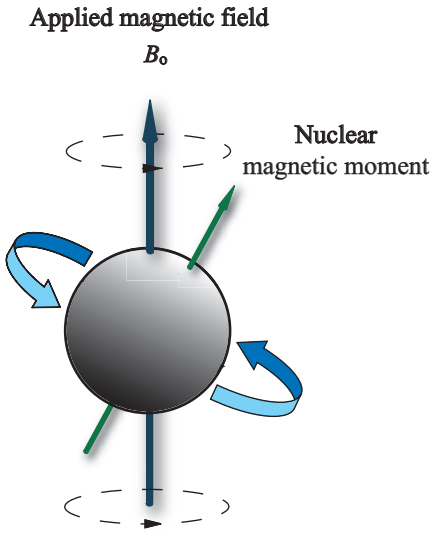

Figure 2.1. Quantum mechanical spin in an applied magnetic field. A nucleus has two possible discrete quantum mechanical spin states: $m = 1/2$ or $m = -1/2$. These states are said to be *degenerate*, which implies they have the same energy. If a nucleus is placed in a magnetic field, B_0, there is an interaction between the nuclear magnetic moment μ_m and the external magnetic field resulting in different energies for the two spin states, thus removing the degeneracy. Thus nuclear spin states have different energies in a non-zero magnetic field. We can imagine the two states of a spin $1/2$ or $-1/2$ as being aligned either with or against the magnetic field.

[5]Figures 2.1 and 2.2 are adapted from diagrams that appear in Phillips (1984).

Figure 2.1 is as an over-simplifed representation of the real physics since we are dealing with *discrete* spin states in reality. With an applied magnetic field, B_0, the energy difference between two spin states is $\Delta E = g\hbar B_0$, where g is called the Lande g-factor that is typically positive and close to unity, and $\hbar$ is the Planck's constant h divided by 2π. When this energy equals $h\nu$ of an incident photon, where ν is the frequency of the photon, resonant absorption occurs. This is the basis of NMR imaging. Thus, magnetic resonance absorption occurs when $\nu = 2\pi g B_0$, which happens also to be the Larmor precession frequency. This typically corresponds to the radio frequency (RF) regime for magnetic fields up to about 20 Tesla.

To be more precise, when there is a misalignment of the magnetic moment μ_m with the applied magnetic field, Larmor precession or rotation of the nuclei spin vector occurs about the magnetic field axis with a specific frequency (Phillips 1984). This rate of precession, or the Larmor frequency, is thus dependent on the magnetic field and a gyromagnetic ratio (Grin 1975, Mudry *et al.* 2003).

In the normal state, the precessing magnetic moments of the proton spins within a body are randomly distributed and therefore their resultant vector sum will approach zero. When the external magnetic field is applied, these spins align parallel and anti-parallel to the direction of the field with the net transverse component approaching zero.

Larmor Precession of Nuclear Magnetisation

Based on a similar type of magnetic field configuration, pulses of radio waves that have magnetic moments perpendicular to the applied magnetic field can cause the hydrogen nuclei to experience a quantum mechanical effect. A nuclear magnetic resonance (NMR) signal from the sample can be obtained by applying a radio frequency (RF) pulse via an RF coil (Fujio *et al.* 1995a, Mudry *et al.* 2003, Mullingera *et al.* 2008). The system of spins can be irradiated with a radio frequency pulse that matches the precessional or Larmor frequency of the nuclei. This causes a time dependent deflection of the net magnetisation from its equilibrium orientation, thereby resulting in the net magnetisation to about B_0 with the Larmor frequency (also known as the resonance frequency), as shown in Figure 2.2. The RF pulse can be represented by a magnetic field, B_1 at right angles to B_0 (Phillips 1984). This causes the magnetisation to move around it with an angle of rotation that is a function of amplitude B_1 and duration of the RF pulse.

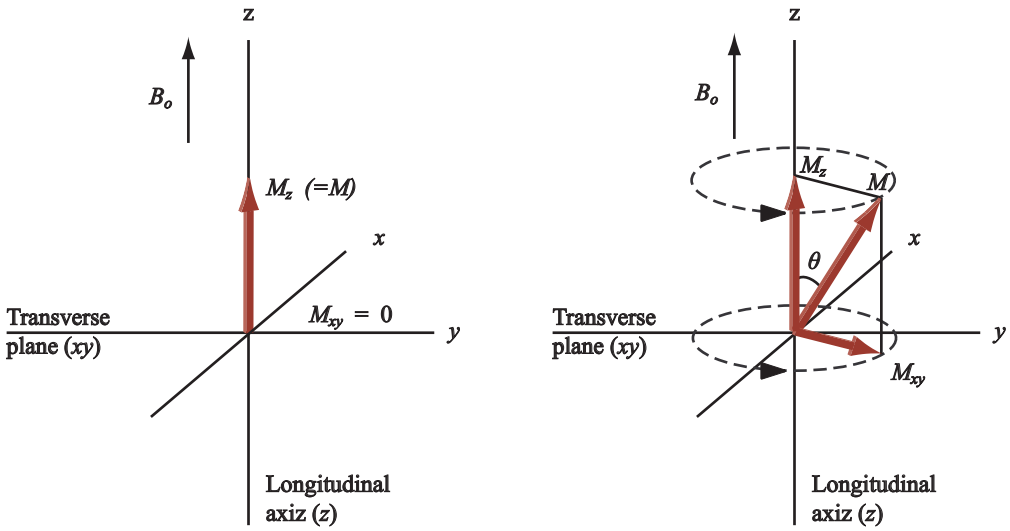

(a) Prior to RF pulse

(b) Post RF pulse

Figure 2.2. Larmor precession and resonance phenomenon. Precessing net magnetisation M which is made up of two vector components, M_z in the direction of B_0 and M_{xy} in the transverse plane. (a) In equilibrium, M aligns with B_0 with zero transverse component. (b) After the RF pulse, M_{xy} has a finite value and allows for detection.

The angle of rotation is also known as the RF flip angle or RF pulse angle. The net magnetisation M is the resultant of M_{xy} that lies in the transverse plane, and M_z in the longitudinal alignment with B_0.

Relaxation Process

Relaxation occurs after termination of an RF pulse and the return of quantum mechanical changes to their initial state (Horowitz 1994). After excitation, nuclei can return to equilibrium by the loss of energy through the emission of electromagnetic radiation. This is known as relaxation, and both the longitudinal (M_z) and transverse (M_{xy}) magnetisation components return to their equilibrium states after the termination of the RF pulse. At this equilibrium, M aligns in the z-direction along B_0 and is denoted by M_0 with $M_{xy} = 0$.

The longitudinal (spin-lattice) relaxation requires a period of time for the longitudinal magnetisation to return to its initial value. We denote the spin-lattice relaxation time T_1 as the time for the longitudinal magnetisation to increase to 63% of this full value, and the spin-spin relaxation time T_2 as the time for the transverse magnetisation to

decrease to 37% of its maximum value. It is to be noted that T_1 and T_2 are independent of each other with T_2 having a smaller value. Figure 2.3 shows the variation of magnetisation versus relaxation times. Different materials affect the relaxation times that are dependent on the size of molecules, physical state of lattice and presence of macromolecules.

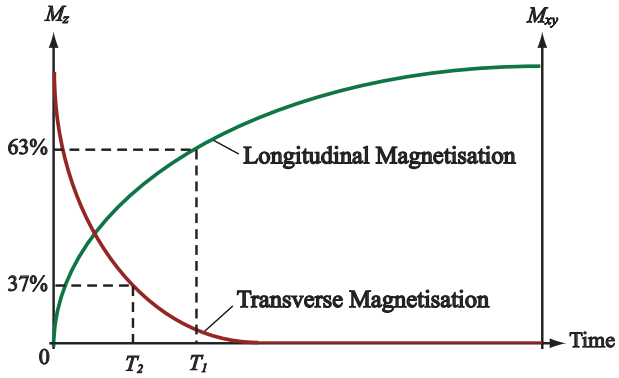

Figure 2.3. Profile of longitudinal and transverse magnetisation during relaxation. Time 1 (T_1) is defined as the duration for nuclei realignment and emission of RF signals that can be registered onto the MR images. Realignment of nuclear spins after this transverse magnetisation has a decay time constant labelled as Time 2 (T_2) for this transverse relaxation.

At this stage, the excitation of the nuclei by the RF pulse causes an induced current signal in the transverse magnetisation that is time-dependent (Fujio *et al.* 1995a). This physical phenomenon can be harnessed to measure magnetic resonance through the induction of the signal using a RF detection coil. This signal receiving coil can be fitted to a patient for detecting the nuclear magnetic resonance signals (Yoshino and Takeuchi 1994, Yau *et al.* 2001). The signal that results from the free precession of net magnetisation in the transverse plane and decays due to the relaxation mechanism is also called the free induction decay (FID) signal. For tissue classification, the rate of decay is dependant upon the material nuclei, and therefore registers differently onto the MR image that is made up of pixels with varying intensity (Worthley 2001).

2.2.2 Magnetic Resonance Imaging Protocols

Two major types of imaging sequences or techniques are used in magnetic resonance imaging. Imaging protocols, such as the spin echo and gradient echo, are based on the principle of magnetic resonance described in previous sections. Other types of imaging

have been developed in the past decade. Thus, we shall briefly review some of these imaging sequences.

Spin echo imaging provides good tissue discrimination of the cardiac structures in heart with flexible contrast characteristics depending on the programmed parameters of imaging sequence. These may include T_1 weighted (T1W), proton density weighted (PDW) and T_2 weighted (T2W) imaging. The spin echo imaging technique is also called *dark blood imaging* as blood within cardiovascular compartments appears black.

Gradient echo imaging is especially useful for assessment of myocardial function and may be acquired rapidly, allowing cine imaging of the heart. It is commonly known as *bright blood imaging* as the imaged blood appears white (Worthley 2001, Worthley and Fayad 2002). However, gradient echo imaging provides poor tissue contrast as compared to a spin echo based technique. Associated with this imaging sequence is the echo time (TE) and repetition time (TR), the details of which will not be defined at this point.

Steady-state free precession (SFP or SSFP) is a method of MR excitation (Bloomer *et al.* 2001, Markl and Pelc 2004, Li *et al.* 2004), which uses steady states of magnetisation. It comprises a gradient echo sequence in which a non-zero steady state develops for both components of magnetisation (transverse and longitudinal) and also when RF pulses are rapidly applied repeatedly with inter-pulse intervals that are short compared to both T_1 and T_2 of the tissue. If the RF pulses are close enough together, the MR signal will never decay completely, so that the spins in the transverse plane will also not dephase completely.

A variant of SSFP is the fast imaging in steady-state free precession that is abbreviated as True FISP[6] (Plein *et al.* 2001, Gleeson *et al.* 2008). This protocol is capable of imaging cross-sections of cardiac structures with unsurpassed soft tissue contrast (Worthley 2001). It is one of the most popular medical imaging modalities for the registration of physiological properties of the heart and arteries. Imaging using this protocol combines both longitudinal and transverse magnetisation (Chen *et al.* 2001). It is characterised by complex T_1/T_2-contrast configurations (Herborn *et al.* 2003) and refocuses all gradients over a repetition interval, thereby achieving fast-imaging with a high signal (Chen *et al.* 2001).

[6]During the course of this PhD, the SSFP protocol by Siemens MRI scanner was utilised for imaging. It is to be noted that several vendor-specific names for this sequence exist: True FISP by Siemens, Balanced FFE by Philips, and FIESTA by General Electric.

Compared with gradient echo sequences, the steady-state free precession protocol allows for a reduced scanning time and a better contrast between blood and myocardium. Based on current studies, steady-state free precession MRI protocol is demonstrated in the literature as providing better quality for cine CMR scans (Carr *et al.* 2001, Fuchsa *et al.* 2003, Kellman *et al.* 2004).

2.3 Asynchronous Precession of Proton in Turbulent Flow

The precessing coherence of nuclear spins is related to the motion state of the fluid, which contains the nuclei, and can give signal contrast that corresponds to its flow.[7] We examine the theory governing the concept of void signal registration due to turbulence within a fluid, where atomic nuclei have been aligned either parallel or anti-parallel to a powerful and uniform magnetic field. As high energy nuclei relax and realign, they emit energy with certain properties that are recorded to provide information about the medium. Image contrast is created by weighting the energy signal during realignment of the nuclear spins with the magnetic field. A signal image is then generated as a result of this quantum mechanical activity.

As the fluid is transported, the nuclear signals within the fluid follows its displacement. In a turbulent flow, the diffusion of magnetic moments occurs (Kuethe 1989). De-phasing (asynchronous precession) of spin due to turbulence in the flow gives a low MR signal during imaging (Globits and Higgins 1995, Lawson 1999) as shown in Figure 2.4. Low MR signals are represented as higher pixel intensities in the MR image (refer to Supplementary Videos 1 to 3 in CD-ROM, listed in Appendix F). The proton spins de-phase in the transverse plane when the RF pulse is terminated. Other than the cause of uncontrolled diffusion of magnetic moments in turbulent fluid, this de-phasing can also be due to intrinsic non-homogeneities of the magnetic field as a result of magnetic susceptibility changes at tissue interfaces.

Therefore, there is a reduction in the signal registration on the image. Effective diffusivity of spin protons at this point is represented by a reduction in signal intensity in the image (Kuethe 1989). As the diffusivity follows the movement of the fluid in a channel, there exists an intensity of change in the direction of flow. This produces a

[7] This is the first description explaining the dynamic magnetic resonance signal contrast that relates to the motion of blood in the heart chamber. We harness this phenomenon and built a technology based on this concept to track blood flow.

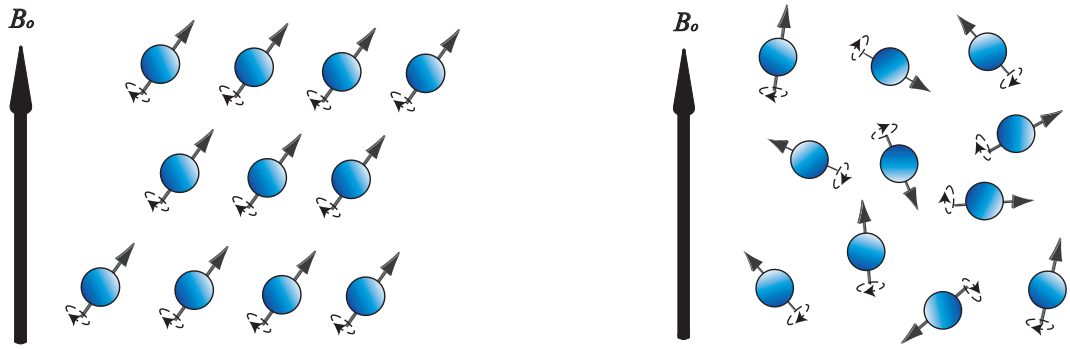

(a) Coherence of spins phases in static fluid (b) De-phasing of spins in turbulent fluid

Figure 2.4. Nature of precessing blood proton spins. Hydrogen-based molecules of blood maintain coherent spin phases when assuming a static fluid state as displayed by (a), but are distributed chaotically in turbulent fluid and this disrupts the alignment of proton spins from their order as shown in (b). Due to the incoherent or random precession of spins, the net magnetisation is weak and gives a low MR signal intensity. Therefore regions of blood at different levels of turbulence appear with contrasting pixel intensities in the cardiac MR image. The groups of incoherently precessing proton spins move along with the global blood flow within the cardiac chamber.

pattern of varying intensity in the magnetic resonance image. The movement of this pattern is called intensity flow. The presence of the temporal intensities, represented by pixels of the image, coincides with the blood flow, and can be visually observed from time-dependent sequences of magnetic resonance images.

2.4 Application of MRI onto Cardiac Diagnosis

It is a well-established fact that cardiac MRI possesses superior resolution, good blood and tissue contrast and offers a wide topological field of view. Unlike computed tomography, it is non-radiative and harmless to humans. The special properties of MRI allow physicians to examine abnormal cardiac morphology as a means of predicting possible heart diseases. Besides morphological imaging, cardiac MRI also allows myocardial wall tracking (Guiterrez *et al.* 1997, Merrifield *et al.* 2001), calculation of ventricular and stroke volumes, mass, ejection fraction (Globits and Higgins 1995, Powell *et al.* 2000), and demonstration of myocardial perfusion in ischemic heart diseases (Higgins *et al.* 1994, Manna *et al.* 2007).

The electrical activity generated by the heart can be recorded as an electrocardiogram (ECG) signal (Chandran *et al.* 2006b, Guyton and Hall 2006) as shown in Figure 2.5. The P wave and the QRS complex are depolarisation waves. The electrical currents by the P wave activation causes the atrial muscles to depolarise and contract. The QRS complex is a representation of the depolarisation and contraction of the ventricular muscles. The repolarisation T wave represents the repolarising of ventricular muscles.

The ECG can be used to synchronise image acquisition with cardiac motion to produce cine-magnetic resonance images (Tetsuya 2003, Larson *et al.* 2004). ECG gating can be performed prospectively or retrospectively (Du *et al.* 2001). In prospective gating, the R-wave triggers image acquisitions in the cardiac cycle. Then, a trigger delay (or trigger window) provides an interval between the R-wave trigger and image acquisition (Ley *et al.* 2007, Koktzoglou *et al.* 2007). For retrospective gating (Achenbach *et al.* 2000, Morgan-Hughes *et al.* 2003, Thompson and McVeigh 2004, Nijm *et al.* 2008), image acquisition occurs continuously along with an ECG tracing. Post-processing of images retrospectively using registered ECG tracing is performed. Cine-MRI of cardiac structures using ECG gating provides information on cardiac flow and function. The first image acquired corresponds to the R-wave trigger (Figure 2.5). Accurate QRS detection (Stallmann and Pipberger 1961, Pan and Tompkins 1985, Friesen *et al.* 1990, Trahanias 1993, Shaw and Savard 1995) is crucial as it indicates reliable identification of the R-waves. Examples of such images can be viewed using Supplementary Videos 1 to 3 (in CD-ROM, listed in Appendix F).

Cardiac MRI allows multiple contiguous slices at various orientations to be scanned at various phases of one cardiac cycle. Typically, the scan pertaining to cardiac analysis can either be short axis (SA) or long axis (LA), and based on the two-chamber (2C), three-chamber (3C) or four-chamber (4C) configurations as shown in Figures 2.6 and 2.7.

Cardiac MRI has been widely utilised for imaging patients with various cardiac conditions, such as diseases of the aorta (Nienaber *et al.* 1993, Deutsch *et al.* 1994, Laissy *et al.* 1995), aneurysm (Moore *et al.* 1984, Dinsmore *et al.* 1986), and human hearts with atrial and ventricular septal aneurysm or defect (Stauder *et al.* 2001, Puvaneswary *et al.* 2003, Webb and Gatzoulis 2006, Beerbaum *et al.* 2008). However, traditionally, only anatomical information of the cardiovascular compartments or structures are used for diagnosis, until the development of phase contrast MRI that is able to provide cardiac

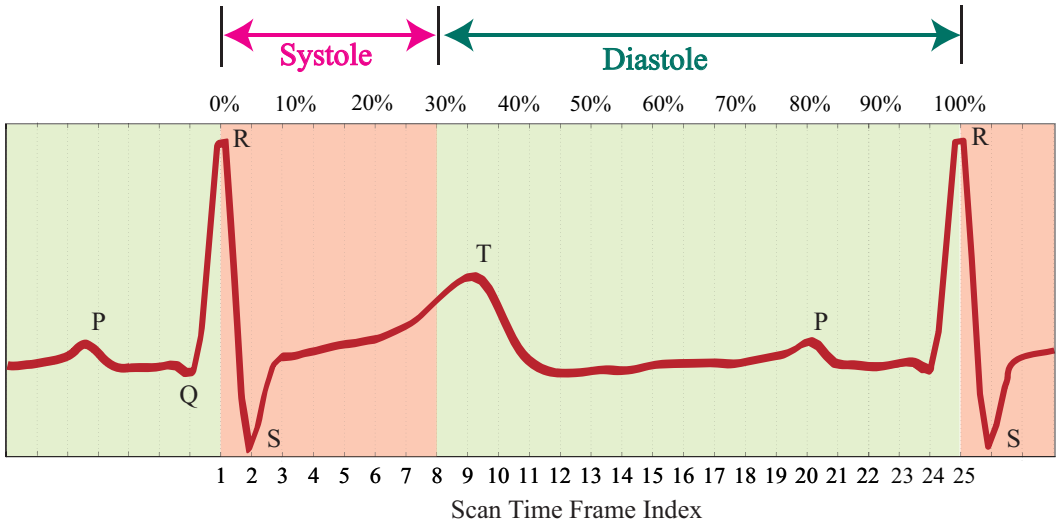

Figure 2.5. Cardiac events with relation to the electrocardiogram. The variation of a generic electrocardiogram (ECG) is correlated to the scan time frames of gated-MRI. The characteristic Q-, R-, S- and T- waves are located at the elevations of the ECG trace. The triggering of image acquisition starts at the occurrence of the R-wave. For a temporal resolution of 25 time frames, the cardiac systole starts from 1 to 8, and the diastole is from 9 to 25.

flow quantification. We summarise the clinical applications of MRI in the cardiovascular system for which the following medical conditions are assessed (English and Moore 1995):

1. Pericardial disease
2. Congenital heart disease
3. Aortic arch heart disease
4. Acquired heart disease
5. Cardiac transplantation
6. Atrial and ventricular septal defects
7. Valve regurgitation
8. Aneurysms
9. Coarctation of the aorta

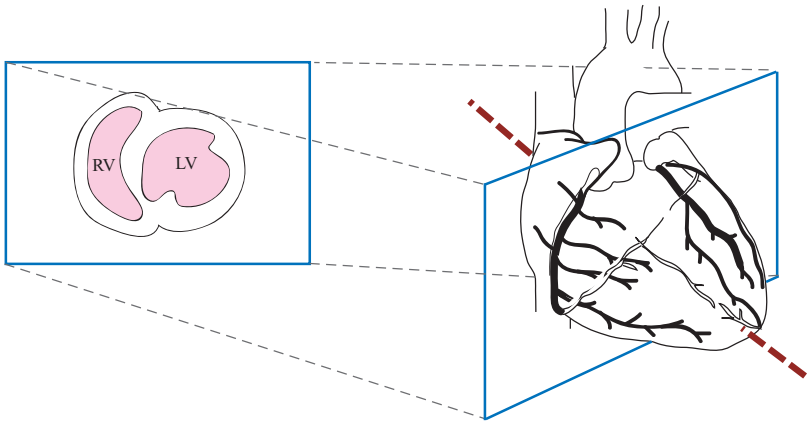

(a) Short axis view configuration

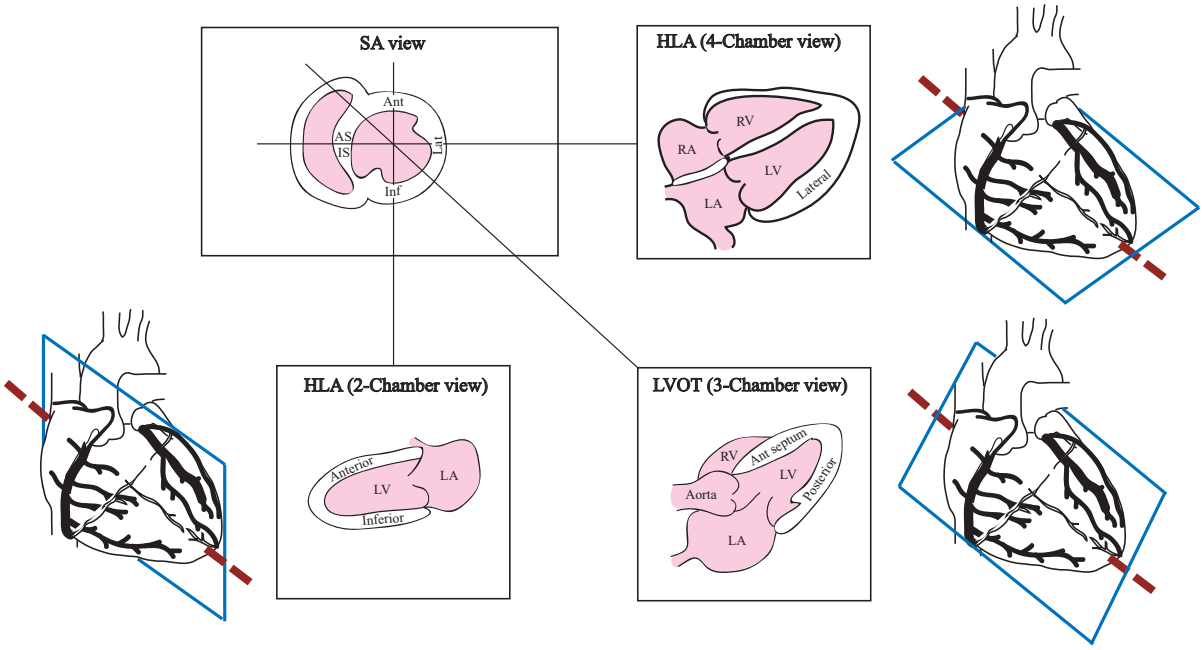

(b) Long axis view configurations

Figure 2.6. Cardiac magnetic resonance imaging based on different configurations. Cardiac magnetic resonance scans can be based on different configurations depending on the cardiac examination such as the short axis view in (a) and long axis view in (b). The abbreviations for the heart structures and scan configurations are: left atrium (LA), left ventricle (LV), right atrium (RA), right ventricle (RV), anterior septum (AS), inferior septum (IS), inferior (Inf), lateral (Lat), and anterior (Ant), left ventricular outflow tract view (LVOT), horizontal long axis (HLA). An appropriate scan view and multiple slices in a scan orientation enables us to examine different portions of the heart effectively.

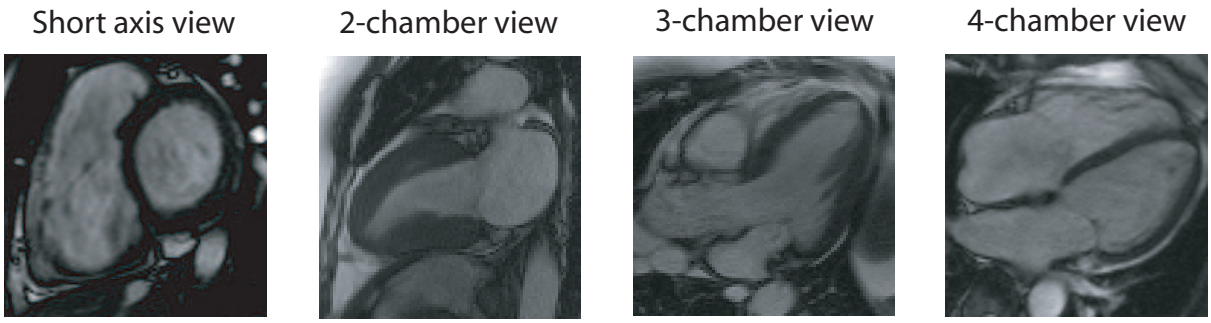

Figure 2.7. Cardiac magnetic resonance image views. Display of cardiac magnetic resonance images is based on the short axis and also on the long axis (with 2-chamber, 3-chamber and 4-chamber views). Each configuration is selected to show the relevant chambers and cardiovascular structures with clarity. Different orientations display the chamber of interest at various positions and bisections.

In this thesis, we emphasise the use of cardiac MRI for the investigation of atrial septal defects with quantitative assessment from the perspective of cardiac chamber flow. Magnetic resonance images based on the short axis two-chamber view of the heart showing the atria are used in our results (Chapters 7 and 8).

2.5 Phase Contrast MRI Velocimetry

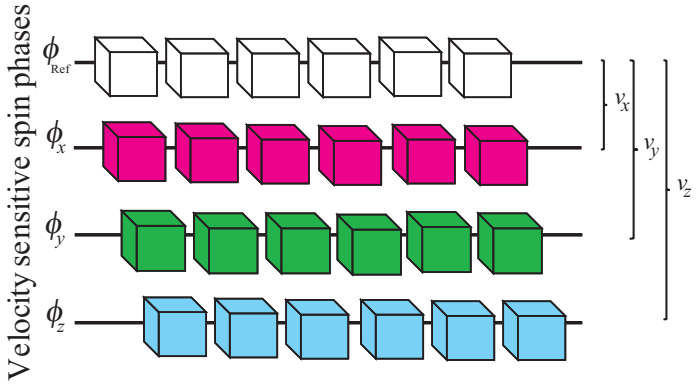

Figure 2.8. Phase contrast MRI velocimetry. Phase contrast MRI works on the concept that hydrogen nuclei from blood that has been exposed to magnetic fields accumulate a phase shift in spin that is proportional to the blood velocity in the x, y, and z directions. Velocities v_x, v_y and v_z are functions of the subtractions of spin phases ϕ_x, ϕ_y and ϕ_z of measured volumes with that of the reference phase ϕ_{Ref}.

2.5.1 Theory of Phase Contrast MRI

Figure 2.8 describes phase contrast in magnetic resonance imaging (MRI) based on spin phase shifts that are proportional to the blood velocity (Markl *et al.* 2003, Yu *et al.* 2003). Phase contrast MRI signals can be represented using intensity images. The intensity of each pixel corresponds to the blood velocity at the measured location. To quantify a velocity in one spatial dimension, at least two phase images must be taken for subtraction of flow-induced phase shift from background phases caused by susceptibility-induced inhomogeneities and coil sensitivity changes (Baltes *et al.* 2005). The flow sensitivity of a phase contrast signal acquisition is given the term velocity encoding and is usually abbreviated as VENC (Svensson 2003). Setting of VENC limits affects flow measurements (Lagerstrand *et al.* 2006). Blood velocity will be aliased to an artificially low value if it exceeds the maximum VENC level by the flow sensitisation gradients.

2.5.2 Phase Contrast MR Imaging of Cardiac Chambers

The phase contrast MRI technology is clinically attractive because it is able to provide quantitative information on blood flow without the need for contrast agent to be introduced into the human body. Moreover, ECG-gated phase contrast MRI can provide cine-images for temporal velocity mapping (Thompson and McVeigh 2004). We present some images based on this MRI protocol in Figure 2.9. The phase contrast images are graphical representations of the velocity components (x- and y- directions) maps. The figure shows the in-plane Foot-Head (F-H) and Anterior-Posterior (A-P) orientation scans.

Combining the two flow maps based on the in-plane x- and y- directions results in velocity mapping of the blood flow as shown below in Figure 2.10. Phase contrast MRI can be extended to three dimensions as well by combining an additional orientation, the through-plane image scans, to obtain the orthogonal z- velocity component map. Although the extraction of the third velocity dimension can give a more accurate description of the flow scenario, the display of three-dimensional vectors in space is visually complicated and visualisation may only be effective with the use of tools such as streamline tracing. Moreover, it is a challenge to incorporate anatomical information into the flow field by using planar MR images insertion into a three-dimensional space that will partially occlude the flow patterns. For this reason, it may be more effective to view projections of velocity vectors onto a slice of interest through the cardiac flow

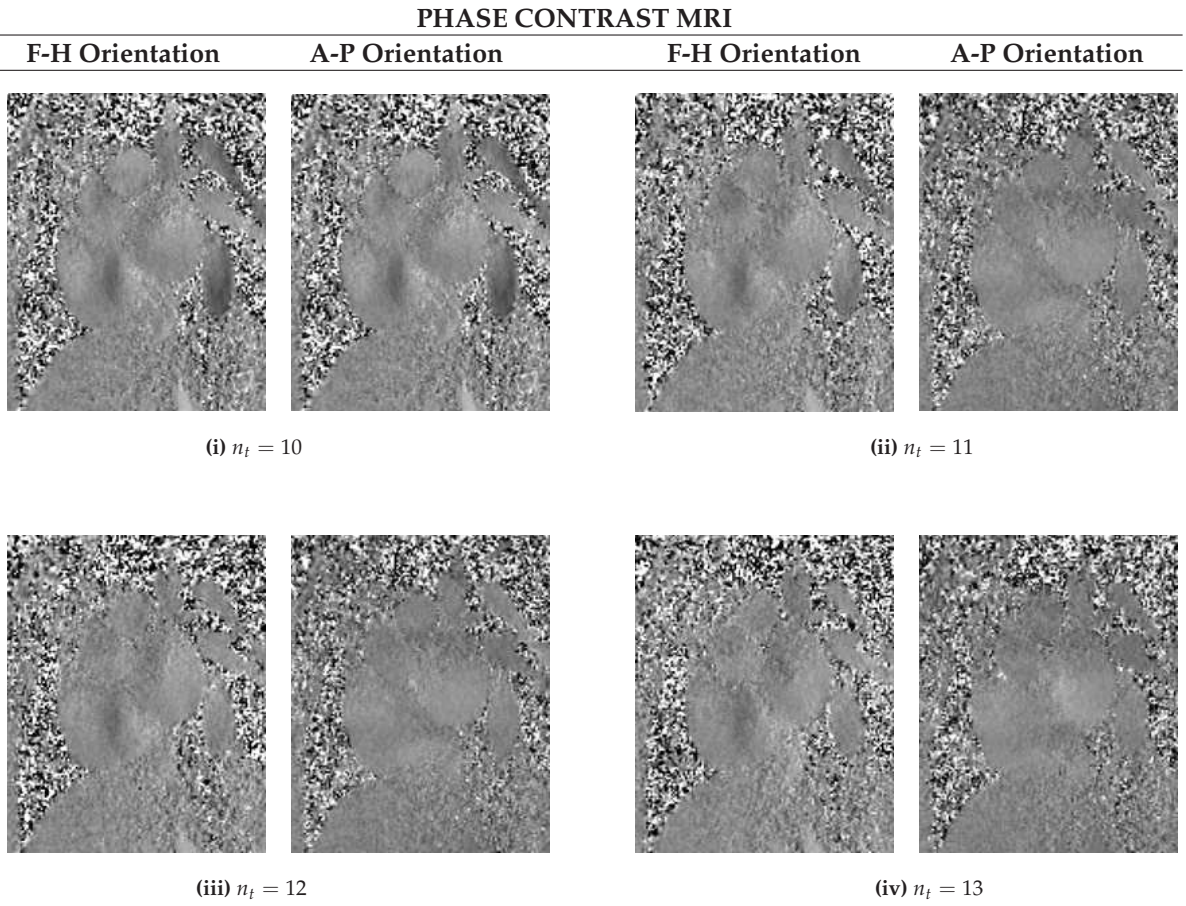

Figure 2.9. Phase contrast MRI of a cardiac chamber. Short axis scans pertaining to time frame indices $n_t = [10, 11, 12, 13]$ out of 25 frames in a cardiac cycle are presented. Scans based on two in-plane x- and y- directions, which pertains to the Foot-Head (F-H) and the Anterior-Posterior (A-P) orientations respectively, are needed for velocity mapping. The intensity of the pixels in the image indicates the magnitude of the velocity component in the specified orientation. Combining two orthogonal velocity-encoded image maps can produce a two dimensional velocity flow field.

field. The flow scenario with respect to the anatomy of the heart can be referenced by superimposing the two-dimensional cardiac flow onto the corresponding MR image. Segmentation of the cardiac chamber will further define the boundary of blood motion and isolate the region of interest for flow analysis[8].

As can be observed, phase contrast MRI encodes velocity information within the output images and we are able to decipher these data to produce velocity field maps for analysis of flow patterns within the cardiac chambers. The phase contrast framework

[8]Refer to Chapter 5 and Supplementary Video 4 (in CD-ROM, listed in Appendix F) which describes cardiac chamber segmentation using active contouring.

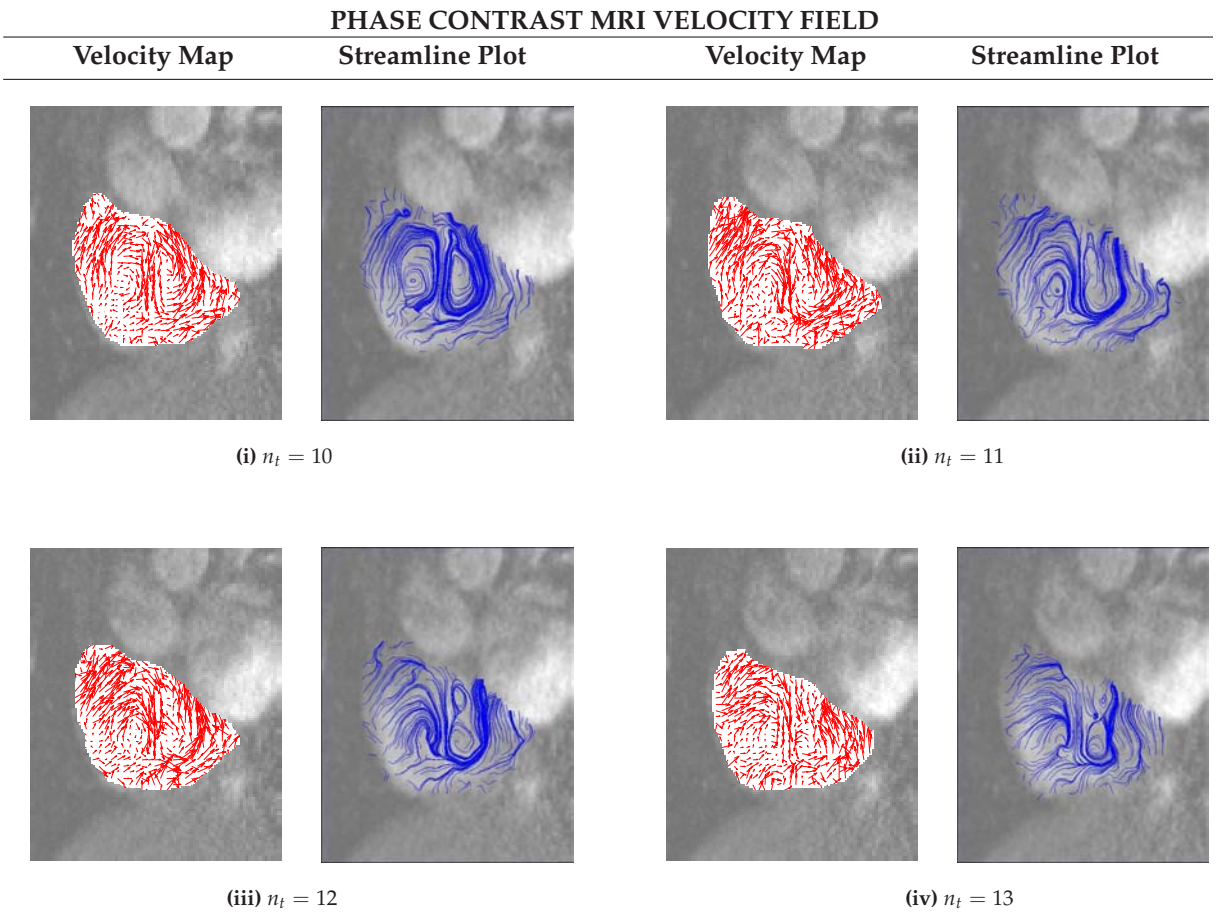

Figure 2.10. Velocity field of cardiac chamber. The velocity fields for time frame indices $n_t = [10, 11, 12, 13]$ out of 25 frames in a cardiac cycle are created by combining the phase contrast images based on the in-plane x- and y- directional scans. The fields are then presented using vector plots made up of multiple red arrows distributed within the region of interest. The flow patterns of the blood may be traced by streamlines (represented in blue) which gives an indication of the direction of flow within user-specified regions of interest.

enables the flow imaging of cardiovascular system non-invasively and with good reliability. This technology is well-established in the medical imaging industry and can serve as a gold standard flow imaging protocol for validation of new and developing methodologies.

2.6 Chapter Summary

This chapter reviews the magnetic resonance imaging (MRI) technology. The concepts explained here can be used in Chapters 3 for implementation of MRI-based tracking, and in Chapter 4 for computational validation of the proposed velocimetry system. In

summary, we review the basic magnetic resonance and quantum mechanical concepts, the terminologies defined for medical imaging, the various protocols in MRI scanning, as well as the techniques related to specific imaging planes. Therefore, this forms one of the pre-requisite chapters underpinning the chapters that build upon techniques related to MRI, as well as those that discuss MRI scanning of the heart. In particular, it facilitates the reading of Chapter 3 that describes the fluid motion tracking of magnetic resonating blood within the cardiac chambers, the implementation of MRI-based velocimetry detailed in Chapter 7, and Chapter 8 which provides an application of magnetic resonance fluid motion tracking on a pathological case of the heart.

Chapter 3

Implementation of Magnetic Resonance Fluid Motion Tracking

MAGNETIC resonance fluid motion tracking is a recent development that leverages on the success of magnetic resonance imaging systems. The system integration of MRI with the motion tracking of non-rigid objects is an important contribution to this thesis. The unique properties of MR images allow the motion tracking of blood proton spin signals by post-processing the information offline after scanning. This has a significant impact on cardiac flow research due to the relatively lower time expenditure and the ability to access information without a scanner in its operational mode at the time of post-processing.

This chapter presents the mathematical and computing algorithm needed to carry out optical flow implementation, which is a class of motion estimation technique. The design of outliers filtering and vector synthesis supplements the flow visualisation output by the system. The motion tracking architecture developed in this research area may also have potential applications in particle image velocimetry, cloud motion tracking using satellite images or multiple human motion monitoring based on video images, and therefore has high versatility in its utilities. However, we limit our focus on the biomedical image processing application in this study.

3.1 Introduction

This chapter reviews the techncial aspects of the existing and well-established multi-resolution motion estimation framework (Anandan 1989, Bouguet 2000, Amiaz *et al.* 2007). The contribution that we make in this study is the description and application of this technique on biomedical image processing. We explore a new concept for flow visualisation based on magnetic resonance imaging of non-rigid materials. A method of performing fluid motion tracking using stead-state free precession (SSFP) magnetic resonance (MR) images of non-stationary flow is proposed. Consequently, we apply magnetic resonance onto the fluid and registered nuclear signals at different phases of its motion onto gray-scale intensity images. By means of tracking the shift of intensity pixels that are the representation of MR signal amplitudes, we can compute the fluid dynamics of the imaged flow. This motion tracking framework has an accuracy depending on the spatial and temporal resolutions of the magnetic resonance scan. The fundamental components that make up MR fluid motion tracking is developed to enable blood flow tracking computationally.

3.2 Overview of Optical Flow

In this section, the optical flow algorithm, in a class of motion estimation methods is described. It may be worthwhile to mention that the term *optical*, as used here, is not related to a particular physical property of electromagnetic waves used to measure velocity or flow of a particular object. Rather, it is related to the graphical aspects of gray-scale pattern representing the camera view of the object that flows from one scene to another. Perspective projection of this moving object onto two-dimensional images generates temporal gray-scale patterns of varying image brightness. Consequently, the optical flow solution is based upon local derivatives in a sequence of high intensity images (Horn and Schunck 1981, Barron *et al.* 1994). By estimating the in-plane distance (in pixels), so that every pixel moves between pairs of two-dimensional images of consecutive phases, we generate flow vectors that correspond to the apparent motion of brightness or intensity patterns in the image. Therefore, optical flow computation is a computer algorithm that performs the tracking of objects captured onto two-dimensional matrices of intensity values. Generally, the basis of differential optical flow is the motion or optical flow constraint that we can derive. We present the mathematical framework by Horn and Schunck (1981) as follows:

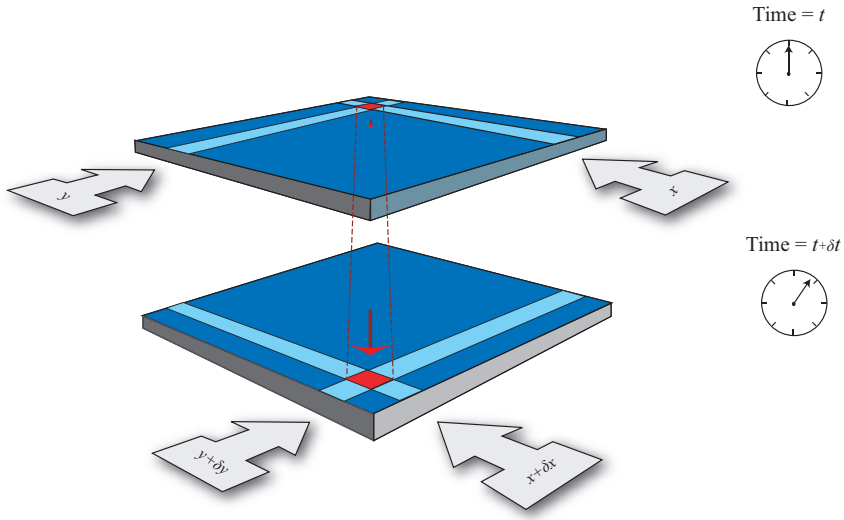

Figure 3.1. Estimating spatial motion of pixel using optical flow. Assume the shift of a pixel from position $(x,\ y,\ t)$ to $(x+\delta x,\ y+\delta y,\ t+\delta t)$. The derivatives of x and y with respect to t gives the x and y components of the spatio-temporal signal flow respectively. The optical flow motion constraint allows us to derive these velocities up to one vector per pixel.

Consider pixel movement from (x, y, t) to $(x+\delta x, y+\delta y, t+\delta t)$ in Figure 3.1. Pixel intensity is denoted by $I(x,y,t)$. Assuming spatio-temporal variation in intensity signal, we obtain

$$I(x,y,t) = I(x+\delta x, y+\delta y, t+\delta t). \tag{3.1}$$

Applying a 1^{st} order Taylor series expansion, Equation 3.1 becomes

$$I(x+\delta x, y+\delta y, t+\delta t) = I(x,y,t) + \frac{\partial I}{\partial x}\delta x + \frac{\partial I}{\partial y}\delta y + \frac{\partial I}{\partial t}\delta t + \varepsilon \tag{3.2}$$

whereby ϵ represents higher order terms. If the temporal intensity or brightness of a particular point in the pattern is constant, we have

$$\frac{\partial I}{\partial x}\delta x + \frac{\partial I}{\partial y}\delta y + \frac{\partial I}{\partial t}\delta t = 0. \tag{3.3}$$

This can also be written as

$$\frac{\partial I}{\partial x}\frac{\delta x}{\delta t} + \frac{\partial I}{\partial y}\frac{\delta y}{\delta t} + \frac{\partial I}{\partial t} = 0. \tag{3.4}$$

Definition of $v_x = \frac{\partial x}{\partial t}$ and $v_y = \frac{\partial y}{\partial t}$ yields

$$\frac{\partial I}{\partial x}v_x + \frac{\partial I}{\partial y}v_y + \frac{\partial I}{\partial t} = 0. \tag{3.5}$$

Therefore, the optical flow constraint equation can be rewritten as

$$\left[I_x, I_y\right] \cdot \left[v_x, v_y\right] = -I_t. \tag{3.6}$$

The optical flow vector $\vec{v}$ has two components v_x and v_y describing the motion of a point feature in x and y direction with the spatial gradient of intensity $\left[I_x, I_y\right]$ is denoted by ∇I. Therefore, the linearised version of the brightness constancy assumption yields the optical flow constraint given by

$$\nabla I \cdot \vec{v} = -I_t. \tag{3.7}$$

It should be noted that the optical flow has been effectively applied onto tracking of rigid objects with no changes of shape. This implies that it actually captures the motion of scene objects with the exclusion of expansions or contractions, as well as deformations (Barron and Thacker 2005).

3.3 Lucas Kanade Optical Flow

In Lucas Kanade optical flow (Lucas and Kanade 1981, Barron *et al.* 1994), we assume that the flow field is smooth locally and solved as a weighted least squares fit of the motion constraint equation. Based on an n by n neighbourhood region the number of pixels is $N = n^2$. The least-squares fit of motion constraint equation and optical flow framework by Barron *et al.* (1994) is presented here. Equation 3.7 can be expressed in matrix format as follows:

$$\begin{bmatrix} \nabla I(x_1, y_1) \\ \nabla I(x_2, y_2) \\ \vdots \\ \nabla I(x_N, y_N) \end{bmatrix} \begin{bmatrix} u \\ v \end{bmatrix} = - \begin{bmatrix} I_t(x_1, y_1) \\ I_t(x_2, y_2) \\ \vdots \\ I_t(x_N, y_N) \end{bmatrix}.$$

Since the solution to this set of equations is under constrained (more equations than unknowns), the least-squares fit of motion constraint equation provides solution for the velocity $\vec{v}$ at a single time t in the spatial region Ω by minimising

$$\sum_{x,y \varepsilon \Omega} \left[\nabla I(x, y, t) \cdot \vec{v} + I_t(x, y, t)\right]^2. \tag{3.8}$$

It will be easier to examine the solution if we can denote the matrices using symbols A, W and $\vec{b}$ such that $A\vec{v} = \vec{b}$ given that

$$A = \Big[\nabla I(x_1, y_1), \ldots, \nabla I(x_N, y_N)\Big], \tag{3.9}$$

$$\vec{v} = \Big[u, v\Big], \tag{3.10}$$

$$\vec{b} = -\Big[I_t(x_1, y_1), \ldots, I_t(x_N, y_N)\Big]. \tag{3.11}$$

Consequently, in terms of expression by the above matrix symbols, we now can solve the optical flow constraint by minimising $||A\vec{v} - \vec{b}||^2$ by which a solution to this minimum least squares problem is given by

$$\vec{v} = \Big[A^T A\Big]^{-1} A^T \vec{b}, \tag{3.12}$$

where

$$A^T A = \begin{bmatrix} \sum_{k=1}^{N} I_x^2(x_k, y_k) & \sum_{k=1}^{N} I_x(x_k, y_k) I_y(x_k, y_k) \\ \sum_{k=1}^{N} I_x(x_k, y_k) I_y(x_k, y_k) & \sum_{k=1}^{N} I_y^2 x_k, y_k) \end{bmatrix},$$

and

$$A^T \vec{b} = -\begin{bmatrix} \sum_{k=1}^{N} I_t(x_k, y_k) I_x(x_k, y_k) \\ \sum_{k=1}^{N} I_t(x_k, y_k) I_y(x_k, y_k) \end{bmatrix},$$

and where all sums are taken over pixels (x,y) in the neighbourhood Ω. The solution to $\vec{v}$ can be solved by decomposition of Equation 3.12 into eigenvalues, such that $\lambda_2 \geq \lambda_1 \geq 0$ and eigenvectors, $\hat{e_1}$ and $\hat{e_2}$. However, some conditions to the solution apply as follows:

1. $A^T A$ should be invertible.

2. $A^T A$ should not be too small. Its eigenvalues λ_1 and λ_2 should not be too small.

3. $A^T A$ should be well conditioned. $\frac{\lambda_2}{\lambda_1}$ and should not be too large.

With regards to condition 2, we usually set a user specified threshold τ_D such that $\lambda_1 \geq \tau_D$ for the computed flow to be accepted as a reliable and full velocity.

3.4 Multi-Resolution Motion Estimation

3.4.1 Definition of Problem

In contrast to the motion estimation of rigid scene objects that can be captured optically via a camera, we track a unique motion of gray-scale patterns based on imaging fluid structure that is deformable in shape and size. Our objective is to measure the movement of an assemblage of nuclear spins within the fluid that is registered using magnetic resonance imaging. The regions that contain an asynchronous precession of protons from the turbulent flow contribute to low MR signals that are registered onto a magnetic resonance image at every time instance. Concatenating a series of images gives the visual display of the 'dynamic clouds' of signals that shows up as moving patterns of dark intensity among a brighter and lest turbulent background flow.

The problem with tracking the suspension of protons having asynchronous phase spins in a fluid is the incoherent movement of MR signal representative pixels that appeared on the MRI. For example, a group of pixels representing a neighbourhood of the *cloud* of asynchronous spins may move at different speeds and direction with respect to each other. As the flow becomes less turbulent at different phases, the intensity of pixels may change and attribute to further complexity in motion estimation. Therefore, there is a need to establish a robust and reliable algorithm for solving optical flow of such complex nature. Some guidelines apply, such that in order to handle large motions, and especially when there are incoherent speeds for groups of pixels, a larger interrogation window is required to capture more details. Conversely, this comes at the expense of local accuracy or flow field resolution, because a smaller interrogation window will be preferable in order not to smooth out details of the moving pattern. This reflects a situation with which we are trying to come to grasps whereby patches of flow potentially move at entirely different velocities.

A pyramidal implementation of the classical Lucas Kanade algorithm had been suggested previously for a solution to such a problem (Bouguet 2000). A multi-resolution implementation of optical flow computation can provide good local tracking accuracy. Hence, for our application, we utilise an extension of the optical flow algorithm to a multi-resolution one in order to maximise our flow image data.

3.4.2 Feature Tracking Using Pyramidal Optical Flow

Our understanding of any feature tracking system is that accuracy and robustness are the two most important considerations for its performance analysis. Accuracy relates to local sub-pixel accuracy involved in tracking, whereas robustness relates to sensitivity of tracking with respect to changes in pattern intensity and speed of motion.

In our optical flow scheme, the pyramidal Lucas Kanade optical flow method (Bouguet 2000), which incorporates a multi-scale approach, has been applied to support large scale fluid motion and for improved accuracy. A lowpass Gaussian filtering operation can produce a Gaussian pyramid to result in a sub-sampling pyramid (Gonzalez and Woods 2002)[9]. A top-down estimation of the flow by using an image pyramid can be performed, with the apex representing the MR image at a coarse scale. Computational results from this level are passed to the next and this process is carried on based on the flow estimated at the preceding scale until the original scale is reached. We refer to the diagram in Figure 3.2[10] to illustrate the computational aspect of pyramidal optical flow. Projection of the computed coarse-level flow field onto the next finer pyramid level is continued for each level of the pyramid until the finest pyramid level has been reached.

For signal emitting nuclei motion that are represented by intensity pixels on MR images, the application of multi-resolution optical flow scheme that predicts fluid motion is based on grey-level constancy assumption or the optical flow constraint (Horn and Schunck 1981). The accuracy of motion estimation critically depends on the magnitude of image motion. In fact, depending on the spatial image frequency, very large motions even may cause aliasing along the time frequency axis. For a fixed global velocity, spatial frequencies moving more than half of their period per frame cause temporal aliasing (Ruhnau *et al.* 2005). Therefore, a suitable temporal resolution of the imaging is required for accurate tracking.

[9] Refer to Section 3.5 for mathematical description of sub-sampling pyramid.
[10] Diagram modified from figure by Gonzalez and Woods (2002).

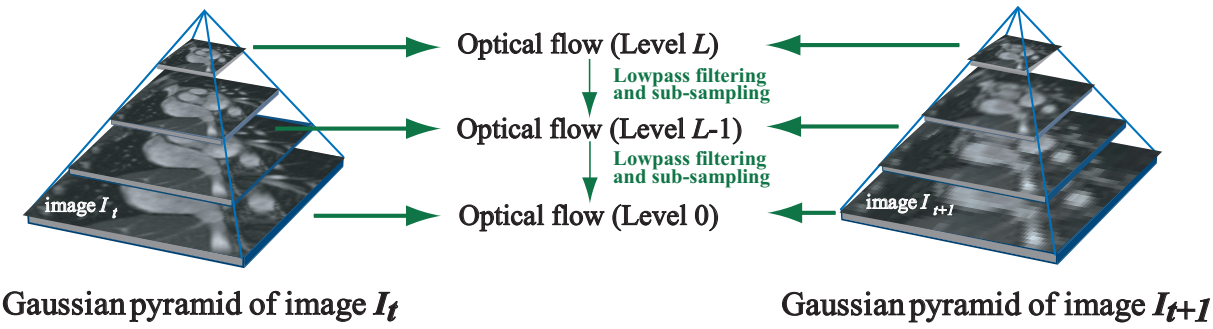

(a) Pyramidal implementation of optical flow

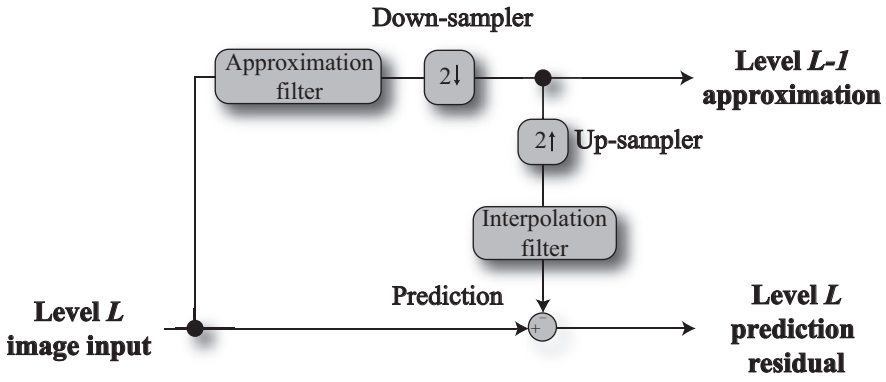

(b) System block diagram for pyramidal optical flow

Figure 3.2. Multi-resolution motion estimation using pyramid implementation. Diagrammatic view of the Gaussian pyramid with optical flow applied onto every image level is presented in (a). Each level in the pyramid is a sub-sampled version of the level below. In the first step, the optical flow between the top level images is computed. We project the computed coarse-level flow field onto the next finer pyramid level and continue this at each level of the pyramid until the finest pyramid level has been reached. The system block diagram in (b) gives an illustration of the algorithmic operation of this pyramidal implementation.

3.5 Pyramidal Lucas Kanade Optical Flow

3.5.1 Initial Definition

We now describe the mathematical implementation of the pyramidal Lucas Kanade optical flow as presented by Bouguet (2000). The technique comprises of pyramidal construction and the Lucas Kanade implementation of the optical flow solution[11].

It should be assumed now that we have two gray-scale intensity images that correspond to consecutive phases of the imaged fluid. The matrix representation of the images for both pre- and post-phases is defined as a function of location $\vec{x} = [x, y]^T$ as $I(\vec{x}) = I(x, y)$ and $J(\vec{x}) = J(x, y)$ respectively. Next, we consider a pixel location $\vec{u} = \left[u_x, u_y\right]^T$ on I and aim to find the shifted location of this pixel defined as $\vec{v} = \vec{u} + \vec{d} = \left[u_x + d_x, u_y + d_y\right]^T$ on J such that $I(\vec{u})$ and $J(\vec{v})$ are most similar. Note that $\vec{d} = \left[d_x, d_y\right]^T$ is the optical flow vector at location x. Assume an interrogation window size $\vec{w} = \left[2w_x + 1, 2w_y + 1\right]$. Finally we can define the optical flow $\vec{d}$ as the vector that will minimise the residual function ϵ defined as follows:

$$\varepsilon\left(\vec{d}\right) = \varepsilon\left(d_x, d_y\right) = \sum_{x=u_x-w_x}^{u_x+w_x} \sum_{y=u_y-w_y}^{u_y+w_y} \left(I(x, y) - J(x + d_x, y + d_y)\right)^2. \tag{3.13}$$

We implement a multi-scale solution of this function by pyramidal representation of the images in the subsequent section.

3.5.2 Pyramidal Representation of Images

We denote an image I^L of size $\left(n_x^L \times n_y^L\right)$, where L represents the level number of the image pyramid. The 0^{th} level means the highest resolution image. Pyramidal construction is built using recursive computation, whereby the current image I^L at the

[11] We acknowledge the use of the mathematical framework presentation by Bouguet (2000) for a pyramidal Lucas Kanade optical flow tracker in Section 3.5.

next higher level is computed from I^{L-1} at the previous level as follows:

$$
\begin{aligned}
&I^L(x,y) = \\
&\quad \frac{9}{64} I^{L-1}(3x,3y) + \\
&\quad \frac{3}{64}\Big(I^{L-1}(3x-1,3y) + I^{L-1}(3x+1,3y) + I^{L-1}(3x,3y-1) + I^{L-1}(3x,3y+1)\Big) + \\
&\quad \frac{3}{128}\Big(I^{L-1}(3x-2,3y) + I^{L-1}(3x+2,3y) + I^{L-1}(3x,3y-2) + I^{L-1}(3x,3y+2)\Big) + \\
&\quad \frac{1}{64}\Big(I^{L-1}(3x-2,3y-1) + I^{L-1}(3x+2,3y-1) + I^{L-1}(3x-2,3y+1) + \\
&\qquad I^{L-1}(3x+2,3y+1) + I^{L-1}(3x-1,3y-2) + I^{L-1}(3x+1,3y-2) + \\
&\qquad\quad I^{L-1}(3x-1,3y+2) + I^{L-1}(3x+1,3y+2)) + \\
&\quad \frac{1}{256}\Big(I^{L-1}(3x-2,3y-2) + I^{L-1}(3x+2,3y+2) + I^{L-1}(3x-2,3y-2) + \\
&\qquad\quad I^{L-1}(3x+2,3y+2).
\end{aligned}
\tag{3.14}
$$

for values of x and y such that $0 \leq x \leq n_x^{L-1} - 1$ and $0 \leq y \leq n_y^{L-1} - 1$. A low-pass Gaussian filter $\left[\frac{1}{16}, \frac{1}{4}, \frac{3}{8}, \frac{1}{4}, \frac{1}{16}\right] \times \left[\frac{1}{16}, \frac{1}{4}, \frac{3}{8}, \frac{1}{4}, \frac{1}{16}\right]^T$ has been implemented for image anti-aliasing before image subsampling.

A border of dummy image pixels around the image $I^L - 1$ are defined for $0 \leq x \leq (n_x^{L-1} - 1)$ and $0 \leq y \leq (n_y^{L-1} - 1)$ such that

$$
\begin{aligned}
I^{L-1}(-1,y) &= I^{L-1}(0,y), \\
I^{L-1}(x,-1) &= I^{L-1}(x,0), \\
I^{L-1}\left(n_x^{L-1},y\right) &= I^{L-1}\left(n_x^{L-1}-1,y\right), \\
I^{L-1}\left(x,n_y^{L-1}\right) &= I^{L-1}\left(x,n_y^{L-1}-1\right), \\
I^{L-1}\left(n_x^{L-1},n_y^{L-1}\right) &= I^{L-1}\left(n_x^{L-1}-1,n_y^{L-1}-1\right).
\end{aligned}
\tag{3.15}
$$

With this definition, the image width and height at the current pyramidal level are based on the computed values from n_x^{L-1} and n_y^{L-1} at the previous level of the pyramid (where the resolution is higher) and the smallest integers not less than these computed values are taken to be image width n_x^L and height n_y^L:

$$
\begin{aligned}
n_x^L &= \left\lceil \frac{n_x^{L-1}+1}{3} \right\rceil, \\
n_y^L &= \left\lceil \frac{n_y^{L-1}+1}{3} \right\rceil.
\end{aligned}
\tag{3.16}
$$

Equations 3.14, 3.15 and 3.16 are used to recursively construct the pyramidal representations of the two images I and J: $\{I^L\}_{L=0,\ldots,L_m}$ and $\{J^L\}_{L=0,\ldots,L_m}$. The height of the pyramid is set by the number of levels $L_m - 1$.

3.5.3 Pyramidal Feature Tracking

We define the position field $\vec{u}^L = \left(u_x^L, u_y^L\right)$ of I at a generic pyramidal level L, and try to find its updated position $\vec{v} = \vec{p} + \vec{d}$ of image J. In our setup, the lowest level of the pyramid is affixed with the largest level number $L = L_m$ all the way to the lowest level $L = 0$. The pyramidal tracking algorithm proceeds as follows: first, the optical flow is computed for image pertaining to the pyramidal level L_m. Next, this flow field is propagated to the next upper level $(L_m - 1)$ as the initial estimate information for pixel displacement. The refined optical flow field is then computed at this level and recursively passed to the next upper level until the optical flow based on original image is processed at $L = 0$.

Assume a generic pyramidal level L whereby the computed optical flow $\vec{g}^L = \left[g_x^L, g_y^L\right]^T$ is available from level L_m down to $(L+1)$ and based on previous calculations. The algorithm is initialised by setting $\vec{g}^L$ for level L_m to zero:

$$\vec{g}^{L_m} = [0,0]^T. \tag{3.17}$$

An interrogation window of size $(2w_x + 1) \times (2w_y + 1)$ is used for all L. The optical flow at level L is based on the residual pixel displacement vector $\vec{d}^L = \left[d_x^L, d_y^L\right]^T$ that minimises the new image matching error function ϵ^L:

$$\varepsilon^L\left(\vec{d}^L\right) = \varepsilon^L\left(d_x^L, d_y^L\right) = \sum_{x=u_x^L-w_x}^{u_x^L+w_x} \sum_{y=u_y^L-w_y}^{u_y^L+w_y} \left(I^L(x,y) - J^L(x + g_x^L + d_x^L, y + g_y^L + d_y^L)\right)^2. \tag{3.18}$$

The initial estimate flow vector $\vec{g}^L$ is used preliminarily to translate the image patch in image J. This restricts huge value fluctuations of flow vector $\vec{d}^L$. The result of this computation is propagated to the next level $(L-1)$ by passing the new initial estimate $\vec{g}^{L-1}$ of expression:

$$\vec{g}^{L-1} = 3\left(\vec{g}^L + \vec{d}^L\right). \tag{3.19}$$

The next new optical flow residual vector $\vec{d}^{L-1}$ is computed by minimising the function $\epsilon^{L-1}(\vec{d}^{L-1})$. This is recursively performed until the final optical flow field $\vec{d}$ is

processed for the highest resolution image:

$$\vec{d} = \vec{g^0} + \vec{d^0}. \tag{3.20}$$

The advantage of the pyramidal implementation is that each residual optical flow vector $\vec{d^L}$ can be of small values while computing a large, overall pixel displacement vector $\vec{d}$. Assuming that each elementary optical flow computation step can handle pixel motions up to $\vec{d}_{\max}$, then the final pixel motion by the algorithm will be $\vec{d}_{\max,\text{final}} = (2^{L_{m+1}} - 1)\vec{d}_{\max}$. The implementation thus enables multi-resolution pixel motions at different magnitude scales while keeping the size of the interrogation window constant.

3.5.4 Iterative Lucas Kanade Optical Flow

The aim of the optical flow algorithm is to find the vector $\vec{d^L}$ that minimises the match error function ϵ^L defined in Equation 3.18. We redefine the symbols that will be used in this section as follows:

$$\begin{aligned} \vec{p} &= \left[p_x, p_y\right]^T = \vec{u}^L, \\ \vec{v} &= \left[v_x, v_y\right]^T = \vec{d}^L. \end{aligned} \tag{3.21}$$

The domains of the images are modified and are now represented using:

$$\begin{aligned} \forall\,(x,y)\,\epsilon\,\left[p_x - w_x - 1, p_x + w_x + 1\right] \times \left[p_y - w_y - 1, p_y + w_y + 1\right], \\ A\,(x,y) = I^L\,(x,y)\,, \end{aligned} \tag{3.22}$$

$$\begin{aligned} \forall\,(x,y)\,\epsilon\,\left[p_x - w_x, p_x + w_x\right] \times \left[p_y - w_y, p_y + w_y\right], \\ B\,(x,y) = J^L\left(x + g_x^L, y + g_y^L\right). \end{aligned} \tag{3.23}$$

Note that $A(x,y)$ is defined over a window size of $(2w_x + 3) \times (2w_y + 3)$ instead of $(2w_x + 1) \times (2w_y + 1)$. This facilitates the computation of the spatial derivatives $I_x(x,y)$ and $I_y(x,y)$, which are numerically determined using the central difference operators in the x and y directions.

With the new symbols, the matching function now becomes

$$\varepsilon\,(\vec{v}) = \varepsilon\,(v_x, v_y) = \sum_{x=p_x-w_x}^{p_x+w_x} \sum_{y=p_y-w_y}^{p_y+w_y} \left(A(x,y) - B(x+v_x, y+v_y)\right)^2. \tag{3.24}$$

To minimise the matching function of Equation 3.18, a standard iterative Lucas Kanade optical flow algorithm can be applied. For optimum values of the matching function based on the flow field, the first derivative of ϵ with respect to $\vec{v}$ is set to zero:

$$\frac{\partial \varepsilon(\vec{v})}{\partial \vec{v}}|_{\vec{v}=\vec{v}_{opt}} = [0,0]\,. \tag{3.25}$$

Without delving further into displaying the steps for solving Equation 3.11 in detail, we use Equation 3.12, Equation 3.3 and Equation 3.3 that will give the optical flow vector solution:

$$\begin{aligned}\vec{v}_{opt} = &\begin{bmatrix} \sum_{k=1}^{N} I_x^2(x_k,y_k) & \sum_{k=1}^{N} I_x(x_k,y_k)I_y(x_k,y_k) \\ \sum_{k=1}^{N} I_x(x_k,y_k)I_y(x_k,y_k) & \sum_{k=1}^{N} I_y^2 x_k,y_k) \end{bmatrix} \\ &\times \begin{bmatrix} -\sum_{k=1}^{N} I_t(x_k,y_k)I_x(x_k,y_k) \\ -\sum_{k=1}^{N} I_t(x_k,y_k)I_x(x_k,y_k) \end{bmatrix}.\end{aligned} \tag{3.26}$$

Note that $(x_1,y_1),(x_2,y_2),\ldots,(x_N,y_N)$ are all the pixel coordinates that exist within the interrogation window of size $(2w_x+3)\times(2w_y+3)$. Expressing Equation 3.26 in terms of $\vec{p}$ and $\vec{w}$ gives

$$\begin{aligned}\vec{v}_{opt} = &\begin{bmatrix} \sum_{x=p_x-w_x}^{p_x+w_x}\sum_{y=p_y-w_y}^{p_y+w_y} I_x^2 & \sum_{x=p_x-w_x}^{p_x+w_x}\sum_{y=p_y-w_y}^{p_y+w_y} I_xI_y \\ \sum_{x=p_x-w_x}^{p_x+w_x}\sum_{y=p_y-w_y}^{p_y+w_y} I_xI_y & \sum_{x=p_x-w_x}^{p_x+w_x}\sum_{y=p_y-w_y}^{p_y+w_y} I_y^2 \end{bmatrix}^{-1} \\ &\times \begin{bmatrix} -\sum_{x=p_x-w_x}^{p_x+w_x}\sum_{y=p_y-w_y}^{p_y+w_y} I_tI_x \\ -\sum_{x=p_x-w_x}^{p_x+w_x}\sum_{y=p_y-w_y}^{p_y+w_y} I_tI_y \end{bmatrix}.\end{aligned} \tag{3.27}$$

Showing how its spatial derivatives $I_x(x,y)$ and $I_y(x,y)$ and temporal image derivatives $I_t(x,y)$ are calculated

$$\begin{aligned} &\forall\,(x,y)\,\epsilon\,[p_x-w_x,p_x+w_x]\times[p_y-w_y,p_y+w_y]\,, \\ I_x(x,y) &= \frac{\partial I(x,y)}{\partial x} = \frac{\partial A(x,y)}{\partial x} = \frac{A(x+1,y)-A(x-1,y)}{2}, \\ I_y(x,y) &= \frac{\partial I(x,y)}{\partial y} = \frac{\partial A(x,y)}{\partial y} = \frac{A(x,y+1)-A(x,y-1)}{2}, \\ I_t(x,y) &= \frac{\partial I(x,y)}{\partial t} = \frac{B(x,y+1)-A(x,y-1)}{1} = B(x,y)-A(x,y). \end{aligned} \tag{3.28}$$

To the optical flow solution, we iterate the procedure to solve $\vec{v}$ recursively using the Newton-Raphson scheme. We assign k as the iterative index where $\vec{v^k}$ is the pixel

displacement vector at the current state of iteration. Assume that the previous calculatons from iterations $1, 2, \ldots, k-1$ provide an initial estimate $\vec{v^{k-1}} = \left[v_x^{k-1}, v_y^{k-1}\right]$ for the pixel displacement $\vec{v^k}$. Then B^k will be the new translated image according to the pixel flow $\vec{v^{k-1}}$ that is based on previous iterations,

$$\begin{aligned} \forall\,(x,y)\,\epsilon\,[p_x - w_x, p_x + w_x] \times [p_y - w_y, p_y + w_y]\,, \\ B^k(x,y) = B(x + v_x^{k-1}, y + v_y^{k-1}). \end{aligned} \tag{3.29}$$

We define an error function such that the aim is to compute the residual pixel motion vector $\vec{\eta^k} = \left[\eta_x^k, \eta_y^k\right]$:

$$\varepsilon^k\left(\vec{\eta}^k\right) = \varepsilon\left(\eta_x^k, \eta_y^k\right) = \sum_{x=p_x-w_x}^{p_x+w_x} \sum_{y=p_y-w_y}^{p_y+w_y} \left(A(x,y) - B^k(x + \eta_x^k, y + \eta_y^k)\right)^2. \tag{3.30}$$

Now, the solution of the minimisation is computed using Equation 3.25

$$\begin{aligned} \vec{\eta}^k = & \begin{bmatrix} \sum_{x=p_x-w_x}^{p_x+w_x} \sum_{y=p_y-w_y}^{p_y+w_y} I_x^2 & \sum_{x=p_x-w_x}^{p_x+w_x} \sum_{y=p_y-w_y}^{p_y+w_y} I_x I_y \\ \sum_{x=p_x-w_x}^{p_x+w_x} \sum_{y=p_y-w_y}^{p_y+w_y} I_x I_y & \sum_{x=p_x-w_x}^{p_x+w_x} \sum_{y=p_y-w_y}^{p_y+w_y} I_y^2 \end{bmatrix}^{-1} \\ & \times \begin{bmatrix} -\sum_{x=p_x-w_x}^{p_x+w_x} \sum_{y=p_y-w_y}^{p_y+w_y} I_t^k I_x \\ -\sum_{x=p_x-w_x}^{p_x+w_x} \sum_{y=p_y-w_y}^{p_y+w_y} I_t^k I_y \end{bmatrix}. \end{aligned} \tag{3.31}$$

Note that the spatial derivates I_x and I_y remains the same, but the k^{th} temporal image derivative I_t^k is defined as follows:

$$\begin{aligned} \forall\,(x,y)\,\epsilon\,[p_x - w_x, p_x + w_x] \times [p_y - w_y, p_y + w_y]\,, \\ I_t^k(x,y) = B^k(x,y) - A(x,y). \end{aligned} \tag{3.32}$$

The computed values of $\vec{\eta^k}$ can be used to update the new pixel displacement estimate $\vec{v^k}$ based on the one obtained from the previous iteration:

$$\vec{v}^k = \vec{v}^{k-1} + \vec{\eta}^k. \tag{3.33}$$

The iterative scheme continues until the computed pixel residual $\vec{\eta^k} \leq \tau_1$ or maximum number of iteration $K \leq \tau$ whereby τ_1 and τ_2 are thresholds that are user-defined. At the first iteration $(k = 1)$, the initial pixel displacement is initialised to zero:

$$\vec{v}^0 = [0,0]^T. \tag{3.34}$$

After K number of iterations, the optimal optical flow vector solution is:

$$\vec{v} = \vec{d}^{L} = \vec{v}^{k} = \sum_{k=1}^{K} \vec{\eta}^{k}. \tag{3.35}$$

The vector d^L is used in Equation 3.19 and the overall procedure is repeated for all subsequent levels $L-1$, $L-2$,...,0.

3.6 Filtration of Flow Vector Outliers

We seek to devise a way of removing outliers in the flow vector field. Optical flow vectors that pertain to very large pixel displacements relative to that of the pixels in its adjacent region are isolated using the median test (Raffel *et al.* 1998). We perform clustering of optical flow vectors with magnitudes above a user defined threshold. The flow vectors within a cluster are classified as outliers provided that two conditions are fulfilled: (1) the difference between the vector magnitude U and the median magnitude U_m in the flow field of size (X, Y) exceeds a threshold denoted by τ_{mag} that can be arbitrarily set; and (2) the number of vector items within the group that is encapsulated by a sampling window size (W_x, W_y) that met the first condition do not fall below a specific value τ_n. The two conditions that qualify the vectors in the flow field as outliers are stated mathematically as follows:

$$\begin{aligned} &\forall\,(x,y)\,\epsilon\,\left[W_x \times W_y\right], \\ &|U(x,y) - U_m| > \tau_{\text{mag}}, \end{aligned} \tag{3.36}$$

$$\begin{aligned} &\forall\,(x,y)\,\epsilon\,\left[W_x \times W_y\right], \\ &\text{count}(|U(x,y) - U_m|) < \tau_n. \end{aligned} \tag{3.37}$$

Voids due to the removal of these outliers must be filled in with new vectors for the flow to be continuous. We devise a simple approach of growing vectors using a flow field synthesising approach. This technique is analogous to the occlusion fill-in algorithm used in texture synthesis by non-parametric sampling (Efros and Leung 1999) except that the sampled elements are flow vectors instead of texels (texture elements). We can also apply reduction in resolution to the flow field. The averaging of vectors within interrogation windows results in a lower resolution of flow field, but can help in smoothing of flow data by negating the effect of high magnitude outliers with more accurate vectors in its neighbourhood regions.

3.7 MR Fluid Motion Estimation Framework

3.7.1 Flow Estimation Using Magnetic Resonance Images

One of the primary objectives, from the perspective of functional medical imaging, is to produce a velocity map of blood flow in the human heart. It is known that at least one vortex is generated during diastolic filling (Kerwin *et al.* 2004). Imaging planar sections of the heart through the cardiac chambers is one of the requirements for tracking vortical blood flow, since a vortex can be best characterised if a sectional slice is taken orthogonal to the axis of rotation and presented in the plan view. Other views may not result in good qualitative characterisation of the flow structure. Therefore, only imaging at a certain specific planar sections of the cardiac chamber can achieve this. MRI scanning protocols allow imaging to be registered within the body at localised planar sections of specific depth and thickness. It also allows access to all anatomical regions in any orientation and is the best choice of imaging modality.

By harnessing the SSFP MRI modality (Plein *et al.* 2001, Merrifield *et al.* 2001, Gleeson *et al.* 2008), we establish the capability for overcoming limitations in flow measurements during scanning. In other words, although this method is unable to encode any velocity measurements, we can still deduce flow movement by assessing signal contrast representation of asynchronous blood proton spins that moves along with blood. We consider a new method of computationally predicting blood movement for planar slices of scan by application of motion estimation algorithm on MR images pertaining to two or more consecutive phases.

It also is worthwhile mentioning that cine-MRI can produce images pertaining to multiple phases of scan for continuous flow tracking throughout the entire cardiac cycle. Generally, retrospective ECG gating enables MR imaging modality to develop images of high temporal resolution. To register changes of a beating heart, data acquisition is gated to cardiac motion to generate a series of images spaced throughout the cardiac cycle. These images can be visually displayed in a cine loop to assess cardiac structures in real time. The capturing of multiple time frames of flow can provide information on the temporal variation of imaged blood within the heart through visual observation of the gray-scale scan images by following the shifting of intensity.

3.7.2 Non-Stationary Patterns of Varying Intensity in Cine-MRI

In the previous chapter, we discuss the non-uniform and temporal intensity of nuclear signal registration of chaotic flow due to de-phasing of the proton spins (Kuethe 1989, Lawson 1999). We also describe the nuclear characteristics of blood within the human heart that is quantum excited under the magnetic resonance scheme. It is also important to emphasise that in the heart chambers, the nuclear spins may move perpendicularly in and out of the imaging plane. Therefore, spins that receive the original excitation in turbulent flow may not experience magnetic resonance gradient refocusing. Likewise, spins that do not receive the original excitation may in fact move into the imaging plane after the RF excitation pulse, and since they are not quantum mechanically stimulated to begin with, no MR-signal may be returned. Extrapolating this concept further, some signal loss due to fast flowing jets is likely due to spins moving too quickly to be excited and refocused, creating signal voids (Lee 2005).

Due to the inhomogeneous presence of asynchronous proton spins, nuclear signals emitted from dynamic fluid appear on MR images as varying patterns of intensity depicting the blood flow movement. It is important to note that poor temporal and spatial resolution imaging may blur the observation of blood movement between consecutive images. For some phases of scans, the presence of low-turbulent regions may also weaken the intensity contrast variation in blood images, so that visual tracking of blood motion declines in accuracy.

3.7.3 Motion Estimation of MR-Signals

A series of MR images are presented in cine-mode as the fluid is in motion. The velocity of dynamic fluid is quantified in real time by numerically computing the shift of intensities within the quantised regions of each set of temporally consecutive images. A velocity flow field can be constructed using a graphical plot and other fluid dynamics properties can be derived from the velocity flow measurement. From the results, the characteristics of the fluid flow can be analysed using these properties.

We can computationally determine the movement of fluid in a vessel based on motion estimation of the contrasting MR-signals. The motion of localised turbulence is influenced by the general flow globally. Motion estimation using multi-resolution optical flow technique is able to track the movement of the flow at various resolutions and resolve them to produce a global flow field in two dimensions. Therefore, we term

this approach MR fluid motion estimation, as it is able to compute the motion of MR imaged fluid.

Application of flow based on the use of motion estimation algorithm (Lucas and Kanade 1981, Bergen *et al.* 1992, Barron *et al.* 1994, Bouguet 2000) allows us to produce flow vectors over the region of defined analysis. This technique makes use of images from two subsequent phases to predict the flow field. Typically, cine MRI scanning results in a sequence of N phases. Post-processing of the data from $(N-1)$ pairs of images gives a series of flow field displays for evaluation and analysis. As such, predicting the ensemble movement of asynchronous proton spins represented in magnetic resonance images of a heart chamber can be technically feasible (Figure 3.3).

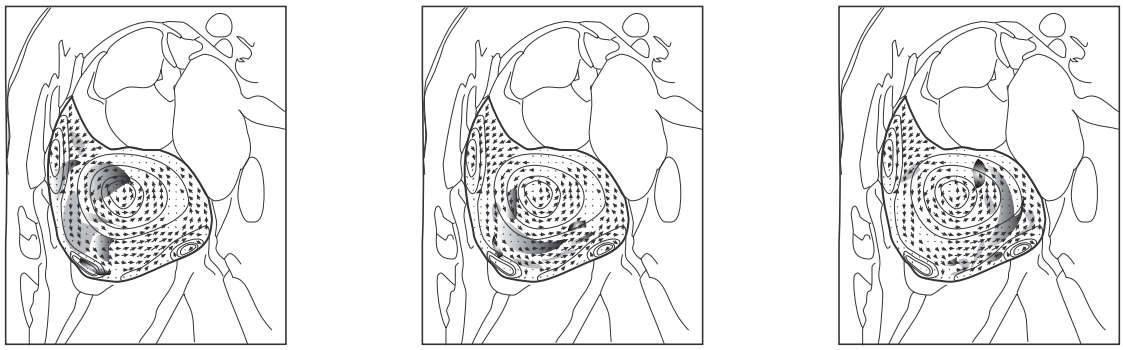

(a) phase (n-1) of N (b) phase n of N (b) phase (n+1) of N

Figure 3.3. Motion estimation of in-plane MR-signals. Based on schematic display of a right atrial flow, the ensembles of asynchronous proton spins that show up as contrasting signal intensity on the cine-magnetic resonance images are represented by grey patches of varying intensity. Using a fluid motion estimation scheme, velocity vector fields pertaining to the blood flow images of arbitrary (n-1), n and (n+1) phases in a cardiac cycle of N phases can be predicted.

3.7.4 Effect of Scan Resolution and Image Quality

A magnetic resonance image is reconstructed using every pixel, where gray-scale intensity (brightness) is proportional to the amplitude of MR signal that corresponds to volume element of specific dimensions in the slice. Therefore, the low turbulent regions will have a higher signal intensity emitted by the region of voxels (or three-dimensional pixels) to contribute brighter pixels in the image. Note that the voxel volume is defined as the pixel area multipied by the slice thickness (Mudry *et al.* 2003).

On the contrary, higher turbulence results in de-phasing of spins within the voxels and tends to reduce the signal intensity that shows up as the darker pixels (Kuethe 1989).

We suggest that for signal emitting nuclei motion that are represented by intensity pixels on MR images, the application of multi-resolution optical flow scheme predicts fluid motion based on grey-level constancy assumption (optical flow constraint). In magnetic resonance imaging terminology, field of view (FOV) is defined as the size of the two- or three-dimensional spatial encoding region of the image, and is usually defined in units of mm. MR imaging spatial resolution (mm/pixel) is defined as the ratio of field of view (mm) to image matrix (pixels). If the imaging resolution improves, more details can be captured within the scanned image and a higher collection of MR signals can be registered per unit area of the magnetic resonance imaged flow. Spatial resolution defines the capability of resolving the turbulent flow details. MR signals from a voxel are collectively averaged and result in loss of micro-turbulence details smaller than the voxel of nuclear information. Therefore, the dimension of the voxel determines the smallest scale of turbulence in fluid that can be registered onto image. Due to aliasing and attenuation, this scale of turbulence may be several voxels wide.

The accuracy of tracking signal motions is dependent on the quality and resolution of the signals represented onto magnetic resonance images. A larger area of measurement scope will give a higher quality of flow field production since a greater information set of signal pixels can be utilised for motion estimation. Ideally, the series of images that will be useful for fluid motion tracking should have a high signal-to-noise ratio, high spatial resolution, superior soft tissue contrast and no ghosting artifacts; which however, comes at the expense of imaging time (Phillips 1984). Noise in MR images is the result of thermally driven Brownian motion of electrons present in the conducting body or even within the receiving coil itself (Redpath 1998). Spatial resolution increases at the cost of reducing signal-to-noise ratio.

3.7.5 MR Fluid Velocity Field

We will describe the implementation of blood motion estimation within a heart based on application of multi-resolution optical flow on cardiac MRI. The motion estimation algorithm proceeds as follows: first, the optical flow is computed at the coarsest pyramid level. Then the result of that computation is propagated to the next level in the

form of an initial estimate for pixel displacement, and this is carried on until the original resolution of the image is reached. The velocity fields of blood in cardiac chambers is provided on a two-dimensional grid. In the visualisation pipeline, we present the flow of time dependent blood movement in a segmented chamber using velocity field plot. In our proposed framework, the scheme computationally measures *intensity flow* based on moving patterns of low nuclear signal blood from MRI and presents a two-dimensional velocity field of user-defined variable resolution. The mathematical details of pyramidal optical flow are outlined in Section 3.5. Note that the averaging of velocity components within sampling frames can be performed to vary the coarseness of the velocity field. Therefore, a dense velocity field of one velocity vector per pixel is computed and a vector averaging for sampling window resolution of w_x by w_y pixels is carried out.

The *field of view* (FOV) with width n_x and height n_y captures the cross-sectional image of a heart and store the anatomical spatial information in a M *row* by N *column* matrix. If the FOV is based on units of millimeters (mm), we can compute the dimension of a single pixel $p = [p_x, p_y]$ in mm as the *pixel spacing* by the formula

$$p = [p_x, p_y] = \left[\frac{n_x}{M}, \frac{n_y}{N}\right]. \tag{3.38}$$

Assuming that the displacement of multiple pixels is given by d_x and d_y in the x and y directions respectively for larger motion. If the time expended during a scan is denoted by t_s in units of milliseconds (ms) , then velocity of the pixel displacement that is denoted by $V = [v_x, v_y]$ is given in units of mms^{-1} using:

$$V = [v_x, v_y] = \left[\frac{d_x p_x}{t_s}, \frac{d_y p_y}{t_s}\right] \times 10^3. \tag{3.39}$$

Note that the imaging time interval may be calculated by taking the *trigger time* of the current scan minus that for the previous scan. The velocity measures that we suggest are computed from the pixel displacement vectors in the motion field. By applying Equation 3.39, we obtain flow velocities in SI units. MRI images are provided in Digital Imaging and Communications in Medicine (DICOM) format. The *field of view* (FOV), *row*, *column*, *pixel spacing* and *trigger time* information can be extracted from DICOM format tags according to the Table 4.1.

MRI DICOM INFORMATION			
Name	Group (G)	Element (E)	Value
TriggerTime	0018	1060	DS
FieldofViewDimension(s)	0018	1149	IS
Rows	0028	0010	US
Columns	0028	0011	US
PixelSpacing	0028	0030	DS

Table 3.1. MRI DICOM information used for calibration of MR fluid motion. MRI DICOM tags group and element information are used to assess scan parameters to scale MR fluid motion quantities into SI metrics units. In DICOM, a data element tag is represented as (G,E), where G equates to the group number and E equates to the element number within that group. Data element tags are represented in hexadecimal notation as specified for each named element in this standard.

3.8 MR Fluid Motion Tracking System Implementation

In this section, we implement the MR fluid motion tracking. It is essential to establish a network of sub-components such that each of the components has a role in preparing the flow image results. The system layout of MR fluid motion tracking is presented in Figure 3.4[12]. The framework serves to produce flow maps of the blood within cardiac chamber that are obtained from MRI of the heart. The core functionality of the system is the visualisation of blood flow. Observation of the vector field generated by the system can assist in identifying flow structures such as vortices or any other interesting flow patterns.

The procedures executed by the system of components are outlined as follows. During pre-processing, we perform imaging of the heart using an MRI Scanner and then store all scan information in the *Disk Drive*. The MR images can be retrieved via a *Receiver* for post-processing at a later stage of the system. Basically, segmentation of the region of interest is semi-automatically determined with external peripherals such as the *Mouse* and *Keyboard*. Tracking of moving signals encoded onto the MR images is carried out by *Motion Estimation* component. The flow field is scaled and displayed via a suitable *Display Element* that can be a *Projector* or *Monitor*. Optionally, other measures of flow such as the vorticity and strain maps can be computed with the *Calculating*

[12]This diagram and the mentioning of its mechanism is adapted from the patent application PCT/AU/2007/000827.dated 15th June 2007

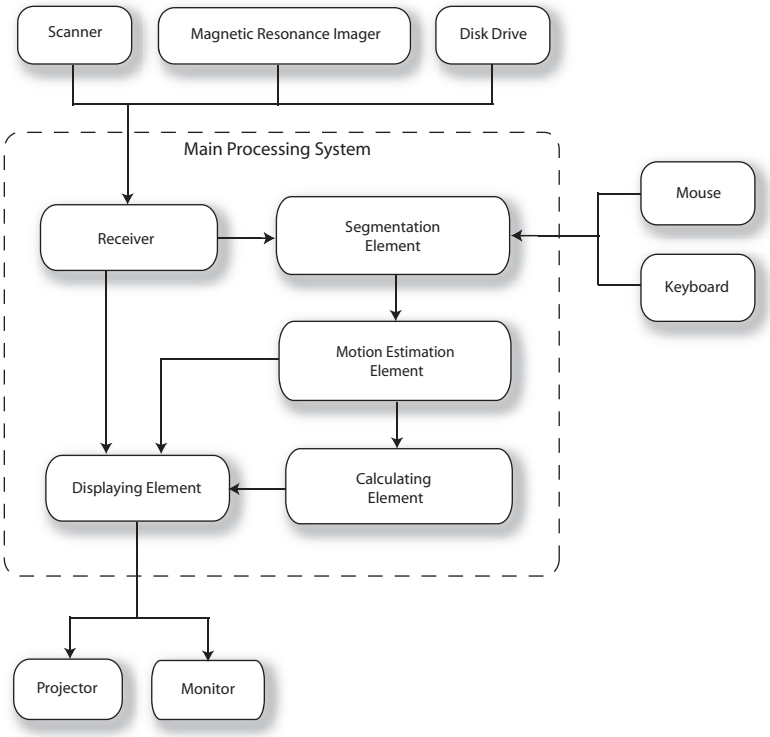

Figure 3.4. Components of MR fluid motion tracking system. In this embodiment diagram, MR images can be taken at two or more different times via a magnetic resonance imager or scanner. The images are then received by a receiver residing in software on a processor. The segmentation element excludes non-fluid or non-relevant structures from analysis of blood flow. The segmentation element allows a user to assist in the segmentation process via an input device such as a keyboard or mouse. Motion estimation algorithm is applied to the images to produce a flow vector field for the fluid, which can be displayed, along with the images, by a display element. Communication with a projector or monitor displays the predicted flow field and/or images.

Element and implemented for analysis. Note that the *Receiver, Segmentation, Motion Estimation, Calculating* and *Display Elements* forms the *Main Processing System* of this velocimetry framework. The components within this processing system are utilised for post-processing MR images. Outside of the motion field or are the physical hardware that facilitates the MR scanning, user inputs and display.

3.9 Discussion

In motion estimation of non-rigid motion such as MR-signal features, we expect to see a wide variation in signal flow behaviour ranging from elastic deformation and segregation to non-uniform volume changes. Motion perception by humans is a natural, well-evolved capability with the facility to rapidly categorise relative motion among fluid structures with respect to multiple coordinate systems. The challenge, therefore, is to develop a fluid motion tracking system that can automatically detect such complex flow.

We provide a framework that enables the development of MR fluid motion tracking such that a successful application of this technique may be able to perform computational flow prediction of blood motion based on nuclear signals measured using magnetic resonance imaging. Estimating motion by harnessing image signals of varying spatio-temporal intensity can be achieved. This theory can be based on observations which we can deduce with our intuitive understanding of visual motion registration. In the context of magnetic resonance signals and based on our knowledge of identifying motion by referencing and contrasting moving light sources, we can state Observations 1 and 2 such that:

Observation 1: *The movement of lines of light can also be perceived as the movement of line shadows on the illuminated background. In our world of vision, light and darkness are the signals of opposite extremities that are used in determining motion.*

Observation 2: *When looking at blood movement in magnetic resonance images of the heart, it is a mixture of observing moving dark shadows of asynchonous proton spins among the bright imaged blood and moving bright shadows of synchronous spins among the black imaged blood.*

However, a reliable computerised system is crucial for the image analysis, especially when the images are displayed at rates higher than human-assisted visual review processes. These two observations form the fundamentals for developing the computational motion estimation that we outline in this study and ultimately leads us to the application of tracking magnetic resonating blood to develop cardiac flow velocity fields.

Some issues still exist at this stage of development. The processing of a smooth velocity field using poor spatial and temporal resolutions image that has large blood

motion displacement causes the flow fields to have a serious degrees of inaccuracies due to the presence of vector outliers. Other than improving the scan quality, one possible solution to address this issues is the use of multiple frames for computing the pixel displacements. While these solutions form the basis for further research in the measurement of visual motion, we highlight that our technique can be readily applicable to the fluid motion tracking using magnetic resonance images provided that proper adjustment of tracking parameters is carried out. Therefore, the current system methodology is used for cardiac flow field measurements as a demonstration of the present theories. We apply a model supported with fundamental concepts to prove its workability. Further developmental suggestions for the system are mentioned in Chapter 9.

3.10 Chapter Summary

This chapter describes a computational framework for the determination of velocity fields based on concomitant image scans. Using this technique, we develop a method for fluid motion tracking of cardiac flow which uses magnetic resonance images.

The next chapter will discuss computation testing of the intensity flow tracking based on the mathematical framework that we provide. Equally important are imaging considerations, such as improvement of quality scans from the modalities, as well as algorithms for accurately processing the velocity information and checking the reliability of the flow tracking. For example, the use of well-established velocity-encoding magnetic resonance imaging can provide reference data for validating the accuracy of fluid motion tracking in Chapter 7. A lot of development is still needed to bring the proposed system to an acceptable standard for use in biomedical image processing. Our work has provided a preliminary working platform for the implementation of these future improvements.

Chapter 4

Computational Validation of Fluid Motion Tracking

CONFIGURATION of the techniques involved in the verification of MR fluid motion tracking based on synthetic gray-scale intensity image data is presented. The computational validation of a system is crucial in any system development and, therefore, the experiments outlined here can deduce if the proposed fluid motion tracking complies with the idealised tracking results. Key parameters designed for modification to the system specifications and assessment of the resulting performance is performed.

A comparison of vector fields generated by analytical and computational methods is presented and the results have demonstrated the successful performance of the system along with its limitations. The testing and validation of MR fluid motion tracking has contributed to proof of system reliability and robustness.

4.1 Introduction

Motion tracking based on spatial-temporal radio-frequency signals from the pixel representation of magnetic resonance imaging (MRI) of a non-stationary fluid is able to provide two-dimensional vector field maps. This supports the underlying fundamentals of magnetic resonance (MR) fluid motion estimation and generates a new methodology for flow measurement that is based on registration of nuclear signals from moving hydrogen nuclei in fluid. However, there is a need to validate the computational aspect of the approach by using velocity flow field data that we will assume as the true reference information or ground truth.

In this study, we create flow vectors based on an ideal analytical vortex, and generate artificial signal-motion image data to verify our computational approach. The analytical and computed flow fields are compared to provide an error estimate of our methodology. The comparison shows that the fluid motion estimation approach using simulated magnetic resonance data is accurate and robust enough for flow field mapping. The results of this work will allow us to progress further in the investigation of fluid motion prediction based on imaging modalities that do not require velocity encoding.

4.2 Data Generation

The validation of a proposed or an implemented system can be achieved if analytical data can be created to calibrate its performance deviation from the perfect situation. We can thereby understand its characteristics and make necessary improvements to the configuration. This section presents the equations for describing analytical flow field that will be used in our system performance calibration.

4.2.1 Analytical Formulation of Vortex

The Lamb-Oseen vortex (Saffman 1992, Meunier *et al.* 2005, Cariteau and Flór 2006) is a theoretical model of the realistic vortex by analytically defining its velocity, vorticity, and circulation. The mathematical presentation of the vortex by Meunier *et al.* (2005) is such that Γ is the circulation, and a is the characteristic core radius. The definition of the angular velocity $\omega(r)$ is expressed by Equation 4.1 as

$$\omega(r) = \frac{\Gamma}{\pi a^2}\left(e^{-\frac{r^2}{a^2}}\right). \tag{4.1}$$

The tangential velocity $v_\theta(r)$ is a function of r in Equation 4.2 such that

$$v_\theta(r) = \frac{\Gamma}{2\pi r}\left(1 - e^{-\frac{r^2}{a^2}}\right). \tag{4.2}$$

The parameters for the data generation are based on $\Gamma = 1$ mm^{2}s^{-1}, and $a = 1$ mm. The size of the vortex image is set as 20 mm by 20 mm in our case. We can digitise the analytic velocity field over an image grid with each coordinate denoted by (x, y), and with velocity interrogation spacing Δ to produce a velocity vector flow field that is given by (u, v). This allows the effect of velocity field resolution based on the analytical data produced for our computational approach to be quantified. The velocity profiles generated by these equations are plotted as a function of r in Figure 4.1. The angular and tangential velocities vary with respect to the radius of the vortex and their magnitudes can be represented using gray-scale intensity. Note that the tangential velocity at the core is zero despite having a finite vorticity. The velocities ω and v_θ vary from 0 to maximum values of $\omega_{\max}$ and $v_{\theta\max}$ respectively.

4.2.2 Generating Vortex Tracks for Artificial Data

We map the analytical velocity field onto a rotational grid to generate discrete vortical tracks with radial intervals in polar coordinates. We shade alternatively spaced intervals and use the gray-scale intensity based image configuration as test data for the fluid motion estimation technique. The spatial dimensions of the track intervals can be varied to quantify the error due to decrement of feature quality.

The contrasting intensity for alternating track intervals provides track features for the motion estimation algorithm in this experiment. The motion of the grid is then represented using a series of these intensity based images, which display the change in positions of the segments according to each track angular velocity to give an optical effect of the rotation. This causes track rings corresponding to specific radial locations to rotate at different speeds uniformly and according to the profile of the angular velocity in Figure 4.2. Such a configuration gives a velocity profile that has discrete values. It is then possible to quantify this rotation from the optical perspective using established motion-tracking algorithms.

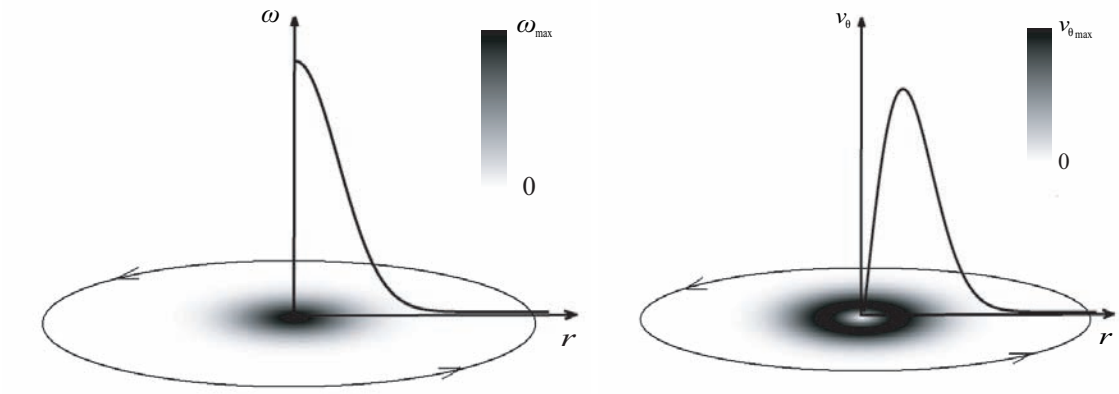

(a) Angular Velocity (b) Tangential Velocity

Figure 4.1. Velocity characteristics of a Lamb-Oseen vortex. Variation of profiles with respect to vortex radius r is shown for the angular and tangential velocities labelled as ω and v_θ in (a) and (b) respectively. The velocity profile for the vortex angular and tangential components can be illustrated using varying gray-scale intensity. We plot the variation of the presented vortex based on analytical formulations (Equations 4.1 and 4.2).

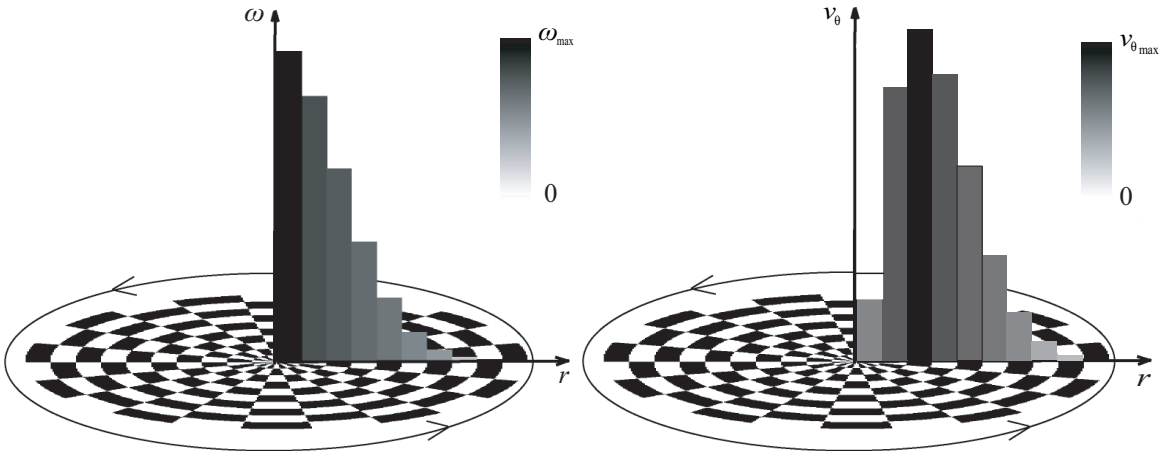

(a) Angular Velocity (b) Tangential Velocity

Figure 4.2. Artificial flow grid based on Lamb-Oseen vortex formulation. Gray-scale intensity based polar grid with alternating contrast track intervals in a rotational fashion representing the vortical tracks of motion is demonstrated with (a) and (b) describing the variation of angular and tangential velocities respectively. The velocity variation is discrete based on the configuration of the grid, which is constructed using alternating dark and bright segments in the radial and angular directions.

4.2.3 Variation of Vortical Track Interval Size

We vary the resolution of track intervals in the vortex to investigate flow tracking accuracy of fluid motion estimation. This may be achieved by varying the spatial density of contrasting grid intervals pertaining to vortical track items of the intensity image in the polar directions. We define the count of track intervals within the entire polar grid to be ν so that

$$\nu = \rho(r)\lambda(\theta) \tag{4.3}$$

and $\rho(r)$ and $\lambda(\theta)$ denote the number of tracks and radial sections respectively at each configuration of the vortical tracks.

4.2.4 Configuration of Tracking Features

The configuration of the polar grid can be modified by using a few parameters. Variation of vortical track intervals can be performed by setting different values of λ for the same image size. In this experiment, the number of tracks ρ is set as a constant. The total number of track intervals varies according to only one parameter as a result. For simpilicty, only three different configurations or levels are chosen to demonstrate the effect of decrease in track intervals and a corresponding increase in their numbers.

The configuration of the polar grid will affect the feature quality used in our tracking experiments. This has to coincide with the settings of the motion estimation algorithm. We design three parameters for conducting our error estimates of the computational approach. The algorithm's sampling size W is varied with increments of 1 pixel from 2 to 20 pixels along with the same number of increments of image size, I at 10 pixels from 160 to 320 pixels. We specify the number of tracks ρ and radial sections λ for levels 1 to 3 as tabulated in Table 4.1.

This track layout is designed to allow the contrasting intensity segments to fall within the algorithm's sampling or interrogation window during tracking. Therefore, the size and numbers of these track segments relative to the sampling window affects the performance of the motion estimation algorithm.

A higher value of λ or more sectioning of the polar grid into tracks at angular intervals gives a smaller track-interval size, and generates finer features that are densely located near the core of rotation. This corresponds to more intensity based track features but at the expense of quality reduction, which has an effect on tracking accuracy of the fluid

TRACK GRID RESOLUTION			
level	ρ	λ	ν
1	20	10	200
2	20	22	440
3	20	30	600

level Identification number of configuration
ρ Number of tracks
λ Number of vortical track intervals
ν Total number of track intervals

Table 4.1. Configuration characteristic of gray-scale track grid. Variation of ρ and λ will adjust the density of the signal features used in motion tracking. The number of track intervals is an indication of the resolution of features in the track grid represented as an image.

motion estimation. Adjustment to the optical flow algorithm, such as the sampling window size, can be carried out to improve tracking.

4.2.5 Variation of Image and Optical Flow Window Size

We demonstrate the effect of the test image size, denoted by I, and also the pyramidal window size, W on the accuracy of the optical flow algorithm. We increase the resolution of the track outlines using increments of image size. Therefore, a larger image size will result in a higher resolution image and quality of features used for tracking. The improvement in quality of signals will have an effect on tracking. Further increasing the size of the sampling window, which is the interrogation mask used in the tracking, will capture a larger quantity of the signals, but at the expense of overly smoothing the velocity flow field due to the larger relative size of the sampling window with respect to the image.

4.2.6 Variation of Noise Addition and Smoothing Filter Mask Size

In a separate study, we use a standard test intensity image. We apply multiplicative Gaussian noise to the image at various percentages, followed by smoothing using a filter based on pixels averaging within a mask of size n. The addition of noise to the images causes the tracking to lose accuracy; however, smoothing of the images subsequently suppresses noise and reduces the error. Nevertheless, there is still a specific

threshold to the addition of noise such that this suppression is able to still maintain accurate tracking.

4.3 Computational and Analytical Data Differencing

Our objective is to compare the velocity field estimate with that of the analytical one based on the direction and magnitude of the vectors represented using a flow image, whereby every pixel stores each of the velocity in the x and y directions. Note that the spatial resolutions of analytical and computational flow images have to be the same for flow image differencing to take place.

4.3.1 Fluid Motion Estimation Flow Predictions

In Chapter 3, we describe the operation of fluid motion tracking system, and its optical flow computation that produces flow map at the pixel resolution; wherein, a dense velocity field (one velocity vector per pixel) is generated. An applied computer algorithm (Stavens 2008) enables the multi-resolution Lucas Kanade feature tracker. We also implement removal of outliers that we classify as high magnitude flow vectors. Replacement of void flow vectors from this removal is performed, by means of image field synthesis from neighbourhood flow maps, using the texture synthesis concept previously described in Chapter 3. Then, calculated vectors are scaled to match the analytical vector set.

4.3.2 Magnitude of Velocity Vectors in Radial Direction

For a track grid of radius R, the average magnitude of tangential vectors (from various angles) obtained from the track location, which is extended by a circumference of radius r, is compared with the analytical velocity magnitude based on the same radius of r. For each track at that radius, the computational velocity is computed by taking the average of N_θ number of tangential velocity vectors arranged circumferentially about the centre of rotation. This procedure is performed based on N_r number of r variables from the vortex centre to edge of the computational domain up to R. Note that V_θ^a and V_θ^c represent the analytical and computational tangential velocity respectively. Error based on the difference between the computational velocity and the analytical velocity

at the defined polar coordinates can be generated using

$$\Delta(r) = \left(\frac{1}{K_\theta} \sum_{k=1}^{K_\theta} V_\theta^c(r, \frac{2n\pi}{N_\theta}) \right) - V_\theta^a(r),$$
$$\text{for} \quad r = (1, 2, , N_r) \times \frac{R}{N_r}. \tag{4.4}$$

A graph of Δ_r versus r can be produced for detecting regions of unacceptable errors due to image signal aliasing, which usually results from poor definition of closely packed track features.

4.3.3 Magnitude of Velocity Vectors in Image Representation

The average magnitude of tangential vectors is compared with the analytical velocity magnitude at every coordinate (x, y) where (I_x, I_x) is the size of the flow field in the x and y directions. Note that (u^a, v^a) and (u^c, v^c) represent the velocity in the x and y directions pertaining to the analytical and computational velocity image grid respectively. The error function based on $\Delta_v(\%)$ for u and v velocity components at every x and y coordinates is given by

$$\Delta_v(\%) = \frac{1}{I_x I_y} \sum_{x=1}^{I_x} \sum_{y=1}^{I_y} \frac{\sqrt{(u_{x,y}^c - u_{x,y}^a)^2 + (v_{x,y}^c - v_{x,y}^a)^2}}{V_{\max}^a} \times 100\%$$
$$\text{where} \quad V_{\max}^a = \max \sqrt{(u_{x,y}^a)^2 + (v_{x,y}^a)^2}$$
$$\text{for} \quad 1 \leq x \leq I_x, 1 \leq y \leq I_y. \tag{4.5}$$

The system response that is based on $\Delta_v(\%)$ can be plotted. This error value will be high if sampling window sizes that falls below a specific threshold value. The mismatch of interrogation sampling window sizes with respect to image size will result in sub-optimal tracking accuracy.

4.3.4 Direction of Velocity Vectors in Image Representation

We take the angular difference in the sets of flow vectors produced using two different systems by performing the following mathematical operation to produce the average

of all absolute angular vector differences in percentage, $\Delta_\theta(\%)$ where θ^a and θ^c represent the orientation of vectors for analytical and computational flow fields respectively. The difference between the computed and the Lamb-Oseen vortex velocity values is

$$\Delta_\theta(\%) = \frac{1}{I_x I_y} \sum_{x=1}^{I_x} \sum_{y=1}^{I_y} \frac{\left|\left(\left|\theta^c_{x,y}\right| - \left|\theta^a_{x,y}\right|\right)\right|}{\theta^{c-a}_{\max}} \times 100\%$$

$$\text{where} \quad \theta^{c-a}_{\max} = \max \left|\left(\left|\theta^c_{x,y}\right| - \left|\theta^a_{x,y}\right|\right)\right|$$

$$\text{for} \quad 1 \leq x \leq I_x, 1 \leq y \leq I_y \quad \text{and} \quad -\pi \leq \theta^a_{x,y} \leq \pi, -\pi \leq \theta^c_{x,y} \leq \pi. \tag{4.6}$$

Graphing this error function for variation of image size I and sampling window size W demonstrates the dependency of feature quality on the increment in image size, and the required increase in sampling window for good tracking.

4.4 Computational Versus Analytical Results

Here, we describe the results of velocity field estimates based on variation of the various parameters mentioned in the previous sections. The aim of this study is to evaluate the performance of fluid motion tracking in terms of computational accuracy.

4.4.1 Velocity in Image Representation

An error analysis is carried out to give an indication of the angular difference of the analytical and computational results. We prepare the graph that depicts the influence of image and sampling window sizes on the discrepancies in the flow vectors for analytical and computational flow results.

High fluctuation of error estimates exist due to small sampling window sizes with dimensions of 2 to 10 pixels (Figure 4.3). Such sampling configurations are undesirable for the motion tracking algorithm. The increment of sizes from sampling window widths of 11 pixels onwards shows relatively small variation in the tracking accuracy.

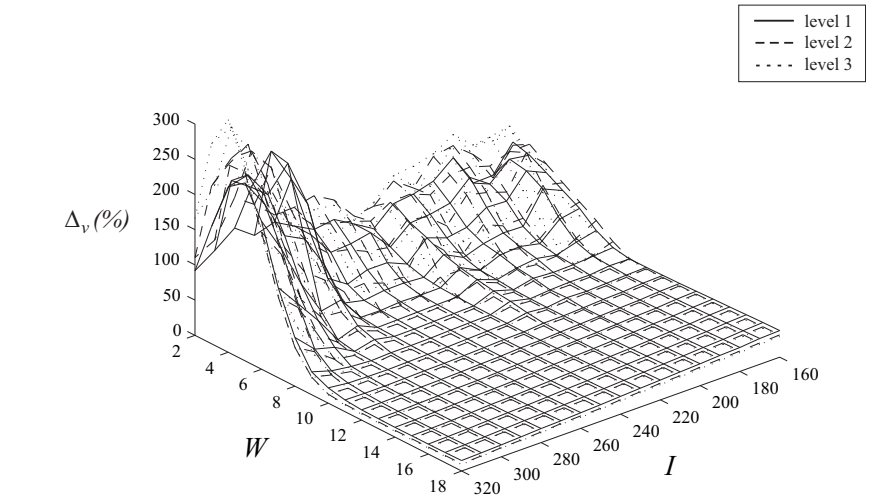

(a) Sampling window size from 2 to 18 pixels

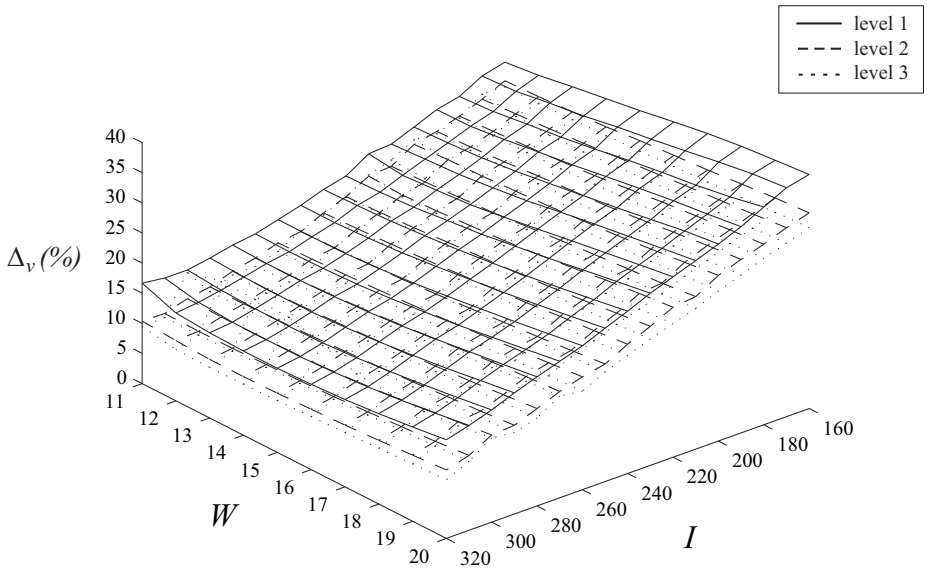

(b) Sampling window size from 11 to 20 pixels

Figure 4.3. Tracking accuracy based on tangential velocities. Flow vector velocity differences based on variation of sampling window size versus image size with different levels of track interval sizes are demonstrated. In this experiment, the sampling window and raw image size dimensions are varied to analyse the tracking effect of the system. Parts (a) and (b) show the results using different ranges of sampling windows. The results demonstrate that tracking improves when the image size increases. That can be accredited to the increase in resolution and corresponding upgrade of the quality of track features.

Larger image sizes give a reduction in error estimates and can be further reduced by a corresponding increment in the sampling window dimension used by the algorithm for image sizes from 260 by 260 pixels onwards (Figure 4.4). The improvement in tracking accuracy due to increase in image size can be explained by enhancement of feature quality due to larger number of pixels used to represent varying space of high and low intensity track intervals. In addition, we can further deduce that an increase of sampling window size, which will encapsulate more features within its interrogation region, will improve tracking accuracy.

Values of image size I and sampling window size W at the upper and lower limits of I and W of our computational domains causes high errors (Figure 4.3 (a) and Figure 4.4 (a)). Note that I and W at the lower and upper limits of the same domains also results in relatively high errors (Figure 4.3 (b) and Figure 4.4 (b)). Both I and W at the upper limits of the domains respectively give the smallest error. There is a reduction in error following an increase in image size. However, for large images, coupling with a proportionally incremented sampling window size used in motion estimation can further reduce error.

4.4.2 Velocity in Radial Direction

We observe the deviation of computational velocities from the analytical ones in the radial direction based on different resolution, noise and smoothing of the artificial intensity track grids that we have mentioned in Section 4.2.2.

Variation of Track Feature Resolution

Motion estimation is performed using a sampling window size of 20 by 20 pixels for a 260 by 260 pixel image. These dimensions are arbitrarily chosen such that the size of the image is 13 times that of the sampling window. The image is a spatial representation of the circular track grid based on three configurations (labeled as levels 1 to 3). A series of images can provide temporal representation of the intensity grid that is rotating. The image and sampling configurations have been set in such a way that the computational profile of the velocity tracking clearly deviates from the analytical one and can give a good illustration of how the track density can affect the motion estimation. Therefore, it is irrelevant to set high image resolutions for achieving accurate tracking here.

We sample the tangential velocity values in the radial directions for N_θ at 10 counts from 0 to 360 degrees at an interval of 36 degrees circumferentially about the centre of rotation. The counts N_r are taken to be 50 samples from $r = 0$ to 5 mm at intervals of 0.1 mm. Note that velocities V_θ and Δ_{V_θ} both have units of mms^{-1}. For a standard comparison, we scale the maximum peak velocity to be 10 mms^{-1}.

Our analysis is based on 10 samples taken in the angular direction. The accuracy of profile of computational velocities can be increased by more sampling. We observe that as spatial density of the tracks increases from levels 1 to 3, average error becomes smaller for radius ranging from 1 to 5 mm due to increment of track features. However, if the track layout becomes too compact from radius 0 to 0.5 mm, error increases due to poor feature quality.

The results demonstrate that the tracking accuracy decreases in regions towards the centre as the grid intervals become denser (Figure 4.5). However, where definition of the tracks becomes clearer due to wider spacing, tracking improves. Increase in track quality can enhance tracking capabilities, but is limited to regions away from the vortex centre. Degradation of track features quality results in higher deviation from the true flow field; nevertheless, it is able to give a more moderate variation of this error and also prevent signal aliasing in the compact grid region.

Variation of Noise and Smoothing

Using the same experimental setup as in the previous section, we analyse the accuracy of profile of computational velocity decline as a result of the addition of noise to images used in tracking, and tried to understand the balance between suppression of noise and loss of signal features due to smoothing. It may be worthwhile noting that we are also interested in examining the tracking effectiveness due to blur track features as well. For this reason, we implement the mean filter for reduction of noise by blurring the image.

We apply different smoothing filter masks at (1×1), (5×5), and (9×9) pixel frames. Gaussian noise is added to the images at percentages (%) of 0, 10, 30, and 50 incrementally. Note that the overall average error increases for radii ranging from 1 to 5 mm for every stage of additional noise input into the images. However, when smoothing is applied, the velocity profile improves in accuracy with respect to the analytical one as a result of the suppression of noise signals. This can be illustrated by parts (a) to (h) of Figure 4.6. Velocity and error profiles derived from tracking are based on 0, 10, and

30% noise addition to image. We also observe that for higher noise added to images, with percentages such as 30% to 50%, over smoothing using a (9×9) pixel filter mask size reduces the tracking accuracy relative to that when a (5×5) pixel smoothing mask is applied.

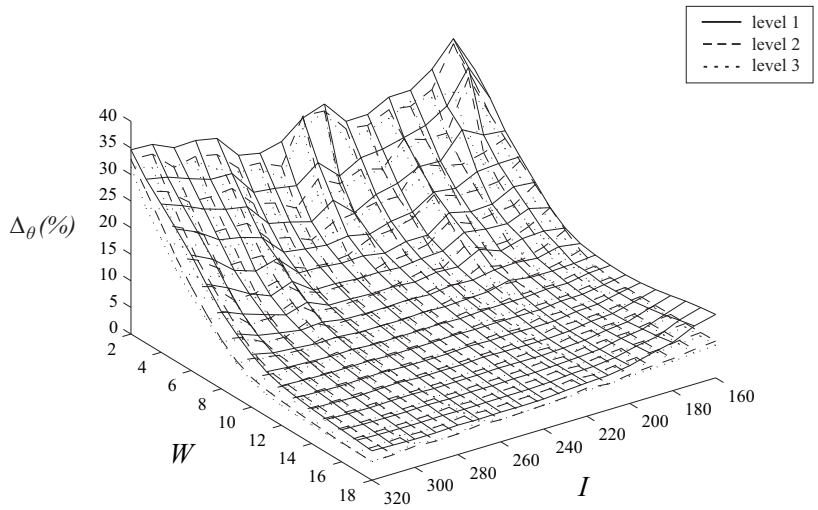

(a) Sampling window size from 2 to 18 pixels

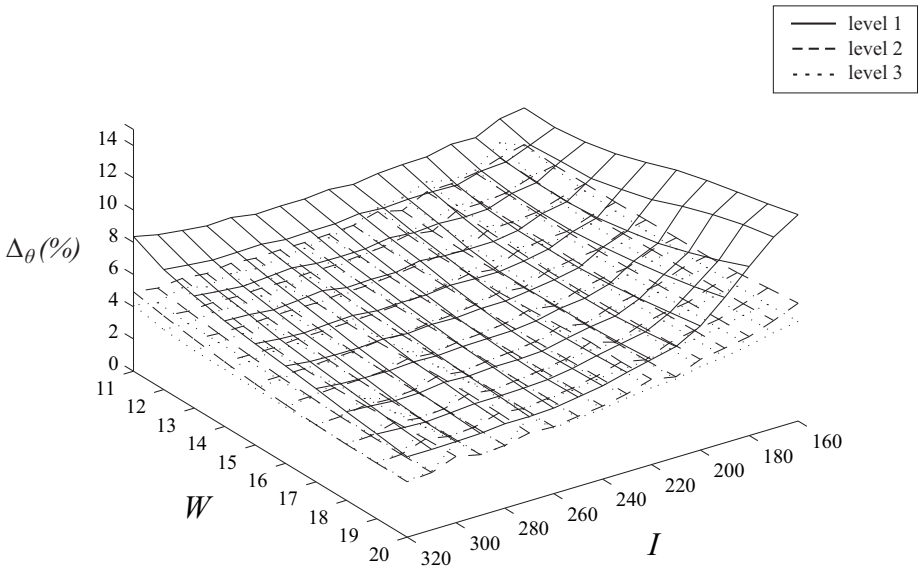

(b) Sampling window size from 11 to 20 pixels

Figure 4.4. Tracking accuracy based on angular velocities. Flow vector angular differences are shown based on variations of sampling window size versus image size with different levels of track interval dimensions (i.e. levels 1 to 3). Parts (a) and (b) show the error variation using different ranges of sampling windows. Similar to the results shown for variation of angular velocity, this set of graphs demonstrates that the tracking is more stable for sampling window sizes from a recommendation of 11 pixels onwards. Angular velocity error decreases as the image becomes-dimensionally bigger.

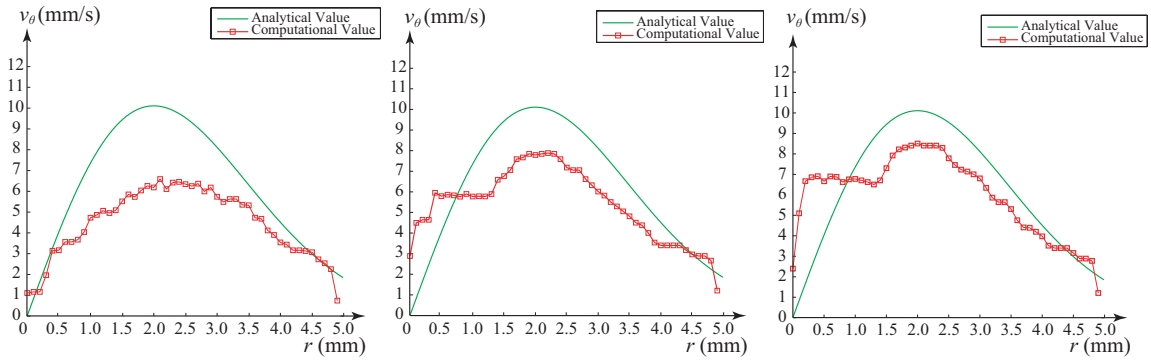

(i) Level 1 (ii) Level 2 (iii) Level 3

(a) Velocity profile with respect to vortex radius r

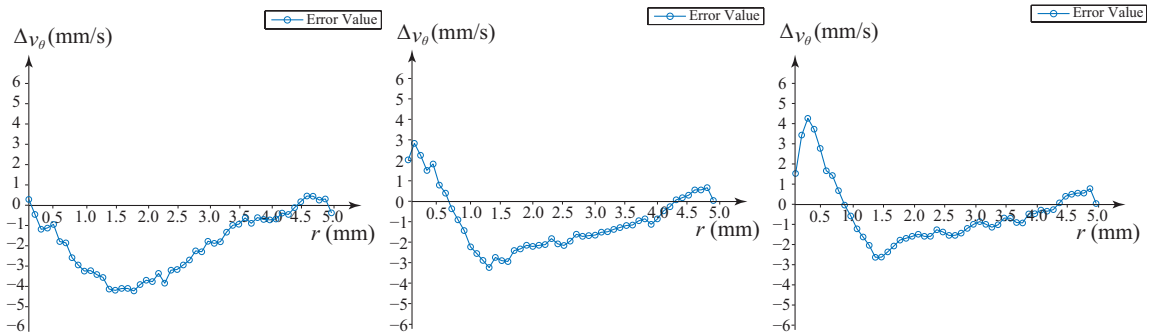

(i) Level 1 (ii) Level 2 (iii) Level 3

(b) Error difference of profiles

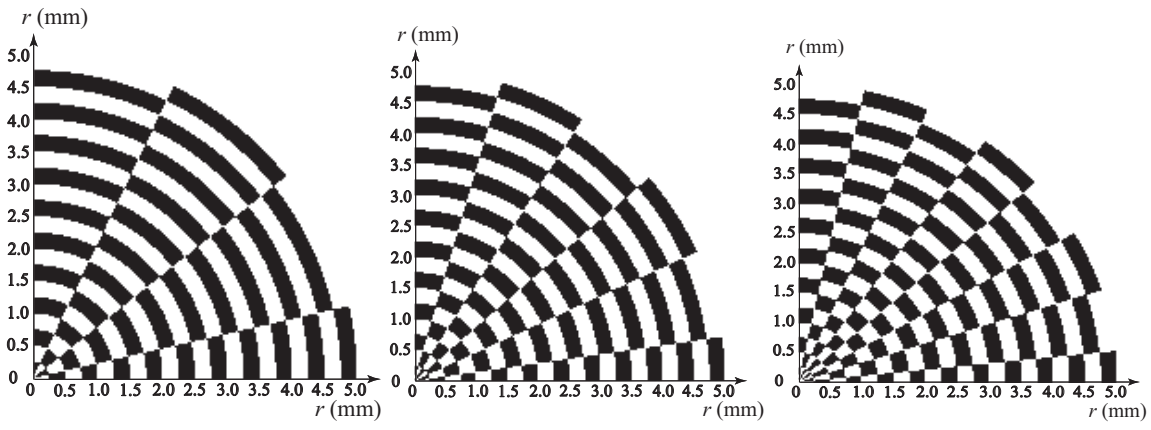

(i) Level 1 (ii) Level 2 (iii) Level 3

(c) Vortical track profiles used for computational studies

Figure 4.5. Tracking accuracy of rotation using motion estimation algorithm. Comparison of analytical and computational flow velocities in the radial direction is illustrated. Velocity profiles and their differences are shown in (a) and (b). Quadrant of the vortical grid is displayed in (c). Variation of feature density adjusts the moderation and extent of flow grid prediction.

0% NOISE

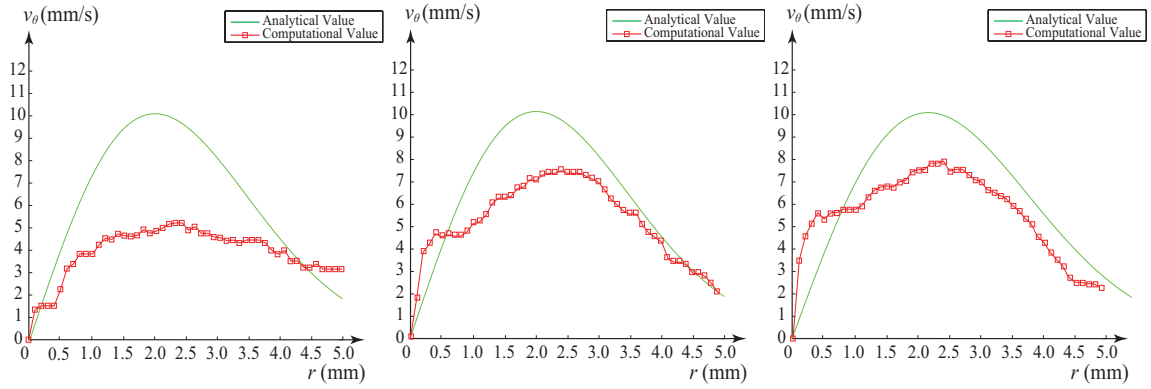

(i) Smoothing filter size 1×1 pixel (ii) Smoothing filter size 5×5 pixels (iii) Smoothing filter size 9×9 pixels

(a) Velocity profile with respect to vortex radius r at 0% noise

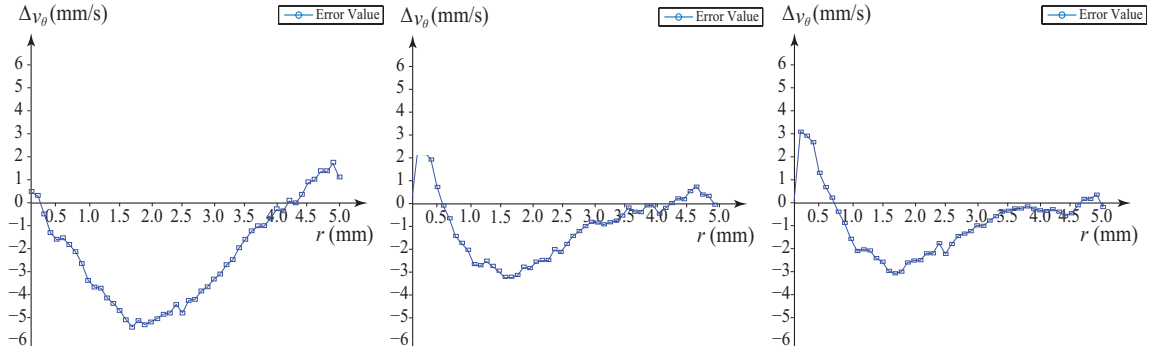

(i) Smoothing filter size 1×1 pixel (ii) Smoothing filter size 5×5 pixels (iii) Smoothing filter size 9×9 pixels

(b) Error difference of profiles at 0% noise

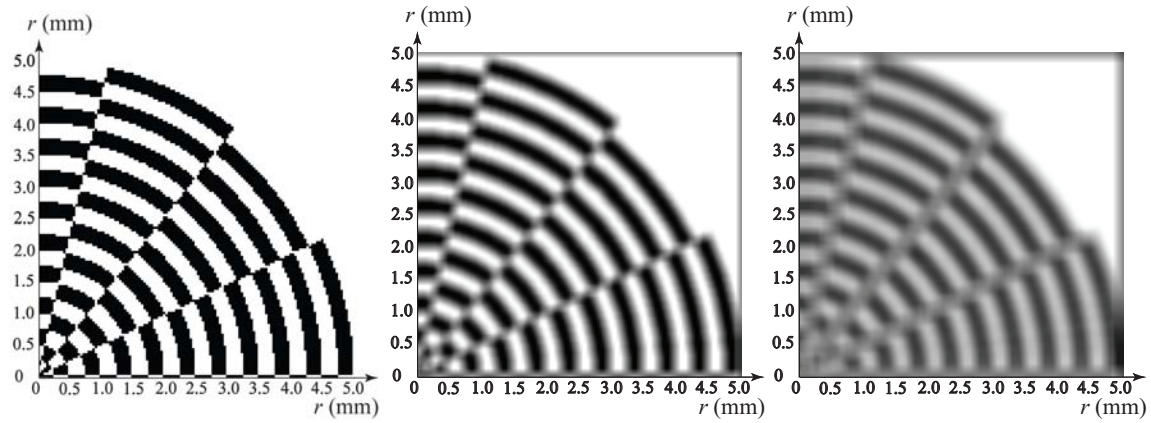

(i) Smoothing filter size 1×1 pixel (ii) Smoothing filter size 5×5 pixels (iii) Smoothing filter size 9×9 pixels

(c) Vortical track profiles used for computational studies at 0% noise

10% NOISE

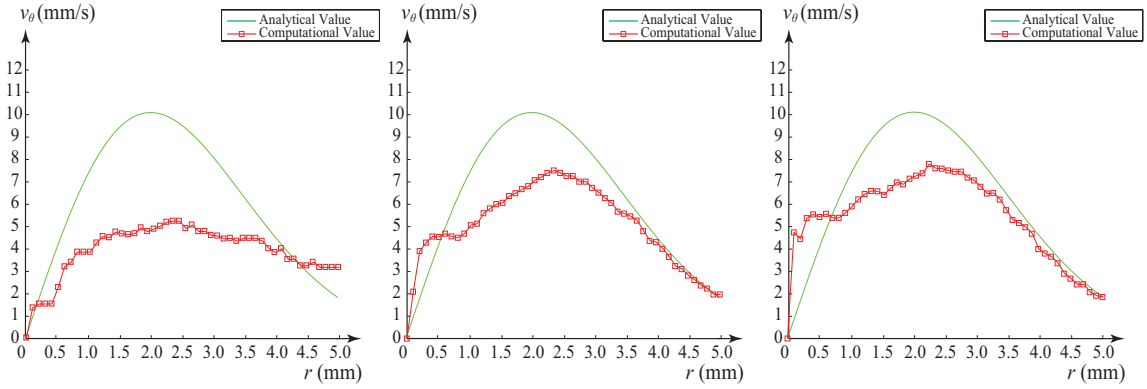

(i) Smoothing filter size 1×1 pixel (ii) Smoothing filter size 5×5 pixels (iii) Smoothing filter size 9×9 pixels

(d) Velocity profile with respect to vortex radius r at 10% noise

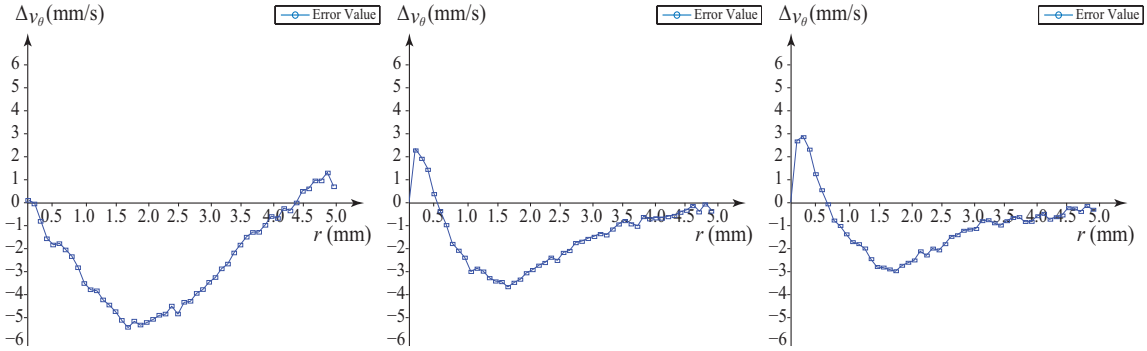

(i) Smoothing filter size 1×1 pixel (ii) Smoothing filter size 5×5 pixels (iii) Smoothing filter size 9×9 pixels

(e) Error difference of profiles at 10% noise

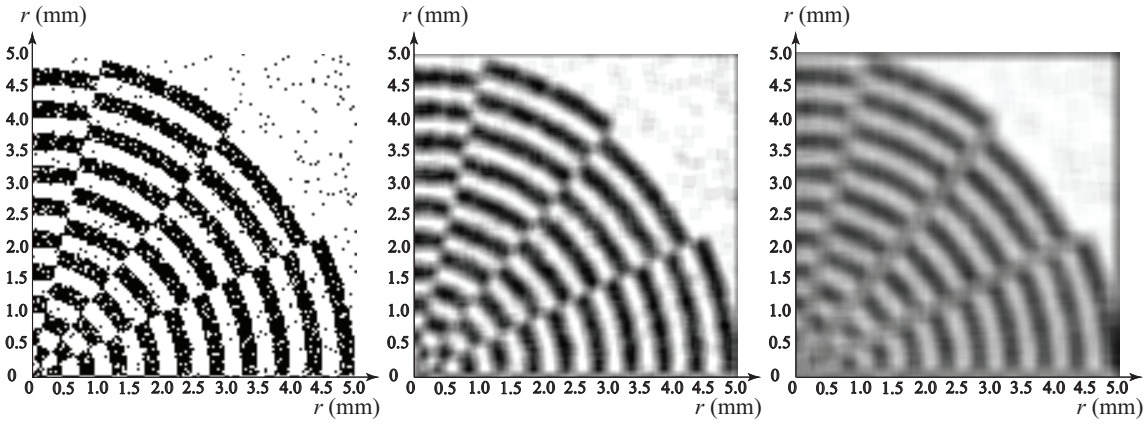

(i) Smoothing filter size 1×1 pixel (ii) Smoothing filter size 5×5 pixels (iii) Smoothing filter size 9×9 pixels

(f) Vortical track profiles used for computational studies at 10% noise

30% NOISE

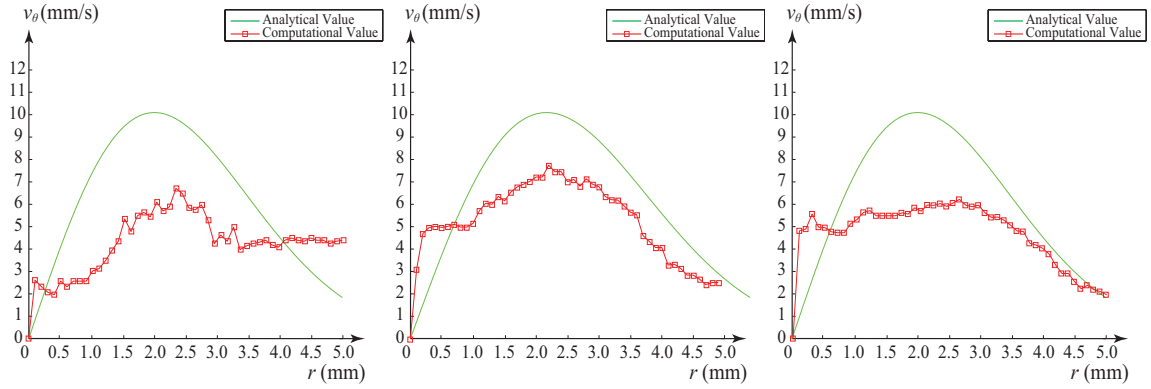

(i) Smoothing filter size 1×1 pixel (ii) Smoothing filter size 5×5 pixels (iii) Smoothing filter size 9×9 pixels

(g) Velocity profile with respect to vortex radius r at 30% noise

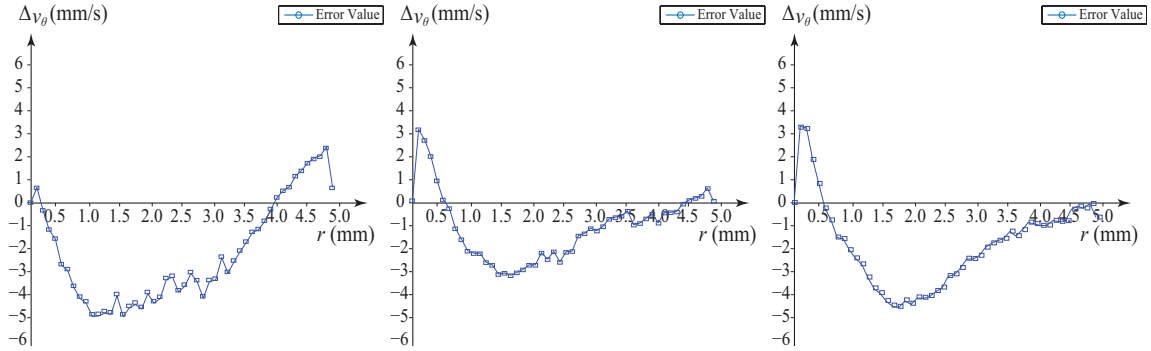

(i) Smoothing filter size 1×1 pixel (ii) Smoothing filter size 5×5 pixels (iii) Smoothing filter size 9×9 pixels

(h) Error difference of profiles at 30% noise

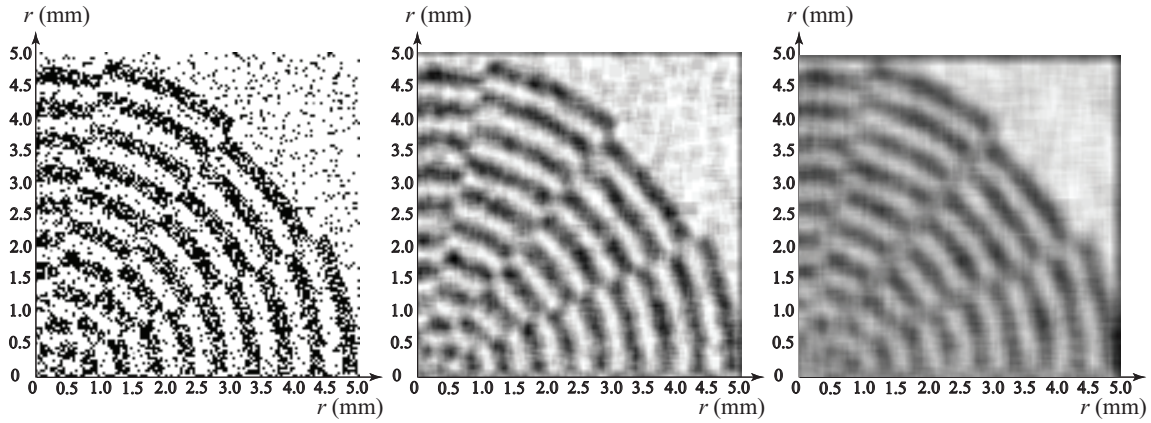

(i) Smoothing filter size 1×1 pixel (ii) Smoothing filter size 5×5 pixels (iii) Smoothing filter size 9×9 pixels

(i) Vortical track profiles used for computational studies at 30% noise

50% NOISE

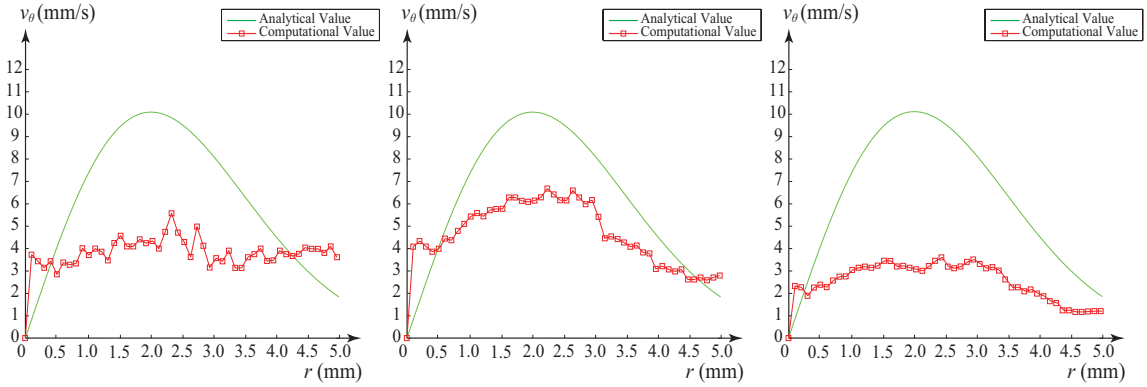

(i) Smoothing filter size 1×1 pixel (ii) Smoothing filter size 5×5 pixels (iii) Smoothing filter size 9×9 pixels

(j) Velocity profile with respect to vortex radius r at 50% noise

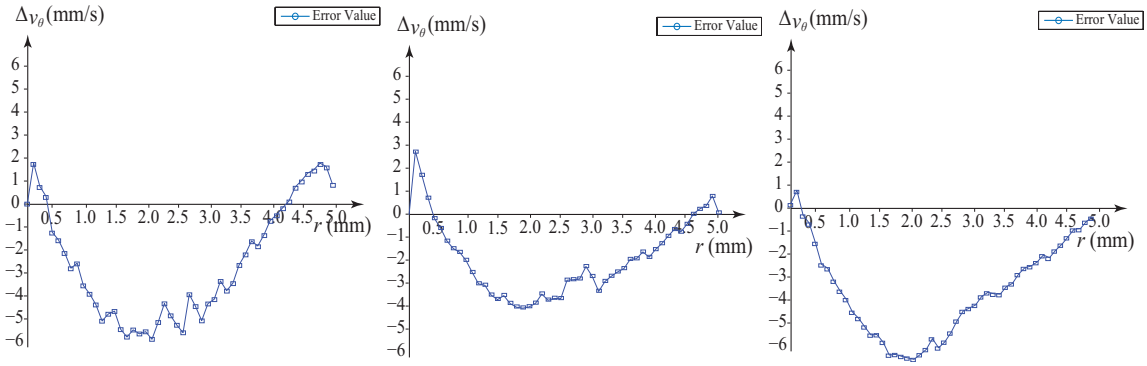

(i) Smoothing filter size 1×1 pixel (ii) Smoothing filter size 5×5 pixels (iii) Smoothing filter size 9×9 pixels

(k) Error difference of profiles at 50% noise

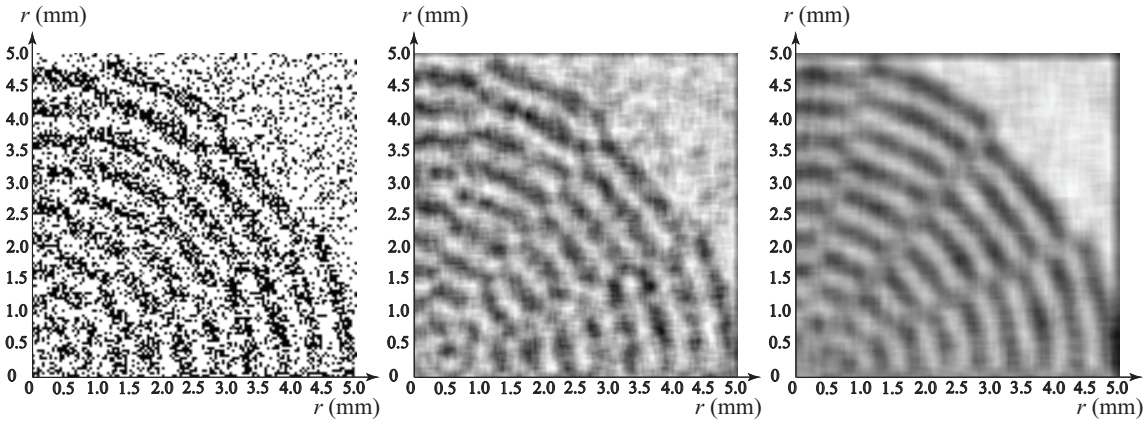

(i) Smoothing filter size 1×1 pixel (ii) Smoothing filter size 5×5 pixels (iii) Smoothing filter size 9×9 pixels

(l) Vortical track profiles used for computational studies at 50% noise

Figure 4.6. Tracking accuracy of rotation based on variation of noise in image. Comparison of analytical and computational flow velocities in the radial direction is illustrated. Velocity profiles and their differences are shown in (a,d,g,j) and (b,e,h,k) respectively. Quadrant of the vortical grid is displayed in (c,f,i,l). Variation of feature density adjusts the moderation and extent of flow grid prediction.

4.5 Limitations of Study

The performed experiments have shown that the proposed method using motion estimation of intensity images can be used to produce flow fields for qualitative analysis. We vary a few study parameters such as the image size, sampling window size of the motion estimation algorithm, signal to noise ratio of the image and smoothing filter mask size. Further studies based on different methods of motion estimation such as block matching (Duan *et al.* 2006a) or affine flow models (Bergen *et al.* 1992) can be carried out to test the tracking system. Nevertheless, in order to maintain the focus of our study, which is to understand the parameters that affect tracking, we use the pyramidal Lucas Kanade optical flow algorithm as the role model here.

We proposed a method of varying spatial features within the images. An increment in the spatial dimension of the vortical track size is followed by a reduction in features and this lowered the tracking accuracy as demonstrated by our surface response error graphs. As the image or sampling window size of the optical flow algorithm increased, the error decreased and tracking can reach an optimal level. The use of analytical data enabled us to validate information for the motion estimation approach as outlined in this chapter. The same principles can be tested using different track feature layouts such as Cartesian grids instead of polar ones. In addition, translation of grids in addition to rotation can be studied as well. But since we are interested to examine rotation of blood, in Chapter 8 using fluid motion tracking, a system validation of tracking rotational features will be more important and therefore is studied here.

Although our results demonstrate that the flow prediction discrepancies are not significant, the accuracy of a computed motion estimation approach may have been affected by the difference in true signal layout when using magnetic resonance images. In our experiments, we devise artificial intensity images simulating the presence of low MR-signals corresponding to incoherent proton spins in an idealised layout. The data set does not, however, reflect the organisation of these signal registrations in non-continuous distribution from the MR image of a vortex. However, since we are trying to verify the underlying computational algorithm of the system, artificial data such as the images that we generated can be used to achieve this.

4.6 Chapter Summary

The purpose of this chapter is to perform a thorough performance evaluation of the suggested theory and implemented system, before it can be further validated using real magnetic resonance images and well-established velocity encoded magnetic resonance imaging. We see the need to organise information related to the system and to optimally present the parameter dependencies.

We are able to provide some validation for a computed motion estimation approach in flow tracking and visualisation. We create artificial signal image data based on an analytical vortex. The images are simulated with an unrealistic assumption of perfect signal intensity contrast at equal geometrical intervals. However, since our main objective is to test the computational tracking mechanism of the approach, it is practical and instructive to produce idealised data sets for calibration and error estimation. Once proven reliable, the proposed system in our study will be useful for non-invasive tracking of blood flow using magnetic resonance images without modification of the standard steady-state free precession (SSFP) MRI scanning.

Additionally, there may be a need to verify fluid motion estimation using experimental data generated from other imaging modalities. The same experiments can be performed using information from other flow measurement techniques as input to fluid motion tracking. In Chapter 6, we describe experiments that perform system verification of our methodology using flow fields derived from phase contrast MRI using a case study of blood flow in the human right atrium. The whole purpose of this study is to perform a thorough performance evaluation of the suggested theory and implemented system before it can be further validated using real magnetic resonance images and well-established velocity encoded magnetic resonance imaging. We see the need to organise information related to the system and to present the parameter dependencies in the best observation possible before proceeding to the next stage of development.

Chapter 5

Visualisation Methods for Cardiac Flow

INTRA-cardiac blood flow imaging and visualisation is challenging due to the processes involved in generating velocity fields of blood within specific chambers of interest. Visual analysis of cardiac flow or wall deformation is crucial for an accurate examination of the heart.

This chapter also sets the practical foundation for flow vector synthesis and visualisation in the cardiac discipline. We outline conceptual development and the construction of flow field based on a three-dimensional Cartesian grid that can give a greater insight into the blood dynamics within the heart.

We develop a framework that is able to present both anatomical as well as flow information by overlaying velocity fields over medical images and displaying them in cine-mode. By addressing most of the methods involved from the programming perspective, procedural execution and memory efficiency have been considered. Our implemented system can be used to examine blood motion patterns in the heart effectively.

5.1 Introduction

An accurate vision of blood flow patterns within cardiovascular structures can assist in the discovery of flow phenomena in a human heart and is useful for investigation of cardiac abnormalities. Therefore, cardiac visualisation dominates the level of data understanding as inaccurate presentation may obscure the crucial details of measurement. We design and construct an interactive visualisation system to achieve good visual display that is suitable for three-dimensional blood flows. Such a framework possesses interactivity so that the state of flow over a cardiac cycle can be deciphered easily and effectively.

In this chapter, we examine the active contour algorithm that is used for semi-automatic segmentation of heart chambers for region segregation and flow analysis. In reality, based on cardiac magnetic resonance images (MRI), it is often difficult to achieve full automation for such applications due to the poor definition of cardiac wall boundary and artefacts within the blood pool. Therefore, we implement a semi-automatic segmentation algorithm when active contouring fails to define internal boundaries of the heart chamber effectively. Flow velocity grids within segmented regions are developed for analysis at a later stage. Useful visualisation tools that can be applied to present flow optimally are described.

Three-dimensional flow reconstructions can be performed using successive planar vector velocity maps. Such a flow field can be constructed based on x-, y- and z- components of each velocity vector in space. The visualisation of the flow can be supported with tools such as streamline tracing. In the absence of the third normal velocity component, due to the limitation of a velocimetry system to determine the rate of movement of blood normal to the plane of scan, we can construct this missing component by superimposing the in-plane components of two planes that are orthogonal to the current plane. Therefore, we can extend two-dimensional flow analysis to a three-dimensional analysis by taking each set of the three planar vectors from the x-y, y-z and x-z planes respectively and constructing them into a single resultant flow in space iteratively using vector addition. Although such technology has been previously implemented (Alsberg *et al.* 1994, Bohs *et al.* 1995), the programming aspect of reconstruction is not discussed and most applications are not of cardiac discipline.

We describe a translation system that is implemented to assist in reconstructing parallel planes of medical images of the heart. Scanned vector maps can be combined using our visualisation framework to present flow with suggested strategies related to

optimal processing of its display. Furthermore, various sections in this chapter outline user-program interacting mechanisms and procedures for controlling operations of the visualisation from a software development perspective. The conceptual framework that is presented can also be utilised in future work related to flow visualisation and fluid analysis in other fields.

5.2 Segmentation of Intra-Cardiac Flow Region

Cardiac chamber boundary detection is one of the key implementations for region definition. To provide intelligible results describing flow within the human heart, cardiac chamber segmentation is a pre-requisite so that fluid motion information can be presented within a region of interest defined by the chamber boundary. A technique that is used to establish contouring along the cardiac wall is described mathematically.

5.2.1 Introduction to Active Contour Technique

A segmentation approach known as active contouring that can be used to define region of interest for flow analysis within the heart. Active contour exists in different forms, such as parametric and geometric deformable models (Xu and Prince 1998). The active contour model can be implemented using a snake contour, which is an energy-minimising spline guided by external constraint forces and influenced by image forces that dynamically pull it toward features such as lines and edges in digital images (Terzopoulos *et al.* 1987, Kass *et al.* 1988, Terzopoulos and Metaxas 1991, Leymarie and Levine 1993, Fua and Brechbühler 1997, Neuenschwander *et al.* 1997, McInerney and Terzopoulos 2000). These are computational curves that deform to localise object shapes represented on these images. In this section, we will focus on describing and utilising the parametric active contour. It is worthwhile mentioning that mechanism of active contouring can be extended to perform three-dimensional segmentation (Ahlberg 1996).

5.2.2 Energy Minimisation of Parametric Snake

Active contouring can be applied onto gray-scale intensity magnetic resonance images for segmentation of cardiac chambers (Goshtasby and Turner 1995). A region of

interest (ROI) is established by the expansion of a preliminary active contour that is positioned within the examined chamber.

Movement of cardiac tissues is effectively excluded by performing contour segmentation on the cardiac walls. The cardiac wall is segmented by placement of a two-dimensional contour that forms a computationally elastic wall within the cardiac chamber. Migration of contour nodes from their origins onto the intense wall region is executed based on an energy minimisation algorithm (Cohen 1991, Jasjit 2000).

Active contouring computes a more accurate contour-line description iteratively by describing the contour as an energy function E_{contour}. It receives information from the preceding contour line and applies energy balancing based on the internal and external energies of this line denoted by E_{int} and E_{ext} respectively to redefine the contour representation. The best fitted contour (Cohen 1991, Jasjit 2000) is one that corresponds to the minimum of this energy:

$$E_{\text{contour}} = \int E_{\text{int}} + \int E_{\text{ext}}. \tag{5.1}$$

The initial curve can be anywhere in the image, and interior contours are automatically detected. In the event of poor segmentation due to over-expansion of the elastic contour, the internal wall of the chamber is manually traced to adapt more to the shape of the region of interest before expansion takes place. Due to the nature of semi-automatic segmentation, contour tracing algorithm set in our program is not the best choice for application. We emphasise that the techniques outlined in this chapter may not be the most efficient and effective methods of implementation at the current stage; however, the principles outlined here can be improved for better performance subsequently.

5.2.3 Implementation of Parametric Snake Model

In the previous section, we describe qualitatively the concept of the snake model and its deformation. Now, we will discuss the mathematical aspects of the model which effectively uses the Kass snake algorithm (Kass *et al.* 1988).

An active contour can be defined as a parametric curve $v(s) = [x(s)y(s)], s \in [0,1]$, with each configuration component being associated with a finite energy. We define the first and second order of $v(s)$ as $v^{'}$ and $v^{''}$ respectively. Expansion of Equation 5.1 gives

$$E_{\text{contour}} = \int E_{\text{elastic}} + \int E_{\text{bending}} + \int E_{\text{ext}} \tag{5.2}$$

where

$$\int E_{\text{elastic}} = \frac{1}{2}\int_0^1 \alpha(s)\left|v'(s)\right|^2 ds, \tag{5.3}$$

$$\int E_{\text{bending}} = \frac{1}{2}\int_0^1 \beta(s)\left|v''(s)\right|^2 ds, \tag{5.4}$$

and

$$\int E_{\text{bending}} = \int_0^1 P\left(v(s)\right) ds. \tag{5.5}$$

The mechanical properties of the contour are controlled by parameters, α and β which determines the entity's tension and rigidity respectively to provide elasticity for snake deformation. The external energy E_{ext} is designed to enable migration of snake nodes towards the step edges of gray-scale image that is an intensity matrix $I(v)$. Here, P is the potential associated with the external forces and proportional to the spatial intensity gradient of the image such that

$$P\left(v(s)\right) = -\left|\nabla I\left(v(s)\right)\right|^2. \tag{5.6}$$

The energy equation can be minimised using the Euler Lagrange differential equation. Using calculus of variations, it can be shown that the minimum energy configuration corresponds to the equation

$$\alpha v''(s) - \beta v''''(s) - \nabla P\left(v(s)\right) = 0. \tag{5.7}$$

In this formulation, each term acts as a force applied to the contour. The whole configuration can be viewed as an equation to balance forces:

$$F_{\text{int}} + F_{\text{ext}} = 0. \tag{5.8}$$

The internal force $F_{\text{int}} = \alpha v''(s) - \beta v''''(s)$ sets the rigidity and elasticity of the snake contour while the external potential force $F_{\text{ext}} = -\nabla P(v(s))$ attracts the contour towards the edges of an image object. The snake migrates towards the local minima of the potential P that is equivalent to the local maxima of the spatial intensity gradient.

5.2.4 Segmentation of Cardiac Chamber Using Active Contouring

Most medical image segmentation of the heart requires expert human intervention to achieve accurate and consistent segregation of the region from the rest of the other

cardiovascular structures. In some cases, active contouring may out-perform other segmentation techniques, such as region growing (Hao *et al.* 2000, Gonzalez and Woods 2002), especially when a user-inserted boundary representing the atrial chamber in the image is required to prevent overflow of pixels into the connecting vessels of an atrium. However, the control of energy pertaining to the snake may be difficult and full automation may not be realisable in a robust and reliable medical image segmentation tool.

Based on Figure 5.1, we demonstrate the use of contour snakes for interactive segmentation of cardiac chambers. Initial plantation of a closed loop contour can be within the chamber of interest. Expansion for a balloon of elemental nodes can be activated semi-automatically by migration of the nodes towards the chamber wall with interactive user control. When there is poor definition of myocardium continuity around an atrium, active contouring of the endocardium may fail and deform out of the geometrical boundary due to weak energy levels to constraint over expansion. Especially for cardiac magnetic resonance imaging of atria, the scanned heart chamber image shows poor definition of the atrial wall and automated contouring using computer algorithms is difficult. In the event of such failures, we take over the automation by supervising the planting and growth of snake contour nodes within the chamber manually. This allows us to obtain a more accurate cardiac chamber contouring and segmentation.

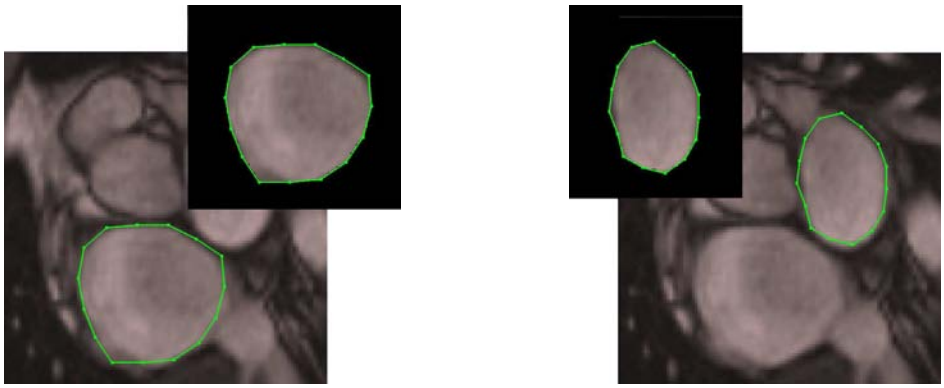

(a) Right atrium segmentation (b) Left atrium segmentation

Figure 5.1. Segmentation of atria based on active contours. Active contouring is applied onto MR images to perform boundary definition of cardiac chambers that can be used for segmentation of the chamber of interest. Active conours in the form of snakes utilise the intensity contrast of the cardiac wall and blood pool within to define the boundary region of the right and left atria, shown in figure part (a) and (b) respectively.

5.3 Two-Dimensional Flow Image Reconstruction

The flow region defined within a region of interest can be displayed using reconstruction of velocity flow vectors by the velocimetry system over the segmented area only. To aid visualisation, anatomic information such as the magnetic resonance images of the scan can be superimposed onto the flow field such that outside the area of interest, the details of the cardiac wall and other cardiovascular chambers are shown. Such a configuration can help in a more concise visualisation of flow in the chamber of examination and the anatomical structures around it.

The system illustrated by Figure 5.2 shows the stages involve in reconstructing a series of temporal flow images that can be played back like a movie clip to aid flow visualisation in the heart. The development of two-dimensional flow images can sometimes be sufficiently informative to explain flow behaviour in the cardiac chambers. It is also easier to quantify two-dimensional flows statistically as compared to three-dimensional ones.

Flow visualisation tools based on colour ribbons, streamlines and vector plots can be applied depending on the user preference and the nature of the fluid flow (Lodha *et al.* 1996). For cardiac examination, it may be useful to determine the speed of blood in cardiovascular systems. Therefore, colour streamlines like the ones shown in Figure 5.3 are commonly used. We emphasise again that cardiac segmentation is performed to limit the display of streamlines within the chamber of interest. The segmented set of streamlines is overlayed onto the medical image to highlight the location of blood flow examination and enables the identification of the chamber easily. In our example, the magnetic resonance image produced as a background canvas, illustrates the anatomical details of the heart while providing flow information at the same time. Multiple flow images can be stitched together to create a movie playback of the changing flow patterns and anatomical deformations. This allows users to view the temporal information related to blood fluid and cardiovascular structural interaction effectively.

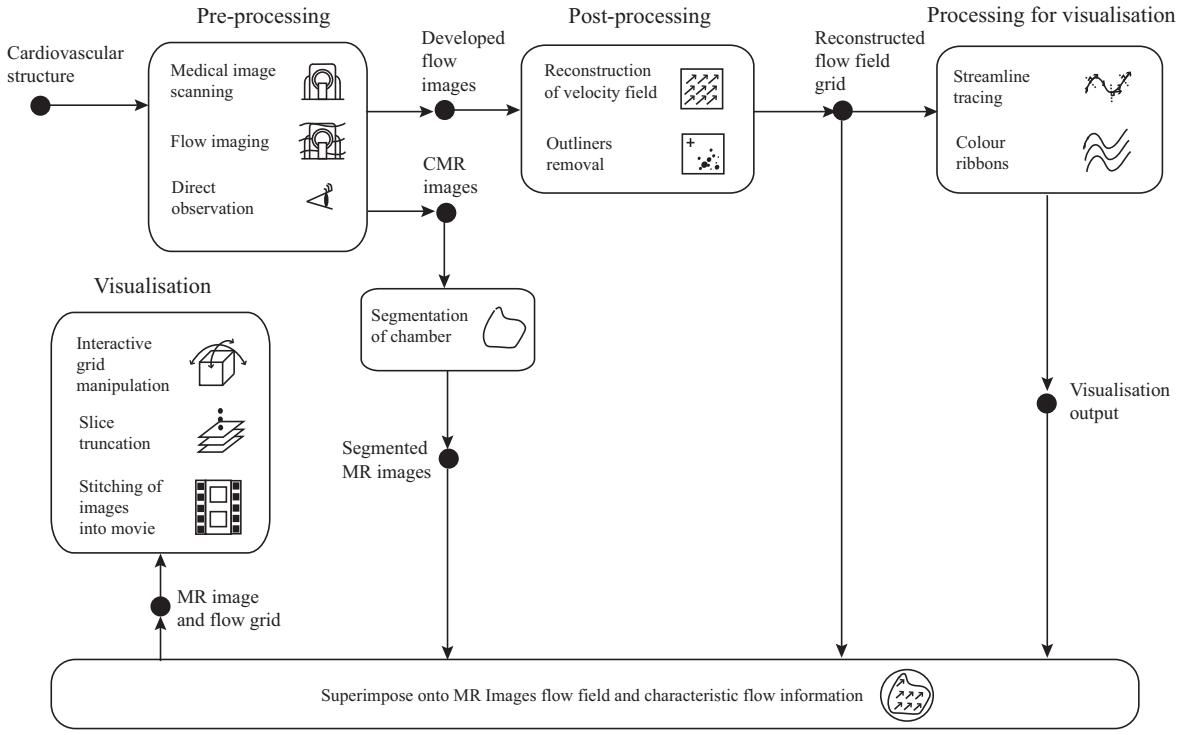

Figure 5.2. A cardiac velocity visualisation system. Visualisation of blood motion is provided by its velocity flow field within the segmented chamber of interest. To achieve this final flow image, various stages such as segmentation, flow field reconstruction, and superimposition of images must be carried out. In addition to the production of flow images, streamline tracing and interactive image slice manipulation can also be performed.

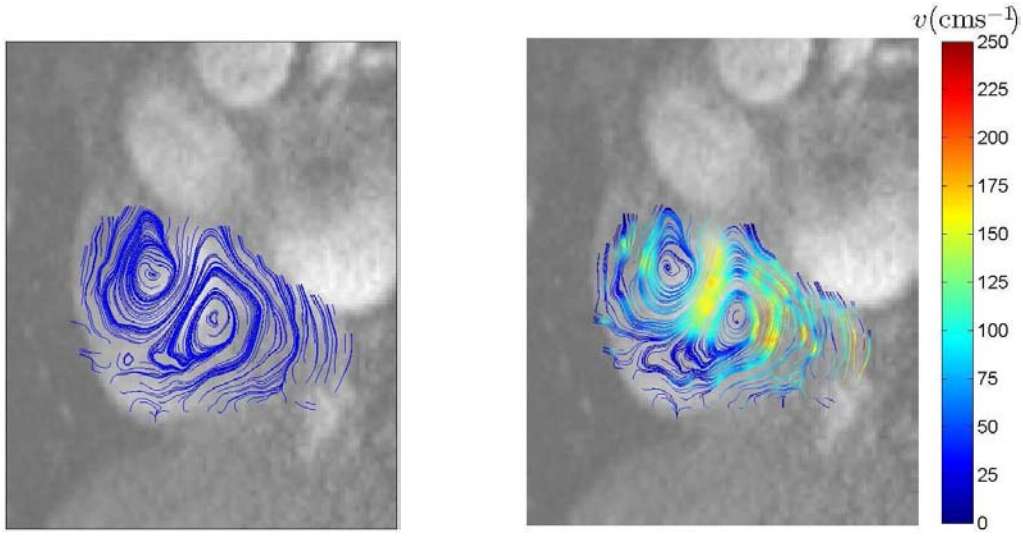

Figure 5.3. Cardiac flow visualisation using streamlines. Streamline plots (with and without colours) are displayed for velocity map based on phase contrast magnetic resonance imaging. It is possible to indicate swirling within a heart chamber with the help of streamline tracing. The colour intensity of the streamlines can be used to describe how fast the blood is rotating within an enclosed space by referencing the velocity scale. Streamline flow visualisation is a useful technqiue to examine cardiac flow phenomena in the heart.

5.4 Three-Dimensional Flow Image Reconstruction

We describe a technique of combining three sets of planar velocity images pertaining to the axial, sagittal and coronal cardiac orientations into a three-dimensional flow field grid. This presents a method for higher-dimensional reconstruction of flow if the imaging system is incapable of scanning the normal velocity component of the planar flow section. An example of imaging system limited by through-plane flow scanning is digital particle image velocimetry (Alahyari and Longmire 1994, Raffel *et al.* 1998). Unlike phase contrast magnetic resonance imaging, the implemented framework requires a longer processing time for flow grid reconstruction due to the extensive memory and computations required.

5.4.1 Cartesian Grid for Image and Flow Display

In Chapter 3, we describe the generation of vector field for in-plane flow based on MR imaging of slices of the heart. In general, we are able to produce vector fields in three orientations if flow images from three sets of planes orthogonal to each other are scanned throughout the heart. Typically, we define the planes as x-y, y-z and x-z in the axial, sagittal and coronal orientations of the flow volume respectively. If every planar slice at an orientation has a two-dimensional in-plane flow grid, then a resultant flow grid from the X, Y and Z flow grids can be reconstructed in three dimensions. A schematic illustration of the image grid over the flow volume is shown in Figure 5.4. Flow vectors within a volume of fluid can be constructed based on the image grid framework that we schematically demonstrate in Figure 5.5.

A segmentation grid is imposed onto the data image construction. Any node of plane intersection and the resultant flow vector associated with it that is outside the region of segmentation will not be displayed. In this figure, a section of the axial, sagittal and coronal slices are hidden for a dissection of the flow volume. The nodes presented spatially in the volume demonstrate how a group of nodes spatially distributed in a three-dimensional space can be volumetrically segmented by applying two-dimensional segmentation for all of the orthogonal planes.

The Cartesian configuration of a field grid can be utilised for a three-dimensional construction of the flow; however, from the perspective of visualisation, it does not help in providing much insight into the flow patterns. Therefore, it is definitely of interest to view flow in-plane from a selected orientation and via a single slice at each time of

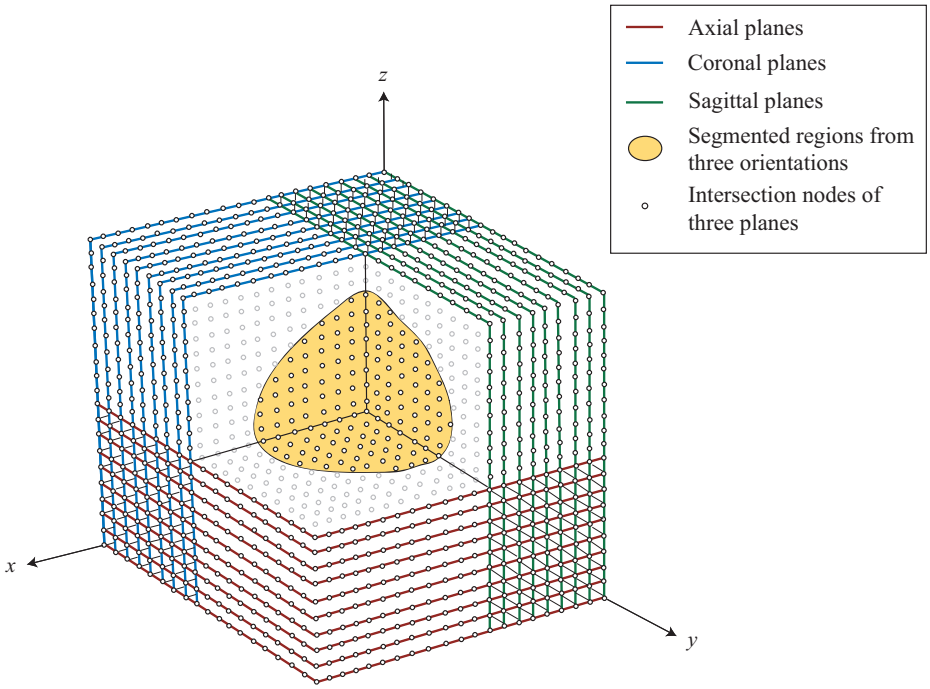

Figure 5.4. Three-dimensional image grid reconstruction. Reconstruction of image grids based on the Cartesian framework can be performed. The nodes representing point of intersection of the three planes in the x, y and z orientations can be displayed. Each of these acts as points for flow construction by vector addition of the flow features associated to the node. The number of nodes will depend on the number of planes within a volume space.

examination. Nevertheless, coupling the display of a three-dimensional grid of flow vectors with user-defined control of the grid in orientation and distance from a reference visual perspective can allow good visual control.

From the programming perspective, the images are stored in a five-dimensional matrix whereby the orientation p, spatial coordinates x, y and z, and time frame index n_t form each of the dimension. Counts of P orientations, with spatial sizes I, J and K, and a total number of time frames T contributes to $P \times I \times J \times K \times T$ number of matrix elements. Figure 5.6 illustrates the image dimensions from a graphical perspective. A more detailed description of this matrix definition can be referenced in Appendix A.

Therefore, for three-dimensional analysis of flow, the MRI slices from the axial, sagittal and coronal scans can be computationally constructed into a stack grid as shown in Figure 5.7[13]. On the display platform, the points of intersection of three orthogonal

[13]Diagrams for three-dimensional grids are generated using Medflovan medical image processing software.

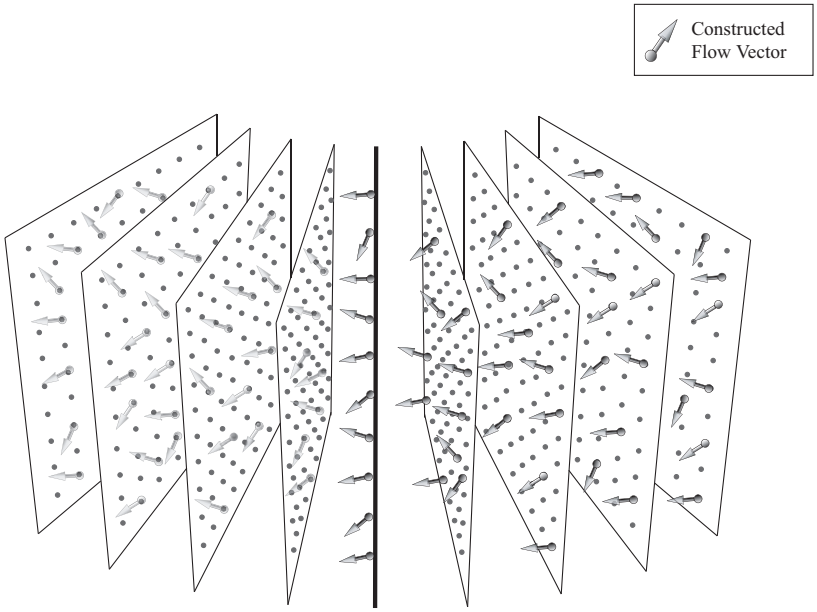

Figure 5.5. Reconstruction of flow using vectors from three orientations. A three-dimensional grid can be constructed from the axial, sagittal and coronal planes. The vectors at the point of intersection of the three planes are added to produce the resultant flow at every node. Flow outside of the segmented region will not be computed. So only the vectors within the region of encapsulation by the contour will be displayed and attributed to the vector addition. Therefore, we will have a display of three-dimensional vectors within the segmented heart chamber that is constructed from three orientations of two-dimensional in-plane vector grids.

planes are represented by spherical points at junctions of intersection. As an example and for good demonstration purposes, the axial planes are hidden and inter-slice distance has been reduced to reveal these points.

In (a), the coronal planes and part of the axial and sagittal planes have been hidden to allow visualisation of the anchored spheres at junctions of plane intersections. Based on (b), the number of junctions in a three-dimensional grid of planes is limited by the number and spacing of the slices for axial, sagittal and coronal orientations. Therefore, a dense image grid is required for accurate three-dimensional computational measurements of flow. However, for demonstration purposes, we display a stack of appropriately spaced images forming a grid structure that is able to reveal the intersectional junctions visually. By setting the planes in schematic outlines, we are able to explain this graphically. Part (c) shows that sections of orthogonal planes are set in hidden mode for clear illustration of the plane intersection junctions in this schematic setup.

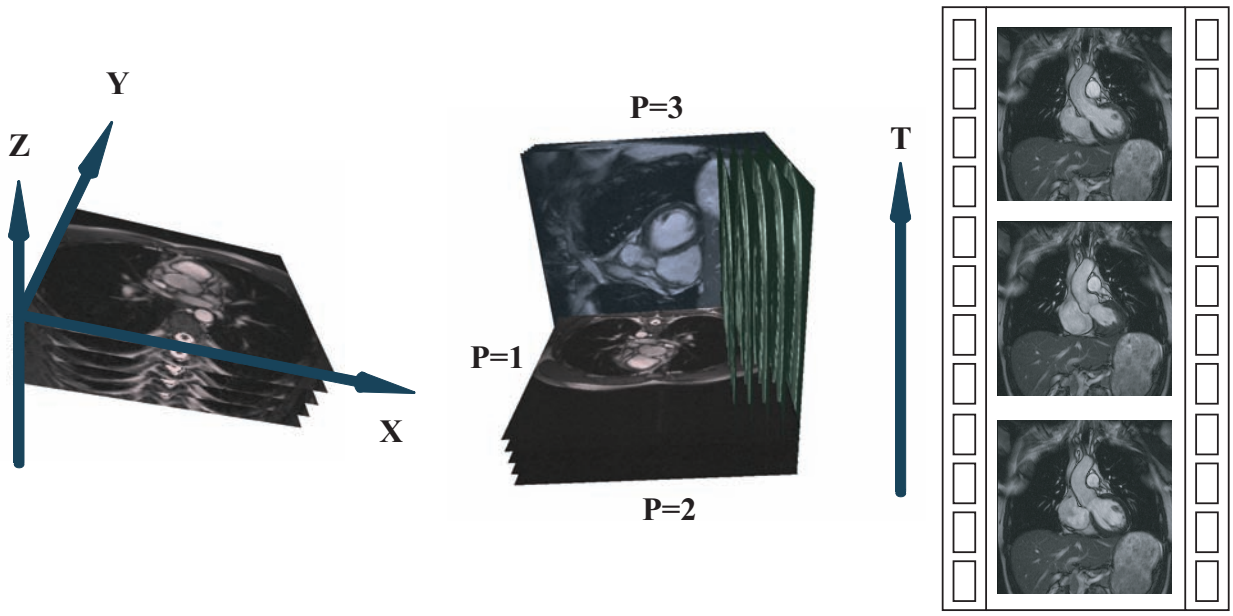

Figure 5.6. Construction of image matrix based on five dimensions. The matrix that is used for processing and display of images has five dimensions. These dimensions are based on arrays labelled as X, Y, Z, P, and T. Due to the huge storage matrix required for allocation of data, good memory management is required in the software application. For example, storage memory during running of program is always released after flow grids are processed. Another strategy in good memory conservation is to resize the matrix when images are cropped or slices are truncated.

A full set of intersecting planes are shown in (d) and the transparency property of the image slice can reveal the number of junctions.

5.4.2 Computation of Flow Grid

We can perform vector addition through addition of the vectors from x-y, y-z and x-z planes. This gives us a three-dimensional flow of designated magnitude and direction at the node of intersection of the three planes as seen in Figure 5.8.

Two-dimensional vectors in-plane at arbitrary coordinates are denoted by

$$\begin{aligned} &\left[v_i^{\text{Axial}}(x_1, y_1, z_1, n_t), v_j^{\text{Axial}}(x_1, y_1, z_1, n_t)\right], \\ &\left[v_i^{\text{Sagittal}}(x_2, y_2, z_2, n_t), v_j^{\text{Sagittal}}(x_2, y_2, z_2, n_t)\right], \\ \text{and} \quad &\left[v_i^{\text{Coronal}}(x_3, y_3, z_3, n_t), v_j^{\text{Coronal}}(x_3, y_3, z_3, n_t)\right], \end{aligned} \tag{5.9}$$

which pertains to the axial, sagittal and coronal orientations respectively. Note that x_p, y_p, z_p for $p = 1, 2$ and 3 measures the spatial position of the point of intersection of the

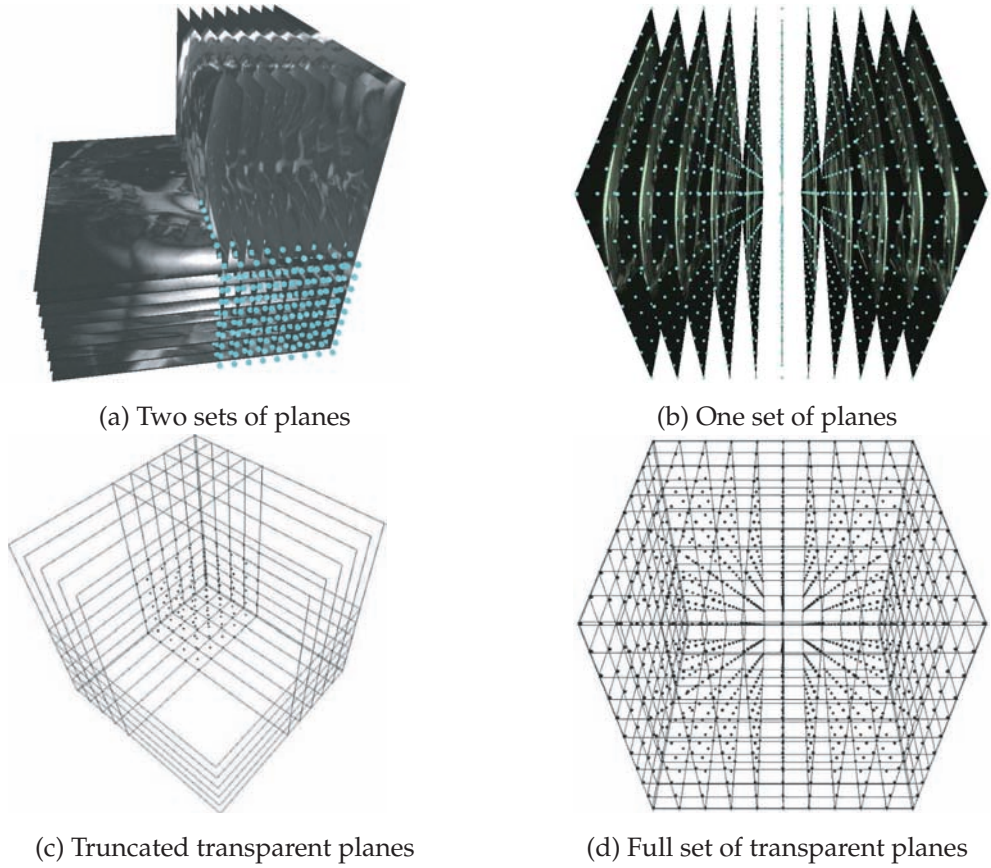

(a) Two sets of planes (b) One set of planes

(c) Truncated transparent planes (d) Full set of transparent planes

Figure 5.7. Intersection nodes of a three-dimensional grid. Reconstruction of MRI slices using three orientations, and with spheres anchored at the points of intersection of the slices in a three-dimensional space. The two diagrams (a) and (b) in the figure show the graphical outputs by our program while (c) and (d) illustrate the construction of nodes in space schematically.

three planes. This intersection node is referenced from an origin at $[0,0,0]$. This flow grid correspond to images pertaining to time frame indices $n_t = 1$ to M. The equations for adding i, j and k directional flow vectors at every point of intersection of the three flow planes give us the orthogonal components V_i, V_j and V_k of the resultant flow as a function of position $[x,y,z]$ and time frame index n_t is:

$$\begin{aligned} V_i(x,y,z,n_t) &= v_i^{\text{Axial}}(x_1,y_1,z_1,n_t) + v_j^{\text{Coronal}}(x_3,y_3,z_3,n_t), \\ V_j(x,y,z,n_t) &= v_i^{\text{Sagittal}}(x_2,y_2,z_2,n_t) + v_j^{\text{Axial}}(x_1,y_1,z_1,n_t), \\ \text{and} \quad V_k(x,y,z,n_t) &= v_i^{\text{Coronal}}(x_3,y_3,z_3,n_t) + v_j^{\text{Sagittal}}(x_2,y_2,z_2,n_t), \end{aligned} \tag{5.10}$$

given that for $1 \leq x \leq I$, $1 \leq y \leq J$ and $1 \leq z \leq K$. We also note that

$$x = x_1 = z_2 = y_3, y = y_1 = x_2 = z_3, z = z_1 = y_2 = x_3. \tag{5.11}$$

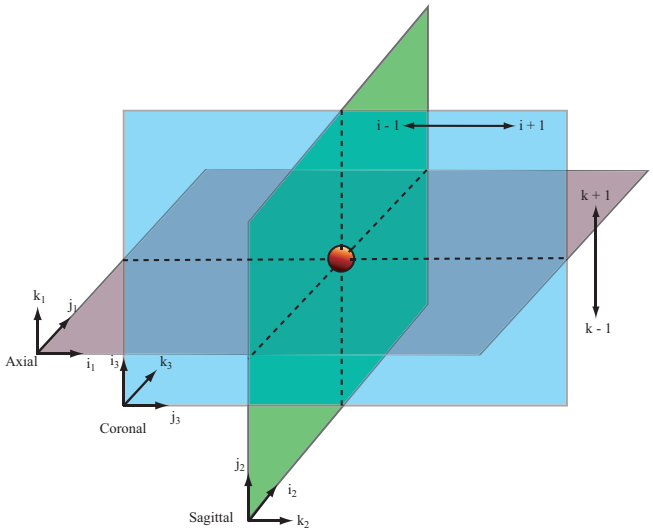

Figure 5.8. Geometrical representation of plane intersection. Reconstruction of flow using vectors from three orientations, namely, the x-y, y-z and x-z planes. Each node that is associated with an orientation has three orthogonal flow vector components in the i, j and k directions. The intersection from each of the other two orientations will contribute a set of two vectors corresponding to each plane. In total, there are altogether six vector components that are associated with a node based on intersection from three planes. Therefore, the attribute of each node is a single flow vector whose i, j and k components are based on the addition of these vectors

Root-mean-square of the vector gives the resultant vector magnitude V_R as

$$|V_R| = \sqrt{(V_i)^2 + (V_j)^2 + (V_k)^2}. \tag{5.12}$$

Figure 5.9 shows the display of arbitrary flow vectors based on intersection of flow image slices in three orientations.[14] For every intersection point, a resultant vector based on the three orthogonal velocity components can be computed. The analysis of three-dimensional flows is limited by the poor inter-slice resolution and lack of contour segmentation. For an illustration of our method, we use a reduced number of anchor spheres for demonstration of an effective visualisation. Flow fields that are used in the generation of these images are arbitrary and has been graphically presented based on the programming strategies that have been discussed.

[14]Flow grids are generated using Medflovan medical image processing software.

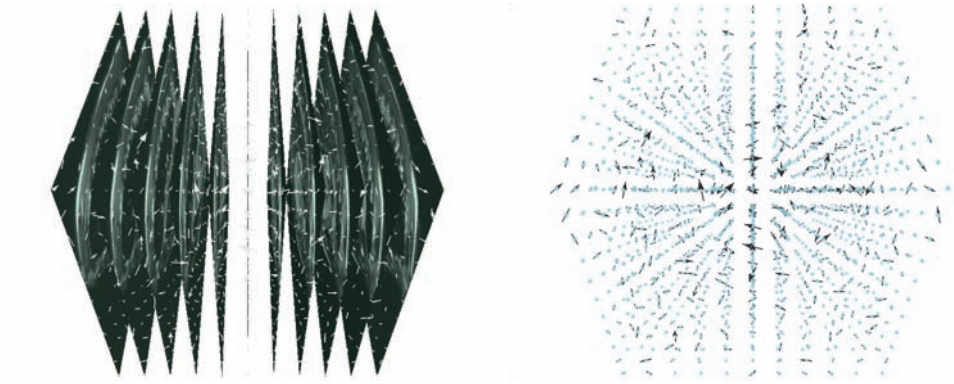

(a) Plane and intersection nodes (b) Intersection nodes only

Figure 5.9. Measured flow vectors in a three-dimensional space through image planes. Based on part (a), we illustrate the augmentation of MR images on three-dimensional grid of the intersected measurements. This enhances a user's view by overlaying graphical and anatomical information onto it. The flow directions can be represented using arrows and its speed correspond to the magnitude of velocity vectors in space. From (b), we see that the configuration of flow vector display in three spatial dimensions is based on the number and density of intersection junctions.

5.5 System Limitations

The mathematical framework derived in this work is designed for a few types of scan protocol only and depends on the dimension of flow analysis. For velocity-encoded imaging modalities, the post processing computational expenses is low considering that most of the processing time is shifted to the physical measurement of localised blood velocity components. Unlike MR fluid motion tracking, system calibration and image registration of the motion-sensitised MR-signal measured during successive scans compensates the reconstruction of velocity grid using intensity flow estimation that is more time consuming. However, comparing the time taken to encode velocities during phase contrast MRI scanning, the overall speed of velocity grid development is much higher.

While MR fluid motion tracking may be efficient based on planar velocity grid construction, the construction of a single three-dimensional grid based on successive planes of flow grids may be computationally inferior to imaging techniques that are able to measure through-plane fluid velocities (an additional velocity component that is perpendicular to in-plane ones). Reconstruction using scans from the latter technique is

able to produce such a flow grid with three sets of velocity-encoded images pertaining to the orthogonal orientations quickly and with low computational cost. However, there may be limitation of an imaging protocol to achieve the through-plane velocity measurement. Emerging technologies such as magnetic resonance fluid motion tracking which can only predict in-plane velocity fields may find our mathematical framework applicable when developing three-dimensional flow grids.

5.6 Chapter Summary

Cardiac flow imaging and visualisation involves a multiple of unique tools that can be combined to produce a system specially targeted for the presentation of blood flow within the heart most effectively. The framework is designed to produce flow field displays with low processing cost and with maximum speed. This chapter also describe the development of framework for performing segmentation using active contouring on two-dimensional images. The flow field of the MR images can be presented with a more focused analysis if active contouring is performed to detect the chamber boundary and any flow vectors outside of the established boundary will be hidden, thereby, presenting a clear overview of the blood pool dynamics within the segmented chamber.

Vector addition based on slices from three planes of orientation allows the development of a volumetric grid of flow vectors. Although a three-dimensional flow grid may not be of much utility in terms of quantification, it may still be of interest to develop interactive display of such information for qualitative flow analysis. In the cardiac flow imagings that we outline in this chapter, we simplify the flow analysis to that of a two-dimensional one. We establish the foundation of this development and to gain preliminary insight into construction of a volumetric flow. The development technique, that is based on the interpolation of multiple orthogonal planar flow planes, can also be applied onto non-cardiac related flow construction. For example, three-dimensional flow grid reconstruction may be based on particle image velocimetry that develops two-dimensional flow grid in any plane.

In the next few chapters, it can be demonstrated that the flow results based on visualisation tools such as colour contour plots, streamline tracing and velocity vector display within segmented regions of interest. The tools described in this chapter can be used effectively for qualitative flow visualisation (Chapters 6, 7 and 8).

Chapter 6

System Design for Visualisation of Vorticity

VORTICITY is a term used to denote rotational fluid flow about a point. Flow visualisation by parametric motion field alone is often insufficient in characterising fluid rotation. Note that although such velocity information is limited in a concise description of the flow, the use of additional quantities such as strain rates can help us to gain more insight into the fluid motion. This chapter discusses the influence of vorticity mapping by flow field noise and sampling window size used in vorticity derivation.

Our work investigates reduction of noise during vorticity calculation based on imperfect flow information without excessive loss of critical flow features, and thereby improves the effectiveness of flow visualisation. We also examine the effect of resolution of field grid on vorticity measurement. This study gives a basic introduction of vorticity from first principles, and aims to prepare the reader for understanding its implications in flow analysis used in subsequent chapters of this thesis.

6.1 Introduction

Flow visualisation is a technique of making fluid motion visible for viewing, and allowing the interpretion of its flow structure through the use of qualitative information on other parameters within the field. Planar flow imaging by two-dimensional particle image velocimetry (Raffel *et al.* 1998, Adrian 2005), phase contrast magnetic resonance velocimetry (Raguin *et al.* 2005) or fluid motion estimation (Cuzol *et al.* 2007) have been used to prepare parametic motion field of the flow. However, imperfect measurement conditions and noise often degrade the flow measurements.

In many instances, post-processing of flow data, such as identification of inconsistent or outlying vectors using the median test (Raffel *et al.* 1998), followed by replacement with interpolated data, can be employed to improve the flow measurement accuracy. Derivative estimation based on the processed data is typically performed for a more detailed flow analysis. Despite efforts to reduce noise in the data and to improve accuracy of the derivative estimation (Etebari and Vlachos 2005), the computed vorticity will often be biased and noisy due to the presence of noise in the flow field. Recent studies have quantified the error of measurement based on different vorticity measurement schemes (Fouras and Soria 1998). The vorticity calculation will be affected by noise based on a minimally sized interrogation window (for example, of a 3×3 grid point array) and such a configuration cannot provide sufficient averaging and inherent smoothing to deliver a representative vorticity field.

To examine fluid rotation and strains, the derivation of differential quantities from flow field grid is necessary. Using a multi-step first order differentiation technique applied over a range of sampling array sizes, we are able to map in two dimensions, strain rates of fluid within a region of investigation. We can then present the distribution of these properties in this space by means of a colour map representing the strain rates values and prepare statistics from the strain fields.

By estimating velocity gradients numerically, we can develop a set of equations for flow derivatives based on interrogation windows of different sizes. Using a larger sampling window, we intrinsically average a larger group of the flow data while providing an indication of the fluid vorticity at a point of interest. However, over-averaging of the data suppresses the flow details. The sampling window configuration of the calculation needs to be selected to produce vorticity maps that relate to that of an acceptable vorticity flow field to a maximum extent. Over-sizing the window destroy the intricate flow features (which can be amplified if resolution of flow grid is high), while

under-sizing it gives a poor global representation of the vorticity map of a vortex. It is therefore of interest to develop a framework for analysing the reliability of vorticity calculations to best represent the vorticity. To solve the problem, we develop a framework that can test the reliability of the computation based on a specific sampling window configuration.

6.2 Methods for Visualisation of Vortices

Vorticity ω (in units of s^{-1}) is defined as the curl of velocity v whereby $\omega = \nabla \times v$ and is a representation of the orientation and angular velocity of local rotation (Potter and Wiggert 1997). The display of a two-dimensional vorticity map of a single vortex based on its velocity field can be used to indicate the vortex core and its rotation. By analysing the vorticity field of a vortex, the strength and length scale of the vortex can be characterised.

Other than the examination of vorticity gradient, we can also visualise vortices using volume reconstruction of uniform vorticity magnitude in space (Silver and Wang 1996). Their iso-volume components can then be used to locate vortex structures that evolve over time. Other techniques include tracing of vortex cores. There are more than one definition of vortex core and its detection. For example, points of maximum enstrophy (one-half the square of the relative vorticity) are defined to exist along the core (Jiminez *et al.* 1993). Other definitions include the local maxima of normalised helicity (Yates and Chapman 1991). Note that helicity is defined as the extent to which fluid travels in a corkscrew-like motion. A study by Banks (1995) uses a vorticity-predictor pressure-corrector scheme to follow vortex cores. In this implementation, low pressure and a large magnitude of vorticity indicates the presence of a vortex. The surface reconstruction of vortex using regions that follow the vortex cores can be performed. Instantaneous streamline mapping is another method to indicate fluid vorticity.

Streamline tracing on a plane normal to the vortex core can be performed to exhibit pattern of lines over the vortex region (Robinson 1991, Robinson 1989, Robinson *et al.* 1989). Nevertheless, this method requires *a priori* knowledge of the vortex core. In addition, vorticity can be present in shear flow without displaying any form of swirling (Sadlo *et al.* 2006).

6.3 Differential Quantities of Flow

From the fluid mechanical perspective, the velocity flow field alone is insufficient in establishing a full physical description of flow. Other measures can be calculated within the scope of the present flow field generation technique. Differential quantities, such as vorticity or strain rate, will be able to provide a better description of the fluid dynamics. If resolved temporally, such fields, in addition to using velocity data, can be used to study the flow field.

6.3.1 First Order Finite Differentiation

A pre-requisite to examining the suggested flow parameters is the requirement to develop a finite element differentiation technique for facilitating the computation of velocity field differentiation using data sampled within an interrogation window. Numerical first order differential operators based on single-level differential operators have been described by Raffel *et al.* (1998). We shall examine the approximation of the gradient of a function based on a point of differentiation with reference to Figures 6.1 and 6.2. .

Assume that $f(x)$ is sampled at discrete locations such that $f_i = f(x_i)$. A first order differential implementation for data spaced at uniform Δx intervals along the x-axis can be given by a central difference (CD) scheme such that:

$$f_i'(2\Delta x) \approx \frac{f_{i+1} - f_{i-1}}{2\Delta x}. \tag{6.1}$$

We sample multiple discrete locations such that $[f_{i-N}, \ldots, f_i, \ldots, f_{i+N}]$ are obtained at $[x_{i-N}, \ldots, x_i, \ldots, x_{i+N}]$. The distance between each pair of sampled points, x_{i-n} and x_{i+n} about x_i is given by $2n\Delta x$.

By averaging of $f_i'(2n\Delta x)$ for $n = 1$ to N, a first order differential at point x_i becomes

$$\left(\frac{\delta f}{\delta x}\right)_i = \frac{1}{N}\sum_{n=1}^{N} f_i'(2n\Delta x) \approx \frac{1}{N}\sum_{n=1}^{N} \frac{f_{i+n} - f_{i-n}}{2n\Delta x}. \tag{6.2}$$

The proposed multi-step gradient averaging also has the advantage of smoothing out local discontinuities and/or noise within the function. It also results in higher errors at points of inflexion. Using this derived equation, we will be able to calculate the

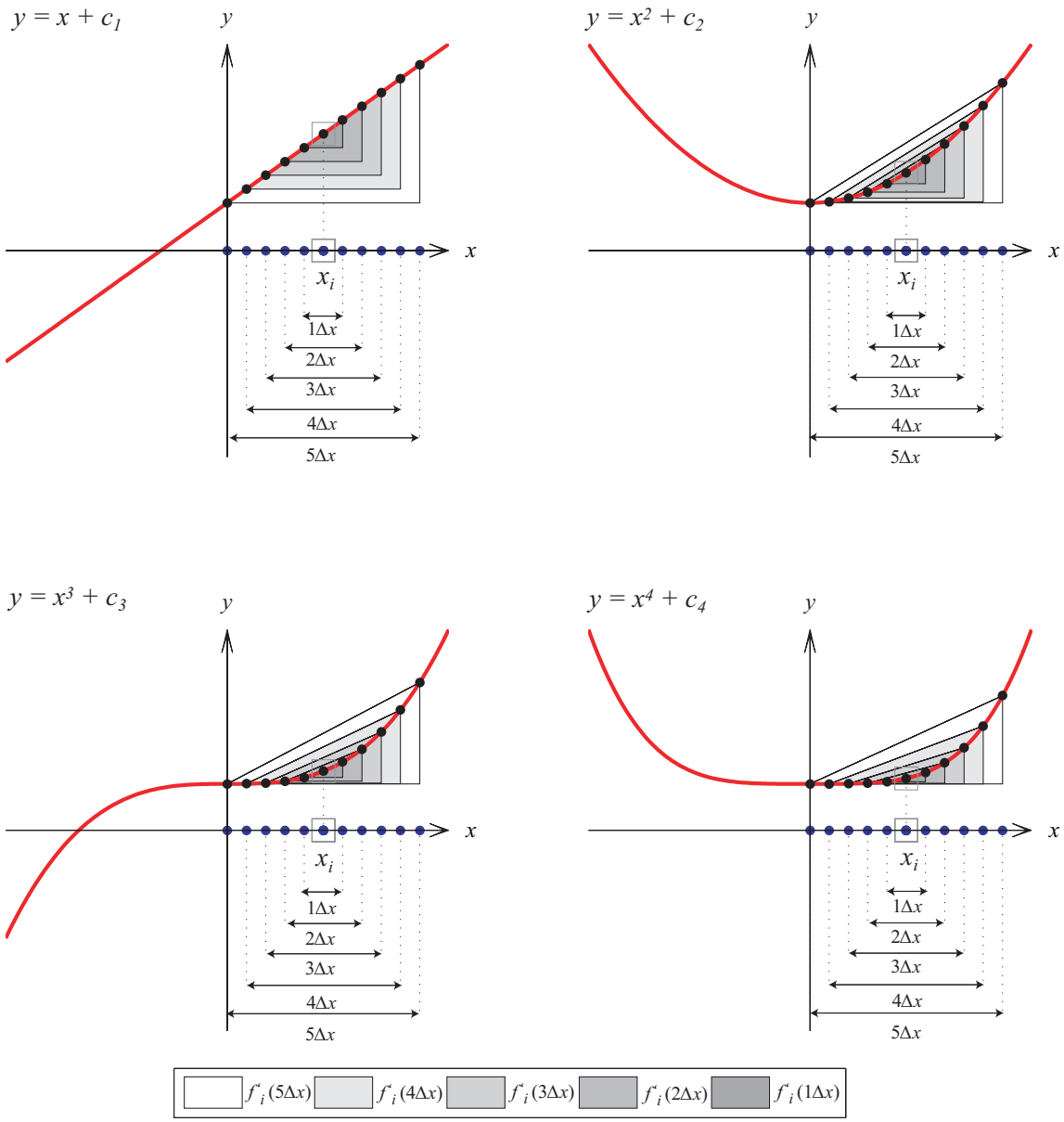

Figure 6.1. First order differentiation using averaging of sampled graph gradients. The graphs of $y = x^k + c_k$ are plotted with the purpose of demonstrating how increase in the rate of change of gradient, as k is incremented from 1 to 4, can affect the results of the multi-step finite differentiation technique. Sampling of y based on equal distanced intervals of Δx for a series of x values about a point of differentiation are used in the computation of multiple gradients. Each of these gradients on the same graph is represented using the slope of a right-angled triangle and its magnitude can be indicated by a gray-scale intensity value. The averaging of these gradients is an approximation of the first order differentiation of y. However, the accuracy of this method declines when the change of gradient over a sampling space becomes higher. For such a condition, it is advisable to use smaller sampling intervals or fewer sampling points about the point of differentiation.

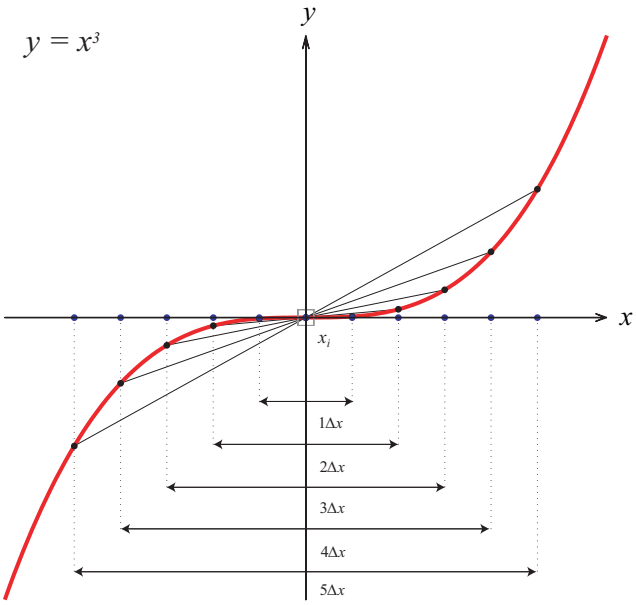

Figure 6.2. Multi-step first order differentiation for graph with a point of inflexion. If the differentiation is performed at the point of inflexion for $y = x^k$ and k are odd number integer values, the accuracy of the multi-step finite differentiation using averaging of multiple sampled gradients decreases as more sampling points taken further away from the point of differentiation is performed. The proposed numerical technique still gives a reasonable estimate of the gradient provided that the sampling set about the differentiation point is taken at y before its curvature changes steeply. This curvature change is more exemplified when k is incremented.

approximate differential quantities of flow by numerical differentiation of flow field in the x and y directions.

Graphs with inflexion points exist for $f(x) = x^k$ given that k assumes odd number integer values. The analytical differentiation of $f(x)$ results in $f^{'}(x) = kx^{k-1}$, where at $x = 0$, this gradient is calculated to be zero. Using finite differentiation method and knowing that $f_{i-n} = -f_{i+n}$, the gradient at each interval step of Δx becomes a finite non-zero value of $\frac{f_{i+n}}{\Delta x}$ since $f_{i+n} > 0$ at $x > 0$. We arrive at the conclusion that

$$\left(\frac{\delta f}{\delta x}\right)_i = kx_i^{k-1} \neq \frac{1}{N}\sum_{n=1}^{N}\frac{(x_{i+n}^k)}{n\Delta x}, \tag{6.3}$$

given the conditions $x_i = 0$ and $x_{i+n} \neq 0$. Note that as n increases when more sampling points are taken, the rate of change of f_{i+n}, as demonstrated by Figure 6.2, increases and results in a higher $\left(\frac{\delta f}{\delta x}\right)_i$. Therefore, we conclude that solution by the proposed multi-step finite differentiation deviates from the exact value more when the degree

of curvature is higher and when the differentiation point coincides with the point of inflexion along the curve. To retain good accuracy, a set of values with its region of interrogation avoiding sampling of x with high degree of change is preferred. Inaccuracy due to such high gradients can be controlled by having a smaller sampling number or interval size.

Let us revisit first order differentiation from a two-dimensional perspective. Based on the velocity field, with its x and y components as $V_x(i,j)$ and $V_y(i,j)$ respectively, about a point of interest located at (i,j), N represents the number of layers of the contour within the interrogation window or sampling frame and Δx and Δy represent the horizontal and vertical intervals between neighboring measurement points. The vorticity, shear strain and normal strain flow characteristics can then be determined based on numerical differentiation when deriving the differential quantities.

6.3.2 Vorticity

The out-of-plane vorticity component is calculated from the in-plane velocity field using the scheme shown in Figure 6.3[15] and Equation 6.4. The circulation is the line integral of the tangential velocity along a circuit (in a counter-clockwise fashion) enclosing a point of interest. The vorticity ω is then equal to the circulation divided by the area enclosed by this circuit.

Mathematically, this translates to

$$\omega = \left(\frac{\partial V_y}{\partial x} - \frac{\partial V_x}{\partial y}\right)_{i,j} = \lim_{\Delta x,\Delta y \to 0} \frac{1}{N^2} \sum_{m=1}^{N} \sum_{n=1}^{N} \left[\frac{V_y(i+m,j+n) - V_y(i-m,j-n)}{2m\Delta x} - \frac{V_x(i+m,j+n) - V_x(i+m,j-n)}{2n\Delta y} \right]. \tag{6.4}$$

From the formulation, positive values signify counter-clockwise (CCW) circulation, whereas negative values represent clockwise (CW) rotation of the fluid. Therefore, the magnitudes of these values give an indication of the rate of rotation and its polarity signifies the direction of the rotation. These may be represented by a colour scale with maximum CCW and CW absolute values corresponding to red and blue respectively.

[15] Diagrams in Figure 6.3, 6.4 and 6.5 are adapted from diagrams that appear in Raffel *et al.* (1998).

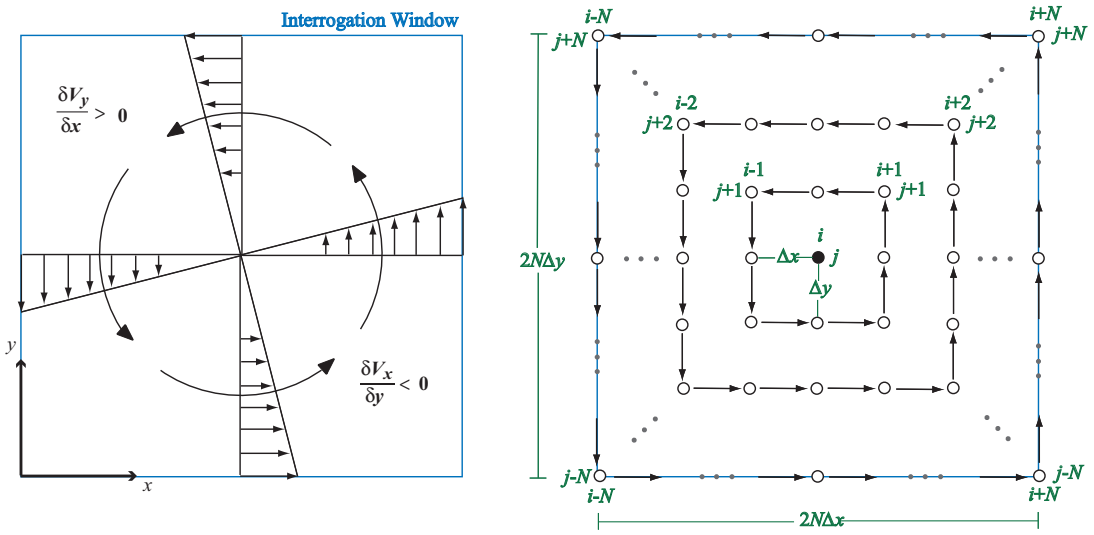

Figure 6.3. Vorticity computation using finite elements. Display of fluid rotation can be represented using finite elements and flow vectors. Vorticity computation is based on the curl of velocity at a point and numerical calculations is carried out using vectors along contour around a point in the flow field. The vorticity is represented by a normal component of the in-plane flow that passes through the plane.

6.3.3 Shear Strain Rate

The shearing of a medium is conceptualised by imagining that the flow is stratified into layers of moving fluid about a point of measurement, and assuming that the finite vectors of the fluid flow is arranged in the configuration as shown by Figure 6.4 and by following Equation 6.5. The schematic illustration of flow shear strain given in this diagram demonstrates that fluid is simultaneously compressed and dilated within the interrogation region. Therefore, for a single layer contour configuration based on a point of measurement, it may be conceived as the summation of partial derivatives $\frac{\partial V_x}{\partial y}$ and $\frac{\partial V_y}{\partial x}$.

Shear strain rate can be computed as

$$\phi = \left(\frac{\partial V_x}{\partial y} + \frac{\partial V_y}{\partial x}\right)_{i,j} = \lim_{\Delta x, \Delta y \to 0} \frac{1}{N^2} \sum_{m=1}^{N} \sum_{n=1}^{N} \left[\frac{V_x(i+m, j+n) - V_x(i+m, j-n)}{2n\Delta y} + \frac{V_y(i+m, j-n) - V_y(i-m, j+n)}{2m\Delta x} \right]. \tag{6.5}$$

From the bio-fluid mechanics perspective, the shear of blood can be visualised as having stratified parallel layers of the bio-fluid moving at different velocities relative to

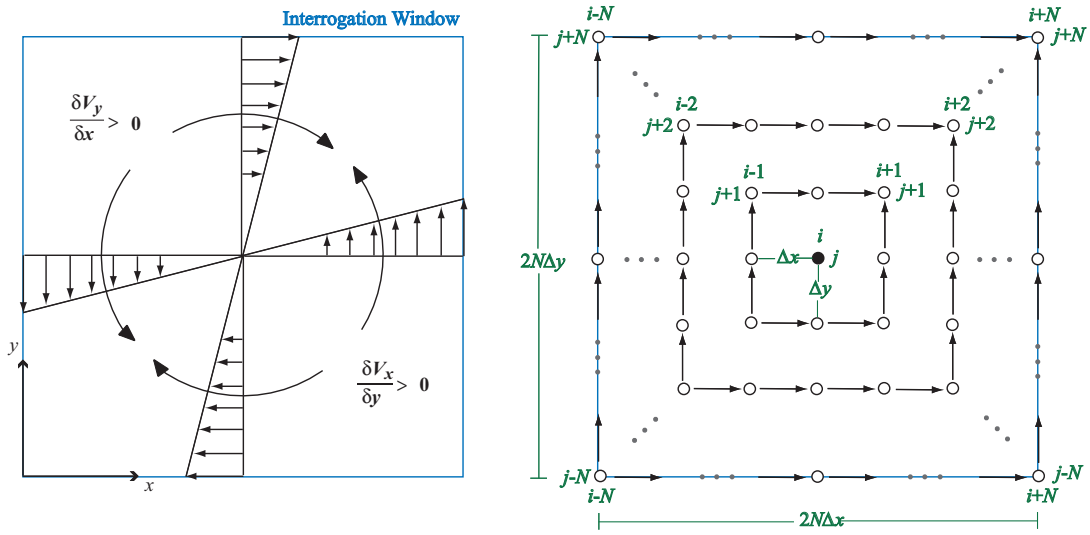

Figure 6.4. Shear strain computation using finite elements. Shear strain calculation based on finite elements and vectors along contour of flow is demonstrated. The flow along the contour co-exists in opposing motion to cause strain for the points at the upper right and lower left corner of the square node mesh respectively. Derivation of shear strain through the entire flow image gives the shear strain map.

one another, thereby creating friction between neighbouring layers. The blood friction induces platelet activation and leads to thrombus formation. Therefore, presenting a shear strain/strain map can provide some indication of the probability of thrombosis in blood. However, it is not the scope of the chapter to discuss this further.

6.3.4 Normal Strain Rate

The normal strain rate Ψ is based on a different configuration as illustrated in Figure 6.5 and Equation 6.6. The normal strain is related to the pressure experienced by the blood at local positions and this has some implications in strain rate of the fluid. The polarity of the parameter determines the direction of compression. A negative compression means fluid dilation.

Normal strain rate can be computed using

$$\psi = -\left(\frac{\partial V_x}{\partial x} + \frac{\partial V_y}{\partial y}\right)_{i,j} = \lim_{\Delta x, \Delta y \to 0} -\frac{1}{N^2} \sum_{m=1}^{N} \sum_{n=1}^{N} \left[\frac{V_x(i+m, j+n) - V_x(i-m, j+n)}{2m\Delta x} + \frac{V_y(i+m, j+n) - V_y(i+m, j-n)}{2n\Delta y} \right]. \tag{6.6}$$

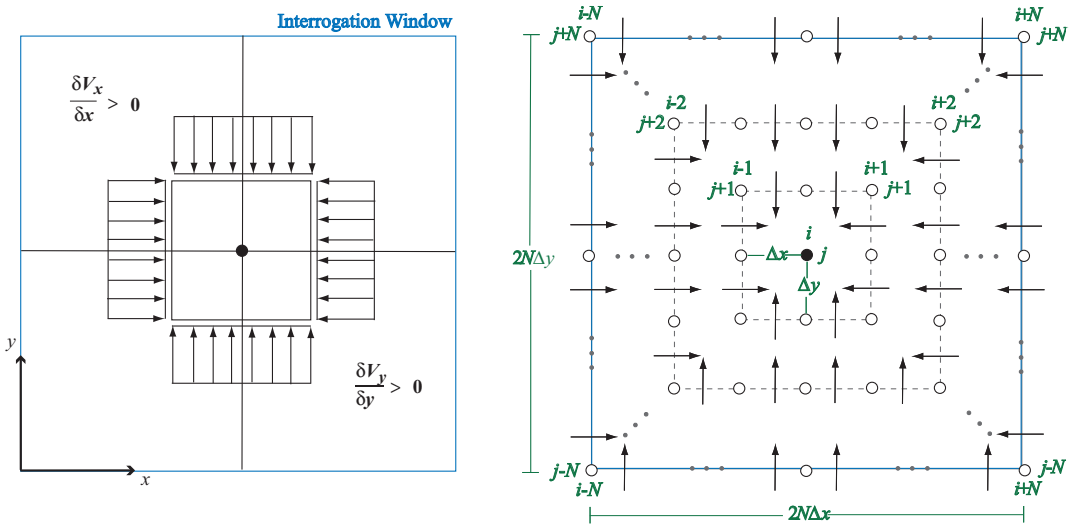

Figure 6.5. Normal strain computation using finite elements. Normal strain is displayed using finte elements and flow vectors. The calculation of this parameter is based on vectors towards a point. An impression of pressure is given by examining how fluid moves towards or away from a point. Polarity of this parameter gives an indication of the direction of compression.

For cardiac flow, strain rate measurements can give the pressure field of blood within the cardiac chamber and can be used to identify potential regions of compression or dilation in blood. Although it may be too crude at this stage to rely on computational prediction of blood dynamics to assess strains within blood in cardiac chamber, a comparative indication of how much strain blood is experiencing among different regions of the fluid can be provided.

With these numerical differential methods, $\frac{\partial V_y}{\partial x}$, $\frac{\partial V_x}{\partial y}$, $\frac{\partial V_x}{\partial x}$ and $\frac{\partial V_y}{\partial y}$ can be obtained to estimate the vorticity, shear strain and normal strain based on the velocity field.

6.4 Statistics of Differential Flow Map

We can perform a statistical analysis of the vorticity distribution using histogram of the map image representation (Gonzalez and Woods 2002, Duan *et al.* 2006b). Assume a map of size M by N pixels, with vorticity or strain magnitude $f_{x,y}$ at a map element location coordinates (x, y). The discrete histogram graph of F versus f is numerically computed by incrementing $F(i)$ with a unit of 1 if $f_{x,y}$ falls within the range of differential flow values specified by n number of bins with each denoted as i. This histogram can be represented using a bar plot in Figure 6.6(a). The mathematical description of

a histogram can be based on Equation 6.7. A parameter $K_{x,y}(i)$ is designated to set its value to 1 or 0 depending on whether it falls within scalar value representation of each bar denoted as i. The sum of $K_{x,y}(i)$ for $1 \geq x \geq M$ and $1 \geq y \geq N$ at every range set by i can be mathematically expressed as:

$$F(i) = \sum_{x=1}^{N} \sum_{y=1}^{M} K_{x,y}(i) \tag{6.7}$$

where $K_{x,y}(i) = \frac{(f_i - f_{x,y}) \times (f_{x,y} - f_{i-1})}{2|(f_i - f_{x,y}) \times (f_{x,y} - f_{i-1})|} + \frac{1}{2}$ and $f_{i-1} > f_{x,y} \geq f_i$ given that $f_i = f_{\min} + \frac{f_{\max} - f_{\min}}{n} i$ for $0 > i \geq n$. Therefore, i is the value of interest pertaining to a histogram bin, n is the total number of bins, and $f_{\min} > f_i \geq f_{\max}$ for all f_i. The formulation forces $K_{x,y}(i)$ to be 1 when the differential flow value $f_{x,y}$ at map coordinates (x, y) falls within the range set by the values of f at $(i-1)$ and i. If the sitaution occurs otherwise, $K_{x,y}(i)$ is set as 0.

The histogram that is produced based on the proportion of map area versus the vorticity values $\omega(s^{-1})$ throughout the entire flow map is featured in Figure 6.6(b). A higher resolution of the graph using more horizontal axis intervals results in smaller histogram bar width.

The histograms pertaining to the vorticity field plots can be computed based on this statistical framework. We are able to calculate the mean, μ and median, m from each of these histograms. The median of the histogram is a single value that is the middle quartile or 50^{th} percentile of the sampling such that at least 50% of the sample values are smaller or greater than this value. Percentiles provide an indication of how the data values are distributed over the interval from the smallest value to the largest value. The median is a robust measure of central tendency in the presence of outlier values. A measure of the average vorticity map value is computed by taking the mean, $\overline{\omega}_\mu$, or median, $\overline{\omega}_m$ of the frequency histograms generated from vorticity maps. The magnitudes of these parameters are represented by superimposing onto the histogram using lines with blue solid and dash formats for the mean and median respectively, while the zero ω line in grey colour represents irrotational flow.

We can extract the vorticity standard deviations from the flow map that measures the relative scatter around the mean and median of the vorticity values in the map respectively. Standard deviation σ with respect to μ can be computed by considering the

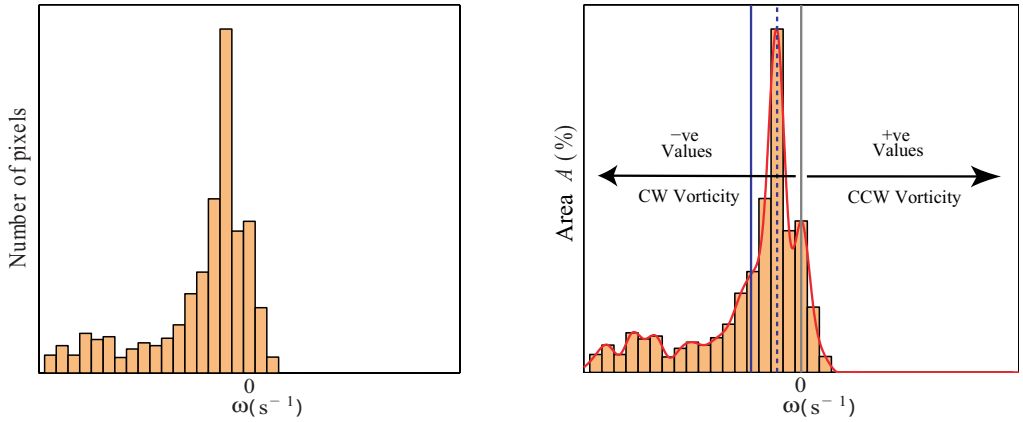

(a) Number of pixels versus vorticity $\omega(s^{-1})$ (b) Area A(%) versus vorticity $\omega(s^{-1})$

Figure 6.6. Histogram of vorticity distribution. A histogram depicting the probability distribution of vorticity or strain within the region of analysis gives some indication of the degree of rotation within the fluid as shown in part (a). Flow investigations can be carried out to a limited extent by analysing normalised histograms with respect to the flow area. In this example, the mean μ and median m, shown by the blue striaght and dash lines respectively, are on the left side of the zero-value centre line shown in grey as illustrated in part (b). Therefore, we can deduce that the flow is dominantly clockwise since vorticity mean and median values are negative.

variation about the mean, and is denoted as σ_μ. Based on a similar mode of computation, calculating the degree of variation about the median will give σ_m.

For standardisation of histogram due to difference in the image sizes for each set of scans, we need to assign the area under the histogram graph (or the sum of all bin arrays) to a constant number. This is performed for a set of images to attain a controlled comparison. Since the total number of grid points measured is now normalised and standardised, if the points are dominated by vorticities of low values, it means that within the region of measurement, the flow is mostly irrotational. Comparatively, if the counts of the points with irrotational flow are smaller, there should be a larger region of rotational flow signified by distribution with non-zero absolute values.

Generally, at a particular time instance, if the velocity field map demonstrates significant irrotational flow regions, the mean vorticity should be close to zero. In the case of a single and dominant vortex, it is likely that the mean vorticity will shift away from the zero flow value, and broaden the distribution of the histogram. Such an analysis methodology can help in assessing the relative intensity of flow property of the fluid. If there are regions of rotational flow with different polarities such that all the fluid

rotation cancels out each other, then the mean will also approximate zero. For this condition, the standard deviation of the histogram can indicate the size of region with rotational versus irrotational flow. Flow visualisation supported with histograms of vorticity and strain flow map can provide a better overview of the swirl and strain present within the fluid.

6.5 Vortex Visualisation Using Theoretical Formulation

6.5.1 Formulation of Vortex Flow Field

We create analytical data using theoretical vortex formulation to test the robustness of our vorticity measurement. The flow fields are generated based on two different configurations of the vortices. In general, we develop flow fields of the single vortex and double vortices pertaining to their two specific sizes respectively.

Single Vortex

Using mathematically generated velocity information based on the Lamb-Oseen vortex, we simulate the principal features of a vortical flow in space. For the purpose of this exercise, we assume that the length scale corresponding to one standard deviation of the Gaussian vorticity distribution, L is 1 mm. The computational domain is $(-5L \leq x \leq 5L)$ and $(-5L \leq y \leq 5L)$, which is equivalent to $(-5 \leq x \leq 5)$ mm and $(-5 \leq y \leq 5)$ mm, whereby (x, y) represents the Cartesian coordinates of the flow field, and the vortex has been scaled such that its maximum tangential velocity is 10 mms^{-1}. An array of 160 by 160 data points represents the velocity flow field of this vortex. Figure 6.7 describes the layout of the velocity magnitudes using flow maps depicting the (a) absolute, (b) horizontal and (c) vertical velocity components.

Double Vortices

We now position two Oseen vortices with core centres at a distance of 5 mm apart from each other. The vortices have different polarities in rotation. This simulates flow consisting of two vortices overlapping partially. Each vortex is constructed in such as way that we computationally set the flow field to span 10 mm by 10 mm in space, and its maximum velocity magnitude to 10 mms^{-1}. Therefore, the maximum absolute velocity in the flow field map can reach up to 20 mms^{-1}. Note that the velocity field of

this flow is represented by a digital image grid with a width of 160 and a height of 240 points matrix size. Figure 6.8 describes the layout of the velocity magnitudes using flow maps depicting the (a) absolute, (b) horizontal and (c) vertical velocity components.

Adding Noise to Flow Field

Noise is added to the perfect flow by modification of field vectors in the form of random realignments and magnitude change to a certain group of dispersed vectors. This is performed by a matrix with elements of range 0 to 1, which are random values based on a Gaussian distribution. The matrix is multiplied onto the x- and y- component maps to modify vector orientation and magnitude, thereby generating outliers within the flow field.

In this study, Gaussian noise is added to the velocity field at percentages of 0 to 25% onto the analytical velocity field to examine the effect of varying sampling window size on vorticity measurements. The effect of increasing vorticity sampling area to its map will be analysed using these data sets. To illustrate the field noise effect on the variation of velocity and vorticity, only the velocity and vorticity flow field maps for 0, 10 and 20% noise addition will be displayed.

Although it is possible to smooth the data before proceeding to vorticity measurement, we are not performing pre-processing of the flow field because our primary purpose is to examine how using different sampling window sizes can average the velocity vectors and inherently smooth the vorticity field. Smoothing the parametric flow field beforehand will not give us a good set of data to experiment on.

6.5.2 Variation of Flow Field Resolution

We vary the field grid resolution from 1 to 16 grid points per mm for a single vortex flow field of 10 by 10 mm (represented using 160 points). In this case, a flow field with no noise is utilised. Sampling window sizes varying from (3×3), (7×7), (11×11) and (15×15) points are used for the field grids at various resolution.

The quality of the vorticity flow map would be affected by the resolution of the grid, since a finer grid contains higher resolution flow features that can be represented using the vorticity map. The results for variation of sampling vorticity windows is dependent on the sampling window ratio and a coarser grid having a lower resolution

vorticity map will affect the vorticity measurement and give rise to a less accurate histogram representation of the map. Therefore the optimal sampling window size to be determined using our framework will be altered, and it is the aim of this experiment to show the nature of this alteration. Examples of flow field showing the absolute values only are illustrated in Figure 6.9.

6.5.3 Configuration for Vorticity Measurement

We examine the concept to generate vorticity that relate to angular velocity of fluid in Section 6.3.2. Based on the calculated velocity field, interrogation areas of some defined sizes are varied for the vorticity calculations. Regions where the sampling windows are exposed partially outside the frame at the edge of the image will be padded with zero velocity vectors. This allows measurement of vorticity near the image borders so as to create vorticity maps of similar dimensions regardless of sampling window size.

From the results describing single and double vortices in the flow field, we are able to visually observe their cores and strength using vorticity flow maps. In addition, from the histogram pertaining to each flow map, we can extract useful statistical properties that reveal some information about the flow scenario, such as the global polarities of vortices in the flow field.

Single Vortex

We apply vorticity calculation of the flow field and represent this at each grid point using colours ranging from blue to red for maximum clockwise to maximum counter-clockwise flow. Various vorticity sampling frame sizes are implemented incrementally to observe their effect in smoothing the vortex calculated vorticity values. Different vortex characteristics and size of the flow field will require unique sampling mask dimensions for capturing the crucial flow information without over- or under-smoothing of vorticity field map.

Histograms of the vorticity maps are devised based on bin resolution of $\omega = 1\ \mathrm{s}^{-1}$ for range of -20 to 20 s^{-1}. Statistical properties of the map such as measures of central tendency and standard deviations are stated for each set of flow field and its histogram.

In this study, we apply sampling mask sizes for vorticity computations ranging from (3×3) to (67×67) points. Each step in the array has a dimension of $\frac{1}{16}$ mm. Therefore we are looking at interrogation window sizes of (0.189×0.189) to (4.19×4.19) mm^2. If

normalised to the flow grid width of 160 points, the sizes range from 0.0188 to 0.419. The analysis is performed for flow fields with 0%, 10% and 20% noise as shown in Figures 6.10, 6.11 and 6.12 respectively.

Double Vortices

For the double vortices, we apply the same sampling mask sizes for vorticity computations ranging from (3×3) to (67×67) points, whereby each step in the array is $\frac{1}{16}$ mm. This is a similar vorticity measurement configuration as the one for single vortex. The vorticity map for these two vortices spans 160 by 240 points. The mean and median of histograms for these flow maps should be ideally zero since there are two vortices with opposite directions of rotation. That will constitute equal number of pixels with the same vorticity values but in two different polarities.

The same configuration for histogram of the maps applies to both the single and double vortices flow field. The bin resolution is set at 1 s^{-1}. Range of ω is -20 to 20 s^{-1}. Statistical properties of the map such as means, medians and standard deviations are computed based on the vorticity distribution in the map. The procedure described above is carried out for flow fields with 0, 10 and 20% noise addition as shown in Figures 6.13, 6.14 and 6.15 respectively.

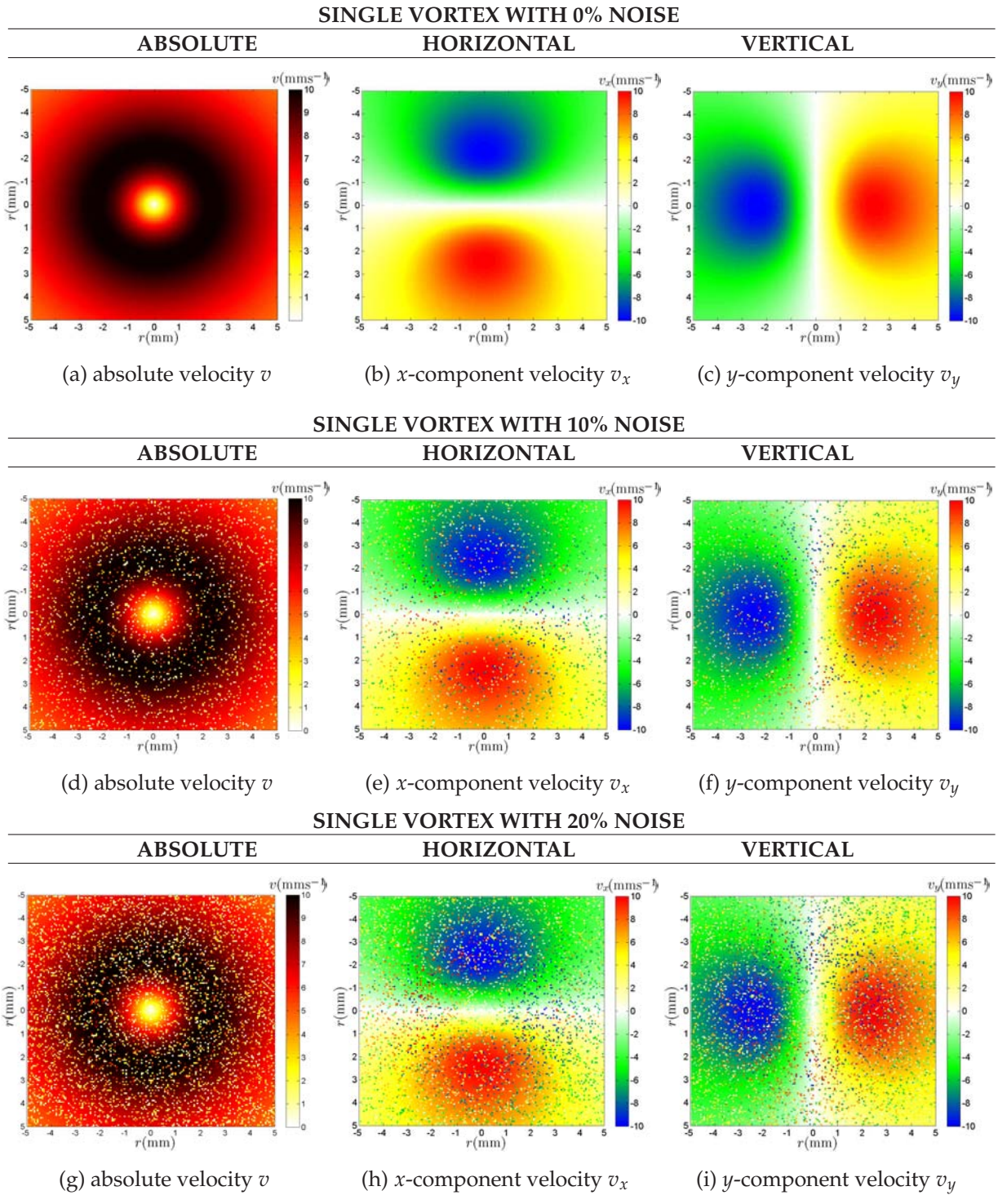

(a) absolute velocity v (b) x-component velocity v_x (c) y-component velocity v_y

(d) absolute velocity v (e) x-component velocity v_x (f) y-component velocity v_y

(g) absolute velocity v (h) x-component velocity v_x (i) y-component velocity v_y

Figure 6.7. Artificially generated single Lamb-Oseen vortex velocity flow field maps. A Lamb-Oseen vortex has a non-uniform distribution of velocity magnitudes that follows a profile defined by a set of equations. The above figure shows the magnitude profile of a vortex in two dimensions using (a,d,g), which can be constructed using velocity flow maps based on the x- and y- components of the counter-clockwise rotation shown by (b,e,h) and (c,f,i) respectively. Vector fields having 10% and 20% of outliers are present to simulate the effect of noise during flow measurement.

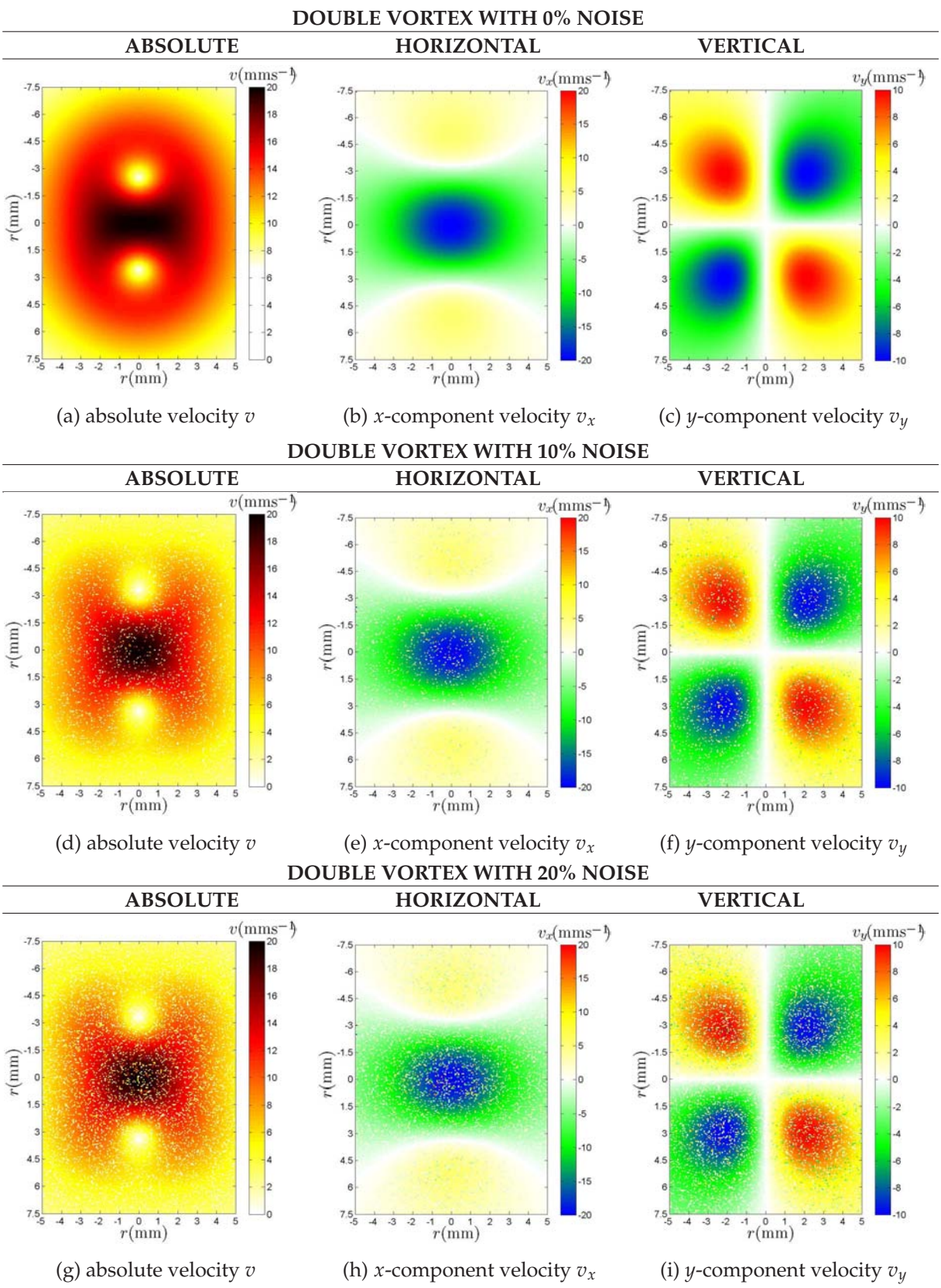

(a) absolute velocity v (b) x-component velocity v_x (c) y-component velocity v_y

(d) absolute velocity v (e) x-component velocity v_x (f) y-component velocity v_y

(g) absolute velocity v (h) x-component velocity v_x (i) y-component velocity v_y

Figure 6.8. Artificially generated double Lamb-Oseen vortices velocity flow field maps. Two Lamb-Oseen vortices with opposite directions of rotation are generated analytically. The two vortices are combined in the field and cover each other partially at a region of overlap. Flow fields having 10% and 20% of outliers are displayed by (a,b,c), (d,e,f) and (g,h,i) respectively.

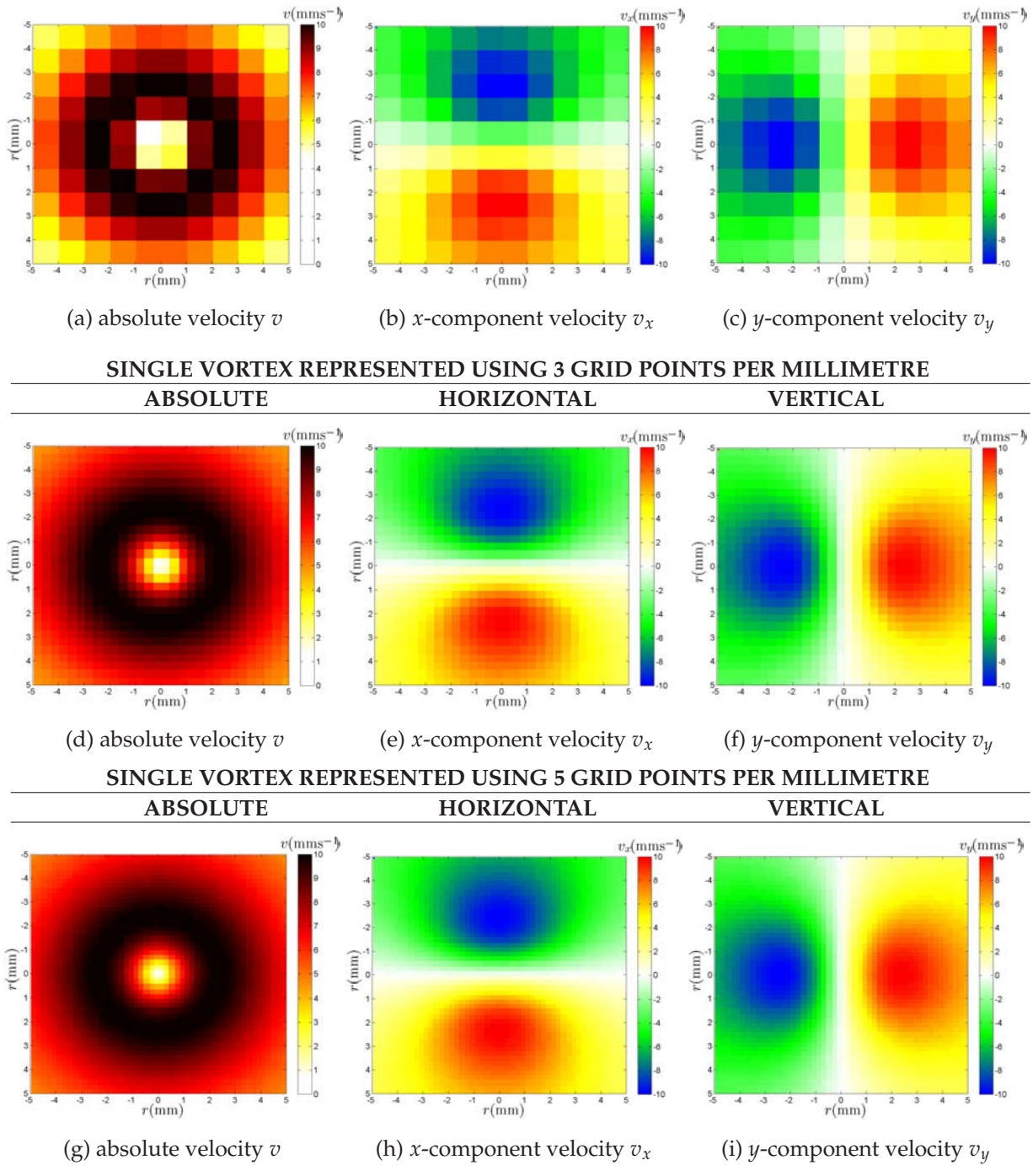

(a) absolute velocity v (b) x-component velocity v_x (c) y-component velocity v_y

(d) absolute velocity v (e) x-component velocity v_x (f) y-component velocity v_y

(g) absolute velocity v (h) x-component velocity v_x (i) y-component velocity v_y

Figure 6.9. Variation of grid resolution for single Lamb-Oseen vortex velocity flow field map. The grid resolution can be varied by resizing the matrix of points used to represent a flow field. The above figure shows the magnitude profile of a vortex in two dimensions using (a,d,g), which can be constructed using velocity flow maps based on the x- and y-components of the counter-clockwise rotation shown by (b,e,h) and (c,f,i) respectively. The resolution of velocity field grid is varied in order to study its influence on vorticity measurement.

SINGLE VORTEX WITH 0% NOISE

CONTOUR MAP	VECTOR MAP	HISTOGRAM

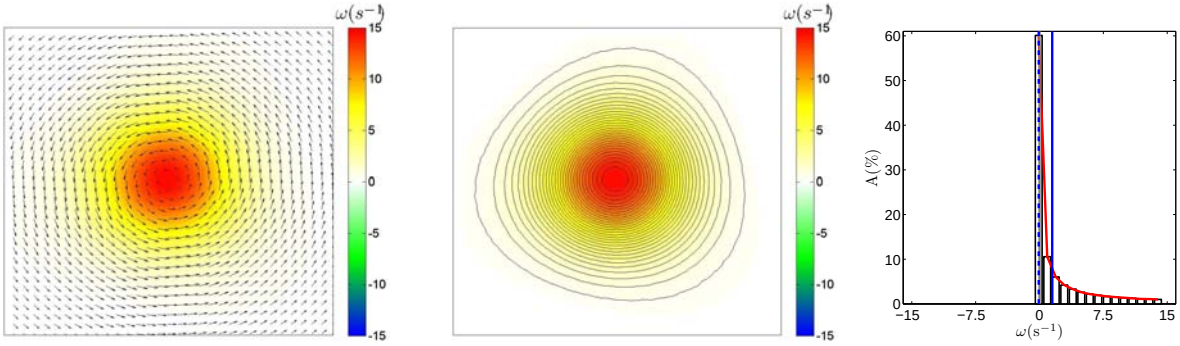

(i) Vorticity sampling window (9×9) grid points, $\begin{bmatrix} \overline{\omega} \\ \sigma \end{bmatrix}_{\mu} = \begin{bmatrix} 2.08 \\ 3.32 \end{bmatrix} \mathrm{s}^{-1}$, $\begin{bmatrix} \overline{\omega} \\ \sigma \end{bmatrix}_{m} = \begin{bmatrix} 0.45 \\ 3.70 \end{bmatrix} s^{-1}$

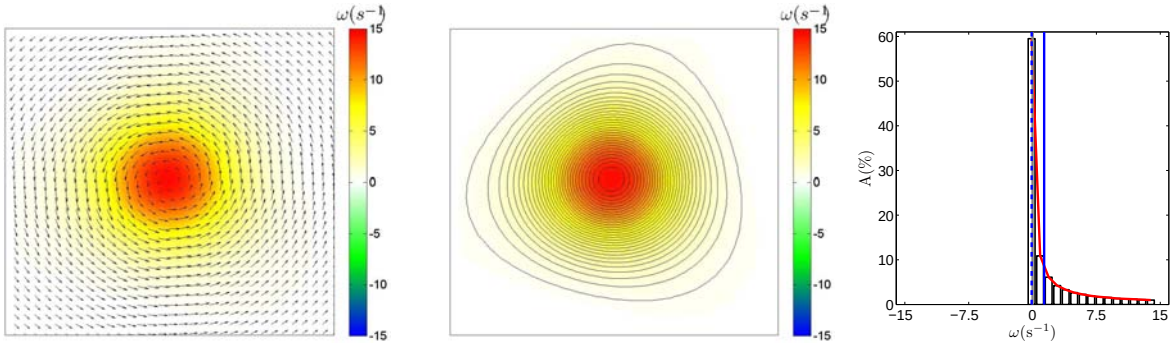

(ii) Vorticity sampling window (13×13) grid points, $\begin{bmatrix} \overline{\omega} \\ \sigma \end{bmatrix}_{\mu} = \begin{bmatrix} 2.08 \\ 3.31 \end{bmatrix} \mathrm{s}^{-1}$, $\begin{bmatrix} \overline{\omega} \\ \sigma \end{bmatrix}_{m} = \begin{bmatrix} 0.46 \\ 3.68 \end{bmatrix} \mathrm{s}^{-1}$

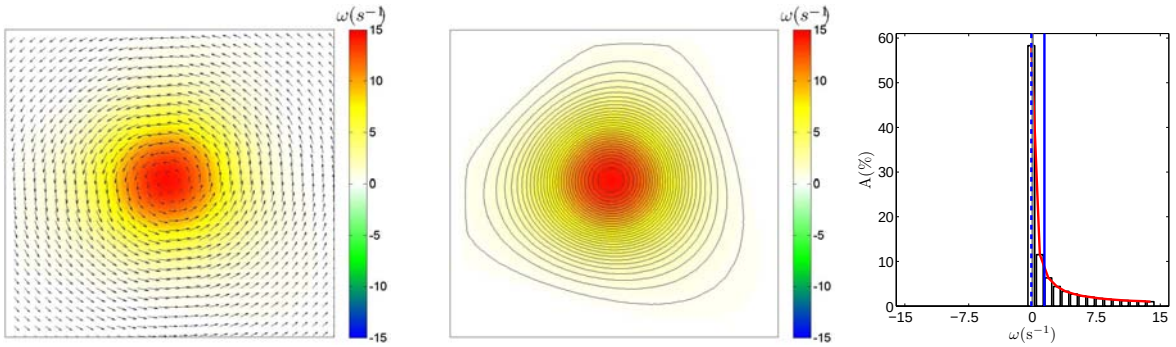

(iii) Vorticity sampling window (17×17) grid points, $\begin{bmatrix} \overline{\omega} \\ \sigma \end{bmatrix}_{\mu} = \begin{bmatrix} 2.08 \\ 3.29 \end{bmatrix} \mathrm{s}^{-1}$, $\begin{bmatrix} \overline{\omega} \\ \sigma \end{bmatrix}_{m} = \begin{bmatrix} 0.48 \\ 3.66 \end{bmatrix} \mathrm{s}^{-1}$

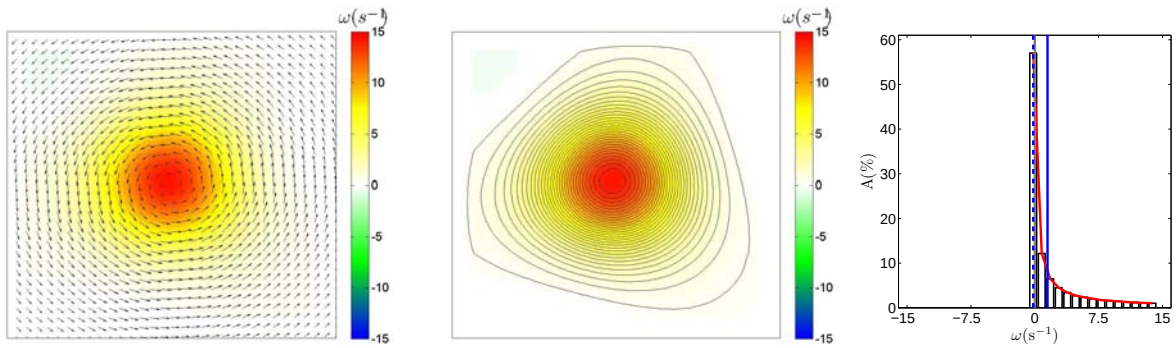

(iv) Vorticity sampling window (21×21) grid points, $\begin{bmatrix} \overline{\omega} \\ \sigma \end{bmatrix}_{\mu} = \begin{bmatrix} 2.07 \\ 3.27 \end{bmatrix} \mathrm{s}^{-1}$, $\begin{bmatrix} \overline{\omega} \\ \sigma \end{bmatrix}_{m} = \begin{bmatrix} 0.49 \\ 3.63 \end{bmatrix} \mathrm{s}^{-1}$

Vorticity sampling windows from (25×25) to (33×33) grid points continues on the next page

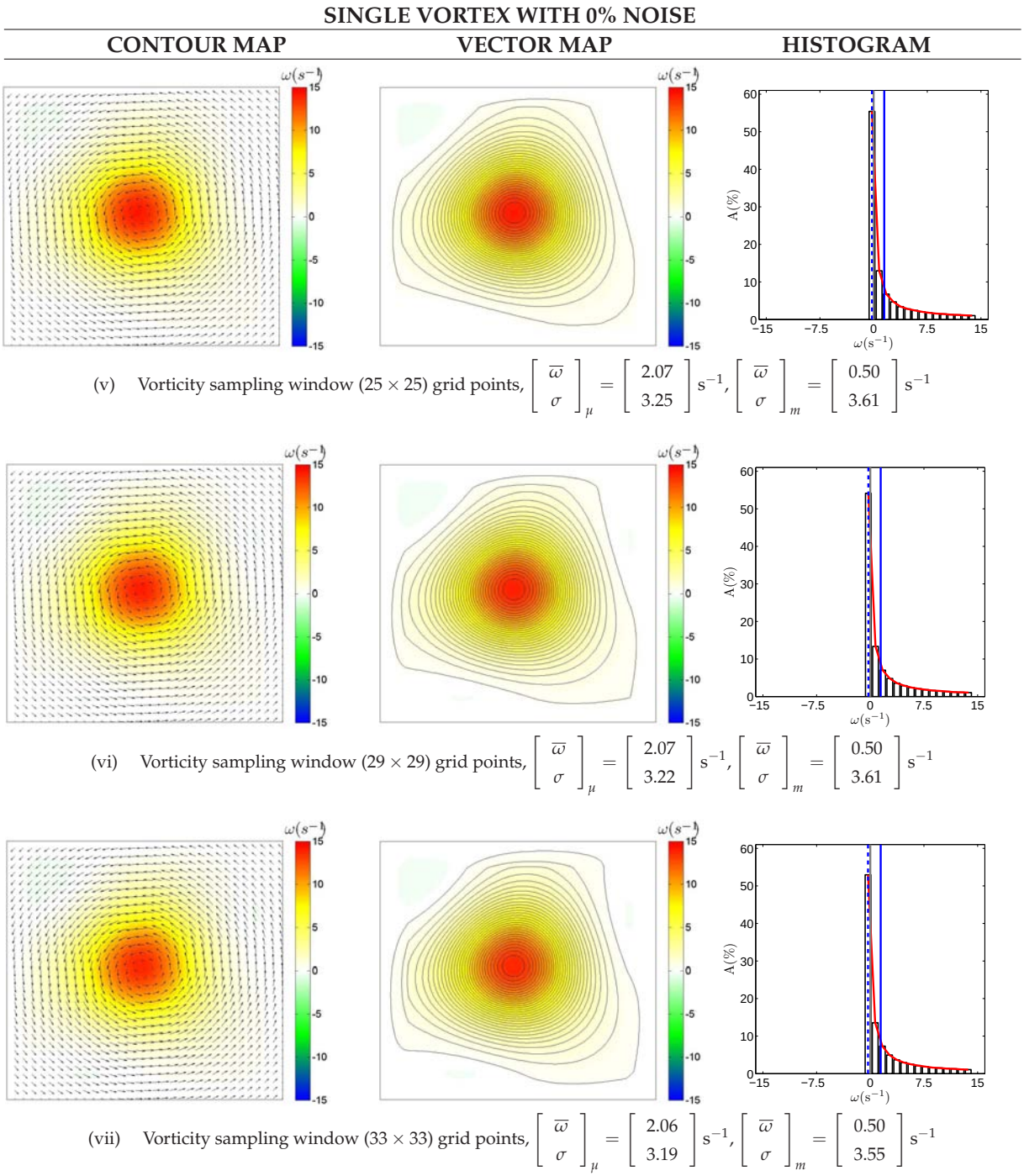

Figure 6.10. Vorticity field of Lamb-Oseen vortex (0% noise). Calculations are performed on the Lamb-Oseen vortex flow field with no noise added to it. The vorticity contour maps are produced based on sampling window size in the range of (9×9) to (33×33) grid points size. This is 5.62×10^{-2} to 2.06×10^{-1} times relative to the grid of 160 by 160 points. Histograms pertaining to each and every of the vortex map are presented in the last column.

SINGLE VORTEX WITH 10% NOISE

CONTOUR MAP	VECTOR MAP	HISTOGRAM

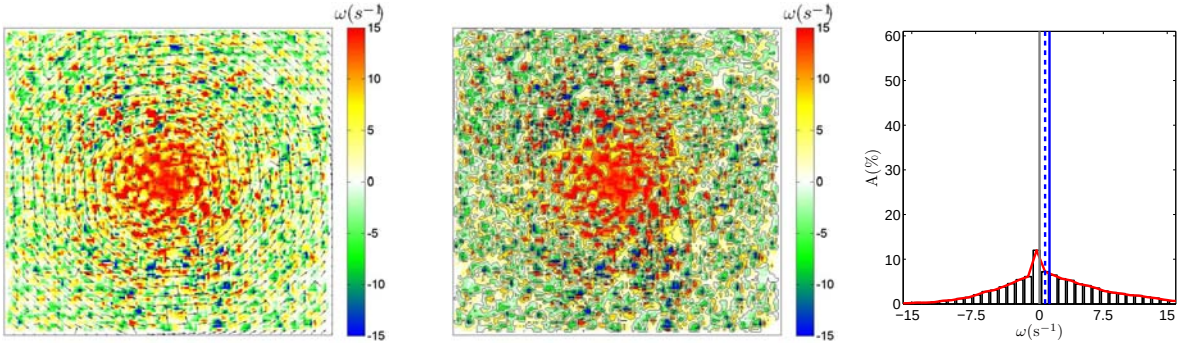

(i) Vorticity sampling window (9×9) grid points, $\begin{bmatrix} \overline{\omega} \\ \sigma \end{bmatrix}_{\mu} = \begin{bmatrix} 1.86 \\ 6.41 \end{bmatrix} \mathrm{s}^{-1}$, $\begin{bmatrix} \overline{\omega} \\ \sigma \end{bmatrix}_{m} = \begin{bmatrix} 1.07 \\ 6.46 \end{bmatrix} s^{-1}$

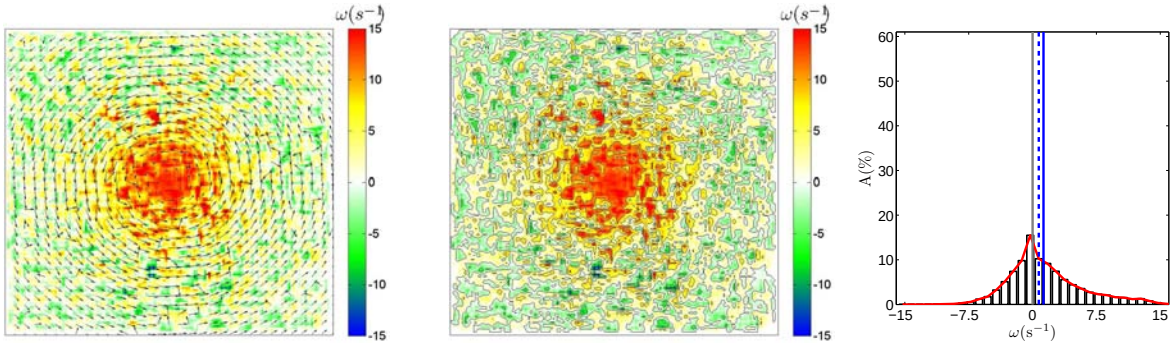

(ii) Vorticity sampling window (13×13) grid points, $\begin{bmatrix} \overline{\omega} \\ \sigma \end{bmatrix}_{\mu} = \begin{bmatrix} 1.86 \\ 4.36 \end{bmatrix} \mathrm{s}^{-1}$, $\begin{bmatrix} \overline{\omega} \\ \sigma \end{bmatrix}_{m} = \begin{bmatrix} 1.01 \\ 4.44 \end{bmatrix} \mathrm{s}^{-1}$

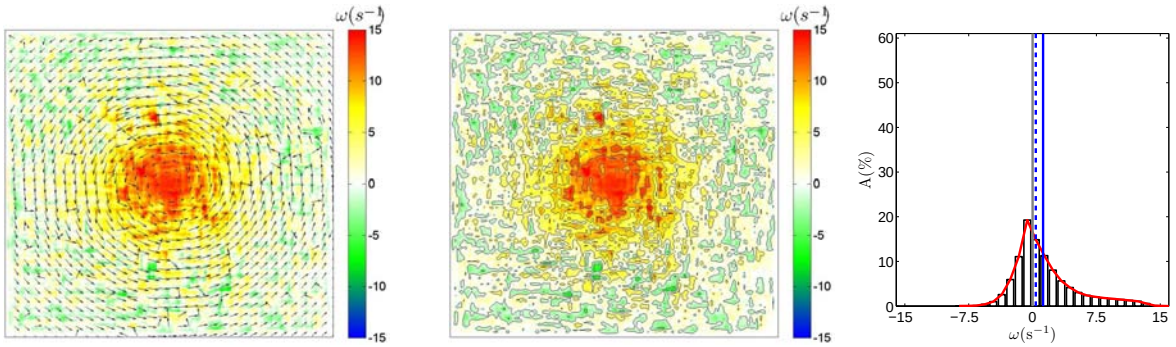

(iii) Vorticity sampling window (17×17) grid points, $\begin{bmatrix} \overline{\omega} \\ \sigma \end{bmatrix}_{\mu} = \begin{bmatrix} 1.86 \\ 3.63 \end{bmatrix} \mathrm{s}^{-1}$, $\begin{bmatrix} \overline{\omega} \\ \sigma \end{bmatrix}_{m} = \begin{bmatrix} 0.91 \\ 3.75 \end{bmatrix} \mathrm{s}^{-1}$

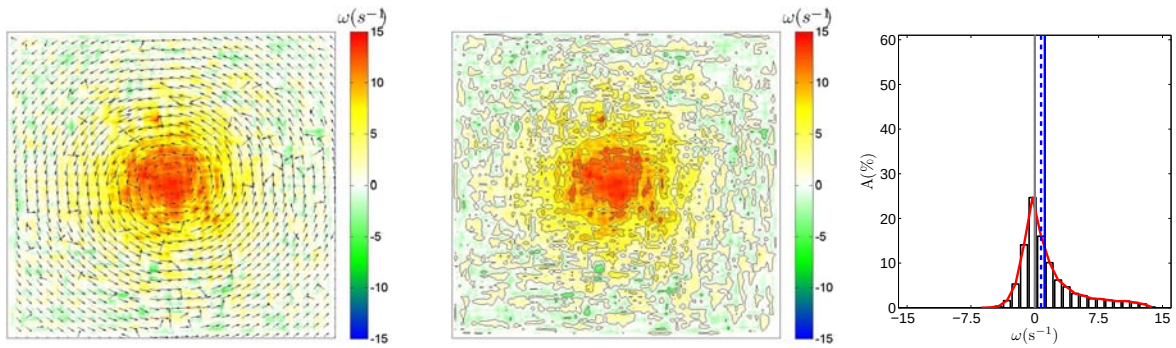

(iv) Vorticity sampling window (21×21) grid points, $\begin{bmatrix} \overline{\omega} \\ \sigma \end{bmatrix}_{\mu} = \begin{bmatrix} 1.86 \\ 3.31 \end{bmatrix} \mathrm{s}^{-1}$, $\begin{bmatrix} \overline{\omega} \\ \sigma \end{bmatrix}_{m} = \begin{bmatrix} 0.79 \\ 3.48 \end{bmatrix} \mathrm{s}^{-1}$

Vorticity sampling windows from (25×25) to (33×33) grid points continues on the next page

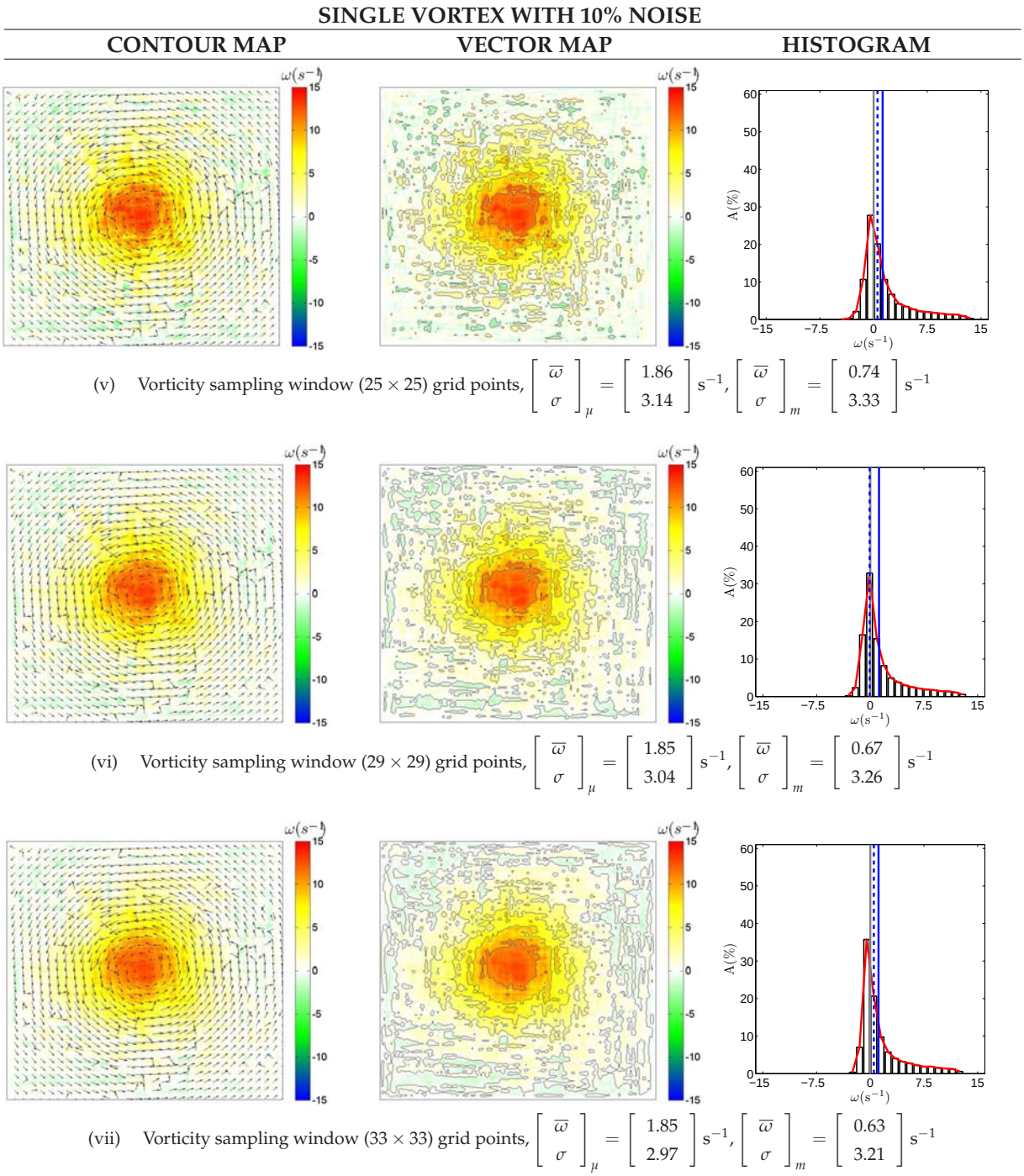

(v) Vorticity sampling window (25×25) grid points, $\begin{bmatrix} \overline{\omega} \\ \sigma \end{bmatrix}_{\mu} = \begin{bmatrix} 1.86 \\ 3.14 \end{bmatrix} \mathrm{s}^{-1}, \begin{bmatrix} \overline{\omega} \\ \sigma \end{bmatrix}_{m} = \begin{bmatrix} 0.74 \\ 3.33 \end{bmatrix} \mathrm{s}^{-1}$

(vi) Vorticity sampling window (29×29) grid points, $\begin{bmatrix} \overline{\omega} \\ \sigma \end{bmatrix}_{\mu} = \begin{bmatrix} 1.85 \\ 3.04 \end{bmatrix} \mathrm{s}^{-1}, \begin{bmatrix} \overline{\omega} \\ \sigma \end{bmatrix}_{m} = \begin{bmatrix} 0.67 \\ 3.26 \end{bmatrix} \mathrm{s}^{-1}$

(vii) Vorticity sampling window (33×33) grid points, $\begin{bmatrix} \overline{\omega} \\ \sigma \end{bmatrix}_{\mu} = \begin{bmatrix} 1.85 \\ 2.97 \end{bmatrix} \mathrm{s}^{-1}, \begin{bmatrix} \overline{\omega} \\ \sigma \end{bmatrix}_{m} = \begin{bmatrix} 0.63 \\ 3.21 \end{bmatrix} \mathrm{s}^{-1}$

Figure 6.11. Vorticity field of Lamb-Oseen vortex (10% noise). Calculations are performed on the Lamb-Oseen vortex flow field with 10% noise added to it. The vorticity contour maps are produced based on sampling window size in the range of (9×9) to (33×33) grid points size. This is 5.62×10^{-2} to 2.06×10^{-1} times relative to the grid of 160 by 160 points. Histograms pertaining to each and every of the vortex map are presented in the last column.

SINGLE VORTEX WITH 20% NOISE

CONTOUR MAP	VECTOR MAP	HISTOGRAM

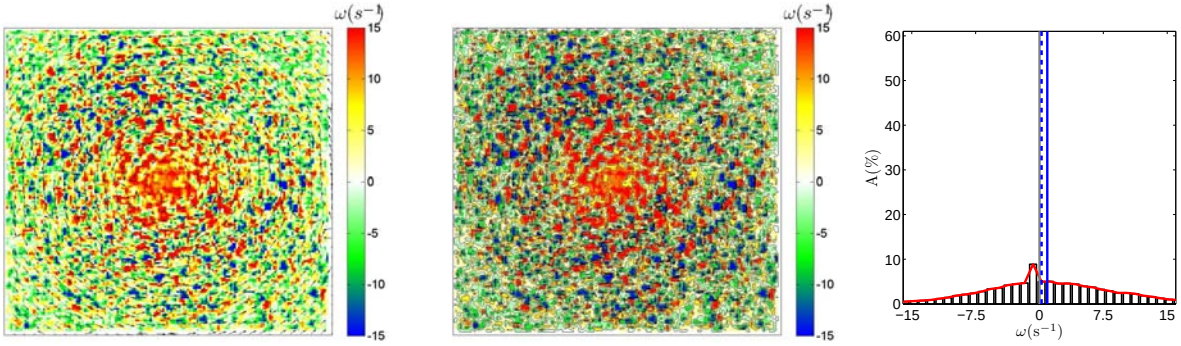

(i) Vorticity sampling window (9×9) grid points, $\begin{bmatrix} \overline{\omega} \\ \sigma \end{bmatrix}_{\mu} = \begin{bmatrix} 1.67 \\ 8.22 \end{bmatrix} \mathrm{s}^{-1}$, $\begin{bmatrix} \overline{\omega} \\ \sigma \end{bmatrix}_{m} = \begin{bmatrix} 1.08 \\ 8.24 \end{bmatrix} s^{-1}$

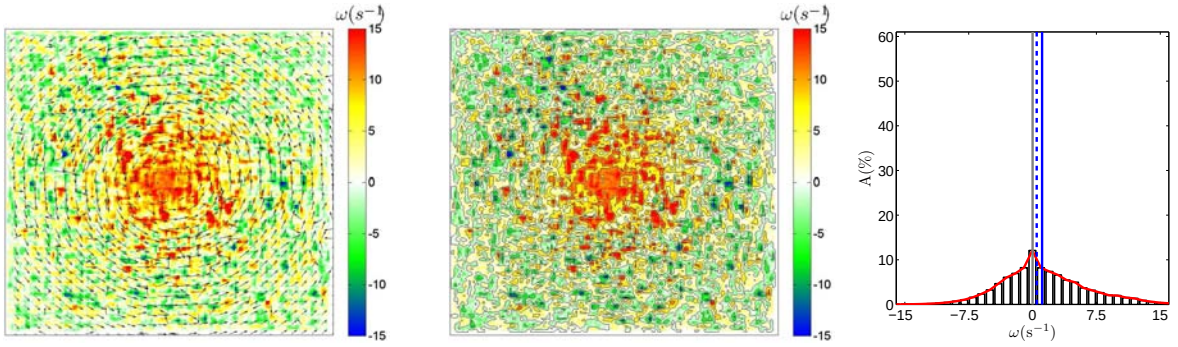

(ii) Vorticity sampling window (13×13) grid points, $\begin{bmatrix} \overline{\omega} \\ \sigma \end{bmatrix}_{\mu} = \begin{bmatrix} 1.67 \\ 5.06 \end{bmatrix} \mathrm{s}^{-1}$, $\begin{bmatrix} \overline{\omega} \\ \sigma \end{bmatrix}_{m} = \begin{bmatrix} 1.03 \\ 5.10 \end{bmatrix} \mathrm{s}^{-1}$

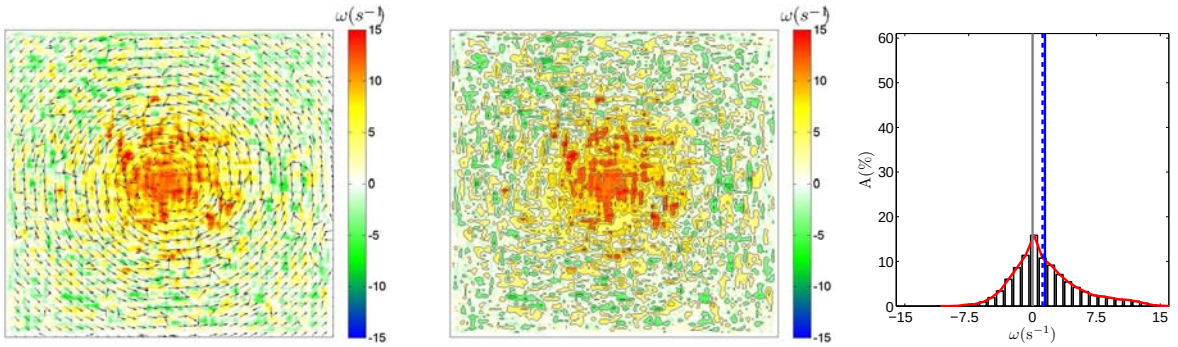

(iii) Vorticity sampling window (17×17) grid points, $\begin{bmatrix} \overline{\omega} \\ \sigma \end{bmatrix}_{\mu} = \begin{bmatrix} 1.67 \\ 3.85 \end{bmatrix} \mathrm{s}^{-1}$, $\begin{bmatrix} \overline{\omega} \\ \sigma \end{bmatrix}_{m} = \begin{bmatrix} 0.93 \\ 3.92 \end{bmatrix} \mathrm{s}^{-1}$

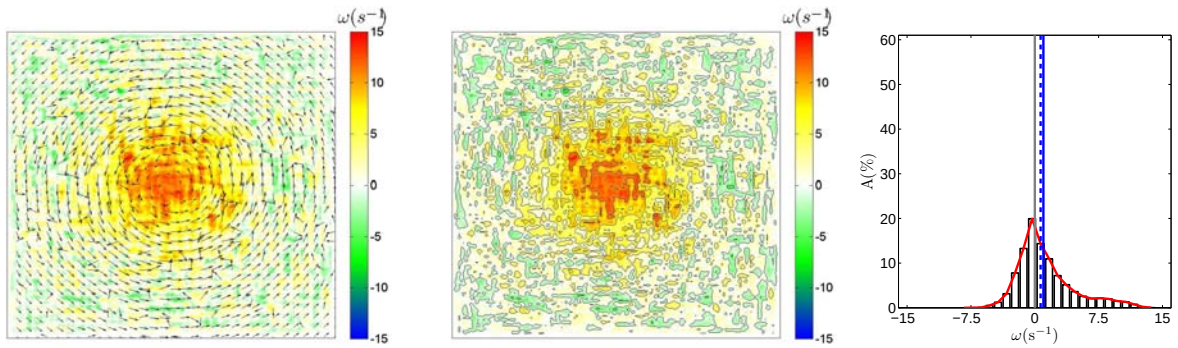

(iv) Vorticity sampling window (21×21) grid points, $\begin{bmatrix} \overline{\omega} \\ \sigma \end{bmatrix}_{\mu} = \begin{bmatrix} 1.66 \\ 3.30 \end{bmatrix} \mathrm{s}^{-1}$, $\begin{bmatrix} \overline{\omega} \\ \sigma \end{bmatrix}_{m} = \begin{bmatrix} 0.85 \\ 3.40 \end{bmatrix} \mathrm{s}^{-1}$

Vorticity sampling windows from (25×25) to (33×33) grid points continues on the next page

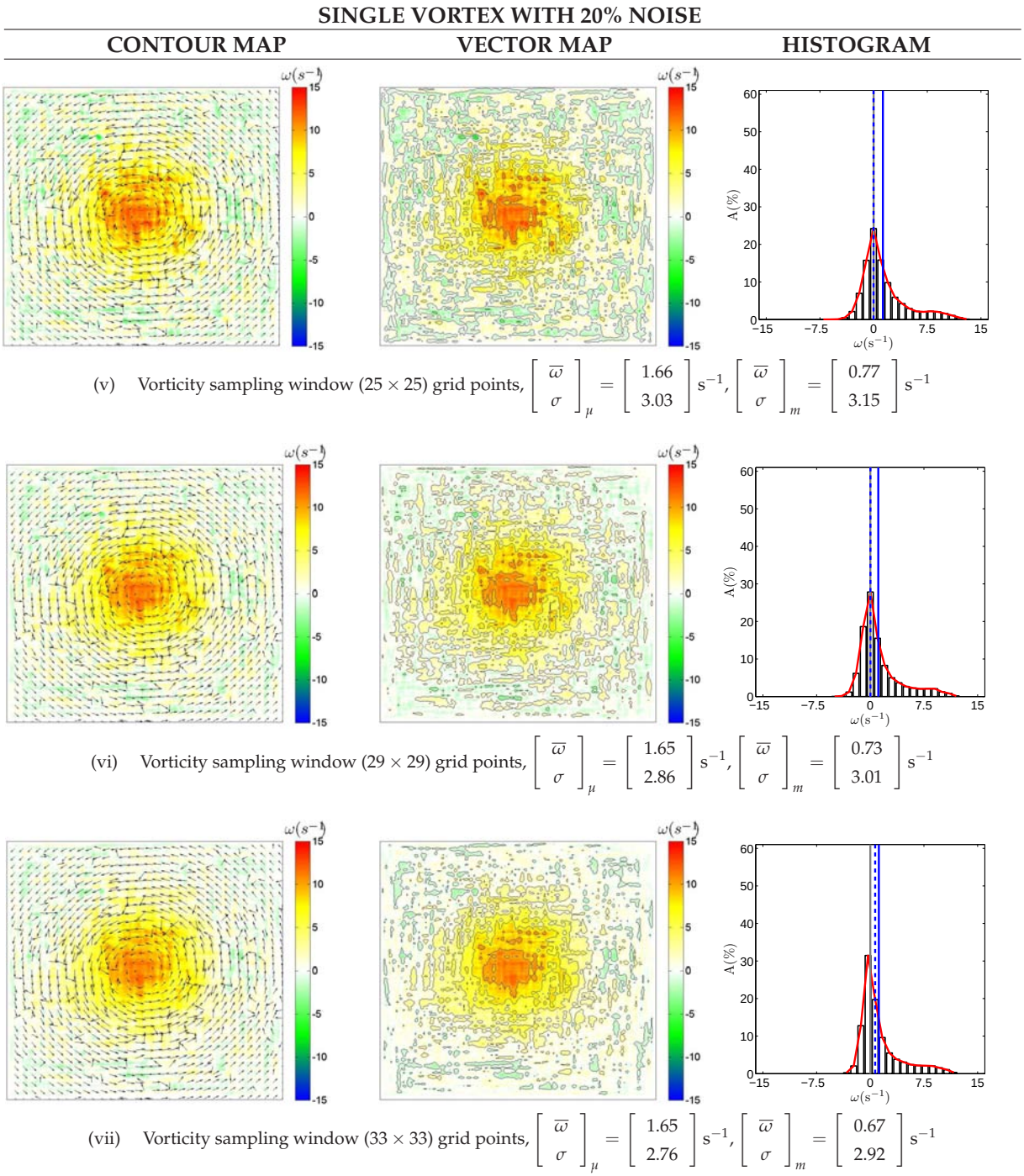

(v) Vorticity sampling window (25×25) grid points, $\begin{bmatrix} \overline{\omega} \\ \sigma \end{bmatrix}_{\mu} = \begin{bmatrix} 1.66 \\ 3.03 \end{bmatrix} \mathrm{s}^{-1}, \begin{bmatrix} \overline{\omega} \\ \sigma \end{bmatrix}_{m} = \begin{bmatrix} 0.77 \\ 3.15 \end{bmatrix} \mathrm{s}^{-1}$

(vi) Vorticity sampling window (29×29) grid points, $\begin{bmatrix} \overline{\omega} \\ \sigma \end{bmatrix}_{\mu} = \begin{bmatrix} 1.65 \\ 2.86 \end{bmatrix} \mathrm{s}^{-1}, \begin{bmatrix} \overline{\omega} \\ \sigma \end{bmatrix}_{m} = \begin{bmatrix} 0.73 \\ 3.01 \end{bmatrix} \mathrm{s}^{-1}$

(vii) Vorticity sampling window (33×33) grid points, $\begin{bmatrix} \overline{\omega} \\ \sigma \end{bmatrix}_{\mu} = \begin{bmatrix} 1.65 \\ 2.76 \end{bmatrix} \mathrm{s}^{-1}, \begin{bmatrix} \overline{\omega} \\ \sigma \end{bmatrix}_{m} = \begin{bmatrix} 0.67 \\ 2.92 \end{bmatrix} \mathrm{s}^{-1}$

Figure 6.12. Vorticity field of Lamb-Oseen vortex (20% noise). Calculations are performed on the Lamb-Oseen vortex flow field with 20% noise added to it. The vorticity contour maps are produced based on sampling window size in the range of (9×9) to (33×33) grid points size. This is 5.62×10^{-2} to 2.06×10^{-1} times relative to the grid of 160 by 160 points. Histograms pertaining to each and every of the vortex map are presented in the last column.

DOUBLE VORTICES WITH 0% NOISE

CONTOUR MAP	VECTOR MAP	HISTOGRAM

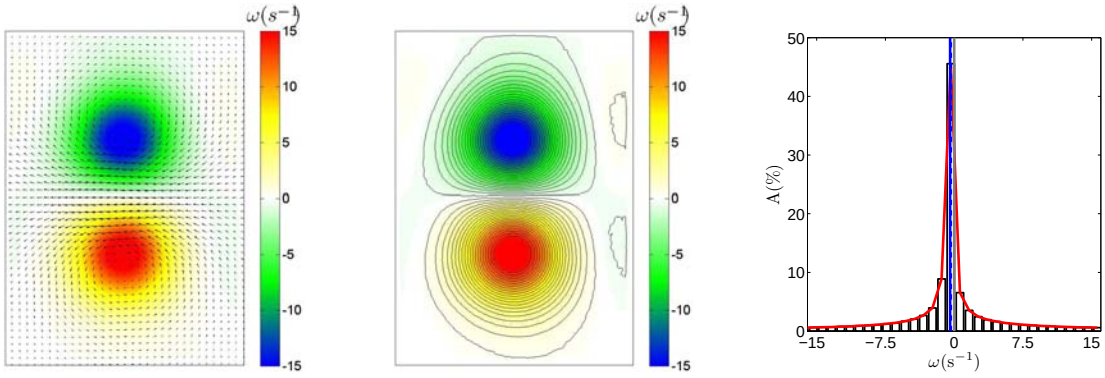

(i) Vorticity sampling window (9×9) grid points, $\begin{bmatrix} \overline{\omega} \\ \sigma \end{bmatrix}_{\mu} = \begin{bmatrix} 0.01 \\ 4.87 \end{bmatrix} s^{-1}, \begin{bmatrix} \overline{\omega} \\ \sigma \end{bmatrix}_{m} = \begin{bmatrix} 0.00 \\ 4.87 \end{bmatrix} s^{-1}$

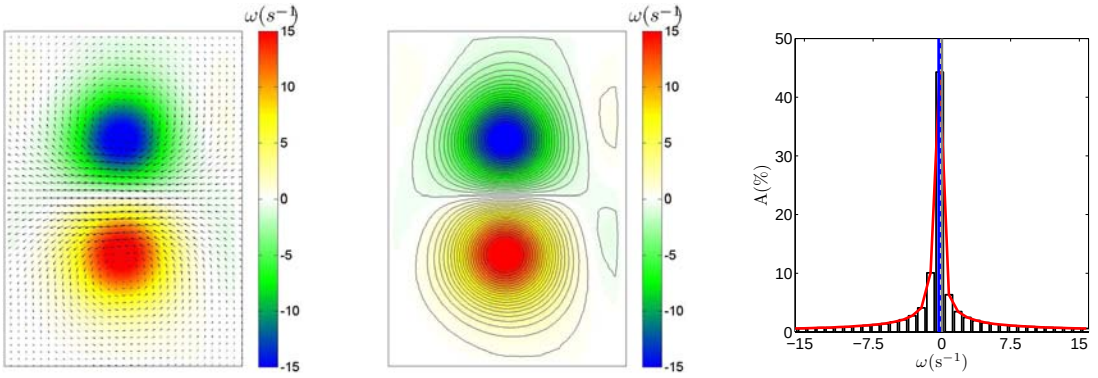

(ii) Vorticity sampling window (13×13) grid points, $\begin{bmatrix} \overline{\omega} \\ \sigma \end{bmatrix}_{\mu} = \begin{bmatrix} 0.02 \\ 4.85 \end{bmatrix} s^{-1}, \begin{bmatrix} \overline{\omega} \\ \sigma \end{bmatrix}_{m} = \begin{bmatrix} 0.00 \\ 4.85 \end{bmatrix} s^{-1}$

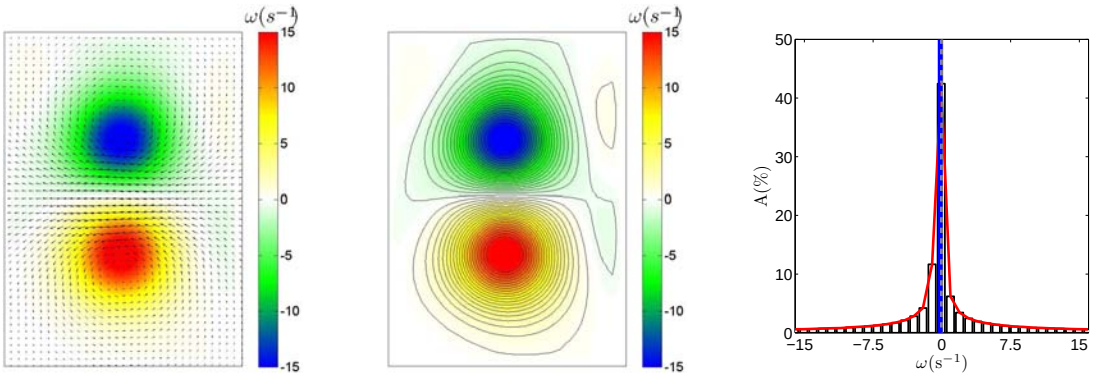

(iii) Vorticity sampling window (17×17) grid points, $\begin{bmatrix} \overline{\omega} \\ \sigma \end{bmatrix}_{\mu} = \begin{bmatrix} 0.02 \\ 4.83 \end{bmatrix} s^{-1}, \begin{bmatrix} \overline{\omega} \\ \sigma \end{bmatrix}_{m} = \begin{bmatrix} 0.00 \\ 4.83 \end{bmatrix} s^{-1}$

Vorticity sampling windows from (21×21) to (29×29) grid points continues on the next page

DOUBLE VORTICES WITH 0% NOISE

CONTOUR MAP	VECTOR MAP	HISTOGRAM

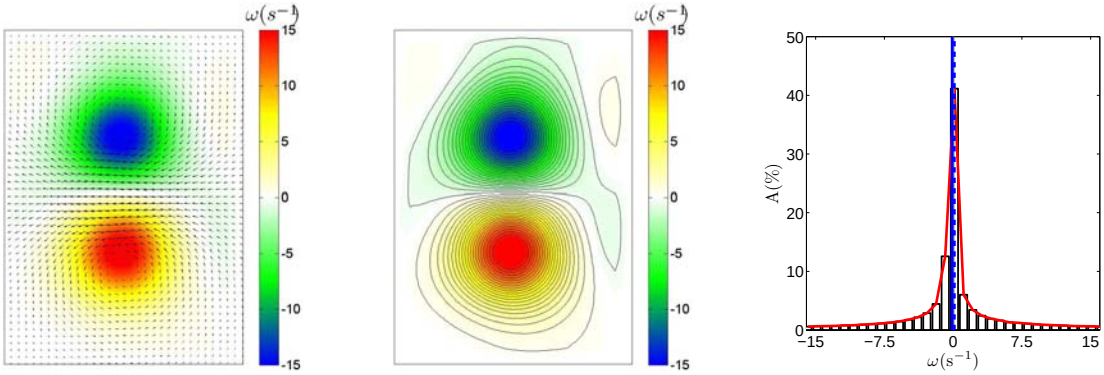

(iv) Vorticity sampling window (21×21) grid points, $\begin{bmatrix} \overline{\omega} \\ \sigma \end{bmatrix}_{\mu} = \begin{bmatrix} 0.03 \\ 4.80 \end{bmatrix} \mathrm{s}^{-1}, \begin{bmatrix} \overline{\omega} \\ \sigma \end{bmatrix}_{m} = \begin{bmatrix} 0.00 \\ 4.80 \end{bmatrix} \mathrm{s}^{-1}$

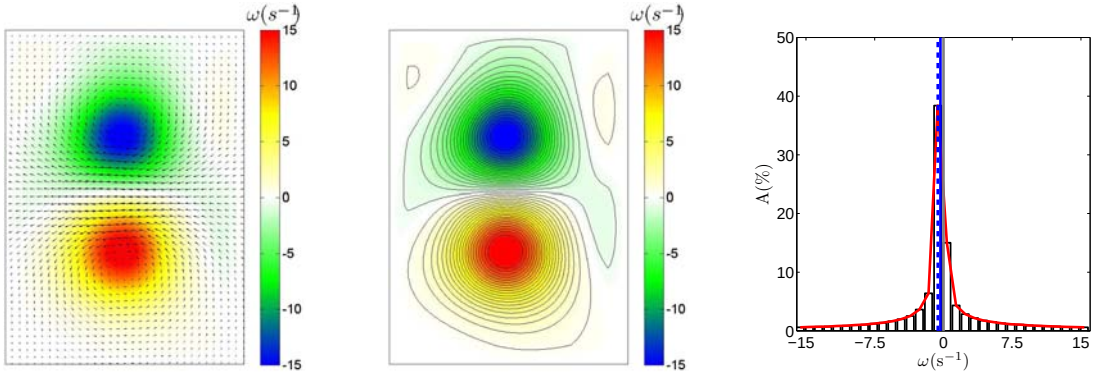

(v) Vorticity sampling window (25×25) grid points, $\begin{bmatrix} \overline{\omega} \\ \sigma \end{bmatrix}_{\mu} = \begin{bmatrix} 0.03 \\ 4.77 \end{bmatrix} \mathrm{s}^{-1}, \begin{bmatrix} \overline{\omega} \\ \sigma \end{bmatrix}_{m} = \begin{bmatrix} 0.00 \\ 4.77 \end{bmatrix} \mathrm{s}^{-1}$

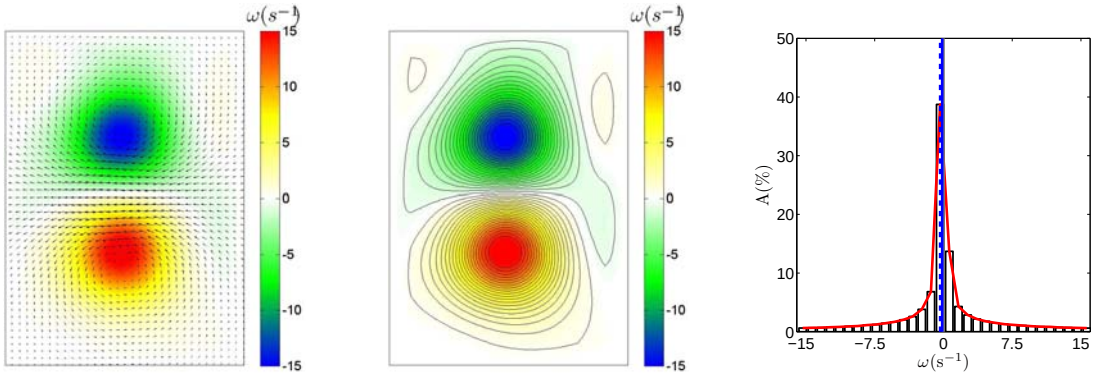

(vi) Vorticity sampling window (29×29) grid points, $\begin{bmatrix} \overline{\omega} \\ \sigma \end{bmatrix}_{\mu} = \begin{bmatrix} 0.04 \\ 4.73 \end{bmatrix} \mathrm{s}^{-1}, \begin{bmatrix} \overline{\omega} \\ \sigma \end{bmatrix}_{m} = \begin{bmatrix} 0.00 \\ 4.73 \end{bmatrix} \mathrm{s}^{-1}$

Figure 6.13. Vorticity field of double Lamb-Oseen vortices (0% noise). Calculations are performed on flow field of two Lamb-Oseen vortices with no noise added to it. The vorticity contour maps are produced based on sampling window size in the range of (9×9) to (29×29) grid points size. This is 5.62×10^{-2} to 1.81×10^{-1} times relative to the grid of 160 by 240 points. Histograms pertaining to each and every of the vortex map are presented in the last column.

DOUBLE VORTICES WITH 10% NOISE

CONTOUR MAP	VECTOR MAP	HISTOGRAM

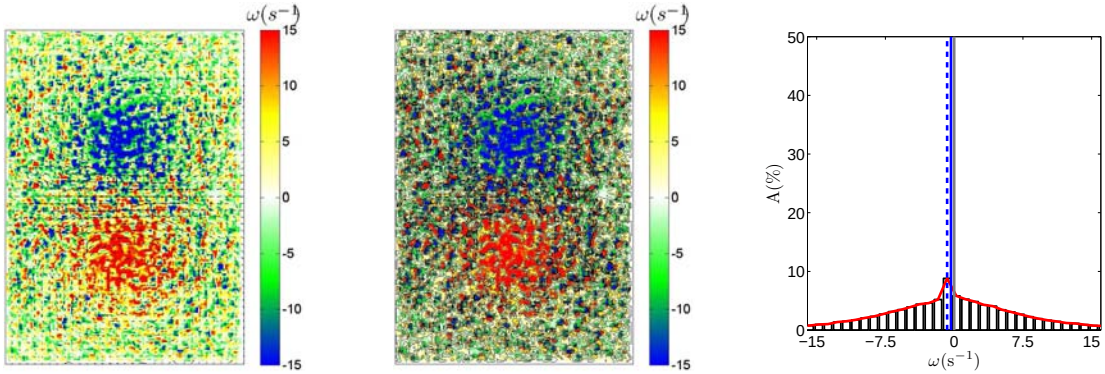

(i) Vorticity sampling window (9×9) grid points, $\begin{bmatrix} \overline{\omega} \\ \sigma \end{bmatrix}_{\mu} = \begin{bmatrix} 0.02 \\ 8.43 \end{bmatrix} \mathrm{s}^{-1}, \begin{bmatrix} \overline{\omega} \\ \sigma \end{bmatrix}_{m} = \begin{bmatrix} 0.00 \\ 8.43 \end{bmatrix} s^{-1}$

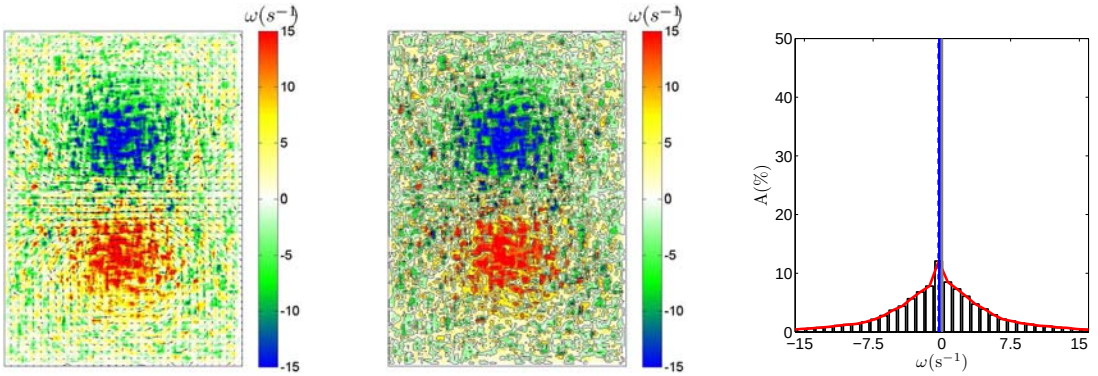

(ii) Vorticity sampling window (13×13) grid points, $\begin{bmatrix} \overline{\omega} \\ \sigma \end{bmatrix}_{\mu} = \begin{bmatrix} 0.02 \\ 6.01 \end{bmatrix} \mathrm{s}^{-1}, \begin{bmatrix} \overline{\omega} \\ \sigma \end{bmatrix}_{m} = \begin{bmatrix} 0.00 \\ 6.01 \end{bmatrix} \mathrm{s}^{-1}$

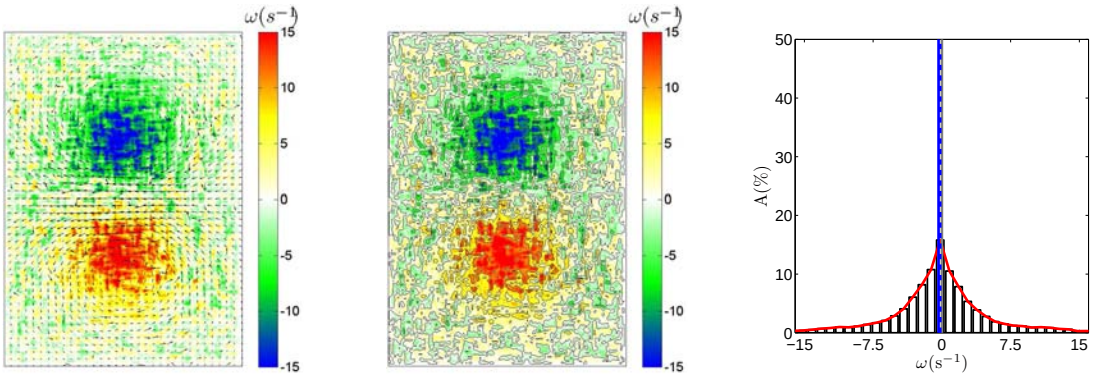

(iii) Vorticity sampling window (17×17) grid points, $\begin{bmatrix} \overline{\omega} \\ \sigma \end{bmatrix}_{\mu} = \begin{bmatrix} 0.02 \\ 5.18 \end{bmatrix} \mathrm{s}^{-1}, \begin{bmatrix} \overline{\omega} \\ \sigma \end{bmatrix}_{m} = \begin{bmatrix} 0.00 \\ 5.18 \end{bmatrix} \mathrm{s}^{-1}$

Vorticity sampling windows from (21×21) to (29×29) grid points continues on the next page

DOUBLE VORTICES WITH 10% NOISE

CONTOUR MAP	VECTOR MAP	HISTOGRAM

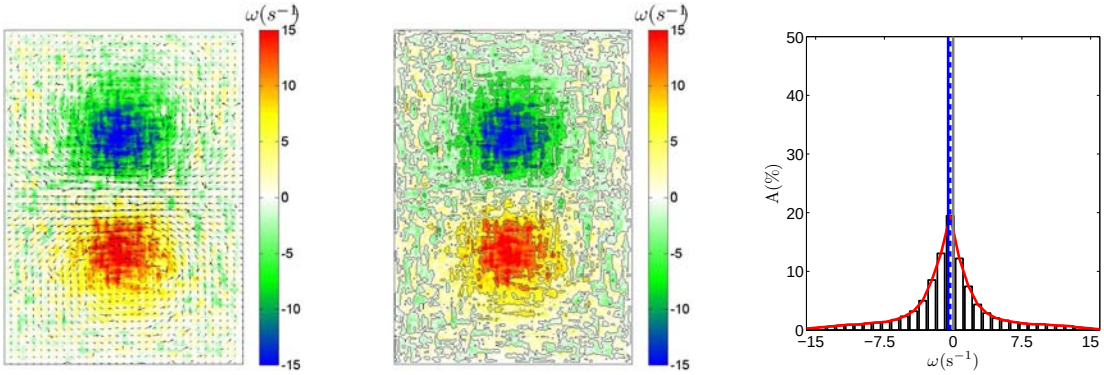

(iv) Vorticity sampling window (21×21) grid points, $\begin{bmatrix} \overline{\omega} \\ \sigma \end{bmatrix}_{\mu} = \begin{bmatrix} 0.03 \\ 4.81 \end{bmatrix} \mathrm{s}^{-1}, \begin{bmatrix} \overline{\omega} \\ \sigma \end{bmatrix}_{m} = \begin{bmatrix} 0.00 \\ 4.81 \end{bmatrix} \mathrm{s}^{-1}$

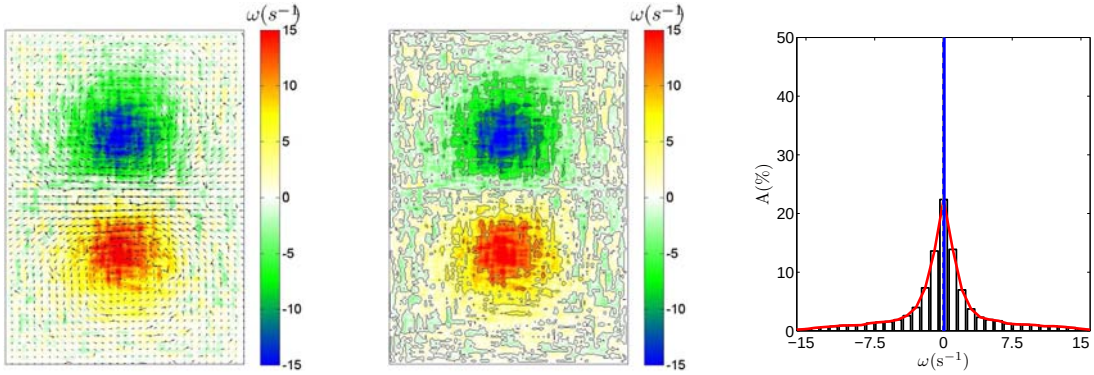

(v) Vorticity sampling window (25×25) grid points, $\begin{bmatrix} \overline{\omega} \\ \sigma \end{bmatrix}_{\mu} = \begin{bmatrix} 0.03 \\ 4.63 \end{bmatrix} \mathrm{s}^{-1}, \begin{bmatrix} \overline{\omega} \\ \sigma \end{bmatrix}_{m} = \begin{bmatrix} 0.00 \\ 4.63 \end{bmatrix} \mathrm{s}^{-1}$

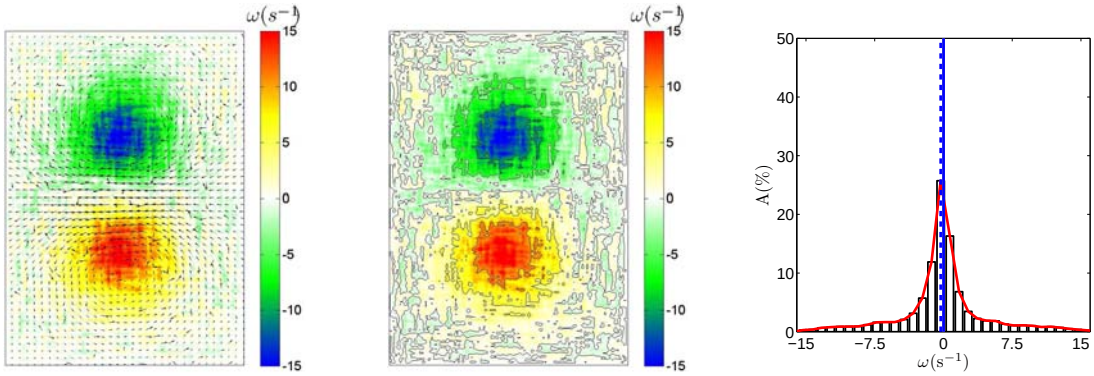

(vi) Vorticity sampling window (29×29) grid points, $\begin{bmatrix} \overline{\omega} \\ \sigma \end{bmatrix}_{\mu} = \begin{bmatrix} 0.04 \\ 4.51 \end{bmatrix} \mathrm{s}^{-1}, \begin{bmatrix} \overline{\omega} \\ \sigma \end{bmatrix}_{m} = \begin{bmatrix} 0.00 \\ 4.51 \end{bmatrix} \mathrm{s}^{-1}$

Figure 6.14. Vorticity field of double Lamb-Oseen vortices (10% noise). Calculations are performed on flow field of two Lamb-Oseen vortices with 10% noise added to it. The vorticity contour maps are produced based on sampling window size in the range of (9×9) to (29×29) grid points size. This is 5.62×10^{-2} to 1.81×10^{-1} times relative to the grid of 160 by 240 points. Histograms pertaining to each and every of the vortex map are presented in the last column.

DOUBLE VORTICES WITH 20% NOISE

CONTOUR MAP	VECTOR MAP	HISTOGRAM

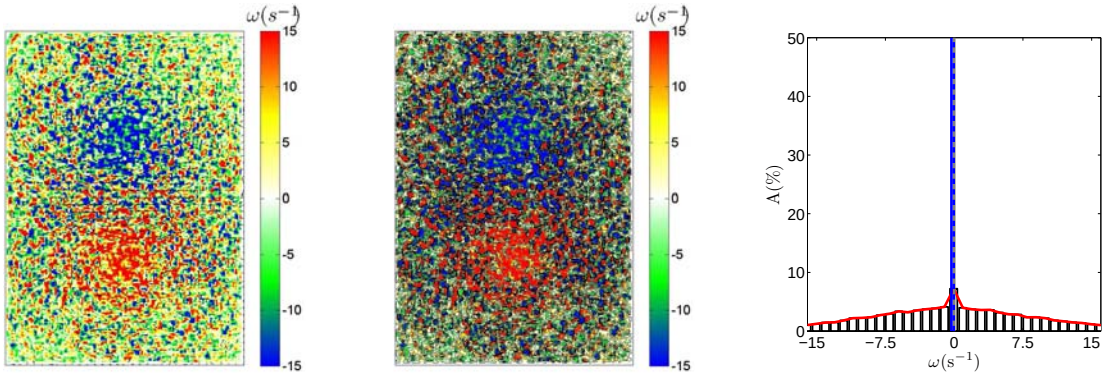

(i) Vorticity sampling window (3×3) grid points, $\begin{bmatrix} \overline{\omega} \\ \sigma \end{bmatrix}_{\mu} = \begin{bmatrix} 0.01 \\ 10.67 \end{bmatrix} \mathrm{s}^{-1}, \begin{bmatrix} \overline{\omega} \\ \sigma \end{bmatrix}_{m} = \begin{bmatrix} 0.00 \\ 10.67 \end{bmatrix} s^{-1}$

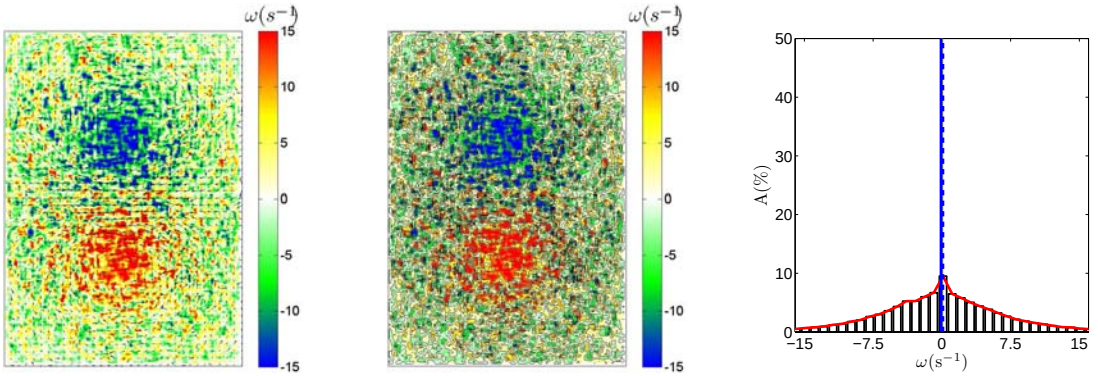

(ii) Vorticity sampling window (13×13) grid points, $\begin{bmatrix} \overline{\omega} \\ \sigma \end{bmatrix}_{\mu} = \begin{bmatrix} 0.02 \\ 6.81 \end{bmatrix} \mathrm{s}^{-1}, \begin{bmatrix} \overline{\omega} \\ \sigma \end{bmatrix}_{m} = \begin{bmatrix} 0.00 \\ 6.81 \end{bmatrix} \mathrm{s}^{-1}$

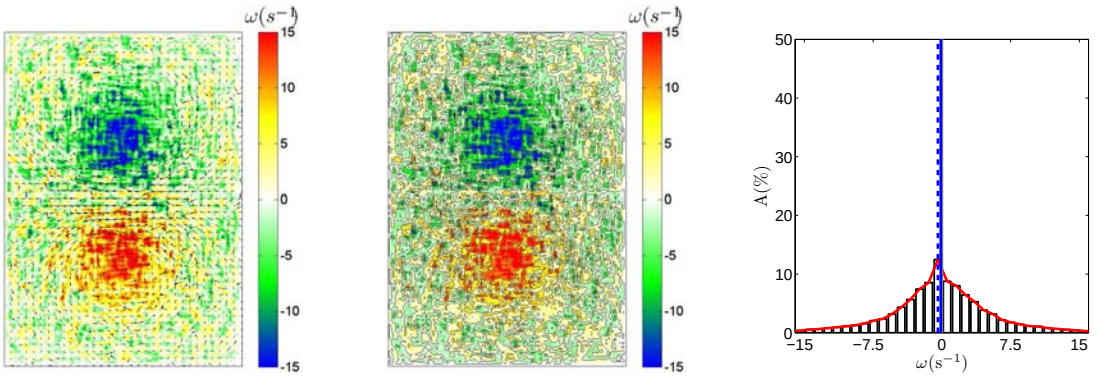

(iii) Vorticity sampling window (17×17) grid points, $\begin{bmatrix} \overline{\omega} \\ \sigma \end{bmatrix}_{\mu} = \begin{bmatrix} 0.02 \\ 5.39 \end{bmatrix} \mathrm{s}^{-1}, \begin{bmatrix} \overline{\omega} \\ \sigma \end{bmatrix}_{m} = \begin{bmatrix} 0.00 \\ 5.39 \end{bmatrix} \mathrm{s}^{-1}$

Vorticity sampling windows from (21×21) to (29×29) grid points continues on the next page

DOUBLE VORTICES WITH 20% NOISE

CONTOUR MAP	VECTOR MAP	HISTOGRAM

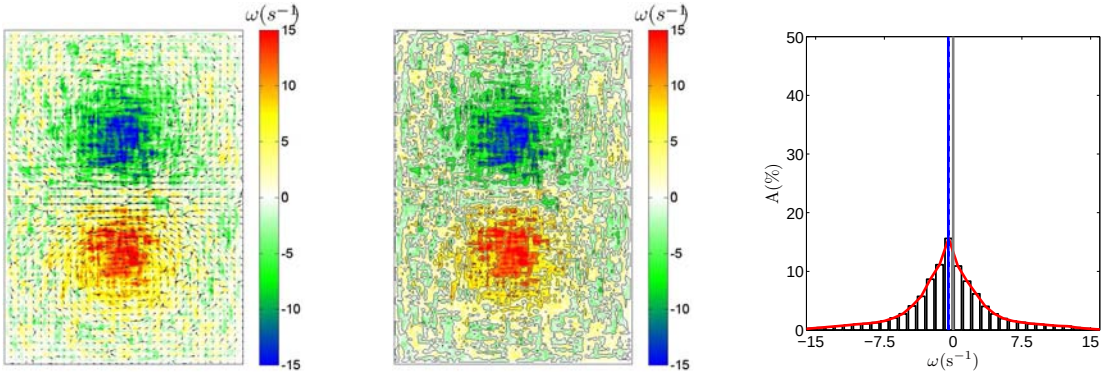

(iv) Vorticity sampling window (21×21) grid points, $\begin{bmatrix} \overline{\omega} \\ \sigma \end{bmatrix}_{\mu} = \begin{bmatrix} 0.03 \\ 4.76 \end{bmatrix} \mathrm{s}^{-1}, \begin{bmatrix} \overline{\omega} \\ \sigma \end{bmatrix}_{m} = \begin{bmatrix} 0.00 \\ 4.76 \end{bmatrix} \mathrm{s}^{-1}$

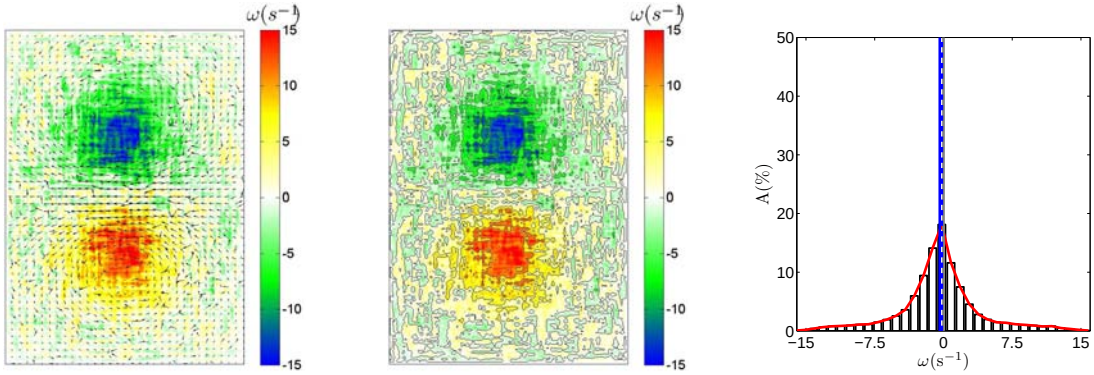

(v) Vorticity sampling window (25×25) grid points, $\begin{bmatrix} \overline{\omega} \\ \sigma \end{bmatrix}_{\mu} = \begin{bmatrix} 0.03 \\ 4.45 \end{bmatrix} \mathrm{s}^{-1}, \begin{bmatrix} \overline{\omega} \\ \sigma \end{bmatrix}_{m} = \begin{bmatrix} 0.00 \\ 4.45 \end{bmatrix} \mathrm{s}^{-1}$

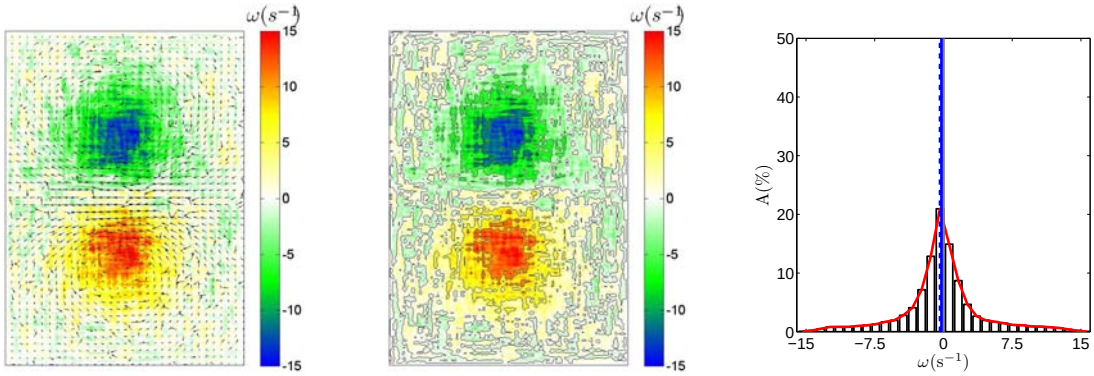

(vi) Vorticity sampling window (29×29) grid points, $\begin{bmatrix} \overline{\omega} \\ \sigma \end{bmatrix}_{\mu} = \begin{bmatrix} 0.04 \\ 4.26 \end{bmatrix} \mathrm{s}^{-1}, \begin{bmatrix} \overline{\omega} \\ \sigma \end{bmatrix}_{m} = \begin{bmatrix} 0.00 \\ 4.26 \end{bmatrix} \mathrm{s}^{-1}$

Figure 6.15. Vorticity field of double Lamb-Oseen vortices (20% noise). Calculations are performed on flow field of two Lamb-Oseen vortices with 20% noise added to it. The vorticity contour maps are produced based on sampling window size in the range of (9×9) to (29×29) grid points size. This is 5.62×10^{-2} to 1.81×10^{-1} times relative to the grid of 160 by 240 points. Histograms pertaining to each and every of the vortex map are presented in the last column.

6.6 Discussion

New parameters are defined for testing reliability of measurement as well as comparing vorticities in order to determine the fidelity of the derived vorticity distribution. The reliability of vorticity measurement from our results shows that the size of the sampling array and noise in the flow field affect the fidelity generation of the computed vorticity fields maps. Based on statistics of these field maps represented by reliability and comparison graphs in this section, we are able to establish an optimised configuration that computes vorticity fields to approximate the ideal vortex statistically.

6.6.1 Reliability of Vorticity Measurement

A study on the influence of sampling window size and perturbation of flow field vectors is conducted using ideal flow maps (Figures 6.10 and 6.13) and flow maps with noise addition (Figures 6.11, 6.12, 6.14 and 6.15). From the visualisation and statistics of the vorticity maps computed from noisy flow fields, sampling window based on smaller number of grid points results in relatively much higher spatial variation of vorticity magnitudes as compared to that of the ideal flow maps. However, as sampling window size increases, the variability in the vorticity map reduces. This is due to intrinsic two-dimensional smoothing of the vorticity map, thereby lowering the distinction between positive and negative rotation values. In the presence of noise and for small sampling window vorticity measurement, flow details cannot be captured sufficiently and ideally for an accurate vorticity mapping. This can be explained by the inability of a small sampling window size grid points to encapsulate enough flow vectors for a concise definition of vorticity. However, it is important to note that a large sampling window, on the contrary, may create an overly smoothed vorticity flow field such that some intricate flow features may be destroyed. It is a good practice to vary the sampling size until the variance of vorticity values is sufficiently small for a clear visualisation of the flow field, and yet large enough without losing intricate flow details.

It is critical to establish a form of measure for reliability of the system to accurately develop vorticity maps of flow imaged by a given technique. The reliability of the vorticity measurement ρ can be defined as the ratio of the true vorticity variance to total variance that comprises the true and error components (Bohrnstedt 1983) such that

$$\rho = \frac{\sigma^2_{\text{True}}}{\sigma^2_{\text{True}} + \sigma^2_{\text{Error}}}, \tag{6.8}$$

where σ^2_{True} is the variance pertaining to the vorticity map of the ideal vortex, which is measured using a (3×3) point sampling window size, whereas that of the measured variance given by vortical flow field with noise is equivalent to $\sigma^2_{\text{True}} + \sigma^2_{\text{Error}}$. To obtain the error map of a vorticity field measured based on a sampling window dimension, grid point by point differencing between the ideal vorticity image with that of the measured one based on a different vorticity configuration is conducted. The computation of the error variance in our measurement is based on the standard deviation of this error map. Reliability curves based on 5 to 25% noise are plotted as a function of sampling window sizes using Equation 6.8 and shown in Figures 6.16 and 6.17. Normalisation of sampling window size with respect to the vorticity grid is carried out by taking the ratio of the window dimension to the width of image grid in terms of grid points.

Note that the reliability of vorticity measurement improves for larger sampling window sizes. The optimal reliability occurs for a specific size and is dependent on the degree of noise added to the vector flow field. From the graphs, the optimal sampling window to use for vorticity maps based on a single vortical flow with 5, 10, 15, 20 and 25% noise is (35×35) points. This corresponds to a metric size ratio of 0.12 mm with respect to the image width of 160 pixels or 10 mm. The same results hold for the double vortices flow field.

6.6.2 Comparison of Vorticity Measurement

Each of the histogram that accompanies a flow map in the illustrated figures is able to provide some information about the vortex. For flow field displaying a single vortex, the counts pertaining to positive values of vorticity ω shown by the histogram of the vorticity map based on Figures 6.10, 6.11, 6.12 and 6.13 signifies the counter-clockwise rotation. The mean of histogram shows consistently small increments in magnitude as sampling is applied on a larger frame. A positive ω mean signifies overall positive rotational flow.

From the histograms of the double vortices illustrated in Figures 6.13, 6.14 and 6.15, we are able to observe a decrease in standard deviations as the sampling size increases,

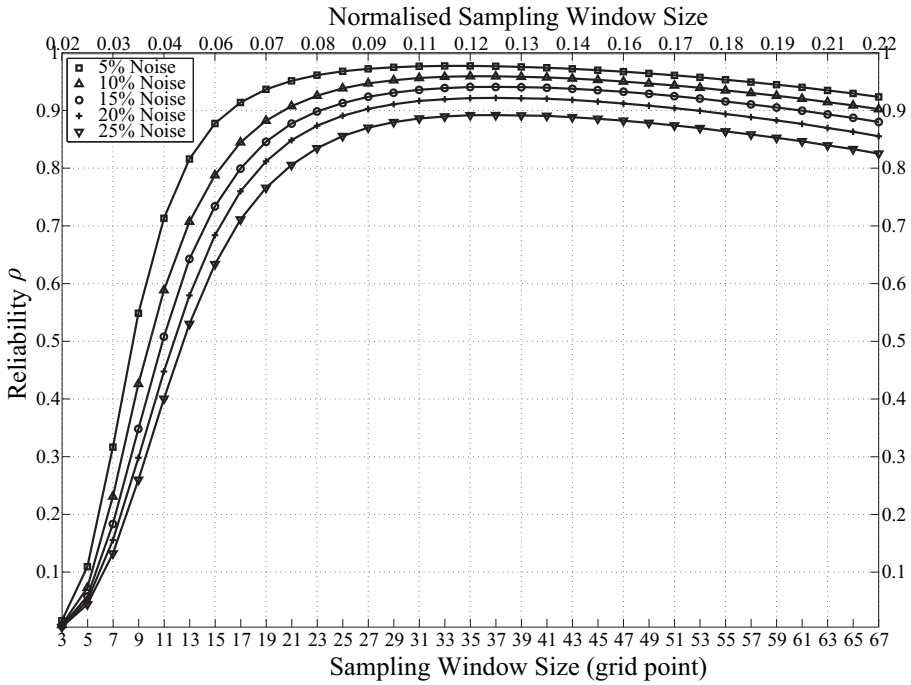

Figure 6.16. Reliability test for single vortex flow fields. Reliability for the flow field ρ calculated based on values σ_μ and σ_m that are standard deviations with respect to mean and median of flow maps respectively. Both sets of reliability graphs are approximately the same, and so only one set based on σ_μ is presented. The variation of vorticity sampling window size can affect the reliability of computational measurement of the vorticity. As the sampling window dimension increases, the reliability of the vorticity map measurement improves. Beyond a specific sampling window size, the reliability starts to drop slightly.

while the means and medians remain at zero regardless of the vorticity sampling. Their histograms are almost symmetrical about the zero centre line as there is an equal distribution of negative and positive rotational flow generated by the vorticies in two different polarities. We also note that higher vorticity sampling windows gives a distribution of vorticity values in the flow map with less fluctuation, and allows us to distinguish the two vortices with better clarity. A zero ω mean signifies overall irrotational flow.

For analytical and measured vorticity maps with the same vorticity sampling window applied, the comparison of their histogram variances γ can be defined as the ratio of the histogram variance from analytically determined vorticity map to the one for measured vorticity map such that

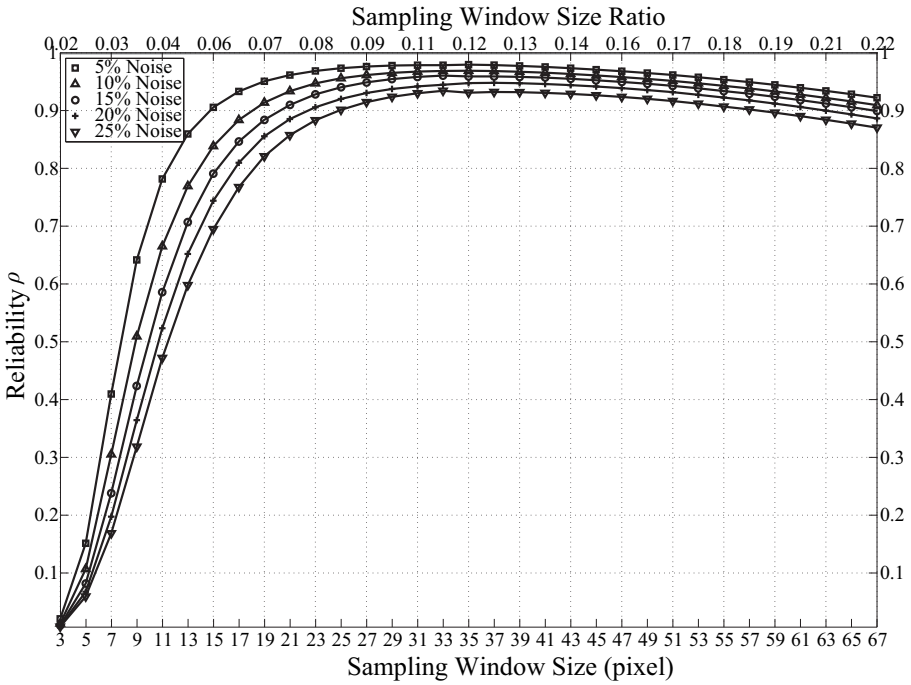

Figure 6.17. Reliability test for double vortex flow fields. Reliability for the flow field ρ based on σ_μ are presented for flow fields with various noise addition. If one were to plot the reliability based on σ_m, the graphs will be almost similar. The reliability curves based on different noise addition follows the same variation as those based on single vortex flow. The optimal sampling size for vorticity measurement may differ for every unique flow field.

$$\gamma = \frac{\sigma^2_{\text{True}}}{\sigma^2_{\text{Measure}}}. \tag{6.9}$$

We now discuss the two factors that will cause the comparison parameter γ to increase in Equation 6.9. The first one is the size of the sampling used for vorticity calculation at every frame. Increments in the vorticity sampling size has an effect on reducing the vorticity variance statistically instead of resulting in a wider distribution of vorticity values in the map because of the increased sampling of field vectors used for vorticity calculation. The second variable is noise within the measured flow field. The addition of noise in the form of generating outlying field vectors has an effect on the absolute value of the calculated vorticity due to the misalignment of vectors from that which is ideally in a uniform contour direction.

If the variance pertaining to the vorticity map of the ideal vortex is σ^2_{True}, and for a perfect flow field, the measured variance given by $\sigma^2_{\text{Measure}}$ is equivalent to σ^2_{True}. This means that the measured vorticity map equals to that of the true flow information and

reliability becomes one. The vector field outliers affect the variance of the measured vorticity map. It is important to note that because of the implications of sampling window size and noise and an existing relationship between the two variables, σ^2_{Error} is not the same as the variance of noise component σ^2_{Noise}. This also implies that $\sigma^2_{\text{Measure}}$ is not equivalent to the sum of contributing variable σ^2_{Noise} and σ^2_{True}. Therefore, the incorporation of the noise and adjustment of sampling window size such that $\sigma^2_{\text{Measured}}$ is equivalent to σ^2_{True} gives the critical point of equilibrium for approximating the measured histogram to the one based on idealised flow condition.

In our case studies, using various sampling windows for vorticity measurement, the flow fields with noise addition at 5 to 25% are tested for comparison against the analytical flow field with no noise based on their histograms. The results of the variance ratio curves with respect to the sampling window size from (3×3) to (41×41) points are shown below in Figure 6.18 and 6.19 for single and double vortex flow fields.

Since the analytically determined vortex is suggested to be the true flow field data, any measured vortex will have elements of noise in its flow field. From the graphs of comparison curves, we observe that variation of noise in the flow field has an effect on their gradients. Addition of flow field outliers has an influence on the variance of its vorticity map, and results in an increasing γ as the sampling size becomes larger.

Vorticity fields created using small sampling size windows during calculation give a poor definition of the vorticity gradient in the map. Increments in the number of vectors being sampled can intrinsically smooth the vorticity map sufficiently to approximate that of the ideal vortex. However, when the sampling size exceeds a specific threshold, the variance of measured vorticity map becomes smaller than that of the analytical one and results in both poor comparison of their histograms and reliability of the vorticity measurement system. This signifies that over-sampling of field vectors have occurred to produce a vorticity map that starts to differ from that of the ideal vortex. This can be explained by the intrinsic over-smoothing of vorticity as a function of overly-large number of vectors that will destroy some features of the vortex.

A critical sampling size can be determined by producing comparison curves of flow fields pertaining to vortices at various degrees of noise. The intersection of these curves occurs at the same position that also coincides approximately with the line of absolute similarity ($\gamma = 1$). This critical point of intersection gives the ideal sampling window size that can be used to extract sufficient contours of vectors and produce vorticity

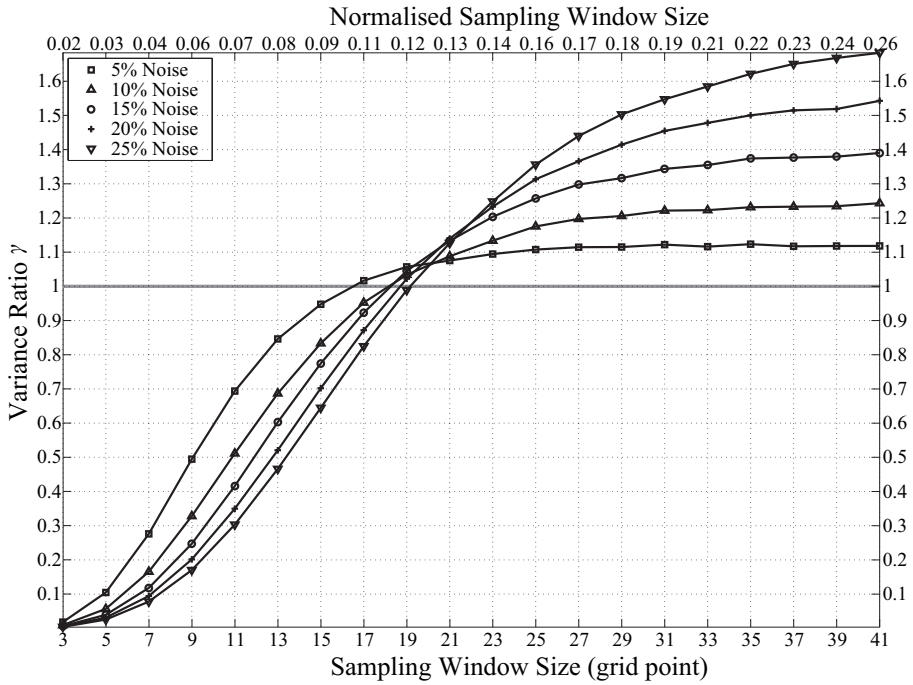

Figure 6.18. Comparison of histograms for single vortex flow fields. Comparison of histograms based on the analytical and measured flow fields are calculated by taking the ratio of their variances γ. The variances σ_{μ}^2 and σ_{m}^2 are based on standard deviations with respect to mean and median of flow maps respectively. Based on our results, both sets of standard deviations are very similar in values. The variation of vorticity sampling window size shows that as the sampling window dimension increases, the histogram variance from measured flow approaches that of the analytical one for the same vorticity measurement configuration. Beyond a specific sampling window size, the measured histogram variance becomes smaller than the analytical one and γ exceeds one.

histograms corresponding as close as possible to the one pertaining to the analytical vortex.

It is worthwhile mentioning that the intersection with the absolute similarity line remains unaffected by any amount of noise added to its flow field. The rate of increment in ratio of histogram variances is based on a specific proportion that corresponds to the sampling size. It may be worthwhile noting that a proportionate addition of outliers to the flow field reduces the vorticity map variance with the same proportion at this critical point of intersection.

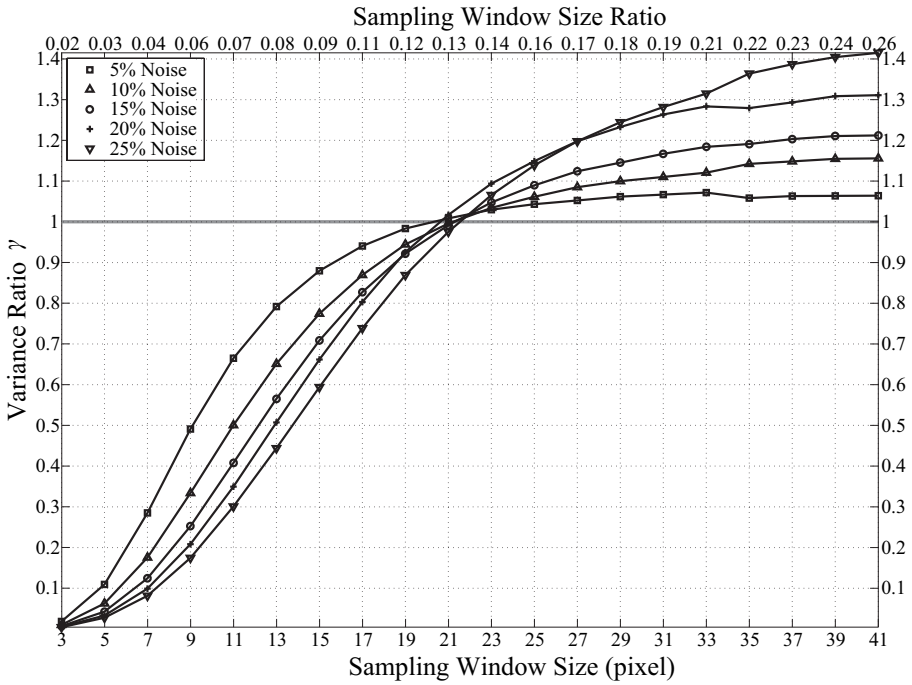

Figure 6.19. Comparison of histograms for double vortices flow fields. Comparison of histogram variances is based on variance pertaining to the analytical flow field divided by variance of the measured one. Both sets of variances, based on standard deviations with respect to the means and medians of the maps, have the same values. This ratio labelled as γ is presented for different sampling window sizes and on flow fields that comprises of double vortices, and with various noise addition. The variance ratio curves based on different noise addition follows the same variation as those pertaining to single vortical flow.

6.6.3 Effect of Grid Resolution on Vorticity Measurement

The presence of both bias and random error exists for grid matrix that has a lower resolution. Note that we use a reference flow field Λ_{ref} with an arbitrary size of (160×160) points at a 16 grid points per mm resolution. We do a point by point differencing of a grid Λ_s that has resolution s grid points per mm with this reference grid to obtain an error matrix. The average of all the elements in that matrix is computed using the function *mean* in Equation 6.10. Note that s ranges from 1 to 16. The maximum error is the subtraction of grids based on resolutions of 1 and 16 grid points per mm (i.e. $\Lambda_1 - \Lambda_{16}$ respectively). Normalisation of the error function Δ is performed by taking the ratio of absolute mean of an arbitrary error grid to the maximum error mean:

$$\Delta(s) = \frac{\text{mean}(|\Lambda_s - \Lambda_{\text{ref}}|)}{\text{mean}(|\Lambda_1 - \Lambda_{\text{ref}}|)} \tag{6.10}$$

$$\text{for} \quad s = 1, ..., 16, \quad \text{and} \quad \Lambda_{\text{ref}} = \Lambda_{16}.$$

Based on this configuration, normalised error Δ ranges from 0 to 1. The equation can give an estimate of the bias error as the result of reduction in grid resolution. We can observe from Figure 6.20 that the error decreases as quality of grid improves. The reliability equation that examines the variability of the difference maps can be used to determine the nature of variation in terms of error fluctuations. Reliability is shown to be close to 1 for higher resolutions of grid. This has shown to be consistent for vorticity maps measured using sampling window sizes of (3×3) to (15×15) points.

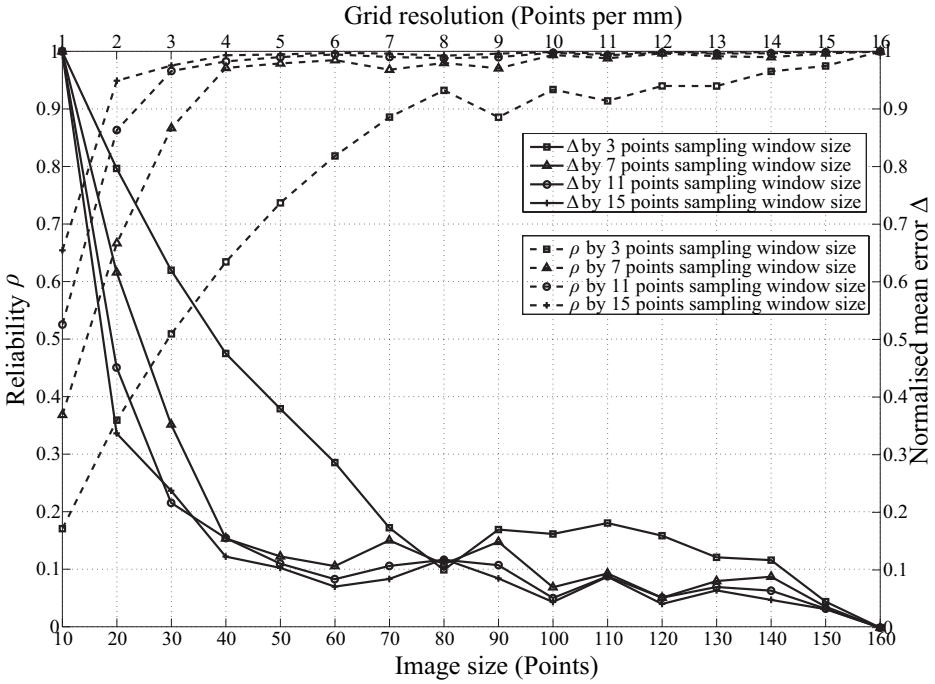

Figure 6.20. Reliability and error deviation for multi-resolutional single vortex flow fields. The reliability ρ of the vorticity measurement depends on the variability in error fluctuation whereas the normalised mean error Δ is a function of the bias error in the differencing of two vorticity fields of dissimilar resolutions. Both parameters are shown to vary in the same fashion based on four sampling window sizes. Reliability is good and error is the lowest for high resolution grids.

The reliability of the vorticity measurement is inversely proportional to the error deviation of the calculated vorticity field with respect to the true field. As the resolution

of the grid increases, the flow detail becomes amplified, and vorticity measurement based on a finer flow grid is able to encapsulate more field vectors for calculation of higher accuracy. The graph demonstrates the nature of this relationship effectively.

6.6.4 Limitations of Study

A statistical framework has been implemented to measure the vorticity field in a fluid flow. To validate this method, we produce analytical flow field maps for testing vorticity measurements based on different noise levels and sampling windows. The experiments show that the sampling window size plays a role in defining the vortex accurately when there is noise in the flow measurement.

We have incorporated random noise into the flow field during our experiments. It is worthwhile mentioning that a bias error may exists in a measurement system as well, but we have not considered it as this will not affect our study of reliability measures. Introducing a bias error in the resulting vorticity field will cause the reliability profiles in Figures 6.16 and 6.17 to be scaled in magnitude, but unaffected in terms of their change in gradients. Note that Equation 6.8 takes only the variances of the true and error fields into the measurement and is independent of their vorticity means. The error map is generated based on a point-by-point differencing of the true and measured vorticity maps. Any bias error introduced to the two flow maps may contribute to a larger mean of the error distribution because it changes the range limits of the vorticity distributions. However, the ratio of error standard deviation to its bias error mean does not change.

Other existing vorticity measurement schemes may improve the accuracy of vorticity field (Fouras and Soria 1998), and a similar study based on comparison of vorticities using a Lamb-Oseen vortex has been previously carried out (Foucaut and Stanislas 2002). However, the key focus in our study is to demonstrate the relationship between noise and sampling window size and the influence of these two variables on vorticity measurement, and therefore it is unnecessary to use a more mathematically enhanced and accurate vorticity measurement to prove this relationship. Moreover, the configured vorticity measurement produces an acceptable vorticity variation as demonstrated by the reliability and comparison results.

6.7 Chapter Summary

This chapter has outlined the methodology used to obtain the vorticity or strain rates within the measured velocity fields from first principles. The primary objective of this study is to quantify characteristics of swirling fluid and, therefore, we emphasise on the basic mathematical and computing aspects of describing flow vorticity and strains based on flow fields without going further into the complicated enhancements to discuss the accuracy of derivation.

Furthermore, the study has successfully illustrated flow field sampling for vorticity calculation based on different sampling window sizes and results are statistically presented such that optimal vorticity measurement configuration can be selected. Using statistical analysis of the vorticity maps, we can deduce the system reliability for the measurement of vorticity field. The procedures outlined in this study for assessing reliability can be used for determining the optimised vorticity measurement.

A good application for our framework is the visualisation of vortical flow within a human heart chamber using a velocity field map obtained by magnetic resonance image velocimetry. This procedure may be followed by a statistical analysis of the vorticity field (Chapter 7). From a clinical perspective, such vorticity information can potentially be used to investigate abnormal cardiac flow in the heart (Chapter 8).

Chapter 7

Methods of Cardiac Flow Analysis

VELOCITY-encoded phase contrast magnetic resonance imaging is performed to produce flow fields of blood in the heart. The aim of this study is to demonstrate the state of change in swirling blood flow within cardiac chambers and to quantify it for clinical analysis. Velocity fields based on the projection of the three dimensional blood flow onto multiple planes are scanned. The flow patterns can be illustrated using streamlines and vector plots to show the blood dynamical behaviour at every cardiac phase. Large-scale vortices can be observed in the heart chambers, and we develop a technique for characterising their locations and strength.

From our results, we are able to acquire an indication of the changes in blood swirls over one cardiac cycle by using temporal vorticity fields of the cardiac flow. This can improve our understanding of blood dynamics within the heart that may have implications in blood circulation efficiency. The results presented in this chapter can establish a set of reference data to compare with unusual flow patterns due to cardiac abnormalities. The calibration of other flow-imaging modalities can also be achieved using this well-established velocity-encoding standard.

7.1 Introduction

Scanning and analysis of cardiac flow is a challenge due to the complexity of blood dynamics and myocardial motion. In a chamber of the heart, vortices are shown to exist as the result of the unique morphological changes of the cardiac chamber wall by using flow-imaging techniques such as phase contrast magnetic resonance imaging. As the characteristics of our vorticity maps vary over a cardiac cycle, there is a need for a robust quantification method to analyse flow.

7.1.1 Importance of Cardiac Flow Analysis

Important contributions to medical imaging and scientific knowledge are made in this study. We devise a methodology to perform cardiac flow visualisation and to be able to quantify flow dynamical changes over time. Measurement of vortex characteristics by means of calculating the vorticity and devising two dimensional vortical flow maps can be performed. The technique relies on determining the vorticity statistics based on different time frames of one cardiac cycle. Our study has shown that a proper measurement of vorticity using the scanned flow field can characterise the location and strengths of large-scale vortices within a cardiac chamber. This approach, which is supported with qualitative flow visualisation, can be utilised to explain cardiac flow behaviour.

The use of phase contrast magnetic resonance imaging (MRI) enables a good assessment of vortices that exist in the cardiac chamber. It is a non-invasive imaging technique that allows study of flow-related physiology and pathophysiology with good spatial and temporal resolutions. Vortical flow behaviour has an effect on blood circulation (Fyrenius *et al.* 2001, Pierrakos and Vlachos 2006). Previously, the study of vortices in the human heart has also been performed using velocity-encoded magnetic resonance (MR) imaging data (Yang *et al.* 1998, Kilner *et al.* 2000, Uterhinninghofen *et al.* 2006). In particular, the study of vortices in the left atrium has been performed using three-dimensional phase contrast MRI (Fyrenius *et al.* 1999, Brandt *et al.* 2001, Ebbers *et al.* 2002). Therefore, this imaging modality is suggested for the flow imaging of cardiac chambers. In addition, we have devise methods of cardiac flow analysis to quantify the dynamic flow properties of blood in various heart chambers.

7.1.2 Details of Methods and Analysis in General

Gated-MRI (Morgan-Hughes *et al.* 2003, Thompson and McVeigh 2004, Tetsuya 2003, Larson *et al.* 2004, Nijm *et al.* 2008) is used in this study. The relationship of the electrocardiogram (ECG) to the cardiac cycle is illustrated in Figure 7.1. The pressure waveforms of the heart chambers and aorta are provided to indicate the onset of atrial and ventricular contraction with respect to the scan time frames. The flow properties of blood can be related to each cardiac event (Guyton and Hall 2006). We note that blood flows from the *vena cavae* into the atria and directly through the tricuspid valves into the ventricles. The ventricles are responsible for pumping blood to the lungs and through the aorta to the rest of the body. It also causes the atrioventricular valves to close so as to prevent backflow of blood. These changes in heart chamber sizes affect the pressure and the flow patterns of the blood. Therefore, the myocardial movements are intrinsically related to the blood dynamics and we present this diagram depicting the occurrence of the various cardiac events in order to relate the scan time frames with the pressure variations. This helps to provide a preliminary introduction to the cardiovascular dynamics of the heart before we can investigate the flow and to explain our observation and analysis using the appropriate terminologies and with relation to the cardiac event occurrence.

We develop planar flow maps of blood flow in the heart chambers and perform flow analysis using the tools described in this chapter. The initial stage involves performing phase contrast MRI of the heart at short axis through the atria. The blood motion can be mapped in two dimensions based on a combination of the velocity signal maps pertaining to the two directions. Vorticity in the flow is computed and mapping of the region of interest is performed. Finally flow statistics are computed globally for the flow region. We identify two dominant vortices of opposite rotation in the right atrium for the initial time frames of one cardiac cycle. Based on another study, using slices from a different scan orientation, we map the influx of blood from the *vena cavae* into the right atrium and then through the mitral valve to the right ventricle. From subsequent studies, we identify the presence of a large-scale vortex in the left atrium as well, and provide an indication of how a vortex in this heart chamber is diminishing as blood in this atrium flows into the left ventricle during the diastolic phase of the cardiac cycle.

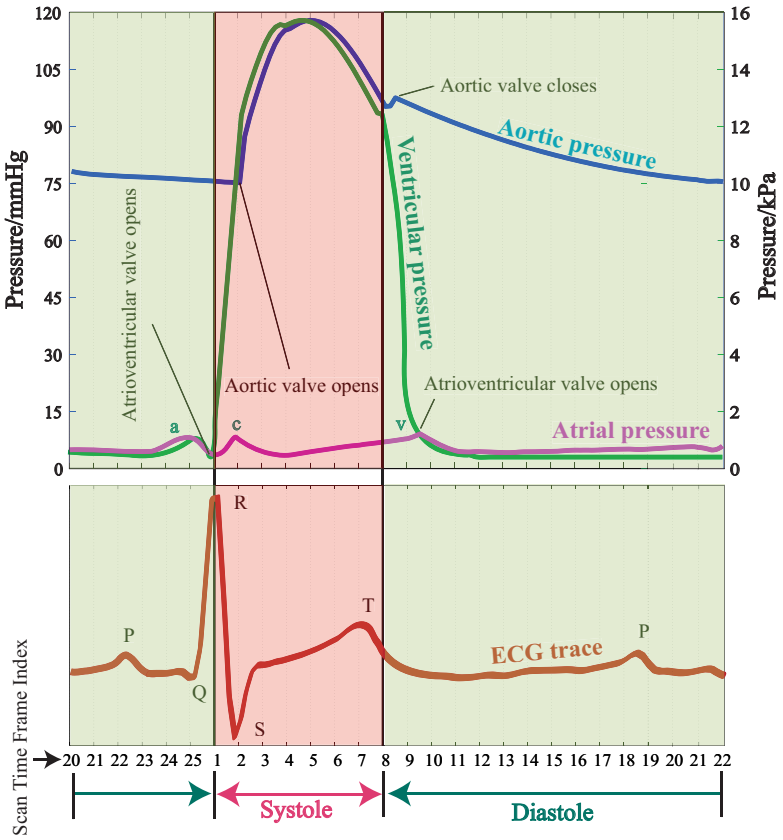

Figure 7.1. Cardiac events with relation to scan time frames. The pressure waveforms of the left ventricle, aorta and right atrium is correlated to the scan time frames of gated-MRI. The triggering of image acquisition starts at the occurrence of the R-wave. For a temporal resolution of 25 time frames, the cardiac systole starts from 1 to 8, and the diastole is from 9 to 25. The pressure changes in the atria can be denoted by the minor elevations labelled as a, c, and v waves that are caused by the dynamics of blood during atrial and ventricular contractions.

7.2 Vorticity Visualisation System Implementation

The components of a vorticity visualisation system have been previously discussed. Here, we examine the integration of imaging procedures, derivative flow measurements, visualisation and results generation into a system dedicated to cardiac flow analysis. Such a system can utilise phase contrast magnetic resonance images, as well as predict flow information from non-velocity encoded images.

7.2.1 Visual Tools for Presentation of Flow Fields

Flow patterns are identified by making the flow visible using a field vector plot. The streamline plot is another useful visual tool for tracing the path of the fluid. An indication of the strength of a large-scale vortex can be given by using a colour contour map. Reconstruction of vorticity map as a colour image displays vorticity values as colour intensities over a spatial grid. The presence of red pixels in a region demonstrates counter-clockwise swirling of blood while the blue region is related to clockwise swirl. Therefore the colours of the image can give indications of the magnitude of vorticity as well as the direction of rotation.

Other flow visualisation tools such as sphere glyphs, colour ribbons, line segment glyphs, adjustable rakes, and barbell glyphs have been developed for use depending on the nature of the fluid flow (Lodha *et al.* 1996). However, it is beyond our scope to examine all of these techniques. Therefore, only streamlines, vector plots and vorticity colour maps are used in the various result figures throughout this thesis.

7.2.2 System Integration

A framework to measure flow within the cardiac structures has been devised based on the described techniques. The system is able to load magnetic resonance images and enables important functions such as segmentation of cardiac chambers, image reconstruction and flow visualisation of blood, and statistical presentation of flow parameters. It can facilitate semi-automatic generation of case study reports of cardiac patients. The augmentation of visualisation using the magnetic resonance image as a background gives a gauge of the location of blood volumes within the cardiac structure. Finally histogram generation and presentation of the vorticity, shear strain and normal strain magnitudes by the case study reports provides a concise indication of the characteristics of flow in the heart.

We discuss the velocity-encoded phase contrast MRI and MR fluid motion tracking configuration in Chapters 2 and 3 respectively. Now we shall improvise the system to allow vorticity and strain rate measurement and display. In addition, we will make our description of the system and its configuration using processing components and their relevant data flow here. In this section, we construct the flow visualisation system based on the theoretical concepts that we have mentioned in previous chapters. It

is essential to establish a network of flow such that each procedure takes place in a systematic sequence to prepare the flow image results.

In order to understand the system of visualisation, we quickly review the data processing pipeline in Figure 7.2. The flow chart illustrates the blocks in an imaging and processing pipeline leading to the analysis of the visualisation output. Beginning with the pre-processing stage, it can be seen that image retrieval from magnetic resonance scanning is carried out. Magnetic resonance imaging using the velocity-encoded phrase contrast as well as standard steady-state free precession protocols can be carried out for the same subject in the scanner. Anatomical details based on the relevant scan slice can be observed. Following the cardiac magnetic resonance image retrieval stage, segmentation of the interested cardiac chamber is performed to isolate the derived fields within the boundary of flow regions from the endocardium.

The cardiac magnetic resonance data are also passed into the velocity grid reconstruction block whereby the flow field can be reconstructed based on deciphering of flow information from the images. For the velocity field, there exist inherent errors and an outlier detection program followed by vector interpolation is carried out to produce a complete smoothed velocity vector field. The output from this stage is the velocity field grid which can include up to one temporal and three spatial dimensions.

During the visualisation stage, different resolutions of the vector plot can be implemented for optimal presentation and observation. Other visualisation tools such as streamline tracing can be carried out for a more qualitative examination of the blood motion. Then the reconstructed velocity field grid are passed into the flow differential calculation stage, whereby each of the field grids is further processed to provide the strain rates or vorticity fields which can give more insight into the flow. The output will be encoded differential flow quantities in image form.

The processed visualisation outputs can be combined in a graphical display platform in the subsequent stage and superimposed onto medical images that depict the anatomy of the heart. This allows positional and size referencing of the flow region against the cardiac structures in the heart. Consolidation of multiple cine-images at various slices can give a three dimensional presentation of the flow images with interactive flow grid manipulation and slice truncation.

Features of interest in the flow study include magnitude, position, and numbers of counts of the vorticity and/or strain units spread throughout the flow map in the visualisation display. The statistical compilation made in the final stage as well as the

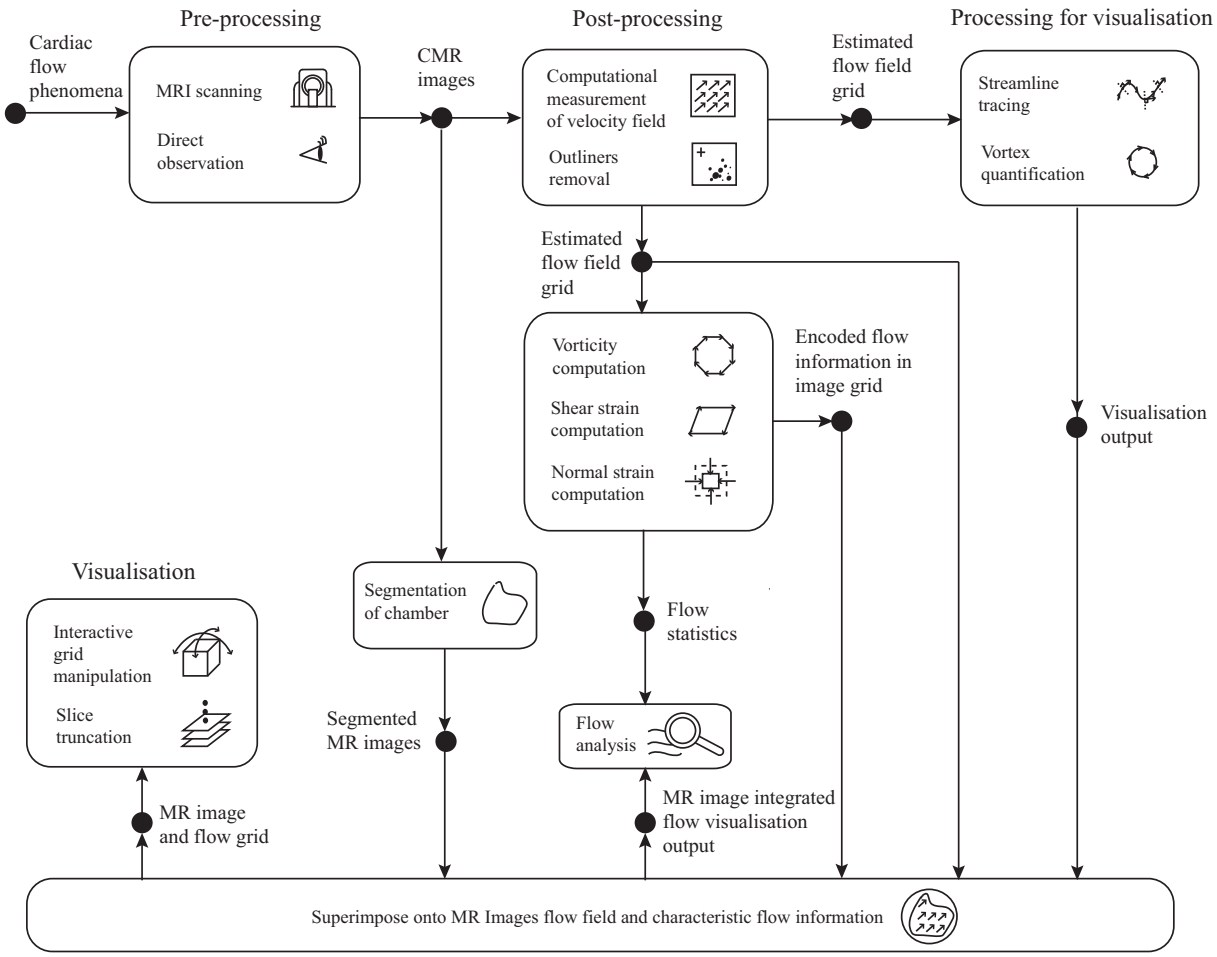

Figure 7.2. Cardiac vorticity visualisation system. Visualisation of flow can be based on a flow imaging framework. This system is a network of various blocks that retrieves information from the previous stage of execution and continuing until visualisation is successful. The vorticity visualisation system flow shows data processed by blocks depicting the MR imaging, which provides data for generation of flow field flows. The calculated flow data is fed into a flow characterisation stage whereby other measures of the flow can be computed. So we observe that this final process information flows systematically along the visualisation pipeline for preparation of flow characterisation and field display using vector plot and/or contour map.

manipulated visualisation outputs can contribute significantly to a more concise flow analysis.

In summary, the implemented system is based on stages of scanning, reconstruction and computation that are constructed into a framework for the purpose of superior flow visualisation and analysis of the heart. The derivation of flow quantities is based on the fluid mechanical properties of blood motion which can be displayed using qualitative and quantitative outputs.

7.3 Experiments

7.3.1 Case Study and MRI Scan Procedure

This section provides the scan information pertaining to each case study. The velocity-encoded magnetic resonance imaging was performed using a Siemens Avanto, 1.5 Tesla, model-syngo MRB15 scanner with Numaris-4, Series No: 26406 software.

Case Study 1

Cine-magnetic resonance imaging was performed in short axis orientation through the atria. All images were acquired with retrospective gating and 25 phases or time frames (for time frame indices from $n_t = 1$ to 25) for each slice.

Using a normal and healthy male subject of age 22 years at the time of our case study, we examine the flow within the right atrium of his heart with a single set of scans pertaining to a slice at two-chamber short axis orientation. Our objective is to analyse the large-scale vortices that exist in the right atrium, and understand their development over the cardiac cycle. This allows us to identify the principal features of the flow in a normal heart versus an abnormal one.

Phase contrast magnetic resonance imaging is used to scan the normal subject. Acquisition parameters include: echo time TR $= 47.1$ ms, repetition time TE $= 1.6$ ms, field of view FOV $= (298 \times 340)$ mm^2 at a (134×256) pixel matrix. The in-plane resolution of 1.54 mm/pixel determined by the pixel spacing and the through-plane resolution is 6 mm based on the slice interval. Velocity encoding (VENC) of 150 cms^{-1} is applied.

Scanning is performed at the section of the heart where the atria are positioned. This section is chosen such that the display of optimal cross-sectional area of the right

atrium is enabled. A chamber size contains more data points to define the features of interest. The scan section is taken at a location shown in Figure 7.3 whereby the scan is perpendicular to the axis joining the top of the heart to the apex through the septum. Eleven slices at this orientation are obtained throughout the atria. However, it is effective to base the velocity mapping on the right atrium of the heart using the scan sections that cut though the middle portion of atria. This corresponds to the maximum region of blood pool within the cardiac chamber in two dimensions. One slice, as shown in the schematic diagram of the heart, is selected for analysis in our study.

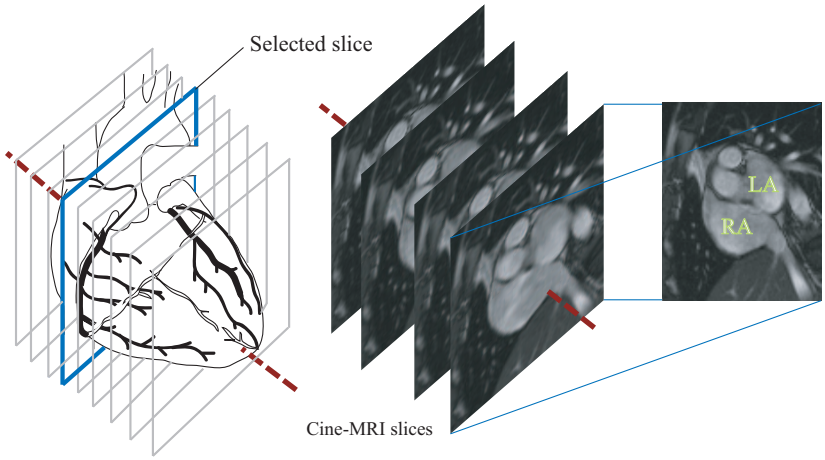

Figure 7.3. MRI scan through heart for case study 1. The scanning of the heart is taken at short axis and through two chambers, namely the left atrium (LA) and right atrium (RA). Therefore, this sectional view pertains to the two-chamber short axis scan. One planar scan is selected for flow examination of the right atrium as the case study.

Case Study 2

Cine-magnetic resonance imaging was performed using a long axis orientation through the heart with displays of the atria and ventricles. All images were acquired with retrospective gating and 20 phases or time frames (for time frame indices from $n_t = 1$ to 20) for each slice.

We map the flow of the heart at a scan (two-chamber configuration) such that, based on two slices, the connections of the *vena cavae* to the right atrium as well as the pulmonary artery to the right ventricle are visible. For the first set of images, the influx of blood from the inferior *vena cavae* (at the bottom of the image) to the right atrium can be visualised. Blood is seen to move along the pulmonary artery (next to the aorta) away from the right ventricle almost simultaneously. This allows us to examine the

effectiveness of the flow of blood from one region to the other. In a second set of scans (four-chamber configuration), we are able to observe the development of a left atrial vortex during diastolic phase of the cardiac cycle.

For the two-chamber view, phase contrast magnetic resonance image acquisition parameters include: echo time TR = 46.85 ms, repetition time TE = 1.97 ms, field of view FOV = (234×340) mm^2 at a (132×192) pixel matrix. For the four-chamber configuration, the image acquisition parameters are: echo time TR = 54.45 ms, repetition time TE = 2.73 ms, field of view FOV = (318×219) mm^2 at a (192×132) pixel matrix. The two sets of multi-slice scans at two-chamber short axis and four-chamber long axis orientations have in-plane resolutions that are determined by the pixel spacing at 1.77 mm/pixel and 1.66 mm/pixel respectively, whereas their through-plane resolution is based on the slice interval of 6 mm.

For this case study, multiple scans at a particular orientation (two-chamber short axis) are taken deliberately to assess the right atrium and its connective channels. The aim is to examine the nature of circulation pertaining to the *vena cavae*, the right atrium and right ventricle over the cardiac cycle. For this study, the imaging planes are tilted at an oblique angle with respect to the ones for case study 1 in order to capture these three anatomical entities. Multiple slices through the heart are scanned. These also correspond to the section that bisect the right atrium, where this chamber and the right ventricle, as well as the mitral valve in between them, can be imaged. Two out of the multiple scan slices are selected such that the inferior *vena cava* is visble in one image scan set, and the superior *vena cava* and pulmonary artery are visible in the other set[16].

Then, multiple scans at four-chamber long axis are performed to study the left and right atrial chambers and how their flow patterns develop over a cardiac cycle. For the right atrial flow, we aim to investigate the presence of swirling in the chamber. Based on a separate experiment, the flow relationship between the left atrium and ventricle is examined to understand the effect of atrial diastole on vortex development, followed by vortex breakup during its systolic phases. The slices that correspond to the middle portion of the left atrium and ventricle are selected. Figure 7.4 summarises the scan orientations carried out for case study 2.

[16]For phase contrast magnetic resonance (magnitude) image based on two-chamber short axis view, refer to Supplementary Videos 9 and 10 in CD-ROM, listed in Appendix F. For the four-chamber long axis view, use Videos 11 and 12

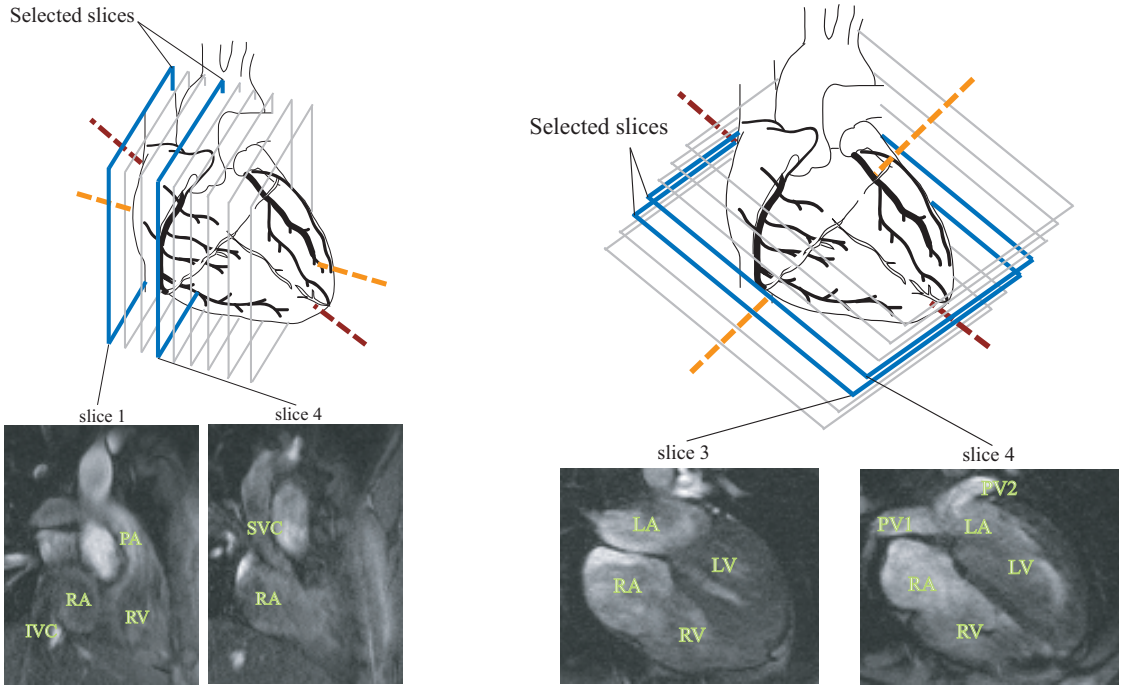

(a) Two-chamber short axis

(b) Four-chamber long axis

Figure 7.4. MRI scan through heart for case study 2. The scanning of the heart is performed using (a) two-chamber short axis to study the right atrium (RA), the right ventricle (RV), the inferior *vena cava* (IVC), the superior *vena cava* (SVC) and the pulmonary artery (PA). The image acquisition based on (b) four-chamber long axis is also carried out to examine flow in the right atrium (RA), the right ventricle (RV), the left atrium (LA), the left ventricle (LV), and two branches of the pulmonary vein (PV1 and PV2). Multiple slices at equal intervals are obtained. Only the appropriate slices, depending on the visibility of each cardiac anatomy, are choosen from each scan set for analysis.

Calibration Parameters

The magnetic resonance imaging parameters for phase contrast velocity encoding protocols are chosen for the flow field generation within the first and second case studies. Table 7.1 is created to summarise the scanning configuration. Note that the image display is a subset of the matrix scan image that is output by the magnetic resonance imaging scanner in order to show the region of interest specifically.

7.3.2 Flow Grid Representation

A dense velocity field (one velocity vector per pixel) is produced and a vector averaging based on a sampling window resolution of n by n pixels is carried out for the

CASE STUDY 1 SCAN SET 1			
Symbol	Quantity	Value	Units
p_s	Pixel spacing	1.54	mm/pixel
t_s	Trigger time interval	29.43	ms
S	Slice thickness	6	mm
X	Image width	120	pixel
Y	Image height	150	pixel

CASE STUDY 2 SCAN SET 1			
Symbol	Quantity	Value	Units
p_s	Pixel spacing	1.77	mm/pixel
t_s	Trigger time interval	48.10	ms
S	Slice thickness	6	mm
X	Image width	120	pixel
Y	Image height	150	pixel

CASE STUDY 2 SCAN SET 2			
Symbol	Quantity	Value	Units
p_s	Pixel spacing	1.66	mm/pixel
t_s	Trigger time interval	47.35	ms
S	Slice thickness	6	mm
X	Image width	100	pixel
Y	Image height	120	pixel

p_s	Size of a pixel in metric unit
t_s	Duration of each time frame
S	Distance of slice interval
X	Width of image display
Y	Height of image display

Table 7.1. Configuration of phase contrast magnetic resonance imaging. The scan properties of three sets of magnetic resonance imaging are presented here. Phase contrast MRI velocimetry is used to produce velocity flow fields. The vorticity flow maps can be determined from velocity information. These parameter values are used to calibrate these flow maps, as well as indicating the sampling vorticity mask size in metric units. Case study 1 scan set 1 pertains to the two-chamber short axis orientation which case study 2 scan sets 1 and 2 are based on the two-chamber and four-chamber long axis orientations respectively.

purpose of an aesthetical vector plot display within a segmented region of interest. We have set n to be 3 in our flow vector fields. The out-of-plane vorticity component is calculated from the in-plane velocity field using a finite element differential scheme (Raffel *et al.* 1998). A vorticity sampling mask size needs to be heristically set during the numerical derivation of the differential quantity. This sampling mask is experimentally determined based on a series of trial computations. It must be noted that the vorticity sampling window size determines the vorticity computation based on a particular vortex scale (Ferziger and Peric 2001, Foucaut and Stanislas 2002, Etebari and Vlachos 2005). There is a need to obtain the optimal vorticity calculation and mapping, which produces vorticity values with the same range in each localised spatial group such that a vortex can be visually observed when the values are mapped onto a colour scale. Typically, setting a large vorticity sampling size can remove noise fluctuations and obtain vorticity maps with minimum intra-class and maximum inter-class vorticity group values. However, this comes at the expense of over smoothing of vorticity values which causes data loss.

For processing of case study 1 scans, a vorticity sampling mask of size (21×21) pixels is set. The 21 pixels dimensional mask corresponds to a (32.34×32.34) mm^2 area. This mask is set to be relatively 7 to 8 times smaller than the displayed scan that is (184.80×231.00) mm^2. The vorticity sampling mask that is established for case study 2 is a (5×5) pixel frame that corresponds to (8.30×8.30) mm^2. The proportion of the scan display size to the sampling window size is approximately 24 times. It is relatively smaller since a smaller window region is to be mapped out of an overall smaller display image of (166.00×199.20) mm^2. Moreover, the spatial resolution of the first case study's scans is much higher and indicates the presence of larger-scale vortices with higher definition.

Here, positive values signify counter-clockwise (CCW) rotation, whereas negative values represent clockwise (CW) motion of the blood. Therefore, the magnitudes of these values give an indication of the angular velocity and their polarity signifies the direction of the rotation. These may be represented by a colour scale with maximum CCW and CW vorticity magnitudes corresponding to red and blue respectively.

7.3.3 Parameters for Data Analysis

The histogram of a vorticity map with a size of n pixels in the range $\omega = [-L, L]\ \mathrm{s}^{-1}$, and with k number of bins (or histogram bars), is a discrete function $h(r_k) = N_k$. Here, r_k is the k^{th} vorticity value and N_k is the number of pixels in the flow map having vorticity value r_k (Gonzalez and Woods 2002). Based on this definition , the vorticity histogram is a probability density function of occurrence of vorticity value r_k, whereby the sum of all components of a normalised histogram is equal to one.

Statistical quantification of the blood vorticity map in the right atrium is performed by translating all the scalar values into histogram format. Normalisation is performed by standardising the total count of pixels within a segmented region of interest to create an equal integral area under the frequency plot of the flow map. Therefore the histogram can be numerically normalised by setting the sum of counts in all bins to an arbitrary value of 100 pixels (which we define as 100% counts achievable). The number of pixels N_k assigned to a bin results in capacity of p_k % of all pixels in a segmented atrial flow map, whereby

$$p_k(\%) = \frac{N_k}{N} \times 100\%. \tag{7.1}$$

The histograms pertaining to the vorticity field plots onto magnetic resonance images is produced for every phase of one cardiac cycle. A measure of the average vorticity value is computed by taking the mean $\overline{\omega}_\mu$ or median $\overline{\omega}_m$ of the frequency histograms that are generated from vorticity maps. Vorticity standard deviation σ with respect to μ are computed by considering the variation about the mean, and is denoted as σ_μ. Standard deviation about the median is denoted by σ_m.

It is useful to characterise the amount of swirl by the circulation Γ. Circulation Γ is calculated using the line integral of a closed and counter-clockwise circuit C (Potter and Wiggert 1997, Raffel *et al.* 1998). By using Stokes' theorem, we may write this as a surface integral in Equation 7.3.3 as follows:

$$\oint_c v \cdot dl = \int_s (\nabla \times v) \cdot dS = \int_s \omega \cdot dS. \tag{7.2}$$

Note that the circulation may be calculated by taking the product of the vorticity mean $\overline{\omega}$ and the area enclosed by the chamber boundary A_c such that

$$\Gamma = \overline{\omega} \times A_c. \tag{7.3}$$

Here, the meaningful and reliable measure of swirling flow is the circulation, and therefore it becomes important to quantify this parameter along with the vorticity statistics.

7.4 Flow Analysis Based on Phase Contrast MR Imaging

This section discusses the flow analysis based on results obtained from the magnetic resonance image velocity-mapping of the cardiac chambers and connective structures of the heart.

7.4.1 Flow in the Right Atrium

We observe the large-scale vortices that appear in the chamber of the heart and analyse their development and changes during selected time frame indices from n_t =8 to 19. The variation of the blood flow field can be visually examined using streamlines, vector plots and vorticity contour maps as shown in Figure 7.12. In addition, we superimpose the corresponding MR images onto these flow fields to give an indication of the location of the flow features with respect to the chamber walls. The time at which the image acquisition takes place can be referenced using an electrocardiogram (ECG) trace at the top right hand corner of every flow map. We use a generic ECG trace for each flow image. The peak of the trace represents the R-wave that triggers the commencement of image acquisition and terminates it at the end of the next cardiac cycle (Stallmann and Pipberger 1961, Pan and Tompkins 1985, Friesen *et al.* 1990, Trahanias 1993, Shaw and Savard 1995). The flow maps for cardiac time frame indices 1 to 24 can be found in Appendix C. The flow maps in cine-mode can be assessed using Supplementary Videos 7 and 8 (in CD-ROM, listed in Appendix F) for vorticity fields and colour flow streamlining of the right atrial flow respectively.

Qualitative Examination of Right Atrial Flow

We present the flow results and analysis of the right atrium for the selected slice of the heart along the short axis orientation. Histograms are computed for each of these vorticity maps. Note that the mean and median of the histograms are denoted by $\overline{\omega}_\mu$ and $\overline{\omega}_m$ respectively. Standard deviations with respect to the mean and median are denoted as σ_μ and σ_m respectively. The magnitude of vorticity using $\overline{\omega}_\mu$ and σ_μ may give an indication of the swirl in the right atrium. Based on our conventions, counter-clockwise and clockwise vorticity are represented in red and blue respectively on the contour map. Vortices in the atrium are shown to be dominantly counter-clockwise in rotation for most of the time frames based on the short axis view.

For a selected set of time frames based on one cardiac cycle, two large-scale vortices exist in the chamber simultaneously. From Figure 7.12, based on the streamline plots and vorticity contour maps[17], we are able to deduce that one counter-clockwise (CCW) vortex in the atrium exists along with a second clockwise (CW) vortex approximately to the upper-left of it.

Vortical flow based on the contour flow maps for the eight selected times frames of a cardiac cycle is characterised using the mean or median of all the map values. With reference to this case, the mean of the vorticity distribution $\overline{\omega}_\mu$ ranges from -0.66 to 2.13 s^{-1} while its median $\overline{\omega}_m$ ranges from -3.05 to 0.00 s^{-1}. Because of higher positive vorticity values generated by a stronger counter-clockwise vortex versus a weaker clockwise vortex, the distribution centroid is offset from the zero value. If the flow is dominantly a counter-clockwise rotation, the vorticity distribution is typically bell-shaped and has a peak that lies in the positive domain of the distribution.

If there is an even number of vortices in the cardiac chamber of analysis, of which half of them pertain to a different direction of rotation, the magnitudes of $\overline{\omega}$ based on the mean or median cannot be used with reliability as a mode of analysis. This is due to the cancellation of positive and negative vorticity values for flow in all clockwise directions and counter-clockwise directions respectively. Therefore, such global analysis is limited in terms of an accurate presentation of vorticity. In this case, visual observation and qualitative analysis will be more appropriate.

[17] We use a medical image processing software named Medflovan, which was developed during the course of preparing this thesis, to produce the results displayed here. This is a system programmed in an object-oriented platform to provide cardiac flow visualisation and analysis.

Another characteristic of the flow is the variance of the vorticity values, which can be based on its mean or median as the distribution centroid. The standard deviation of vorticity map σ that is based on the mean and median ranges from 7.13 to 12.64 s^{-1} and 7.53 to 12.81 s^{-1} respectively. Vorticity images with high pixel colour contrast result from maps with large standard deviations. There are a few reasons for a high σ, so it is of little value to use it for flow interpretation. Some possible reasons can be the presence of an odd number of equally strong vortices in the flow or numerous small vortices of different strengths, and the new vorticity that may be generated near the chamber wall regions.

In Figure 7.6, we display the vorticity fields based on directional and absolute scalar map values. The absolute magnitude flow map will have a higher average vorticity as compared to the directional one whereas its standard deviation will remain the same. This can give an insight into the overall vorticity of the blood regardless of the rotation direction. The absolute vorticity means range from 5.67 to 9.99 s^{-1}. The corresponding median is 0 s^{-1} for almost all of the cardiac phases. Both distributions have standard deviations which ranges from 7.15 to 12.57 s^{-1}.

Vorticity Analysis of Right Atrial Flow

We observe qualitatively, based on the display of velocity and vorticity maps, two large-scale vortices of opposite rotations that appear in the right atrial flow. Note that each of them exists as a dominant vortex at some occasions throughout the cardiac cycle. We are able to indicate the relative strengths of the two vortices by plotting the directional means of vorticity maps with respect to cardiac time frames. If two vortices of equal strength but different polarities are developed in the region of analysis, the average of the vorticity field which is denoted by $\overline{\omega}$ is zero. When one vortex becomes stronger than the other one, the directional vorticity distribution centroid shifts to the positive or negative domain depending on the mean direction of rotation.

We take the ratio of directional vorticity mean to the absolute one as the normalised vorticity mean. As a vortex dominates the flow and the second vortex disappears completely, the normalised mean $\overline{\omega}_N$ approaches 1. When two equal and opposite vortices appear, μ_N becomes 0. Intermediate levels of dominance can be indicated for $\overline{\omega}_N$ in the range of 0 to 1. The variation of $\overline{\omega}_N$ in Figure 7.7 shows that a counter-clockwise vortex is present in the beginning. Then a vortex of opposite rotation grows in magnitude until it is slightly stronger than the first one. Eventually, this vortex diminishes

and the initial dominant vortex occupies the chamber again. In conclusion, based on the statistics of these vorticity maps, we are able to describe the vortex development in a quantitative manner.

In the absence of other slices for the same analysis carried out here, there is a lack of evidence to show that the variation in vortex magnitude could be due to the changes in vortex locations over time. Therefore, to gain an accurate insight of the flow behaviour in the cardiac chamber, we need to either examine the temporal variation of $\overline{\omega}_N$ for multiple slices in short axis orientations over the entire cardiac chamber, or a single long axis scan slice. The aim is to explore if the reduction in overall vortex strengths displayed by a vorticity map during subsequent time frames is the result of a vortex moving in the perpendicular direction of the slice, away from the sectional scan. Therefore, we generate flow maps of the right atrium and ventricle along the long axis orientation and examine the dynamics of blood in this view. It can be observed that in Figure 7.8, based on selected time phases during atrial systole, there is a movement of blood from the right atrium into the ventricle and this may account for the motion of vortex away from the short axis plane of view towards the ventricle. It may be interesting to note that the linear or curvilinear translation of a vortex results in a spiral flow known as a helix (Bogren and Buonocore 1999, Morbiducci *et al.* 2007, Morbiducci *et al.* 2009).

7.4.2 Circulation of Blood in the Right Atrium and Ventricle

Here, we present the flow visualisation of blood which circulates in the right atrium, right ventricle and connective veins and arteries to these chambers. Using the streamline trace diagrams, we are able to deduce the direction and speed of blood flow within the regions of interest. In Figure 7.9 (a), we can observe the flow from superior *vena cava* at the onset of right atrial dilation. This event is seen to occur during the ventricular systolic phases. The pressures in the pulmonary arteries and veins are approximately 20 mmHg and 5 mmHg respectively (Chandran 1992, Chandran *et al.* 2006b). Towards the end-systole, the flow slows down and a corresponding dilation of the right atrium induces the flow in the inferior and superior *vena cavae* to accelerate. We note that the blood streams entering the right atrium from these two channels interact to form a vortex (Kilner *et al.* 2000).

With the opening of the atrioventricular valves during atrial systole, the blood surges into the relaxed ventricles, and then channels into the pulmonary artery (Kilner *et al.* 2000). We note that there is an accelerated flow of blood in the pulmonary artery after the onset of the ventricular contraction (Figure 7.9 (b)). The ventricular contraction is triggered by the electrocardiographic R-wave which can lead to a rising pressure of up to 100 mmHg or greater (Gertsch and Cannon 2003). The absolute duration of a ventricular systole is defined as the time interval between the onset of the R-wave and the minimal ventricular volume on the volume-time activity curve (Plehn *et al.* 2008).

The velocity of blood in the pulmonary artery is measured to reach up to 155 cms^{-1} at some localised points in time. The average flow in the *vena cavae* are generally slower than the one in the artery, which typically ranges from approximately 0 to 80 cms^{-1}. It is important to highlight that while a localised maximum velocity v_{max} can give an indication of the fastest blood flow at a specific region, it may not necessarily be higher than the ensemble average of the velocities in a region of interest. However, we observe that the maximum velocities measureable in our velocity maps also have a high range of velocities in the region, and so this quantity can be taken as an indicator of maximum global flow velocity here. The velocities measured are consistent with the typical range determined by pulsed Doppler examination (Mielke and Benda 2002, Freedom *et al.* 2003).

We highlight that a heart may have different numbers and strengths of large-scale vortices in the right atrium. The flow imaging in our study shows that the right atrial vortex is predominantly counter-clockwise. This is due to the oblique alignment of the inferior and superior *vena cavae* in such a way that the flow presented from each vein introduces counter-clockwise angular momentum to the blood pool in the right atrium. The flow into the atrium increases during the atrial diastolic phases, thereby causing blood to gain this angular momentum and developing a counter-clockwise vortex.

7.4.3 Analysis of Vorticity in Left Atrial Flow

Streamline tracing of the velocity field pertaining to the atrium and ventricle on the left side of the heart is performed. The traces in Figure 7.10 clearly demonstrate that a large-scale vortex exists in the left atrium during the cardiac systole. At this stage, no indication of swirling is observed in the ventricle . During the ventricular systole, pressure of the blood in the ventricular chamber causes the mitral and triscupid valves

to close so that blood does not flow back into the left atrium (Chandran 1992, Chandran *et al.* 2006a). When the atrial systole takes place, the left atrium dilates. The counter-clockwise swirling in the left atrium is observed to be due to flow interaction from blood exiting out of the two branches of the pulmonary vein (PV1 and PV2) into the chamber. Due to the oblique alignment of the PV1 and PV2 flows, the interaction of these inflows from the two branches results in a diversion from their original courses of flow, and contributes to an angular momentum to the blood such that a counter-clockwise vortex is developed (Kilner *et al.* 2000). This large-scale vortex is formed during the time frame indices $n_t = 7$ to 9. It moves away from the atrium during the atrial systolic phase as the atrioventricular valves open and the blood surges into the left ventricle (Kilner *et al.* 2000, Narula *et al.* 2007). The velocity of the blood becomes maximum at time frame index $n_t = 10$ and can reach up to 175 cms^{-1} at some local positions as it moves from the left atrium to the ventricle through the mitral valve. The surge jet leads to an asymmetric development of the initial vortex ring (Schenkel *et al.* 2009). Flow decelerates slowly as the end stage of the atrial systole approaches. Some smaller-scale clockwise swirling is seen in the left ventricle subsequently during the onset of the cardiac systole (note $n_t = 11$ and 12). This observation is due to the formation of the vortex rings after the mitral flow (Pierrakos and Vlachos 2006, Gharib *et al.* 2006).

NORMAL SUBJECT

COLOUR STREAMLINE PLOT	VECTOR & CONTOUR MAP	HISTOGRAM

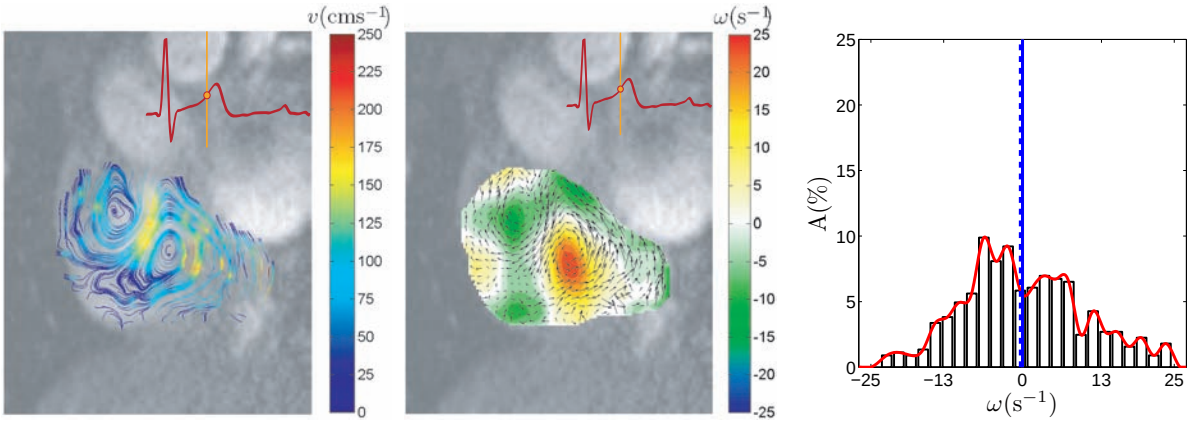

(i) $n_t = 8, \begin{bmatrix}\overline{\omega}\\ \sigma\end{bmatrix}_{\mu} = \begin{bmatrix}1.77\\ 9.71\end{bmatrix}\mathrm{s}^{-1}, \begin{bmatrix}\overline{\omega}\\ \sigma\end{bmatrix}_{m} = \begin{bmatrix}0.00\\ 9.87\end{bmatrix}\mathrm{s}^{-1}, \Gamma = 8.44\mathrm{m}^2\mathrm{s}^{-1}$

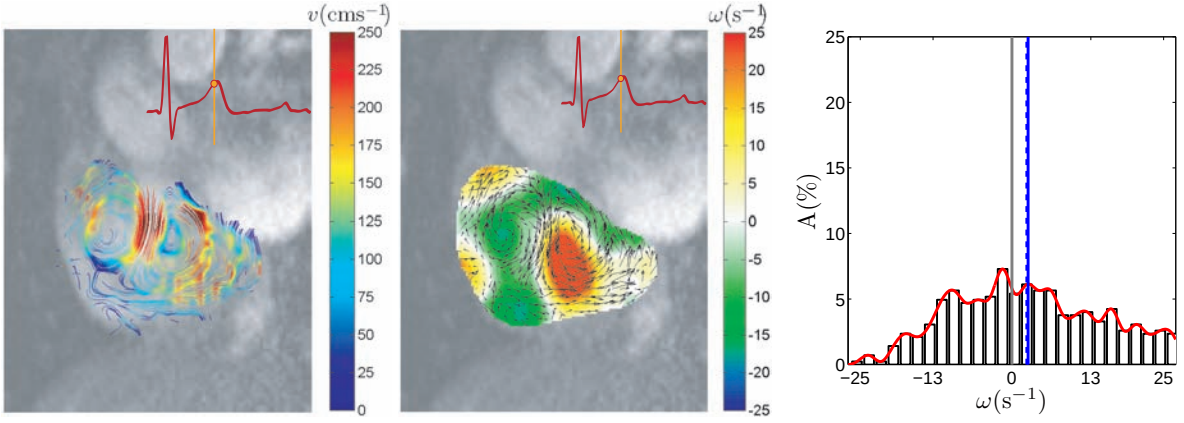

(ii) $n_t = 9, \begin{bmatrix}\overline{\omega}\\ \sigma\end{bmatrix}_{\mu} = \begin{bmatrix}2.13\\ 12.64\end{bmatrix}\mathrm{s}^{-1}, \begin{bmatrix}\overline{\omega}\\ \sigma\end{bmatrix}_{m} = \begin{bmatrix}0.00\\ 12.81\end{bmatrix}\mathrm{s}^{-1}, \Gamma = 12.57\mathrm{m}^2\mathrm{s}^{-1}$

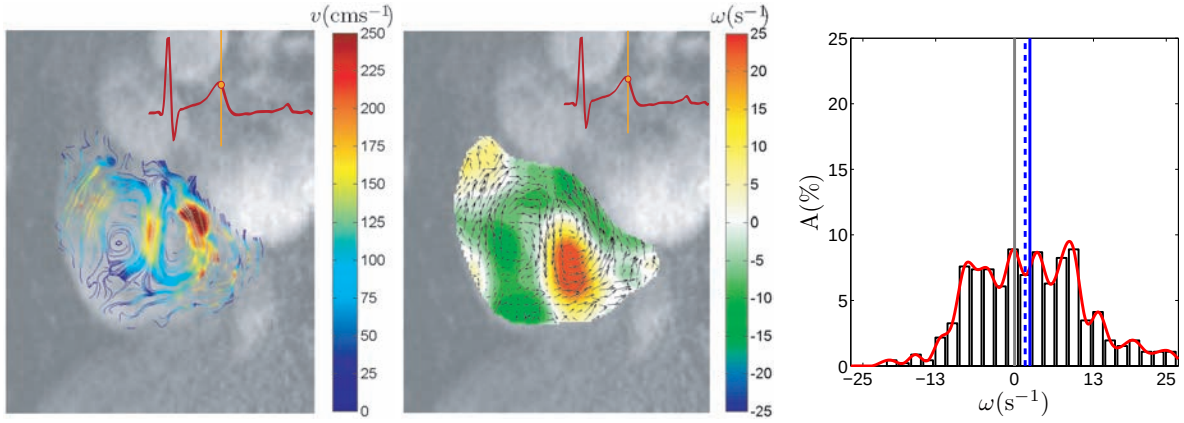

(iii) $n_t = 10, \begin{bmatrix}\overline{\omega}\\ \sigma\end{bmatrix}_{\mu} = \begin{bmatrix}0.23\\ 9.59\end{bmatrix}\mathrm{s}^{-1}, \begin{bmatrix}\overline{\omega}\\ \sigma\end{bmatrix}_{m} = \begin{bmatrix}-1.75\\ 9.79\end{bmatrix}\mathrm{s}^{-1}, \Gamma = 1.58\mathrm{m}^2\mathrm{s}^{-1}$

Time frame indices from 11 to 13 out of 25 frames in a cardiac cycle continues on the next page

NORMAL SUBJECT

COLOUR STREAMLINE PLOT	VECTOR & CONTOUR MAP	HISTOGRAM

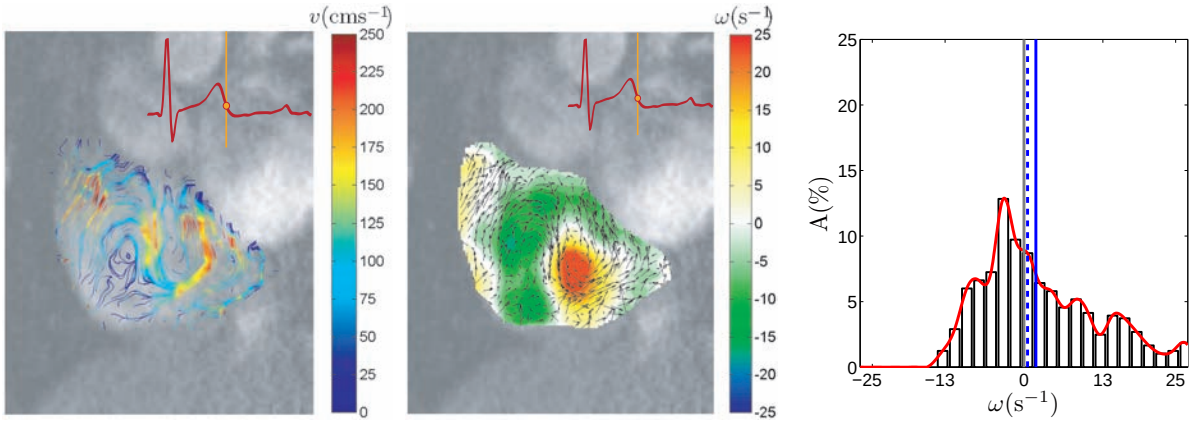

(iv) $n_t = 11, \begin{bmatrix}\overline{\omega}\\ \sigma\end{bmatrix}_{\mu} = \begin{bmatrix}0.02\\ 9.10\end{bmatrix}\mathrm{s}^{-1}, \begin{bmatrix}\overline{\omega}\\ \sigma\end{bmatrix}_{m} = \begin{bmatrix}-1.87\\ 9.30\end{bmatrix}\mathrm{s}^{-1}, \Gamma = 0.66\mathrm{m}^2\mathrm{s}^{-1}$

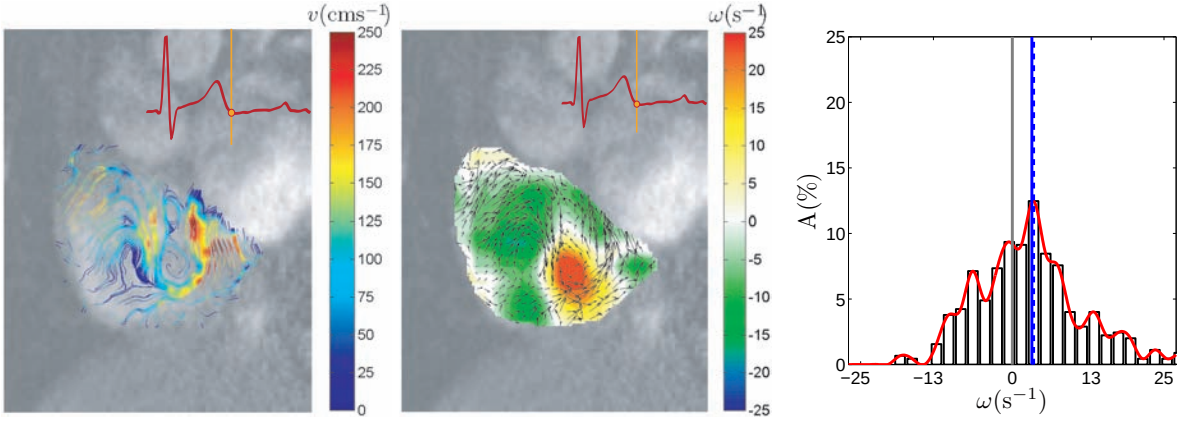

(v) $n_t = 12, \begin{bmatrix}\overline{\omega}\\ \sigma\end{bmatrix}_{\mu} = \begin{bmatrix}-0.66\\ 9.35\end{bmatrix}\mathrm{s}^{-1}, \begin{bmatrix}\overline{\omega}\\ \sigma\end{bmatrix}_{m} = \begin{bmatrix}-3.4\\ 9.74\end{bmatrix}\mathrm{s}^{-1}, \Gamma = -4.33\mathrm{m}^2\mathrm{s}^{-1}$

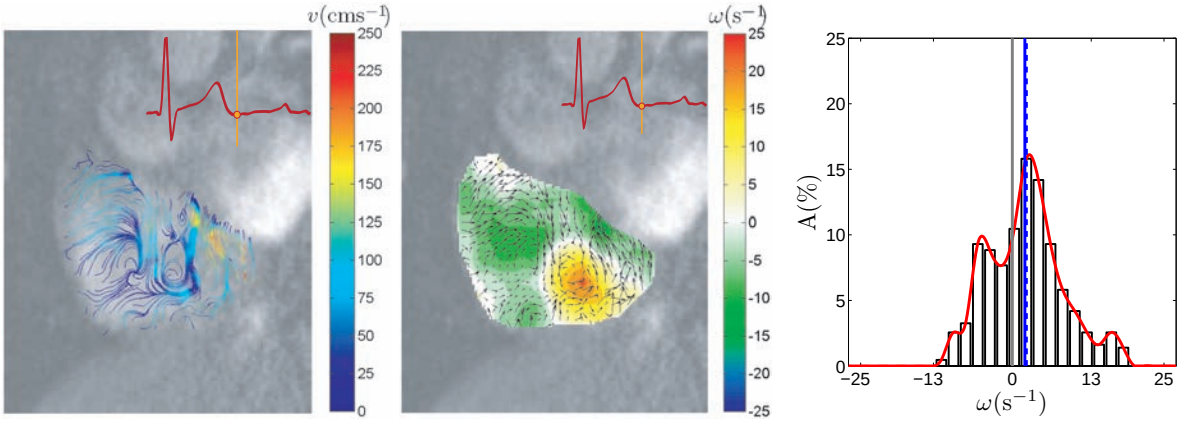

(vi) $n_t = 13, \begin{bmatrix}\overline{\omega}\\ \sigma\end{bmatrix}_{\mu} = \begin{bmatrix}-0.6\\ 7.13\end{bmatrix}\mathrm{s}^{-1}, \begin{bmatrix}\overline{\omega}\\ \sigma\end{bmatrix}_{m} = \begin{bmatrix}-3.05\\ 7.53\end{bmatrix}\mathrm{s}^{-1}, \Gamma = -3.82\mathrm{m}^2\mathrm{s}^{-1}$

Time frame indices from 14 to 16 out of 25 frames in a cardiac cycle continues on the next page

NORMAL SUBJECT

COLOUR STREAMLINE PLOT	VECTOR & CONTOUR MAP	HISTOGRAM

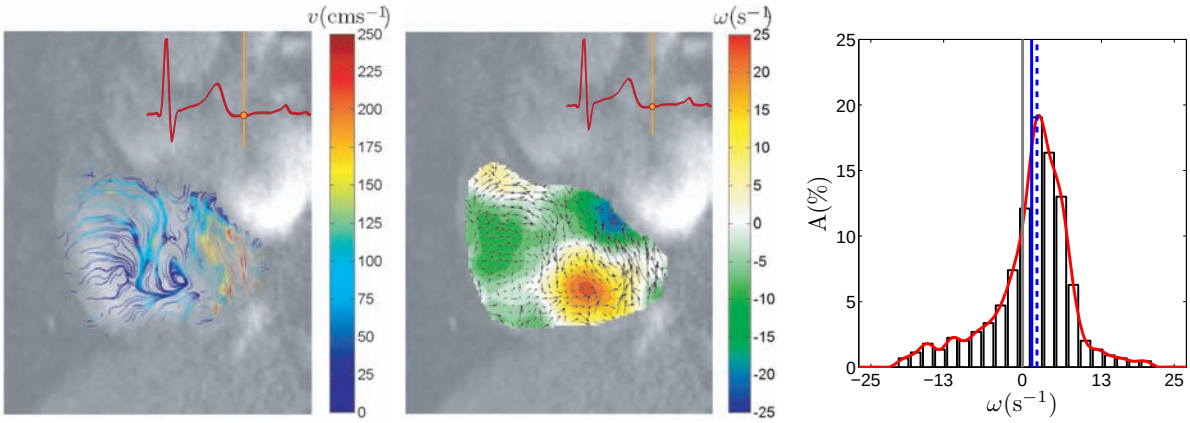

(vii) $n_t = 14, \begin{bmatrix}\overline{\omega}\\ \sigma\end{bmatrix}_\mu = \begin{bmatrix}-0.25\\ 9.25\end{bmatrix}\mathrm{s}^{-1}, \begin{bmatrix}\overline{\omega}\\ \sigma\end{bmatrix}_m = \begin{bmatrix}-1.87\\ 9.39\end{bmatrix}\mathrm{s}^{-1}, \Gamma = -2.44\mathrm{m}^2\mathrm{s}^{-1}$

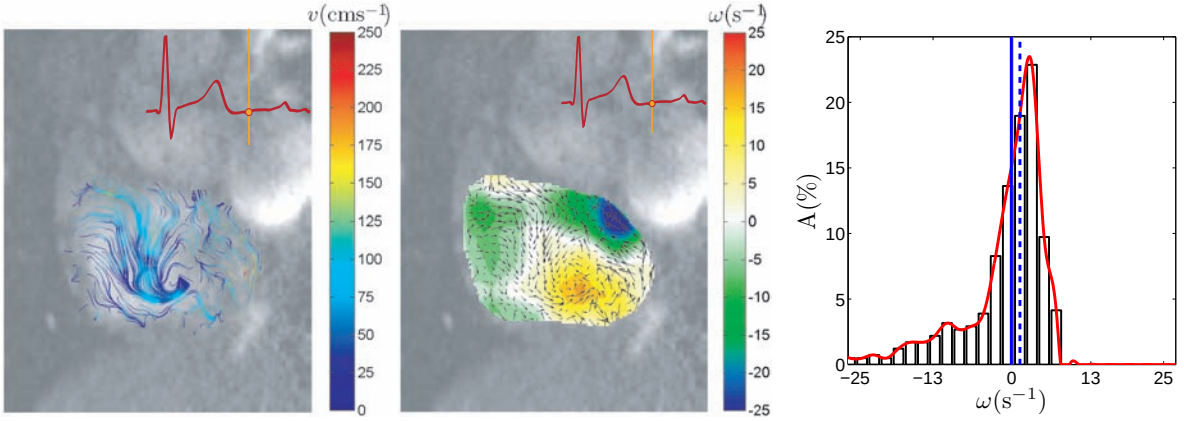

(viii) $n_t = 15, \begin{bmatrix}\overline{\omega}\\ \sigma\end{bmatrix}_\mu = \begin{bmatrix}-0.54\\ 9.40\end{bmatrix}\mathrm{s}^{-1}, \begin{bmatrix}\overline{\omega}\\ \sigma\end{bmatrix}_m = \begin{bmatrix}-1.7\\ 9.47\end{bmatrix}\mathrm{s}^{-1}, \Gamma = -3.06\mathrm{m}^2\mathrm{s}^{-1}$

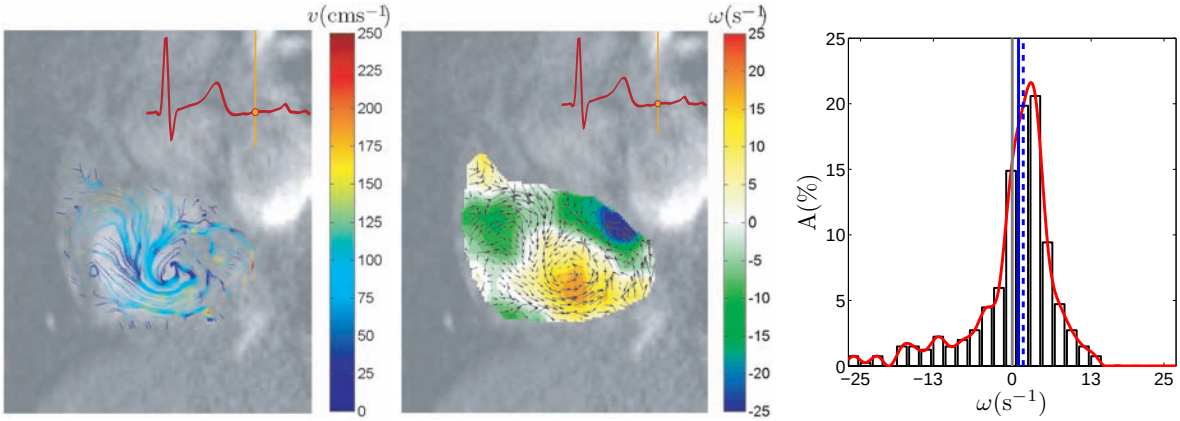

(ix) $n_t = 16, \begin{bmatrix}\overline{\omega}\\ \sigma\end{bmatrix}_\mu = \begin{bmatrix}-0.56\\ 10.62\end{bmatrix}\mathrm{s}^{-1}, \begin{bmatrix}\overline{\omega}\\ \sigma\end{bmatrix}_m = \begin{bmatrix}0\\ 10.64\end{bmatrix}\mathrm{s}^{-1}, \Gamma = -3.89\mathrm{m}^2\mathrm{s}^{-1}$

Time frame indices from 17 to 18 out of 25 frames in a cardiac cycle continues on the next page

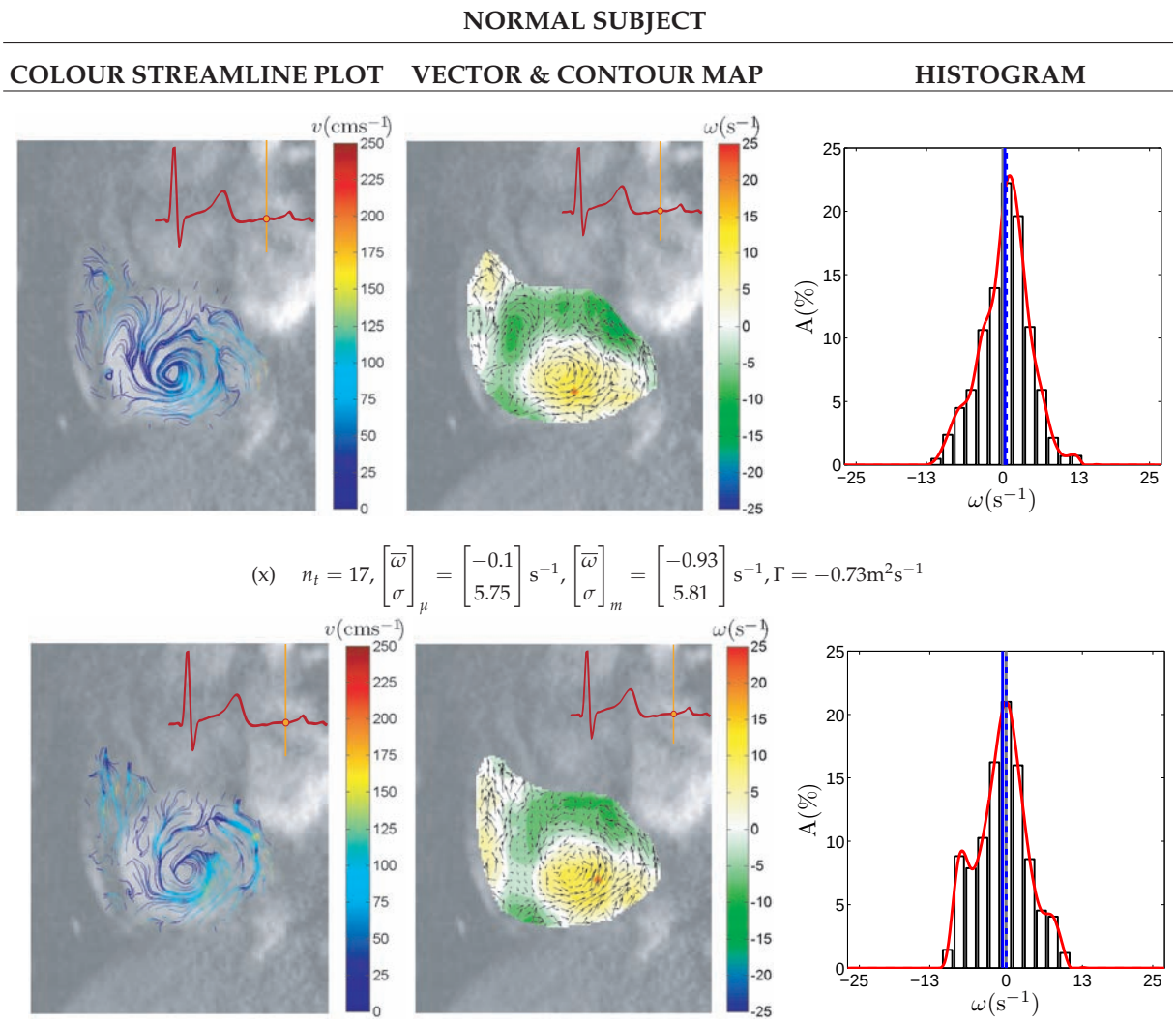

Figure 7.5. Flow visualisation of normal right atrium. The visualisation of flow in the right atrium of a normal subject is presented for investigation of the vortex behaviour during the systolic and diastolic phases from time frame indices $n_t = 8$ to 18 of one cardiac cycle with 25 phases. The examination of flow patterns shows that the blood is swirling in both the clockwise and counter-clockwise directions simultaneously for some cardiac phases. Streamline plots are produced to illustrate the direction of blood in the chamber. Streamlines, with the colour at every patch of the line indicates the magnitude of the velocity (in cms^{-1}) and presents both the direction and speed of flow. A vector plot that is superimposed onto the vorticity contour map is also produced to indicate the location and strength of vortices. Each event of a cardiac cycle is indicated by a reference line on an echocardiogram (ECG) trace located on the top right hand corner of every image. This line updates its position as the time frame index increases.

Cardiac time frame indices $n_t = 8$ to 11	Cardiac time frame indices $n_t = 12$ to 15

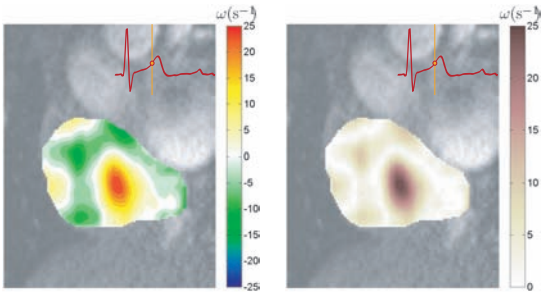

(i) $n_t = 8$, $\begin{bmatrix}\overline{\omega}\\ \sigma\end{bmatrix}_{\text{Dir}} = \begin{bmatrix}1.38\\ 7.78\end{bmatrix}\,\text{s}^{-1}$, $\begin{bmatrix}\overline{\omega}\\ \sigma\end{bmatrix}_{\text{Abs}} = \begin{bmatrix}7.32\\ 7.78\end{bmatrix}\,\text{s}^{-1}$

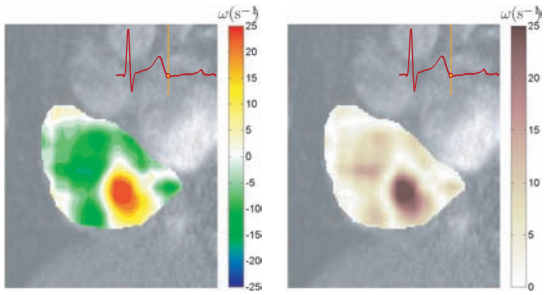

(v) $n_t = 12$, $\begin{bmatrix}\overline{\omega}\\ \sigma\end{bmatrix}_{\text{Dir}} = \begin{bmatrix}-0.71\\ 9.23\end{bmatrix}\,\text{s}^{-1}$, $\begin{bmatrix}\overline{\omega}\\ \sigma\end{bmatrix}_{\text{Abs}} = \begin{bmatrix}7.32\\ 9.23\end{bmatrix}\,\text{s}^{-1}$

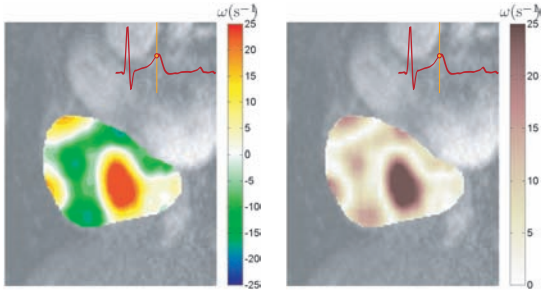

(ii) $n_t = 9$, $\begin{bmatrix}\overline{\omega}\\ \sigma\end{bmatrix}_{\text{Dir}} = \begin{bmatrix}2.17\\ 12.64\end{bmatrix}\,\text{s}^{-1}$, $\begin{bmatrix}\overline{\omega}\\ \sigma\end{bmatrix}_{\text{Abs}} = \begin{bmatrix}9.99\\ 12.64\end{bmatrix}\,\text{s}^{-1}$

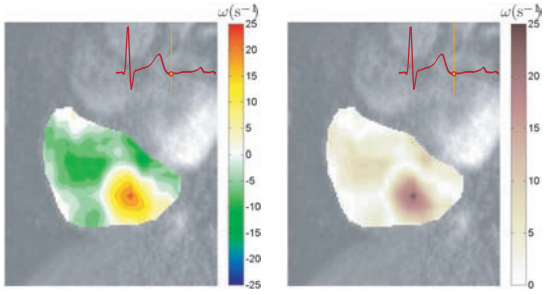

(vi) $n_t = 13$, $\begin{bmatrix}\overline{\omega}\\ \sigma\end{bmatrix}_{\text{Dir}} = \begin{bmatrix}-0.65\\ 7.10\end{bmatrix}\,\text{s}^{-1}$, $\begin{bmatrix}\overline{\omega}\\ \sigma\end{bmatrix}_{\text{Abs}} = \begin{bmatrix}5.67\\ 7.10\end{bmatrix}\,\text{s}^{-1}$

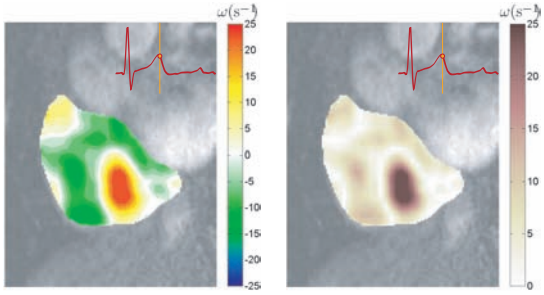

(iii) $n_t = 10$, $\begin{bmatrix}\overline{\omega}\\ \sigma\end{bmatrix}_{\text{Dir}} = \begin{bmatrix}0.25\\ 9.54\end{bmatrix}\,\text{s}^{-1}$, $\begin{bmatrix}\overline{\omega}\\ \sigma\end{bmatrix}_{\text{Abs}} = \begin{bmatrix}7.40\\ 9.54\end{bmatrix}\,\text{s}^{-1}$

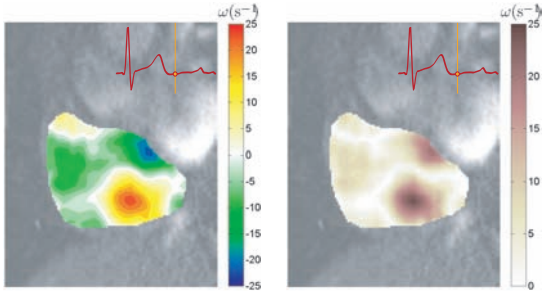

(vii) $n_t = 14$, $\begin{bmatrix}\overline{\omega}\\ \sigma\end{bmatrix}_{\text{Dir}} = \begin{bmatrix}-0.40\\ 9.21\end{bmatrix}\,\text{s}^{-1}$, $\begin{bmatrix}\overline{\omega}\\ \sigma\end{bmatrix}_{\text{Abs}} = \begin{bmatrix}7.26\\ 9.21\end{bmatrix}\,\text{s}^{-1}$

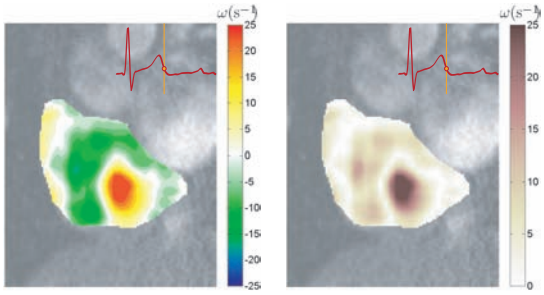

(iv) $n_t = 11$, $\begin{bmatrix}\overline{\omega}\\ \sigma\end{bmatrix}_{\text{Dir}} = \begin{bmatrix}0.10\\ 9.06\end{bmatrix}\,\text{s}^{-1}$, $\begin{bmatrix}\overline{\omega}\\ \sigma\end{bmatrix}_{\text{Abs}} = \begin{bmatrix}6.84\\ 9.06\end{bmatrix}\,\text{s}^{-1}$

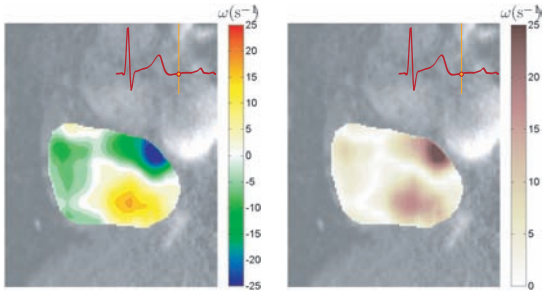

(viii) $n_t = 15$, $\begin{bmatrix}\overline{\omega}\\ \sigma\end{bmatrix}_{\text{Dir}} = \begin{bmatrix}-0.54\\ 9.38\end{bmatrix}\,\text{s}^{-1}$, $\begin{bmatrix}\overline{\omega}\\ \sigma\end{bmatrix}_{\text{Abs}} = \begin{bmatrix}7.20\\ 9.38\end{bmatrix}\,\text{s}^{-1}$

Figure 7.6. Flow quantification of normal right atrium. The statistics of each flow map based on mean and standard deviations for directional (Dir) and absolute (Abs) vorticity fields are provided for time frame indices $n_t = 8$ to 15 of one cardiac cycle with 25 frames. A directional field consists of polarised vorticity values that can depict clockwise or counter-clockwise fluid rotations. An absolute field displays vorticity magnitudes only.

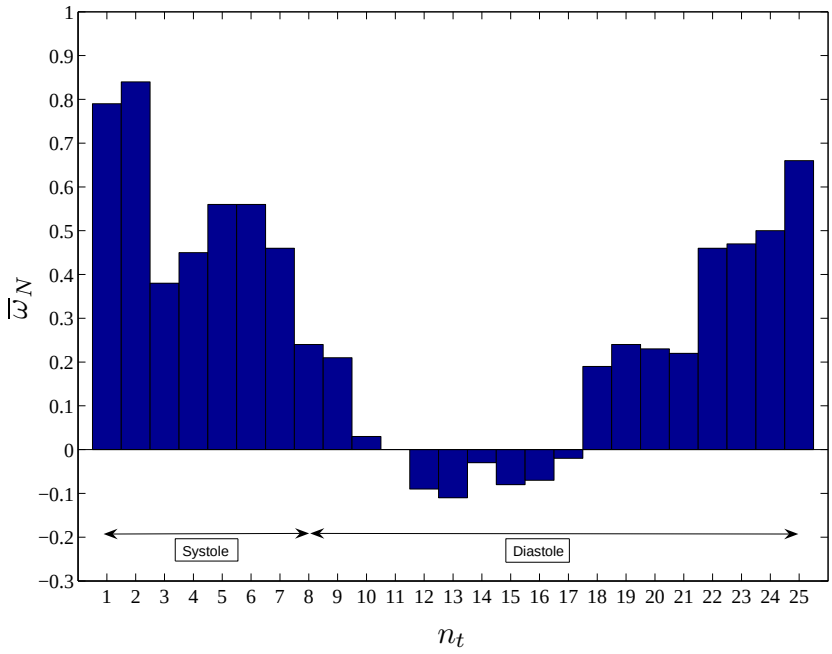

Figure 7.7. Chart of normalised vorticity mean based on a cardiac cycle. The relative strengths of vortices in a flow field can be indicated using the ratio of the directional mean to that of the absolute one. The plot of such normalised mean $\overline{\omega}_N$ with respect to time frame index n_t of a cardiac cycle demonstrates a smooth transition in positive vorticities losing dominance to the negative ones during time frame indices from $n_t = 10$ onwards and becoming higher in values again after $n_t = 18$.

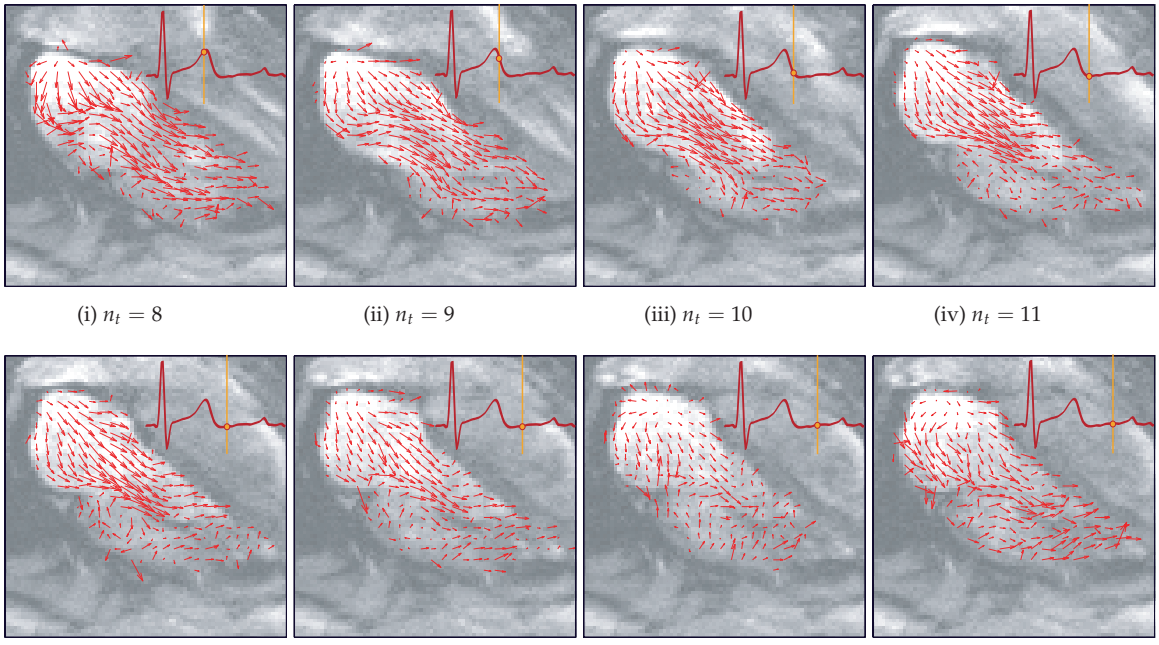

(i) $n_t = 8$ (ii) $n_t = 9$ (iii) $n_t = 10$ (iv) $n_t = 11$

(v) $n_t = 12$ (vi) $n_t = 13$ (vii) $n_t = 14$ (viii) $n_t = 15$

Figure 7.8. Qualitative visualisation of flow in the right atrium and ventricle. The vector plots for selected time frame indices of $n_t = 8$ to 15 of a cardiac cycle with 20 frames demonstrates the movement of blood from the right atrium (RA) into the right ventricle (RV). There is no sign of large scale vortex formation in the RA during these atrial diastolic phases. The image set that is used here corresponds to slice 3 of the four-chamber long axis scan.

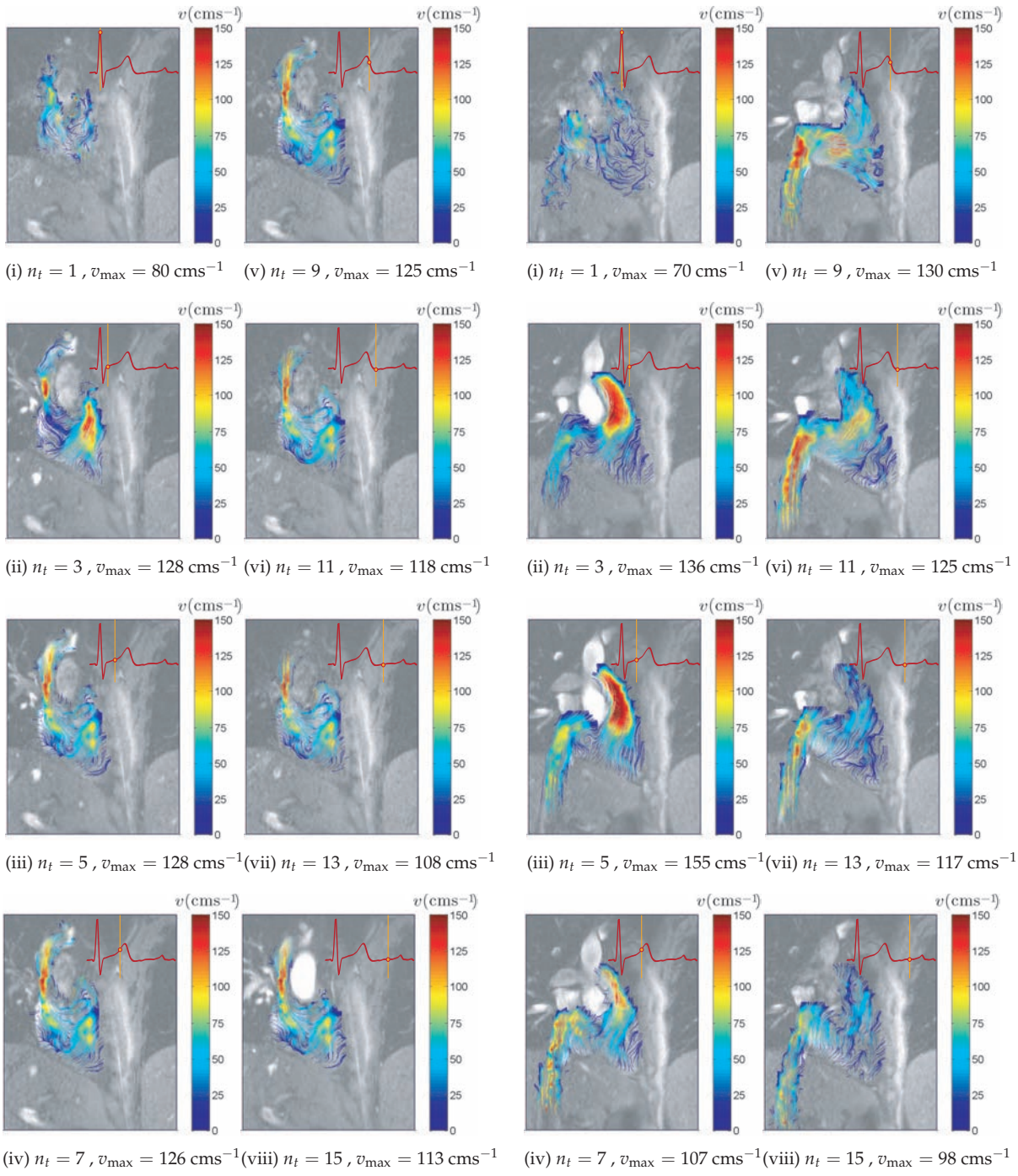

Figure 7.9. Qualitative visualisation of right atrial flow circulation. The visualisation of flow in the (a) inferior *vena cava* (IVC) and pulmonary artery (PA) and (b) superior *vena cava* (SVC) can be demonstrated by using streamline plots based on a cardiac cycle of 20 time frame indicess. Flow is accelerated in the pulmonary artery during time frame indices from $n_t = 3$ onwards and its $v_{\max}$ is 155 cms^{-1} at $n_t = 5$. The flow in the inferior *vena cava* are shown to be accelerated during time frame indices $n_t = 9$ to 13 and has a maximum velocity $v_{\max}$ of 128 cms^{-1} at $n_t = 3$ and 5. These first and second events correspond to the systolic and diastolic phases respectively.

LEFT ATRIAL AND VENTRICULAR CIRCULATION

Cardiac time frame indices $n_t = 6$ to 9	Cardiac time frame indices $n_t = 10$ to 13

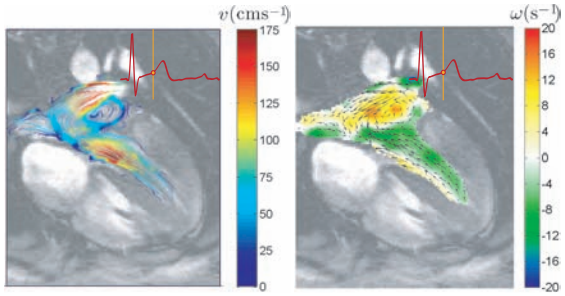

(i) $n_t = 6$, $\begin{bmatrix}\overline{\omega}\\ \sigma\end{bmatrix}_\mu = \begin{bmatrix}-0.79\\ 6.79\end{bmatrix}\text{s}^{-1}$, $\begin{bmatrix}\overline{\omega}\\ \sigma\end{bmatrix}_m = \begin{bmatrix}-1.46\\ 6.83\end{bmatrix}\text{s}^{-1}$

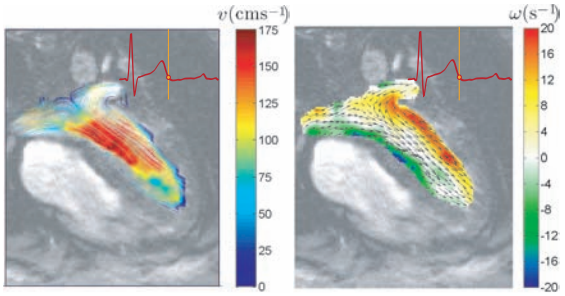

(v) $n_t = 10$, $\begin{bmatrix}\overline{\omega}\\ \sigma\end{bmatrix}_\mu = \begin{bmatrix}3.35\\ 7.69\end{bmatrix}\text{s}^{-1}$, $\begin{bmatrix}\overline{\omega}\\ \sigma\end{bmatrix}_m = \begin{bmatrix}2.47\\ 7.74\end{bmatrix}\text{s}^{-1}$

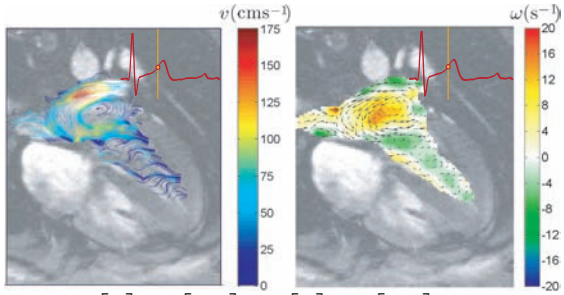

(ii) $n_t = 7$, $\begin{bmatrix}\overline{\omega}\\ \sigma\end{bmatrix}_\mu = \begin{bmatrix}1.07\\ 5.64\end{bmatrix}\text{s}^{-1}$, $\begin{bmatrix}\overline{\omega}\\ \sigma\end{bmatrix}_m = \begin{bmatrix}0.00\\ 5.74\end{bmatrix}\text{s}^{-1}$

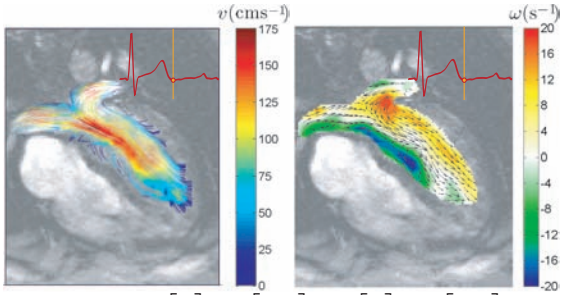

(vi) $n_t = 11$, $\begin{bmatrix}\overline{\omega}\\ \sigma\end{bmatrix}_\mu = \begin{bmatrix}1.45\\ 8.53\end{bmatrix}\text{s}^{-1}$, $\begin{bmatrix}\overline{\omega}\\ \sigma\end{bmatrix}_m = \begin{bmatrix}1.53\\ 8.53\end{bmatrix}\text{s}^{-1}$

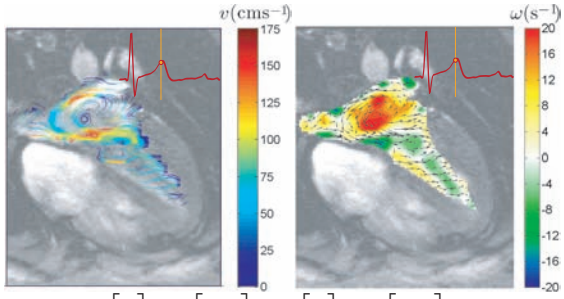

(iii) $n_t = 8$, $\begin{bmatrix}\overline{\omega}\\ \sigma\end{bmatrix}_\mu = \begin{bmatrix}3.38\\ 4.73\end{bmatrix}\text{s}^{-1}$, $\begin{bmatrix}\overline{\omega}\\ \sigma\end{bmatrix}_m = \begin{bmatrix}2.94\\ 4.75\end{bmatrix}\text{s}^{-1}$

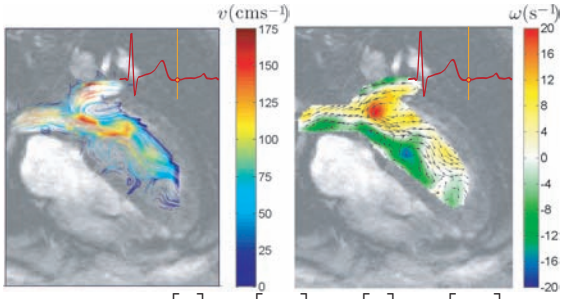

(vii) $n_t = 12$, $\begin{bmatrix}\overline{\omega}\\ \sigma\end{bmatrix}_\mu = \begin{bmatrix}0.35\\ 7.53\end{bmatrix}\text{s}^{-1}$, $\begin{bmatrix}\overline{\omega}\\ \sigma\end{bmatrix}_m = \begin{bmatrix}0.00\\ 7.54\end{bmatrix}\text{s}^{-1}$

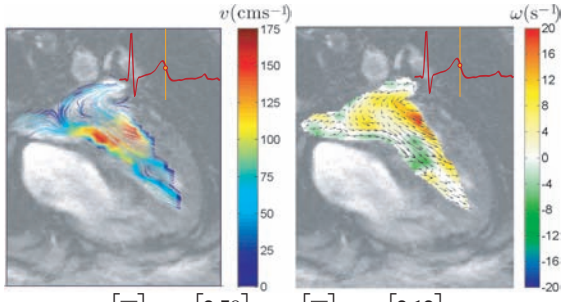

(iv) $n_t = 9$, $\begin{bmatrix}\overline{\omega}\\ \sigma\end{bmatrix}_\mu = \begin{bmatrix}2.59\\ 5.57\end{bmatrix}\text{s}^{-1}$, $\begin{bmatrix}\overline{\omega}\\ \sigma\end{bmatrix}_m = \begin{bmatrix}2.12\\ 5.59\end{bmatrix}\text{s}^{-1}$

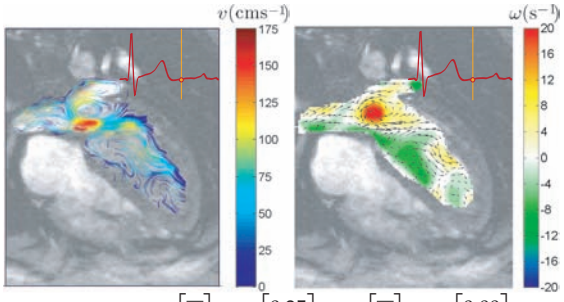

(viii) $n_t = 13$, $\begin{bmatrix}\overline{\omega}\\ \sigma\end{bmatrix}_\mu = \begin{bmatrix}0.35\\ 6.13\end{bmatrix}\text{s}^{-1}$, $\begin{bmatrix}\overline{\omega}\\ \sigma\end{bmatrix}_m = \begin{bmatrix}0.00\\ 6.14\end{bmatrix}\text{s}^{-1}$

Figure 7.10. Flow quantification of normal left atrium and left ventricle. Streamline tracing and vorticity flow maps based on time frame indices $n_t = 6$ to 13 of one cardiac cycle with 20 frames. A counter-clockwise vortex is observed to form as flow through the two branches of the pulmonary vein (PV1 and PV2) into the left atrium (LA) from $n_t = 6$ to 8 gives the atrial blood an angular momentum.

7.5 Introduction to Cardiac Flow Component Analysis

This section describes the procedures for vorticity-based segmentation using K-means clustering and how analysis can be broken down into examination of individual vortices using histogram plots of the isolated vorticity region. Here, segmentation is the process of partitioning a digital image representing the vorticity field into multiple regions or sets of pixels such that each region represents a large-scale vortex. The goal of segmentation is to change the representation of an image into information that is more meaningful for analysis (Shapiro and Stockman 2001).

We attempt to quantify vortex characteristics using component analysis by segmenting the vortices before histograms of their vortical distribution are generated. We can determine the properties of vorticity using a statistical quantification of the flow maps and comparison of these quantities over a cardiac cycle.

The proposed approach is utilised for examining vortices within the human heart chamber. Our study has shown that quantification of vorticity after vortex isolation can generate statistical properties that characterise the vortex components individually.

The purpose of this study is to demonstrate the working principles of our proposed framework that is devised to perform component flow analysis. The mathematical and technical information presented in this chapter can lay the fundamentals for further successful flow analysis of any cardiac circulation. Since our objective is not to establish the number of vortices in the heart or to discover new flow phenomenon, but to present an engineering methodology to achieve effective flow analysis, We can justify the testing of this platform using a sample case study of the right atrial flow.

7.5.1 Colour-Based K-Means Clustering Segmentation

Data clustering based on a colour image is described here. The pixel classification is based on target colours in the segmentation. The technique of colour image segmentation based on K-means clustering (Kanungo *et al.* 2002) is applied. The number of clusters denoted by K affects the colour differentiation as a large number of clusters may result in over-segmentation of the image and a small number will not enable sufficient region segregation (Hase *et al.* 2003). The colour quantisation allows us to differentiate cluster regions which have unique class properties and therefore breaks down the analysis into components.

We examine how the algorithm partitions data into K clusters as described by Wu *et al.* (2007). Assume that the feature vectors are denoted by $X = \{x_i | i = 1, 2, ..., n\}$. The generalised algorithm initiates K cluster centroids C, given that $C = \{c_j | j = 1, 2, ..., K\}$ and $K < n$, by randomly selecting K feature vectors from X. The feature vectors are assigned into each group labelled as j such that their Euclidean distances to the centroid of the group $G_j = ||x_i - c_j||$ are minimum given that $\forall \left(x_i, c_j\right) \epsilon X \times C$. The cluster centroids are computed again based on their group members and the new selection of the feature vectors according to the new cluster centroids is performed. The procedure terminates when there is no change in position of cluster centroids.

7.5.2 Segregation of Vortices

As an illustration, we ideally position two Lamb-Oseen vortices (Saffman 1992, Meunier *et al.* 2005, Cariteau and Flór 2006) with core centres at a distance of 5 mm apart from each other. The vortices have different directions of rotation. Each vortex is constructed in such as way that we computationally set the flow field to span 10 mm by 10 mm in space, and its maximum velocity magnitude to 10 mms^{-1}. Note that the velocity field of this flow is represented by a digital image grid with a width of 160 and a height of 240 points matrix size.

From the results describing double vortices in the flow field (Figure 7.11 (a) and (b)), we are able to visually observe their cores and strength using vorticity flow maps. In addition, from the histogram pertaining to each flow map in Figure 7.11 (c), we can extract useful statistical properties that reveal some information about the flow field, such as the global directions of the vortices.

We can apply region segmentation of the vorticity map based on the proximity of similar map elements to determine the number of vortices that are present in a flow, and also to produce histogram plots of each distribution cluster (Figure 7.11 (d) to (i)). We can determine regions with high intra-class and low inter-class similarities (Kaufman and Rousseeuw 1990, Biswas *et al.* 1998) using a K-means algorithm, whereby each set of regional clusters with such a characteristic is given a unique label. Therefore, we can localise vortices within the flow and provide a discriminant measure based on the mean $\overline{\omega}$ and variance σ^2 of the cluster distribution. The discrimination of spatial separation for N number of vortices is given by

$$D = \frac{1}{N} \sum_{k=1}^{N} \frac{|\overline{\omega}_k|}{\sigma_k^2}. \tag{7.4}$$

If D is large, it means that the vortices are defined with good intra-class similarities and inter-class dissimilarities. Figure 7.11 shows the results of applying segmentation on a pair of idealised Lamb-Oseen vortices and examination of each segmented region using histogram plot of its vorticity distribution. Each homogeneous group of vorticity values is a representation of a vortex. An incorrect input for number of clusters into the K-means segmentation framework will result in one or more clusters having almost similar vorticity distribution. It is important that an accurate number of large-scale clusters can be automatically determined by a reliable unsupervised clustering algorithm.

The circulation Γ_j of a vortex component j can be obtained by taking the product of the component vorticity mean $\overline{\omega}_j$ (from the segmented vorticity region) and the area A_j covered by the vortex cluster j such that

$$\begin{aligned} \Gamma_j &= \overline{\omega}_j \times A_{\text{vor}} \\ \text{where} \quad A_{\text{vor}} &= \frac{N_j}{N_c} \times A_c. \end{aligned} \tag{7.5}$$

Here, N_j and N_c are the number of pixels that makes up the vortex component and segmented heart chamber respectively. A_c is defined as the actual area of the heart chamber in units of m^2. The measure of swirling flow using Γ is quantified along with the other statistics based on vorticity.

7.5.3 Component Flow Analysis Results

We observe the vortices that appear during the diastolic and systolic phases of the heart beat cycle, and analyse its course of development and changes over the cardiac cycle. The change in polarity of rotation can be easily and visually observed using the streamlines, contour maps, and vector plots as shown in Figure 7.12. In addition, we superimpose the corresponding MR images onto these flow fields to give an indication of the location of the vortex with respect to the chamber in which it resides. A vorticity sampling mask of size (21×21) pixels is used. This corresponds to

(32.34×32.34) mm^2 window size. The rectangular encapsulation of the displayed scan is (184.80×231.00) mm^2.

We present the flow results and analysis of the right atrium for the selected slice based on one time frame of the cardiac cycle to illustrate the concept of vortex component analysis using real atrial flow data. From vorticity maps that can be represented using a pixel image, histograms are computed based on the vorticity distribution. Note that the mean and median of the histogram are denoted by $\overline{\omega}_\mu$ and $\overline{\omega}_m$ respectively. Standard deviations with respect to the mean and median are denoted as σ_μ and σ_m respectively.

We focus on a more thorough examination of the flow using the entire set of time frames in the cardiac cycle. For brevity, we present the flow regions based on a selected series of time frame indices from $n_t = 8$ to 15 out of 25 frames of a cardiac cycle as an illustration (Figure 7.13). The full range of vorticity maps can be assessed using Supplementary Video 7. The statistical entities for every time frame, mean, median and their standard deviations, are displayed to indicate the global properties of the flow. The velocity vector plots show that there are two vortices in the same flow region for the presented time frames. The intensity of vorticity using $\overline{\omega}_\mu$ and σ_μ gives a good estimation of the swirl structure in the right atrium. Based on our conventions, counter-clockwise and clockwise vorticity are represented in red and blue respectively on the contour map. Vortices in the atrium are visually shown to be both clockwise and counter-clockwise in rotation upon investigation. This observation needs to be quantified. In Figure 7.13, based on $n_t = 8$ to 11, $\overline{\omega}_\mu$ is greater than zero, and the flow is overall counter-clockwise. For $n_t = 12$ to 15, $\overline{\omega}_\mu$ is negative, and the flow becomes clockwise globally. It is reasonable to reach this deduction as the sign of $\overline{\omega}_\mu$ is the same as that of Γ.

Next, we perform segmentation on the flow region to segregate the vortices into their components. This can provide a more detailed analysis. In Figure 7.14, we present the component analysis for clockwise (CW) and counter-clockwise (CCW) vortices for $n_t = 8$ to 15. The variation of the vortex pattern at every time frame is visible from the intensity contours. The colour bar on the right of every vorticity field is scaled to show the actual vorticity range of the segmented vortex.

7.5.4 Statistics of Component Flow

Flow analysis can be based on the entire flow region (Figure 7.12) and also on individual segregated sub-regions such that each of them comprises a vortex (Figure 7.13). A concise analysis of cardiac flow in a heart chamber may be based on the statistical properties of the regional vorticity field. We highlight the systolic phases from approximately $n_t = 1$ to 8 and the diastolic phases from $n_t = 9$ to 25.

In Figure 7.15, we note the differences between the means and the medians for time frame indices from $n_t = 8$ to 21. Therefore, such global analysis is limited in terms of an accurate presentation of vorticity. In this case, visual observation and qualitative analysis will be more appropriate.

The vorticity and circulation charts in Figure 7.15 are able to provide evidence of the physical flow occurence that is related to the cardiac events. It can be observed that the vorticity and circulation properties of flow are generally higher and positive (overall clockwise rotation) during the systole and at the transition stage to diastole, the values decrease to zero. For the diastolic events, the flow properties reduce to negative magnitudes (overall counter-clockwise rotation) and slowly increase in value towards the end of the diastole. This section provides an indication of the overall direction of flow circulation. Further analysis can be achieved by analysing each segmented vortex individually.

Breaking down the vorticity analysis into examination of individual vortices allows us to characterise the blood flow behaviour more accurately. Two main vortices are identified: one of clockwise motion with $\overline{\omega}_\mu$ with range from = -14.85 to -2.42 s^{-1} and $\overline{\omega}_m$ with range -14.29 to -3.20 s^{-1}, while the other vortex has $\overline{\omega}_\mu$ with range 5.59 to 18.87 s^{-1} and $\overline{\omega}_m$ with range 5.33 to 16.89 s^{-1}. Based on the mean of vorticity distribution, the standard deviations σ_μ of the negative and positive vorticities ranges from 0.91 to 8.02 s^{-1}, and 2.61 to 8.53 s^{-1} respectively. Standard deviation σ_m of the positive and negative vorticities are of range 0.93 to 8.48 s^{-1} and 2.61 to 8.76 s^{-1} respectively. The region of nominally irrotational flow has a low mean of range -1.64 to 1.57 s^{-1} and small standard deviation of range 1.20 to 4.94 s^{-1}.

If we combine the vortices in the flow, the ensemble average of the positive and negative vorticities result in a mean of range -0.71 to 7.35 s^{-1} and standard deviation of range 4.87 to 12.64 s^{-1} (Figure 7.15). The larger variance in vorticity shows that the global flow differs from those of the components. This will not give a correct insight

into the actual flow characteristics. Therefore, we can deduce that vorticity segmentation is crucial for an accurate flow analysis of the blood motion behaviour in the heart.

We find that, based on normal conditions, two vortices appear during the cardiac cycle (Figure 7.16). However, one dominant vortex exists at some time frames. In particular, the presence of a stronger counter-clockwise vortex from $n_t = 1$ to 9 and $n_t = 18$ to 25 can be noted. The clockwise vortex is more dominant from $n_t = 12$ to 16. This is consistent with the global vorticity means presented by Figure 7.15. There is a smaller difference between the vorticity mean and median for each time frame, and this is expected because of the smaller standard deviation of vorticity distribution after breaking down the flow regions into their vortex components.

In terms of the temporal variation of flow circulation, the range of Γ for global flow is given by -4.33 to 42.81 m^2s^{-1}. The counter-clockwise and clockwise vortices have circulation ranges of -24.00 to -1.30 m^2s^{-1} and 12.46 to 49.92 m^2s^{-1} respectively. Based on Figure 7.16, we may not be able to see much difference in absolute magnitudes between the vorticity means of the clockwise and counter-clockwise vortices. However, the circulation magnitudes of these two vortices are clearly distinguishable during the systole and diastole of the cardiac cycle.

7.5.5 Mechanics of Flow with Reference to the Cardiac Events

Based on Figure 7.1, we attempt to link the flow results to the cardiac events during a heart beat cycle. We highlight the possibility of delay in changes of flow that are caused by the myocardial dynamics at some of these events. This may be due to the time required for the blood to gain momentum. Based on the pressure wave in Figure 7.1, the *a* wave that is caused by right atrial contraction (at time frame indices $n_t = 23$ to 25, and restarting at 1) can cause the pressure to increase up to 6 mmHg (Guyton and Hall 2006). This may account for the rise in vorticity and circulation from $n_t = 23$ to 25 and then from 1 to 4. Then, the *c* wave occurs during cardiac systole (from $n_t = 1$ to 8), which causes a slight regurgitation of blood into the atrium at the onset of the ventricular contraction. At this instance, the mitral and tricuspid valves close due to the back pressure of blood flow into the atrium. We can relate this event to the reduction of vorticity and circulation magnitude resulting in decreasing values from $n_t = 5$ to 11. The *v* wave that occurs towards the end of cardiac systole ($n_t = 9$) is the cause of blood flow into the atrium from the *vena cavae*. This may be observed in the

slow increase of vorticity and circulation in the opposite direction (negative values) from $n_t = 12$ to 14. After ventricular contraction, the atrioventricular valves open allowing the stored atrial blood to flow rapidly into the ventricles and causing the v wave to disappear ($n_t = 11$). At the same time, it also causes the vorticity and circulation to drop to zero values during $n_t = 15$ to 18. From this instance to the starting of the next atrial contraction, the two flow properties increase slightly. There should be a marked increase in their values at the onset of the atrial systole ($n_t = 23$).

7.5.6 Limitations of Study

We have not presented the flow results for all the time frames of one cardiac cycle, as it is not the aim of this chapter to consider the number of vortices in the right atrial flow. Rather, it is to demonstrate the measurement of vorticity and the analytical framework that has been developed. We test the methodology on one test subject as an illustrative example. A full clinical study is beyond the scope of this engineering thesis, and this work therefore motivates the need for future clinical studies.

We idealise the study by selecting test subject scans that show the presence of two vortices in the right atrium. It may not be definite that two vortices appear in the right atrial flow consistently for all individuals. Nevertheless, this case enables us to test the working principles of the vortex segmentation effectively.

The vorticity measurement produces an acceptable vorticity variation as demonstrated by the flow maps. The key focus is to demonstrate the effectiveness of vorticity measurement and segmentation. At this stage, it is not important to use an accurate but complicated vorticity measurement to prove this concept. The main aim is to present our approach using a simplified model that is supported with fundamental concepts.

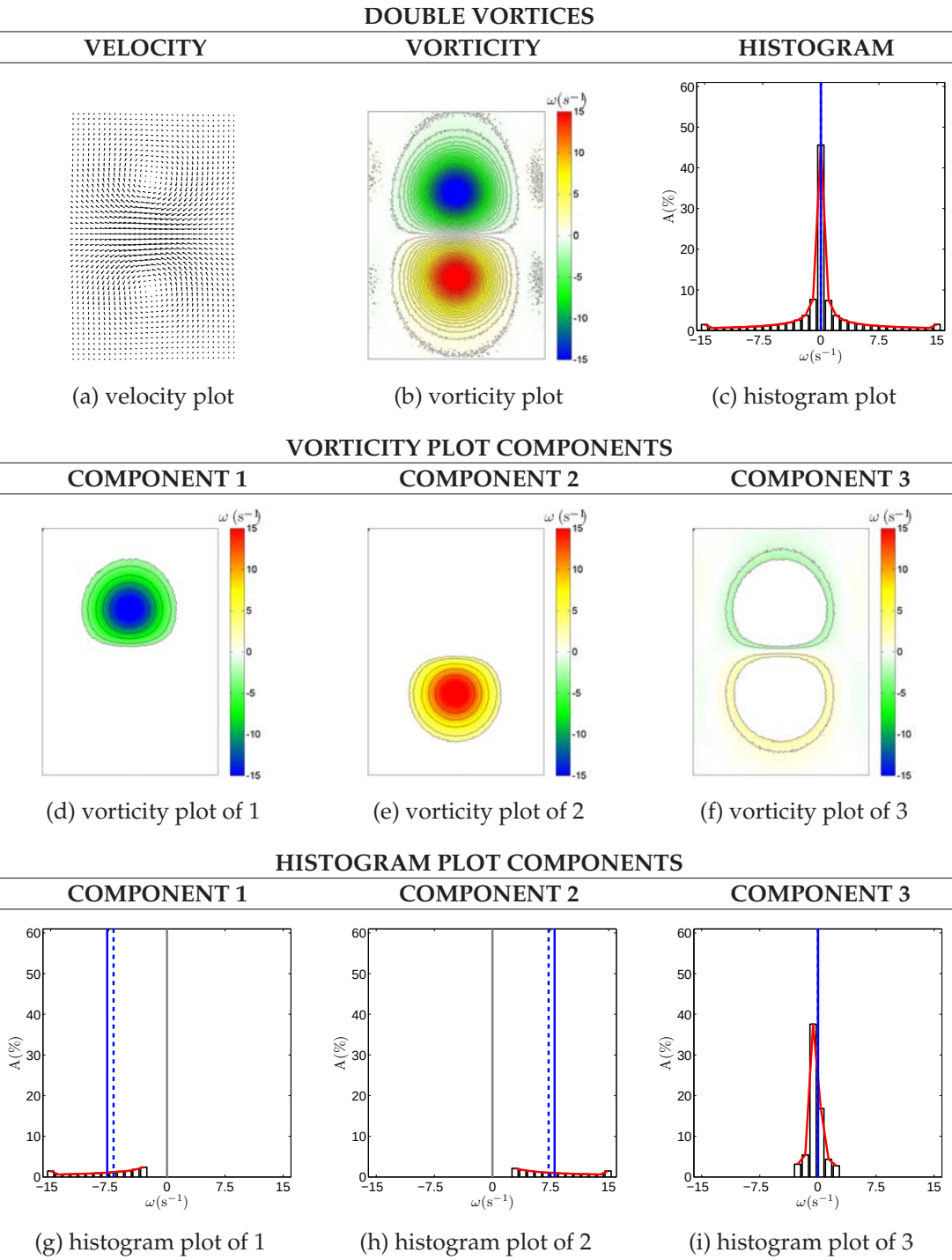

(a) velocity plot (b) vorticity plot (c) histogram plot

(d) vorticity plot of 1 (e) vorticity plot of 2 (f) vorticity plot of 3

(g) histogram plot of 1 (h) histogram plot of 2 (i) histogram plot of 3

Figure 7.11. Localisation and analysis of vortices. Segmentation of flow field isolates the vortices and allows us to perform histogram analysis on its distribution. This enables breakdown of the analysis into components that can be quantified with more quantitative information. In this example, we have two Lamb-Oseen vortices in a flow field and application of K-means algorithm segregates the flow region into three partitions. The histogram plot of each partition provides the mean and variance of the isolated vortex which can indicate its vorticity or speed of fluid rotation. Combining the segmented regions results in the same combination of their histograms.

NORMAL SUBJECT		
COLOUR STREAMLINE PLOT	VECTOR & CONTOUR MAP	HISTOGRAM

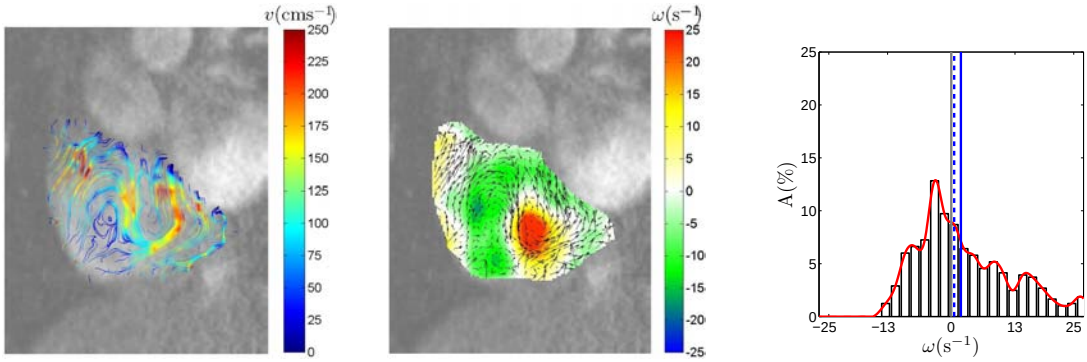

Statistical details: $n_t = 11, \begin{bmatrix}\overline{\omega}\\ \sigma\end{bmatrix}_\mu = \begin{bmatrix}0.10\\ 9.06\end{bmatrix}\mathrm{s}^{-1}, \begin{bmatrix}\overline{\omega}\\ \sigma\end{bmatrix}_m = \begin{bmatrix}-1.63\\ 9.23\end{bmatrix}\mathrm{s}^{-1}, \Gamma = 0.66\ \mathrm{m}^2\mathrm{s}^{-1}$

(a) Flow visualisation of right atrium blood motion

COMPONENT 1	COMPONENT 2	COMPONENT 3

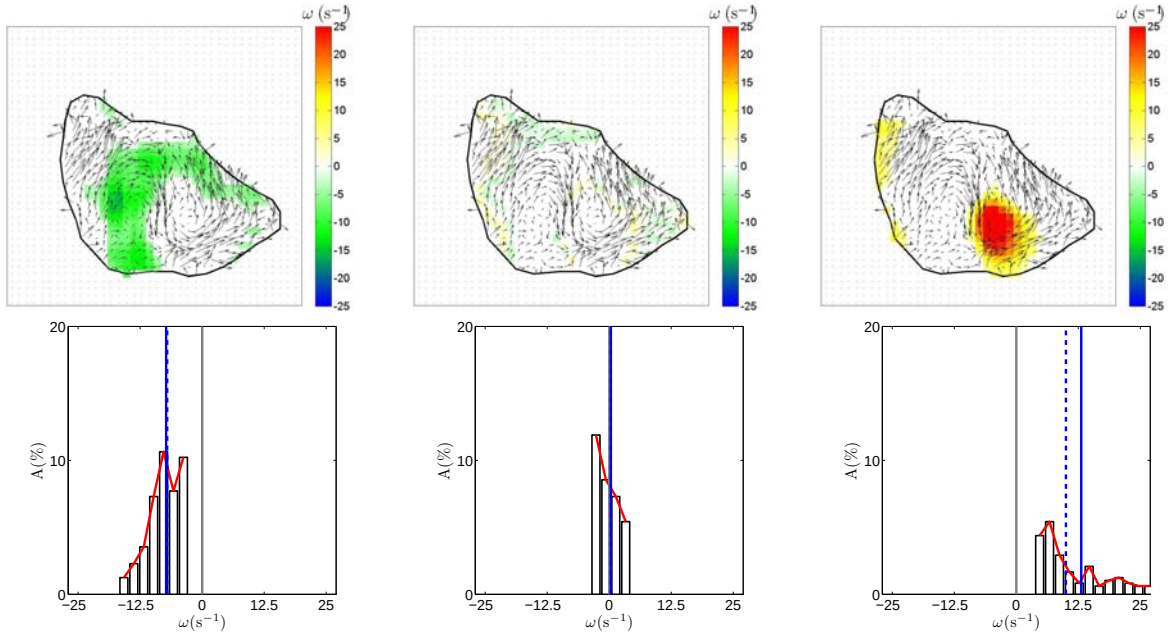

$\begin{bmatrix}\overline{\omega}\\ \sigma\end{bmatrix}_\mu = \begin{bmatrix}13.09\\ 7.47\end{bmatrix}\mathrm{s}^{-1}, \begin{bmatrix}\overline{\omega}\\ \sigma\end{bmatrix}_m = \begin{bmatrix}10.00\\ 8.09\end{bmatrix}\mathrm{s}^{-1}, \Gamma = -20.00\ \mathrm{m}^2\mathrm{s}^{-1}$

$\begin{bmatrix}\overline{\omega}\\ \sigma\end{bmatrix}_\mu = \begin{bmatrix}0.33\\ 2.00\end{bmatrix}\mathrm{s}^{-1}, \begin{bmatrix}\overline{\omega}\\ \sigma\end{bmatrix}_m = \begin{bmatrix}0.32\\ 2.00\end{bmatrix}\mathrm{s}^{-1}, \Gamma = -0.01\ \mathrm{m}^2\mathrm{s}^{-1}$

$\begin{bmatrix}\overline{\omega}\\ \sigma\end{bmatrix}_\mu = \begin{bmatrix}-7.27\\ 3.04\end{bmatrix}\mathrm{s}^{-1}, \begin{bmatrix}\overline{\omega}\\ \sigma\end{bmatrix}_m = \begin{bmatrix}-7.04\\ 3.05\end{bmatrix}\mathrm{s}^{-1}, \Gamma = 20.68\ \mathrm{m}^2\mathrm{s}^{-1}$

(b) Segmented flow components and visualisation

Figure 7.12. Component analysis of normal right atrium flow. (a) The visualisation of flow in the right atrium of a normal subject is presented for investigation of the vortex behaviour for time frame $n_t = 11$ of one cardiac cycle. The statistical properties are based on the chamber flow region. (b) The segmentation of vortical flow using K-means into individual vortices can be performed effectively.

GLOBAL ANALYSIS

Cardiac time frames $n_t = 8$ to 11	Cardiac time frames $n_t = 12$ to 15

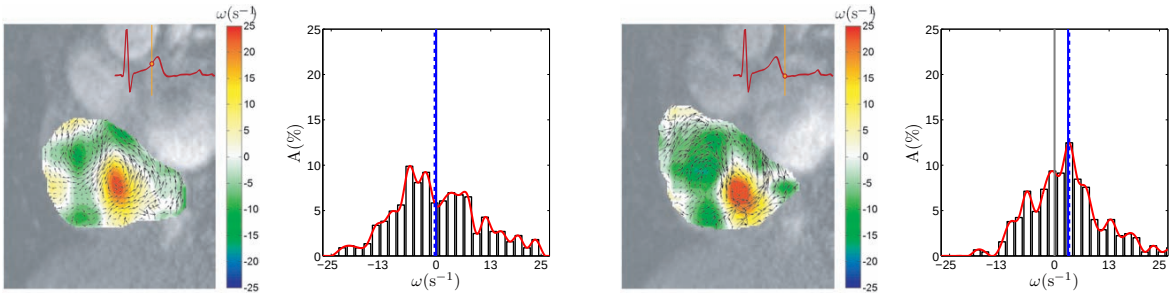

(i) $n_t = 8$, $\begin{bmatrix}\overline{\omega}\\ \sigma\end{bmatrix}_\mu = \begin{bmatrix}1.38\\ 7.78\end{bmatrix}$ s^{-1}, $\Gamma = 8.44$ m^{2}s^{-1}

(v) n_t=12, $\begin{bmatrix}\overline{\omega}\\ \sigma\end{bmatrix}_\mu = \begin{bmatrix}-0.71\\ 9.23\end{bmatrix}$ s^{-1}, $\Gamma = -4.33$ m^{2}s^{-1}

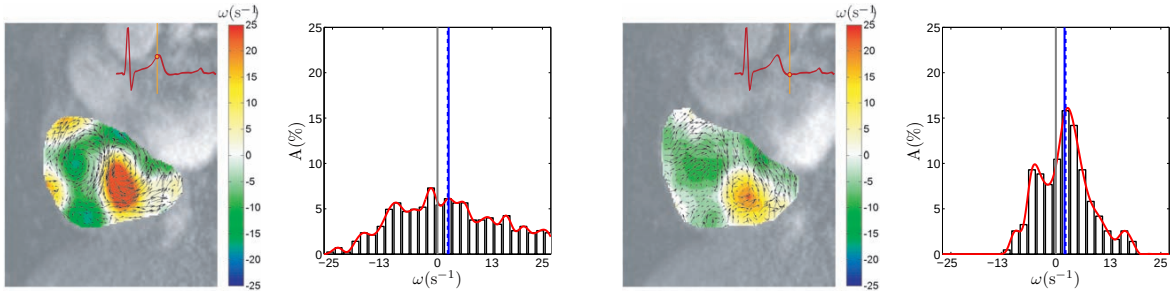

(ii) $n_t = 9$, $\begin{bmatrix}\overline{\omega}\\ \sigma\end{bmatrix}_\mu = \begin{bmatrix}2.17\\ 12.64\end{bmatrix}$ s^{-1}, $\Gamma = 19.19$ m^{2}s^{-1}

(vi) n_t=13, $\begin{bmatrix}\overline{\omega}\\ \sigma\end{bmatrix}_\mu = \begin{bmatrix}-0.65\\ 7.10\end{bmatrix}$ s^{-1}, $\Gamma = -3.82$ m^{2}s^{-1}

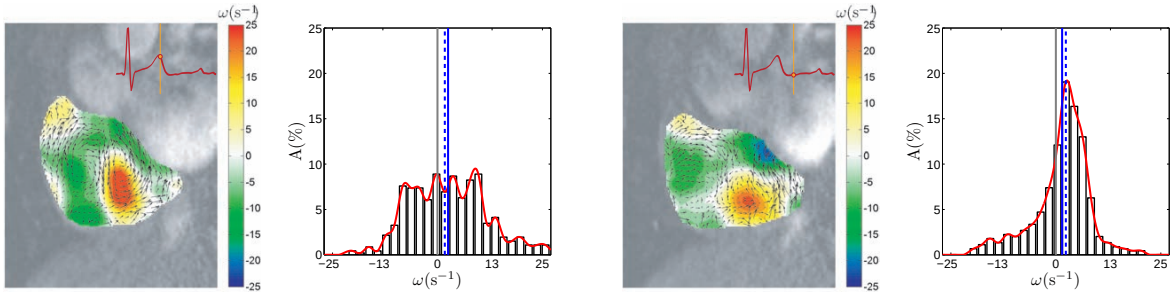

(iii) $n_t = 10$, $\begin{bmatrix}\overline{\omega}\\ \sigma\end{bmatrix}_\mu = \begin{bmatrix}0.25\\ 9.54\end{bmatrix}$ s^{-1}, $\Gamma = 1.58$ m^{2}s^{-1}

(vii) n_t=14, $\begin{bmatrix}\overline{\omega}\\ \sigma\end{bmatrix}_\mu = \begin{bmatrix}-0.40\\ 9.21\end{bmatrix}$ s^{-1}, $\Gamma = -2.44$ m^{2}s^{-1}

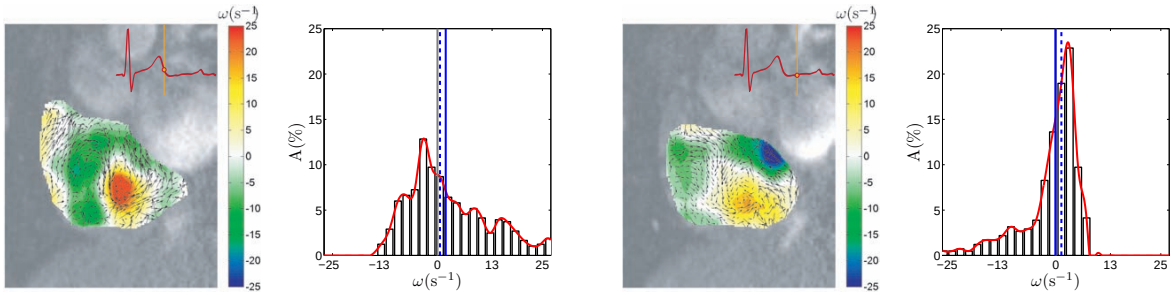

(iv) $n_t = 11$, $\begin{bmatrix}\overline{\omega}\\ \sigma\end{bmatrix}_\mu = \begin{bmatrix}0.10\\ 9.06\end{bmatrix}$ s^{-1}, $\Gamma = 0.66$ m^{2}s^{-1}

(viii) n_t=15, $\begin{bmatrix}\overline{\omega}\\ \sigma\end{bmatrix}_\mu = \begin{bmatrix}-0.54\\ 9.38\end{bmatrix}$ s^{-1}, $\Gamma = -3.06$ m^{2}s^{-1}

Figure 7.13. Global analysis for normal right atrium flow. Flow in the right atrium of a normal subject for time frames $n_t = 8$ to 15 out of a cardiac cycle of 25 time phases is displayed. The change in flow patterns can be analysed using statistical paramaters of mean $\overline{\omega}_\mu$, standard deviations σ_μ and circulation Γ.

COMPONENT 1 ANALYSIS

Cardiac time frame indices $n_t = 8$ to 11	**Cardiac time frame indices $n_t = 12$ to 15**
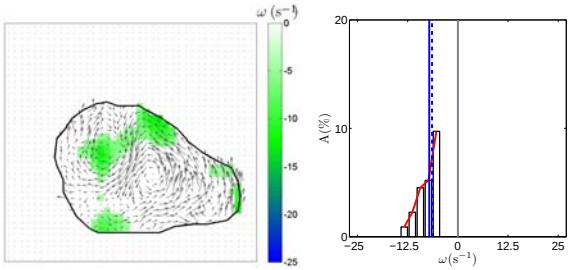	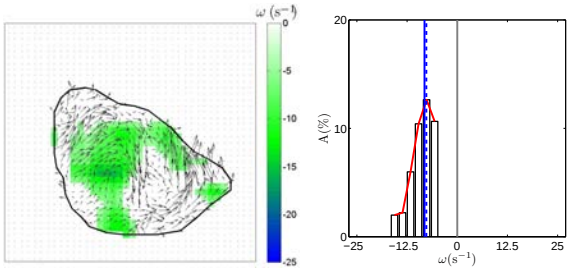
(i) $n_t = 8, \begin{bmatrix}\overline{\omega}\\ \sigma\end{bmatrix}_\mu = \begin{bmatrix}-7.13\\ 2.25\end{bmatrix}$ s^{-1}, $\Gamma = -9.84$ m^{2}s^{-1}	(v) $n_t = 12, \begin{bmatrix}\overline{\omega}\\ \sigma\end{bmatrix}_\mu = \begin{bmatrix}-8.16\\ 2.63\end{bmatrix}$ s^{-1}, $\Gamma = -21.97$ m^{2}s^{-1}
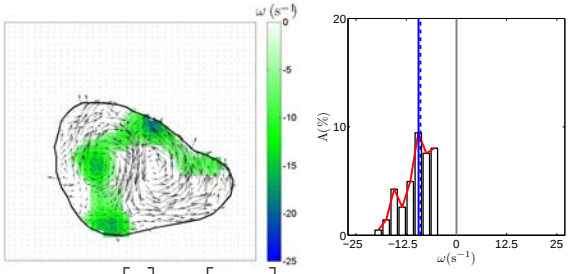	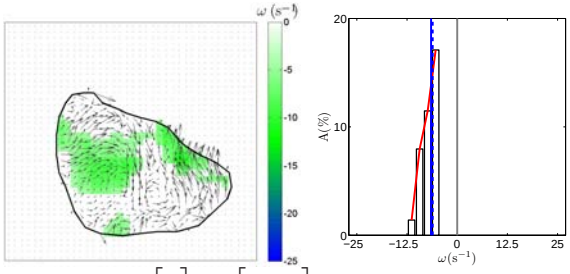
(ii) $n_t = 9, \begin{bmatrix}\overline{\omega}\\ \sigma\end{bmatrix}_\mu = \begin{bmatrix}-9.44\\ 3.49\end{bmatrix}$ s^{-1}, $\Gamma = -21.25$ m^{2}s^{-1}	(vi) $n_t = 13, \begin{bmatrix}\overline{\omega}\\ \sigma\end{bmatrix}_\mu = \begin{bmatrix}-6.50\\ 1.66\end{bmatrix}$ s^{-1}, $\Gamma = -14.56$ m^{2}s^{-1}
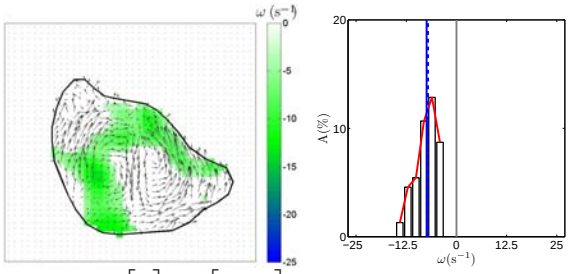	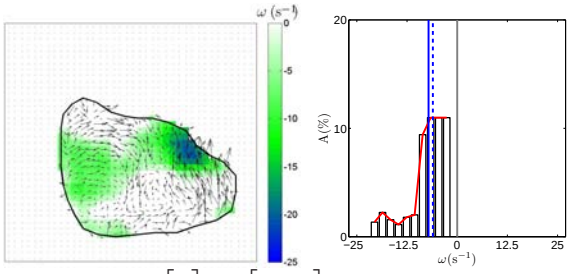
(iii) $n_t = 10, \begin{bmatrix}\overline{\omega}\\ \sigma\end{bmatrix}_\mu = \begin{bmatrix}-7.44\\ 2.44\end{bmatrix}$ s^{-1}, $\Gamma = -20.45$ m^{2}s^{-1}	(vii) $n_t = 14, \begin{bmatrix}\overline{\omega}\\ \sigma\end{bmatrix}_\mu = \begin{bmatrix}-7.14\\ 4.44\end{bmatrix}$ s^{-1}, $\Gamma = -22.84$ m^{2}s^{-1}
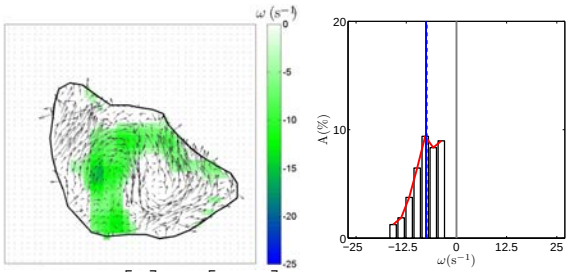	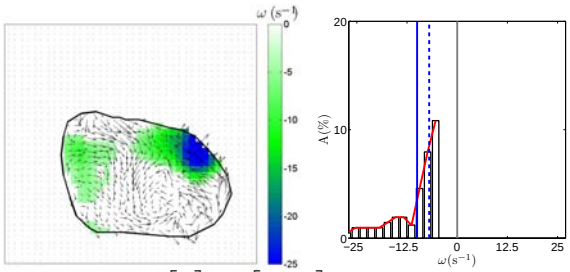
(iv) $n_t = 11, \begin{bmatrix}\overline{\omega}\\ \sigma\end{bmatrix}_\mu = \begin{bmatrix}-7.59\\ 2.90\end{bmatrix}$ s^{-1}, $\Gamma = -20.00$ m^{2}s^{-1}	(viii) $n_t = 15, \begin{bmatrix}\overline{\omega}\\ \sigma\end{bmatrix}_\mu = \begin{bmatrix}-9.98\\ 6.83\end{bmatrix}$ s^{-1}, $\Gamma = -20.13$ m^{2}s^{-1}

(a) Component analysis for clockwise vortex

Component 3 analysis for counter-clockwise vortex continues on the next page

COMPONENT 3 ANALYSIS

Cardiac time frame indices $n_t = 8$ to 11	**Cardiac time frame indices $n_t = 12$ to 15**
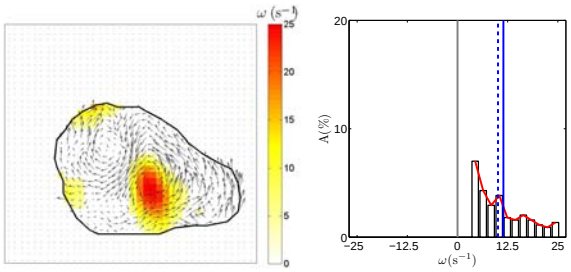	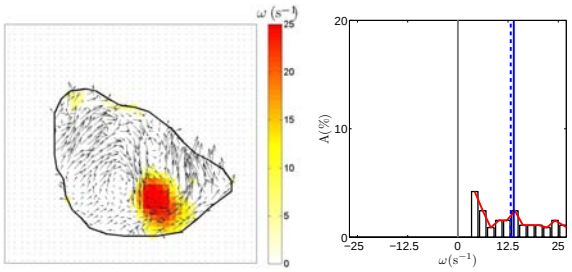
(i) $n_t = 8$, $\begin{bmatrix}\overline{\omega}\\ \sigma\end{bmatrix}_\mu = \begin{bmatrix}11.44\\ 5.84\end{bmatrix}$ s^{-1}, $\Gamma = 19.90$ m^{2}s^{-1}	(v) $n_t = 12$, $\begin{bmatrix}\overline{\omega}\\ \sigma\end{bmatrix}_\mu = \begin{bmatrix}13.92\\ 7.43\end{bmatrix}$ s^{-1}, $\Gamma = 17.60$ m^{2}s^{-1}
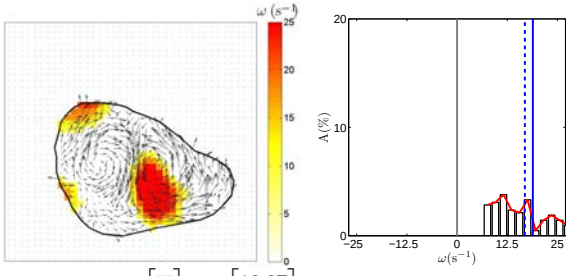	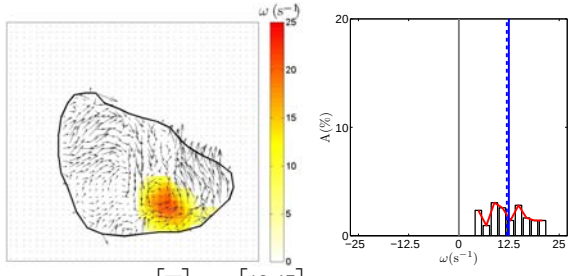
(ii) $n_t = 9$, $\begin{bmatrix}\overline{\omega}\\ \sigma\end{bmatrix}_\mu = \begin{bmatrix}18.87\\ 8.53\end{bmatrix}$ s^{-1}, $\Gamma = 30.81$ m^{2}s^{-1}	(vi) $n_t = 13$, $\begin{bmatrix}\overline{\omega}\\ \sigma\end{bmatrix}_\mu = \begin{bmatrix}12.45\\ 4.49\end{bmatrix}$ s^{-1}, $\Gamma = 12.91$ m^{2}s^{-1}
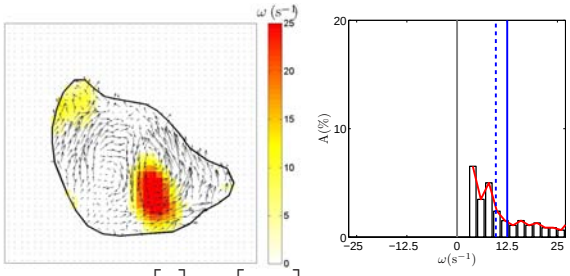	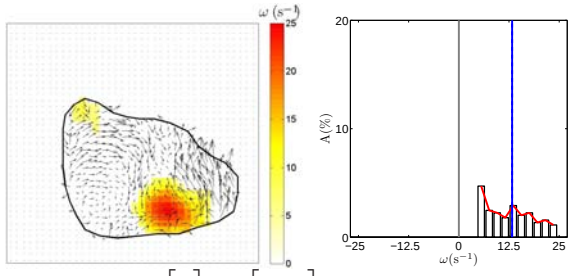
(iii) $n_t = 10$, $\begin{bmatrix}\overline{\omega}\\ \sigma\end{bmatrix}_\mu = \begin{bmatrix}12.50\\ 7.83\end{bmatrix}$ s^{-1}, $\Gamma = 22.86$ m^{2}s^{-1}	(vii) $n_t = 14$, $\begin{bmatrix}\overline{\omega}\\ \sigma\end{bmatrix}_\mu = \begin{bmatrix}13.28\\ 5.43\end{bmatrix}$ s^{-1}, $\Gamma = 18.14$ m^{2}s^{-1}
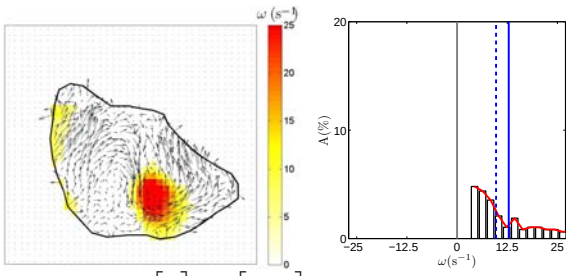	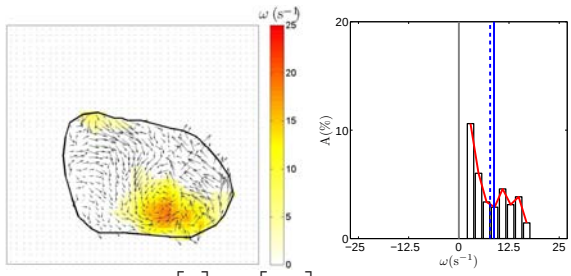
(iv) $n_t = 11$, $\begin{bmatrix}\overline{\omega}\\ \sigma\end{bmatrix}_\mu = \begin{bmatrix}12.87\\ 7.50\end{bmatrix}$ s^{-1}, $\Gamma = 20.68$ m^{2}s^{-1}	(viii) $n_t = 15$, $\begin{bmatrix}\overline{\omega}\\ \sigma\end{bmatrix}_\mu = \begin{bmatrix}8.77\\ 4.67\end{bmatrix}$ s^{-1}, $\Gamma = 17.92$ m^{2}s^{-1}

(b) Component analysis for counter-clockwise vortex

Figure 7.14. Component analysis for normal right atrium flow. Flow in the right atrium of a normal subject is presented based on clockwise (CW) and counter-clockwise (CCW) vortices for analysis of vortex component 1 and 3 respectively. Time frame indices $n_t = 8$ to 15 out of one cardiac cycle of 25 time phases are selected for illustration. The statistical properties are based on the segmented and coloured flow region.

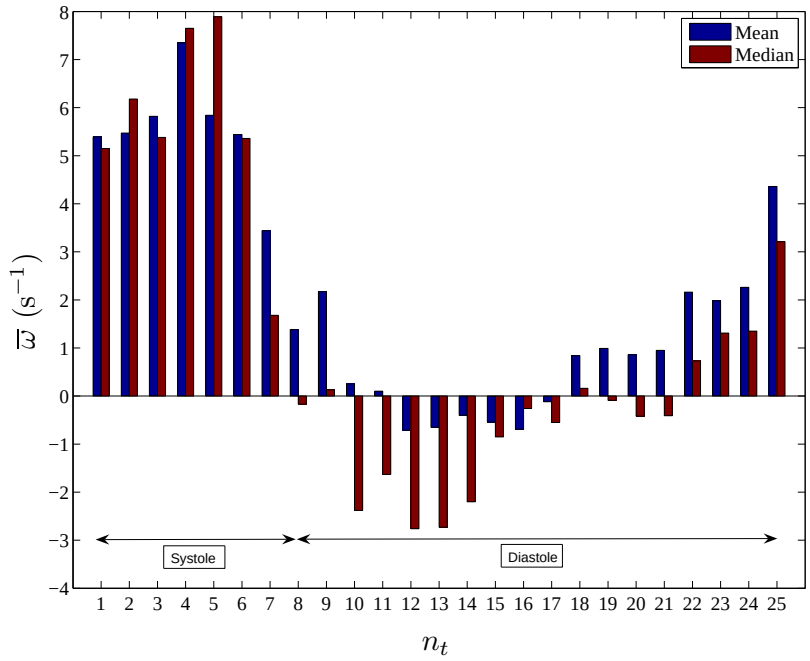

(a) Vorticity mean

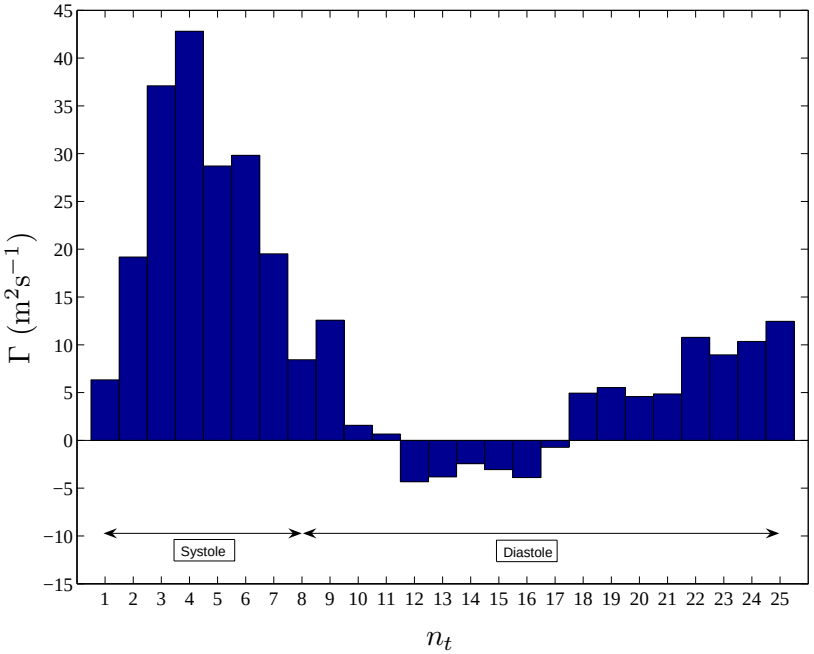

(b) Circulation

Figure 7.15. Variation of global vorticity mean and circulation. The variation of (a) vorticity mean $\overline{\omega}$ and (b) circulation for a cardiac cycle of 25 time frames shows that both positive and negative average map values can exist as the result of having two vortices in the flow. The sign of the average map value can indicate the dominance of positive vorticities over the other negative ones.

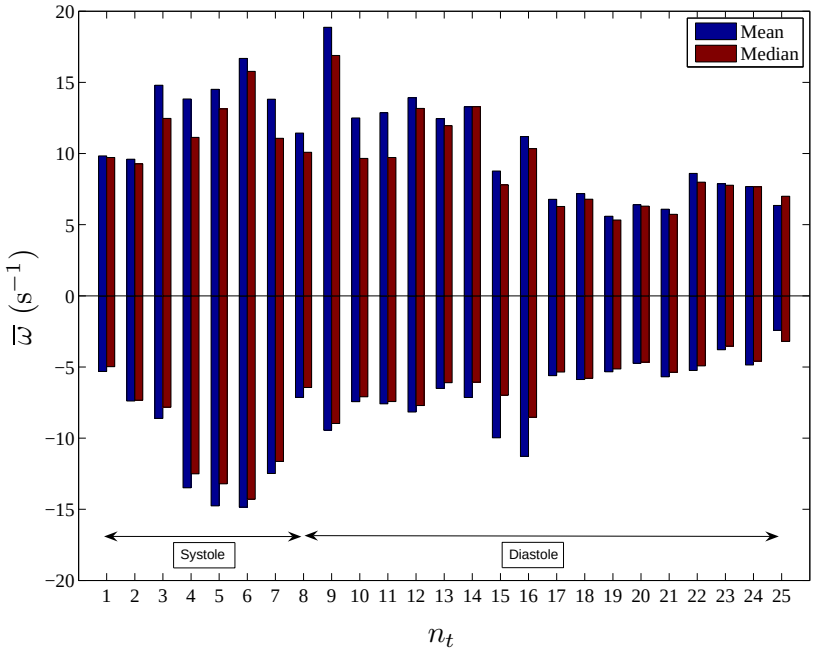

(a) Vorticity mean

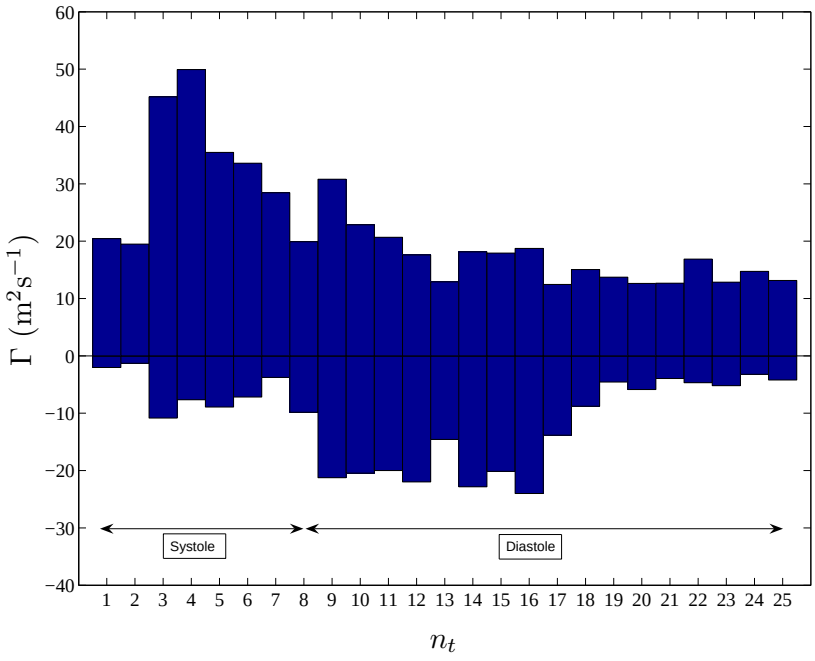

(b) Circulation

Figure 7.16. Variation of vorticity mean and circulation of vortex components. The variation of (a) vorticity mean $\overline{\omega}$ and (b) circulation for clockwise and counter-clockwise vorticities are presented by their values at the negative and positive domains of the bar chart respectively. Note the relatively smaller difference between mean and median values in contrast to those presented in the variation of the statistical properties that pertain to global vorticity.

7.6 Validating Intra-cardiac Flow Tracking Using Velocity-encoded Imaging

Velocity-encoded phase contrast MRI to validate magnetic resonance fluid motion tracking. This velocimetry system relies on motion estimation of blood signal shifts that appears as changes in intensity distribution over the entire registered signal image.

The speed of processing flow is dependent on the computational platform and the machine that runs it. A strong limitation, however, is the accuracy of the motion predication that is highly affected by the configuration of the algorithm as well as the clarity of signal contrast temporally. It is the key purpose of this study to validate the output flow fields of MR fluid motion tracking against those produced by phase contrast magnetic resonance images.

It is necessary to establish a form of measure for reliability of a system to accurately develop vorticity maps of flow field imaged by other flow-imaging techniques such as MR fluid motion tracking. To achieve this, we implement a dual flow imaging and comparison system that enables processing of phase contrast data as well as MR fluid motion tracking of non-velocity encoded MR images (with system features outlined in Appendix A). Since velocity flow field is limited in terms of comparison of two flow images, vorticity measurement has been devised to facilitate the quantification of difference based on different fields. In addition, we describe a concise flow visualisation system that encompasses flow imaging, flow vector presentation, and vorticity mapping, to analysis of vorticity pertaining to the imaged fluid.

7.6.1 Imaging and Flow Visualisation Parameters

One slice of the heart is selected as shown in Figure 7.3 and selected for modality comparison analysis here. Some samples of the magnetic resonance images are presented in Figure 7.17. The full set of images in cine-mode can be viewed using Supplementary Video 1 (in CD-ROM, listed in Appendix F). The same set of phase contrast MR images for the x- and y- directions that is based on the previous study (Supplementary Videos 5 and 6) is used here.

The MR imaging parameters for SSFP and phase contrast velocity encoding protocols, as well as motion tracking algorithm configuration are chosen for the flow field generation within the right atrium. Table 7.2 shows the configuration of tracking. The

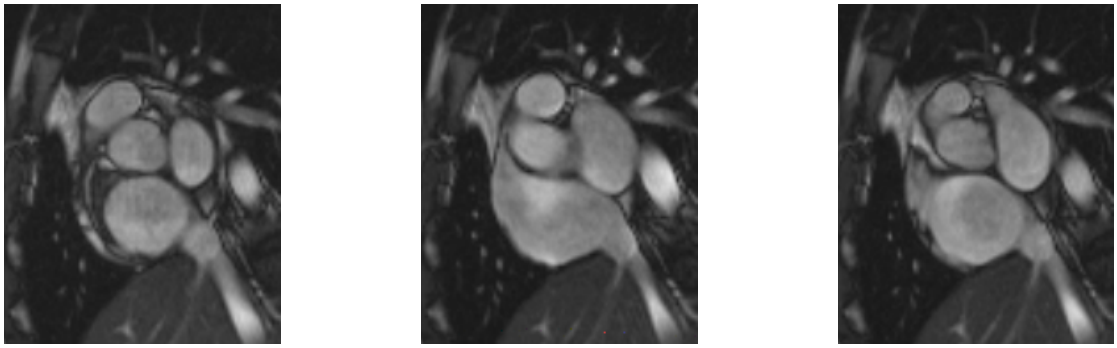

(a) Time frame index 1 of 25 (b) Time frame index 7 of 25 (c) Time frame index 21 of 25

Figure 7.17. Magnetic resonance images of normal right atrium. Magnetic resonance imaging is carried out to generate cine-images with 25 time frames in a cardiac cycle. Sample images at time frame indices $n_t = 1$, 7 and 21 are presented. Note the relative size of the right atrium with respect to the left one.

in-plane and through-plane resolution of the scans are determined by the pixel spacing (at 1.67 mm/pixel for SSFP and 1.54 mm/pixel for phase contrast MRI protocols) and slice interval of 6 mm (for both protocols) respectively. It is important that the flow data by both protocols is correctly calibrated using the relevant information from Digital Imaging and Communications in Medicine (DICOM) images.

7.6.2 Implementation of Vorticity Field Differencing

Using Figure 7.18, we demonstrate the systematic implementation of vorticity field differencing based on four stages. The first stage starts with scanning of a normal heart with steady-state free precession MR imaging and on a separate occasion, the same scanning using phase contrast MR imaging. During this pre-processing stage, blood motion information is encoded within images in a different manner. The cardiac MR images contain temporal positions of magnetic resonating blood, whereas the phase contrast images have local blood velocities encoded within them. The flow fields are reconstructed using the two different sets of information retrieved. MR fluid motion estimation is used to post-process the cardiac MR images to give a predicted flow field grid whereas phase contrast MR velocimetry system reconstructs the velocity-encoded images to produce measured flow field grid. In the visualisation processing stage, both field grids are further processed to give their respective vorticity fields, which are then differenced. Statistical quantification such as histograms of the field is processed and useful data can be retrieved to perform a reliability test of MR fluid motion tracking.

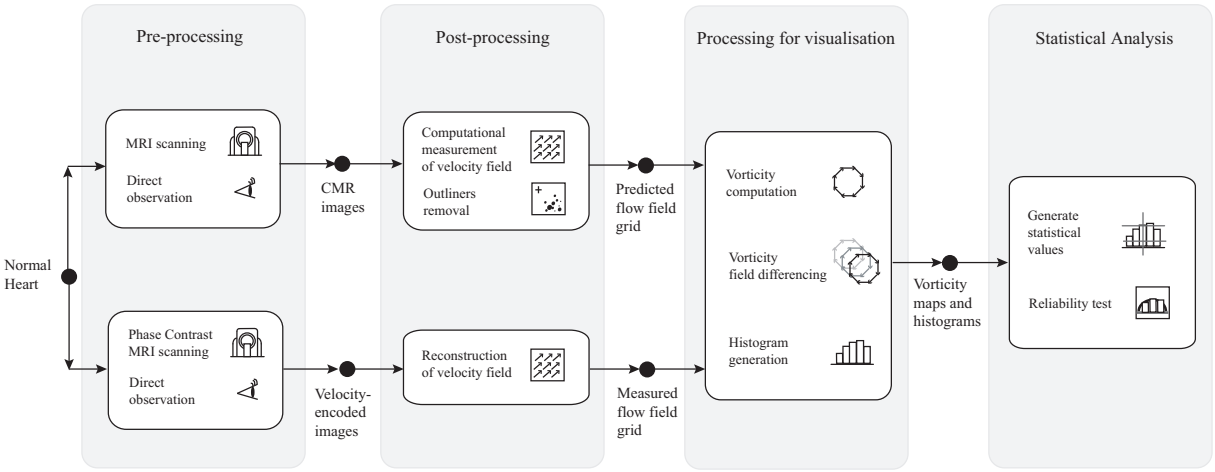

Figure 7.18. Validation system for imaging modality based on vorticity differencing. This system is specially constructed to calibrate the performance of a test imaging modality such as MR fluid motion tracking against the well-established phase contrast MR image velocimetry system. The measurement of vorticity field based on predicted and measured flow field grids can be utilised for differencing, which can then be used to provide an indication of how close the tracking is for fluid motion estimation as compared to phase contrast MR imaging.

SSFP MRI SCAN			
Symbol	Quantity	Value	Units
p_s	Pixel spacing	1.67	mm/pixel
t_s	Trigger time interval	35.72	ms
S	Slice thickness	6	mm
M_X	Matrix width	134	pixel
M_Y	Matrix height	256	pixel
X	Image width	120	pixel
Y	Image height	150	pixel

PHASE CONTRAST MRI SCAN			
Symbol	Quantity	Value	Units
p_s	Pixel spacing	1.54	mm/pixel
t_s	Trigger time interval	29.43	ms
S	Slice thickness	6	mm
M_X	Matrix width	134	pixel
M_Y	Matrix height	256	pixel
X	Image width	120	pixel
Y	Image height	150	pixel

MOTION TRACKING PARAMETERS			
Symbol	Quantity	Value	Units
W	Optical flow sampling window	4×4	pixel
L	Number of pyramid levels	5	
W_v	Velocity interrogation window	3×3	pixel

p_s	Size of a pixel in metric unit
t_s	Duration of each time frame
S	Distance of slice interval
X	Width of matrix scan
Y	Height of matrix scan
X	Width of image display
Y	Height of image display
W	Size of sampling window used in tracking
L	Number of pyramid level used in tracking
W_v	Resolution of velocity grid

Table 7.2. Configuration of phase contrast MRI and MR fluid motion tracking. The scan properties of standard SSFP and phase contrast MR imaging are presented here. MR fluid motion tracking as well as phase contrast MRI velocimetry are used to produce velocity flow fields. The vorticity flow maps can be determined from velocity information. These parameter values are used to calibrate flow maps, as well as indicating the sampling vorticity mask size in metric units.

7.6.3 Experimental Parameters for Flow Comparison

We utilise the framework described in the previous section to calculate the vorticity in the right atrial blood flow of a normal human subject using two different techniques of flow imaging. Measured flow fields using phase contrast MRI and predicted ones calculated by the fluid motion estimating algorithm using cardiac MRI are compared to assess the difference when a configuration such as the sampling window size for tracking is altered. We vary this parameter from (3×3) to (33×33) pixels with increments of (2×2) pixels at each interval to chart the reliability of flow measurement using MR fluid motion tracking versus phase contrast MR imaging technique. From Table 7.2, the average pixel size is 1.60 mm, and we set the interrogation window to a 3 by 3 pixels frame. Therefore, we are varying vorticity sampling window sizes of range (14.4×14.4) mm^2 to (158.4×158.4) mm^2 within a rectangular encapsulation of the atrium with dimensions 192 mm by 240 mm. We observe vorticity flow maps pertaining to time frame indices $n_t = [17, 18, 19, 20]$ out of a maximum of 25 frames in a cardiac cycle for a series of sampling window sizes in Figure 7.19. In Appendix C, more vorticity contour maps based on sampling window size from (3×3) to (27×27) pixels and time frame indices $n_t = 17$ to 19 is provided[18].

7.6.4 Comparison of Flow-Imaging Results

The reliability of a flow field prediction can be defined as the ratio of the true variance to the total measured variance of vorticity maps (Bohrnstedt 1983). In this respect, based on an arbitrary time frame of the cardiac cycle, a vorticity map from the flow field by phase contrast MRI velocimetry is assumed as the true data. The map produced from flow field developed by MR fluid motion tracking (hereby termed the predicted map) has inherent noise and is a combination of the true and error data.

In this study using a normal atrium, with regard to Equation 6.8, we assume that the true-score variance σ^2_{True} is the equivalent of the vorticity variance based on a true map measured by phase contrast MRI. We note that the error variance with the expression σ^2_{Error} is the variance of an error map that is produced by differencing the predicted and

[18]For results that appear in Appendix C, no ECG trace is present in flow maps to indicate the time of image acquisition. This is because the purpose of the study is on the affect of different vorticity sampling windows on flow visualisation, and not on cardiac flow analysis where the indication of time is important.

PREDICTED FLOW	MEASURED FLOW	VORTICITY DIFFERENCE
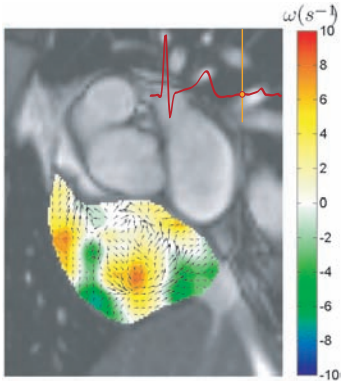	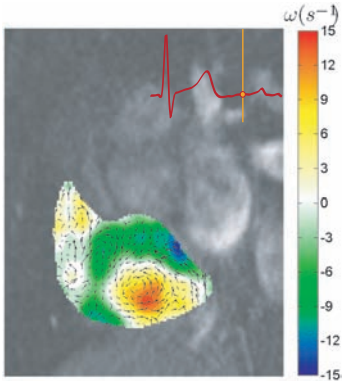	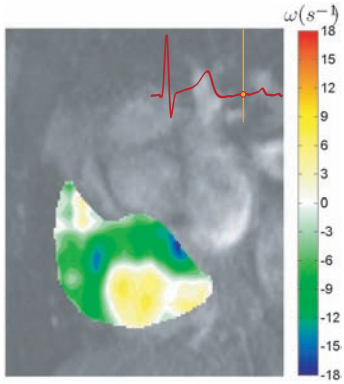
$\begin{bmatrix}\overline{\omega}\\ \sigma\end{bmatrix}_{\mu} = \begin{bmatrix}1.32\\ 3.34\end{bmatrix} s^{-1}, \begin{bmatrix}\overline{\omega}\\ \sigma\end{bmatrix}_{m} = \begin{bmatrix}1.43\\ 3.34\end{bmatrix} s^{-1}$	$\begin{bmatrix}\overline{\omega}\\ \sigma\end{bmatrix}_{\mu} = \begin{bmatrix}-0.24\\ 6.19\end{bmatrix} s^{-1}, \begin{bmatrix}\overline{\omega}\\ \sigma\end{bmatrix}_{m} = \begin{bmatrix}6.19\\ 6.19\end{bmatrix} s^{-1}$	$\begin{bmatrix}\overline{\omega}\\ \sigma\end{bmatrix}_{\mu} = \begin{bmatrix}-2.45\\ 5.79\end{bmatrix} s^{-1}, \begin{bmatrix}\overline{\omega}\\ \sigma\end{bmatrix}_{m} = \begin{bmatrix}-2.87\\ 5.81\end{bmatrix} s^{-1}$
$(a) \quad n_t = 17$		
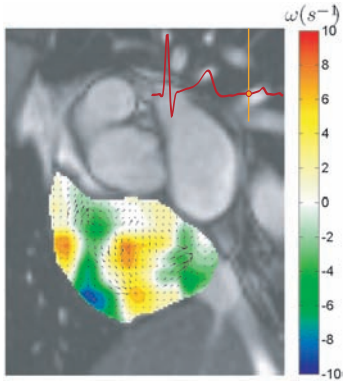	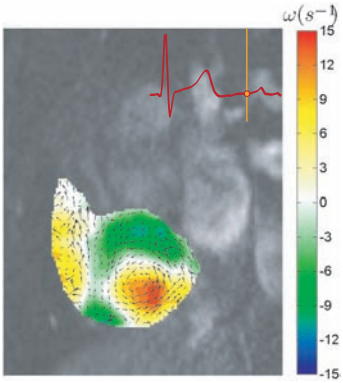	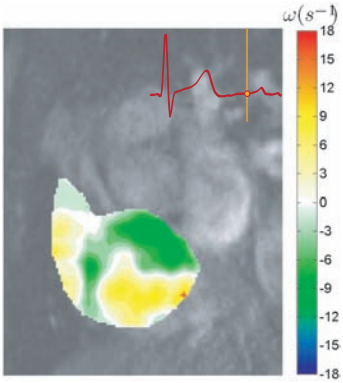
$\begin{bmatrix}\overline{\omega}\\ \sigma\end{bmatrix}_{\mu} = \begin{bmatrix}0.49\\ 3.65\end{bmatrix} s^{-1}, \begin{bmatrix}\overline{\omega}\\ \sigma\end{bmatrix}_{m} = \begin{bmatrix}0.39\\ 3.65\end{bmatrix} s^{-1}$	$\begin{bmatrix}\overline{\omega}\\ \sigma\end{bmatrix}_{\mu} = \begin{bmatrix}1.40\\ 6.27\end{bmatrix} s^{-1}, \begin{bmatrix}\overline{\omega}\\ \sigma\end{bmatrix}_{m} = \begin{bmatrix}1.06\\ 6.28\end{bmatrix} s^{-1}$	$\begin{bmatrix}\overline{\omega}\\ \sigma\end{bmatrix}_{\mu} = \begin{bmatrix}0.25\\ 5.38\end{bmatrix} s^{-1}, \begin{bmatrix}\overline{\omega}\\ \sigma\end{bmatrix}_{m} = \begin{bmatrix}0.09\\ 5.39\end{bmatrix} s^{-1}$
$(b) \quad n_t = 18$		
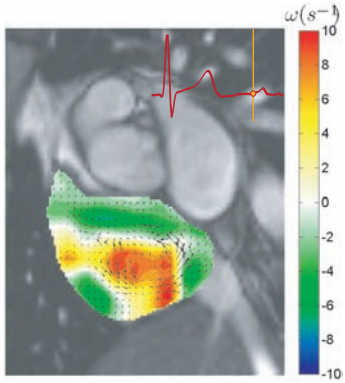	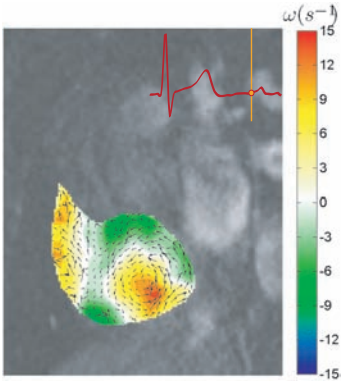	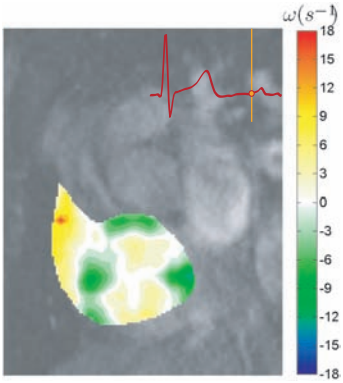
$\begin{bmatrix}\overline{\omega}\\ \sigma\end{bmatrix}_{\mu} = \begin{bmatrix}0.98\\ 4.52\end{bmatrix} s^{-1}, \begin{bmatrix}\overline{\omega}\\ \sigma\end{bmatrix}_{m} = \begin{bmatrix}-0.74\\ 4.84\end{bmatrix} s^{-1}$	$\begin{bmatrix}\overline{\omega}\\ \sigma\end{bmatrix}_{\mu} = \begin{bmatrix}2.24\\ 5.66\end{bmatrix} s^{-1}, \begin{bmatrix}\overline{\omega}\\ \sigma\end{bmatrix}_{m} = \begin{bmatrix}1.52\\ 5.70\end{bmatrix} s^{-1}$	$\begin{bmatrix}\overline{\omega}\\ \sigma\end{bmatrix}_{\mu} = \begin{bmatrix}1.01\\ 4.60\end{bmatrix} s^{-1}, \begin{bmatrix}\overline{\omega}\\ \sigma\end{bmatrix}_{m} = \begin{bmatrix}1.32\\ 4.61\end{bmatrix} s^{-1}$
$(c) \quad n_t = 19$		

Flow fields for time frame $n_t = 20$ continues on the next page

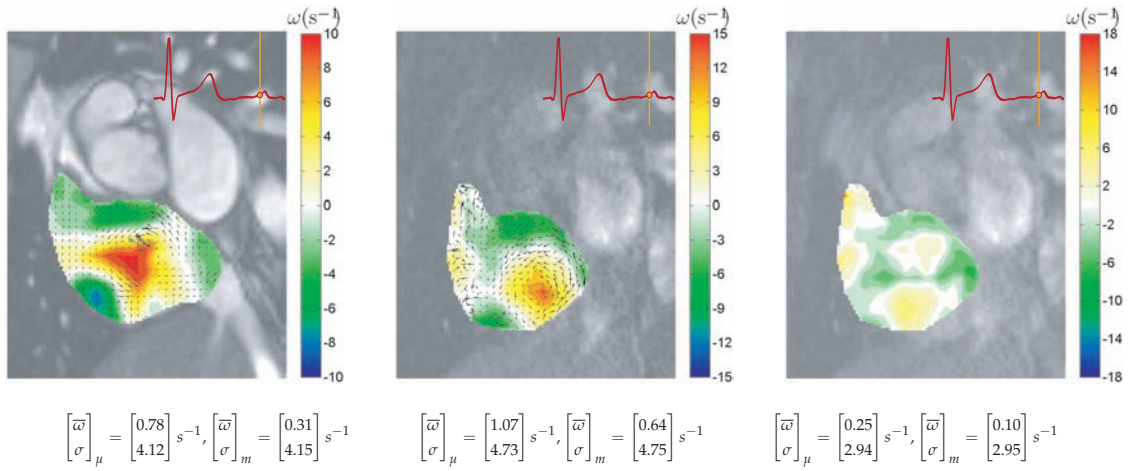

Figure 7.19. Vorticity differencing based on MR fluid motion field and phase contrast MR image field. Predicted flow fields by MR fluid motion tracking are verified against measured ones based on phase contrast magnetic resonance image velocimetry. The former technique post-processes temporal MR signals, while the latter velocimetry system measures the signal during scan and encodes the velocity information in images. The set of results presented here illustrates the difference between predicted and measured blood flow fields in the human right atrium. Phase contrast data is taken as ground truth here. Therefore their vorticity map differences can be taken as the deviation of MR fluid motion field from the true flow field. We have performed flow field differencing using time frame indices $n_t = [17, 18, 19, 20]$ out of 25 frames in a cardiac cycle. Vorticity measurement is based on sampling window size of (19×19) pixels.

true vorticity maps. The components of this error can come from existence of other smaller vortices along with the dominant single vortex in the right atrium that escape detection by the fluid motion estimation due to inferior quality of tracking features. The reliability of flow field prediction using MR fluid motion tracking defined as ρ is the ratio of true vorticity variance σ^2_{True} to total measured variance given by $\sigma^2_{\text{True}} + \sigma^2_{\text{Error}}$. Ideally, if the system can generate flow fields that correspond close enough to those that are measured by an imaging modality such as phase contrast MRI, the error tends to approximate zero and reliability becomes one.

Implementing an appropriate sampling window size for vorticity measurement can bring the vorticity maps to be as close as possible to the physically measured one. Generating the variation of its reliability with respect to the sampling window size can give us an indication of the ideal sampling window size value.

The use of the reliabilty equation involving σ^2_{True} and σ^2_{Error} is an indicator for the accuracy of measurement based on MR fluid motion flow field, which varies as the vorticity sampling window size increases. The graph of reliability measurement is shown in Figure 7.20 for sampling window dimensions of (3×3) to (33×33) pixels. The results are based on four cardiac time frame indices from $n_t = 17$ to 20 to illustrate variation of measurement reliability. For right atrial vorticity flow computation and examination based on the optimal reliability, we suggest an appropriate sampling window size to be from (17×17) to (21×21) pixels. This corresponds to a metric width range of 81.6 mm to 100.8 mm in dimension, or a sampling window ratio (which is sampling window dimension with respect to image height) from range of 0.544 to 0.672 mm. Such sampling window size ranges can be a guide to the configuration of the vorticity calculation applied to flow maps for every cardiac phase, which is dependent on the size of the heart chamber. Although we use only four sets of flow maps, such partial analysis of the entire cardiac flow set will not affect the determination of the vorticity configuration significantly.

Considering that the SSFP and phase contrast magnetic resonance imaging are performed on two separate occasions with slight dissimilarities in planar imaging configuration, perfect alignment of the right atria regions is difficult. Therefore, a near zero error map of the vorticity maps resulting from the flow images of MR fluid motion tracking and velocity-encoded MRI is hard to achieve. Based on this discrepancy, we have to take into account additional error contributed by the imperfect comparison scheme. This justifies that the large error margin exhibited by MR fluid motion tracking and the qualitative observation of the velocity flow field as well as vorticity differencing results can suggest that the reliability of MR fluid motion tracking is good enough for cardiac flow assessment.

Motion prediction based on MRI generates a flow field of the blood pool that can have limitations in terms of accuracy if the signals emitted by the blood vary poorly in contrast spatially. Therefore, the motion estimation algorithm needs to be robust and reliable enough to enable good prediction of the blood motion globally. The velocity-flow data also needs to be processed a second time to provide differential flow measures such as vorticity. It may be worthwhile to highlight that phase contrast MRI can produce much more accurate flow information, however; scanning time is significantly higher than standard MRI. Although the tracking system trades off accuracy

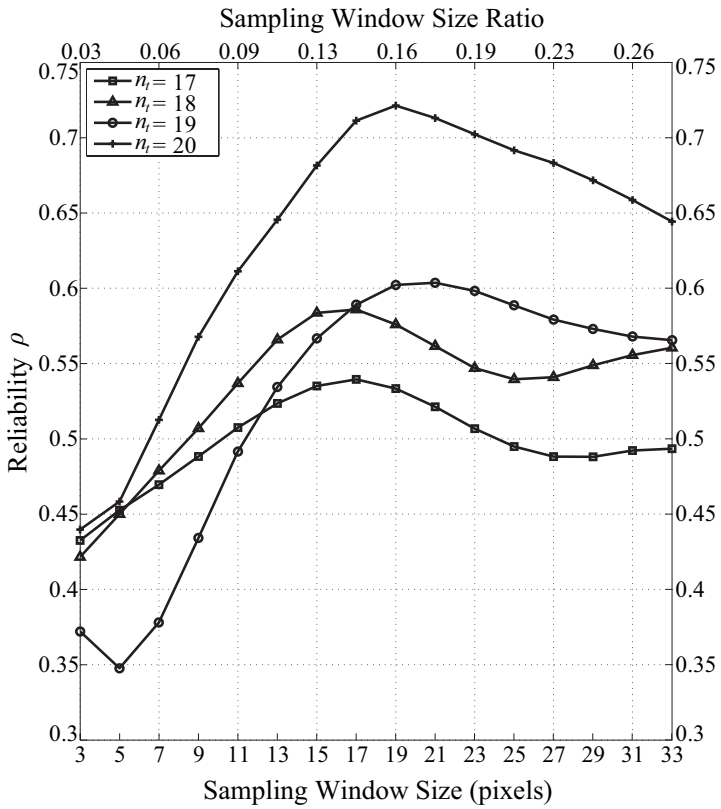

Figure 7.20. Reliability of computed flow field. Reliability of the predicted MR fluid motion field data ρ with respect to the phase contrast MRI data (taken as the true data) is computed. This graph is generated based on values σ_μ and σ_m that are standard deviations with respect to mean and median of flow maps respectively. The variations of standard deviations for both sets of reliability curves are similar. The vorticity sampling window size can affect the reliability of computational measurement of the vorticity. As the sampling window dimension increases, the reliability of the vorticity mapping improves. However, there is a specific threshold such that over-sizing using larger sampling window parameter has a negative effect on vorticity measurement.

with processing time, it can deliver a good prediction of flow structures within the heart.

We also note the low resolution of the (120×150) pixel image representing a (184.8×231.0) mm^2 window view that are used here in this experiment. If higher signal-to-noise ratio imaging with superior resolution is implemented, the tracking of the magnetic resonating fluid will generate flow fields that approximate more closely to the truth. In any case, the aim is to identify the location and strength of vortices can be achieved by MR fluid motion tracking. Although the flow plot may differ in terms

of localised vector-to-vector comparison, the general fluid paths are similar and the large-scale vortices can still be observed using appropriate vorticity mapping.

7.6.5 Discussion of System Performance

The full advantage of a flow imaging and visualisation system lies in its integrated components, with focus on the data that each of them can generate, how the components are networked and the overall benefit that it can bring to clinical evaluation. Therefore, a successful application needs to be able to distinguish cardiac pathology from a normal heart part, such as pertaining to pre- and post-surgical intervention of cardiac structures, or to provide comparison of results from two different flow imaging modalities. It should also be able to provide a quantifiable indication of the difference. We develop a system that is able to achieve these aims.

The disadvantages of the system are that velocity-encoding scans take a considerably longer duration than other MR imaging protocols such as the steady-state free precession (SSFP) (Plein *et al.* 2001, Li *et al.* 2004). Dual sets of flow-component images are required to produce a two-dimensional flow field, and so at least twice the scanning time is required as compared to imaging the anatomical structures using the SSFP protocol. Availability of the protocol as well as a medical image processing tool for deciphering the velocity values encoded within the phase contrast images also dictates the use of this flow mapping and visualisation technology.

Note that the computational reconstruction of flow based on intensity-based medical images is not immune to false intensity flow detection due to the different sources of magnetic field distortions during magnetic resonance imaging. For example, lung tissue occludes the heart, which results in a distortion of the static magnetic field (Edelman 2004), can lead to detection of false blood signals. It is therefore crucial to use good quality images for computational reconstruction of the motion field in all our studies. In addition, image sizes have to be standardised when comparing flow before and after surgical intervention or when patient to patient comparisons are made.

The construction of a flow grid using more than one set of orthogonal planes can provide a better indication of three-dimensional vortex flow structures. Nevertheless, the use of planar flow map slices provides a sufficient representation of the volumetric flow. At the preliminary stage, we can present flow analysis in the two-dimensional

plane. The use of scans in one plane is sufficient to reveal flow behaviour for characterisation.

7.7 Chapter Summary

The use of velocity-encoded magnetic resonance imaging can reveal flow patterns within the human heart chambers, thereby opening up an understanding of the functional aspect of the heart. Extending this technique by the computation of vorticity maps can allow us to determine the characteristics of the vortices to an extent. The use of statistics and histograms of vorticity maps can aid in the analysis of the blood circulation at various time frames of a cardiac cycle.

The velocity fields are based on the phase contrast magnetic resonance images that the scanner provides. The flow can be calibrated and streamline traces of the field can provide a clear visualisation of blood movement with information such as the speed and direction. Vorticity is generated from the motion vector field to display the location and strength of vorticities in the flow. We illustrate the usefulness of these qualitative information displays in this chapter.

The study has shown that swirling flow is present in the right and left atria of the heart. However, such movements vary over time and are influenced by the movement of the myocardium[19]. Using scans of the right atrium in the short axis orientation, we determine the characteristics of the vortices within the chamber. Based on long axis scans, we also observe that blood is drawn into the heart chamber at different events of the cardiac cycle. Finally, from the four-chamber long axis view, we produce visualisation of left atrial vortex using streamline tracing and vorticity mapping. The evolution of the vortex can be analysed qualitatively and quantitatively.

The velocity-mapping framework that we develop can be applied to assess flow in various heart chambers and circulation in the veins and arteries. A benefit of our framework is the coupling of flow visualisation with quantifiable data that may give an indication of the vorticity changes in the cardiac flow. The flow quantification methods in this work is new, and further studies based on a larger population group and other portions of the heart or circulation can be performed in future to validate the cardiac flow analytical framework. The results may also be used to validate computational

[19]This is the heart's muscular wall. The internal and external linings of the wall are known as the endocardium and epicardium respectively.

fluid dynamics simulations (Zhao *et al.* 2003, Long *et al.* 2002, Glor *et al.* 2008), and techniques such as magnetic resonance fluid motion tracking (Wong *et al.* 2009e) can be verified in terms of accuracy based on velocity-encoded flow maps. In addition, we can try to develop three-dimensional streamline visualisation of the blood flow which can eliminate the use of multiple slices to cover the flow details adequately. Although we understand that complicated flow patterns may clutter the three dimensional flow visualisation and cause qualitative analysis to be difficult, it may be worthwhile performing flow modelling using interactive manipulation of the flow field display to gain a clearer insight of the flow.

Imaging the cardiac chamber using phase contrast magnetic resonance imaging can establish a set of results for validation of new flow imaging modalities. While preparing our investigation and scan sets, we select the right atrium as a case study so that we can use the same methodologies described in this chapter to measure large-scale vortices while analysing right atrial flow in the heart of a patient with atrial septal defect (Chapter 8).

Chapter 8

Study of Cardiac Flow in a Heart with Atrial Septal Defect

THIS chapter focuses on the integration of the complete software system and its application to cardiac flow velocity measurement. It gives evidence of the practical implementation on medical image outputs by the magnetic resonance imaging technique. It also highlights the scanning and management of cardiac patients, identification of the effect of atrial septal defect on blood flow, performance of cardiac tracking, system deliverables for analysis of blood flow behaviour, which all contribute to the success of non-invasive visualisation and quantification using MR imaging and post-processing of heart sectional scans.

Adjacent to this successful and practical application on standard magnetic resonance images is the landmark investigation and confirmation of the existence of vortical blood flow in the counter-clockwise direction within the right atrium of a human heart with qualitative and quantitative compilation of its characteristics. Apart from that, the study provides outlines for an investigation of flow behaviour for atrial septal defect (ASD) patients pre- and post-ASD occlusion and this establishes the route to development of a possible imaging and assessment scheme for surgical correction of heart defects.

8.1 Introduction

Most types of cardiac problems such as atrial septal defect (ASD) have an implication on blood flow. For example, turbulent flow in the heart and arteries may have an effect on thrombosis leading to risk of stroke. Currently, medical technology such as cardiac magnetic resonance imaging (CMRI), positron emission tomography (PET), single photon emission computed tomography (SPECT), X-ray computed tomography (CT), and ultrasound imaging modalities are utilised in the management of cardiac patients. In particular, cardiac magnetic resonance imaging provides a unique and non-invasive approach for imaging patients with abnormalities. For example, a study of vortices generated within the right atrium during the diastolic phase of the cardiac cycle can provide useful information on the change in the magnitude of vorticity pre- and post-ASD occlusion. Atrial septal defect (ASD) closure or occlusion is also termed *atrial septal occlusion* (ASO) in some literature (Calvert and Klein 2008). In this study, we apply the new MRI-based measurement system to the analysis of vortical blood flow within the human heart. We present using two case studies, two-dimensional visualisation of in-vivo right atrial flow. This is constructed using flow velocities measured from the pixel intensity shifts of asynchronous blood proton spin regions in MR images. In particular, the strength of the vorticities within the flow can be measured against different patients with cardiac abnormalities, to extend medical knowledge of ASD and their hemodynamic effects.

8.2 Overview of Atrial Septal Defect

Atrial septal defect, often abbreviated as ASD, is a congenital cardiac abnormality that affects the health and fitness of the individual. In this medical condition, a puncture in the septum exists to create a left-to-right shunt of atrial blood to maintain equalisation of pressure in the heart. Due to this flow phenomenon, oxygenated blood seeps through the left atrium to the right one instead of being effectively circulated to the rest of the body. As a result, the patient experiences a lower efficiency of oxygenated blood circulation. The schematic diagram in Figure 8.1 illustrates the inefficient replenishment of oxygenated blood and its reduced flow from the left atrium to left ventricle and ultimately through the aorta to the rest of the body.

Atrial septal occlusion is the surgical correction to this cardiac situation by delivery of the right atrial disc to the loction of the defect using catheterisation (Cross *et al.* 2001,

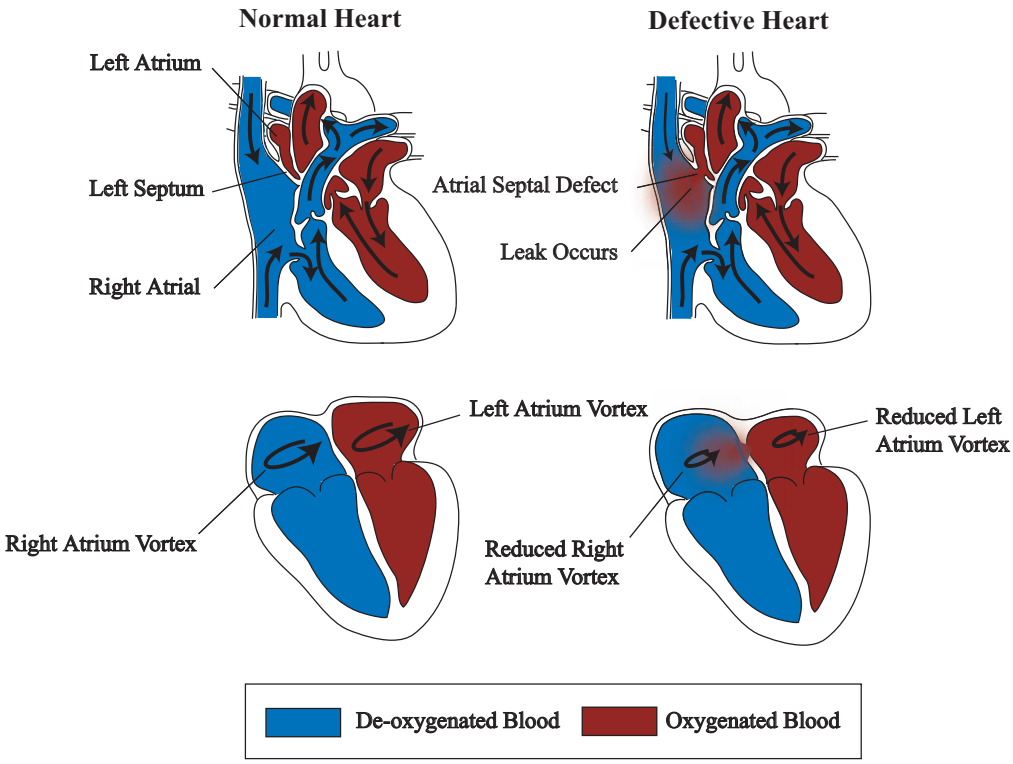

Figure 8.1. Circulation in a heart with atrial septal defect. Cardiac defect such as atrial septal defect can affect the efficiency of circulation of oxygenated blood through the human body. In this diagram, we examine the leak of oxygenated blood from the left atrium into the right. Therefore, a patient with the septal defect may not have the same health fitness standard in comparison with someone who has a normal healthy heart.

Kim *et al.* 2007, Balzer *et al.* 2008, Duncan *et al.* 2008) as demonstrated in Figure 8.2. It is proposed that an indication of difference in the pre- and post-surgical intervention exists. The natural flow of blood in a rotational fashion is disturbed in a cardiac chamber with a septal defect. One of the hypothesis for a less consistent blood flow rotation before the operation is the reduction in the velocity of blood circulating in a larger chamber as a result of left-to-right shunt that causes the right atrial dilation. The other reason is that the leak produces a jet of fluid through the defect to break up the normal flow in the right atrium. Once the septal occluder is inserted to close the defect, the left and right chambers are restored to their more normal sizes, and a more consistent right atrial blood rotation may be effected.

The use of steady-state free precession (SSFP) MRI has been effective in examination of myocardial defects (Duncan *et al.* 2008). In Figure 8.3, we observe the discontinuity in the septum that allows blood to shunt from the left atrium (LA) to the right atrium (RA). In a normal right atrium, the chamber blood is supposed to be flowing in

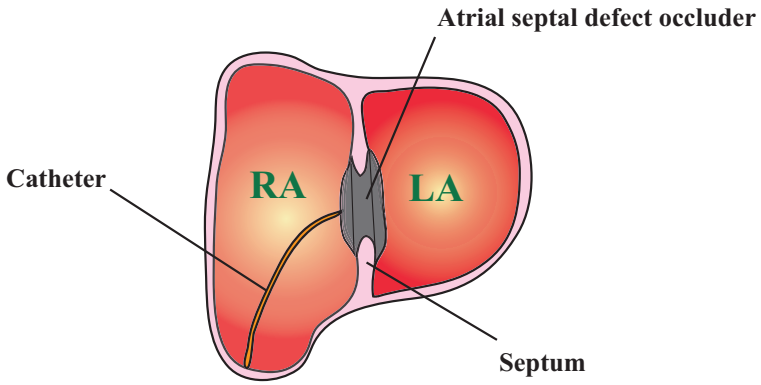

Figure 8.2. Schematic illustration of atrial septal occlusion. Surgical intervention such as atrial septal occlusion (ASO) can help to seal the leakage from left atrium (LA) to right atrium (RA). This schematic diagram, illustrates how the septal occluder is inserted via a catheter using minimally invasive surgical intervention. The occluder is a cicular mesh mechanism that is secured in a canister of the catheter, and upon reaching the site of defect, can be released to open up like an umbrella that locks itself onto the septum, and becoming part of it. The double folds of this mesh acts as a self centering device that stablise the position of occlusion and ensure an optimal ASD closure. Over time, the cardiac tissue grows into the occluder mesh and seals up the defect. This prosthetic device stays in the patient permanently.

a rotational manner. This vortical flow is disturbed by the shunting of blood to cause multiple small-scale vortices to appear. As a result, the efficiency in blood circulation is affected. In addition, we also note the difference in right atrial chamber size between the pre- and post-ASO conditions since the percutaneous closure of ASD can reduce the right heart volumes by removing the left-to-right shunting (Teo *et al.* 2008). We can make use of this knowledge to diagnose ASD patients, and to use MR images to examine the difference in blood flow patterns.

The investigation of vortical blood flow in cardiovascular structures and cardiac chambers sets a new direction for the exploration of hemodynamics within the human heart. In the literature there is limited discussion of the significance of vortices in relation to cardiac function, nevertheless we know that vortical flow behaviour is essential in efficient heart operation and blood circulation (Fyrenius *et al.* 2001, Pierrakos and Vlachos 2006). Flow information can be used to examine the amount of energy wasted by a heart with structural abnormalities such as ASD or valvular disease. The study of vortices in the human heart has been extensively performed using phase-contrast data (Yang *et al.* 1998). From previous studies, vortex formation and characteristics is

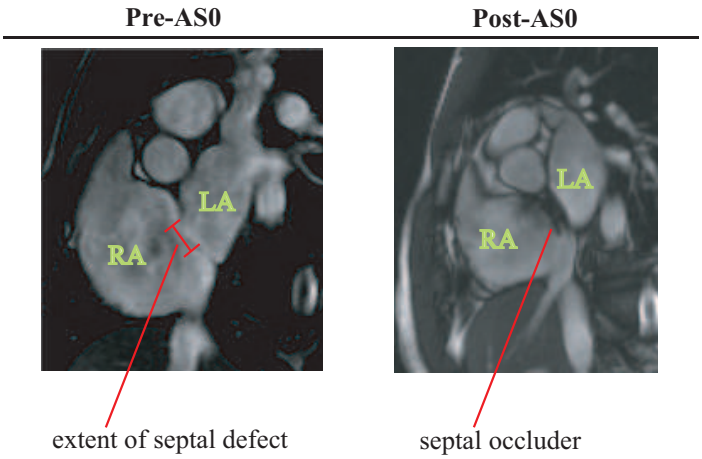

Figure 8.3. Myocardial discontinuity in a heart with atrial septal defect. The MRI imaging of a heart based on short axis orientation is able to demonstrate the physical discontinuity of the myocardium that separates the left atrium (LA) and right atrium (RA) within the heart of an ASD patient. Medical examination based on this method can determine the location, size and extent of the defect. This can effectively diagnose the medical condition and plan for surgical preparation.

related to the nature of heart chamber wall relaxation, as well as its cavity size and shape (Kerwin *et al.* 2004) since it is clear that the chamber wall interaction with the blood fluid within will influence the behaviour of both blood and cardiac chamber. It is hypothesed in this study that large-scale, well organised vortices are beneficial, and that an ASD condition causes this flow pattern to break down resulting in poor blood circulation within the heart.

Vorticity is a quantity that is closely related to the angular velocity of the fluid at a point, and it is evaluated from the fluid velocity gradients (Raffel *et al.* 1998). The measurement of a three-dimensional vortex structure is dependent on the angle of the measurement plane. When vortices are skewed with respect to the measurement plane, the results are affected by the skew angle (Brandt *et al.* 2001). However, presentation of resolved vector components of spiralling flows or skewed vortical flow in a three-dimensional space is visually complicated and will make the analysis of vorticity difficult. We see in this study that visual examination of vortices in cardiac MR images of the human chamber using two-dimensional slices of the scan is sufficient. We compare magnitude and occupancy of a single vortex on a specific slice and phase of the cardiac cycle for a patient who has been scanned pre- and post-septal occlusion.

Based on our preliminary investigations, we discover that most flow analyses carried out are based on the left instead of the right atrium (Brandt *et al.* 2001, Ebbers *et al.* 2002,

Fyrenius *et al.* 2001, Uterhinninghofen *et al.* 2006). Although the study of vortices in the right atrium may not be of great utility in terms of cardiac related clinical end-points, such as thrombosis and stroke risk, it is nevertheless important to have an understanding of how the vortex strength is diminished during atrial left-to-right shunting. This presents new knowledge on atrial flow for ASD patients.

8.3 Current Methods in Diagnosing Atrial Septal Defect

The use of medical imaging modalities can enable visualisation of the intrinsic structure of the heart and/or determine flow properties within the heart chambers and arteries. This section provides a review of imaging methods that can be used to diagnose cardiac abnormalities. The purpose of this section is to provide motivation for our system to be used as an alternative to these current existing modalities.

8.3.1 Echocardiogram

Ultrasound has been used widely in imaging cardiovascular flow in human for diagnosis. Doppler colour flow imaging is now a widely accepted technique to measure subtle fluctuations in arteries and veins. Ultrasound images of flow are based on the Doppler effect in which a series of pulses is transmitted to non-stationary blood to record echo signals from it. A colour flow image or sonogram can be produced by recording the Doppler frequency shift.

The echocardiogram is an ultrasound scan of the heart that may be used for assessing ASD patients (McMahon *et al.* 2002, Webb and Gatzoulis 2006, Linguraru *et al.* 2008). Using standard ultrasound scans, two-dimensional slices of the heart can be imaged and used for flow visualisation. In addition to creating scans of the cardiovascular system, the echocardiogram can also produce an assessment of the velocity of blood and cardiac tissue at any arbitrary point using pulsed or continuous wave Doppler ultrasound (Sprecher *et al.* 1987, Tamai *et al.* 1990, Walker *et al.* 2004). This allows assessment of abnormal communications between the left and right side of the heart, such as any shunting of blood through an ASD.

Ultrasound is sensitive to blood flow, which makes it potentially applicable to flow visualisation. However, this technique is mostly used only as a qualitative technique and is liable to error depending on the plane of imaging. Contrast agents, such as a

suspension of microscopic gas bubbles, are used to enhance ultrasound performance. Ultrasound is, however, an inexpensive alternative to MRI, PET and CT methods, and therefore more commonly used to diagnose ASD.

Ultrasound techniques avoid the use of harmful radiation to the body, but produce relatively poor spatial resolution and are often limited by the availability of a clear acoustic window between the external surface and imaged region. Moreover, it is difficult for ultrasound imaging to be performed on a cross-sectional plane of the chamber. Ultrasound scans typically measure channel flow in the blood vessels and not planar flow through the heart chamber. As a result of this limitation, it is difficult to investigate the vortices in the blood within the heart chamber using ultrasound.

8.3.2 Cardiac Magnetic Resonance Imaging

Magnetic resonance imaging (MRI) is the application of magnetic fields, employing the use of radio frequency pulses to image different tissues in the human body (Horowitz 1994, Hirsch *et al.* 1994, Hoppe *et al.* 1996, Worthley 2001). Magnetic resonance registration is based on the response of specific nuclei to the exposed radio frequency energy and can be represented using an intensity-based image (Markl *et al.* 2003, Yu *et al.* 2003). The emitted signal can be encoded in such a way that the components that correspond to the spatial position of radiation emitting nuclei are used for construction of an image slice. An MRI scanner is effectively a device that creates a map of spin relaxation times of hydrogen nuclei within the tissue. This allows the structures to be scanned at a planar section (Phillips 1984). MRI also allows multiple contiguous slices at various sections of the body to be scanned at various phases of one cardiac cycle. Therefore, cine-MRI can be presented at various phases continuously for motion analysis of cardiac structures.

As discussed in Chapter 2, MR images of the heart, at a short axis two-chamber view, may be performed and used for visual flow analysis. In Chapter 3, we discuss the observation of signal voids, within the local region with poor gradient refocusing, as the result of chaotic and dynamic blood flow in more than one plane is discussed. As these local turbulent regions move along with the global flow of the blood, we are able to visually track their magnitude and direction of movement and determine the flow structure. However, there has been no method that performs flow quantification and as such, only a qualitative examination of the flow can be performed. The assessment

of ASD has been performed on cardiac MR imaging effectively. Examination using spin-echo cine-MRI, which gives a good intensity contrast for the cardiac wall, is able to reveal ASD (Duncan *et al.* 2008). In addition, gradient-echo T1-weighted cine-MRI of cardiac chambers allows visualisation of blood movement, based on the shifting intensity in the image shown up as signal voids due to de-phasing of nuclear spins. Apart from the left-to-right shunting of blood that can be observed, the enlargement of the right atrium can also be detected using MR images.

8.3.3 Chest Radiography

Radiographic techniques produce image films by registering the intensity of X-rays passing through a human body. The two-dimensional chest radiograph can be represented using an intensity image (Mudry *et al.* 2003, Park *et al.* 2007). Variation in the density of tissues results in different degrees of attenuation of X-ray photons within the structure under exposure and gives the intensity contrast of tissues captured on film by casting a distinctive image of shadows on it. The use of ionising radiation may harm the body if there is excessive exposure. Due to the inability to register signals from localised regions, the scan is unable to produce an image registering a projection slice at a specific depth through the body. The conventional chest X-ray can detect and monitor cardiac disease (Gleeson 2006). Chest X-rays can show up abnormalities in patients with severe ASD. Right heart dilation can be observed in lateral films. The central pulmonary arteries are characteristically enlarged with pulmonary plethora indicating increased pulmonary flow, and this can be used to diagnose ASD (Webb and Gatzoulis 2006, Egeblad *et al.* 1980).

8.3.4 Computed Tomography

Three-dimensional computed tomography (CT) provides a volumetric visualisation of the human body from a series of two-dimensional X-ray scans taken about an axis of rotation (Wolbarst 1999, Mudry *et al.* 2003). These images are synthesised into a model that allows the volume of data to be reformatted to present slices of structure within the human body at localised sections. Images of high temporal resolution can be registered using retrospective ECG gating. Computed tomography scans provide better soft tissue and bone contrast as compared to conventional X-rays and MRI. However,

computed tomography does not provide any information on the hemodynamic significance of ASDs and is associated with a significant radiation exposure. Hence, it is rarely used in the diagnosis and management of patients with ASDs. Computed tomography scans are often used to check if the right heart chambers are dilated or the location of a septal defect, which can serve as an indication for the severity of ASD.

8.4 Methodology

8.4.1 Subject for Case Study

In this study, we focus on two sets of investigations, one on the right atrium of an atrial septal defect (ASD) subject before treatment, and the other set on that of the same patient after atrial septal occlusion (ASO) surgically. The flow information from these two types of heart can be used to explain the behaviour of vortices that develop in the right atrium of a heart with a septal defect before and after ASO.

Scans were performed on a set of patients diagnosed with atrial septal defect for pre- and post-occlusion conditions[20]. Since the flow mechanisms are generally the same for all of the patients, it is sufficient to display the image sets and results that pertain to one of these patients for an effective case study demonstration. We note the difficulty in presenting all of the detailed results for every patient due to the large number of flow images that pertains to each case study, and the redundancy in displaying all the images which will be used to show the same mechanism of myocardial movement, and flow behaviour in a heart with an atrial septal defect. Instead, we aim to summarise the study results of all patients in Section 8.7 in order to demonstrate our theory.

The case subject is a male patient, aged 18 years. The subject had an ASD and was assessed using cardiac MR imaging. Implantation of the septal occluder device in the patient was performed 79 days later and another scan was carried out 210 days after the ASD closure.

[20]Human studies were approved by the Royal Adelaide Hospital Committee and by the Institutional Review Board. MR imaging was conducted in accordance with guidelines defined by the Wakefield Hospital to achieve safe and reliable scanning. Informed consent was obtained from each case subject after the imaging procedures had been conveyed.

8.4.2 MRI Scan Procedure

Cardiac MR imaging was performed on the patient using a Siemens Sonata, 1.5 Tesla, model–syngo MR 2004A scanner with Numaris–4, Series No: 21609 software. Steady-state free precession cine-MR imaging was performed using contiguous slices in the short axis orientation through the ASD. All images were acquired with retrospective gating and 25 phases (time frame indices of $n_t = 1$ to 25) for each slice are obtained.

SSFP magnetic resonance imaging is used to scan the patient before and after atrial septal occlusion. Acquisition parameters include: TR = 47.1 ms, TE = 1.6 ms, FOV = (298×340) mm^2 at a (134×256) pixel matrix for pre-septal occlusion scans and TR = 40.3 ms, TE = 1.2 ms, FOV = (260×320) mm^2 at a (156×192) pixel matrix for post-atrial septal occlusion scans.

8.4.3 Clinical Investigation

Cardiac MR image slices of the patient that correspond to diastolic phases of the cardiac cycle are selected. We observe the vortices that are generated pre- and post-septal occlusion at the selected phases. The right atrium was enlarged due to a left-to-right shunt, and the changes in the signal intensity of blood using MRI are more easily detected than in the other chambers. Note that we choose the right atrial flow for analysis, since this is the chamber where we can observe the shunting of blood into it from the left atrium. A region of interest of width 120 pixels and height 150 pixels is truncated from the selected slice showing the sectioning of the right and left atria, where the septal defect is most apparent. This is to be displayed for qualitative examination.

8.4.4 Parameters for Data Analysis

The images for pre- and post-septal occlusion are standardised to sizes of (156×192) pixels or grid point dimensions in order to maintain consistency for MR fluid motion computation and analysis. If a sampling window frame size given by $W = (w_x, w_y)$ is such that $w = w_x = w_y$, this corresponds to $\frac{w-1}{2}$ grid points from an interrogation point to the edge of the interrogated region. Each region uses a different number of sampling vectors depending on its number of grid points. Based on the measured velocity field, a sampling window of size $W = (21 \times 21)$ pixels is used on the velocity grid for calculation. This corresponds to a total number of 441 pixels (or grid points)

within the window. Reduction of velocity grid resolution is carried out by addition of vector components within 3 pixels by 3 pixels window throughout the flow grid.

Statistical histograms are produced by counting the number of frames with the specified range of vorticity values and then consolidating them to create a frequency versus vorticity value plot. The frequency of the image frames can be normalised to become the area $A(\%)$ of region in terms of percentage.

8.4.5 Investigation Procedure

This section sets the parameters for measurement and examination of right atrial flow using MR fluid motion tracking. The flow results for the heart of an atrial septal defect (ASD) subject are developed for pre- and post-ASO imaging. Comparison of the pre- and post-surgical intervention based on the right atrial flow patterns and vorticity measures can provide an indication of the cardiac abnormality as well as the recovery conditions after atrial septal occlusion.

We investigate the flow patterns of blood in the right atrium by analysing the strength of vortices in the vorticity maps. It is hypothesised that the vortices in a patient with an ASD will be stronger and more coherent after atrial septal occlusion. We quantify the strength of vortices using the flow visualisation system described in Chapter 7. Based on the system framework, an indication of the vorticity in a flow map can be provided by grouping pixels into subsets of range of flow values and generating a histogram that depicts the counts of pixels in bins of various values.

MR image slices from the contiguous scans, in short axis orientation through the ASD, are illustrated in Figure 8.4. Mapping of atrial flow are carried out during the diastolic phases of the heart. The time frames in a cardiac cycle selected for analysis corresponds approximately to those that occur for maximum left-to-right shunting of blood during atrial systole.

A review of the right atrium from these scans has been performed. The selected MR images that correspond to the sectioning of the atria are labelled as slices numbering from 1 to 3, starting at the top of the heart to its apex through an axis oblique to the direction from head to foot, for examination and flow analyses.

The observations of vortices and statistical analyses are performed for the right atrium and displayed in all the flow result figures. The global estimation of flow velocity

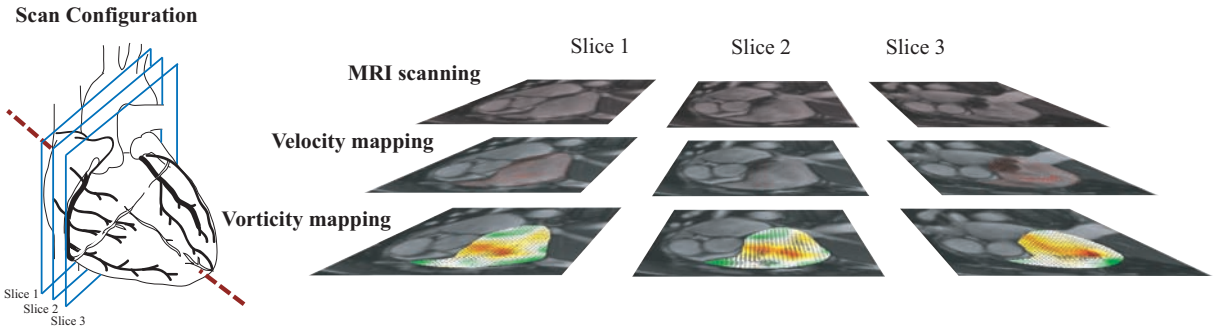

Figure 8.4. Planar dissection of heart based on three MR scan slices. Steady-state free precession MR scans of the cardiac chambers were performed in the short axis view at slice intervals of 6 mm and labelled as 1, 2 and 3, starting from the top to apex of the heart. Velocity and vorticity maps can be generated based on MR motion flow field for every slice and phase.

vector fields over the whole image provides useful information on the presence of vortices within the atrium that can be used to assess the vorticity. The strength of the vortical motion can be indicated by the mean vorticity $\overline{\omega}$ and its standard deviation σ from the vorticity map.

In this study, only flow fields at selected phases observed with the most obvious vortical flow are presented for all the patients. The flow maps superimposed onto MR images for pre- and post-ASO are shown in Figure 8.9, but are only based on selected scans pertaining to 4 out of 25 time frames for the entire cardiac cycle.

The study for examination of vorticity in post-ASO condition applies the same order of sequence for the patient as during the pre-ASO scan. Vorticity maps of the segmented atrium at four selected phases of cardiac cycle are presented. From preliminary observations, we can deduce that there is a difference in the flow (refer to Supplementary Videos 2 and 3 in CD-ROM, listed in Appendix F) that is highlighted in more detail in the subsequent results.

Table 8.1 summarises the MR imaging and tracking properties of the algorithm used in producing the velocity flow fields for case subject with ASD, as well as for pre- and post-ASO scans. Vorticity maps are computed using the computationally measured velocity data. The in-plane resolution of the scans is determined by the pixel spacing (at 1.33 mm/pixel and 1.67 mm/pixel for pre- and post-ASO images) and its through-plane resolution is based on a slice interval of 6 mm (for both images). The planes are chosen to be approximately normal to the mean flow direction. The sampling window sizes used for vorticity computation are (27.93×27.93) and (35.07×35.07) mm^2 for

PRE-ASO SCAN			
Symbol	Quantity	Value	Units
p_s	Pixel Spacing	1.33	mm/pixel
t_s	Trigger Time Step	30.73	ms
S	Slice thickness	6	mm
X	Image width	120	pixels
Y	Image height	150	pixels

POST-ASO SCAN			
Symbol	Quantity	Value	Units
p_s	Pixel Spacing	1.67	mm/pixel
t_s	Trigger Time Step	33.32	ms
S	Slice thickness	6	mm
X	Image width	120	pixels
Y	Image height	150	pixels

MOTION TRACKING PARAMETERS			
Symbol	Quantity	Value	Units
W	Optical flow sampling window	6×6	pixel
L	Number of pyramid levels	5	
W_v	Velocity interrogation window	1×1	pixel

p_s	Size of a pixel in metric unit
t_s	Duration of each time frame
S	Distance of slice interval
X	Width of image
Y	Height of image
W	Size of sampling window used in tracking
L	Number of pyramid level used in tracking
W_v	Resolution of velocity grid

Table 8.1. MR imaging and fluid motion tracking properties of ASD case subject. MR imaging and fluid motion tracking parameters for processing cardiac flow fields of study is presented. This table gives the information for adjustment of tracking algorithm and metric calibration that produces the flow visualisation for the cardiac flow in the right atrium for both pre- and post-ASO scans of the right atria.

pre- and post-ASO scans represented by (159.60 $\times$ 199.50) and (200.40 $\times$ 250.50) mm^2 respectively. This corresponds to sampling window areas of 780 and 1230 mm^2 for pre- and post-ASO scan images of area 31840 and 50200.20 mm^2 respectively. The tracking and vorticity sampling windows are configured appropriately to generate the vorticity maps that is able to provide an optimal visual presentation of the large-scale vortices.

8.4.6 Flow Visualisation System Implementation

We implement a vorticity visualisation system dedicated to the examination of flow behaviour in the heart chambers. In Figure 8.5, we examine the system flow stages from imaging of a patient with an atrial septal defect to the visualisation of cardiac flow field and statistical analysis of the vortical flow in the atrium of the imaged heart. Flow visualisation is performed at the post-processing stage whereby a vector plot is computed based on image intensity motion vectors for every pixel. The segmentation is required for isolating the region within the chamber for observation (refer to Supplementary Video 4 in CD-ROM, listed in Appendix F) and also for selecting only the relevant vorticity values in the atrium to be used statistically for analysis.

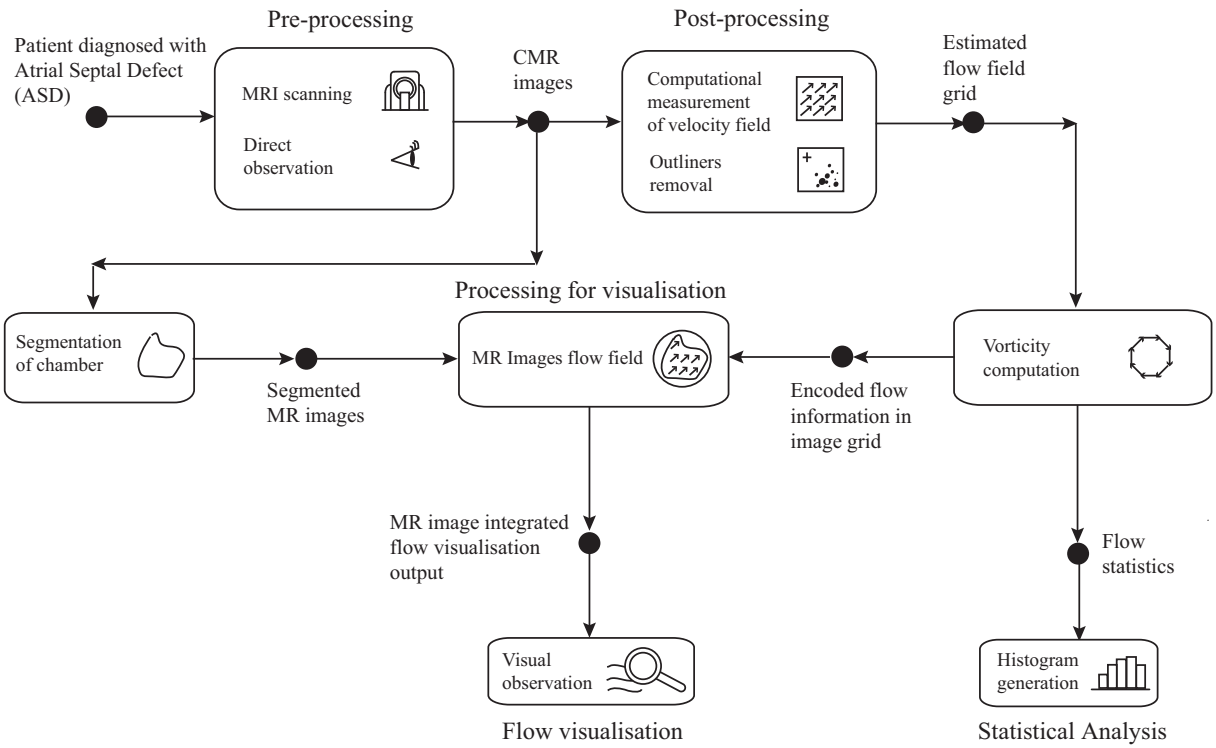

Figure 8.5. Cardiac vorticity visualisation system for ASD investigation. This system is specially constructed to review vorticity characteristics in a patient with an atrial septal defect (ASD) and relies on computational post-processing of MR images. The vorticity visualisation system flow shows data processed by blocks depicting the MR imaging which provides data for generation of flow field flows. Flow visualisation is achieved by field display using a vector plot with the superposition of MR intensity images. Statistical analysis is supported by histograms of the vorticity maps.

8.5 Results and Discussion

Medical examiners and/or radiologists usually confirm the existence of septal defects by observation of a left-to-right shunt of blood through the septum using cine magnetic resonance images and also from the broken definition of the cardiac wall between two chambers (Durongpisitkul *et al.* 2004). Both indications of abnormality can be detected based on the intensity of the image signals captured on MRI scans. Examples for magnetic resonance images of the short axis atrial scans are presented in Figure 8.6.

We propose the examination of blood rotation speed in the right atrium using MR fluid motion tracking. The tracing of blood within this chamber can be used to assess the severity of the cardiac abnormality in atrial septal defect patients. The cardiac phases or time frames that correspond to the maximum pressure in the left atrium and the minium pressure in the right one is chosen to analyse the optimal shunting of blood

in this instance. Vector field mapping of the flow in the sectional planes is presented for pre- and post-ASO in Figure 8.7 based on selected phases of the cardiac phases. Streamline plots using the flow vector information can be created by seeding the entire chamber region of interest and tracing the streamline flow from each seed as shown in Figure 8.8. In addition to the direction of the flow that is given, we are able to track the blood vortical motion using a series of colour streamlines, which have variations of colours that correspond to different speeds of flow. This visual tool allows perception on the location and strength of the vortices in the right atrium. Flow visualisation using streamline depicts the motion of flow from computed MR fluid motion field of segmented atrium at four selected phases of cardiac cycle.

We highlight the poor tracking of blood made by the implemented technique, which is mainly due to the poor quality of tracking features present in the image. This demonstrates a limitation of MR fluid motion tracking as compared with phase contrast MR velocimetry. Nevertheless, the motion tracking technique makes it possible to show both quickly and conveniently that a more consistent vortical structure is present for the post-ASO case.

From Figures 8.7 and 8.8, we can visually deduce that the vortical features in the post-ASO atrium are more concentrated and coherent than those in the pre-ASO. Furthermore, the size and magnitude of the vorticity concentrations given in vorticity maps indicate the strength of blood rotation during one cardiac cycle (Fyrenius *et al.* 2001). Comparison of the pre- and post-surgical intervention based on the right atrial flow patterns and vorticity maps can provide an indication of the cardiac abnormality as well as the recovery conditions after atrial septal occlusion.

We present the flow results and analysis of the right atrium pre- and post-ASO for multiple selected slices and phases of the heart in Figure 8.9. Histograms are represented using a spline interpolated line plot of the bar frequency height levels. The mean μ and median m of the histogram are represented by the straight and dotted vertical blue line indictors. The centre line that represents the zero mark of the histogram vorticity axis (where $\omega = 0$) is coloured in grey. For the pre-ASO flow maps, the spread of the vorticity ω approximates that of a normal (or Gaussian) distribution since there is a lack of a single strong vortex. For the ASO histograms, note the development of a second hump in the normal curve as the migration of the mean and median indicators away from the centre line as a vortex develops in strength over the four phases. Further details of analysis for scans at various other slice and phases can be obtained from Appendices D and E.

We perform cardiac flow assessment of a pathological heart to provide an example of the MR fluid motion field of a patient that is diagnosed with atrial septal defect. Limited by the absence of the velocity-encoding (VENC) protocol during the MRI scanning of this patient, only steady-state free precession (SSFP) MR images are obtained to assess the septal defect by examining the discontinuity along the myocardium. The strategy of attaining a stronger assessment of the defect is by utilising the same SSFP MR images for both anatomical and flow evaluation. Figure 8.7 shows the derived velocity field from intensity motion tracking for both pre- and post-atrial septal occlusion at 4 sample time frames out of 25 frames in one cardiac cycle.

Our set of results illustrates the potential clinical interest to analyse local blood motion behaviour or to discover flow phenomena based on pathological conditions. For example, medical experts will be able to provide a study of a defective heart and to compare it against the normal or the post-operation case. It also has the foundation to open up discussion on the difference that can be captured via our methodology, with the aim of flow grid reconstruction that requires short processing time and lower memory, for an effective and efficient diagnosis.

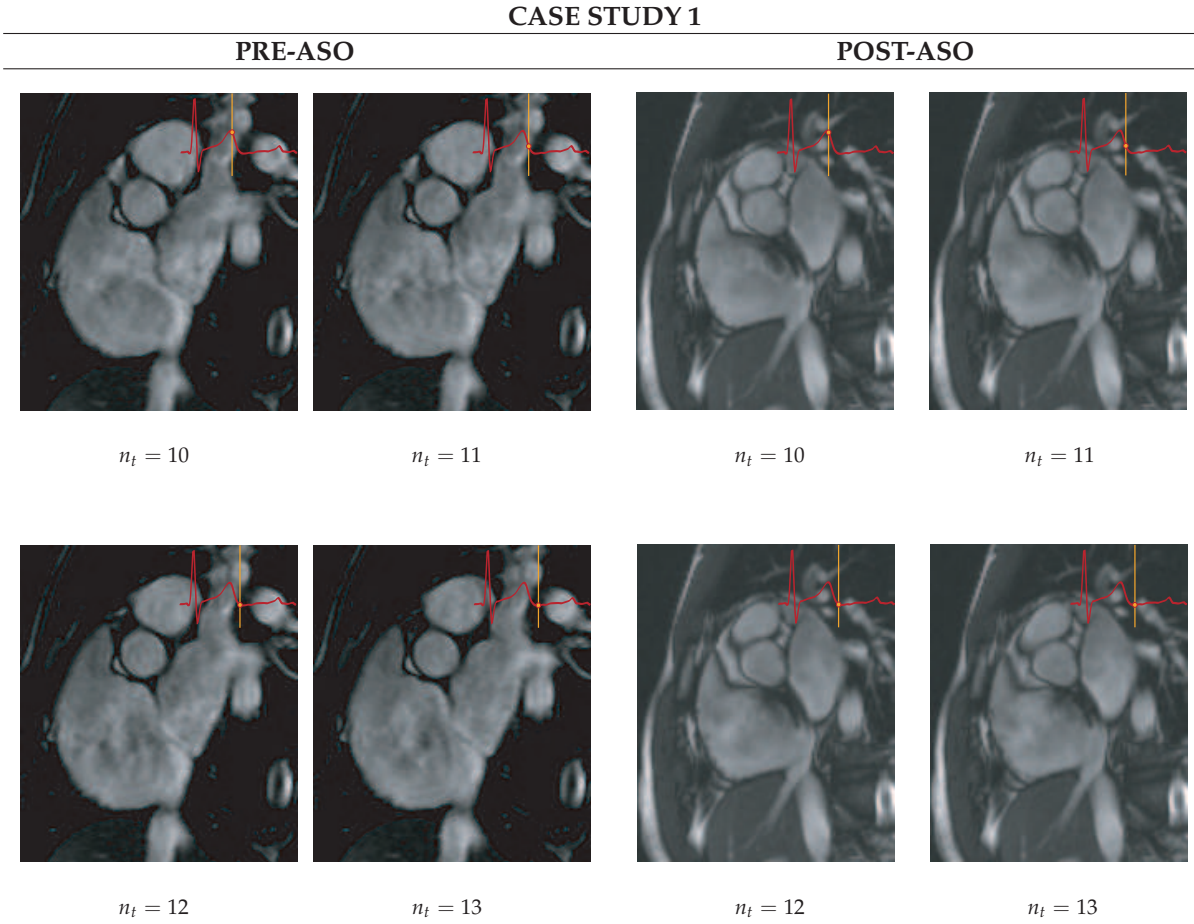

Figure 8.6. MRI Scans of right atrial flow pre- and post-ASO. One slice that passes through the septal defect has been choosen for flow analysis here. The size of the pre-ASO atrium is shown to be larger than that of the post-ASO one. It can be deduced from this scans that there is an inbalance of pressure maintained by both atria. In this case, pressure is increased in the right atrium due to the left to right shunting of blood that causes the blood circulation in the heart to lose efficiency.

VECTOR PLOT
PRE-ASO

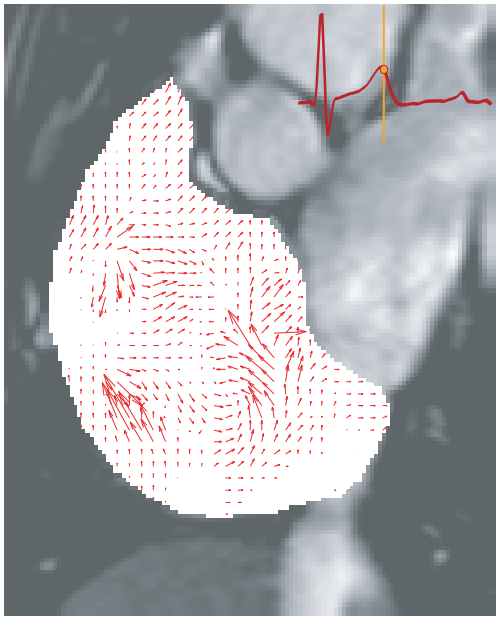

(i) $n_t = 10$

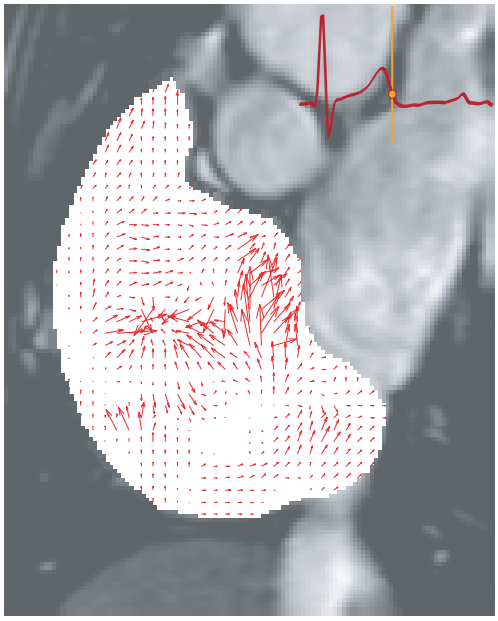

(ii) $n_t = 11$

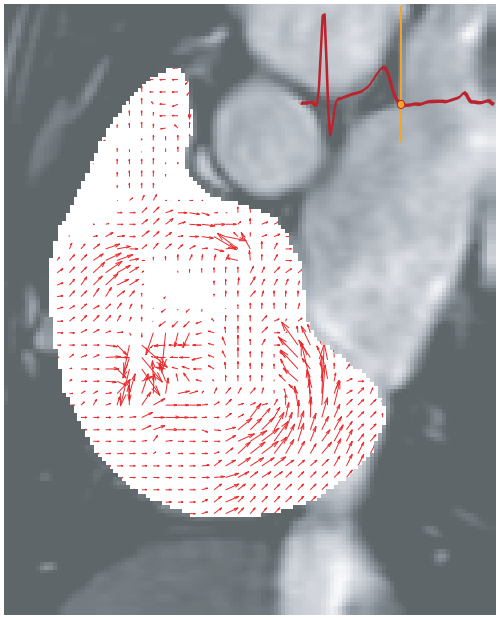

(iii) $n_t = 12$

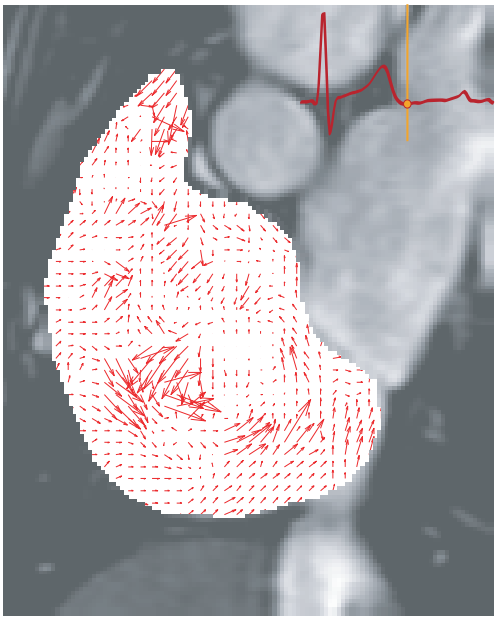

(iv) $n_t = 13$

(a) Subject 1: Selected time frame indices $n_t = [10, 11, 12, 13]$ of pre-ASO scans

Vector plots for post-ASO scans continues on next page

VECTOR PLOT
POST-ASO

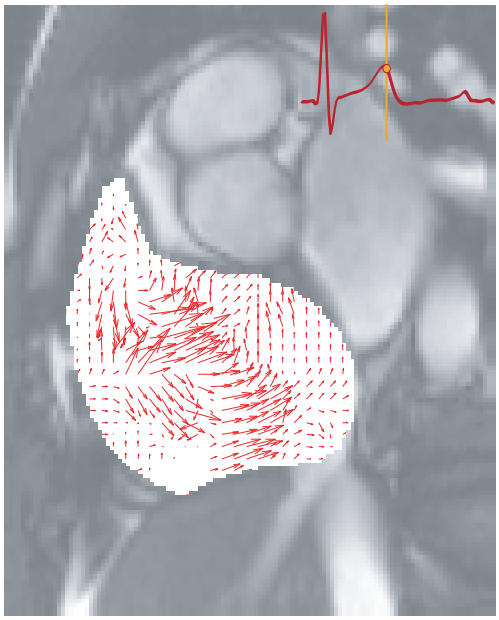

(i) $n_t = 10$

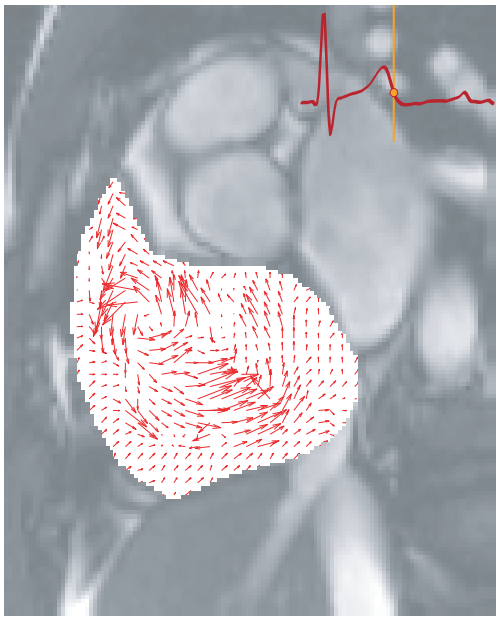

(ii) $n_t = 11$

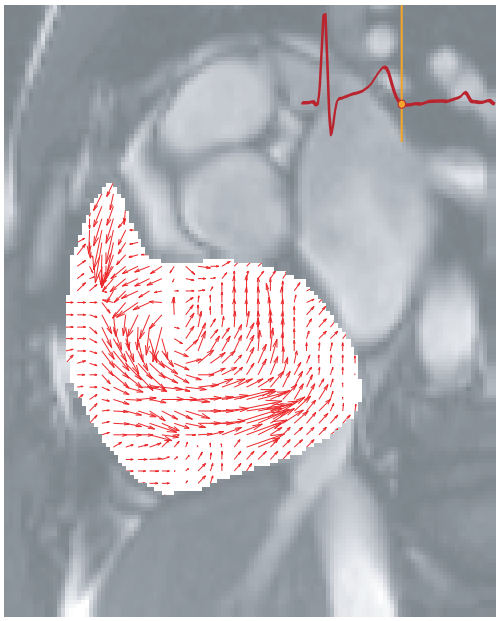

(iii) $n_t = 12$

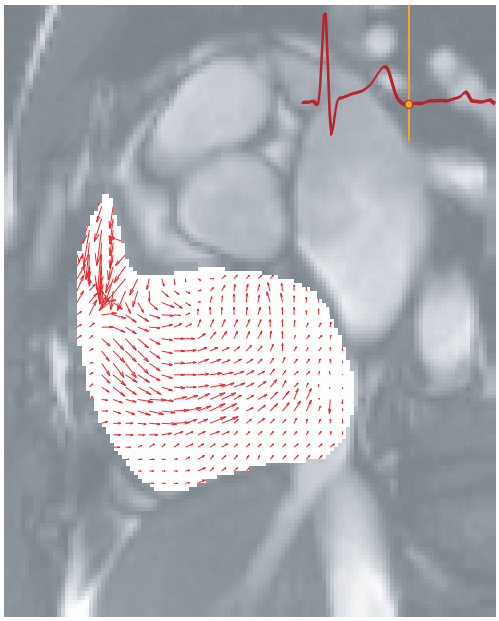

(iv) $n_t = 13$

(b) Subject 1: Selected time frame indices $n_t = [10, 11, 12, 13]$ of post-ASO scans

Figure 8.7. Vector flow plot of right atrial flow pre- and post-ASO. The motion field of blood can be produced rapidly by using MR fluid motion tracking to give an estimation of the direction and magnitude of flow. The method can give a quick insight into the fluid flow behaviour and the swirling of blood based on cardiac time frame indices $n_t = [10, 11, 12, 13]$ of one cardiac cycle (which comprises of 25 frame) can be observed clearly before and after atrial septal occlusion shown by parts (a) and (b) respectively.

COLOUR STREAMLINE PLOT

PRE-ASO

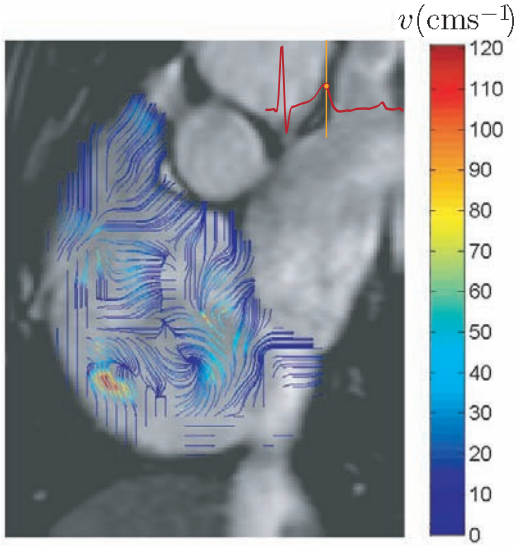

(i) $n_t = 10$

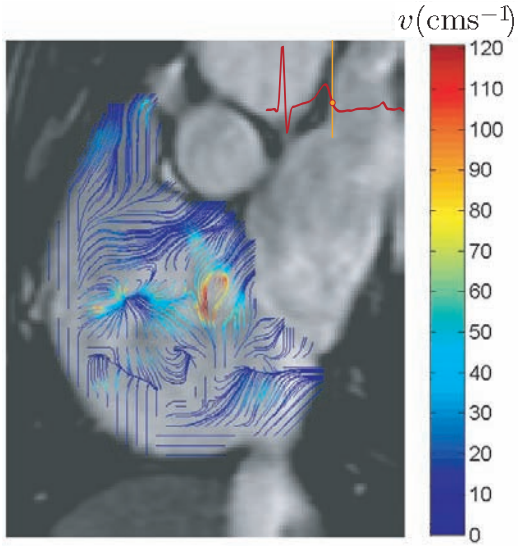

(ii) $n_t = 11$

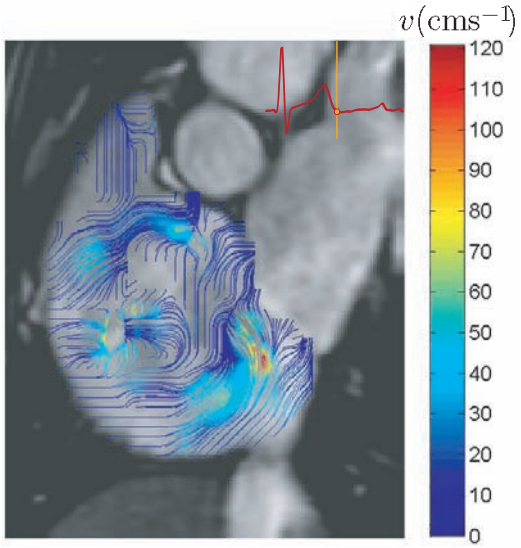

(iii) $n_t = 12$

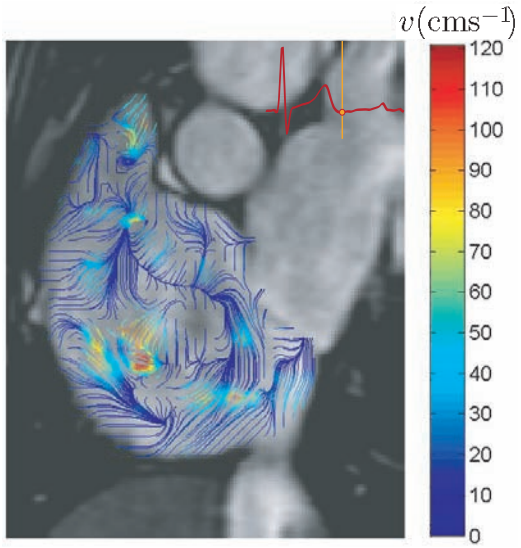

(iv) $n_t = 13$

(a) Subject 1: Selected time frame indices $n_t = [10, 11, 12, 13]$ of pre-ASO scans

Streamline plots for post-ASO scans continues on next page

COLOUR STREAMLINE PLOT
POST-ASO

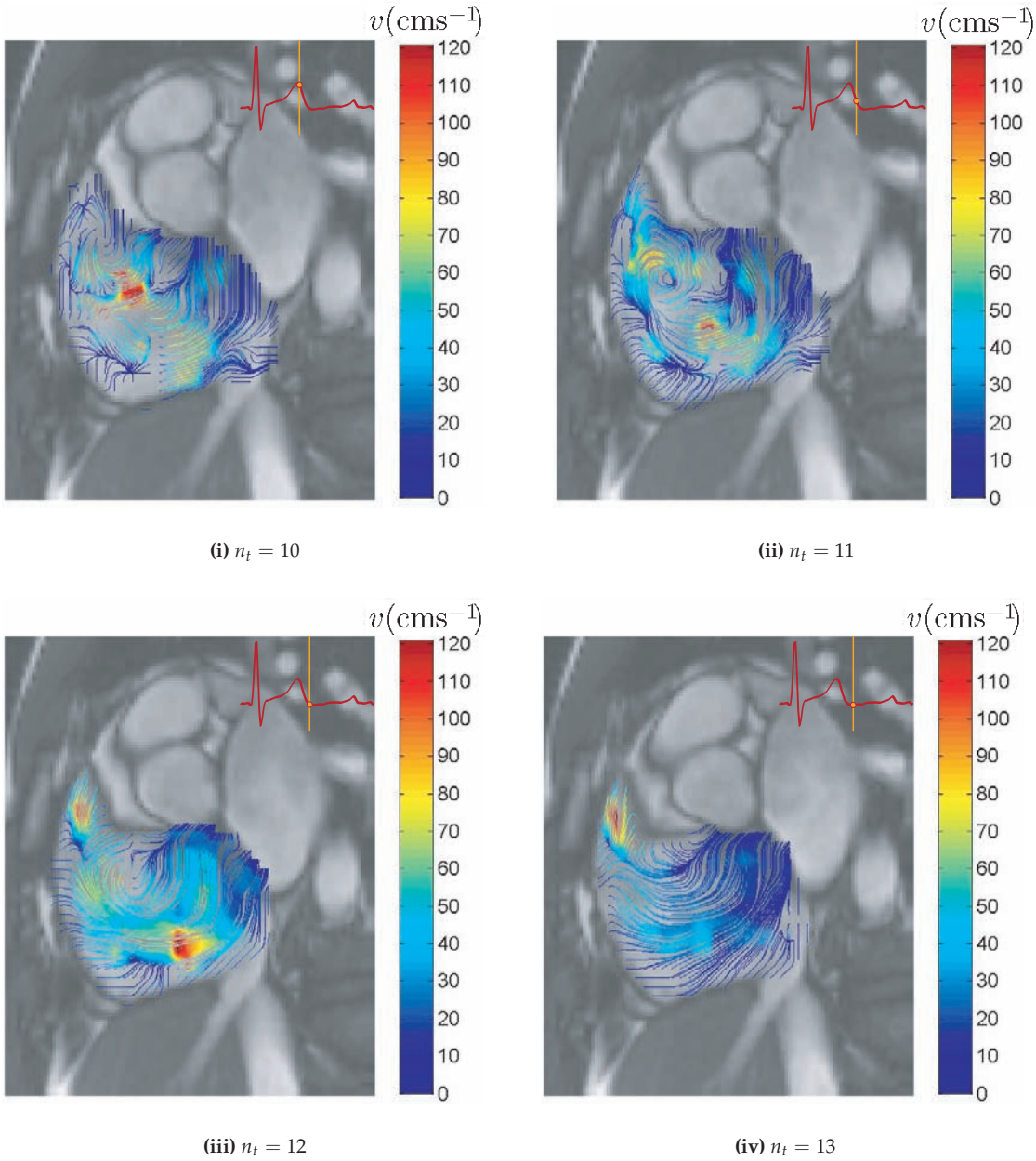

(i) $n_t = 10$ **(ii)** $n_t = 11$

(iii) $n_t = 12$ **(iv)** $n_t = 13$

(b) Subject 1: Selected time frame indices $n_t = [10, 11, 12, 13]$ of post-ASO scans

Figure 8.8. Streamline visualisation of right atrial flow pre- and post-ASO. The swirling traced by the streamlines within the chamber region of interest shows the existence of vortices during cardiac time frame indices $n_t = [10, 11, 12, 13]$ of a cardiac cycle with 25 frames. In part (a), prior to occlusion, there is no clear identification of a single large blood swirl. The tracing of blood movement within the right atria indicates a more consistent swirling motion within the right atrium after atrial septal occlusion (ASO) as shown by part (b).

CASE STUDY 1 - PRE - ASO

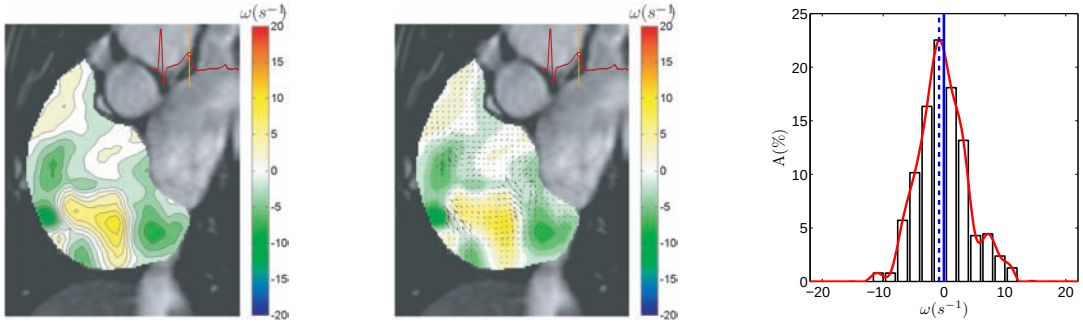

(i) $n_t = 10, \begin{bmatrix} \overline{\omega} \\ \sigma \end{bmatrix}_{\mu} = \begin{bmatrix} 0.16 \\ 4.32 \end{bmatrix} \text{s}^{-1}, \begin{bmatrix} \overline{\omega} \\ \sigma \end{bmatrix}_{md} = \begin{bmatrix} 0 \\ 4.33 \end{bmatrix} \text{s}^{-1}$

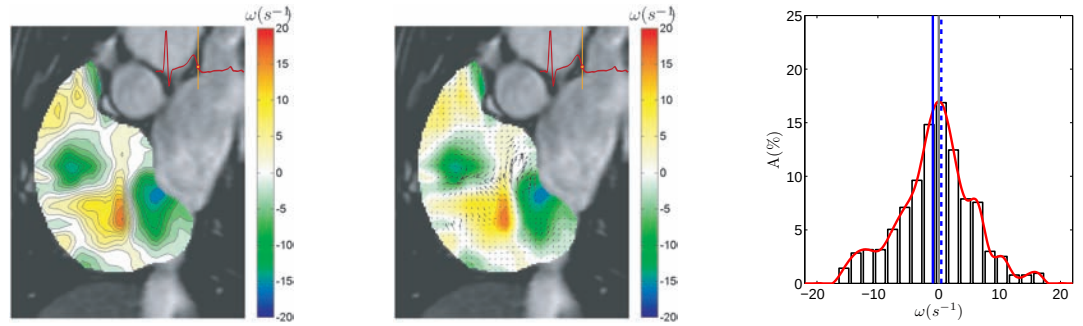

(ii) $n_t = 11, \begin{bmatrix} \overline{\omega} \\ \sigma \end{bmatrix}_{\mu} = \begin{bmatrix} 0.13 \\ 3.75 \end{bmatrix} \text{s}^{-1}, \begin{bmatrix} \overline{\omega} \\ \sigma \end{bmatrix}_{md} = \begin{bmatrix} 0 \\ 3.76 \end{bmatrix} \text{s}^{-1}$

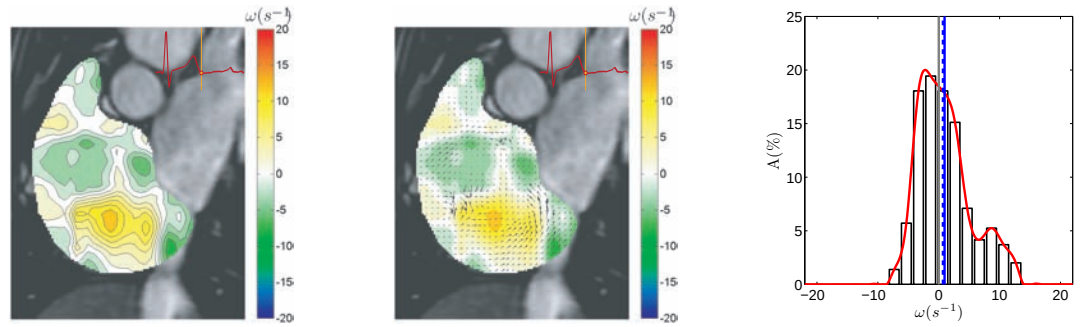

(iii) $n_t = 12, \begin{bmatrix} \overline{\omega} \\ \sigma \end{bmatrix}_{\mu} = \begin{bmatrix} 0.24 \\ 6.12 \end{bmatrix} \text{s}^{-1}, \begin{bmatrix} \overline{\omega} \\ \sigma \end{bmatrix}_{md} = \begin{bmatrix} 0 \\ 6.12 \end{bmatrix} \text{s}^{-1}$

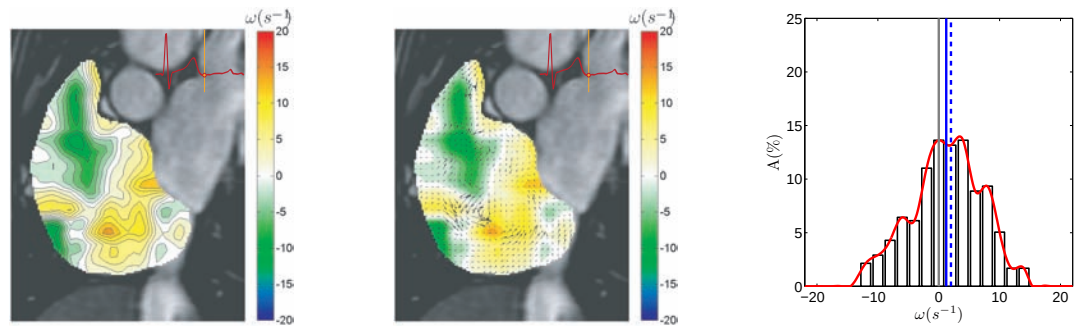

(iv) $n_t = 13, \begin{bmatrix} \overline{\omega} \\ \sigma \end{bmatrix}_{\mu} = \begin{bmatrix} 1.38 \\ 0.76 \end{bmatrix} \text{s}^{-1}, \begin{bmatrix} \overline{\omega} \\ \sigma \end{bmatrix}_{md} = \begin{bmatrix} 4.18 \\ 4.19 \end{bmatrix} \text{s}^{-1}$

(a) Subject 1: Selected phases n_t = [10, 11, 12, 13] of pre-ASO scans

CASE STUDY 1 - POST - ASO

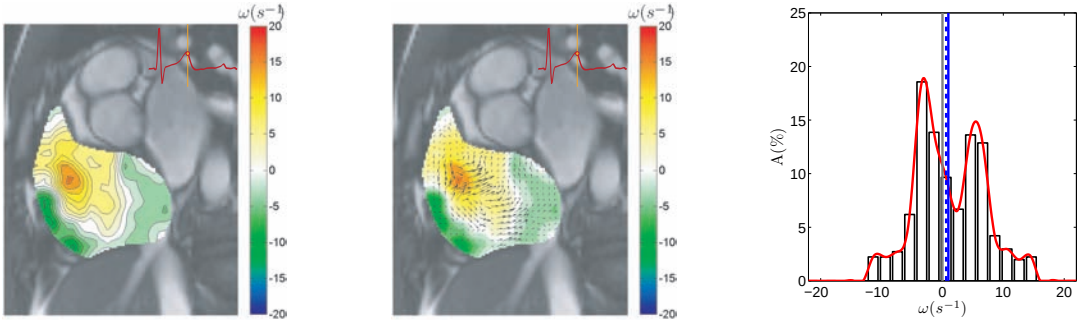

(i) $n_t = 10, \begin{bmatrix} \overline{\omega} \\ \sigma \end{bmatrix}_{\mu} = \begin{bmatrix} 2.39 \\ 1.88 \end{bmatrix} \mathrm{s}^{-1}, \begin{bmatrix} \overline{\omega} \\ \sigma \end{bmatrix}_{md} = \begin{bmatrix} 5.57 \\ 5.59 \end{bmatrix} \mathrm{s}^{-1}$

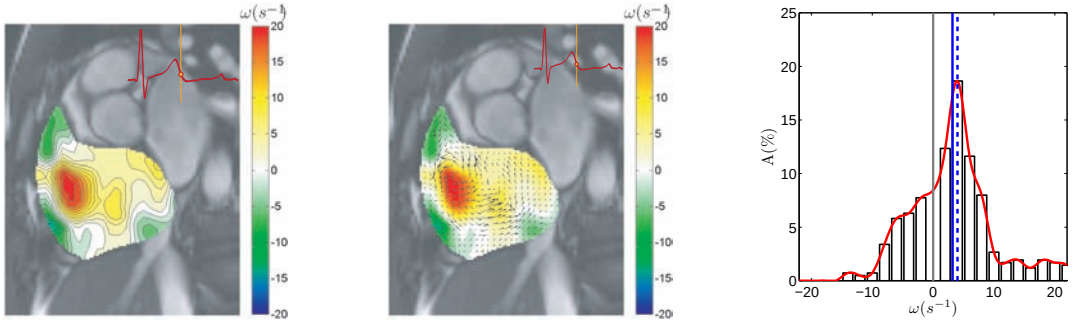

(ii) $n_t = 11, \begin{bmatrix} \overline{\omega} \\ \sigma \end{bmatrix}_{\mu} = \begin{bmatrix} 2.34 \\ 1.88 \end{bmatrix} \mathrm{s}^{-1}, \begin{bmatrix} \overline{\omega} \\ \sigma \end{bmatrix}_{md} = \begin{bmatrix} 5.60 \\ 5.62 \end{bmatrix} \mathrm{s}^{-1}$

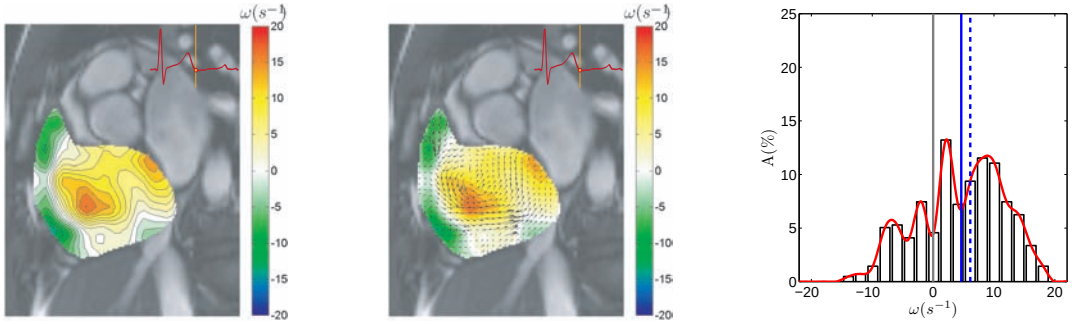

(iii) $n_t = 12, \begin{bmatrix} \overline{\omega} \\ \sigma \end{bmatrix}_{\mu} = \begin{bmatrix} 4.15 \\ 4.06 \end{bmatrix} \mathrm{s}^{-1}, \begin{bmatrix} \overline{\omega} \\ \sigma \end{bmatrix}_{md} = \begin{bmatrix} 6.46 \\ 6.46 \end{bmatrix} \mathrm{s}^{-1}$

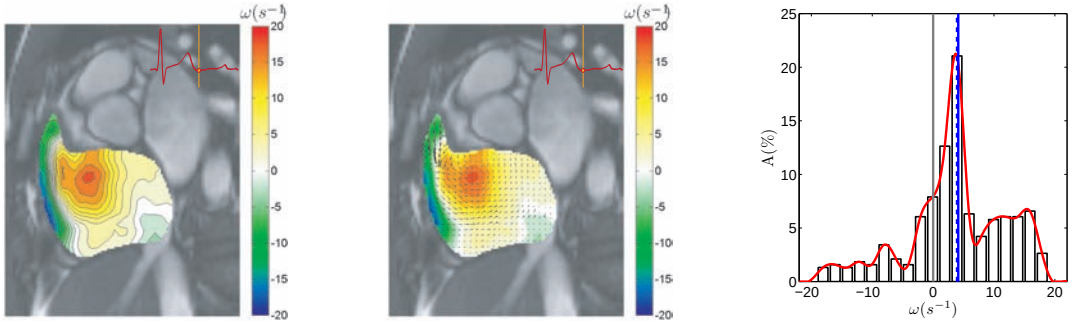

(iv) $n_t = 13, \begin{bmatrix} \overline{\omega} \\ \sigma \end{bmatrix}_{\mu} = \begin{bmatrix} 5.17 \\ 6.71 \end{bmatrix} \mathrm{s}^{-1}, \begin{bmatrix} \overline{\omega} \\ \sigma \end{bmatrix}_{md} = \begin{bmatrix} 6.39 \\ 6.57 \end{bmatrix} \mathrm{s}^{-1}$

(b) Subject 1: Selected time frame indices $n_t = [10, 11, 12, 13]$ of post-ASO scans

CASE STUDY 1

PRE-ASO	POST-ASO	VORTICITY COMPARISON
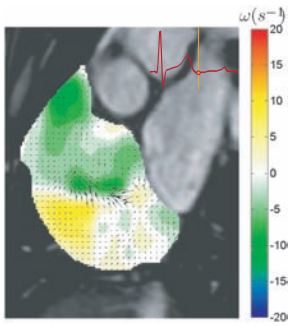	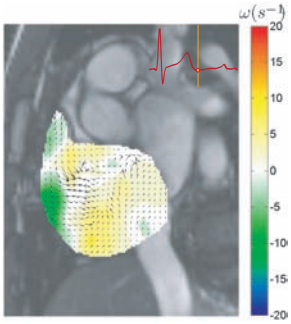	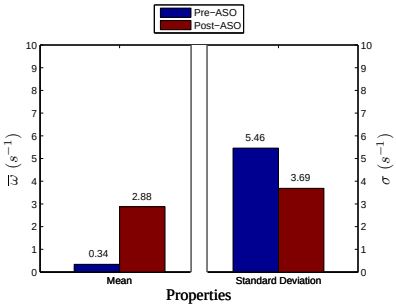
Pre-ASO: $\begin{bmatrix} \overline{\omega} \\ \sigma \end{bmatrix}_{\mu} = \begin{bmatrix} 0.78 \\ 4.18 \end{bmatrix} \text{s}^{-1}$	Post-ASO: $\begin{bmatrix} \overline{\omega} \\ \sigma \end{bmatrix}_{\mu} = \begin{bmatrix} 4.58 \\ 5.20 \end{bmatrix} \text{s}^{-1}$	Ratio of $\overline{\omega} = 5.87$ Ratio of $\sigma = 1.24$
(i) Slice 1		
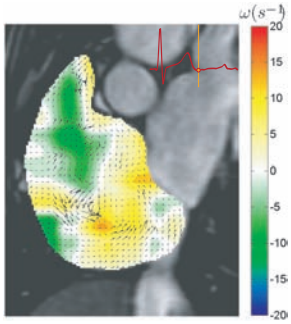	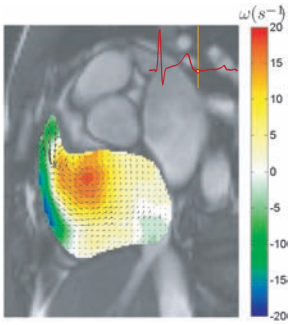	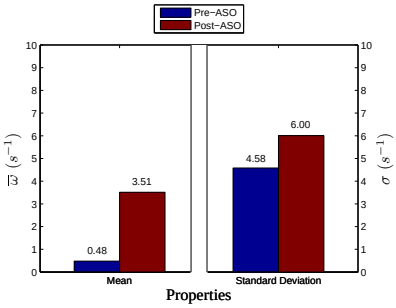
Pre-ASO: $\begin{bmatrix} \overline{\omega} \\ \sigma \end{bmatrix}_{\mu} = \begin{bmatrix} 1.38 \\ 4.18 \end{bmatrix} \text{s}^{-1}$	Post-ASO: $\begin{bmatrix} \overline{\omega} \\ \sigma \end{bmatrix}_{\mu} = \begin{bmatrix} 5.17 \\ 6.39 \end{bmatrix} \text{s}^{-1}$	Ratio of $\overline{\omega} = 3.75$ Ratio of $\sigma = 1.53$
(ii) Slice 2		
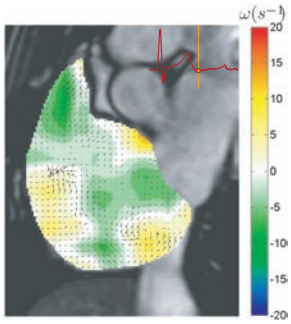	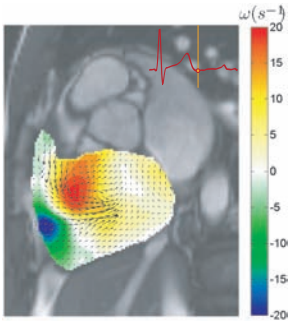	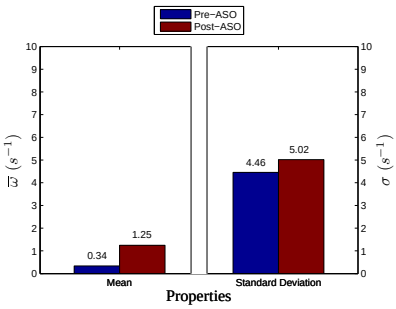
Pre-ASO: $\begin{bmatrix} \overline{\omega} \\ \sigma \end{bmatrix}_{\mu} = \begin{bmatrix} 0.61 \\ 3.36 \end{bmatrix} \text{s}^{-1}$	Post-ASO: $\begin{bmatrix} \overline{\omega} \\ \sigma \end{bmatrix}_{\mu} = \begin{bmatrix} 2.50 \\ 5.86 \end{bmatrix} \text{s}^{-1}$	Ratio of $\overline{\omega} = 4.10$ Ratio of $\sigma = 1.74$
(iii) Slice 3		

(c) Subject 1: Selected time frame index $n_t = 13$ of pre-ASO scans and $n_t = 13$ of post-ASO scans

Figure 8.9. Vorticity visualisation of right atrial flow pre- and post-ASO. Vorticity contour maps are superimposed onto cardiac MR images and presented. The vorticity representation by the flow map in colour codes can be referenced against scales (in metric units of per second) on the right hand side. Pre- and post-ASO vorticity maps are presented by parts (a) and (b) respectively while part (c) shows the comparison of the two sets of maps. Three slices of the scan are selected for this comparison.

8.6 Flow Analysis

This section describes the flow characteristics of the vortices within the right atrium pre- and post-ASO. We base our analysis on quantitative data pertaining to vorticity calculations and support the flow scenario with superimposed qualitative data such as velocity vector plots and streamlines. The purpose of our analysis is to reach the conclusion that a difference in the vorticity after surgical intervention is visible, and we use our implemented technique to support this claim. The characteristics for the vorticity map can be presented in histograms as an indication of vorticity magnitudes represented by colour pixels in the flow grid. The patient has his cardiac flow results presented. Swirl within segmented right atrium for pre- and post-ASO at three scan slices of the heart are presented and comparison of vorticity for both conditions is carried out.

8.6.1 Qualitative Flow Analysis

In the velocity vector plots depicting the rotation of blood, we are able to visually deduce that pre-ASO closure at our selected phases of examination (based on time frame indices $n_t = 10$, 11, 12 and 13) have flows that are of lower vorticities than those for post-ASD closure. This signifies that the rotation of blood is higher after septal occlusion. Note that this pressure acts as a mechanism for delivering blood effectively into the pulmonary arteries for oxygenation. Ideally, the pressure due to the contraction of the left atrium is responsible for pushing the oxygenated blood into the left ventricle without seepage into the right atrium and diffusing into the de-oxygenated blood. The presence of an ASD reduces the pressure in the left atrium and increases the pressure within the right atrium. As an extension of our explanation, the existence of strong vortices in the human atrium is suggested as being normal and the reduction in its intensity will have an abnormal effect on the human heart.

We also analyse the flow patterns from Figure 8.8 and discover that a clockwise and counter-clockwise vortex appear before atrial septal defect occlusion. This is due to the shunting of blood from the left to right atria as a result of the pressure difference in the two chambers. The left-to-right shunt through a small defect relative to the entire chamber introduces swirling of blood in different directions on both sides of the jet. For case study 1, after the septal defect has been repaired, the blood is able to flow

more normally and a single vortex is present within the right atrium without any flow interference.

8.6.2 Quantitative Flow Analysis

The intensity of vorticity based on $\overline{\omega}$ gives a good estimation of the swirl structure in the right atrium. The vortices in the right atrium are shown to be counter-clockwise in rotation upon investigation, and counter-clockwise vorticity has a positive magnitude based on our conventions. This can also be correlated with the shear and normal strain that is experienced by the blood but this is beyond the scope of this study.

From Figure 8.9, pre-ASO flow maps have vorticity means for four selected phases that are characterised by low magnitudes of $\overline{\omega}$ in range of 0.13 to 1.38 s^{-1}. This is different from flow characteristics of the post-ASO, where $\overline{\omega}$ has much higher values ranging from 2.34 to 5.17 s^{-1}. In a similar way, the magnitude of standard deviation for pre-ASO maps σ varies from 3.75 to 6.12 s^{-1}, which is lower than those for post-ASO flow maps with σ that varies from 5.57 to 6.46 s^{-1}.

The magnitudes of σ are dependent on the characteristic of the flow map. A high intensity contrast vorticity image results in a larger standard deviation as compared to a low contrast one made up of vorticity values that do not have a large variance. When there are even numbers of vortices in the cardiac chamber of analysis, magnitudes of $\overline{\omega}$ cannot be used with confidence as a mode of comparison as the sum of vorticity values for flow in clockwise (CW) directions will cancel those in counter-clockwise (CCW) directions. Using magnitudes of σ is a more accurate comparison for the intensity of the vortices in the flow map. It is worthwhile mentioning that using the statistical properties of the vorticity map based on median m can also provide the same mode of comparison.

In Figure 8.9, we observe that vorticity is increased in the right atrium for the same patient and at the same cardiac phase after septal occluder insertion. We also note the enlargement of the atrium before septal occlusion. We observe that there is an increase in vorticity of flow and a more defined vortex after occlusion. Increase in vorticity occurs as a result of the decrease in chamber size following an increase in pressure that strengthens the actuating mechanism for circulating blood in the heart.

Figure 8.9 shows the mapping of vorticity components normal to the measurement planes, i.e. in the principal direction of the most significant planar flow rotation. From

these results, we observe that the septal occlusion produces two significant effects. The first one is that it leads to an increase in strength of a single dominant counter-clockwise vortex within the cardiac chamber. Secondly, it reduces the concentration of clockwise vortical regions at the same time. For the post-occlusion condition, a strong negative vorticity region exists adjacent to the chamber wall that has less curvature relative to the septum that is associated with flow of positive vorticity. This is due to the quick motion of blood parallel to the endocardium of a relatively motionless and flat chamber wall. Consistent with this effect, there is a broader distribution of absolute vorticity in the right atrium for the same patient and at the same cardiac phase after septal occlusion. This deduction can be supported using statistical properties of the vorticity distributions. We note the atrial enlargement pre-occlusion, which may in part explain the reduction on the strength of the vorticity concentrations before occlusion. Another possible cause of the differences between the pre-and post-occlusion cases is the presence of left-to-right shunting of blood that disrupts the normal dominant vortex to introduce vortices of a smaller scale (refer to Supplementary Video 2 in CD-ROM, listed in Appendix F).

8.6.3 Statistical Comparison of Vorticity Maps

The statistical properties of vorticity maps for flow maps for pre- and post-ASD pertaining to cardiac phases based on frames of 10 to 13 (out of 25 time frames) are presented in histograms (Figure 8.10) for comparison. The averaging of these properties is performed and illustrated using histograms as well.

The variation in the level of statistical parameters of flow maps at each phase can be used to determine the degree of abnormality in the cardiac structure. For pre-ASO condition, we are able to observe from the streamline plots and vorticity maps that multiple vortices exist because of the left-to-right shunting of blood during the ASD condition. As the vortices are of relatively the same strength in different rotation directions, the vorticity mean of the map based on averaging of all vorticity values approaches zero. This is consistent with our results from which Figure 8.9 has shown that measures of central tendency for each vorticity map, which are mean $\overline{\omega}_{\mu}$ and median $\overline{\omega}_{m}$, have magnitudes that are considerably smaller for pre-ASO vorticity maps. And we observe that the standard deviation of mean σ_{μ} and of median σ_{m} are consistently smaller for pre-ASO vorticity maps as well. On the contrary, once the shunting is minimised after atrial septal occlusion, and the atria are restored to a more normal size,

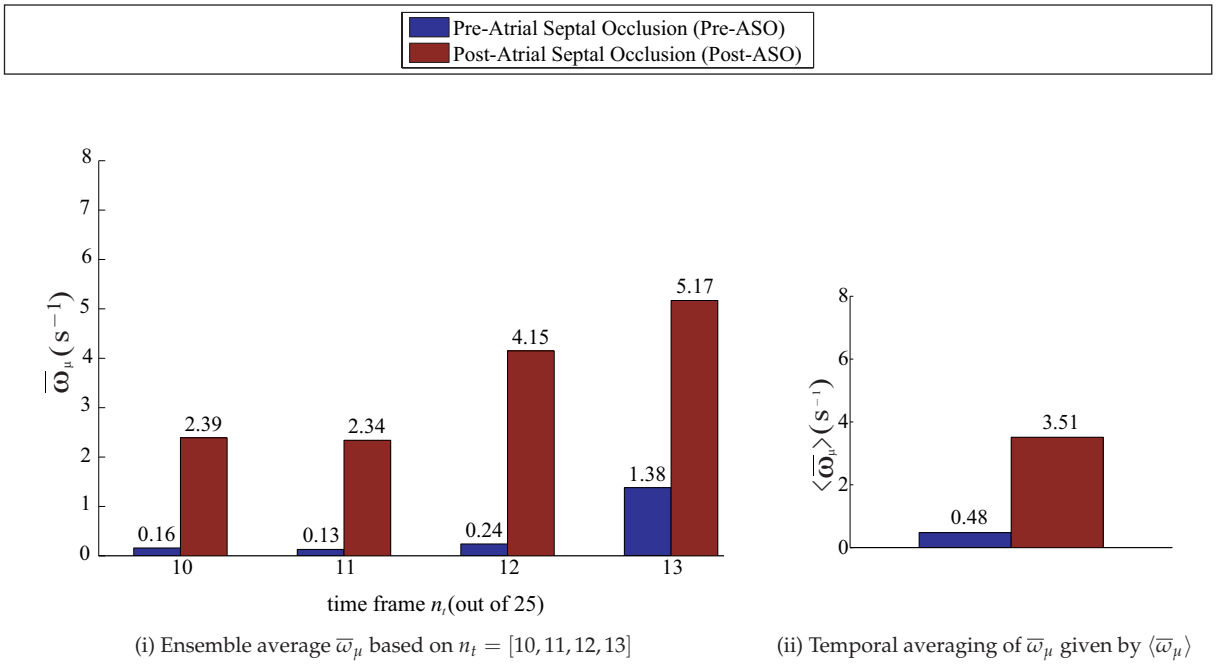

(i) Ensemble average $\overline{\omega}_\mu$ based on $n_t = [10, 11, 12, 13]$ (ii) Temporal averaging of $\overline{\omega}_\mu$ given by $\langle\overline{\omega}_\mu\rangle$

(a) Ensemble averages of vorticity maps for $n_t = 10$ to 13 and their temporally averaged values

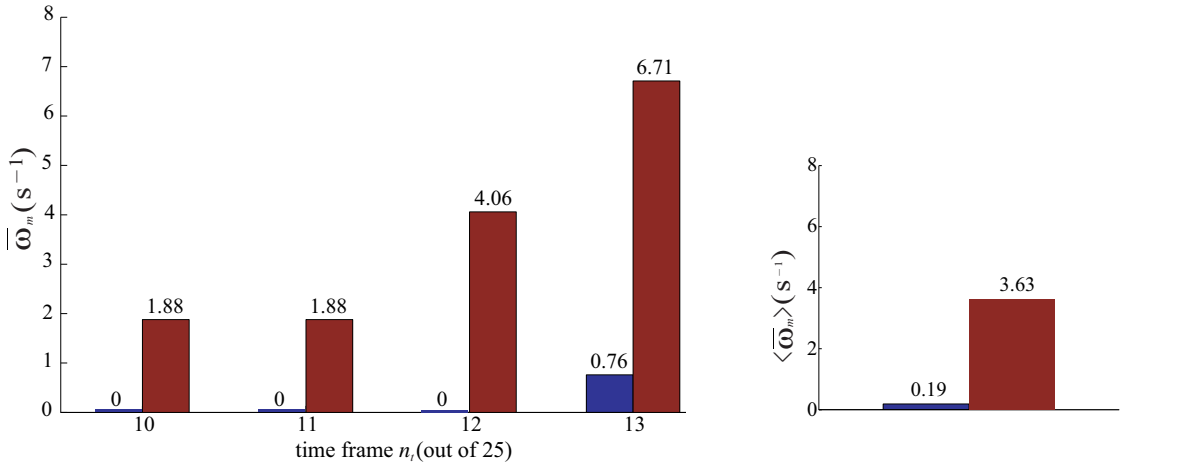

(i) Median $\overline{\omega}_m$ based on $n_t = [10, 11, 12, 13]$ (ii) Temporal averaging of $\overline{\omega}_m$ given by $\langle\overline{\omega}_m\rangle$

(b) Medians of vorticity maps for $n_t = 10$ to 13 and their temporally averaged values

Standard deviations of vorticity maps continue on next page

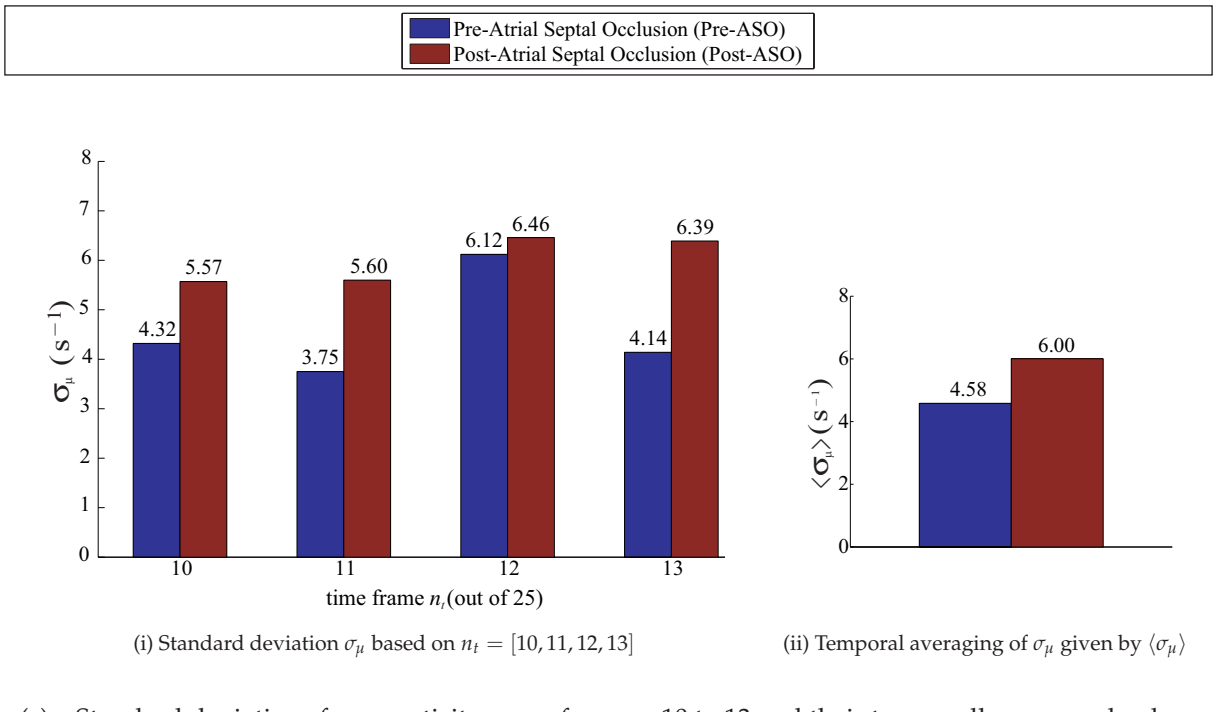

(i) Standard deviation σ_μ based on $n_t = [10, 11, 12, 13]$ (ii) Temporal averaging of σ_μ given by $\langle\sigma_\mu\rangle$

(c) Standard deviations from vorticity mean for $n_t = 10$ to 13 and their temporally averaged values

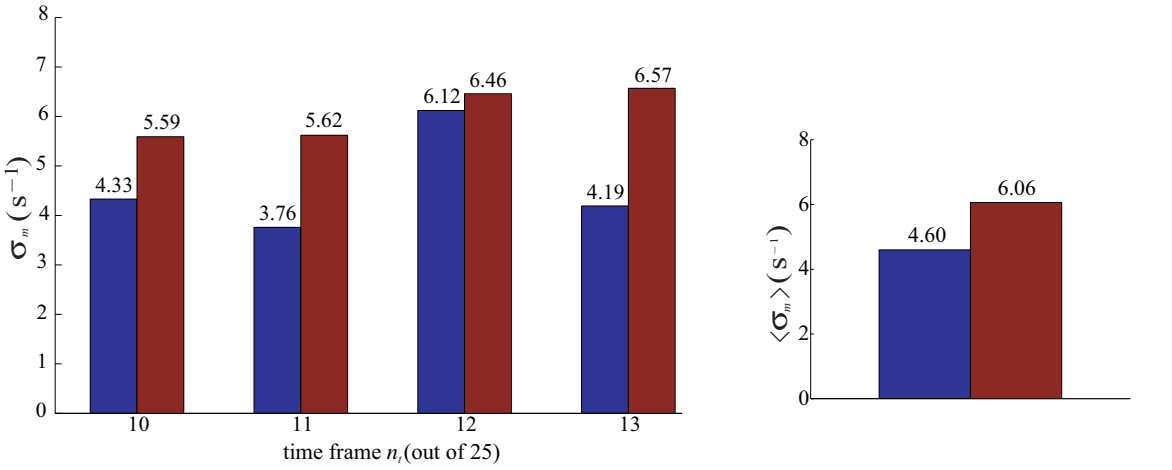

(i) Standard deviation σ_m based on $n_t = [10, 11, 12, 13]$ (ii) Temporal averaging of σ_m given by $\langle\sigma_m\rangle$

(d) Standard deviations from vorticity median for $n_t = 10$ to 13 and their temporally averaged values

Figure 8.10. Time-variation of vorticity properties for pre- and post-ASO flow maps. Ensemble measures of central tendencies such as mean $\overline{\omega}_\mu$ and median $\overline{\omega}_m$, shown in (a) and (b), as well as their standard deviations σ_μ and σ_m, shown in (c) and (d), are based on histograms of the vorticity maps pertaining to time frame indices $n_t = 10$ to 13 out of 25 frames in a cardiac cycle. Temporal averages of central measures and of standard deviations are given by $\langle\overline{\omega}\rangle$ and $\langle\sigma\rangle$ respectively. Both parameters are shown to be higher for post-ASO vorticity flow maps as compared to pre-ASO ones.

only a single vortex is expected to be present in the ideal case after surgical correction. This contributes to a higher absolute ensemble vorticity average and variance.

Figure 8.10 demonstrates the verification of results in Figure 8.9 that shows that, for case study of one patient with ASD, the vorticity mean and variance of the right atrial flow map for post-ASD closure are consistently higher for the selected phases than those for pre-ASD closure. This implies that there is an increase in their measures of central tendency following the appearance of a more well defined vortex and the disappearance of the multiple smaller vortices that has an opposite vortical flow. The temporal mean of these measures for $n_t = 10$ to 13 gives $\langle\overline{\omega}\rangle$, and the average of standard deviations based on the same time frames gives $\langle\sigma\rangle$. These statistical parameters have subscripts μ and m which denote mean and median respectively, and may be used reliably to gauge the relative strength of vortices in the atrium pertaining to the pre- and post-ASO conditions. The results in this study show that flow imaging and the statistics of vorticity maps at selected time frames of a cardiac cycle can be utilised to find a difference in flow patterns before and after surgical intervention.

8.7 Summary of Cardiac Investigation

We carried out the same experiments on the twenty-six patients. We will not display the flow images of all these patients due to the immense number of flow images involved. Moreover, it may be more effective to present the statistical flow characteristics to verify our flow analyses. Temporal averaging of the ensemble vorticity means based on four or more selected time frames (when the vortices are the strongest) is performed. The results can be summarised in Figure 8.11.

The higher strength of the vortices in the right atrium after an effective septal occlusion can demonstrate that the original vortical flow has indeed been disturbed in the event of left-to-right shunting of blood into the right atrial blood pool. This verifies our qualitative analyses in the previous chapters.

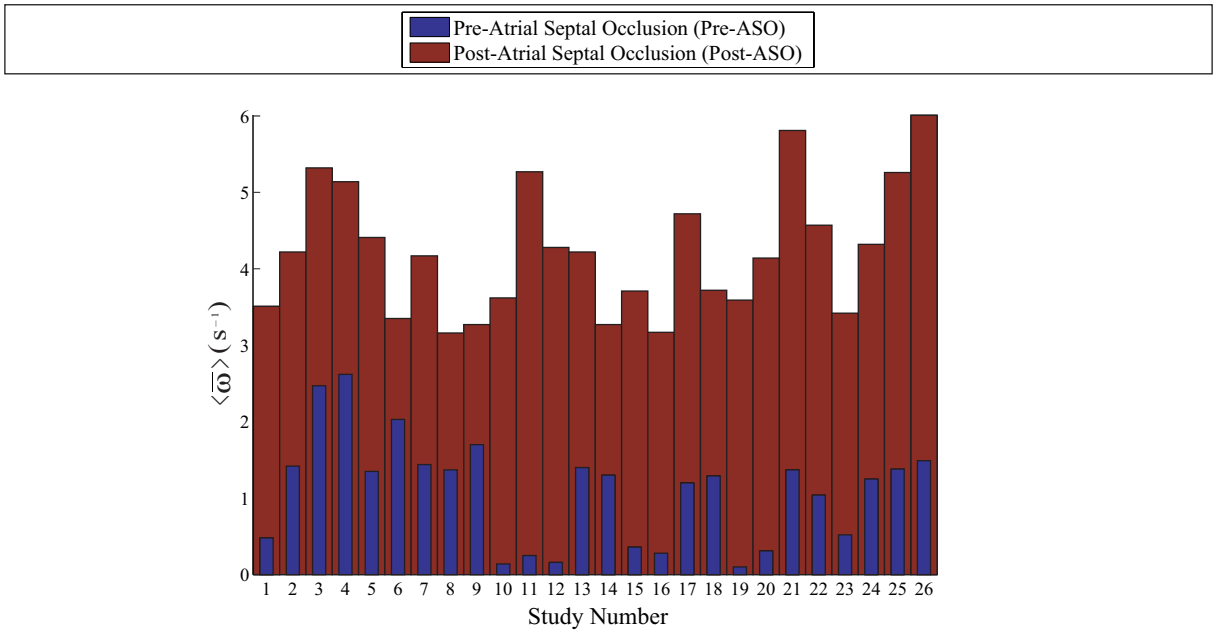

Figure 8.11. Summary of ASD investigation. The graph for pre- versus post-atrial septal occlusion.shows that there is a distinct difference between the temporal average of the vorticity means using a set of selected time frames. Twenty-six studies are performed using the framework presented in this study. This investigation may be able to show that the use of vorticity statistics is possible in characterising normal and abnormal flows in a heart chamber.

8.8 Discussion of Investigation

MRI measurements of blood flow in a heart chamber have been described as an illustration. Although one specific region (right atrium) is demonstrated by the results, the developed framework can be extended to assess flow in the other heart chambers or cardiovascular structures. It can conveniently predict flow information with superior processing speed to improve our understanding of blood motion within the heart, which may have implications in the study of blood circulation efficiency. This is extremely useful when MRI scanning is limited by the absence of a velocity-encoding protocol. The implemented study is neither to show with high accuracy the existence of vortices or flow structures in the cardiac chambers nor to verify what has already been established in earlier studies. Rather, it aims to highlight feasibility of the framework for visualising the flow as well as measuring or comparing vorticities, and with high system versatility to be executed on future batches of case subjects.

Some scan sets can be ineffective for fluid motion tracking. There are a variety of reasons for the inability to develop flow fields from them: such as low image resolution,

presence of ghosting artifacts due to respiration during scanning, and absence of vortices that are large enough to be quantified.

It is difficult to achieve high accuracy velocity mapping with low scan duration at the same time. The method that is proposed trades imaging speed with accurate flow field scanning, but still achieves the desired flow analysis for the cardiac abnormalities. This ultimately leads to flow evaluation for septal defect patients using the available steady-state free precession (SSFP) magnetic resonance images without performing the additional and time-consuming velocity-encoding MRI.

8.9 Chapter Summary

As an extension to well known medical imaging-based diagnostic and prognostic techniques discussed in the literature, we apply fluid motion tracking to magnetic resonance images, and perform flow quantification to analyse blood movement in an atrium based on the measured flow field. This is carried out after the visual examination of defective myocardium of these medical images. The results from this study have successfully proved the working principles of our proposed framework. As such, this technique offers potential for non-invasive flow visualisation in cardiac structures before and after septal occluder insertion for ASD patients.

We examine vorticity during the diastolic phase for a heart with an ASD pre- and post-atrial septal closure. Based on the calculations of vorticity, it is possible to measure the strength of vorticity that exists in the right atrium. This increases due to septal closure and may therefore be used as one of the components in the assessment of the ASD. The technique may also be used to assess growth of cardiac tissue into the mesh of the occluder by examining blood leakage through the ASD. As quantitative as well as qualitative data is provided for flow, it serves potentially as a diagnostic system for medical experts to assess surgical success or healing of septal defect over time.

The display of information using histograms of vorticity provides an overview of the swirl patterns by the blood flow. We discover that after ASD closure, vortices increase in magnitude scale. This is consistent with our investigation of all other ASD patients, although not presented here. Due to poor signals from moving blood, the tracking may depreciate in accuracy. Nevertheless, the framework gives some indication of swirl observed from the velocity field; and it has enabled us to assess the vorticity of flow within the heart chamber.

Chapter 9

Conclusion

CARDIAC flow imaging and analysis that is the main focus of this thesis, concentrates on a comprehensive coverage of research stages leading to the development, system testing and verification, and finally application of MRI velocimetry. It has now come to a stage of concluding the study and making suggestions for extending this work to produce improved results and reliability.

The broad range of implementation that is made has brought together the fields of magnetic resonance imaging, computer vision, and flow visualisation. It concentrates on the development of software algorithms towards the goal of a cardiac flow imaging and analysis system, and supports the underlying theory by concise computational and experimental validation of the implemented velocimetry system.

9.1 Introduction

Magnetic resonance imaging (MRI) has been widely accepted as a robust, reliable, reproducible and non-invasive scanning modality for assessment of structural and functional parameters for management of cardiac patients. As previously discussed, the clinical utility of MRI is based on its capability to assess morphological structures of heart and arteries, regional and global ventricular flow properties, cardiac perfusion as well as aortic or arterial flow data. In this thesis, we outline the design of a new framework for assessing flow functionalities as a parameter in diagnosing patients with heart problems, particularly structural defects. In addition, we are able to overlap both anatomical and functional data to give a more informative description of the flow with reference to morphology of the heart. The research has been successfully carried out to deliver flow assessment based on a new type of computational prediction from MR images. An application based on this methodology is implemented.

9.2 Thesis Summary

The primary aims of this thesis are specifically directed at validating a novel framework for post-processing magnetic resonance images with specific application in flow visualisation of blood within cardiac chambers of the heart. This involves the use of multi-resolution motion estimation onto SSFP MRI and confirmation of the capability in processing the flow field for characterisation and subsequent analysis of interesting flow phenomenon for diagnosis of cardiac problems, in particular, atrial septal defect. We term the introduced technique as *MR fluid motion tracking* as it is a system that performs computational tracking of fluid flow based on MRI.

An extensive review of the cardiac blood flow visualisation establishes the relevance of flow in heart as a functional parameter in the examination of cardiac health, and also access the conventional phase contrast MRI in flow imaging of chamber-blood. This imaging modality has been widely accepted for non-invasive flow quantification; nevertheless, scan times are undesirably long and like most other imaging modality, requires software components to process the velocity-encoded information in flow visualisation. The aim of this research is to develop an alternative technique for post-processing standard MRI without encoding velocity information on the scan images. This shifts some of the additional the work in physical scan processing time to computational time used for prediction of velocity-flow data. Since the latter processing

does not exhaust much time, the overall time from scanning to flow visualisation will be less than that for phase contrast MRI. Although, we sacrifice accuracy in flow field presentation for processing time, this does not pose significant problems for cardiac flow analysis. In practice, the optimal trade-off can be adjusted depending on the application.

In Chapter 2, we examine the theory of magnetic resonance imaging to be able to utilise important terminologies for usage throughout the thesis. This literature review provides a fundamental understanding of the medical imaging modality, establishes a theoretical description for the phenomenon that is observed in gray-scale imaging of cardiac blood, and paves the way that allows us to harness the unique properties of this observation in flow field prediction.

The review in Chapter 3 provides the theoretical and practical outlines of decoding MRI for presence of moving nuclear signal contrast and preparing velocity-data based on signal intensity flow. More importantly, the mathematical formulation of multi-resolution optical flow estimation allows us to gain a clear insight into the mechanics of MR fluid motion tracking system.

Chapter 4 mentions validatation of the computational accuracy of the proposed methodology using artificial image data generated. It provides definitive confirmation that velocity field by MR fluid motion estimation is accurate enough by processing the artificial images. It also describes the trend of accuracy and robustness subjected to parametric settings of the tracking system and image configurations.

A review on segmentation and flow region configuration of the heart is performed in Chapter 5. The description of active contour gives an outline of the energy balancing technique employed by the mathematical snake contour of the heart chamber. We note that two-dimensional segmented flow regions can be reconstructed into a three-dimensional scaffold for volumetric flow analysis.

Chapter 6 revises and describes the implementation of the system for flow visualisation and analysis to provide definitive confirmation of the proposed methodology. This provides the first step for application of the system onto real-life applicable MR data. Having discussed the theoretical ability of MR fluid motion estimation to perform cardiac flow visualisation, the next step will be to show that application of the methodology onto MRI scans of the heart can be successful. This is crucial in confirming the ability of MR fluid motion tracking in flow field prediction and characterisation of blood motion with heart chambers. In Chapter 7, the comparability of the MR fluid

motion tracker and phase contrast MRI provides compelling evidence that the proposed technique is promising for cardiac flow tracking.

Chapter 8 describes the work in managing atrial septal defect patients using cardiac MR fluid motion field information. In the case of examining patients with atrial septal defects, the characterisation of the flow and its utilisation can help to determine the seriousness of myocardial wall defect and its impact on flow behaviour.

Chapters 3 to 8 of the thesis are designed to permit a stepwise progression from examining intensity contrast in MRI as a potential property for enabling flow prediction, to the implementation of a tracking system applied to clinical cardiac MRI for analysis. This now sets the stage for future work in diagnosis of heart problems and we have now shown the potential for MR fluid motion tracking in cardiac management of atrial septal defect patients. Further studies are necessary to assess management of patients diagnosed with other heart diseases.

Appendix A gives a detailed presentation of the computing aspect of the software that is developed to present MR fluid motion fields, where ergonomics of Medflovan medical image processor is presented. Appendix B gives a detailed flow chart for retrieving MR images and processing them. The procedures outlined here can be used to perform further experiments related to cardiac flow imaging and analyses in future. Appendix C provides flow images of a healthy right atrium developed using phase contrast magnetic resonance imaging velocimetry. These results can be used as a reference for normal right atrial flow. Appendices D and E are flow results predicted by MR fluid motion tracking for right atria of defective hearts pre- and post-atrial septal occlusion respectively. We can observe the quality of flow image generation using this proposed methodology. Appendix F lists some of the video clips that illustrate MR imaging and the flow maps produced. These supplementary videos can assist concept understanding, and provides full details of some flow results. Appendix G demonstrates particle image velocimetry based on fluid motion estimation. This section shows that motion estimation can also be applied onto particle image data effectively.

9.3 Research Novelty

The inventive features of cardiac flow analysis system are described in this section. Each of these features on its own does not constitute useful clinical application, but

coupling of all the features together gives a working system and a unique framework that is useful in terms of research and clinical applications.

9.3.1 Motion Estimation of Degradable Non-Rigid Objects

In machine vision, optical flow has been applied on various images ranging from object differentiation to tracking of mobile items. Application of motion estimation on video sequences of images depicting objects of interests has been known to be able to trace boundaries of moving items or determine their motion field. These implementations allow motion tracking of rigid objects, and in most instances, it can be used for automated vehicle steering or human motion tracking.

Application of a multi-resolution motion estimation technique, such as the optical flow algorithm onto magnetic resonance imaging of heart can produce the magnetic resonance (MR) blood motion field. There are well-established studies describing motion estimation on computed tomography, magnetic resonance images, and ultrasonic scans that highlight morphological details of cardiac structures. However, these applications are directly targeted for myocardial wall segmentation. For example, optical flow is known to be workable on medical scans of the heart, which is deformable, elastic in size and shape, and is often used in medical imaging for myocardial wall tracking. While noting that there are new fluid motion estimation techniques that are developed recently (Cuzol *et al.* 2007), the same working principle of predicting flow motion is the same as the one applied in our framework. A cost function exists behind the mechanism of fluid motion estimating. It generates the direction and velocity of flow based on a series of image sequences depicting fluid flows.

It is important to note that current application of motion estimation are specifically workable for the items of interest that are non-degradable, and works best for rigid objects. In tracking of multiple targets that moves at different speeds and directions relative to one another, a multi-resolution optical flow can be applied. It is also realised in this research that on cardiac magnetic resonance images of heart chambers, volatile motional items such as agglomeration of nuclear signals from blood may degrade in intensities. Note that signal intensity of magnetic resonance is inversely related to image intensity. In many instances, nuclear blood signals may be moderated subjected to the increase in turbulence or emittance of non-gradient focused blood through-plane. The application of multi-resolution Lucas Kanade optical flow onto images of volatile

signals can give the blood motion field since MR signalling provides information on flow properties of the dynamic blood; where in this case, low MR signals can serve as tracking artefacts within the signal emitting blood. Nevertheless, this technique of tracking blood movement is limited in terms of accuracy due to the condition of tracking features subjected to changes in intensity temporally.

9.3.2 Measures from Cardiac Flow Field

The measurement of vorticity based on the cardiac flow field generated from either MR fluid motion tracking or phase contrast MRI velocimetry is performed. By characterising flow using these parameters, and statistically presenting them for every phase of the flow, we are able to extract more information from the flow model. Flow quantification needs to be carried out so that it can have research value and clinical usage. Note that no detailed and quantifiable flow analysis has ever been adequately documented from cardiac blood flow field for diagnostic usage. Even though it may be desirable to analyse the flow quantitatively using planar measurements, it will be inaccurate because the actual flow is three-dimensional. However, we demonstrate that examination and measurement in two-dimensional planes is sufficient in characterising cardiac abnormalities. Although transthoracic and transesophoegal echocardiography are now regarded as the standard for ASD assessment (Hirsch *et al.* 1994, Hoppe *et al.* 1996, Abdel-Massih *et al.* 2005, Kasliwal *et al.* 2005, Bartel *et al.* 2008, Roldán *et al.* 2008, Piatkowski *et al.* 2009, Skolnick *et al.* 2009), clinical trials will be the subject of a future study to show incremental value in using cardiac MRI flow analysis. Advancements in software support for magnetic resonance imaging technology can pave way for future diagnosis of cardiac defects by means of flow analysis within cardiac chambers.

9.3.3 Three-Dimensional Grid Reconstruction Using Images

Active contouring is currently used in the implementation of cardiac chamber segmentation. The flow field is displayed within the region of interest. Construction of multiple segmented flow field images into a scaffold of slices presents a volumetric flow grid that can be used to illustrate flow in three dimensions. Although this component of the system is not used during the flow visualisation implementation stage of the project, it may be worthwhile highlighting the technical description of it which may be harnessed for future flow analysis of much more complex nature. In fact, assessment in

cardiac pathologies can be more qualitative clinical use if three-dimensional flow data can be provided. However, at the current stage of research, we plan to establish a more solid foundation in the engineering and calibration of *MR fluid motion tracking* without expanding into more complexities. The extension of two dimensions into three dimensions can be carried out definitely. Special flow visualisation tools such as streamline tracing can be incorporated into the system to enhance flow display.

9.4 Generation of Interest to Scientific Community

This research entails the marriage of computer science, engineering and physics applied to medical engineering and analysis of a cardiac abnormality that will spin off interests among specialists in these fields. It also comprises of the development of a flow imaging system that has been validated against the well-established velocity encoded MRI framework. The statistical analysis developed in our case studies will have useful application on characterising patient's cardiac conditions such as septal defects, and can be used regardless of the flow imaging methods utilised. This may generate interest into the study of vortices in fluids that may be studied further by statisticians looking into fluid behaviour. In addition to that, the suggest flow imaging technology may have its place in off-line post-processing of magnetic resonance images or be incorporated into magnetic resonance scanners during its mature stage of development. This may influence radiographers that will benefit from the publication of this new method.

9.4.1 Clinical Relevance

The clinical relevance of intra-cardiac flow characteristics is critical. For example, pulmonary artery velocity measurements can evaluate cardiac conditions such as pulmonary hypertension, pulmonary stenosis and insufficiency, intracardiac shunts and congenital abnormalities (Gardin *et al.* 1988, Freedom *et al.* 2003). In addition, approximately 20% of cerebrovascular events have a cardiac source of embolis, and structural cardiac predictors (i.e. left atrium size and left ventricular function) are imperfect at identifying which patients are at risk. The ability to characterise intra-cardiac flow offers a new index that may provide risk predictors for certain individuals with embolic cardiovascular conditions. Clearly, further work is required to fully understand the normal range of intra-cardiac flow characteristics and to predict future embolic events.

9.5 Future Directions

The use of flow examination as a means of examining humans in terms of heart functions or diagnosis of patients with other heart problems can be further investigated as outlined in Chapter 1. In addition, *MR fluid motion tracking* can be used to analyse fluid motion patterns in mechanical flow systems. It has clear applicability in relation to the design and testing of biomedical devices such as artificial hearts or mechanical heart valves, for example, by maintaining a small difference in operation between the natural cardiac structures and prosthetic ones through examination of their blood flow patterns. It may even be used for widespread, non-biological applications where flow analysis is required, such as the analysis of fluid flow through mechanical devices or within hollow structures. The use of *MR fluid motion tracking* can be wide depending on the type of analysis required and has the advantage of imaging flow through opaque vessels. This attributes superiority over particle image velocimetry (PIV) technique which relies on the optics of the flow volume in retrieval of velocity data. However, the fall back of the technique is that no metals can be present in the construction of the flow test device. For the PIV technqiue, fluid motion estimation can also be applied onto particle images (Corpetti *et al.* 2006, Cuzol *et al.* 2007), and we demonstrate the utilisation of pyramidal Lucas Kanade optical flow for parametric motion field generation based on PIV data (Appendix G).

In relation to flow measurement within biological structures, the implementation of MR fluid motion tracking is only applicable to examining arteries if the resolution of the MR images is sufficient to capture MR blood signals sufficiently. The improvement of magnetic resonance imaging in terms of resolution will help to increase the accuracy of flow tracking since more signal features can be encoded within the images. Therefore, an important criterion is the required increment in pixel resolution of magnetic resonance imaging for micro scale arteries. However, this will come at the expense of computational cost, and lead to increased processing time.

It may be useful to improve the motion estimation algorithm for tracking of volatile fluid imaging. This may then help in enhancing the flow field tracking accuracy. Investigating the tracking of deformable objects (Palaniappan *et al.* 1995, Giachetti and Torre 1995, Giachetti and Torre 1996) can give us a better insight into improving fluid motion tracking, and the studies have shown that it is possible to obtain a meaningful optical flow of deformable liquids and gases. These techniques developed in computer vision may be worthwhile investigating and employing these algorithms as an

alternative to multi-resolution Lucas Kanade optical flow used in the MR fluid motion tracking system may be carried out.

Extension of magnetic resonance imaging to the study of flow phenomena is not new and can be applied to problems of direct relevance to multi-phase flow visualisation and analysis (Gladden 1994, Gladden and Alexander 1996, Akpa *et al.* 2007a, Akpa *et al.* 2007b, von der Schulenburg *et al.* 2008). The state-of-the-art in magnetic resonance flow imaging studies is previously discussed and the framework can be applied to investigate cardiac blood motion as well. Emerging technologies, such as magnetic resonance global coherent free precession (GCFP) (Rehwald *et al.* 2004), can provide a new platform for the usage of MR fluid motion tracking, which generates a potential scheme for cardiac flow tracking now and in the future. Such MRI protocols can be applied to blood spin labelling techniques for acquisition of multiple temporal slices of gray-scale intensity blood flow or cine-angiograms without a contrast agent and use of ionising radiation (Alsop 2007). Currently available segmentation techniques (Luo and Jin 2005) can be applied to quantify or visualise the magnetic resonance angiography (MRA) data. The movement of blood can be tracked as a result of processing such information using fluid motion estimation. Sample GCFP images provide information about vascular function and morphology just as steady-state free precession (SSFP) MR images do. Moreover, it provides with a more definite contrast of spin labelled dynamic blood into the non-spin labelled region because of the tagging of blood protons every few milliseconds as they travel through an arbitrary region in space.

Last, we note that although we have implemented the active contouring technique for segregration of cardiac chambers, other types of segmentation tools may exist to perform the same task more effectively. Moreover, the preferred segmentation is typically dependent on the imaging modality and the type of images obtained. For example, levels sets may be used for segmentation of neurological structures based on diffusion MRI (Jonasson *et al.* 2003, Jonasson *et al.* 2007) and also on defining the endocardium and myocardium in ECG-triggered MRI images (Paragios 2003, Fritscher *et al.* 2005). It may be worthwhile developing new techniques of cardiac segmentation to define the region of interest more effectively and efficiently. In addition, the use of three-dimensional contouring techniques based on volumetric MRI data grid (Ahlberg 1996,

Mille *et al.* 2007) may be more efficient and can perform better than the current two-dimensional active contouring method that we have implemented. It is also worthwhile noting that active contour technique may even be combined with the tensor-based orientation gradient force and velocity-encoded magnetic resonance imaging to develop a velocity-aided cardiac segmentation method (Choa and Benkeser 2006). Other methods such as atlas-based segmentation may also be applied to tracking three-dimensioanl cardiac MRI (Lorenzo-Valdés *et al.* 2002).

9.6 Summary of Original Contributions

We utilise a procedural approach to achieve the development of various tools described in this thesis. The documentation of a nuclear-based phenomenon related to the use of signal contrast from asynchonous proton spins during magnetic resonance imaging enables us to develop a novel tool for blood flow tracking. The harnessing of this new knowledge spurs forth the discovery of a new cardiac flow behaviour related to atrial vorticity. In addition, we use the implemented tracking methodology and this discovery to develop a cardiac diagnostics framework. Figure 9.1 shows the chain of events that generated the successful deliverables from our work.

The original contributions represented by this work are discussed in Section 1.7. In summary, the developed methodologies and/or frameworks include:

1. **MR fluid motion tracking.** Development of a cardiac flow tracking system has been demonstrated. The techniques and mathematical frameworks are described and thoroughly tested (Wong *et al.* 2009e). Tracking of temporal MR signals output, which corresponds to the blood motion, is performed using steady-state free precession MRI, followed by computational and experimental validation.

2. **Flow visualisation.** Methods for visualisation of cardiac flow within the anatomy are proposed and developed. We implement colour streamlines, velocity vector plotting and cardiac segmentation procedures for optimal display of flow structures effectively and efficiently. The techniques can be applied to flow fields generated by other flow-imaging modalities or simulation platforms (Wong *et al.* 2009b).

3. **Velocity-encoded MRI visualisation.** The phase contrast magnetic resonance images can be processed to develop high quality flow maps for analysis. We can

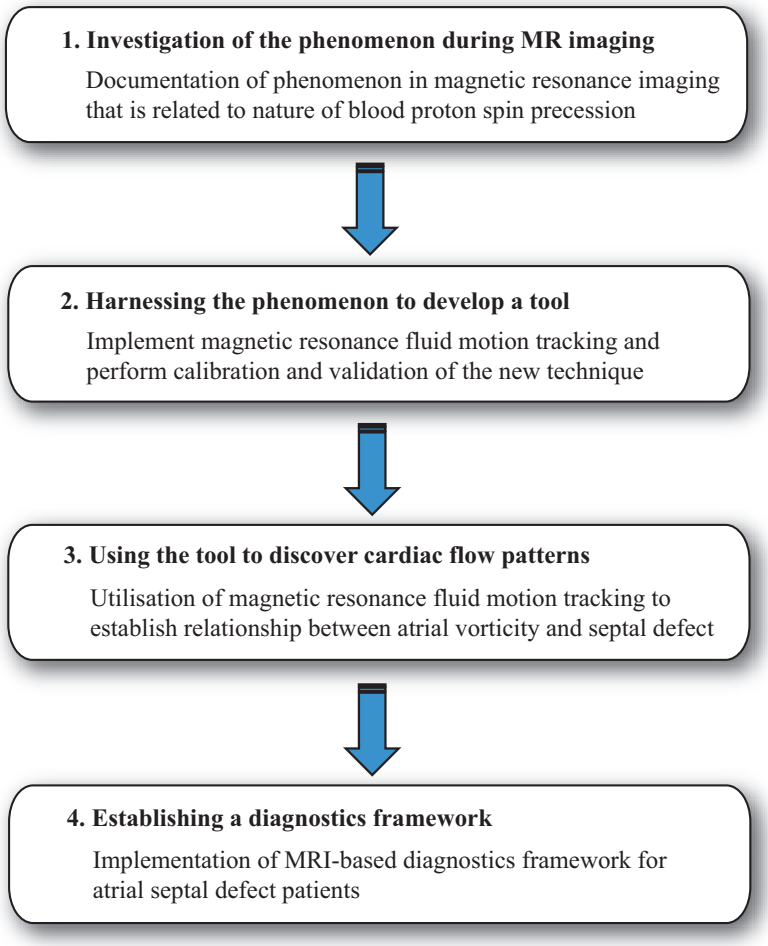

Figure 9.1. Stages leading to successful deliverables in the thesis. The stage-by-stage implementation of our tools and understanding of the new phenomena are systematically described by the block diagram. The nature of investigation and contributions made can be broken down into four important stages.

successfully develop a system for deciphering the velocity encoded information within the images and to map out the flow field for visualisation (Wong *et al.* 2009a). We have also used the generated flow results to validate those produced by *MR fluid motion tracking*.

4. **Flow analysis.** Flow analysis by devising measures of central tendencies and standard deviations can help us gain better insights into the vorticity flow fields. The quantification of these parameters can be used to assist fluid mechanics reseachers in examining differences in flow structures on top of qualitative tools such as flow visualisation methods (Wong *et al.* 2009d).

5. **Atrial vorticity and septal defect analysis.** The relationship between atrial vorticity and spetal defect is established using flow information generated by MR fluid motion tracking. The comparison of atrial blood rotation for pre- and post-atrial septal occlusion has been performed and discussed (Wong *et al.* 2009c). We can image vortices in a normal heart chamber using phase contrast MRI to contribute as reference information.

6. **Investigation procedures for cardiac anomalies.** We outline procedures and flow charts for scanning and information processing to achieve a reliable investigation of cardiac abnormalities such as septal defects. The technical details of effective scans and productive examination of patients are also suggested. The methodologies can be used on investigation of other cardiac abnormalities as well.

7. **Development of medical image processing software.** We develop a software system named Medflovan that facilitates all of our experiments. This system is capable of cardiac boundary segmentation, deciphering of phase contrast magnetic resonance images, motion tracking using steady-state free precession magnetic resonance images, flow analysis, and statistical report generation. More details of Medflovan is described in Appendix A. The system featuring and demonstration of this research tool can be referenced using Supplementary Videos 13 and 14 in CD-ROM, listed in Appendix F.

9.7 In Closing

With the technological advancement in medical imaging and analysis, there is born a wealth of industries to research and improve the technology for the investigation of cardiac functions, and for the upgrading of medical diagnosis. The current development of the *MR fluid motion tracking* system is still in its infancy and is severely limited in delivering accurate velocity information as compared to more established measurements, such as phase contrast MRI. This thesis has contributed to the progress by developing the post-processing architecture for MR signal motion tracking in order to establish a new flow imaging technology. Towards the goal of *MR fluid motion tracking* is novel research on two parallel fronts. The first concerns harnessing of signal contrast to perform motion tracking. Multi-resolution optical flow is adapted to apply on gray-scale intensity MR images. On the second front, a flow characterisation framework is

designed to develop flow and strain maps, and quantify flow behaviour in the heart chamber. The *MR fluid motion tracking* framework is also demonstrated in case studies focusing on cardiac analysis of atrial septal defect patients. These represent just a myriad of potential non-invasive cardiac flow measurement and analysis applications.

Appendix A

Software Implementation of Medflovan

MEDFLOVAN is the medical image processing (MIP) software that is developed by the author during the course of his PhD study with the intention to support medical image processing research. Its capabilities include imaging, computer vision and flow visualisation applications.

This appendix states the software components used to enable a system that reads in magnetic resonance images. The system can computationally produce flow field of blood in the heart based on fluid motion estimation, or decipher phase contrast velocity encoded information, and then generate the desired information for analysis. Included within the libraries are class functions to deal with interactive visualisation, region of interest segmentation and statistical analysis of blood flow within heart chambers. The software architecture integrating the supporting libraries will be described here. The list of user forms with their specifications and purposes are also detailed.

Software code listing will be limited in the thesis due to the immense size of the system implementation. However, description of its system architecture, libraries, software components and user manual is sufficient to describe this software concisely.

A.1 Imaging and Visualisation Computing Libraries

A.1.1 OpenGL

The OpenGL library was initiated by SGI as an Application Programming Interface (API) for the development of two and three-dimensional graphics applications. OpenGL is designed for high-performance graphics on multiple hardware platforms. The software utilises this library to display magnetic resonance images and to blend in flow measurement display such as velocity field, as well as vorticity and strain rates represented using colour maps.

The visualisation component of the Medflovan medical image processing (MIP) software comes with an interactive three-dimensional display of MR image grid stored in a matrix with five dimensions, namely, the orientation P, in-plane horizontal X, in-plane vertical Y, through-plane Z, and time frame T. The visualisation of the grid is operated by OpenGL driver components and its speed of display is dependent on the computing resources available.

A.1.2 OpenCV

The OpenCV library was initiated by Intel to develop a collection of algorithms for computer vision applications. The library is compatible with Intel Imaging Library

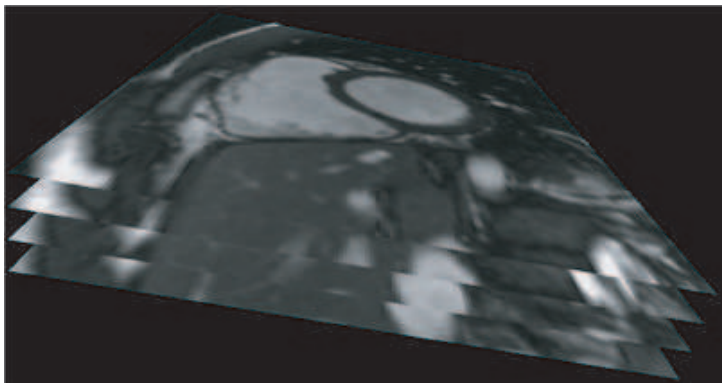

Figure A.1. Three-dimensional display of MR image planes. A display of gray-scale MR images can be achieved using OpenGL library implementation. Note that the morphological changes of the heart can be presented in media mode by updating the pixels of each slice temporally. Zoom-in and rotation capabilities are also built into the system. The software supports interactive display and update of slices in its temporal and spatial dimensions.

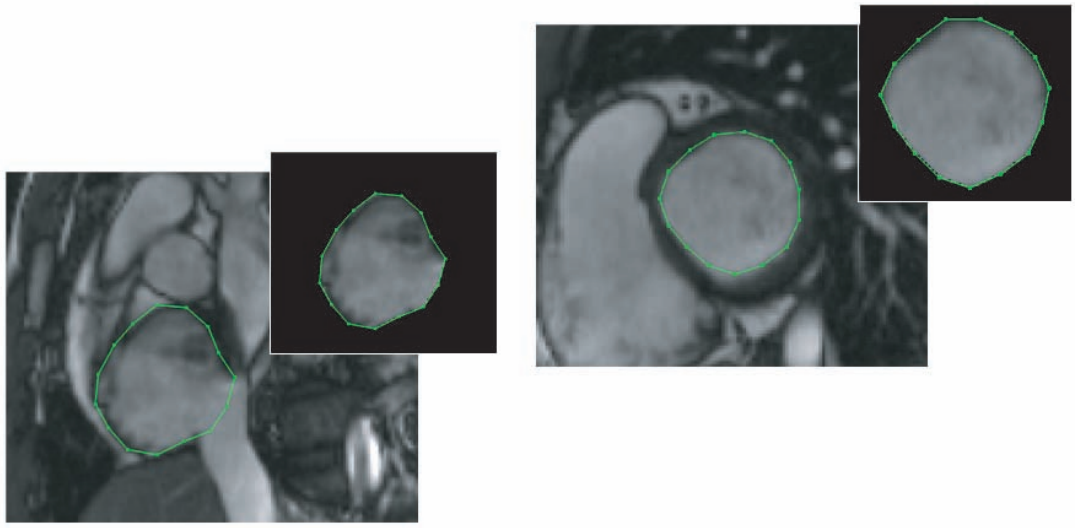

Figure A.2. Segmentation of cardiac chamber imaged by MRI. Segmentation of cardiac chambers based on MR images can be achieved using OpenCV library implementation. The enclosed boundaries of atrium and ventricle of heart has been defined as region of interests using active contouring by growing an expanding closed loop snake contour within the chamber. Placement and migration of nodes can be performed easily using the MIP segmentation template.

(IIL) and utilises Intel Integrated Performance Primitives (IPP) for high performance, thereby enabling it to focus mainly on real-time Imaging. The IPL includes functions for arithmetic and logical operations on images. It has a range of algorithms which include filters, morphological operators, geometric operators, statistics, Fourier transform, etc. OpenCV also consists of many algorithms relating to computer vision and runs cross-platform on various operating systems. The software development utilised applications on Segmentation and Motion Tracking algorithms in this library.[21] The mathematical framework for enabling cardiac segmentation is described in Section 5.2 (Chapter 5).

Flow maps can be generated with colour bar scales and superimposed medical images such as those pertaining to magnetic resonance images as illustrated in Figure A.3. The graphical outputs demonstrating the vorticity maps of the segmented flow can also be displayed without any background images. The flow results using such configurations are presented in various sections of the thesis (Chapters 5, 7 and 8).

[21] Active contouring is ultised by Medflovan medical image processing software for cardiac chamber segmentation.

MRI WITH CONTOUR MAPS

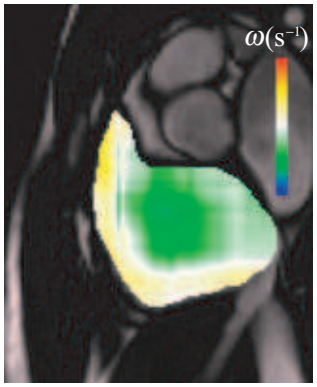

(a) Contour flood vorticity flow field

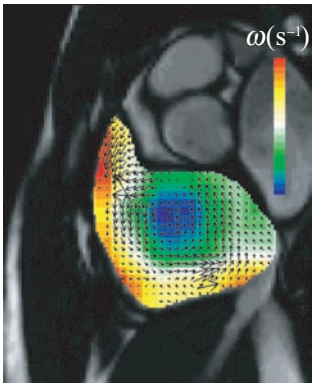

(b) Vorticity flow field with vector plot

SEGMENTED CONTOUR MAPS

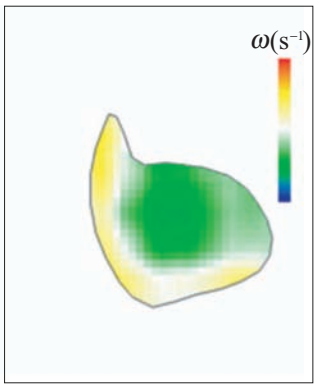

(c) Vorticity flow field without MR image

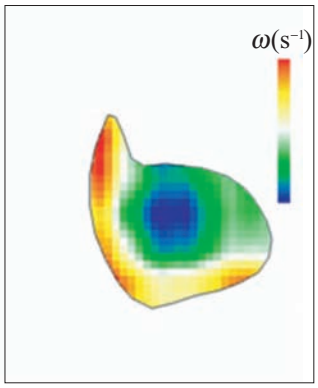

(d) Flow map with smaller bar scale limits

Figure A.3. Velocity and vorticity flow maps superimposed onto MR image. Computation of flow vectors and display using OpenCV library can present a two dimensional visualisation platform using Medflovan. The pyramidal optical flow algorithm has been utilised by the software in this example to show the vorticity of blood inside the dilated right atrium. The polarity of the vorticity can be inversed to display either blue or red for counter-clockwise vortex. In (a) and (b), the MR image of the heart can be superimposed onto the vorticity fields that can be presented using contour flood and/or vector flow maps. Adjustment of the vorticity bar scale limits can be performed to intensify the distinction of vorticity magnitudes in flow maps as illustrated in (c) and (d). The range of vorticity ω for each map ranges from -18 to 18 s^{-1}, and can be represented by the colour intensities from blue to red. Within the cardiac chamber, the white colour represents irrorational flow. Positive and negative values correspond to clockwise and counter-clockwise flows respectively. The vorticty values on the scale legend in the images are hidden as it is not our intention to analyse the vortical flow here.

A.2 DICOM Decoder Library

Two DICOM decoding libraries (DCMTK and TDICOMDecoder) are utilised in the implementation. Their system information are given briefly below:

DCMTK is a collection of ANSI C and C++ libraries and applications implementing DICOM decoding. Codes are implemented to run the DICOM decoder program in command script. This is an open-source library of version 3.5.4.

TDICOMDecoder is a library designed to read DICOM30, ACRNEMA10, ACRNEMA20 medical image files and extract tag information from it. It is developed using the Borland Delphi programming platform and is compatible with all Borland products. This is a commercial product. Its file list includes:

1. TDICOMDecoder[Prog][Ver].bpk

   This package exists in Delphi and C++ builder for [Prog] = 'D' and 'C' respectively and can support version number 5 and 6 depending on the value of field [Ver].

2. DICOMDecoderReg.pas

   This package registers TDICOMDecoder into the Delphi or C++ builder platform.

3. DICOMDecoder.pas

   This is main file executing the DICOM decoder.

4. DICOMDefines.pas

   This is the data type definition of the package.

5. DICOMDictionary.pas

   This is a dictionary file that includes tag groups and elements from DICOM3.0

A.3 The Medflovan Software Architecture

Medflovan is a software technology that enables flow visualisation by processing magnetic resonance images (MRI) offline. The name MEDFLOVAN or Medflovan is based on the extraction of alphabets from the description: MEDical FLOw Visualisation and ANalysis software. Medflovan supports image and flow grid visualisation, imaging

and measurement analysis functionalities. It is specifically designed to create a platform for investigation of blood behaviour in the heart by enabling quantitative analysis of the cardiac flow using interactive image visualisation and quantitative analysis based on statistical characterisation of flow maps. Medflovan is created during the course of this thesis to provide flow measurements based on standard gated-MRI datasets. It is a system that can assist biomedical engineers and doctors in characterising cardiac flow structures.

Medflovan is developed using an objected-oriented programming platform. An image mapping class is developed for visualisation of MRI data. It utilises a segmentation class component for active contouring and region definition, as well as a computer vision component for flow field computation and assessment. A statistic class component has been implemented for flow analysis that allows histograms of flow distribution in image maps to be plotted.

This section focuses on building the architecture of the Medflovan software which includes the package and use case diagram (Figure A.4 and Figure A.5) that is helpful for clarifying the functionality of the software system. The package diagram demonstrates how the forms and library components are integrated together. This provides a clear overview of software implementation and operation. The use case model bridge the gap between user requirement and system functionality by presenting the user intention and system response for each step in a particular interaction. This model is important for designer and end user to identify the specific functionality and design.

A.3.1 Package Diagram

Figure A.4 presents the integrated components of forms in the Medflovan package. The display of its structure can help to identify the relationship between each and every form used. By demonstrating how the forms and library components are integrated together, it provides a concise description of software implementation and operation.

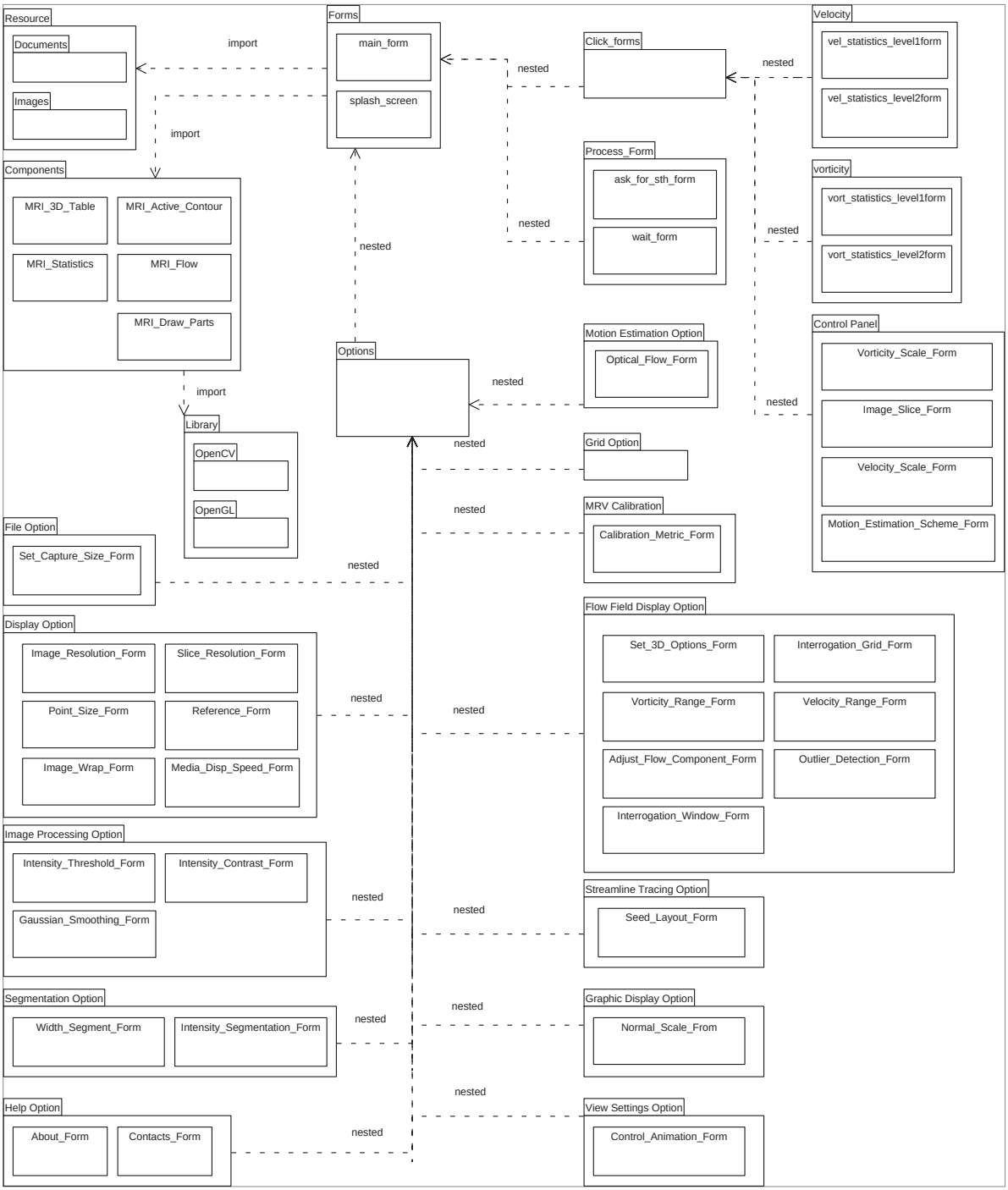

Figure A.4. Medflovan package diagram. This diagram illustrates all the linkages between the class forms and their inter-relationships. These forms are integrated together to allow ease of data entry and selection of format during flow map generation and other operations. Ergonomics with relation to ease of program use has been taken into account during the design of these forms.

A.3.2 Use Case Diagram

Medflovan system is composed of five subsystems: image grid visualisation, segmentation, flow grid generation, and statistics generation. There are two primary users for our system: data entry personnel, and analyst. The overview of the use case model demonstrates interaction between the primary users and the system user interface. This model is helpful for examining the detailed functionality in each subsystem.[22] The program is designed in such a way that it assists the investigation of atrial septal defect outlined in Chapter 8 of this thesis.

Actors

1. Data Entry Personnel: This staff inputs the unprocessed MR images into Medflovan and backups the processed flow information.
2. Analyst: This staff imports the flow data files into Medflovan and prints out the cardiac flow maps based on single/multiple selected flow formats.

Use Case

Load Image

Use Case Identifier: load image
Description: Import image into Medflovan Control Panel system
Actors: Data entry personnel
Assumptions: MR images format is compatible with import formats of Medflovan
Pre-condition: User can use this system
Triggers: User clicks the *load image* button
Steps:

1. User select directory where MR images are stored
2. Program loads images into system
3. User crop section of image that illustrates cardiac flow
4. User set up session for processing of images

[22] Diagrams in unified model language (UML) are generated using Poseidon for UML SE 6.0.2.

Post-condition: Program stores MR image data

Segment Image

Use Case Identifier: segment image
Description: Segment image using Medflovan Control Panel platform
Actors: Data entry personnel
Assumptions: MR images loaded into Medflovan system
Pre-condition: User selects image slice and phase
Triggers: User clicks the *Region* tab in control panel of software
Steps:

1. User activates *Trace Region Contour* or *Insert Region Contour* checkboxes
2. User inserts nodes onto MR image displayed on screen
3. User adjusts nodes to define region boundary on screen
4. User saves contour information as segment information

Post-condition: Program stores active contour grid

Calculate Flow

Use Case Identifier: calculate flow
Description: Process MR image into flow image grid
Actors: Data entry personnel
Assumptions: MR images loaded into Medflovan Control Panel system
Pre-condition: User set parameters for flow calibration
Triggers: User activates the *Differential Flow* selection in control panel of software
Steps:

1. User activates relevant motion estimation algorithm checkbox to use
2. User adjust motion estimation algorithm parameters

Post-condition: Program stores flow image grid

Show Statistics

Use Case Identifier: show statistics
Description: Process flow maps to obtain histogram statistics
Actors: Data entry personnel
Assumptions: Flow map grid stored into Medflovan Control Panel system
Pre-condition: User set parameters for computing histogram statistics
Triggers: User clicks the *Vorticity* tab in control panel of software
Steps:

1. User activates *Display Graph* checkbox
2. User adjusts the *Bin Number* slider bar to vary the histogram resolution

Post-condition: Program saves statistics grid and plots histogram pertaining to flow map

Plot Flow

Use Case Identifier: plot flow
Description: Plot flow maps
Actors: Data entry personnel
Assumptions: Flow image grid stored into Medflovan Control Panel system
Pre-condition: User set parameters for displaying flow map plot
Triggers: User clicks the *Vorticity* tab in control panel of software
Steps:

1. User activates *Velocity*, *Vorticty*, *Shear Strain* or *Normal Strain* checkboxes
2. User activates the *Vel*, *Vort*, *SS* or *NS* checkboxes to display flow map on screen
3. User adjusts the velocity scale and interrogration frame window size to display flow map aesthetically

Post-condition: Program plots flow map grid

Plot Segment

Use Case Identifier: plot segment
Description: Plot segment nodes and contour lines

Actors: Data entry personnel
Assumptions: Active contour grid stored into Medflovan Control Panel system **Post-condition:** Program plots active contour grid

Save Segment

Use Case Identifier: save segment
Description: Save segment nodes
Actors: Data entry personnel
Assumptions: Active contour grid stored into Medflovan Control Panel system
Pre-condition: User views segment contour as acceptable
Triggers: User clicks the *Segmentation* system menu of software
Steps:

1. User activates *Save Contour Grid*

2. User enters filename for segment data to be saved

Post-condition: Program saves segmentation grid in a file

Save Flow

Use Case Identifier: save flow
Description: Save flow velocity and differential flow data
Actors: Data entry personnel
Assumptions: Flow image grid stored into Medflovan Control Panel system
Pre-condition: User views flow map as acceptable
Triggers: User clicks the *File*$->$*Save* system menu of software
Steps:

1. User selects *Save Flow Field* under the *Save* subsystem menu

2. User enters filename for flow data to be saved

Post-condition: Program saves flow map grid in a file

Save Statistics

Use Case Identifier: save statistics
Description: Save histogram statistics data
Actors: Data entry personnel
Assumptions: Statistics grid stored into Medflovan Control Panel system
Pre-condition: User views histogram settings as acceptable
Triggers: User double clicks the histogram plot in control panel of software to display a second level form depicting the histogram plot.
Steps:

1. User double clicks histogram plot in the second level form to display a third level form
2. User clicks on *Save Statistics in Excel*
3. User enters filename for statistical data to be saved

Post-condition: Program saves statistics grid in a file

Select Slice

Use Case Identifier: select slice
Description: Use a single/multiple selection of slices from the full range
Actors: Data entry personnel, Analyst
Assumptions: MR image grid stored into Medflovan Control Panel system
Pre-condition: User performs segmentation and/or single-slice flow analysis
Steps:

1. If user update current slice, EXTENSION update image
2. User double clicks *Image* button to display the *Image Slice Adjustment* menu
3. User adjusts two *Slice Truncation Z* slider bars to truncate the non-selected slices from bottom up and top down directions

Post-condition: Program replots image for only selected slice

Select Phase

Use Case Identifier: select phase
Description: Use a single/multiple selection of phases from the full range
Actors: Data entry personnel, Analyst
Assumptions: MR image grid stored into Medflovan Control Panel system
Pre-condition: User performs segmentation and/or single-phase flow analysis
Steps:

1. If user update current slice, EXTENSION update image
2. User clicks on *Forward* and *Backward* buttons to traverse the phases

Post-condition: Program replots image for only selected phases

Choose Flow Format

Use Case Identifier: choose flow format
Description: Choose desired flow display format depending on analysis requirements
Actors: Analyst
Assumptions: Flow map grid stored into Medflovan Control Panel system
Pre-condition: User plots flow map on display
Steps:

1. If user update flow format, EXTENSION update image
2. User activate *Contour flood* or *Contour lines* checkboxes
3. User activate/deactivate *Velocity* and *Vel* checkboxes

Post-condition: Program replots image based on flow format

Update Image Display

Use Case Identifier: update image display
Description: Plot MR image and/or flow maps depending on selected slice, phase and display format
Actors: Data entry personnel, Analyst
Assumptions: MR image and/or flow map grid stored into Medflovan Control Panel

system
Pre-condition: User plots MR image and/or flow map on display
Steps:

1. If user update flow format, EXTENSION update image
2. If user select slice, EXTENSION update image
3. If user select phase, EXTENSION update image
4. Program refresh the main panel display screen

Post-condition: Program replots image based on selected slice, phase and flow format

Load Flow

Use Case Identifier: load flow
Description: Import flow data files into Medflovan Control Panel system
Actors: Analyst
Assumptions: Flow data file format is compatible with import formats of Medflovan
Pre-condition: User can use this system
Triggers: User clicks the *load flow file* button
Steps:

1. User select directory where flow data files are stored
2. Program loads flow image grid into system
3. User crop section of image that illustrates cardiac flow
4. User set up session for processing of images

Post-condition: Program stores flow image data

Load Segment

Use Case Identifier: load segment
Description: Import segment data files into Medflovan Control Panel system
Actors: Analyst

Assumptions: Segment data file format is compatible with import formats of Medflovan
Pre-condition: User can use this system
Triggers: User clicks the *load segment file* button
Steps:

1. User select segment data file
2. Program loads segment contour grid into system
3. Optionally, user increase opacity of image that lies outside segment

Post-condition: Program stores segmentation contour data

Print Flow

Use Case Identifier: print flow
Description: Print flow maps onto graphics file for evaluation of flow
Actors: Analyst
Assumptions: Flow image grid stored into Medflovan Control Panel system
Pre-condition: User set parameters for displaying flow map print
Triggers: User clicks the *File*$->$*Print* system menu of software
Steps:

1. User selects *Print Flow* under the *Print* subsystem menu
2. User enters filename for flow map to be printed

Post-condition: Program prints flow map display in a file

Load Statistics

Use Case Identifier: load statistics
Description: Import statistics data files into Medflovan Statistics Panel subsystem
Actors: Analyst
Assumptions: Statiatical data file format is compatible with import formats of Medflovan
Pre-condition: User can use this system
Triggers: User clicks the *load statistics file* button
Steps:

1. User select statistics data file
2. Program loads statistics grid into system
3. User activates *Display Graph* checkbox
4. Optionally, user adjust colour and drawing format of histogram bar display

Post-condition: Program stores statistics data

Update Graph Display

Use Case Identifier: update graph display
Description: Plot histogram graph depending on selected slice, phase and display format
Actors: Analyst
Assumptions: Statistics grid stored into Medflovan Statistics Panel subsystem
Pre-condition: User plots statistics using histograms on display
Steps:

1. If user update histogram format, EXTENSION update graph display
2. Program refresh the Medflovan Plot Statistics subpanel display screen

Post-condition: Program replots histogram based on drawing format

Print Histogram

Use Case Identifier: print histogram
Description: Print histogram onto graphics file for evaluation of flow
Actors: Analyst
Assumptions: Statistics grid stored into Medflovan Statistics Panel subsystem
Pre-condition: User set parameters for displaying histogram print
Triggers: User clicks the *File*$-$ $>$*Print* system menu of software
Steps:

1. User selects *Print Histogram* under the *Print* subsystem menu
2. User enters filename for histogram to be printed

Post-condition: Program prints single/multiple histograms in a file

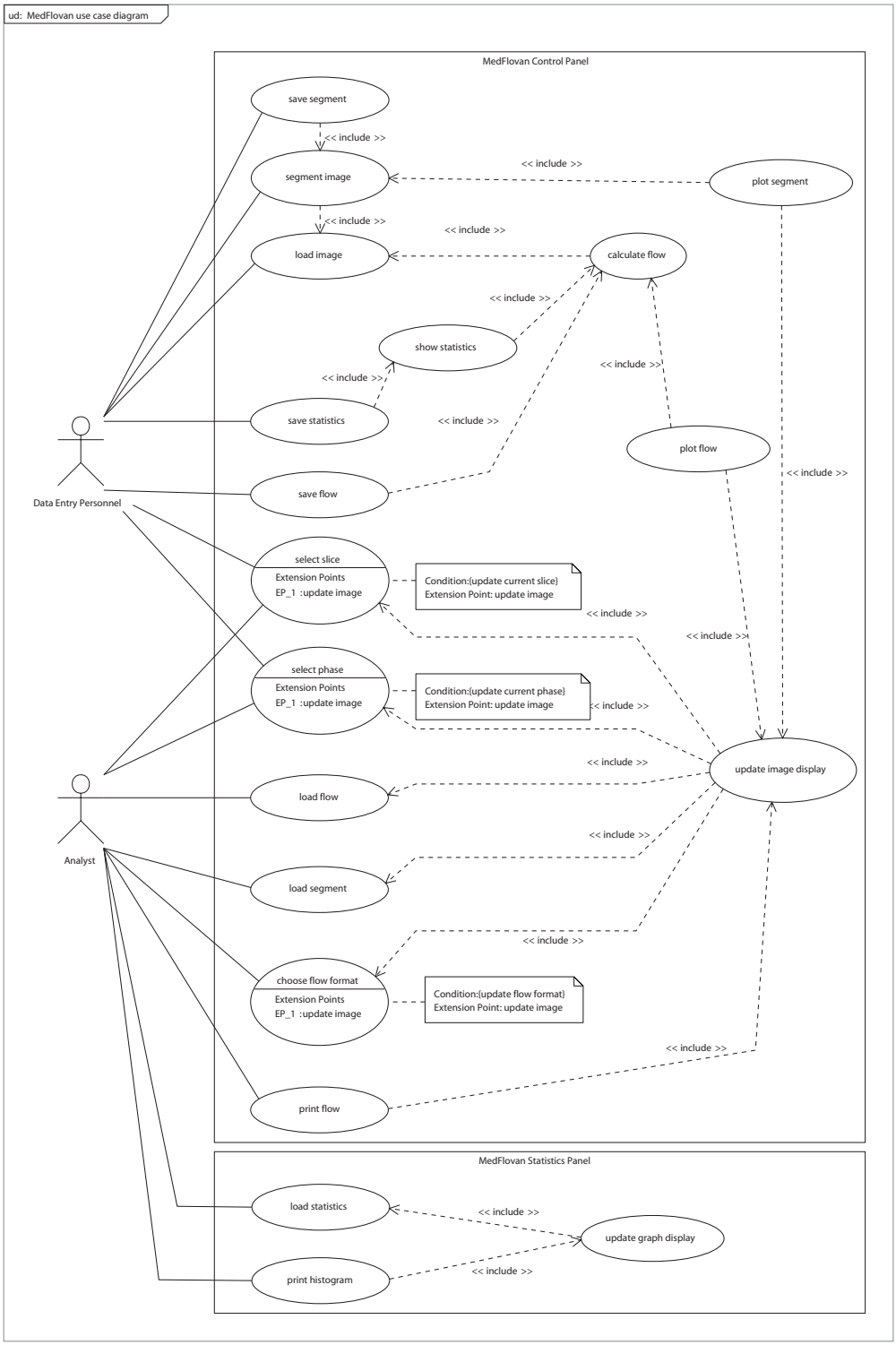

Figure A.5. Medflovan use case diagram. The application use case diagram allows a clear overview of software in terms of user functions and actors involved. Two primary actors, one for data entry and the other for analyst of information processed are required. The model illustrates how the operators work by entering the MR images into the system and processing them to print the desired flow maps with reference to the use cases.

A.3.3 Component Class Diagrams

This section lists all the classes and its associated attributes. There are five main component classes in the system. These classes are listed as follows:

1. MRI_3D_Table_class
2. MRI_Active_Contour_class
3. MRI $_{F}low\_classMRI\ _{S}tatistics\_class$
4. MRI_Draw_Parts_class

They operate engines of the software with specialisations in *Visualisation*, *Segmentation*, *Flow Measurements*, *Flow Statistics* and *Plotting* respectively. They comprise of procedures that carry out specific functions to perform image grid display, active contouring and segmentation, flow measurements, calculation of statistical measures of histograms, and plotting of flow and image elements.

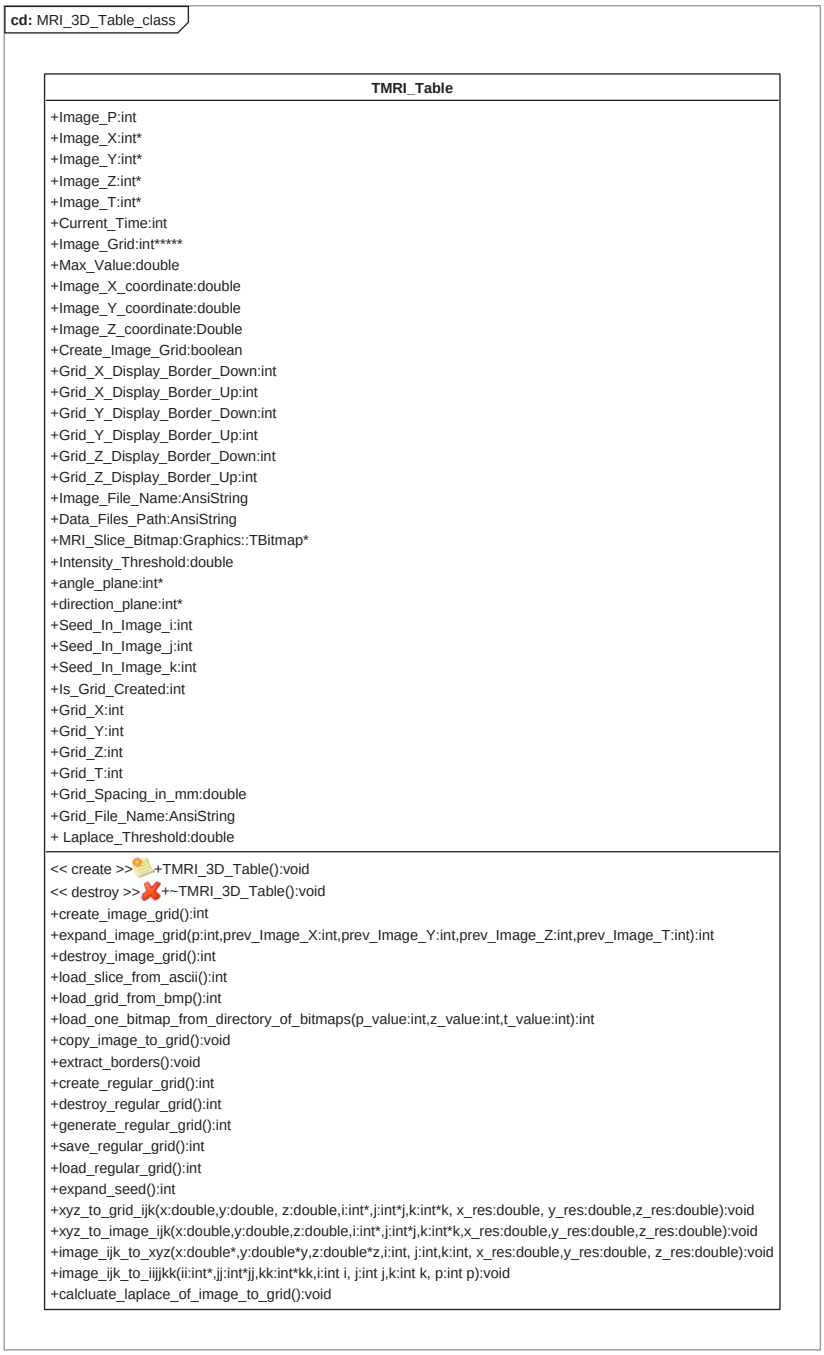

Figure A.6. TMRI_Table class. Medflovan software is supported by five main class components that controls the velocity field computation, visualisation and display, as well as statistics of the flow. Out of the five classes, the one that is presented here performs the memory allocation and storage of magnetic resonance image data.

Figure A.7. TMRI_Active_Contour, TMRI_Statistics and TMRI_Draw_Parts classes. These classes perform the segmentation of cardiac chambers, computation of statistical quantification of flow and the visualisation display of flow fields and images respectively.

Figure A.8. TMRI_Flow class. This class component performs the velocity field computation based on motion tracking of magnetic resonance fluid or decipher flow information from phase contrast images for flow reconstruction.

Some sample codes in C++ programming language are presented as well. However, we highlight that these is a small section of the entire software framework developed. We find difficulty in displaying all of the forms, source, header and project files that are system components of the programming architecture required to compile the medical image processing software Medflovan. Therefore, as an illustration, we describe only

some of the functions that are used for the key operations. These codes can be found in the following class components of Medflovan.

MRI_3D_Table_class

MRI_3D_Table_class is specially written to store MR image data in a matrix grid of integer type for up to five dimensions, namely, the slice orientation labelled as P, in-plane horizontal dimensions as X and Y, through-plane dimension as Z, and the time dimension as T. The loading of image slices, spatial and intensity calibration, plotting and truncation of MR pixels with interactive display capabilities is controlled by functions from this class component. Variable expansion of the matrix grid is incorporated to conserve memory storage for display of MR image grid by the *expand_image_grid* function. Clicking on a displayed pixel on the screen interactively can assess the display of pixel properties such as dimension, intensity and orientation in a form.

MRI_3D_Table_class: Initialisation of Image Grid

```
void TMRI_3D_Table::create_image_grid()
{
    // Allocate memory for image grid up to 5 dimensions
    Image_Grid = (int*****) malloc((unsigned)(Image_P)*sizeof(int***));
    for( int p=0; p<Image_P; p++)
    {
        Image_Grid[p] = (int****) malloc((unsigned)(Image_X[p])*sizeof(int***));
        if (!Image_Grid[p])
            exit(0);
    }
    for (int p=0; p<Image_P; p++)
    for (int i=0; i<Image_X[p]; i++)
    {
        Image_Grid[p][i] = (int***) malloc((unsigned)(Image_Y[p])*sizeof(int**));
        if (!Image_Grid[p][i])
            exit(0);
    }
    for (int p=0; p<Image_P; p++)
    for (int i=0; i<Image_X[p]; i++)
    for (int j=0; j<Image_Y[p]; j++)
    {
        Image_Grid[p][i][j] = (int**) malloc((unsigned)(Image_Z[p])*sizeof(int*));
        if (!Image_Grid[p][i][j])
            exit(0);
    }
    for (int p=0; p<Image_P; p++)
    for (int i=0; i<Image_X[p]; i++)
```

```
    for (int j=0; j<Image_Y[p]; j++)
    for (int k=0; k<Image_Z[p]; k++)
    {
        Image_Grid[p][i][j][k] = (int*) malloc((unsigned)(Image_T[p])*sizeof(int));
        if (!Image_Grid[p][i][j][k])
            exit(0);
    }
    // Reset grid initialisation condition
    Exist_Image_Grid = true;
}
```

MRI_Active_Contour_class

This class component is responsible for performing active contouring and also comes with manual contour insertion capabilities. An active contour represented by a snake can have up to five dimensions, which are the orientation P, the slice Z that it lies on, the time frame T, that are represented in integers and the in-plane X and Y coordinates which are of CvPoint data type definition by OpenCV library. Expansion of the contour is executed by *calculate_active_contour* that activates the boundary detection of a cardiac chamber by the energy minimisation technique. The segmentation of the contour is executed by implementing point in polygon detection using the function *point_polygon_test*, which controls the pixel properties pertaining to segmentation regions. The final snake can be saved as a segment boundary using *save_segment* and loaded into the display platform using *load_segment*. Variability in snake creation is rendered possible depending on the number of image slices loaded and segments can be destroyed to release memory if the segmentation option is deactivated.

MRI_Active_Contour_class: Initialisation of Active Contour Grid

```
void TMRI_Active_Contour::TMRI_Active_Contour()
{
    // Allocation of memory
    Image_P = 3;
    Image_Z = (int*) malloc((unsigned)(Image_P)*sizeof(int));
    Image_T = (int*) malloc((unsigned)(Image_P)*sizeof(int));
    // Temporary initialisation of matrices
    for (int p=0; p<Image_P; p++)
    {
        Image_Z[p] = 2;
        Image_T[p] = 1;
    }
    // Initialise the vectors
```

```
    Create_Image_File_List = false;
    create_image_file_list();
    // Maximum number of 80 contour nodes allowed
    snk = new CvPoint[80];
}
```

MRI_Flow_class

The flow vector grid is presented by two in-plane flow matrices $Velx$ and $Vely$ which comes in five dimensions P, X, Y, Z, and T that is similar to the configuration of the image grid. Therefore the use of terminology for image grid and vector grid are interchangeable since the flow information is represented in the Cartesian coordinates system like an image. Using the same strategy for efficient memory utilisation, flow image grid can be varied in its dimensions depending on the orientation, numbers and sizes of image slice loaded into the program by the user. The grid is destroyed to release memory space if the checker box selection for display of flow grid is deactivated

The computation of flow vectors using motion estimation can be executed by running the functions depending on the type of optical flow algorithm utilised:

1. *calculate_optical_flow_Lk*
2. *calculate_optical_flow_HS*
3. *calculate_optical_flow_BM*
4. *calculate_optical_flow_PryLk*

The procedure *remove_outliers_from_velocity_grid* is implemented to remove vectors whose magnitudes are exceptionally large enough to exceed a specific threshold set by the user (which is typically the maximum distance that blood can possibly travel in between two cardiac time frame). The void vector is then replaced by the average of vectors within the interrogation window.

MRI_Flow_class: Initialisation of Velocity Grid

```
void TMRI_Flow::create_velocity_grid()
{
    int Region_Size_TrackBar_Max = 33;
```

```
    // Check grid initialisation condition
    if (Create_Velocity_Grid == false)
    {
        // Expand merged velocity x grid
        Vel_x_matrix = (double**) malloc((signed)(Image_X+(2*Region_Size_TrackBar_Max-1))*sizeof(double*));
        for ( int i=0; i < Image_X+(2*Region_Size_TrackBar_Max-1); i++)
            Vel_x_matrix[i] = (double*) malloc((signed)(Image_Y+(2*Region_Size_TrackBar_Max-1))*sizeof(double));
        // Expand merged velocity y grid
        Vel_y_matrix = (double**) malloc((signed)(Image_X+(2*Region_Size_TrackBar_Max-1))*sizeof(double*));
        for ( int i=0; i < Image_X+(2*Region_Size_TrackBar_Max-1); i++)
            Vel_y_matrix[i] = (double*) malloc((signed)(Image_Y+(2*Region_Size_TrackBar_Max-1))*sizeof(double));
    }
    // Reset grid initialisation condition
    Create_Velocity_Grid = true;
}
```

MRI_Flow_class: Initialisation of Velocity Range Array

```
void TMRI_Flow::create_flow_grid()
{
    max_Vel = (double**) malloc((unsigned)(Image_P)*sizeof(double*));
    // Expand maximum velocity storage grid
    for (int p=0; p<Image_P; p++)
        max_Vel[p] = (double*) malloc((unsigned)(Image_Z[p])*sizeof(double));
    min_Vel = (double**) malloc((unsigned)(Image_P)*sizeof(double*));
    // Expand minimum velocity storage grid
    for (int p=0; p<Image_P; p++)
        min_Vel[p] = (double*) malloc((unsigned)(Image_Z[p])*sizeof(double));
    // Initialisation of velocity storage grid
    for (int p=0; p<Image_P; p++)
    for (int k=0; k<Image_Z[p]; k++)
    {
        min_Vel[0][0] = -0;
        max_Vel[0][0] = +100;
    }
}
```

MRI_Flow_class: Calibration of Velocity Grid Based on S.I. Metrics

```
// Calculates the new velocity grid based on merging of arrows with an interrogation grid
void TMRI_Flow::scale_velocity_grid_SI_metrics(int p_value, int z_value, int Image_X, int Image_Y,
    double**** Vel_x, double**** Vel_y, double Pixel_Spacing_X, double Pixel_Spacing_Y,
    double Trigger_Time_Interval)
{
    // Thickness of one layer
    int k = z_value;
    int p = p_value;
    // Scale velocity magnitude for every pixel of dense velocity grid
```

```
    for (int i=0; i<Image_X; i++)
    for (int j=0; j<Image_Y; j++)
    {
        // Calibrate in units of mm/s
        Vel_x[p][i][j][k] = Vel_x[p][i][j][k]*((Pixel_Spacing_X*1000.0)/Trigger_Time_Interval);
        Vel_y[p][i][j][k] = Vel_y[p][i][j][k]*((Pixel_Spacing_Y*1000.0)/Trigger_Time_Interval);
    }
}
```

MRI_Flow_class: Scaling of Velocity Grid

```
// Scale differential flow grid
void TMRI_Flow::scale_differential_flow_grid(int p_value, int z_value, int Image_X, int Image_Y,
    double** Flow, double min_Flow, double max_Flow, double set_min_Flow, double set_max_Flow)
{
    // Thickness of one layer
    int k = z_value;
    int p = p_value;
    if (max_Flow-min_Flow == 0)
    return;
    // Scale velocity magnitude for every pixel of dense velocity grid
    for (int i=0; i<Image_X; i++)
    for (int j=0; j<Image_Y; j++)
    {
        Flow[i][j] = ((Flow[i][j]-min_Flow)/(max_Flow-min_Flow))*(set_max_Flow - set_min_Flow);
        Flow[i][j] = ((Flow[i][j]-min_Flow)/(max_Flow-min_Flow))*(set_max_Flow - set_min_Flow);
    }
}
```

MRI_Flow_class: Renewal of Velocity Grid Based on Updated Resolution

```
// Calculates the new velocity grid based on merging of arrows with an interrogation grid
void TMRI_Flow::vector_average_velocity_grid(int p_value, int z_value, int Image_X, int Image_Y,
    int d, int D, double**** Vel_x, double**** Vel_y, int** Img_Mask)
{
    // Thickness of one layer
    int k = z_value;
    int p = p_value;
    // Offsets the flow velocity grid so that it lies in the centre of the image
    int interrog_win_size = (2*D+1);
    int sampling_win_size = (2*d+1);
    // Assign zero velocity magnitude for every pixel of temporary velocity grid
    // A frame of width equal to the boundary of pixels for the sampling window included
    for (int ii=0; ii<Image_X/interrog_win_size+(sampling_win_size-1); ii++)
    for (int jj=0; jj<Image_Y/interrog_win_size+(sampling_win_size-1); jj++)
    {
        // Assign zero velocity values to matrices
        Vel_x_matrix[ii][jj] = 0.0;
```

```
            Vel_y_matrix[ii][jj] = 0.0;
        }
        // Determine velocity magnitude for every pixel
        for (int ii=0; ii<Image_X/interrog_win_size; ii++)
        for (int jj=0; jj<Image_Y/interrog_win_size; jj++)
        {
            // Convert matrix index (offset by one neighbourhood interrogation window)
            int i = (ii*interrog_win_size + D) + grid_offsetX1;
            int j = (jj*interrog_win_size + D) + grid_offsetY1;
            // Initialise merged velocity grid
            double Velx = 0.0;
            double Vely = 0.0;
            // Calculate sum of each arrow about the inspected pixel
            for (int x=-D; x<=D; x++)
            for (int y=-D; y<=D; y++)
            {
                // Extract neighbourhood velocity magnitudes
                double Vx = Vel_x[p][i+x][j+y][k];
                double Vy = Vel_y[p][i+x][j+y][k];
                // Euclidean distance of vector away from centre of interrogation window (IW) is computed
                // Vectors that are further away from the centre of IW are given a lower weighting during averaging
                double weight = (double) max((sqrt(2.0*pow(D,2.0)) - sqrt(pow(x,2.0) + pow(y,2.0))),1.0);
                // Averaging of arrows within current IW
                Velx = Velx + weight*Vx;
                Vely = Vely + weight*Vy;
            }
            Velx = Velx / (2*D + 1);
            Vely = Vely / (2*D + 1);
            // Assign zero values to neighbour pixels in inspected window
            for (int x=-D; x<=D; x++)
            for (int y=-D; y<=D; y++)
            {
                Vel_x[p][i+x][j+y][k] = 0.0;
                Vel_y[p][i+x][j+y][k] = 0.0;
            }
            // Assign arrow values to centre pixel in inspected window
            Vel_x[p][i][j][k] = Velx;
            Vel_y[p][i][j][k] = Vely;
            // Assign merged velocity arrows to the velocity grid (excluding the boundary width)
            Vel_x_matrix[ii+d][jj+d] = Velx;
            Vel_y_matrix[ii+d][jj+d] = Vely;
        }
        // Assign zero velocity magnitude for border pixels
        for (int i=d; i<Image_X; i++)
        for (int j=d; j<Image_Y; j++)
        {
            if (i>=Image_X-grid_offsetX2||j>=Image_Y-grid_offsetY2||i<grid_offsetX1||j<grid_offsetY1)
            {
                Vel_x[p][i][j][k] = 0.0;
                Vel_y[p][i][j][k] = 0.0;
            }
        }
}
```

MRI_Flow_class: Destruction of Velocity Range Array

```
void TMRI_Flow::destroy_flow_grid()
{
    // Release maximum velocity storage grid
    for (int p=0; p<Image_P; p++)
        free ((int*) (max_Vel[p]));
    free ((int**) (max_Vel));
    // Release minimum velocity storage grid
    for (int p=0; p<Image_P; p++)
        free ((int*) (min_Vel[p]));
    free ((int**) (min_Vel));
}
```

MRI_Flow_class: Destruction of Velocity Grid

```
void TMRI_Flow::destroy_velocity_grid()
{
    int Region_Size_TrackBar_Max = 33;
    // Check grid initialisation condition
    if (Create_Velocity_Grid == true)
    {
        // Delete merged velocity x grid
        for ( int i=0; i < Image_X+(2*Region_Size_TrackBar_Max-1); i++)
            free ((double*) (Vel_x_matrix[i]));
        free ((double**) (Vel_x_matrix));
        // Delete merged velocity y grid
        for ( int i=0; i < Image_X+(2*Region_Size_TrackBar_Max-1); i++)
            free ((double*) (Vel_y_matrix[i]));
        free ((double**) (Vel_y_matrix));
    }
    //Reset grid initialisation condition
    Create_Velocity_Grid = false;
}
```

Phase contrast magentic resonance imaging velocimetry can be performed by executing *calculate_phase_contrast_flow*. This function takes in at least two sets of MR images and deciphers the intensity pixels to derive the velocity flow fields based on the cardiac scan.

The MRI_Flow_class component class also comes with vorticity, shear strain and normal strain computation that creates a colour map display of these differential velocity values stored using a flow image grid. The *calculate_differential_flow_image_grid* uses the previously processed velocity grid and numerically determines the differentiation

with respect to the X and Y dimensions. These data can also be exported out of Medflovan and may be imported into a third party program, such as Tecplot (developed by Amtec Engineering, Inc), for flow visualisation. Nevertheless, Medflovan can also output flow images based on various visualisation tools implemented. The visualisation package that we have designed is more suited for medical image and cardiac flow applications.

MRI_Statistics_class

MRI_Statistics_class deals mainly with the statistical aspects of the flow characteristic that is predicted by Medflovan. The statistics of differential flow is generated via use of histogram plots of the flow or strain map values. Properties such as mean, quartile, median, standard deviation as well as the maximum and minimum values of the map are computed. The histogram, as well as this statistical information, can be displayed using TChart library package incorporated in Borland C++ platform. The data depicting these statistics can be exported out into Microsoft Excel spreadsheet format.

MRI_Statistics_class: Calculation of Statistical Properties

```
void TMRI_Statistics::Graph_Display(Tvort_statistics_level1form* vort_statistics_level1form)
{
    int p = Main_Form1->p_value;
    int Bin_Number;
    double X_Interval;
    double Series1_Lower_Limit, Series1_Upper_Limit,
           Series2_Lower_Limit, Series2_Upper_Limit,
           Series3_Lower_Limit, Series3_Upper_Limit;
    int Series1_Bin[100], Series2_Bin[100], Series3_Bin[100];
    double Series1_X_Val[100], Series2_X_Val[100], Series3_X_Val[100];
    double min_Rot, max_Rot, min_SS, max_SS, min_NS, max_NS;
    double max_Rot_Val, max_SS_Val, max_NS_Val, max_Val;
    Graph_Reset(vort_statistics_level1form);
    if (Main_Form1->Disp_Graph_CheckBox2->State==cbChecked)
    {
        //Set initial number of bins
        Bin_Number = vort_statistics_level1form->Bin_Number_TrackBar->Position;
        //Determine minimum and maximum vorticity and strain rates values
        min_Rot = Main_Form1->min_Rot;
        max_Rot = Main_Form1->max_Rot;
        max_Rot_Val = max(abs(min_Rot), abs(max_Rot));
        min_SS = Main_Form1->min_SS;
        max_SS = Main_Form1->max_SS;
        max_SS_Val = max(abs(min_SS), abs(max_SS));
```

```
            min_NS = Main_Form1− >min_NS;
            max_NS = Main_Form1− >max_NS;
            max_NS_Val = max(abs(min_NS), abs(max_NS));
            max_Val = max(max(max_Rot_Val, max_SS_Val), max(max_SS_Val, max_NS_Val));
            //Series 1
            min_Rot = -max_Val;
            max_Rot = +max_Val;
            //Series 2
            min_SS = -max_Val;
            max_SS = +max_Val;
            //Series 3
            min_NS = -max_Val;
            max_NS = +max_Val;
            //Traverse for every bin
            for (int Curr_Bin = 0; Curr_Bin < Bin_Number; Curr_Bin++)
            {
                //Series_bin[] records how many pixels in current bin
                //Series_X_Val records current x position in X Axis
                Series1_Bin[Curr_Bin] = 0;
                Series2_Bin[Curr_Bin] = 0;
                Series3_Bin[Curr_Bin] = 0;
                Series1_X_Val[Curr_Bin] = 0;
                Series2_X_Val[Curr_Bin] = 0;
                Series3_X_Val[Curr_Bin] = 0;
                //Traverse every pixel of window
                for (int j = Main_Form1− >min_win_y; j < Main_Form1− >max_win_y; j++)
                for (int i = Main_Form1− >min_win_x; i < Main_Form1− >max_win_x; i++)
                {
                    //Apply Segmentation Mask
                    //Neglect counts for pixels that lies outside segment
                    if (Main_Form1− >Img_Mask[p][i][j] == 1)
                    {
                        //Update histogram series
                        Main_Form1− >Add_Series_Bin[Curr_Bin]
                    }
                }
            }
            Graph_Display(vort_statistics_level2form);
        }
}
```

MRI_Draw_Parts_class

The last stage of program execution is the graphical display of the processed information pertaining to the magnetic resonance, velocity, and differential flow image grids. The pixels of these maps are displayed using polygon drawing by OpenGL library package. Segmentation boundaries represented by the active contouring of cardiac walls can be graphically plotted during semi-automatic segmentation procedures using line drawing by the same graphics library. This library also controls

three-dimensional display of these polygons and lines. In addition, simple image processing capabilities such as intensity thresholding and colour scaling of flow maps with colour bar display is also made available by this component class. In summary, MRI_Draw_Parts_class component deals mainly with only graphical aspects of the program using the input and processed data generated by the other class components.

MRI_Draw_Parts_class: Plotting of Vector Using OpenGL

```
inline static TMRI_Draw_Parts::Draw_3D_Arrow_Head(double x_pt1, double y_pt1, double z_pt1,
    double x_pt2, double y_pt2, double z_pt2)
{
    double x_pt3,y_pt3,z_pt3,x_pt4,y_pt4,z_pt4;
    double arrow_length = sqrt( pow((x_pt2-x_pt1), 2) + pow((y_pt2-y_pt1), 2));
    double tip_length = 0.5*arrow_length;
    //Angle that the arrow on the plane makes in the x-y base
    double angle = atan2((y_pt2-y_pt1), (x_pt2-x_pt1));
    //Angle of planes affects the transformation of arrows
    double transform_x, transform_y, transform_tip1_x, transform_tip1_y, transform_tip2_x, transform_tip2_y;
    transform_x = +cos(angle);
    transform_y = +sin(angle);
    transform_tip1_x = +cos(angle + M_PI / 8);
    transform_tip1_y = +sin(angle + M_PI / 8);
    transform_tip2_x = +cos(angle - M_PI / 8);
    transform_tip2_y = +sin(angle - M_PI / 8);
    //Dimensions of arrow head
    x_pt3 = (double) (x_pt2 - tip_length * transform_tip1_x);
    y_pt3 = (double) (y_pt2 - tip_length * transform_tip1_y);
    z_pt3 = (double) z_pt2 - (tip_length/arrow_length)*(z_pt2 - z_pt1);
    x_pt4 = (double) (x_pt2 - tip_length * transform_tip2_x);
    y_pt4 = (double) (y_pt2 - tip_length * transform_tip2_y);
    z_pt4 = (double) z_pt2 - (tip_length/arrow_length)*(z_pt2 - z_pt1);
    //Draw Arrow Head
    glBegin(GL_QUADS);
    glLineWidth (0.5);
    glVertex3f(x_pt2, y_pt2, z_pt2);
    glVertex3f(x_pt3, y_pt3, z_pt3);
    glVertex3f(x_pt4, y_pt4, z_pt4);
    glVertex3f(x_pt2, y_pt2, z_pt2);
    glEnd();
}
```

Appendix B

Procedures for MRI Preparation and Processing

CARDIAC flow investigation procedures for atrial septal defect (ASD) patients are detailed in this appendix. They describe the process of performing MRI and decoding of MR images from DICOM format to graphic files for post-processing of patient scans pre- and post-surgical intervention.

All the procedural components, along with their critical specifications and execution are listed in point format for the user. A flow chart has been created for ease of reference and usage.

B.1 MRI Equipment

Cardiac SSFP MR imaging is performed using a Siemens Sonata, 1.5 Tesla, model–syngo MR 2004A scanner with Numaris–4, Series No: 21609 software. For phase contrast VENC MR imaging, the Siemens Avanto, 1.5 Tesla, model-syngo MRB15 scanner with Numaris-4, Series No: 26406 software is used.

For DICOM decoding and viewing of scan images, the syngo MultiModality Workplace station is used. The usage of Siemen's syngo software applications can be referenced using the syngo MultiModality Workplace operator manual (Siemens 2007). Flow investigations are performed using Medflovan medical imaging software outlined in Appendix A.

B.2 Imaging and Analysis Procedures

The flowchart presented in Figure B.1 provides an illustration of the procedures for the investigation of ASD. Each procedural step is described in point form and provides a guide for the radiologists and/or investigators in its execution. Flexibility in adjustments of the steps can be made or additional operations can be incorporated into this activity depending on the configuration of the machines and setup used in the facilities. The flowchart is designed to guide the medical imaging, processing of velocity vector field information and analysis of the vortical flow information for investigation of atrial vorticity in relation to septal defects (Chapter 8).

1. Steady-state free precession imaging (SSFP)[23] is performed using contiguous slices in short axis two-chamber orientation through the heart. Alternatively, the phase contrast MR imaging protocol can be used if it is available. All images can be acquired with retrospective gating and a typical number of 25 phases (or time frames) for each slice are obtained. Acquisition parameters may be different for scans of pre- and post- occlusion of ASD. The scanned images are loaded into Siemens syngo MultiModality Workplace system. The MultiModality Workplace is a stand-alone evaluation system that can be embedded in a workplace network.

2. The cardiac abnormality is further verified by viewing the cine-MRI of the patient using media player incorporated within the system. The subjects with cardiac

[23]The True Fast Imaging with Steady-state Precession (True FISP) imaging protocol is provided by the Siemens MRI scanner.

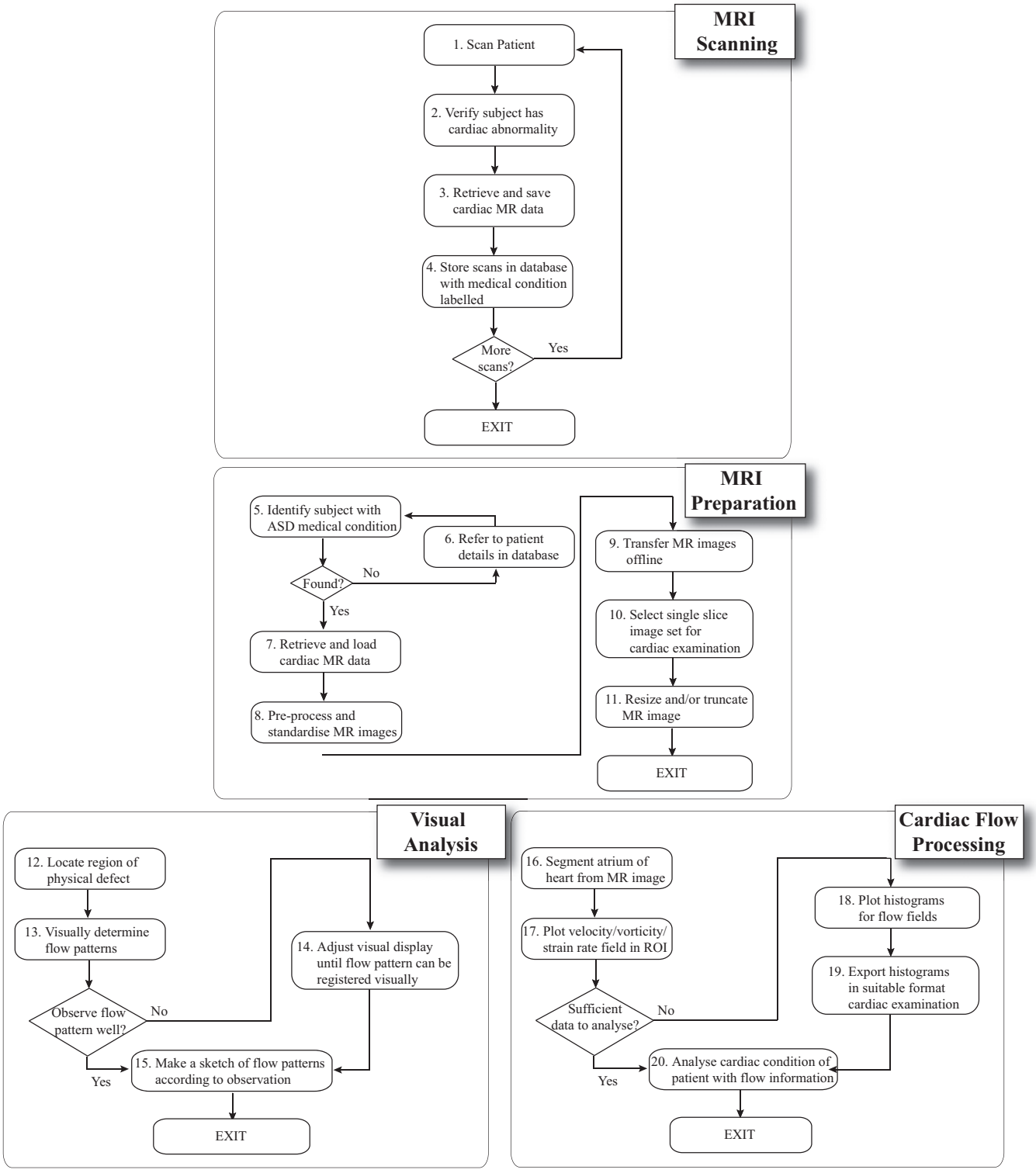

Figure B.1. Flow chart for guiding investigation of cardiac abnormalities. A flow chart for MRI preparation and processing pertaining to those of cardiac patients is presented for systematic retrieval of cases and analysis of flow behaviour in heart. The breakdown of the cardiac investigation into stages allows a clear understanding of the rationale behind each activity and provides clear instruction for running them.

abnormalities (ASD) can be identified based on morphological defects such as the discontinuity of the atrial septum and/or dilation of the right atrium. Left-to-right shunting of blood through the septal defect can be observed by playing the cine-MRI.

3. The scanned images in DICOM format are transferable to a removable storage device (i.e. CD-Rs/DVD-Rs and CD/DVD drives, magneto-optical discs and drives, or diskette drives) for storage and transfer. The syngo Media Viewer, which is a DICOM viewing application, can be burned to CD or DVD so that imaging studies can be viewed on personal computers. Images may then be processed offline without the MR scanner in operation.

4. Patient particulars and scan records are entered into a patient database. With the labelling of scan information, future retrieval of cases pertaining to the different types of cardiac condition can be performed by labelling the cardiac condition field accordingly.

5. A new database of ASD patients is to be created for study.

6. Retrieval of cases pertaining to ASD is performed by referencing the database of patients who underwent scans. In this activity, subjects with severe ASD are to be identified using the cardiac condition labels of the general patient database.

7. When a patient is identified from the database, records and images pertaining to scans are extracted for data preparation and post-processing. The scanned images may be reloaded into the syngo MultiModality Workplace system.

8. A section of each image is cropped from MR scans pertaining to all the phases at user-specified regions of interest. Due to the truncation in size, the image decreases in resolution to maintain a size with the same dimensions as the original one. Range of gray-scale intensity for all images is standardised. The images are converted into graphic files in BITMAP format. Alternatively, they may remain as DICOM format depending on the image format dictated by the medical imaging application.

9. The prepared MR images can be transferred out of the work station by means of a removable storage device or through a network cable. The user may now exit the syngo MultiModality Workplace software.

10. The region of defect is examined. The extent of ASD is recorded. The size of the defect can be measured and calibrated in S.I. units. The abnormal dilation of the right atrium is noted. Any other anomalies are observed and recorded.

11. The right chamber is selected for observation. The temporal velocity flow field within the segmented chamber region of interest (ROI) is deduced heuristically.

12. The visual display rate is adjusted the registration of motion by human perception is optimal.

13. A manual sketch of the flow patterns is carried out. This gives an illustration of the general flow.

14. The MR images are loaded into Medflovan, and the images of the slice that dissects the left and right atria, showing the atrial septal defect (ASD), are selected for processing. This slice will demonstrate the abnormal cardiac flow through the ASD. The regions showing the right atria are truncated to the same dimensions for all images to prepare for flow visualisation.

15. The images for pre- and post-septal occlusion are standardised at the same sizes (i.e. 156×192 pixels) in order to maintain consistency during computation and analysis.

16. The region of defect is examined and the extent of the ASD is recorded. The size of the defect can be measured and calibrated in S.I. units. The abnormal dilation of the right atrium is noted. Any other anomalies are observed and recorded.

17. The right chamber is selected for observation. The temporally varying flow pattern within the segmented chamber region of interest (ROI) is deduced heuristically.

18. The visual display rate is adjusted so that the registration of motion by human perception is optimal.

19. A manual sketch of the flow patterns may be prepared to give an illustration of the general flow.

20. Within the Medflovan platform, the atrium of the heart for all images are segmented manually using external peripheral attached to the computer by tracing

a contour along the edge of the atria wall. Alternatively, a closed loop active contour can be planted within the chamber and interactively expanded to fit along the boundary of the endocardium.

21. The temporal velocity flow field within the segmented chamber region of interest (ROI) is plotted either on its own or superimposed onto gray-scale intensity MR image to show blood flow with reference to myocardial morphology. The computed flow maps can be displayed using animated sequences of flow maps (by means of media player incorporated within Medflovan) for flow pattern investigation.

22. Frequency graphs or histograms depicting the measures of vorticity, shear strain and normal strain is presented optionally. They show the characteristic distribution of the examined flow parameter within the segmented region of interest. The means and variances of these histograms versus time frame index are optionally plotted.

23. Information on the velocity, vorticity, shear strain and normal strain provides an indication of the flow characteristics within the heart chamber, and can be exported out to electronic spreadsheets for reference. The flow information is used to compile a case study report of the patient. This comprises of the patient's information, atrial blood flow vorticity field plots, and charts for pre- and post- ASD occlusion scans pertaining to every time frame. The user may exit Medflovan software after that.

24. The observation of ASD can be based on the flow fields as well as quantitative and qualitative measures in the report. The patient is analysed by comparing the vorticity level against a specified threshold to determine his cardiac condition. A strategy for cardiac management of the patient can be devised based on the case study report. This is transferred electronically or in hard copy document to medical professionals for investigation.

Appendix C

Flow Visualisation of Blood in Normal Atrium

CARDIAC cardiac magnetic resonance image scans of heart in short axis orientation are presented here. The vorticty flow maps and histograms are displayed as well. This information can give an indication of the flow condition within the right atrium of a healthy human subject. Variation in tracking configuration such as sampling window size onto three different phases of the cardiac cycle is performed for the generation of the flow maps to illustrate the degree of smoothing vorticity information.

This section presents a series of flow images to demonstrate the nature of right atrial vorticity within a normal heart. They can be used as a reference for analysing vorticity maps for a heart with atrial septal defect. A set of figures that shows the vorticity map differencing between fields produced by the MR fluid motion tracking and the phase contrast magnetic resonance imaging techniques is also included with a reduced version presented in Section 7.6 of the thesis.

NORMAL SUBJECT

COLOUR STREAMLINE PLOT **VECTOR & CONTOUR MAP** **HISTOGRAM**

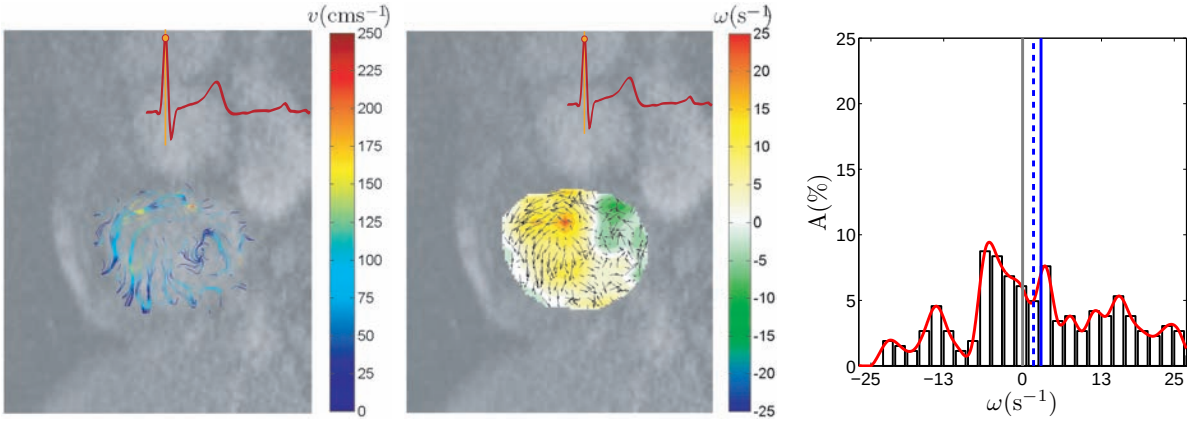

(i) $n_t = 1, \begin{bmatrix}\overline{\omega}\\ \sigma\end{bmatrix}_{\mu} = \begin{bmatrix}5.41\\ 6.29\end{bmatrix}\mathrm{s}^{-1}, \begin{bmatrix}\overline{\omega}\\ \sigma\end{bmatrix}_{m} = \begin{bmatrix}4.94\\ 6.31\end{bmatrix}\mathrm{s}^{-1}, \Gamma = 19.43\mathrm{m}^2\mathrm{s}^{-1}$

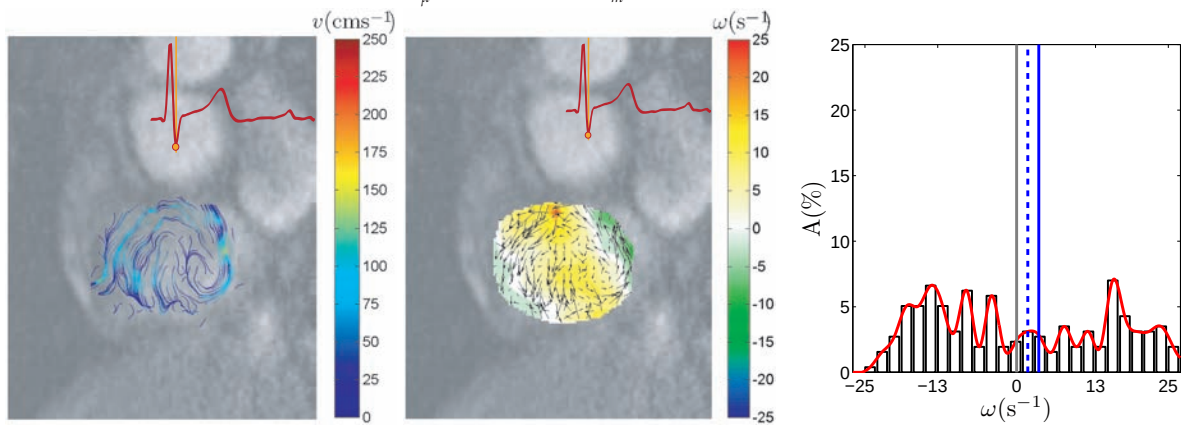

(ii) $n_t = 2, \begin{bmatrix}\overline{\omega}\\ \sigma\end{bmatrix}_{\mu} = \begin{bmatrix}5.63\\ 5.65\end{bmatrix}\mathrm{s}^{-1}, \begin{bmatrix}\overline{\omega}\\ \sigma\end{bmatrix}_{m} = \begin{bmatrix}5.88\\ 5.65\end{bmatrix}\mathrm{s}^{-1}, \Gamma = 19.19\mathrm{m}^2\mathrm{s}^{-1}$

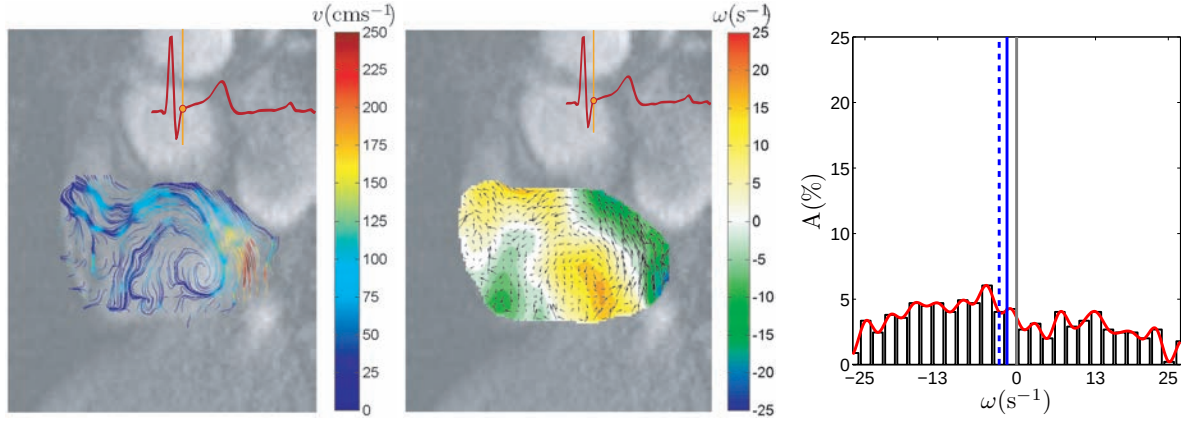

(iii) $n_t = 3, \begin{bmatrix}\overline{\omega}\\ \sigma\end{bmatrix}_{\mu} = \begin{bmatrix}2.91\\ 8.71\end{bmatrix}\mathrm{s}^{-1}, \begin{bmatrix}\overline{\omega}\\ \sigma\end{bmatrix}_{m} = \begin{bmatrix}4.24\\ 8.81\end{bmatrix}\mathrm{s}^{-1}, \Gamma = 37.10\mathrm{m}^2\mathrm{s}^{-1}$

Flow fields for time frame indices $n_t = 4$ to 6 out of 25 frames continues on the next page

NORMAL SUBJECT

COLOUR STREAMLINE PLOT VECTOR & CONTOUR MAP HISTOGRAM

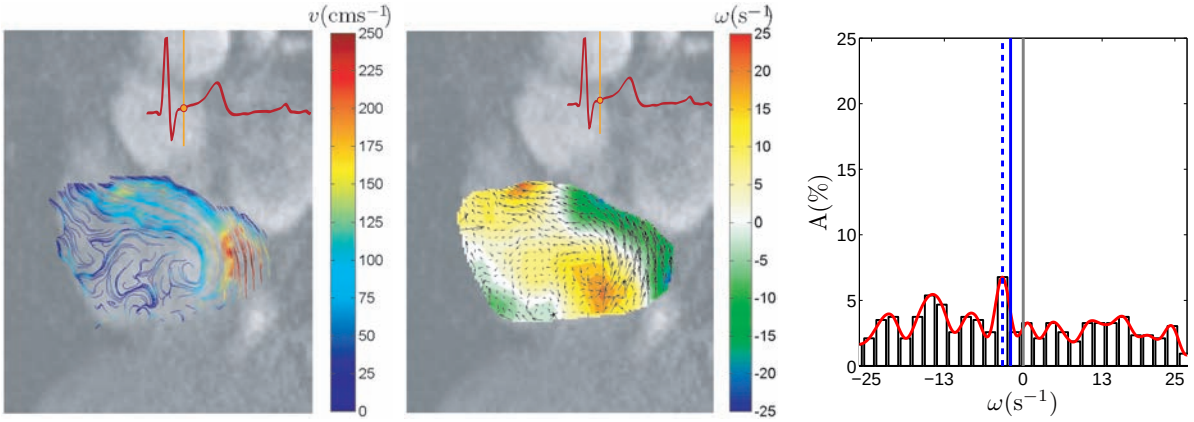

(iv) $n_t = 4, \begin{bmatrix}\overline{\omega}\\ \sigma\end{bmatrix}_{\mu} = \begin{bmatrix}4.00\\ 9.68\end{bmatrix}\mathrm{s}^{-1}, \begin{bmatrix}\overline{\omega}\\ \sigma\end{bmatrix}_{m} = \begin{bmatrix}5.29\\ 9.76\end{bmatrix}\mathrm{s}^{-1}, \Gamma = 42.81\mathrm{m}^2\mathrm{s}^{-1}$

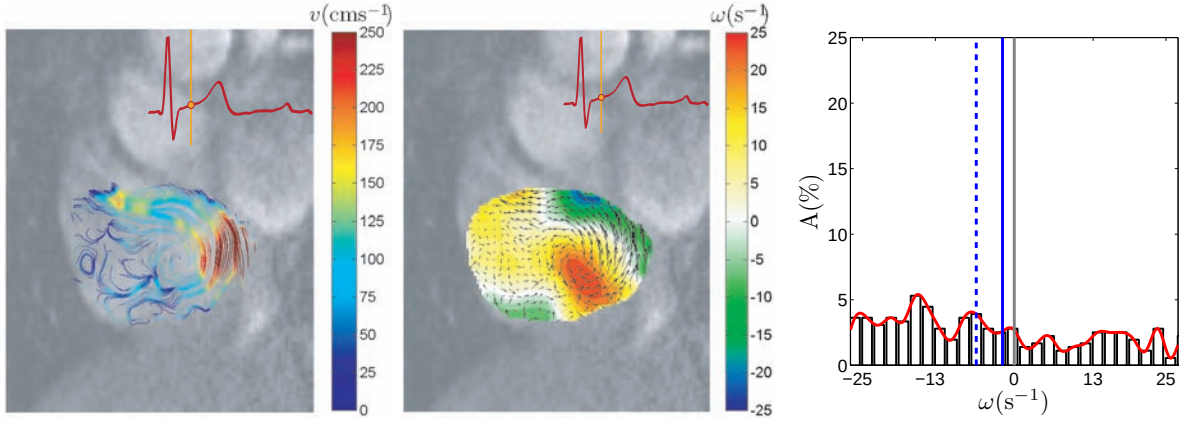

(v) $n_t = 5, \begin{bmatrix}\overline{\omega}\\ \sigma\end{bmatrix}_{\mu} = \begin{bmatrix}5.98\\ 11.05\end{bmatrix}\mathrm{s}^{-1}, \begin{bmatrix}\overline{\omega}\\ \sigma\end{bmatrix}_{m} = \begin{bmatrix}7.53\\ 11.16\end{bmatrix}\mathrm{s}^{-1}, \Gamma = 28.71\mathrm{m}^2\mathrm{s}^{-1}$

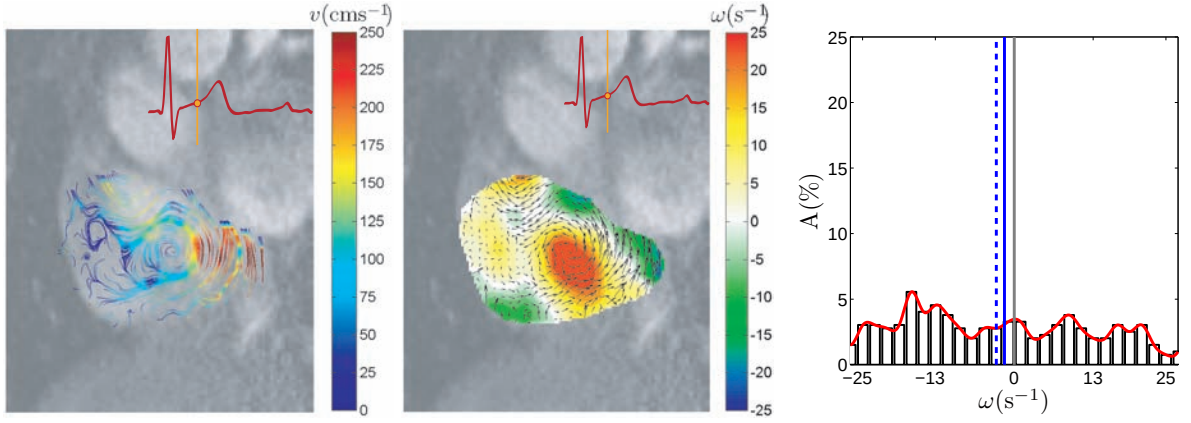

(vi) $n_t = 6, \begin{bmatrix}\overline{\omega}\\ \sigma\end{bmatrix}_{\mu} = \begin{bmatrix}5.50\\ 11.03\end{bmatrix}\mathrm{s}^{-1}, \begin{bmatrix}\overline{\omega}\\ \sigma\end{bmatrix}_{m} = \begin{bmatrix}6.00\\ 11.04\end{bmatrix}\mathrm{s}^{-1}, \Gamma = 29.82\mathrm{m}^2\mathrm{s}^{-1}$

Flow fields for time frame indices $n_t = 7$ to 9 out of 25 frames continues on the next page

COLOUR STREAMLINE PLOT VECTOR & CONTOUR MAP HISTOGRAM

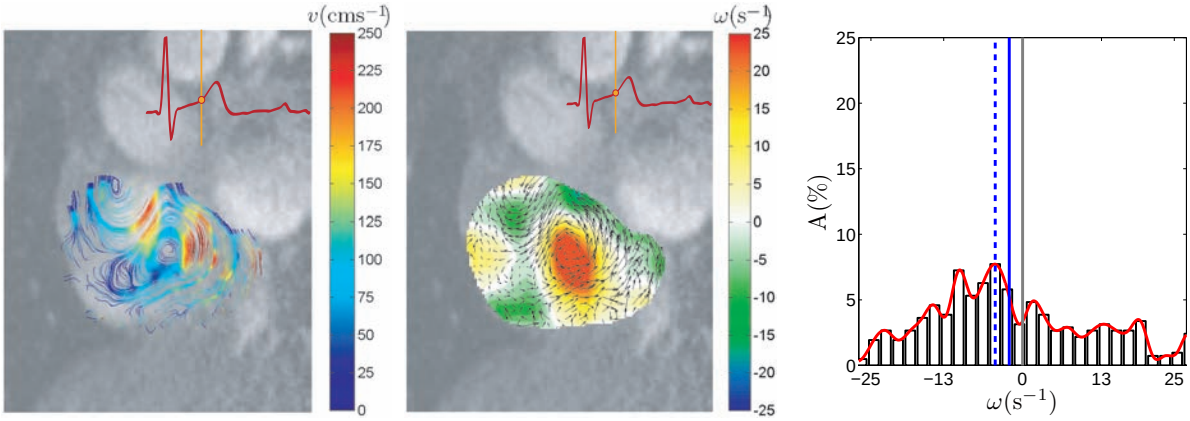

(vii) $n_t = 7, \begin{bmatrix}\overline{\omega}\\ \sigma\end{bmatrix}_\mu = \begin{bmatrix}3.50\\ 1.76\end{bmatrix}\mathrm{s}^{-1}, \begin{bmatrix}\overline{\omega}\\ \sigma\end{bmatrix}_m = \begin{bmatrix}9.81\\ 9.96\end{bmatrix}\mathrm{s}^{-1}, \Gamma = 19.52\mathrm{m}^2\mathrm{s}^{-1}$

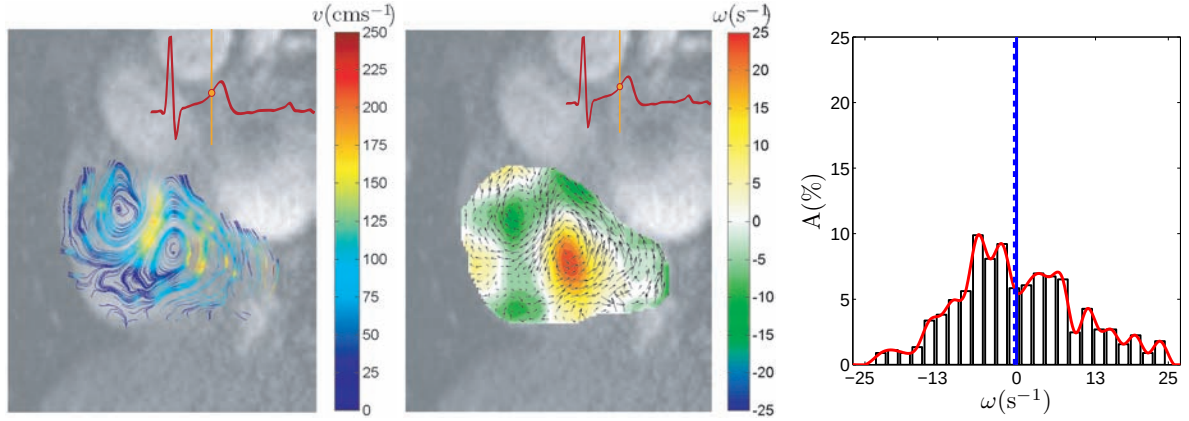

(viii) $n_t = 8, \begin{bmatrix}\overline{\omega}\\ \sigma\end{bmatrix}_\mu = \begin{bmatrix}3.33\\ 12.09\end{bmatrix}\mathrm{s}^{-1}, \begin{bmatrix}\overline{\omega}\\ \sigma\end{bmatrix}_m = \begin{bmatrix}0.00\\ 12.54\end{bmatrix}\mathrm{s}^{-1}, \Gamma = 8.44\mathrm{m}^2\mathrm{s}^{-1}$

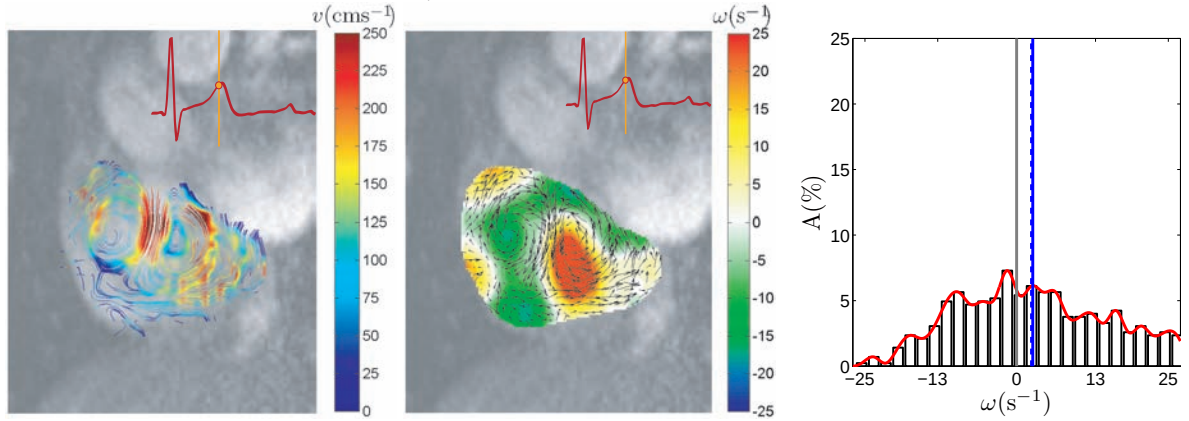

(ix) $n_t = 9, \begin{bmatrix}\overline{\omega}\\ \sigma\end{bmatrix}_\mu = \begin{bmatrix}2.59\\ 11.13\end{bmatrix}\mathrm{s}^{-1}, \begin{bmatrix}\overline{\omega}\\ \sigma\end{bmatrix}_m = \begin{bmatrix}0.00\\ 11.43\end{bmatrix}\mathrm{s}^{-1}, \Gamma = 12.57\mathrm{m}^2\mathrm{s}^{-1}$

Flow fields for time frame indices $n_t = 10$ to 12 out of 25 frames continues on the next page

NORMAL SUBJECT

COLOUR STREAMLINE PLOT VECTOR & CONTOUR MAP HISTOGRAM

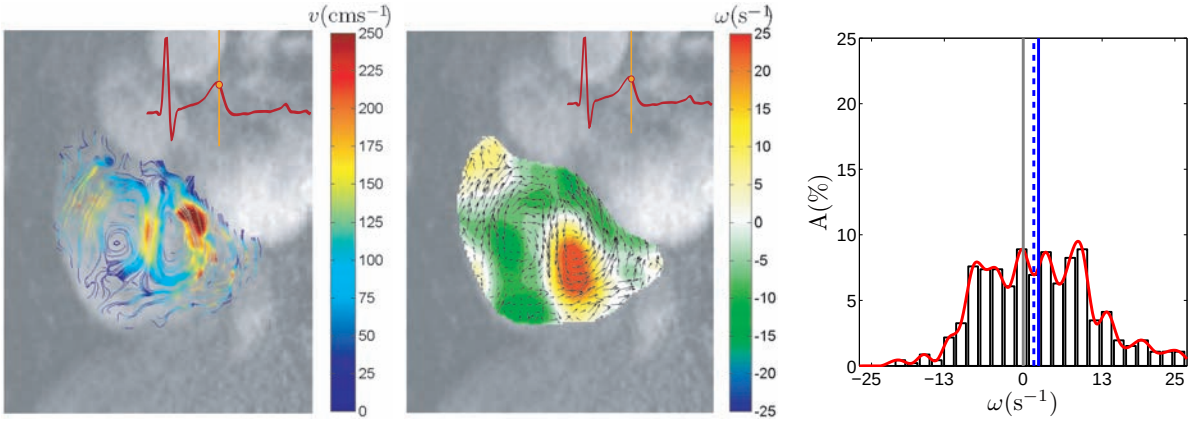

(x) $n_t = 10, \begin{bmatrix}\overline{\omega}\\ \sigma\end{bmatrix}_\mu = \begin{bmatrix}0.23\\ 9.59\end{bmatrix}\mathrm{s}^{-1}, \begin{bmatrix}\overline{\omega}\\ \sigma\end{bmatrix}_m = \begin{bmatrix}-1.75\\ 9.79\end{bmatrix}\mathrm{s}^{-1}, \Gamma = 1.58\mathrm{m}^2\mathrm{s}^{-1}$

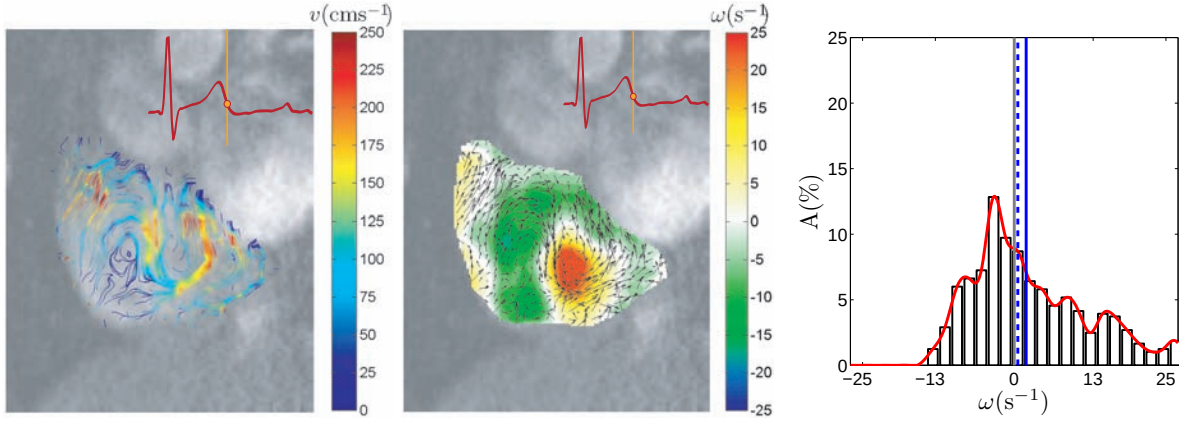

(xi) $n_t = 11, \begin{bmatrix}\overline{\omega}\\ \sigma\end{bmatrix}_\mu = \begin{bmatrix}0.02\\ 9.10\end{bmatrix}\mathrm{s}^{-1}, \begin{bmatrix}\overline{\omega}\\ \sigma\end{bmatrix}_m = \begin{bmatrix}-1.87\\ 9.30\end{bmatrix}\mathrm{s}^{-1}, \Gamma = 0.66\mathrm{m}^2\mathrm{s}^{-1}$

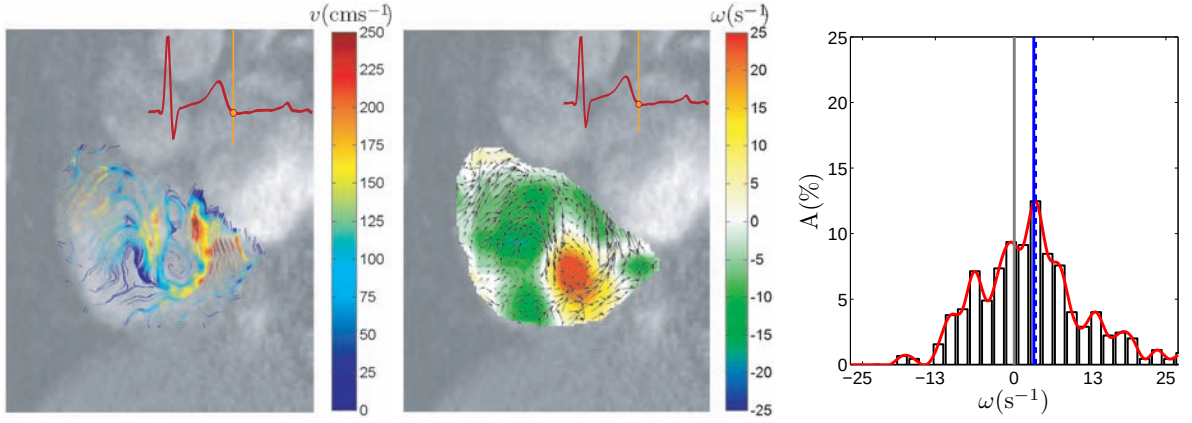

(xii) $n_t = 12, \begin{bmatrix}\overline{\omega}\\ \sigma\end{bmatrix}_\mu = \begin{bmatrix}-0.66\\ 9.35\end{bmatrix}\mathrm{s}^{-1}, \begin{bmatrix}\overline{\omega}\\ \sigma\end{bmatrix}_m = \begin{bmatrix}-3.4\\ 9.74\end{bmatrix}\mathrm{s}^{-1}, \Gamma = -4.33\mathrm{m}^2\mathrm{s}^{-1}$

Flow fields for time frame indices $n_t = 13$ to 15 out of 25 frames continues on the next page

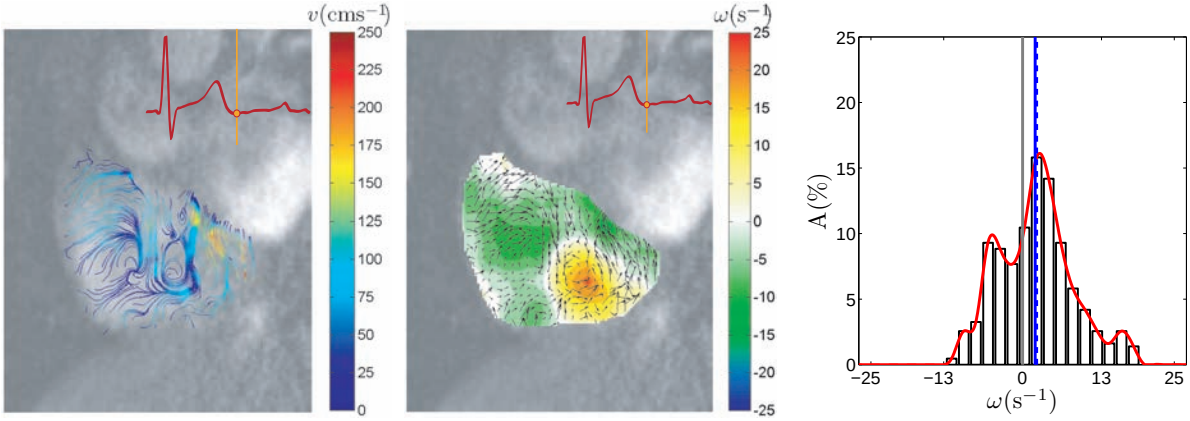

(xiii) $n_t = 13, \begin{bmatrix}\overline{\omega}\\ \sigma\end{bmatrix}_\mu = \begin{bmatrix}-0.6\\ 7.13\end{bmatrix}\mathrm{s}^{-1}, \begin{bmatrix}\overline{\omega}\\ \sigma\end{bmatrix}_m = \begin{bmatrix}-3.05\\ 7.53\end{bmatrix}\mathrm{s}^{-1}, \Gamma = -3.82\mathrm{m}^2\mathrm{s}^{-1}$

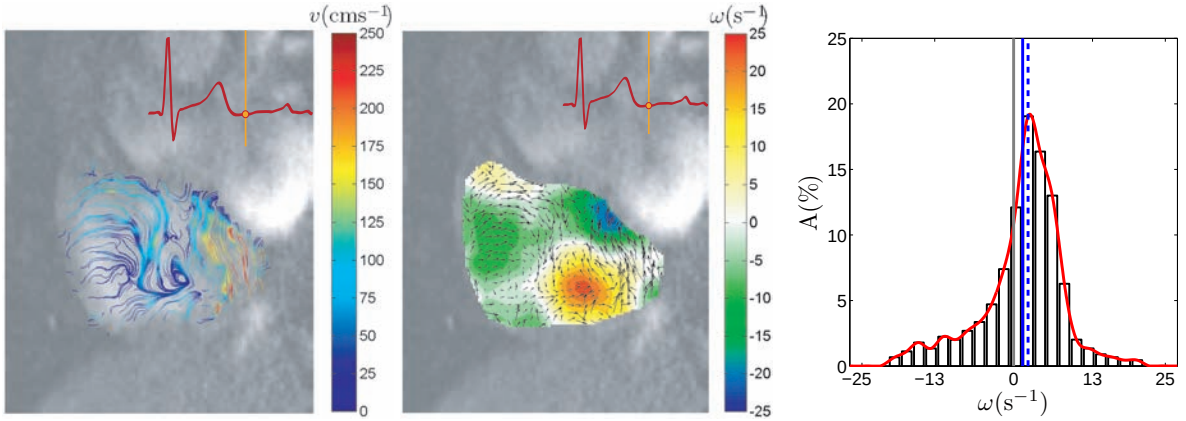

(xiv) $n_t = 14, \begin{bmatrix}\overline{\omega}\\ \sigma\end{bmatrix}_\mu = \begin{bmatrix}-0.25\\ 9.25\end{bmatrix}\mathrm{s}^{-1}, \begin{bmatrix}\overline{\omega}\\ \sigma\end{bmatrix}_m = \begin{bmatrix}-1.87\\ 9.39\end{bmatrix}\mathrm{s}^{-1}, \Gamma = -2.44\mathrm{m}^2\mathrm{s}^{-1}$

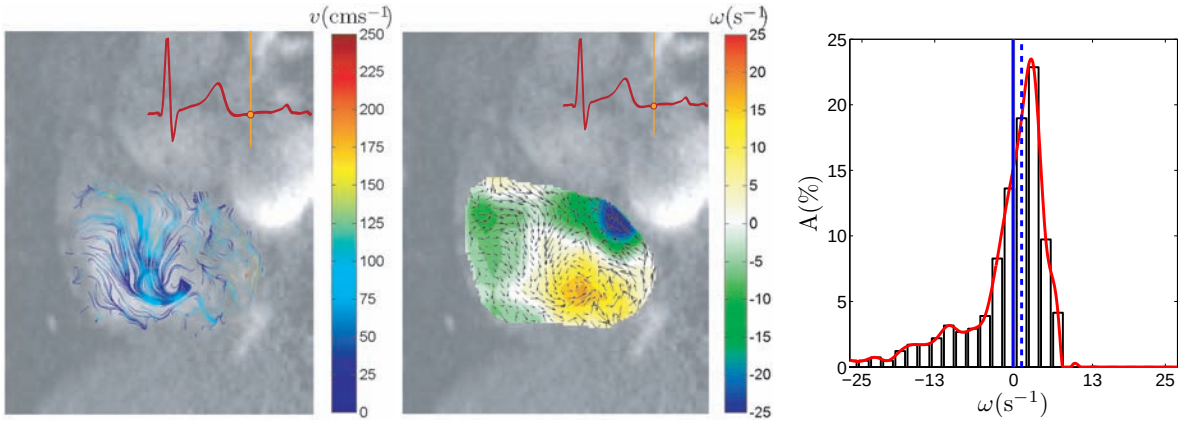

(xv) $n_t = 15, \begin{bmatrix}\overline{\omega}\\ \sigma\end{bmatrix}_\mu = \begin{bmatrix}-0.54\\ 9.40\end{bmatrix}\mathrm{s}^{-1}, \begin{bmatrix}\overline{\omega}\\ \sigma\end{bmatrix}_m = \begin{bmatrix}-1.7\\ 9.47\end{bmatrix}\mathrm{s}^{-1}, \Gamma = -3.06\mathrm{m}^2\mathrm{s}^{-1}$

Flow fields for time frame indices $n_t = 16$ to 18 out of 25 frames continues on the next page

NORMAL SUBJECT

COLOUR STREAMLINE PLOT VECTOR & CONTOUR MAP HISTOGRAM

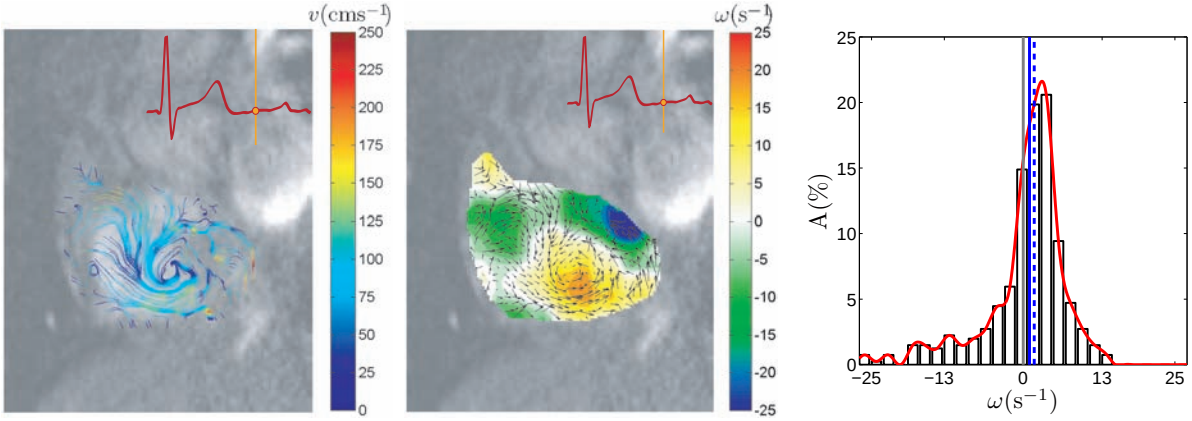

(xvi) $n_t = 16, \begin{bmatrix}\overline{\omega}\\ \sigma\end{bmatrix}_\mu = \begin{bmatrix}-0.56\\ 10.62\end{bmatrix}\mathrm{s}^{-1}, \begin{bmatrix}\overline{\omega}\\ \sigma\end{bmatrix}_m = \begin{bmatrix}0\\ 10.64\end{bmatrix}\mathrm{s}^{-1}, \Gamma = -3.89\mathrm{m}^2\mathrm{s}^{-1}$

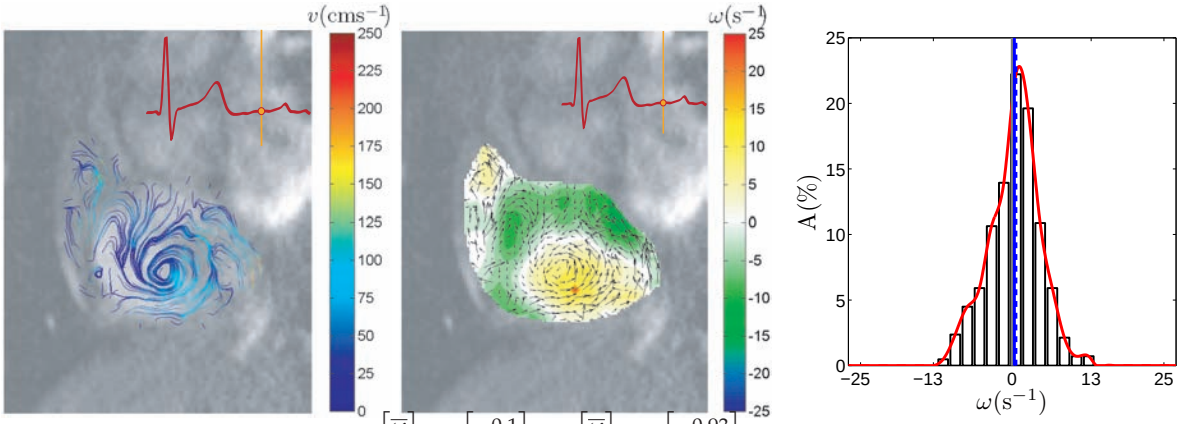

(xvii) $n_t = 17, \begin{bmatrix}\overline{\omega}\\ \sigma\end{bmatrix}_\mu = \begin{bmatrix}-0.1\\ 5.75\end{bmatrix}\mathrm{s}^{-1}, \begin{bmatrix}\overline{\omega}\\ \sigma\end{bmatrix}_m = \begin{bmatrix}-0.93\\ 5.81\end{bmatrix}\mathrm{s}^{-1}, \Gamma = -0.73\mathrm{m}^2\mathrm{s}^{-1}$

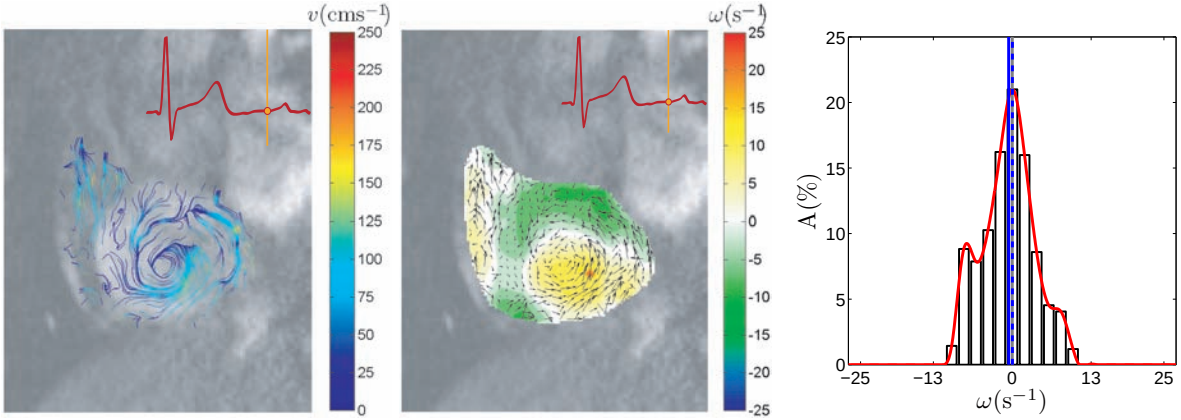

(xviii) $n_t = 18, \begin{bmatrix}\overline{\omega}\\ \sigma\end{bmatrix}_\mu = \begin{bmatrix}0.89\\ 5.66\end{bmatrix}\mathrm{s}^{-1}, \begin{bmatrix}\overline{\omega}\\ \sigma\end{bmatrix}_m = \begin{bmatrix}0\\ 5.73\end{bmatrix}\mathrm{s}^{-1}, \Gamma = 4.94\mathrm{m}^2\mathrm{s}^{-1}$

Flow fields for time frame indices $n_t = 19$ to 21 out of 25 frames continues on the next page

COLOUR STREAMLINE PLOT VECTOR & CONTOUR MAP HISTOGRAM

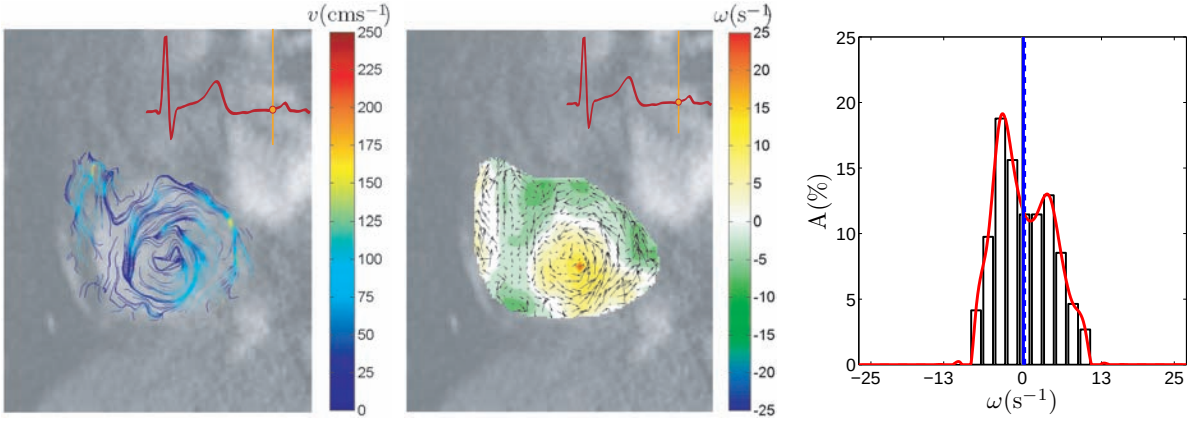

(xix) $n_t = 19, \begin{bmatrix}\overline{\omega}\\ \sigma\end{bmatrix}_{\mu} = \begin{bmatrix}0.97\\ 4.89\end{bmatrix}\mathrm{s}^{-1}, \begin{bmatrix}\overline{\omega}\\ \sigma\end{bmatrix}_{m} = \begin{bmatrix}0.00\\ 4.99\end{bmatrix}\mathrm{s}^{-1}, \Gamma = 5.52\mathrm{m}^2\mathrm{s}^{-1}$

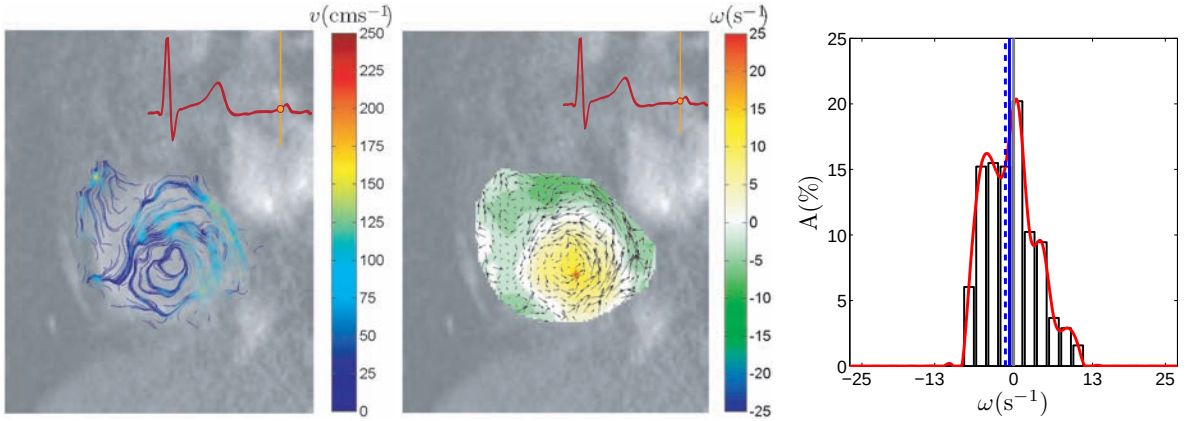

(xx) $n_t = 20, \begin{bmatrix}\overline{\omega}\\ \sigma\end{bmatrix}_{\mu} = \begin{bmatrix}0.92\\ 5.01\end{bmatrix}\mathrm{s}^{-1}, \begin{bmatrix}\overline{\omega}\\ \sigma\end{bmatrix}_{m} = \begin{bmatrix}-0.75\\ 5.28\end{bmatrix}\mathrm{s}^{-1}, \Gamma = 4.58\mathrm{m}^2\mathrm{s}^{-1}$

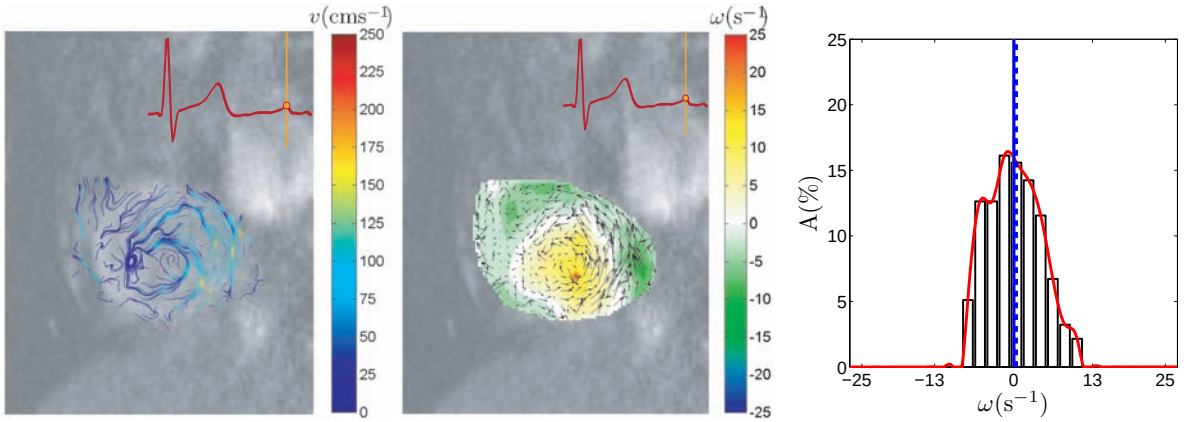

(xxi) $n_t = 21, \begin{bmatrix}\overline{\omega}\\ \sigma\end{bmatrix}_{\mu} = \begin{bmatrix}0.90\\ 5.12\end{bmatrix}\mathrm{s}^{-1}, \begin{bmatrix}\overline{\omega}\\ \sigma\end{bmatrix}_{m} = \begin{bmatrix}-0.81\\ 5.40\end{bmatrix}\mathrm{s}^{-1}, \Gamma = 4.86\mathrm{m}^2\mathrm{s}^{-1}$

Flow fields for time frame indices $n_t = 22$ to 24 out of 25 frames continues on the next page

NORMAL SUBJECT

COLOUR STREAMLINE PLOT | VECTOR & CONTOUR MAP | HISTOGRAM

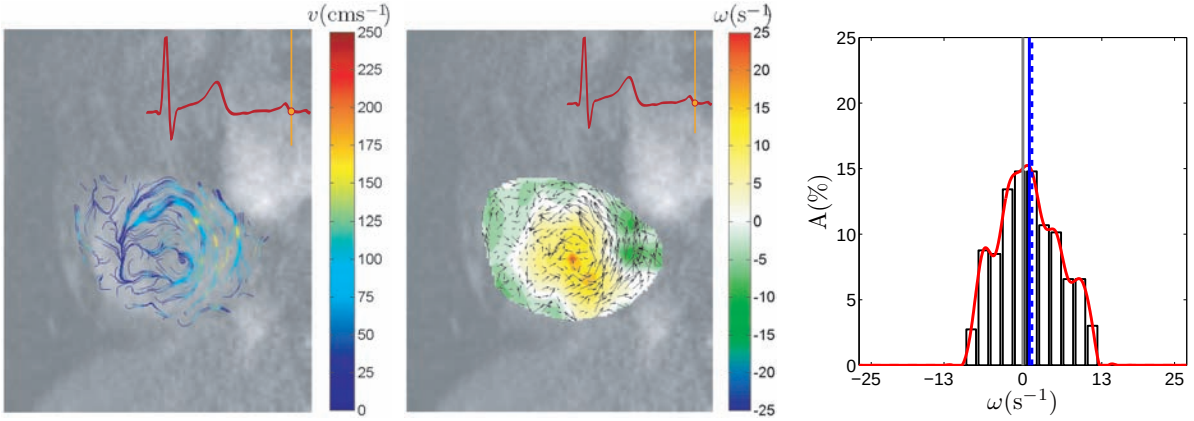

(xxii) $n_t = 22, \begin{bmatrix}\overline{\omega}\\ \sigma\end{bmatrix}_{\cdot\cdot} = \begin{bmatrix}2.31\\ 6.11\end{bmatrix}\mathrm{s}^{-1}, \begin{bmatrix}\overline{\omega}\\ \sigma\end{bmatrix}_{\cdot\cdot\cdot} = \begin{bmatrix}0.94\\ 6.26\end{bmatrix}\mathrm{s}^{-1}, \Gamma = 10.78\mathrm{m}^2\mathrm{s}^{-1}$

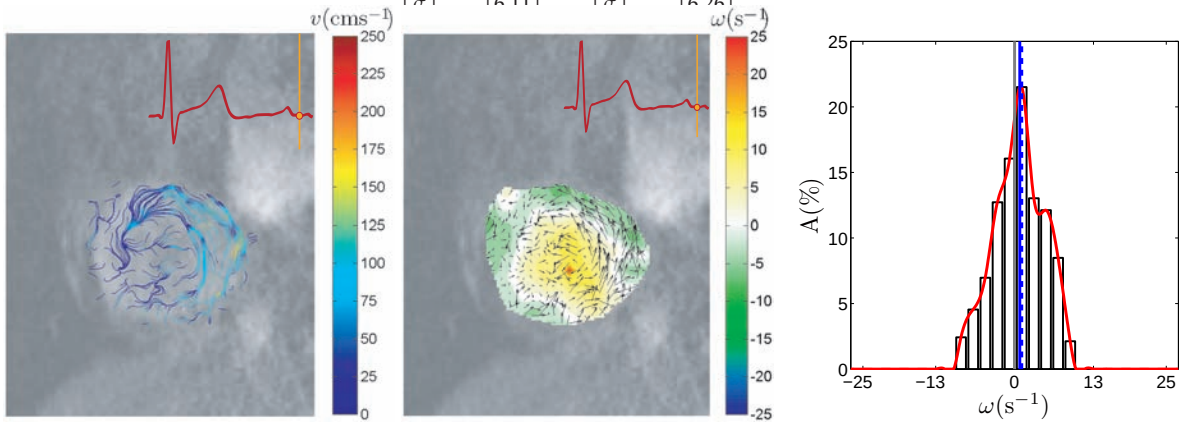

(xxiii) $n_t = 23, \begin{bmatrix}\overline{\omega}\\ \sigma\end{bmatrix}_{\cdot\cdot} = \begin{bmatrix}2.09\\ 5.18\end{bmatrix}\mathrm{s}^{-1}, \begin{bmatrix}\overline{\omega}\\ \sigma\end{bmatrix}_{\cdot\cdot\cdot} = \begin{bmatrix}1.76\\ 5.19\end{bmatrix}\mathrm{s}^{-1}, \Gamma = 8.95\mathrm{m}^2\mathrm{s}^{-1}$

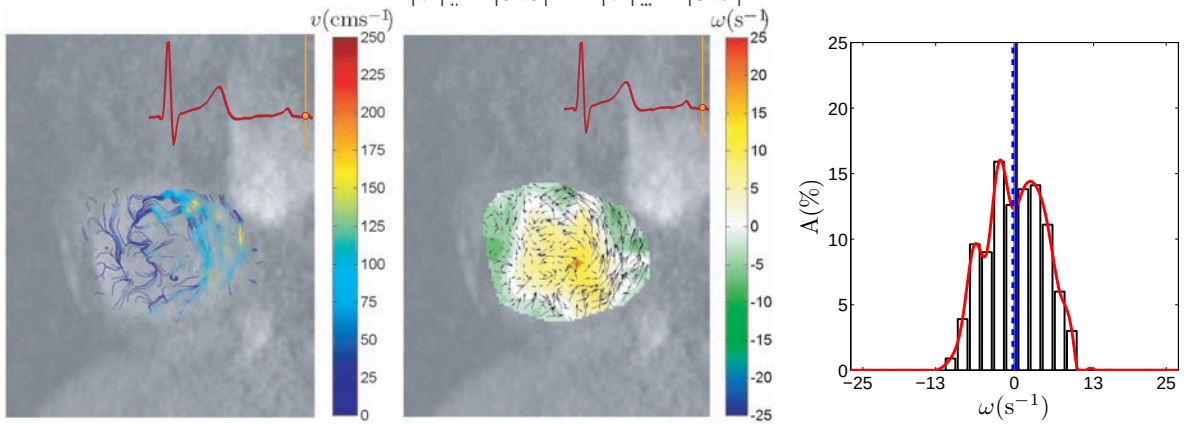

(xxiv) $n_t = 24, \begin{bmatrix}\overline{\omega}\\ \sigma\end{bmatrix}_{\mu} = \begin{bmatrix}2.33\\ 5.25\end{bmatrix}\mathrm{s}^{-1}, \begin{bmatrix}\overline{\omega}\\ \sigma\end{bmatrix}_{m} = \begin{bmatrix}1.53\\ 5.31\end{bmatrix}\mathrm{s}^{-1}, \Gamma = 10.35\mathrm{m}^2\mathrm{s}^{-1}$

Figure C.1. Flow visualisation of normal right atrium based on one cardiac cycle. Visualisation of flow in the right atrium of a normal subject is presented for investigation of the vortex behaviour during the systolic and diastolic phases from time frame indices $n_t = 1$ to 24 of one cardiac cycle.

VORTICITY SAMPLING SIZE (9×9) PIXELS		
PREDICTED FLOW	**MEASURED FLOW**	**VORTICITY DIFFERENCE**
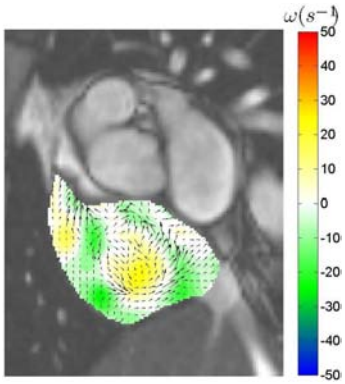	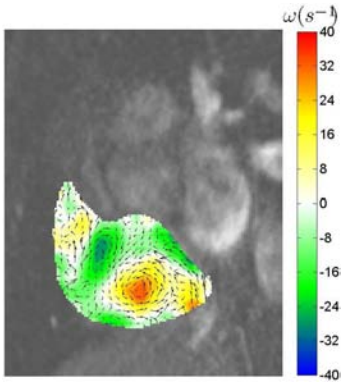	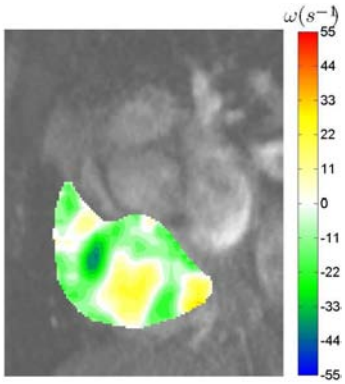
$\begin{bmatrix}\overline{\omega}\\ \sigma\end{bmatrix}_{\mu} = \begin{bmatrix}0.78\\ 9.39\end{bmatrix} s^{-1}, \begin{bmatrix}\overline{\omega}\\ \sigma\end{bmatrix}_{m} = \begin{bmatrix}0.19\\ 9.41\end{bmatrix} s^{-1}$	$\begin{bmatrix}\overline{\omega}\\ \sigma\end{bmatrix}_{\mu} = \begin{bmatrix}0.76\\ 13.87\end{bmatrix} s^{-1}, \begin{bmatrix}\overline{\omega}\\ \sigma\end{bmatrix}_{m} = \begin{bmatrix}-0.92\\ 13.97\end{bmatrix} s^{-1}$	$\begin{bmatrix}\overline{\omega}\\ \sigma\end{bmatrix}_{\mu} = \begin{bmatrix}-2.16\\ 14.20\end{bmatrix} s^{-1}, \begin{bmatrix}\overline{\omega}\\ \sigma\end{bmatrix}_{m} = \begin{bmatrix}-3.31\\ 14.24\end{bmatrix} s^{-1}$
$(i) \quad n_t = 17$		
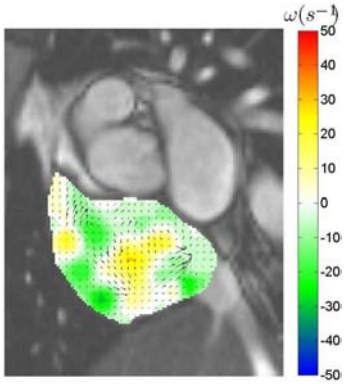	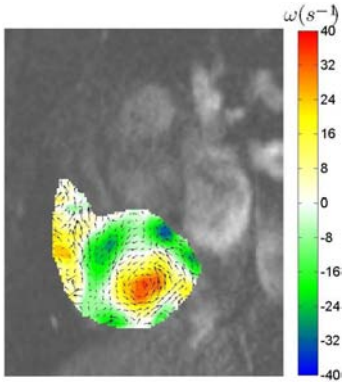	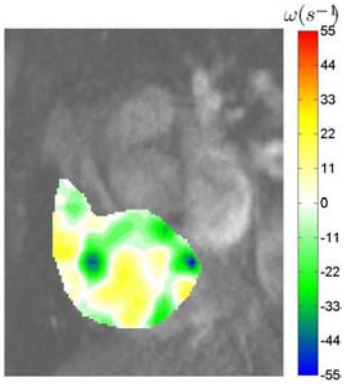
$\begin{bmatrix}\overline{\omega}\\ \sigma\end{bmatrix}_{\mu} = \begin{bmatrix}-0.03\\ 10.99\end{bmatrix} s^{-1}, \begin{bmatrix}\overline{\omega}\\ \sigma\end{bmatrix}_{m} = \begin{bmatrix}-1.29\\ 11.06\end{bmatrix} s^{-1}$	$\begin{bmatrix}\overline{\omega}\\ \sigma\end{bmatrix}_{\mu} = \begin{bmatrix}2.27\\ 15.29\end{bmatrix} s^{-1}, \begin{bmatrix}\overline{\omega}\\ \sigma\end{bmatrix}_{m} = \begin{bmatrix}1.57\\ 15.31\end{bmatrix} s^{-1}$	$\begin{bmatrix}\overline{\omega}\\ \sigma\end{bmatrix}_{\mu} = \begin{bmatrix}0.43\\ 15.11\end{bmatrix} s^{-1}, \begin{bmatrix}\overline{\omega}\\ \sigma\end{bmatrix}_{m} = \begin{bmatrix}1.80\\ 15.13\end{bmatrix} s^{-1}$
$(ii) \quad n_t = 18$		
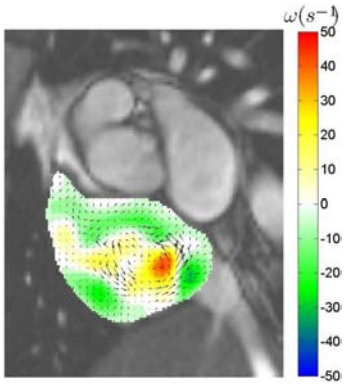	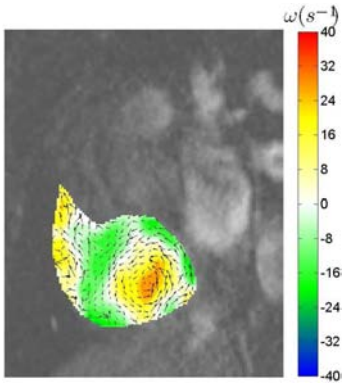	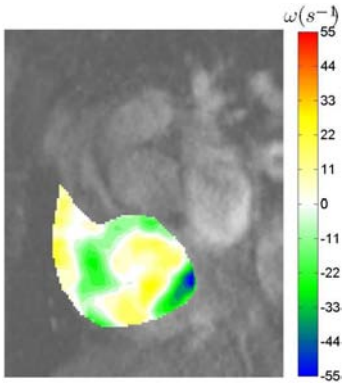
$\begin{bmatrix}\overline{\omega}\\ \sigma\end{bmatrix}_{\mu} = \begin{bmatrix}-0.50\\ 12.77\end{bmatrix} s^{-1}, \begin{bmatrix}\overline{\omega}\\ \sigma\end{bmatrix}_{m} = \begin{bmatrix}-1.16\\ 12.88\end{bmatrix} s^{-1}$	$\begin{bmatrix}\overline{\omega}\\ \sigma\end{bmatrix}_{\mu} = \begin{bmatrix}3.39\\ 13.48\end{bmatrix} s^{-1}, \begin{bmatrix}\overline{\omega}\\ \sigma\end{bmatrix}_{m} = \begin{bmatrix}1.82\\ 13.57\end{bmatrix} s^{-1}$	$\begin{bmatrix}\overline{\omega}\\ \sigma\end{bmatrix}_{\mu} = \begin{bmatrix}1.28\\ 15.39\end{bmatrix} s^{-1}, \begin{bmatrix}\overline{\omega}\\ \sigma\end{bmatrix}_{m} = \begin{bmatrix}3.39\\ 15.53\end{bmatrix} s^{-1}$
$(iii) \quad n_t = 19$		

(a) Vorticity sampling window size (9×9) pixels

Vorticity sampling window size (11×11) pixels continues on the next page

VORTICITY SAMPLING SIZE (11×11) PIXELS

PREDICTED FLOW	MEASURED FLOW	VORTICITY DIFFERENCE
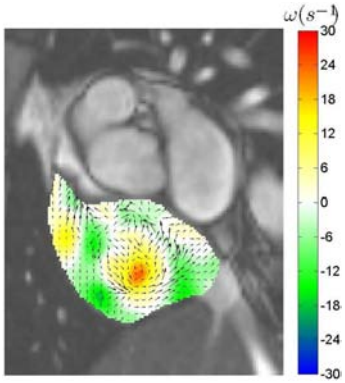	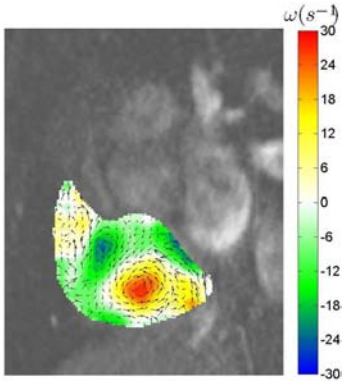	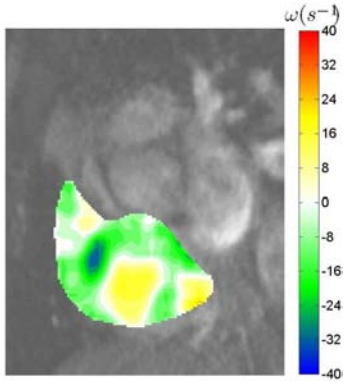
$\begin{bmatrix}\overline{\omega}\\ \sigma\end{bmatrix}_{\mu} = \begin{bmatrix}0.93\\ 7.70\end{bmatrix} s^{-1}, \begin{bmatrix}\overline{\omega}\\ \sigma\end{bmatrix}_{m} = \begin{bmatrix}0.48\\ 7.72\end{bmatrix} s^{-1}$	$\begin{bmatrix}\overline{\omega}\\ \sigma\end{bmatrix}_{\mu} = \begin{bmatrix}0.60\\ 11.53\end{bmatrix} s^{-1}, \begin{bmatrix}\overline{\omega}\\ \sigma\end{bmatrix}_{m} = \begin{bmatrix}-0.47\\ 11.58\end{bmatrix} s^{-1}$	$\begin{bmatrix}\overline{\omega}\\ \sigma\end{bmatrix}_{\mu} = \begin{bmatrix}-2.14\\ 11.36\end{bmatrix} s^{-1}, \begin{bmatrix}\overline{\omega}\\ \sigma\end{bmatrix}_{m} = \begin{bmatrix}-3.29\\ 11.42\end{bmatrix} s^{-1}$
$(i) \quad n_t = 17$		
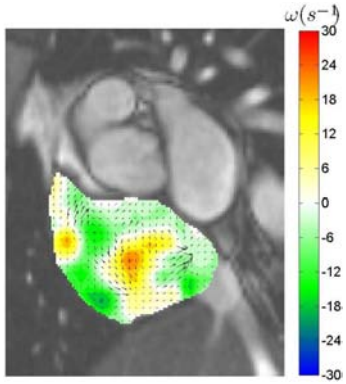	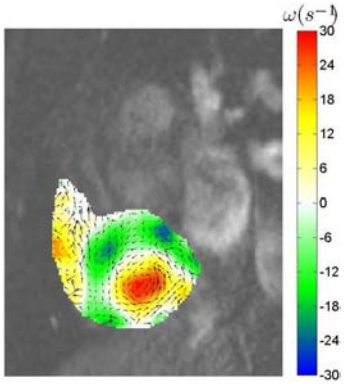	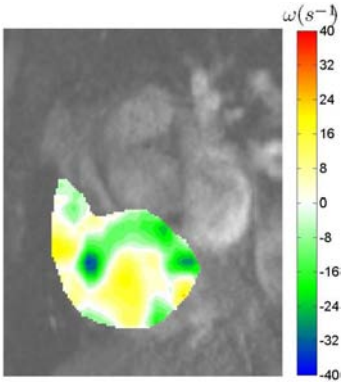
$\begin{bmatrix}\overline{\omega}\\ \sigma\end{bmatrix}_{\mu} = \begin{bmatrix}0.14\\ 8.81\end{bmatrix} s^{-1}, \begin{bmatrix}\overline{\omega}\\ \sigma\end{bmatrix}_{m} = \begin{bmatrix}-1.52\\ 8.97\end{bmatrix} s^{-1}$	$\begin{bmatrix}\overline{\omega}\\ \sigma\end{bmatrix}_{\mu} = \begin{bmatrix}2.24\\ 12.63\end{bmatrix} s^{-1}, \begin{bmatrix}\overline{\omega}\\ \sigma\end{bmatrix}_{m} = \begin{bmatrix}1.50\\ 12.66\end{bmatrix} s^{-1}$	$\begin{bmatrix}\overline{\omega}\\ \sigma\end{bmatrix}_{\mu} = \begin{bmatrix}0.63\\ 11.73\end{bmatrix} s^{-1}, \begin{bmatrix}\overline{\omega}\\ \sigma\end{bmatrix}_{m} = \begin{bmatrix}1.34\\ 11.75\end{bmatrix} s^{-1}$
$(ii) \quad n_t = 18$		
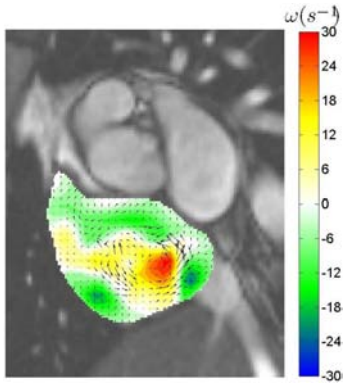	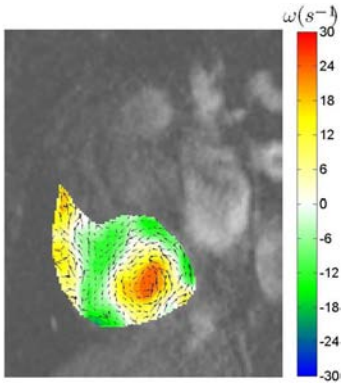	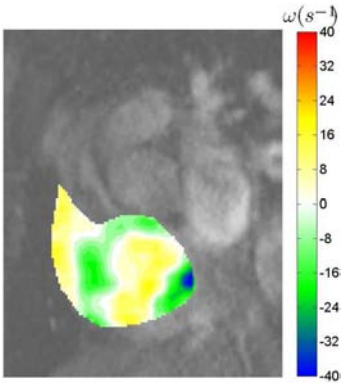
$\begin{bmatrix}\overline{\omega}\\ \sigma\end{bmatrix}_{\mu} = \begin{bmatrix}0.71\\ 9.86\end{bmatrix} s^{-1}, \begin{bmatrix}\overline{\omega}\\ \sigma\end{bmatrix}_{m} = \begin{bmatrix}-0.72\\ 9.96\end{bmatrix} s^{-1}$	$\begin{bmatrix}\overline{\omega}\\ \sigma\end{bmatrix}_{\mu} = \begin{bmatrix}3.17\\ 11.26\end{bmatrix} s^{-1}, \begin{bmatrix}\overline{\omega}\\ \sigma\end{bmatrix}_{m} = \begin{bmatrix}2.15\\ 11.31\end{bmatrix} s^{-1}$	$\begin{bmatrix}\overline{\omega}\\ \sigma\end{bmatrix}_{\mu} = \begin{bmatrix}1.37\\ 11.45\end{bmatrix} s^{-1}, \begin{bmatrix}\overline{\omega}\\ \sigma\end{bmatrix}_{m} = \begin{bmatrix}3.17\\ 11.60\end{bmatrix} s^{-1}$
$(iii) \quad n_t = 19$		

(b) Vorticity sampling window size (11×11) pixels

Vorticity sampling window size (13×13) pixels continues on the next page

VORTICITY SAMPLING SIZE (13×13) PIXELS		
PREDICTED FLOW	**MEASURED FLOW**	**VORTICITY DIFFERENCE**
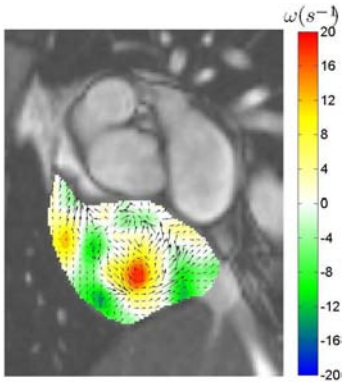	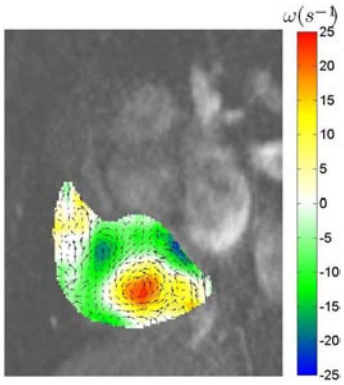	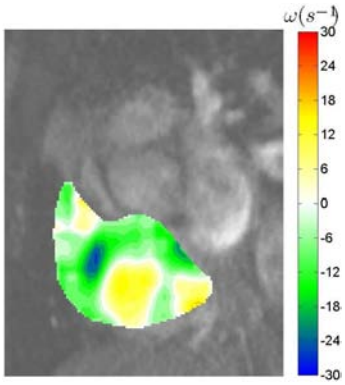
$\begin{bmatrix}\overline{\omega}\\ \sigma\end{bmatrix}_{\mu} = \begin{bmatrix}1.07\\ 6.28\end{bmatrix} s^{-1}, \begin{bmatrix}\overline{\omega}\\ \sigma\end{bmatrix}_{m} = \begin{bmatrix}0.78\\ 6.29\end{bmatrix} s^{-1}$	$\begin{bmatrix}\overline{\omega}\\ \sigma\end{bmatrix}_{\mu} = \begin{bmatrix}0.42\\ 9.80\end{bmatrix} s^{-1}, \begin{bmatrix}\overline{\omega}\\ \sigma\end{bmatrix}_{m} = \begin{bmatrix}-0.36\\ 9.83\end{bmatrix} s^{-1}$	$\begin{bmatrix}\overline{\omega}\\ \sigma\end{bmatrix}_{\mu} = \begin{bmatrix}-2.14\\ 9.35\end{bmatrix} s^{-1}, \begin{bmatrix}\overline{\omega}\\ \sigma\end{bmatrix}_{m} = \begin{bmatrix}-3.25\\ 9.42\end{bmatrix} s^{-1}$
$(i) \quad n_t = 17$		
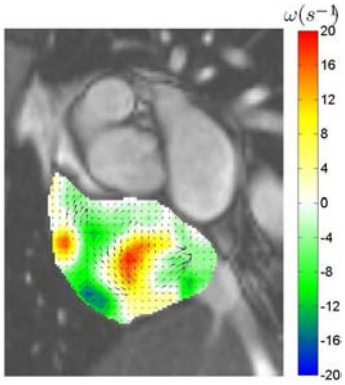	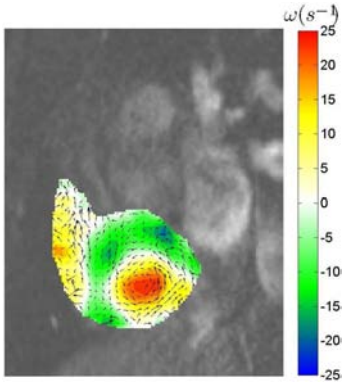	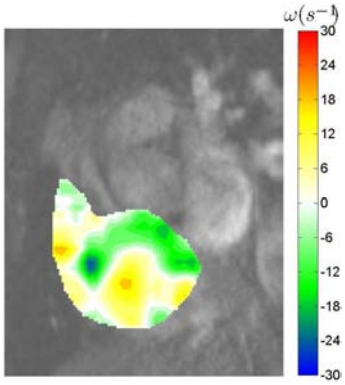
$\begin{bmatrix}\overline{\omega}\\ \sigma\end{bmatrix}_{\mu} = \begin{bmatrix}0.29\\ 7.02\end{bmatrix} s^{-1}, \begin{bmatrix}\overline{\omega}\\ \sigma\end{bmatrix}_{m} = \begin{bmatrix}-0.95\\ 7.13\end{bmatrix} s^{-1}$	$\begin{bmatrix}\overline{\omega}\\ \sigma\end{bmatrix}_{\mu} = \begin{bmatrix}2.08\\ 10.48\end{bmatrix} s^{-1}, \begin{bmatrix}\overline{\omega}\\ \sigma\end{bmatrix}_{m} = \begin{bmatrix}1.84\\ 10.48\end{bmatrix} s^{-1}$	$\begin{bmatrix}\overline{\omega}\\ \sigma\end{bmatrix}_{\mu} = \begin{bmatrix}0.64\\ 9.18\end{bmatrix} s^{-1}, \begin{bmatrix}\overline{\omega}\\ \sigma\end{bmatrix}_{m} = \begin{bmatrix}1.48\\ 9.21\end{bmatrix} s^{-1}$
$(ii) \quad n_t = 18$		
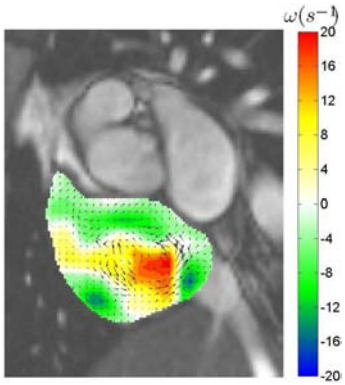	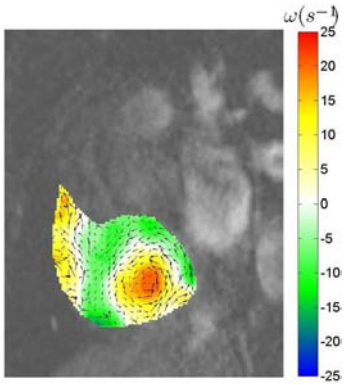	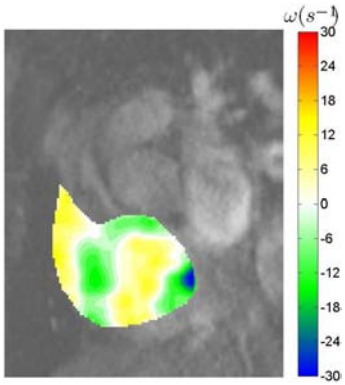
$\begin{bmatrix}\overline{\omega}\\ \sigma\end{bmatrix}_{\mu} = \begin{bmatrix}0.90\\ 7.83\end{bmatrix} s^{-1}, \begin{bmatrix}\overline{\omega}\\ \sigma\end{bmatrix}_{m} = \begin{bmatrix}-1.10\\ 8.07\end{bmatrix} s^{-1}$	$\begin{bmatrix}\overline{\omega}\\ \sigma\end{bmatrix}_{\mu} = \begin{bmatrix}2.92\\ 9.47\end{bmatrix} s^{-1}, \begin{bmatrix}\overline{\omega}\\ \sigma\end{bmatrix}_{m} = \begin{bmatrix}2.13\\ 9.50\end{bmatrix} s^{-1}$	$\begin{bmatrix}\overline{\omega}\\ \sigma\end{bmatrix}_{\mu} = \begin{bmatrix}1.33\\ 8.84\end{bmatrix} s^{-1}, \begin{bmatrix}\overline{\omega}\\ \sigma\end{bmatrix}_{m} = \begin{bmatrix}1.87\\ 8.85\end{bmatrix} s^{-1}$
$(iii) \quad n_t = 19$		

(c) Vorticity sampling window size (13×13) pixels

Vorticity sampling window size (15×15) pixels continues on the next page

VORTICITY SAMPLING SIZE (15×15) PIXELS

PREDICTED FLOW	MEASURED FLOW	VORTICITY DIFFERENCE
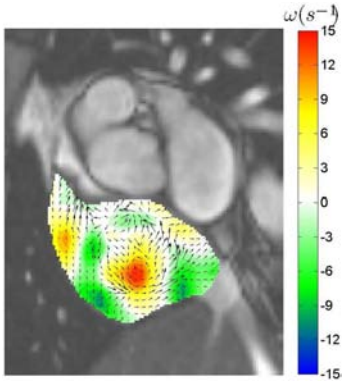	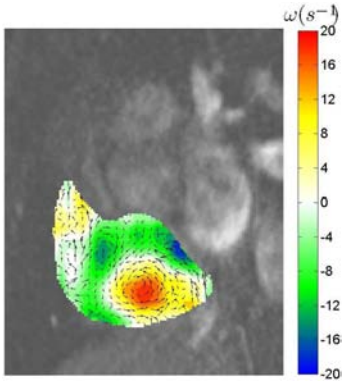	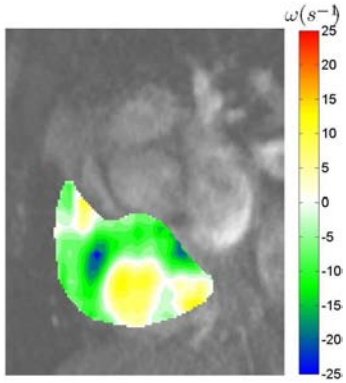
$\begin{bmatrix}\overline{\omega}\\ \sigma\end{bmatrix}_{\mu} = \begin{bmatrix}1.19\\ 5.08\end{bmatrix} s^{-1}, \begin{bmatrix}\overline{\omega}\\ \sigma\end{bmatrix}_{m} = \begin{bmatrix}0.82\\ 5.09\end{bmatrix} s^{-1}$	$\begin{bmatrix}\overline{\omega}\\ \sigma\end{bmatrix}_{\mu} = \begin{bmatrix}0.17\\ 8.40\end{bmatrix} s^{-1}, \begin{bmatrix}\overline{\omega}\\ \sigma\end{bmatrix}_{m} = \begin{bmatrix}-0.60\\ 8.43\end{bmatrix} s^{-1}$	$\begin{bmatrix}\overline{\omega}\\ \sigma\end{bmatrix}_{\mu} = \begin{bmatrix}-2.26\\ 7.83\end{bmatrix} s^{-1}, \begin{bmatrix}\overline{\omega}\\ \sigma\end{bmatrix}_{m} = \begin{bmatrix}-2.75\\ 7.84\end{bmatrix} s^{-1}$
$(i) \quad n_t = 17$		
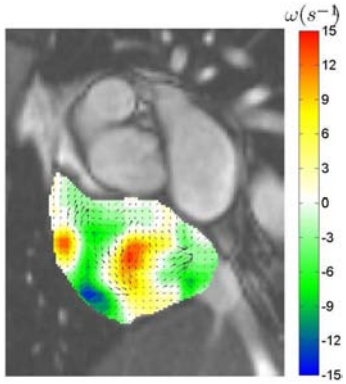	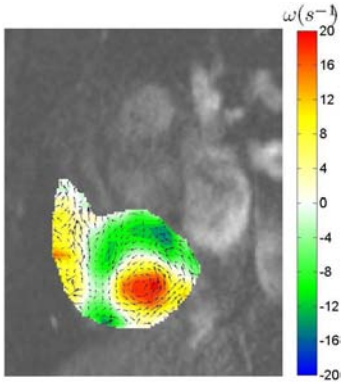	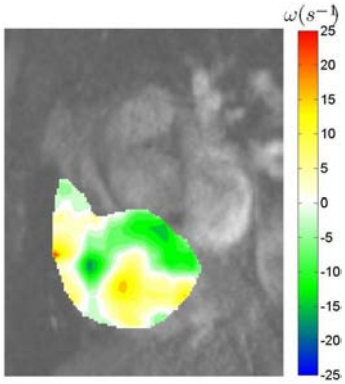
$\begin{bmatrix}\overline{\omega}\\ \sigma\end{bmatrix}_{\mu} = \begin{bmatrix}0.39\\ 5.59\end{bmatrix} s^{-1}, \begin{bmatrix}\overline{\omega}\\ \sigma\end{bmatrix}_{m} = \begin{bmatrix}-0.40\\ 5.65\end{bmatrix} s^{-1}$	$\begin{bmatrix}\overline{\omega}\\ \sigma\end{bmatrix}_{\mu} = \begin{bmatrix}1.85\\ 8.75\end{bmatrix} s^{-1}, \begin{bmatrix}\overline{\omega}\\ \sigma\end{bmatrix}_{m} = \begin{bmatrix}1.11\\ 8.78\end{bmatrix} s^{-1}$	$\begin{bmatrix}\overline{\omega}\\ \sigma\end{bmatrix}_{\mu} = \begin{bmatrix}0.53\\ 7.39\end{bmatrix} s^{-1}, \begin{bmatrix}\overline{\omega}\\ \sigma\end{bmatrix}_{m} = \begin{bmatrix}0.78\\ 7.39\end{bmatrix} s^{-1}$
$(ii) \quad n_t = 18$		
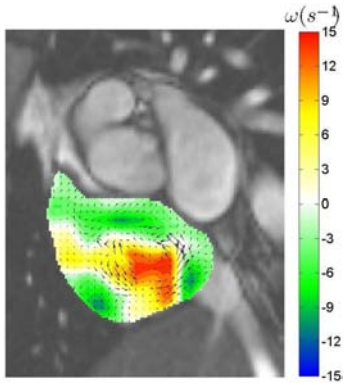	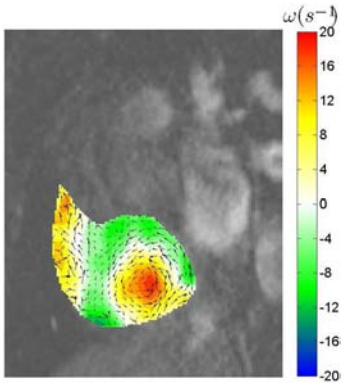	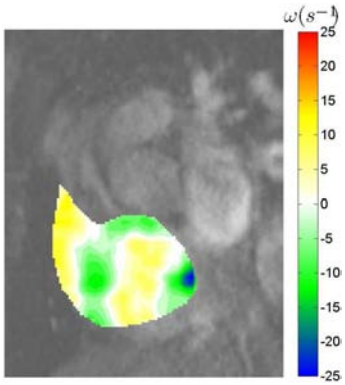
$\begin{bmatrix}\overline{\omega}\\ \sigma\end{bmatrix}_{\mu} = \begin{bmatrix}1.00\\ 6.38\end{bmatrix} s^{-1}, \begin{bmatrix}\overline{\omega}\\ \sigma\end{bmatrix}_{m} = \begin{bmatrix}-1.07\\ 6.71\end{bmatrix} s^{-1}$	$\begin{bmatrix}\overline{\omega}\\ \sigma\end{bmatrix}_{\mu} = \begin{bmatrix}2.68\\ 7.97\end{bmatrix} s^{-1}, \begin{bmatrix}\overline{\omega}\\ \sigma\end{bmatrix}_{m} = \begin{bmatrix}2.01\\ 7.99\end{bmatrix} s^{-1}$	$\begin{bmatrix}\overline{\omega}\\ \sigma\end{bmatrix}_{\mu} = \begin{bmatrix}1.22\\ 6.97\end{bmatrix} s^{-1}, \begin{bmatrix}\overline{\omega}\\ \sigma\end{bmatrix}_{m} = \begin{bmatrix}1.38\\ 6.97\end{bmatrix} s^{-1}$
$(iii) \quad n_t = 19$		

(d) Vorticity sampling window size (15×15) pixels

Vorticity sampling window size (17×17) pixels continues on the next page

VORTICITY SAMPLING SIZE (17×17) PIXELS		
PREDICTED FLOW	**MEASURED FLOW**	**VORTICITY DIFFERENCE**
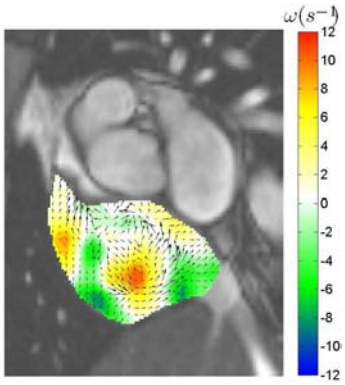	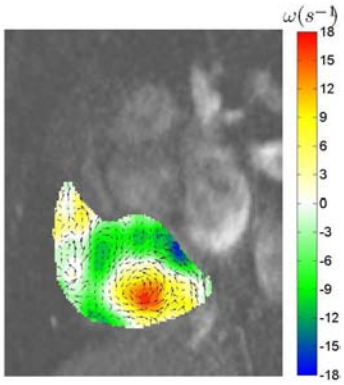	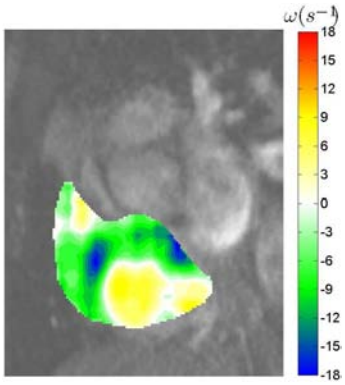
$\begin{bmatrix}\overline{\omega}\\ \sigma\end{bmatrix}_{\mu} = \begin{bmatrix}1.28\\ 4.09\end{bmatrix} s^{-1}, \begin{bmatrix}\overline{\omega}\\ \sigma\end{bmatrix}_{m} = \begin{bmatrix}1.17\\ 4.10\end{bmatrix} s^{-1}$	$\begin{bmatrix}\overline{\omega}\\ \sigma\end{bmatrix}_{\mu} = \begin{bmatrix}-0.05\\ 7.23\end{bmatrix} s^{-1}, \begin{bmatrix}\overline{\omega}\\ \sigma\end{bmatrix}_{m} = \begin{bmatrix}-0.52\\ 7.24\end{bmatrix} s^{-1}$	$\begin{bmatrix}\overline{\omega}\\ \sigma\end{bmatrix}_{\mu} = \begin{bmatrix}-2.36\\ 6.68\end{bmatrix} s^{-1}, \begin{bmatrix}\overline{\omega}\\ \sigma\end{bmatrix}_{m} = \begin{bmatrix}-2.90\\ 6.70\end{bmatrix} s^{-1}$
$(i) \quad n_t = 17$		
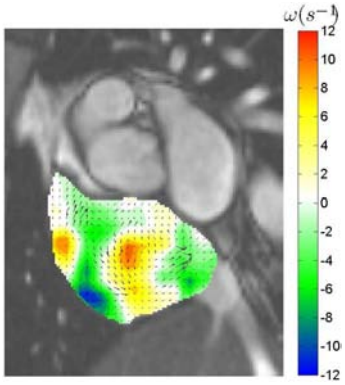	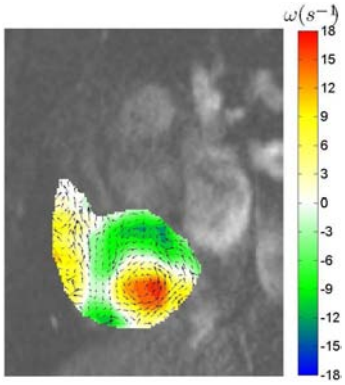	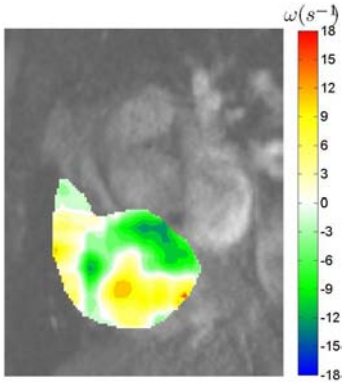
$\begin{bmatrix}\overline{\omega}\\ \sigma\end{bmatrix}_{\mu} = \begin{bmatrix}0.46\\ 4.48\end{bmatrix} s^{-1}, \begin{bmatrix}\overline{\omega}\\ \sigma\end{bmatrix}_{m} = \begin{bmatrix}0.10\\ 4.49\end{bmatrix} s^{-1}$	$\begin{bmatrix}\overline{\omega}\\ \sigma\end{bmatrix}_{\mu} = \begin{bmatrix}1.62\\ 7.41\end{bmatrix} s^{-1}, \begin{bmatrix}\overline{\omega}\\ \sigma\end{bmatrix}_{m} = \begin{bmatrix}1.15\\ 7.42\end{bmatrix} s^{-1}$	$\begin{bmatrix}\overline{\omega}\\ \sigma\end{bmatrix}_{\mu} = \begin{bmatrix}0.40\\ 6.23\end{bmatrix} s^{-1}, \begin{bmatrix}\overline{\omega}\\ \sigma\end{bmatrix}_{m} = \begin{bmatrix}0.69\\ 6.24\end{bmatrix} s^{-1}$
$(ii) \quad n_t = 18$		
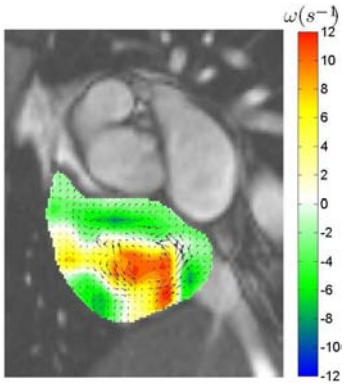	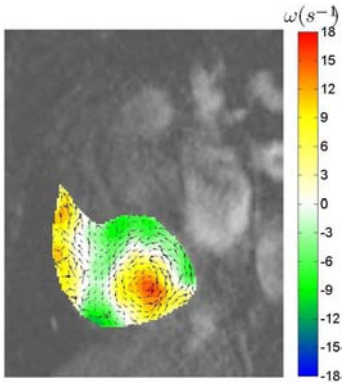	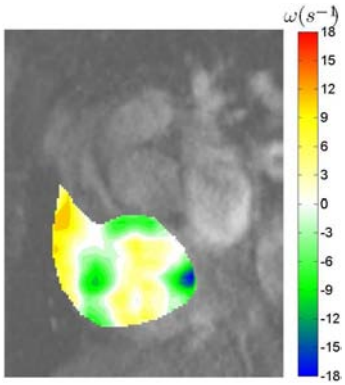
$\begin{bmatrix}\overline{\omega}\\ \sigma\end{bmatrix}_{\mu} = \begin{bmatrix}1.02\\ 5.33\end{bmatrix} s^{-1}, \begin{bmatrix}\overline{\omega}\\ \sigma\end{bmatrix}_{m} = \begin{bmatrix}-0.92\\ 5.67\end{bmatrix} s^{-1}$	$\begin{bmatrix}\overline{\omega}\\ \sigma\end{bmatrix}_{\mu} = \begin{bmatrix}2.46\\ 6.68\end{bmatrix} s^{-1}, \begin{bmatrix}\overline{\omega}\\ \sigma\end{bmatrix}_{m} = \begin{bmatrix}1.54\\ 6.74\end{bmatrix} s^{-1}$	$\begin{bmatrix}\overline{\omega}\\ \sigma\end{bmatrix}_{\mu} = \begin{bmatrix}1.12\\ 5.58\end{bmatrix} s^{-1}, \begin{bmatrix}\overline{\omega}\\ \sigma\end{bmatrix}_{m} = \begin{bmatrix}1.62\\ 5.60\end{bmatrix} s^{-1}$
$(iii) \quad n_t = 19$		

(e) Vorticity sampling window size (17×17) pixels

Vorticity sampling window size (19×19) pixels continues on the next page

VORTICITY SAMPLING SIZE (19×19) PIXELS

PREDICTED FLOW	MEASURED FLOW	VORTICITY DIFFERENCE
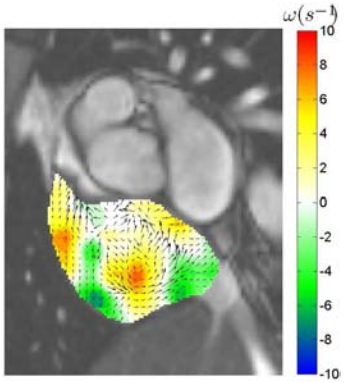	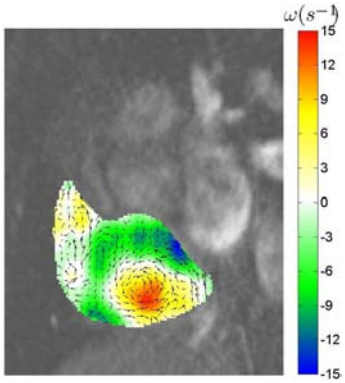	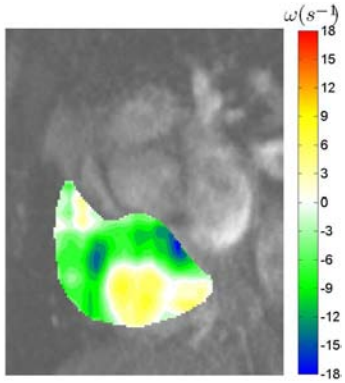
$\begin{bmatrix}\overline{\omega}\\ \sigma\end{bmatrix}_{\mu} = \begin{bmatrix}1.32\\ 3.34\end{bmatrix} s^{-1}, \begin{bmatrix}\overline{\omega}\\ \sigma\end{bmatrix}_{m} = \begin{bmatrix}1.43\\ 3.34\end{bmatrix} s^{-1}$	$\begin{bmatrix}\overline{\omega}\\ \sigma\end{bmatrix}_{\mu} = \begin{bmatrix}-0.24\\ 6.19\end{bmatrix} s^{-1}, \begin{bmatrix}\overline{\omega}\\ \sigma\end{bmatrix}_{m} = \begin{bmatrix}-2.45\\ 5.79\end{bmatrix} s^{-1}$	$\begin{bmatrix}\overline{\omega}\\ \sigma\end{bmatrix}_{\mu} = \begin{bmatrix}-2.45\\ 5.79\end{bmatrix} s^{-1}, \begin{bmatrix}\overline{\omega}\\ \sigma\end{bmatrix}_{m} = \begin{bmatrix}-2.87\\ 5.81\end{bmatrix} s^{-1}$
$(i) \quad n_t = 17$		
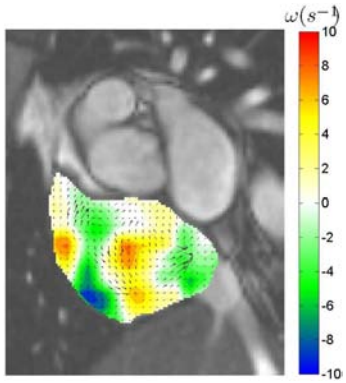	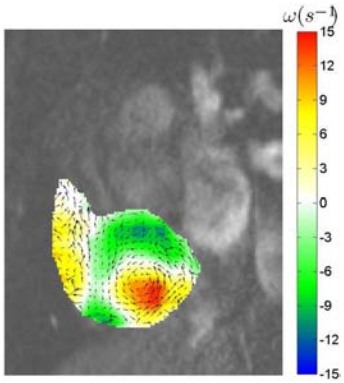	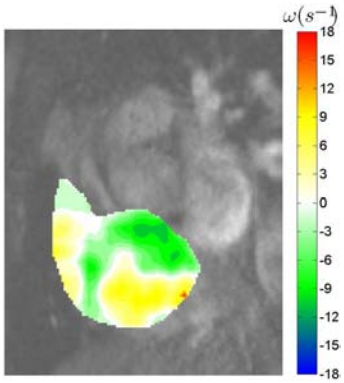
$\begin{bmatrix}\overline{\omega}\\ \sigma\end{bmatrix}_{\mu} = \begin{bmatrix}0.49\\ 3.65\end{bmatrix} s^{-1}, \begin{bmatrix}\overline{\omega}\\ \sigma\end{bmatrix}_{m} = \begin{bmatrix}0.39\\ 3.65\end{bmatrix} s^{-1}$	$\begin{bmatrix}\overline{\omega}\\ \sigma\end{bmatrix}_{\mu} = \begin{bmatrix}1.40\\ 6.27\end{bmatrix} s^{-1}, \begin{bmatrix}\overline{\omega}\\ \sigma\end{bmatrix}_{m} = \begin{bmatrix}1.06\\ 6.28\end{bmatrix} s^{-1}$	$\begin{bmatrix}\overline{\omega}\\ \sigma\end{bmatrix}_{\mu} = \begin{bmatrix}0.25\\ 5.38\end{bmatrix} s^{-1}, \begin{bmatrix}\overline{\omega}\\ \sigma\end{bmatrix}_{m} = \begin{bmatrix}0.09\\ 5.39\end{bmatrix} s^{-1}$
$(ii) \quad n_t = 18$		
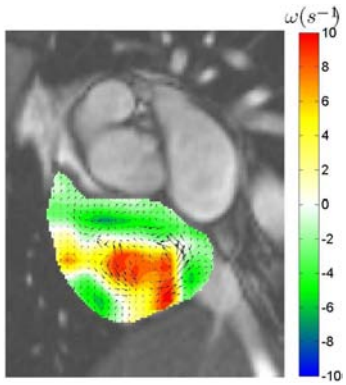	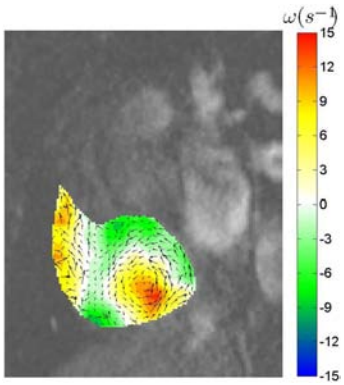	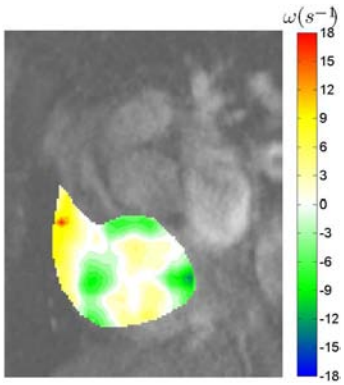
$\begin{bmatrix}\overline{\omega}\\ \sigma\end{bmatrix}_{\mu} = \begin{bmatrix}0.98\\ 4.52\end{bmatrix} s^{-1}, \begin{bmatrix}\overline{\omega}\\ \sigma\end{bmatrix}_{m} = \begin{bmatrix}-0.74\\ 4.84\end{bmatrix} s^{-1}$	$\begin{bmatrix}\overline{\omega}\\ \sigma\end{bmatrix}_{\mu} = \begin{bmatrix}2.24\\ 5.66\end{bmatrix} s^{-1}, \begin{bmatrix}\overline{\omega}\\ \sigma\end{bmatrix}_{m} = \begin{bmatrix}1.52\\ 5.70\end{bmatrix} s^{-1}$	$\begin{bmatrix}\overline{\omega}\\ \sigma\end{bmatrix}_{\mu} = \begin{bmatrix}1.01\\ 4.60\end{bmatrix} s^{-1}, \begin{bmatrix}\overline{\omega}\\ \sigma\end{bmatrix}_{m} = \begin{bmatrix}1.32\\ 4.61\end{bmatrix} s^{-1}$
$(iii) \quad n_t = 19$		

(f) Vorticity sampling window size (19×19) pixels

Vorticity sampling window size (21×21) pixels continues on the next page

VORTICITY SAMPLING SIZE (21×21) PIXELS		
PREDICTED FLOW	**MEASURED FLOW**	**VORTICITY DIFFERENCE**
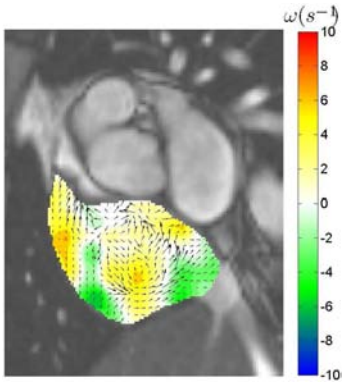	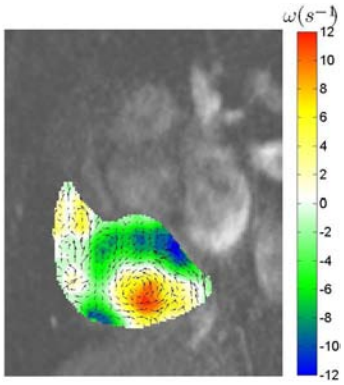	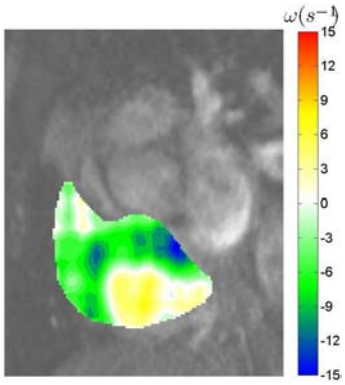
$\begin{bmatrix}\overline{\omega}\\ \sigma\end{bmatrix}_{\mu} = \begin{bmatrix}1.30\\ 2.78\end{bmatrix} s^{-1}, \begin{bmatrix}\overline{\omega}\\ \sigma\end{bmatrix}_{m} = \begin{bmatrix}1.52\\ 2.79\end{bmatrix} s^{-1}$	$\begin{bmatrix}\overline{\omega}\\ \sigma\end{bmatrix}_{\mu} = \begin{bmatrix}-0.39\\ 5.28\end{bmatrix} s^{-1}, \begin{bmatrix}\overline{\omega}\\ \sigma\end{bmatrix}_{m} = \begin{bmatrix}-0.36\\ 5.28\end{bmatrix} s^{-1}$	$\begin{bmatrix}\overline{\omega}\\ \sigma\end{bmatrix}_{\mu} = \begin{bmatrix}-2.51\\ 5.06\end{bmatrix} s^{-1}, \begin{bmatrix}\overline{\omega}\\ \sigma\end{bmatrix}_{m} = \begin{bmatrix}-2.79\\ 5.06\end{bmatrix} s^{-1}$
$(i) \quad n_t = 17$		
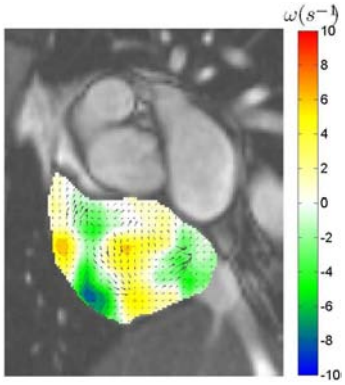	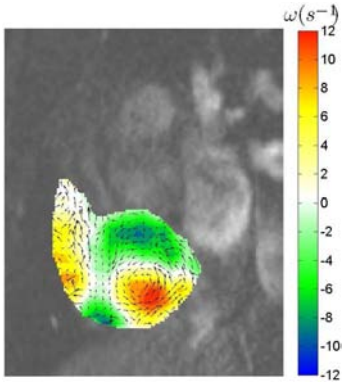	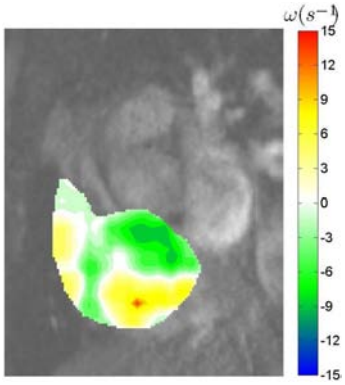
$\begin{bmatrix}\overline{\omega}\\ \sigma\end{bmatrix}_{\mu} = \begin{bmatrix}0.48\\ 3.05\end{bmatrix} s^{-1}, \begin{bmatrix}\overline{\omega}\\ \sigma\end{bmatrix}_{m} = \begin{bmatrix}0.57\\ 3.06\end{bmatrix} s^{-1}$	$\begin{bmatrix}\overline{\omega}\\ \sigma\end{bmatrix}_{\mu} = \begin{bmatrix}1.19\\ 5.33\end{bmatrix} s^{-1}, \begin{bmatrix}\overline{\omega}\\ \sigma\end{bmatrix}_{m} = \begin{bmatrix}0.83\\ 5.34\end{bmatrix} s^{-1}$	$\begin{bmatrix}\overline{\omega}\\ \sigma\end{bmatrix}_{\mu} = \begin{bmatrix}0.12\\ 4.71\end{bmatrix} s^{-1}, \begin{bmatrix}\overline{\omega}\\ \sigma\end{bmatrix}_{m} = \begin{bmatrix}-0.08\\ 4.72\end{bmatrix} s^{-1}$
$(ii) \quad n_t = 18$		
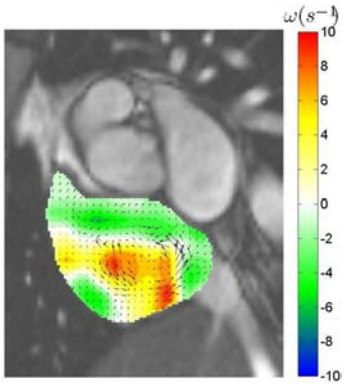	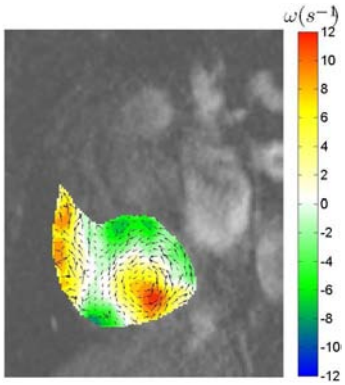	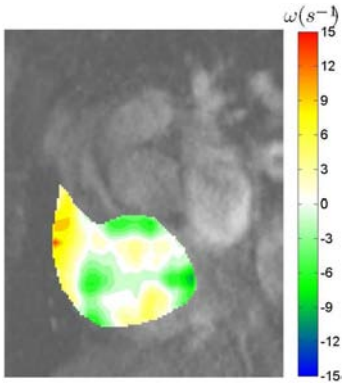
$\begin{bmatrix}\overline{\omega}\\ \sigma\end{bmatrix}_{\mu} = \begin{bmatrix}0.91\\ 3.88\end{bmatrix} s^{-1}, \begin{bmatrix}\overline{\omega}\\ \sigma\end{bmatrix}_{m} = \begin{bmatrix}-0.50\\ 4.13\end{bmatrix} s^{-1}$	$\begin{bmatrix}\overline{\omega}\\ \sigma\end{bmatrix}_{\mu} = \begin{bmatrix}2.03\\ 4.86\end{bmatrix} s^{-1}, \begin{bmatrix}\overline{\omega}\\ \sigma\end{bmatrix}_{m} = \begin{bmatrix}1.09\\ 4.94\end{bmatrix} s^{-1}$	$\begin{bmatrix}\overline{\omega}\\ \sigma\end{bmatrix}_{\mu} = \begin{bmatrix}0.91\\ 3.93\end{bmatrix} s^{-1}, \begin{bmatrix}\overline{\omega}\\ \sigma\end{bmatrix}_{m} = \begin{bmatrix}0.69\\ 3.94\end{bmatrix} s^{-1}$
$(iii) \quad n_t = 19$		

(g) Vorticity sampling window size (21×21) pixels

Vorticity sampling window size (23×23) pixels continues on the next page

VORTICITY SAMPLING SIZE (23×23) PIXELS

PREDICTED FLOW	MEASURED FLOW	VORTICITY DIFFERENCE
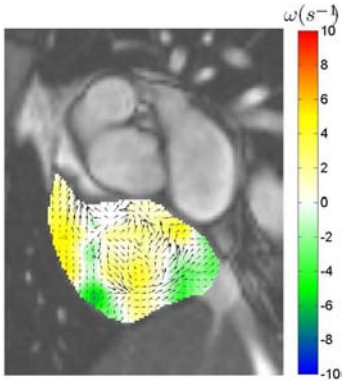	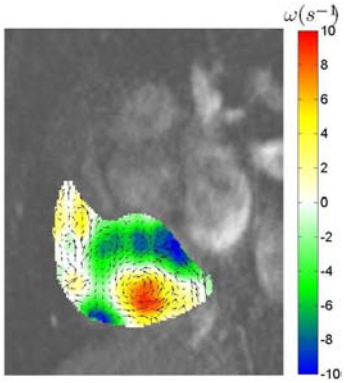	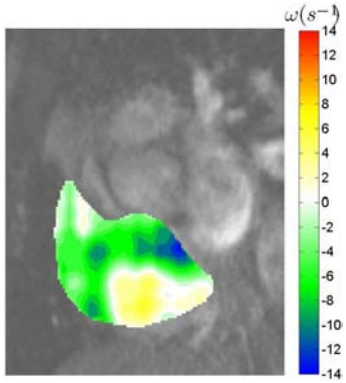
$\begin{bmatrix}\overline{\omega}\\ \sigma\end{bmatrix}_{\mu} = \begin{bmatrix}1.21\\ 2.40\end{bmatrix} s^{-1}, \begin{bmatrix}\overline{\omega}\\ \sigma\end{bmatrix}_{m} = \begin{bmatrix}1.37\\ 2.40\end{bmatrix} s^{-1}$	$\begin{bmatrix}\overline{\omega}\\ \sigma\end{bmatrix}_{\mu} = \begin{bmatrix}-0.51\\ 4.50\end{bmatrix} s^{-1}, \begin{bmatrix}\overline{\omega}\\ \sigma\end{bmatrix}_{m} = \begin{bmatrix}-0.11\\ 4.52\end{bmatrix} s^{-1}$	$\begin{bmatrix}\overline{\omega}\\ \sigma\end{bmatrix}_{\mu} = \begin{bmatrix}-2.54\\ 4.44\end{bmatrix} s^{-1}, \begin{bmatrix}\overline{\omega}\\ \sigma\end{bmatrix}_{m} = \begin{bmatrix}-2.83\\ 4.45\end{bmatrix} s^{-1}$
$(i) \quad n_t = 17$		
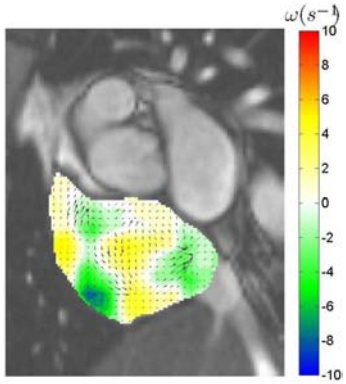	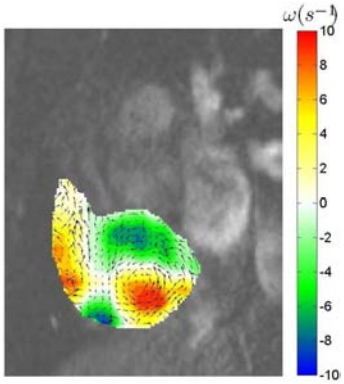	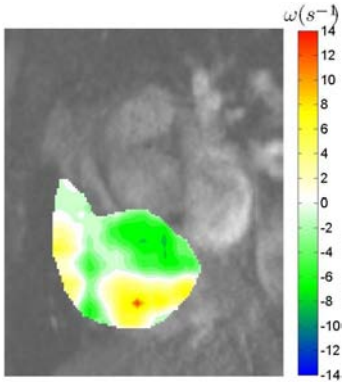
$\begin{bmatrix}\overline{\omega}\\ \sigma\end{bmatrix}_{\mu} = \begin{bmatrix}0.45\\ 2.64\end{bmatrix} s^{-1}, \begin{bmatrix}\overline{\omega}\\ \sigma\end{bmatrix}_{m} = \begin{bmatrix}0.67\\ 2.64\end{bmatrix} s^{-1}$	$\begin{bmatrix}\overline{\omega}\\ \sigma\end{bmatrix}_{\mu} = \begin{bmatrix}1.01\\ 4.58\end{bmatrix} s^{-1}, \begin{bmatrix}\overline{\omega}\\ \sigma\end{bmatrix}_{m} = \begin{bmatrix}0.94\\ 4.56\end{bmatrix} s^{-1}$	$\begin{bmatrix}\overline{\omega}\\ \sigma\end{bmatrix}_{\mu} = \begin{bmatrix}0.01\\ 4.15\end{bmatrix} s^{-1}, \begin{bmatrix}\overline{\omega}\\ \sigma\end{bmatrix}_{m} = \begin{bmatrix}-0.45\\ 4.17\end{bmatrix} s^{-1}$
$(ii) \quad n_t = 18$		
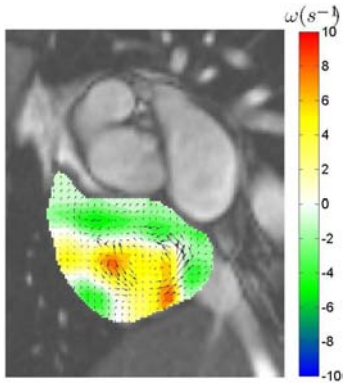	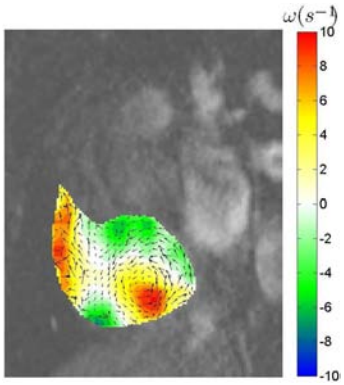	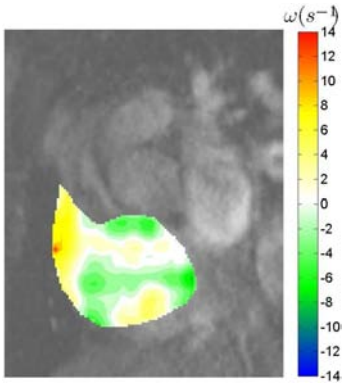
$\begin{bmatrix}\overline{\omega}\\ \sigma\end{bmatrix}_{\mu} = \begin{bmatrix}0.83\\ 3.37\end{bmatrix} s^{-1}, \begin{bmatrix}\overline{\omega}\\ \sigma\end{bmatrix}_{m} = \begin{bmatrix}-0.32\\ 3.56\end{bmatrix} s^{-1}$	$\begin{bmatrix}\overline{\omega}\\ \sigma\end{bmatrix}_{\mu} = \begin{bmatrix}1.84\\ 4.21\end{bmatrix} s^{-1}, \begin{bmatrix}\overline{\omega}\\ \sigma\end{bmatrix}_{m} = \begin{bmatrix}1.35\\ 4.23\end{bmatrix} s^{-1}$	$\begin{bmatrix}\overline{\omega}\\ \sigma\end{bmatrix}_{\mu} = \begin{bmatrix}0.83\\ 3.45\end{bmatrix} s^{-1}, \begin{bmatrix}\overline{\omega}\\ \sigma\end{bmatrix}_{m} = \begin{bmatrix}0.40\\ 3.48\end{bmatrix} s^{-1}$
$(iii) \quad n_t = 19$		

(h) Vorticity sampling window size (23×23) pixels

Vorticity sampling window size (25×25) pixels continues on the next page

VORTICITY SAMPLING SIZE (25×25) PIXELS		
PREDICTED FLOW	**MEASURED FLOW**	**VORTICITY DIFFERENCE**
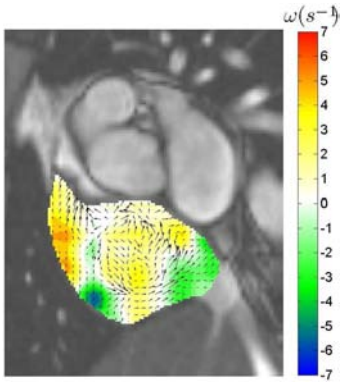	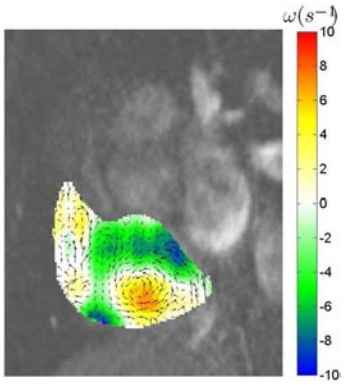	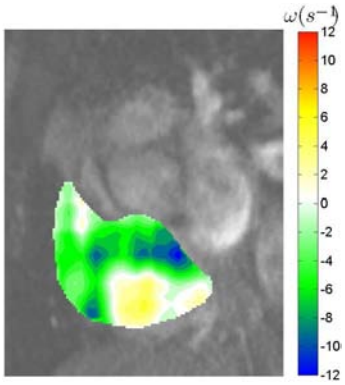
$\begin{bmatrix}\overline{\omega}\\ \sigma\end{bmatrix}_{\mu} = \begin{bmatrix}1.10\\ 2.15\end{bmatrix} s^{-1}, \begin{bmatrix}\overline{\omega}\\ \sigma\end{bmatrix}_{m} = \begin{bmatrix}1.25\\ 2.15\end{bmatrix} s^{-1}$	$\begin{bmatrix}\overline{\omega}\\ \sigma\end{bmatrix}_{\mu} = \begin{bmatrix}-0.60\\ 3.87\end{bmatrix} s^{-1}, \begin{bmatrix}\overline{\omega}\\ \sigma\end{bmatrix}_{m} = \begin{bmatrix}-0.10\\ 3.90\end{bmatrix} s^{-1}$	$\begin{bmatrix}\overline{\omega}\\ \sigma\end{bmatrix}_{\mu} = \begin{bmatrix}-2.53\\ 3.90\end{bmatrix} s^{-1}, \begin{bmatrix}\overline{\omega}\\ \sigma\end{bmatrix}_{m} = \begin{bmatrix}-2.77\\ 3.90\end{bmatrix} s^{-1}$
$(i) \quad n_t = 17$		
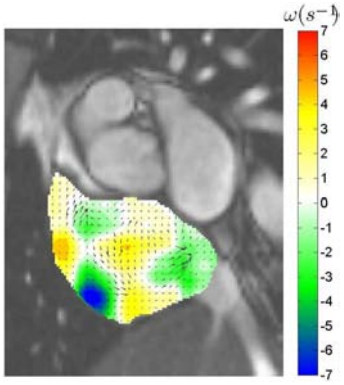	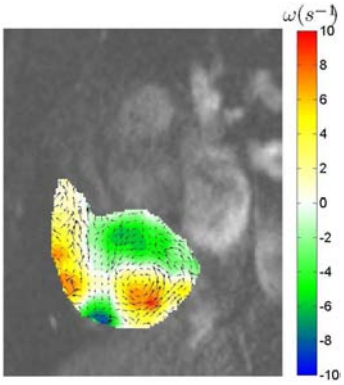	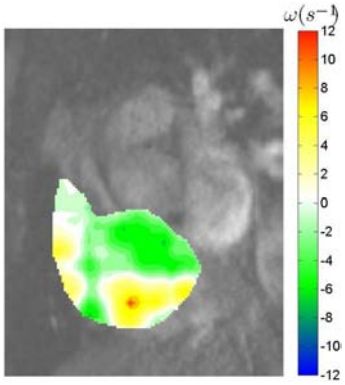
$\begin{bmatrix}\overline{\omega}\\ \sigma\end{bmatrix}_{\mu} = \begin{bmatrix}0.39\\ 2.32\end{bmatrix} s^{-1}, \begin{bmatrix}\overline{\omega}\\ \sigma\end{bmatrix}_{m} = \begin{bmatrix}0.70\\ 2.34\end{bmatrix} s^{-1}$	$\begin{bmatrix}\overline{\omega}\\ \sigma\end{bmatrix}_{\mu} = \begin{bmatrix}0.83\\ 3.94\end{bmatrix} s^{-1}, \begin{bmatrix}\overline{\omega}\\ \sigma\end{bmatrix}_{m} = \begin{bmatrix}0.78\\ 3.94\end{bmatrix} s^{-1}$	$\begin{bmatrix}\overline{\omega}\\ \sigma\end{bmatrix}_{\mu} = \begin{bmatrix}-0.09\\ 3.64\end{bmatrix} s^{-1}, \begin{bmatrix}\overline{\omega}\\ \sigma\end{bmatrix}_{m} = \begin{bmatrix}-0.60\\ 3.67\end{bmatrix} s^{-1}$
$(ii) \quad n_t = 18$		
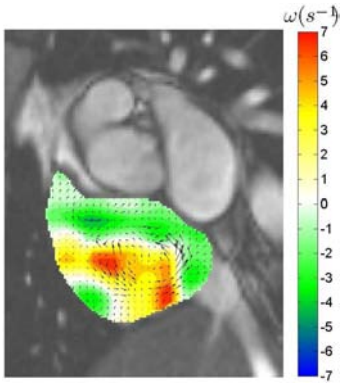	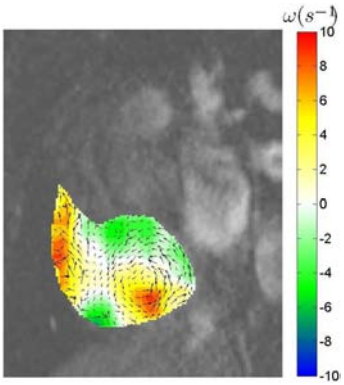	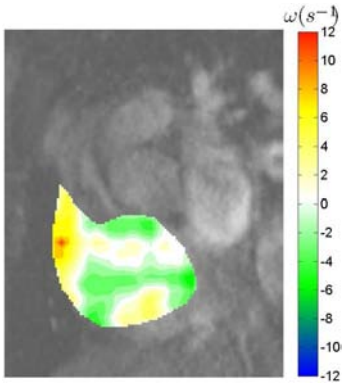
$\begin{bmatrix}\overline{\omega}\\ \sigma\end{bmatrix}_{\mu} = \begin{bmatrix}0.75\\ 2.97\end{bmatrix} s^{-1}, \begin{bmatrix}\overline{\omega}\\ \sigma\end{bmatrix}_{m} = \begin{bmatrix}-0.19\\ 3.11\end{bmatrix} s^{-1}$	$\begin{bmatrix}\overline{\omega}\\ \sigma\end{bmatrix}_{\mu} = \begin{bmatrix}1.68\\ 3.72\end{bmatrix} s^{-1}, \begin{bmatrix}\overline{\omega}\\ \sigma\end{bmatrix}_{m} = \begin{bmatrix}1.40\\ 3.73\end{bmatrix} s^{-1}$	$\begin{bmatrix}\overline{\omega}\\ \sigma\end{bmatrix}_{\mu} = \begin{bmatrix}0.74\\ 3.11\end{bmatrix} s^{-1}, \begin{bmatrix}\overline{\omega}\\ \sigma\end{bmatrix}_{m} = \begin{bmatrix}0.41\\ 3.12\end{bmatrix} s^{-1}$
$(iii) \quad n_t = 19$		

(i) Vorticity sampling window size (25×25) pixels

Vorticity sampling window size (27×27) pixels continues on the next page

VORTICITY SAMPLING SIZE (27×27) PIXELS

PREDICTED FLOW	MEASURED FLOW	VORTICITY DIFFERENCE
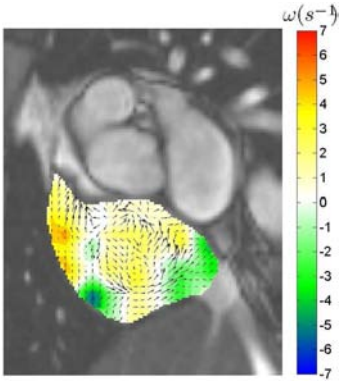	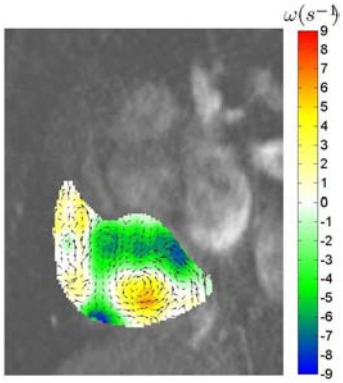	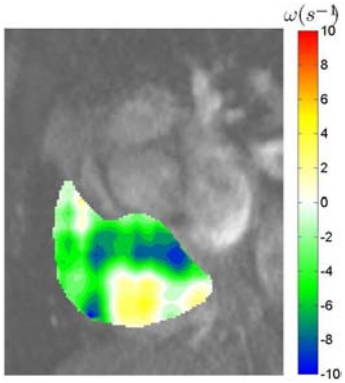
$\begin{bmatrix}\overline{\omega}\\ \sigma\end{bmatrix}_{\mu} = \begin{bmatrix}0.99\\ 1.97\end{bmatrix} s^{-1}, \begin{bmatrix}\overline{\omega}\\ \sigma\end{bmatrix}_{m} = \begin{bmatrix}1.27\\ 2.00\end{bmatrix} s^{-1}$	$\begin{bmatrix}\overline{\omega}\\ \sigma\end{bmatrix}_{\mu} = \begin{bmatrix}-0.64\\ 3.33\end{bmatrix} s^{-1}, \begin{bmatrix}\overline{\omega}\\ \sigma\end{bmatrix}_{m} = \begin{bmatrix}-0.16\\ 3.36\end{bmatrix} s^{-1}$	$\begin{bmatrix}\overline{\omega}\\ \sigma\end{bmatrix}_{\mu} = \begin{bmatrix}-2.48\\ 3.41\end{bmatrix} s^{-1}, \begin{bmatrix}\overline{\omega}\\ \sigma\end{bmatrix}_{m} = \begin{bmatrix}-2.61\\ 3.41\end{bmatrix} s^{-1}$
$(i) \quad n_t = 17$		
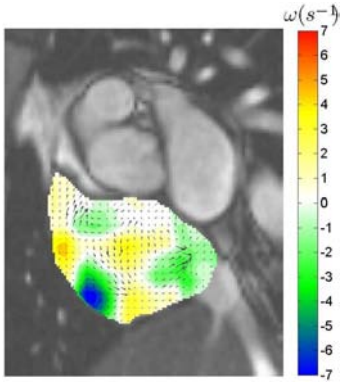	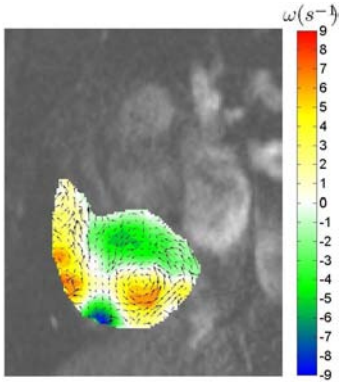	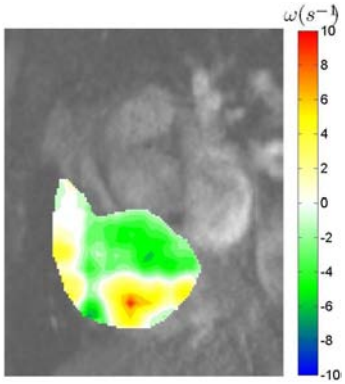
$\begin{bmatrix}\overline{\omega}\\ \sigma\end{bmatrix}_{\mu} = \begin{bmatrix}0.33\\ 2.08\end{bmatrix} s^{-1}, \begin{bmatrix}\overline{\omega}\\ \sigma\end{bmatrix}_{m} = \begin{bmatrix}0.65\\ 2.10\end{bmatrix} s^{-1}$	$\begin{bmatrix}\overline{\omega}\\ \sigma\end{bmatrix}_{\mu} = \begin{bmatrix}0.69\\ 3.43\end{bmatrix} s^{-1}, \begin{bmatrix}\overline{\omega}\\ \sigma\end{bmatrix}_{m} = \begin{bmatrix}0.69\\ 3.43\end{bmatrix} s^{-1}$	$\begin{bmatrix}\overline{\omega}\\ \sigma\end{bmatrix}_{\mu} = \begin{bmatrix}-0.16\\ 3.16\end{bmatrix} s^{-1}, \begin{bmatrix}\overline{\omega}\\ \sigma\end{bmatrix}_{m} = \begin{bmatrix}-0.74\\ 3.21\end{bmatrix} s^{-1}$
$(ii) \quad n_t = 18$		
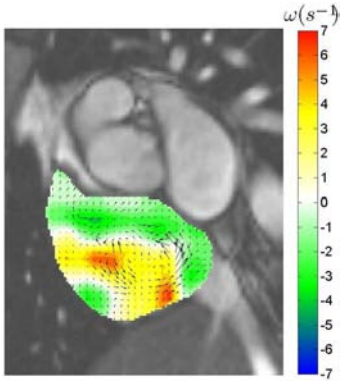	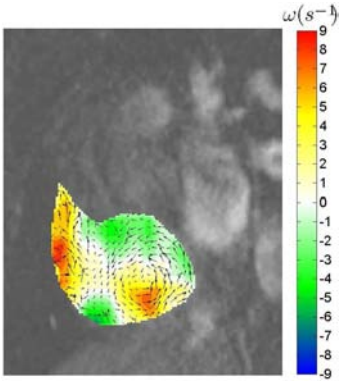	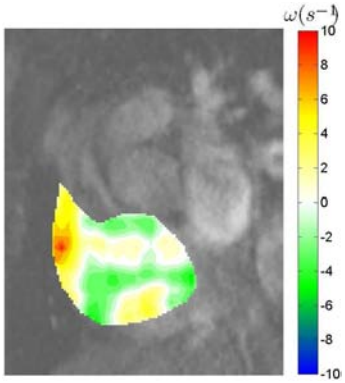
$\begin{bmatrix}\overline{\omega}\\ \sigma\end{bmatrix}_{\mu} = \begin{bmatrix}0.66\\ 2.62\end{bmatrix} s^{-1}, \begin{bmatrix}\overline{\omega}\\ \sigma\end{bmatrix}_{m} = \begin{bmatrix}-0.13\\ 2.74\end{bmatrix} s^{-1}$	$\begin{bmatrix}\overline{\omega}\\ \sigma\end{bmatrix}_{\mu} = \begin{bmatrix}1.53\\ 3.32\end{bmatrix} s^{-1}, \begin{bmatrix}\overline{\omega}\\ \sigma\end{bmatrix}_{m} = \begin{bmatrix}1.19\\ 3.34\end{bmatrix} s^{-1}$	$\begin{bmatrix}\overline{\omega}\\ \sigma\end{bmatrix}_{\mu} = \begin{bmatrix}0.67\\ 2.84\end{bmatrix} s^{-1}, \begin{bmatrix}\overline{\omega}\\ \sigma\end{bmatrix}_{m} = \begin{bmatrix}0.40\\ 2.85\end{bmatrix} s^{-1}$
$(iii) \quad n_t = 19$		

(j) Vorticity sampling window size (27×27) pixels

Figure C.2. Normal atrial flow visualisation using different vorticity measurements. Visualisation of flow in the right atrium of a normal subject based on different vorticity measurement sampling window sizes from (9×9) to (27×27) grid points is presented.

Appendix D

Visualisation of Right Atrial Flow (Pre-Atrial Septal Occulsion)

PATIENT with atrial septal defect is scanned using cardiac magnetic resonance imaging and processed for flow information. The velocity streamline plots and vorticty contour flow maps are presented. Flow measurement has been performed based on MR fluid motion tracking. This information can give an indication of the flow condition within the right atrium of the patient with atrial septal defect before atrial septal occlusion.

The set of flow images in this section are presented to demonstrate abnormal flow situation before atrial septal occlusion. A reduced version of the image set is in Section 8.5 of the thesis. The flow fields may be referenced against those for the heart chamber after surgical occlusion to determine any differences in the flow patterns.

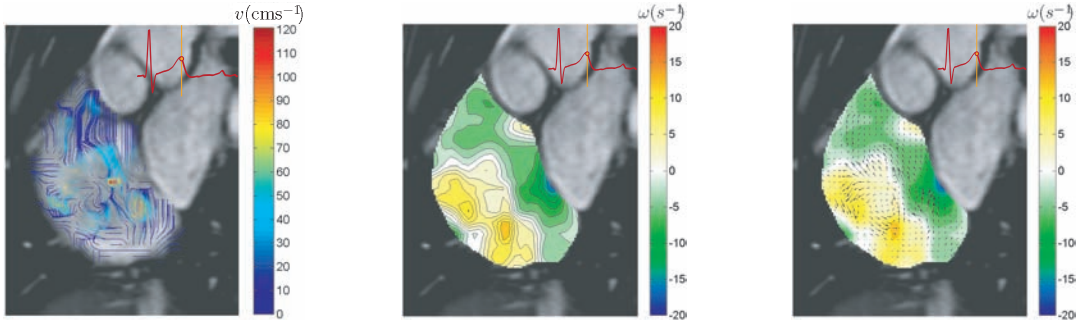

(i) $n_t = 10, \begin{bmatrix} \overline{\omega} \\ \sigma \end{bmatrix}_{\mu} = \begin{bmatrix} -0.05 \\ 5.55 \end{bmatrix} \mathrm{s}^{-1}, \begin{bmatrix} \overline{\omega} \\ \sigma \end{bmatrix}_{md} = \begin{bmatrix} -1.05 \\ 5.64 \end{bmatrix} \mathrm{s}^{-1}$

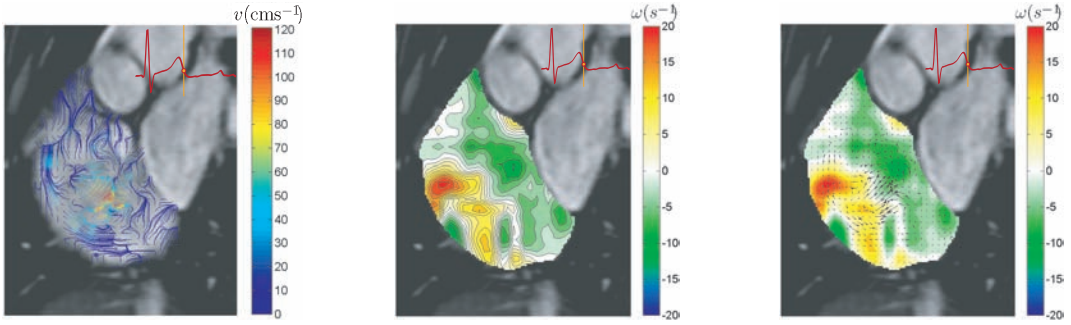

(ii) $n_t = 11, \begin{bmatrix} \overline{\omega} \\ \sigma \end{bmatrix}_{\mu} = \begin{bmatrix} -0.04 \\ 5.48 \end{bmatrix} \mathrm{s}^{-1}, \begin{bmatrix} \overline{\omega} \\ \sigma \end{bmatrix}_{md} = \begin{bmatrix} -1.05 \\ 5.57 \end{bmatrix} \mathrm{s}^{-1}$

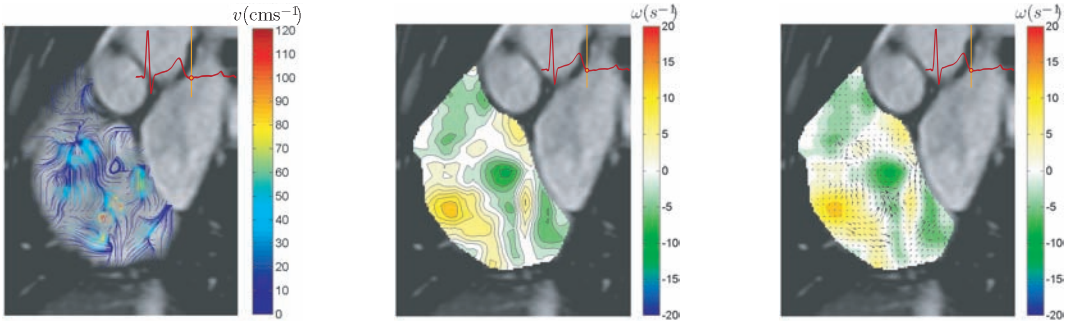

(iii) $n_t = 12, \begin{bmatrix} \overline{\omega} \\ \sigma \end{bmatrix}_{\mu} = \begin{bmatrix} 0.48 \\ 6.62 \end{bmatrix} \mathrm{s}^{-1}, \begin{bmatrix} \overline{\omega} \\ \sigma \end{bmatrix}_{md} = \begin{bmatrix} -1.28 \\ 6.85 \end{bmatrix} \mathrm{s}^{-1}$

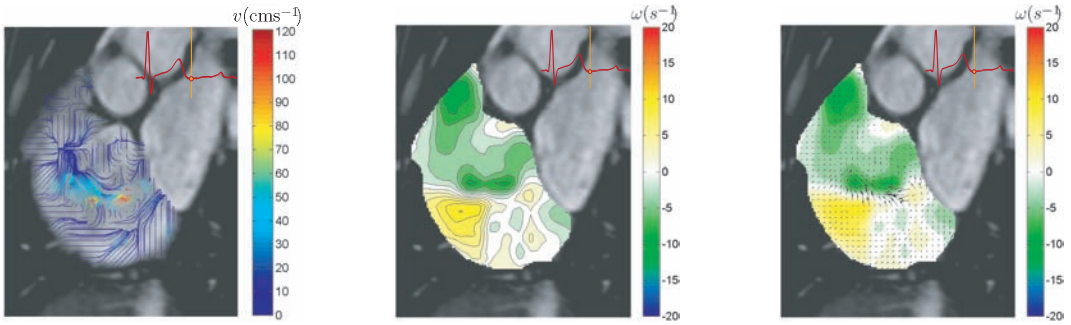

(iv) $n_t = 13, \begin{bmatrix} \overline{\omega} \\ \sigma \end{bmatrix}_{\mu} = \begin{bmatrix} 0.78 \\ 4.18 \end{bmatrix} \mathrm{s}^{-1}, \begin{bmatrix} \overline{\omega} \\ \sigma \end{bmatrix}_{md} = \begin{bmatrix} 0 \\ 4.25 \end{bmatrix} \mathrm{s}^{-1}$

Figure D.1. Slice = 1 and time frame indices n_t = 10 to 13 of pre-ASO scan. The first slice of rotating blood flow within the right atrium pre-ASO using magnetic resonance images, streamline plots, velocity vector plots, and vorticity contour maps.

CASE STUDY 1

SLICE 2

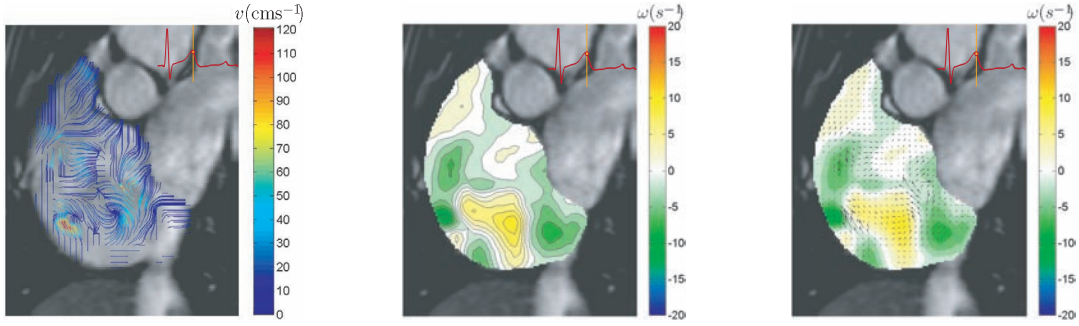

(i) $n_t = 10, \begin{bmatrix} \overline{\omega} \\ \sigma \end{bmatrix}_{\mu} = \begin{bmatrix} 0.16 \\ 0 \end{bmatrix} \mathrm{s}^{-1}, \begin{bmatrix} \overline{\omega} \\ \sigma \end{bmatrix}_{md} = \begin{bmatrix} 4.32 \\ 4.33 \end{bmatrix} \mathrm{s}^{-1}$

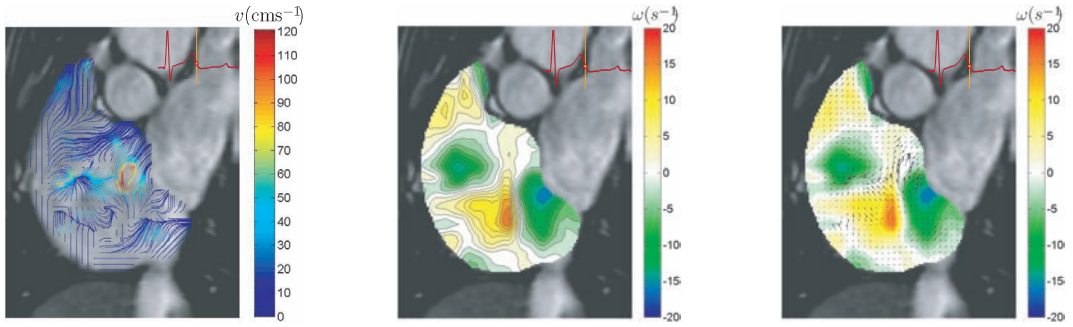

(ii) $n_t = 11, \begin{bmatrix} \overline{\omega} \\ \sigma \end{bmatrix}_{\mu} = \begin{bmatrix} 0.13 \\ 0 \end{bmatrix} \mathrm{s}^{-1}, \begin{bmatrix} \overline{\omega} \\ \sigma \end{bmatrix}_{md} = \begin{bmatrix} 3.75 \\ 3.76 \end{bmatrix} \mathrm{s}^{-1}$

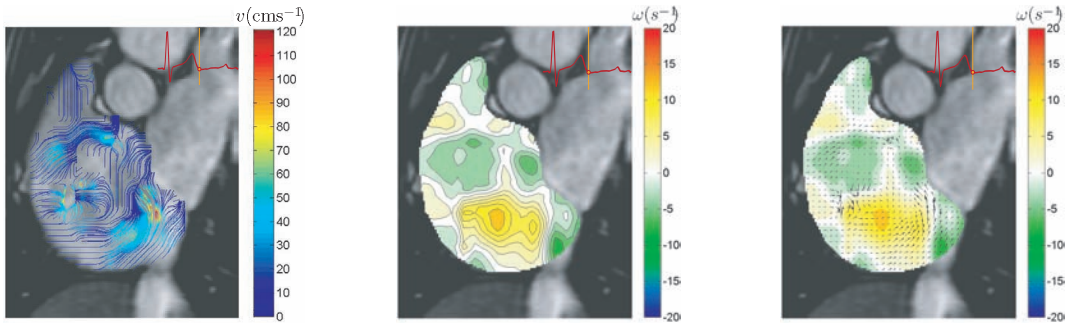

(iii) $n_t = 12, \begin{bmatrix} \overline{\omega} \\ \sigma \end{bmatrix}_{\mu} = \begin{bmatrix} 0.24 \\ 0 \end{bmatrix} \mathrm{s}^{-1}, \begin{bmatrix} \overline{\omega} \\ \sigma \end{bmatrix}_{md} = \begin{bmatrix} 6.12 \\ 6.12 \end{bmatrix} \mathrm{s}^{-1}$

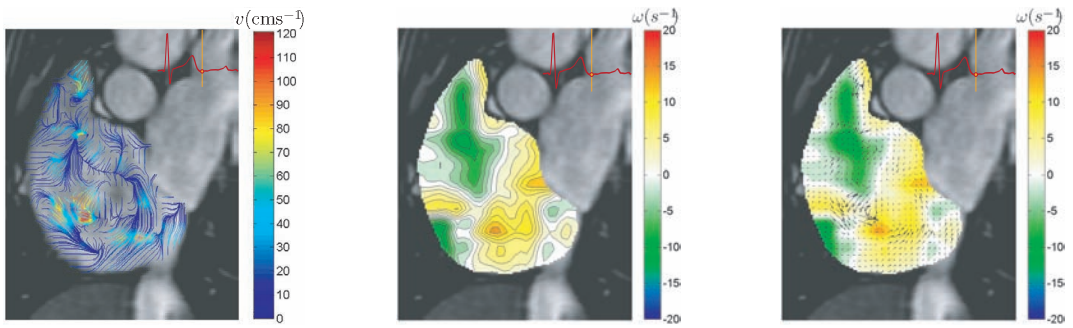

(iv) $n_t = 13, \begin{bmatrix} \overline{\omega} \\ \sigma \end{bmatrix}_{\mu} = \begin{bmatrix} 1.38 \\ 0.76 \end{bmatrix} \mathrm{s}^{-1}, \begin{bmatrix} \overline{\omega} \\ \sigma \end{bmatrix}_{md} = \begin{bmatrix} 4.18 \\ 4.19 \end{bmatrix} \mathrm{s}^{-1}$

Figure D.2. Slice = 2 and time frame indices n_t = 10 to 13 of pre-ASO scan. The second slice of rotating blood flow within the right atrium pre-ASO using magnetic resonance images, streamline plots, velocity vector plots, and vorticity contour maps.

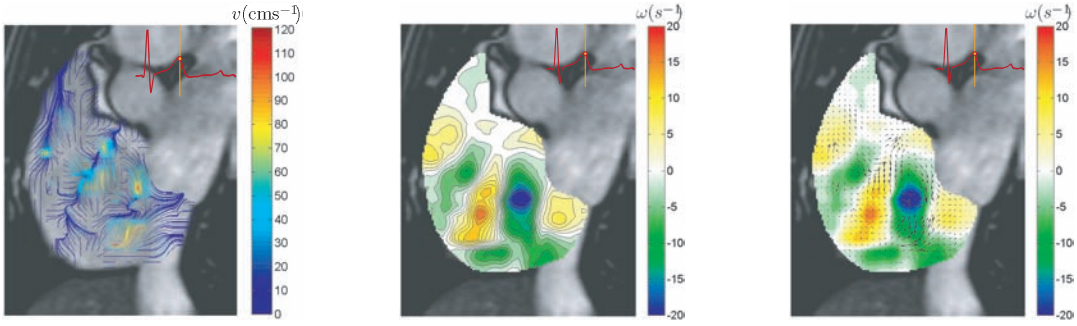

(i) $n_t = 10, \begin{bmatrix} \overline{\omega} \\ \sigma \end{bmatrix}_{\mu} = \begin{bmatrix} 0.09 \\ 0 \end{bmatrix} \mathrm{s}^{-1}, \begin{bmatrix} \overline{\omega} \\ \sigma \end{bmatrix}_{md} = \begin{bmatrix} 6.38 \\ 6.38 \end{bmatrix} \mathrm{s}^{-1}$

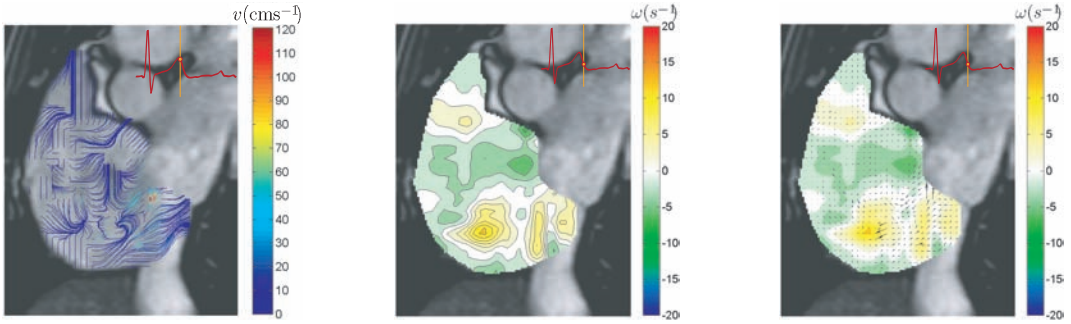

(ii) $n_t = 11, \begin{bmatrix} \overline{\omega} \\ \sigma \end{bmatrix}_{\mu} = \begin{bmatrix} 0.08 \\ 0 \end{bmatrix} \mathrm{s}^{-1}, \begin{bmatrix} \overline{\omega} \\ \sigma \end{bmatrix}_{md} = \begin{bmatrix} 5/07 \\ 5.07 \end{bmatrix} \mathrm{s}^{-1}$

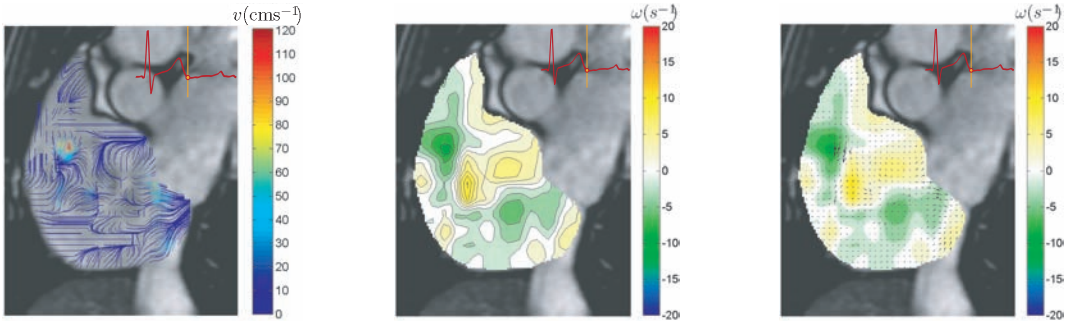

(iii) $n_t = 12, \begin{bmatrix} \overline{\omega} \\ \sigma \end{bmatrix}_{\mu} = \begin{bmatrix} 0.56 \\ 0 \end{bmatrix} \mathrm{s}^{-1}, \begin{bmatrix} \overline{\omega} \\ \sigma \end{bmatrix}_{md} = \begin{bmatrix} 3.02 \\ 3.07 \end{bmatrix} \mathrm{s}^{-1}$

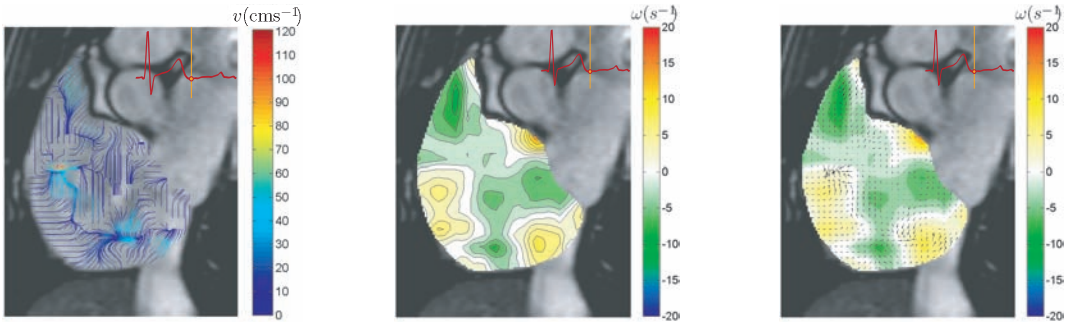

(iv) $n_t = 13, \begin{bmatrix} \overline{\omega} \\ \sigma \end{bmatrix}_{\mu} = \begin{bmatrix} 0.61 \\ 0.71 \end{bmatrix} \mathrm{s}^{-1}, \begin{bmatrix} \overline{\omega} \\ \sigma \end{bmatrix}_{md} = \begin{bmatrix} 3.36 \\ 3.36 \end{bmatrix} \mathrm{s}^{-1}$

Figure D.3. Slice = 3 and time frame indices $n_t = 10$ to 13 of pre-ASO scan. The third slice of rotating blood flow within the right atrium pre-ASO using magnetic resonance images, streamline plots, velocity vector plots, and vorticity contour maps.

Appendix E

Visualisation of Right Atrial Flow (Post-Atrial Septal Occulsion)

POST-atrial septal occlusion is performed and the patient is scanned using cardiac magnetic resonance imaging. Velocity streamline plots and vorticty contour flow maps are presented here. These information can give an indication of the flow condition within the right atrium of the patient with atrial septal defect after atrial septal occlusion. The flow can also be compared with the one before septal occlusion.

The set of flow images provided here can demonstrate the difference in flow patterns after surgical atrial septal occlusion. A section of these flow image set is presented in Section 8.5 of the thesis. They are to be referenced against the vorticity maps based on scans before the occlusion (in Appendix D).

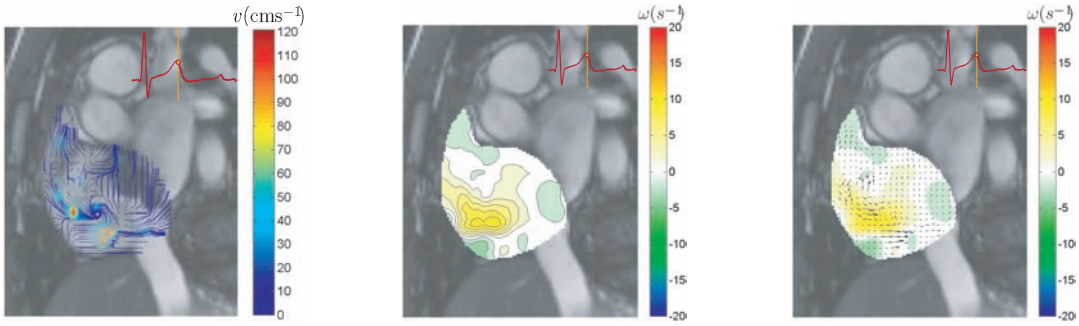

(i) $n_t = 10, \begin{bmatrix} \overline{\omega} \\ \sigma \end{bmatrix}_{\mu} = \begin{bmatrix} 2.02 \\ 1.29 \end{bmatrix} \mathrm{s}^{-1}, \begin{bmatrix} \overline{\omega} \\ \sigma \end{bmatrix}_{md} = \begin{bmatrix} 2.91 \\ 3.00 \end{bmatrix} \mathrm{s}^{-1}$

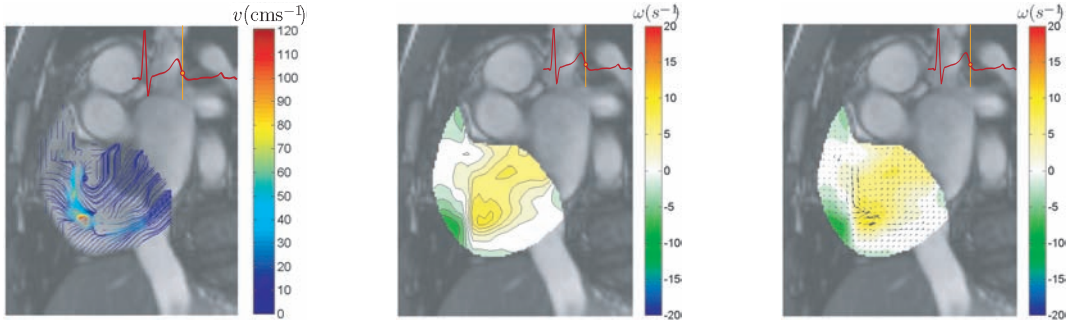

(ii) $n_t = 11, \begin{bmatrix} \overline{\omega} \\ \sigma \end{bmatrix}_{\mu} = \begin{bmatrix} 2.04 \\ 1.29 \end{bmatrix} \mathrm{s}^{-1}, \begin{bmatrix} \overline{\omega} \\ \sigma \end{bmatrix}_{md} = \begin{bmatrix} 2.89 \\ 2.99 \end{bmatrix} \mathrm{s}^{-1}$

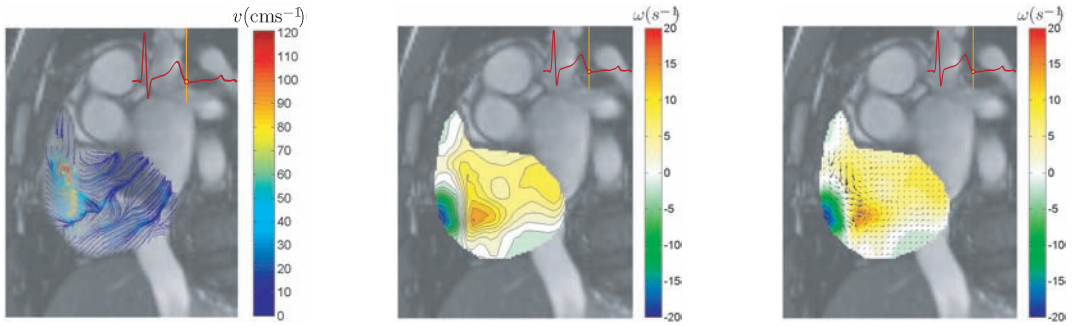

(iii) $n_t = 12, \begin{bmatrix} \overline{\omega} \\ \sigma \end{bmatrix}_{\mu} = \begin{bmatrix} 2.87 \\ 2.35 \end{bmatrix} \mathrm{s}^{-1}, \begin{bmatrix} \overline{\omega} \\ \sigma \end{bmatrix}_{md} = \begin{bmatrix} 3.74 \\ 3.78 \end{bmatrix} \mathrm{s}^{-1}$

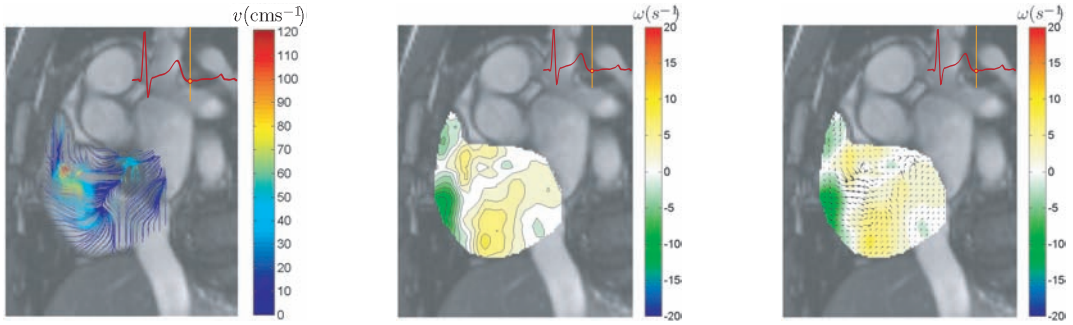

(iv) $n_t = 13, \begin{bmatrix} \overline{\omega} \\ \sigma \end{bmatrix}_{\mu} = \begin{bmatrix} 4.58 \\ 5.88 \end{bmatrix} \mathrm{s}^{-1}, \begin{bmatrix} \overline{\omega} \\ \sigma \end{bmatrix}_{md} = \begin{bmatrix} 5.20 \\ 5.36 \end{bmatrix} \mathrm{s}^{-1}$

Figure E.1. Slice = 1 and time frame indices n_t = 10 to 13 of post-ASO scan. The first slice of rotating blood flow within the right atrium post-ASO using magnetic resonance images, streamline plots, velocity vector plots, and vorticity contour maps.

CASE STUDY 1

SLICE 2

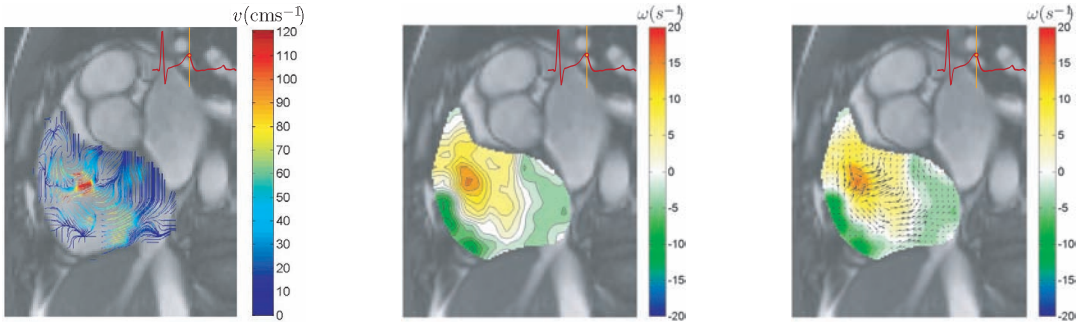

(i) $n_t = 10, \begin{bmatrix} \overline{\omega} \\ \sigma \end{bmatrix}_{\mu} = \begin{bmatrix} 2.39 \\ 1.88 \end{bmatrix} \mathrm{s}^{-1}, \begin{bmatrix} \overline{\omega} \\ \sigma \end{bmatrix}_{md} = \begin{bmatrix} 5.57 \\ 5.59 \end{bmatrix} \mathrm{s}^{-1}$

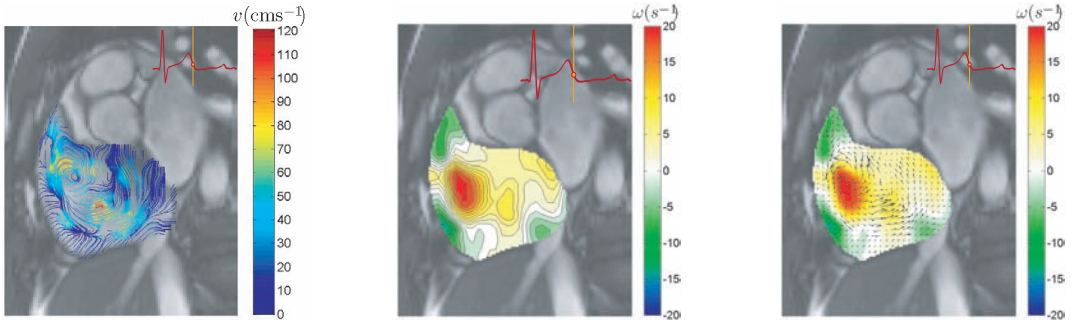

(ii) $n_t = 11, \begin{bmatrix} \overline{\omega} \\ \sigma \end{bmatrix}_{\mu} = \begin{bmatrix} 2.34 \\ 1.88 \end{bmatrix} \mathrm{s}^{-1}, \begin{bmatrix} \overline{\omega} \\ \sigma \end{bmatrix}_{md} = \begin{bmatrix} 5.60 \\ 5.62 \end{bmatrix} \mathrm{s}^{-1}$

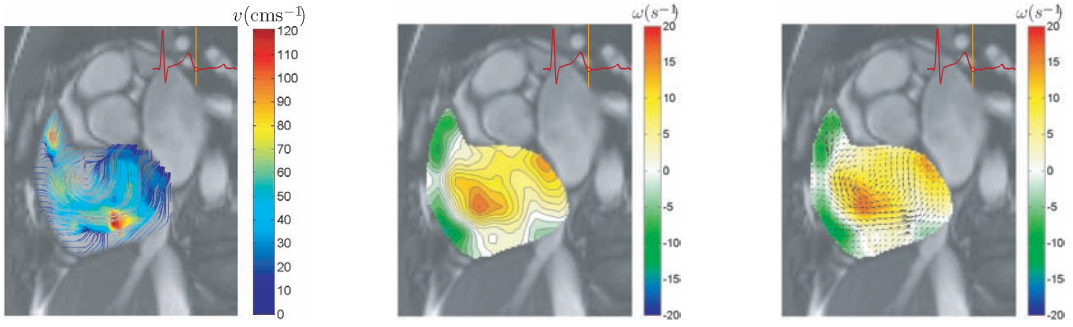

(iii) $n_t = 12, \begin{bmatrix} \overline{\omega} \\ \sigma \end{bmatrix}_{\mu} = \begin{bmatrix} 4.15 \\ 4.06 \end{bmatrix} \mathrm{s}^{-1}, \begin{bmatrix} \overline{\omega} \\ \sigma \end{bmatrix}_{md} = \begin{bmatrix} 6.46 \\ 6.46 \end{bmatrix} \mathrm{s}^{-1}$

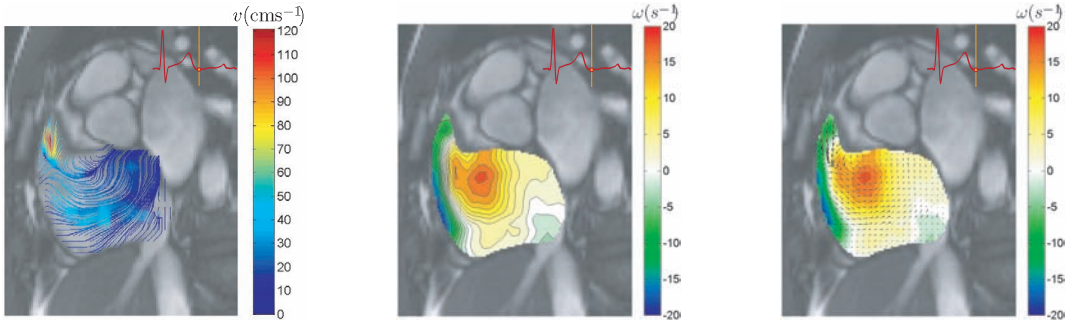

(iv) $n_t = 13, \begin{bmatrix} \overline{\omega} \\ \sigma \end{bmatrix}_{\mu} = \begin{bmatrix} 5.17 \\ 6.71 \end{bmatrix} \mathrm{s}^{-1}, \begin{bmatrix} \overline{\omega} \\ \sigma \end{bmatrix}_{md} = \begin{bmatrix} 6.39 \\ 6.57 \end{bmatrix} \mathrm{s}^{-1}$

Figure E.2. Slice = 2 and time frame indices n_t = 10 to 13 of post-ASO scan. The second slice of rotating blood flow within the right atrium post-ASO using magnetic resonance images, streamline plots, velocity vector plots, and vorticity contour maps.

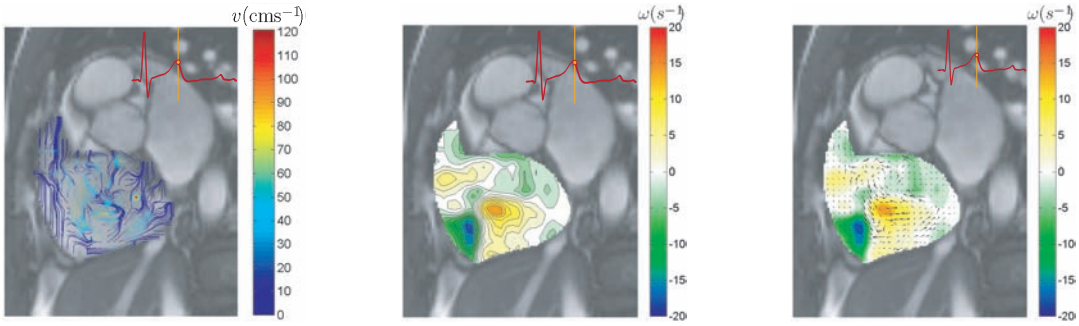

(i) $n_t = 10, \begin{bmatrix} \overline{\omega} \\ \sigma \end{bmatrix}_{\mu} = \begin{bmatrix} 0.51 \\ 0 \end{bmatrix} \text{s}^{-1}, \begin{bmatrix} \overline{\omega} \\ \sigma \end{bmatrix}_{md} = \begin{bmatrix} 5.15 \\ 5.18 \end{bmatrix} \text{s}^{-1}$

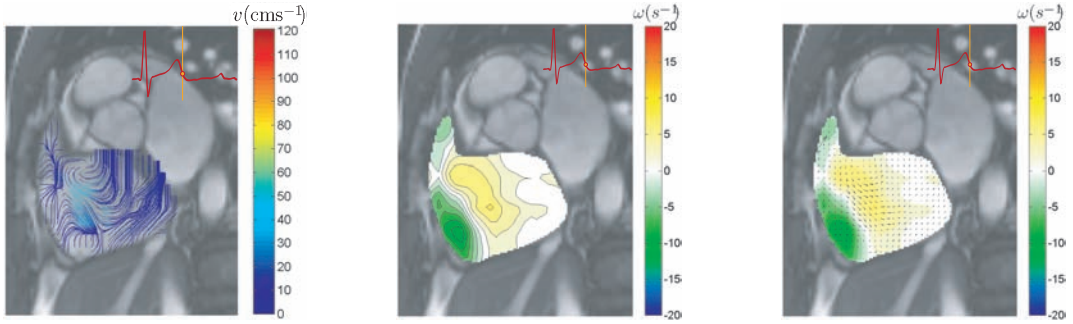

(ii) $n_t = 11, \begin{bmatrix} \overline{\omega} \\ \sigma \end{bmatrix}_{\mu} = \begin{bmatrix} 0.48 \\ 0 \end{bmatrix} \text{s}^{-1}, \begin{bmatrix} \overline{\omega} \\ \sigma \end{bmatrix}_{md} = \begin{bmatrix} 5.12 \\ 5.14 \end{bmatrix} \text{s}^{-1}$

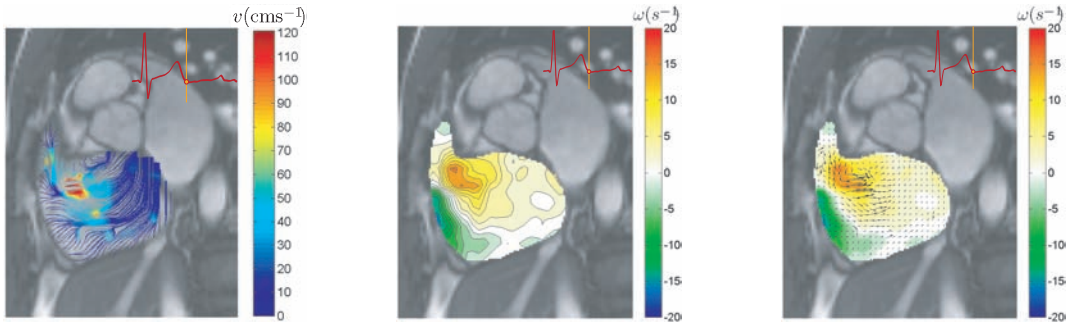

(iii) $n_t = 12, \begin{bmatrix} \overline{\omega} \\ \sigma \end{bmatrix}_{\mu} = \begin{bmatrix} 1.49 \\ 1.94 \end{bmatrix} \text{s}^{-1}, \begin{bmatrix} \overline{\omega} \\ \sigma \end{bmatrix}_{md} = \begin{bmatrix} 3.95 \\ 3.97 \end{bmatrix} \text{s}^{-1}$

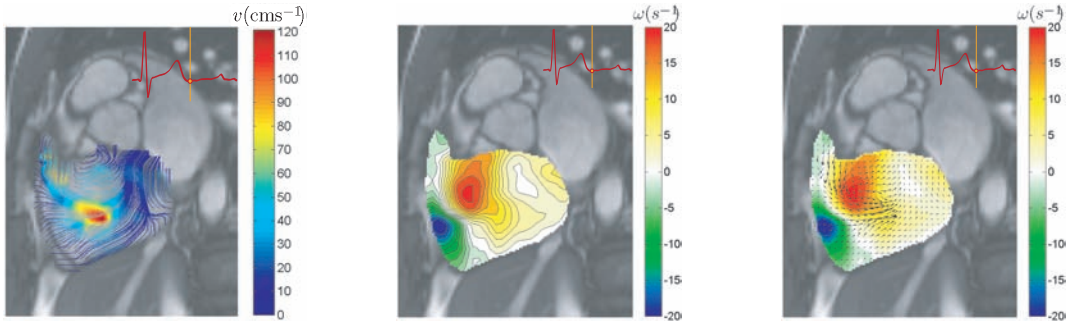

(iv) $n_t = 13, \begin{bmatrix} \overline{\omega} \\ \sigma \end{bmatrix}_{\mu} = \begin{bmatrix} 2.50 \\ 2.82 \end{bmatrix} \text{s}^{-1}, \begin{bmatrix} \overline{\omega} \\ \sigma \end{bmatrix}_{md} = \begin{bmatrix} 5.86 \\ 5.87 \end{bmatrix} \text{s}^{-1}$

Figure E.3. Slice = 3 and time frame indices $n_t = 10$ to 13 of post-ASO scan. The first slice of rotating blood flow within the right atrium post-ASO using magnetic resonance images, streamline plots, velocity vector plots, and vorticity contour maps.

Appendix F

Supplementary Video Clips

CINE-cardiac magnetic resonance images, segmentation procedures, as well as flow results, in the form of video clips, are listed in this appendix. The resource contents of these supplementary materials can be assessed from a CD-ROM labeled *Supplementary Videos* that forms a portion of this thesis.

These video clips are designed to assist the reading of Chapters 2, 5, 7 and 8 in terms of understanding the various concepts and referencing the full version of results that appears here.

The list of supplementary video clips is as follows:

List of video clips			
Video No.	Description	File name	File size
1	MRI of normal case subject	Normal_Subject1_MRI.mov	259 KB
2	MRI of patient pre-ASO	Pre_ASO_MRI.mov	320KB
3	MRI of patient post-ASO	Post_ASO_MRI.mov	333 KB
4	MRI atrial segmentation	Atrial_MRI_segmentation.mov	155 KB
5	Phase contrast MRI of normal case subject in x-direction	Normal_Subject1_PCMRI_X.mov	1372 KB
6	Phase contrast MRI of normal case subject in y-direction	Normal_Subject1_PCMRI_Y.mov	1526 KB
7	Vorticity and vector flow maps of normal right atrium	Normal_Subject1_Vorticity_Maps.mov	1847 KB
8	Colour flow streamlines of normal right atrium	Normal_Subject1_Streamline_Maps.mov	1906 KB
9	PC-MRI magnitude images based on two-chamber short axis (Slice 1)	MRI_2_Chamber_Short_Axis_Slice1.mov	287 KB
10	PC-MRI magnitude images based on two-chamber short axis (Slice 4)	MRI_2_Chamber_Short_Axis_Slice4.mov	284 KB
11	PC-MRI magnitude images based on four-chamber long axis (Slice 3)	MRI_4_Chamber_Long_Axis_Slice3.mov	391 KB
12	PC-MRI magnitude images based on four-chamber long axis (Slice 4)	MRI_4_Chamber_Long_Axis_Slice4.mov	386 KB
13	Medflovan version 1.0 Brochure	Medflovan_brochure.mov	4420 KB
14	Medflovan version 1.0 System Demonstration	Medflovan_demo.mov	15201 KB

Each thumbnail showing the one screen capture of the supplementary video clips is presented in Figure F.1. There are altogether 14 video clips in the list:

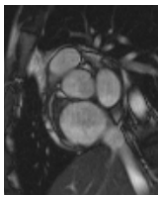

(a) Video No. 1

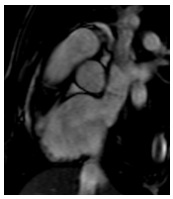

(b) Video No. 2

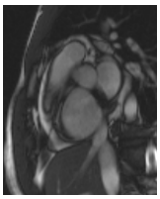

(c) Video No. 3

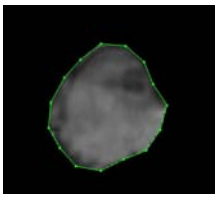

(d) Video No. 4

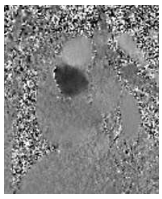

(e) Video No. 5

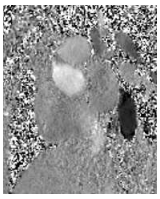

(f) Video No. 6

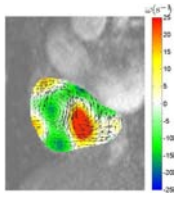

(g) Video No. 7

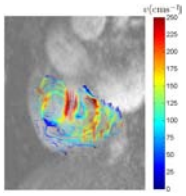

(h) Video No. 8

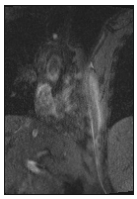

(i) Video No. 9

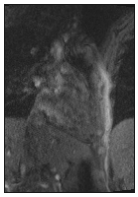

(j) Video No. 10

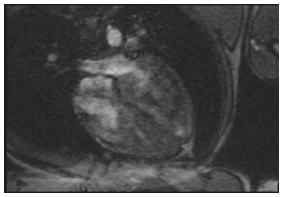

(k) Video No. 11

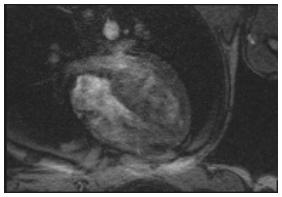

(l) Video No. 12

(m) Video No. 13

(n) Video No. 14

Figure F.1. Thumbnails of supplementary videos. One screen capture of every video is presented in thumbnail graphics to describe the contents of each of the media resource. The movie videos are in mov format. Picture and transition duration are set as 0.5 seconds for Videos 1 to 12. The durations set for Video 13 are set to be slower at 2 and 0.75 seconds. The movie playback can be paused for closer visual analysis. Video 14 is a screen capture of the Medflovan system demonsration. We can observe the graphical user interface of the software from this video.

The descriptive contents of supplementary video clips are provided below:

1. Magnetic resonance images of a normal case subject at 2-chamber short axis configuration is presented. We can visually observe a rotation of blood within the right atrium based on the motional ensembles of asynchronous blood proton spins.

2. Use of SSFP magnetic resonance imaging to detect atrial septal defect (ASD). Note the multiple vortices in the right atrial flow.

3. This is the SSFP magnetic resonance imaging of the atrium after atrial septal occlusion (ASO). We observe a faster blood rotation based on the intensity contrast exhibited by asynchronous blood proton spins for a series of time frames. There is a dominant vortex in the right atrium.

4. Segmentation using semi-automatic active contouring based on the Kass snake algorithm is shown. Region of interest (ROI) is defined after atrial contouring. The flow analysis is baded on blood within the isolated chamber.

5. Phase contrast magnetic resonance images of a normal case subject in the x-direction is performed with a VENC of 150 cms^{-1}.

6. Phase contrast magnetic resonance images of a normal case subject in the y-direction is performed with a VENC of 150 cms^{-1}.

7. Vorticity and vector flow maps of right atrial flow shows the spiralling of blood as it circulates within the heart chamber that undergoes deformation.

8. Colour streamline tracing of the right atrial flow presents the spiralling of blood more clearly as the traces of lines through the vectors can give an indication of the direction and magnitude of velocity with better clarity.

9. Phase contrast magnetic resonance images (magnitude values) that is based on slice 1 of the heart at two-chamber short axis configuration can be presented in this video clip. We can visually observe the inferior *vena cava*.

10. Phase contrast magnetic resonance images (magnitude values) that is based on slice 4 of the heart at two-chamber short axis configuration can be presented in this video clip. We can visually observe the superior *vena cava* and pulmonary artery.

11. Phase contrast magnetic resonance images (magnitude values) that is based on slice 3 of the heart at four-chamber long axis configuration can be presented in this video clip. The formation of left atrial vortex and variation of flow in the left atrium and ventricle can be investigated.

12. Phase contrast magnetic resonance images (magnitude values) that is based on slice 4 of the heart at four-chamber long axis configuration can be presented in this video clip. The formation of left atrial vortex due to flow interaction from the two branches of the pulmonary vein can be investigated.

13. Introduction to medical image processor (Medflovan version 1.0). This version has extended functionalities and is designed with ergonomics of use being considered and speed of its operation.

14. Software System Demonstration (Medflovan version 1.0). The demonstration of software usage and the display of software interface components are presented. The example of generating flow fields based on phase contrast magnetic resonance images is used.

Appendix G

Particle Image Velocimetry Based on Fluid Motion Estimation

PARTICLE image velocimetry (PIV), which uses images based on digital scanning of illuminated fluid suspended microscopic glass seeds, is described here. Particle image scans are presented with flow fields generated by a cross-correlation technique and a multi-resolution Lucas Kanade motion estimation algorithm. Vector fields calculated by both methods are presented. The experiments carried out here demonstrate the capability of optical flow in estimating parametric motion field using particle images.

G.1 Fluid Motion Estimation Using Particle Images

G.1.1 Particle Image Velocimetry

Over the past few decades, particle image velocimetry (Alahyari and Longmire 1994, Raffel *et al.* 1998) has been an established method of performing flow tracking based on optical scanning of fluid suspended particles. Nano-particles in the form of glass beads can act as velocity trackers when illuminated by a two-dimensional sheet of high-powered laser source. Cross-correlation of concomitant scans (Weng *et al.* 2001) is performed based on imaging of the flow scenario at two instances. This process is dictated by a measurement interval that is dependent on the speed of the flow. The computation of collective particle displacements gives a flow visualisation of the fluid. However, the limitation of PIV in imaging flow through non-compatible optic structures has been an obstacle in studying cardiovascular flow in the human body. We have developed magnetic resonance fluid motion tracking to perform high speed prediction of blood flow. The underlying algorithm in parametric motion estimation in this new development is based on a class of multi-resolution optical flow (OF) method, in particular, the pyramidal Lucas Kanede optical flow which we have applied to perform motion estimation of groups of pixels with varying intensities over time. It will be interesting to apply such a variational optical flow estimation on PIV images, as this can indicate extensions of the prototypical approach onto images output by other scanners. Previously, motion estimation flow studies on such optical-based images has been conducted with good results (Ruhnau *et al.* 2005, Corpetti *et al.* 2006, Cuzol *et al.* 2007).

G.1.2 Cross-Correlation Versus Pyramidal Optical Flow

We produce two parametric motion fields from the same set of particle images using the cross-correlation technique and the pyramidal optical flow algorithm. The latter method belongs to a class of multi-resolution motion estimation approach. The key objective is to demonstrate that the image intensity based motion estimation method is able to match the former technique in terms of accuracy of flow prediction. Tables G.1, G.2 and G.3 illustrate the specifications of the two algorithms. We will not

PIV Measurement (Double vortices)			
No.	Specification	Value	Units
1	Sampling rate	10	Hz
2	Resolution	19.6	pixel/mm
3	time difference between images	11	ms
4	Jet diameter	25	mm
5	Jet velocity	46	mm/s
6	Image size	1008×1018	pixel
7	Interrogation window size	32×32	pixel
8	Overlap region	16×16	pixel

Table G.1. PIV measurement of double vortices particle images. The physical properties of flow is presented in this table. Specifications for cross-correlation technique used to generate the flow field is listed in point number 7 and 8.

Optical Flow Measurement (Double vortices)			
No.	Specification	Value	Units
1	Optical flow sampling window size	23×23	pixel
2	Number of pyramid levels	5	
3	Image size	1008×1018	pixel
4	Velocity grid window size	15×15	pixel
5	Velocity resolution	294	pixel/mm

Table G.2. Multi-resolution OF measurement of double vortices particle images. Variational optical flow technique can also be used to produce the flow field based on particle images using PIV.

go into further explanation of the mathematical details as it is beyond the scope of this investigation. [24]

[24]For a better understanding of the background literature on fluid mechanics of optical-based velocimetry system, we recommend that the reader study a book titled *Particle Image Velocimetry* by Raffel et al.

Optical Flow Measurement (Single vortex)			
No.	Specification	Value	Units
1	Optical flow sampling window size	10×10	pixel
2	Number of pyramid levels	5	
3	Image size	800×977	pixel
4	Velocity grid window size	15×15	pixel
5	Velocity resolution	294	pixel/mm

Table G.3. Multi-resolution OF measurement of single vortex particle images. The counter-clockwise vortex is mapped using multi-resolution motion estimation. The optical flow sampling window size that controls the accuracy of flow field mapping is adjusted to improve tracking based on the higher resolution of the particle images.

G.2 Results Generated by Particle Image Velocimetry

We present the PIV results of flow comprising two vortices in this section. The parametric motion field is processed by the cross-correlation algorithm (Figure G.1). In general, the technique will require a high density of data captured by the image recording device, and other various considerations are required for an accurate measurement of flow which we will not investigate further here. The PIV images presented were developed and stored in a database of graphics files. [25]

[25] Images are provided by School of Mechanical Engineering, The University of Adelaide.

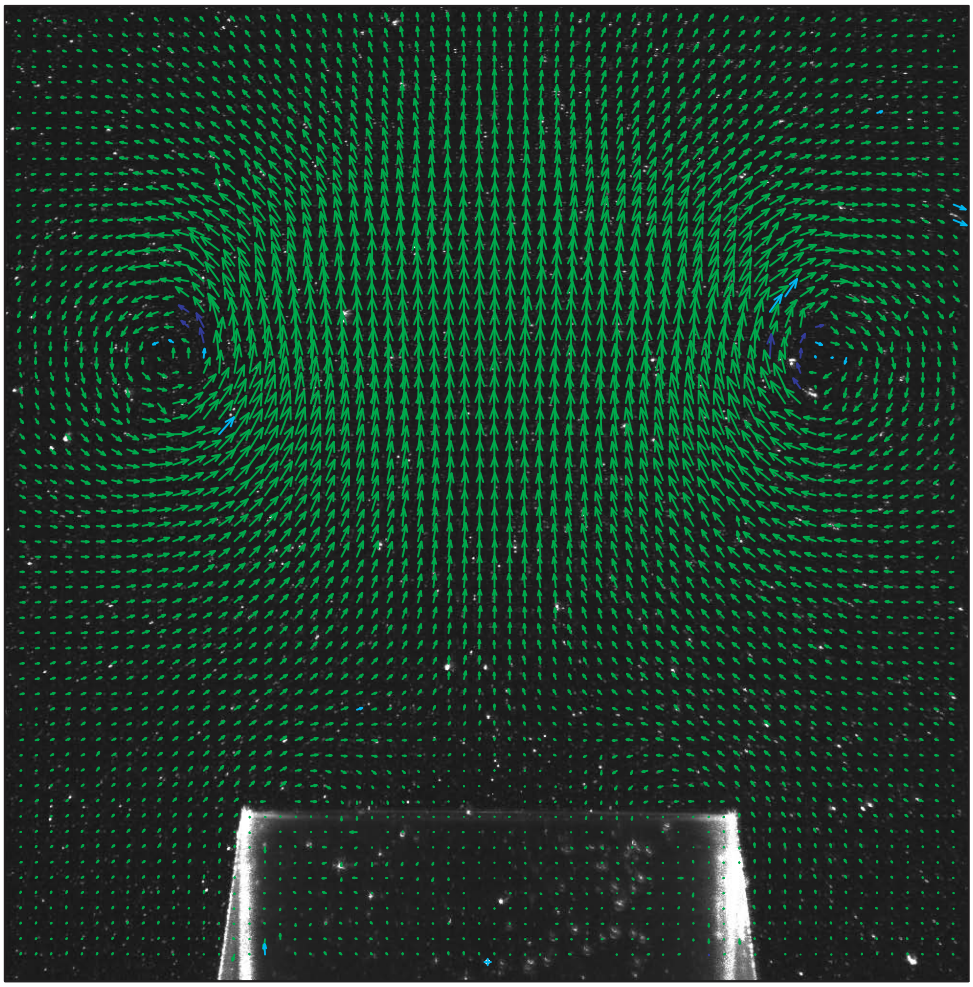

Figure G.1. Double vortices flow field using particle image velocimetry. This flow was generated by producing a jet via a pipe into a tank of water with microscopic glass seeds. The double vortices appear on opposite sides of the jet with clockwise and counter-clockwise rotations. Cross-correlation of concomitant images is applied to obtain the superimposed parametric vector field data. The blue vectors represent replacements of outliers during the imperfect measurement. They are calculated by averaging of neighbouring vectors.

G.3 Results Generated by Optical Flow

This section presents the motion field produced by multi-resolution optical flow method which is based on intensity measurements over time. The PIV image has been reduced in size in our experiments and an appropriate sampling window size for predicting intensity shifts of pixels is applied. Flow maps for the double vortices and a single vortiex are displayed in Figures G.2 and G.3 respectively. [26]

[26] We have used Medflovan software to produce these parametric motion fields. Also note that the clarity of the parametric motion fields may be better in the electronic version of this thesis.

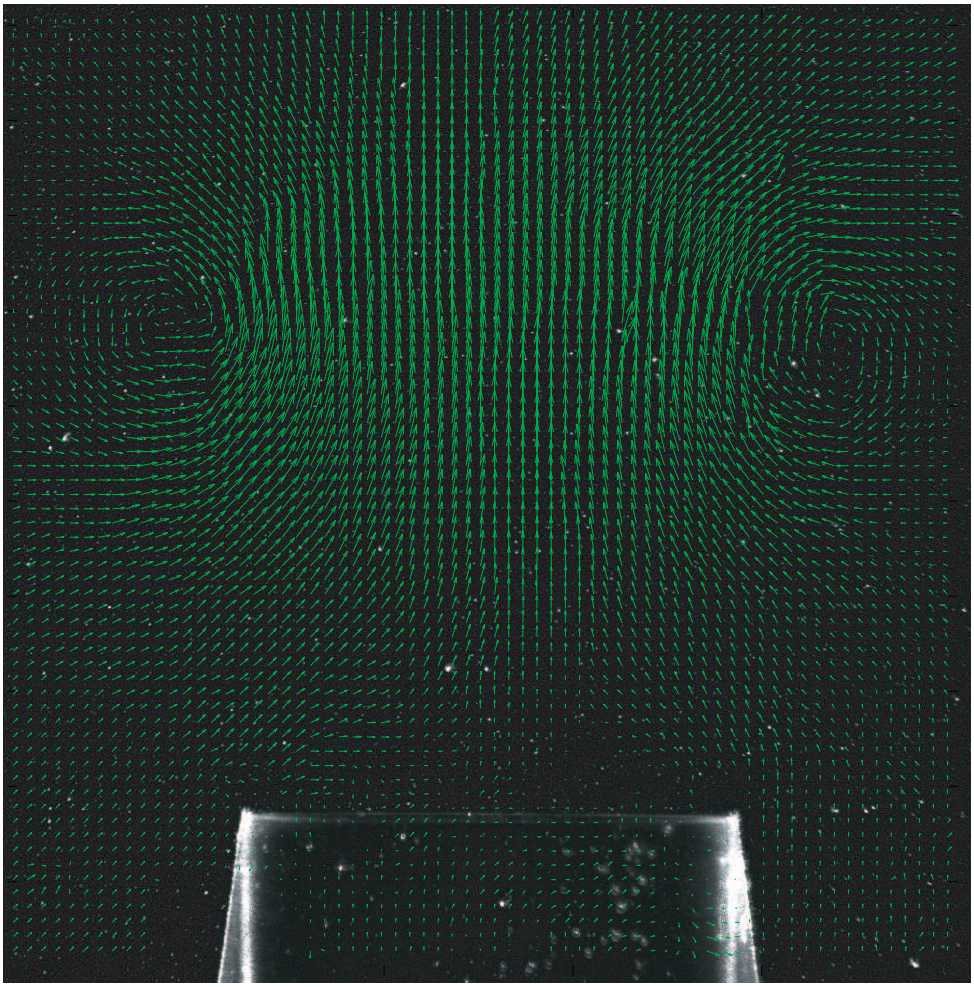

Figure G.2. Double vortices flow field computed by optical flow. The same PIV images are used in our experiments. Multi-resolution optical flow was applied to produce the vector flow field that is superimposed onto the image. Visual observation is able to indicate, to a certain extent, good correlation between the flow fields generated by cross-correlation technique and motion estimation algorithm.

The increase in resolution of scan can improve tracking accuracy. However, this comes at the expense of computational time. It is critical to set the algorithm parameters to achieve the optimal tracking using the least resources but not compromising the accuracy of motion estimation to an unacceptable extent. Figure G.3 was generated at a higher resolution and requires more processing resources as compared to images of the single vortex cropped out from Figure G.2.

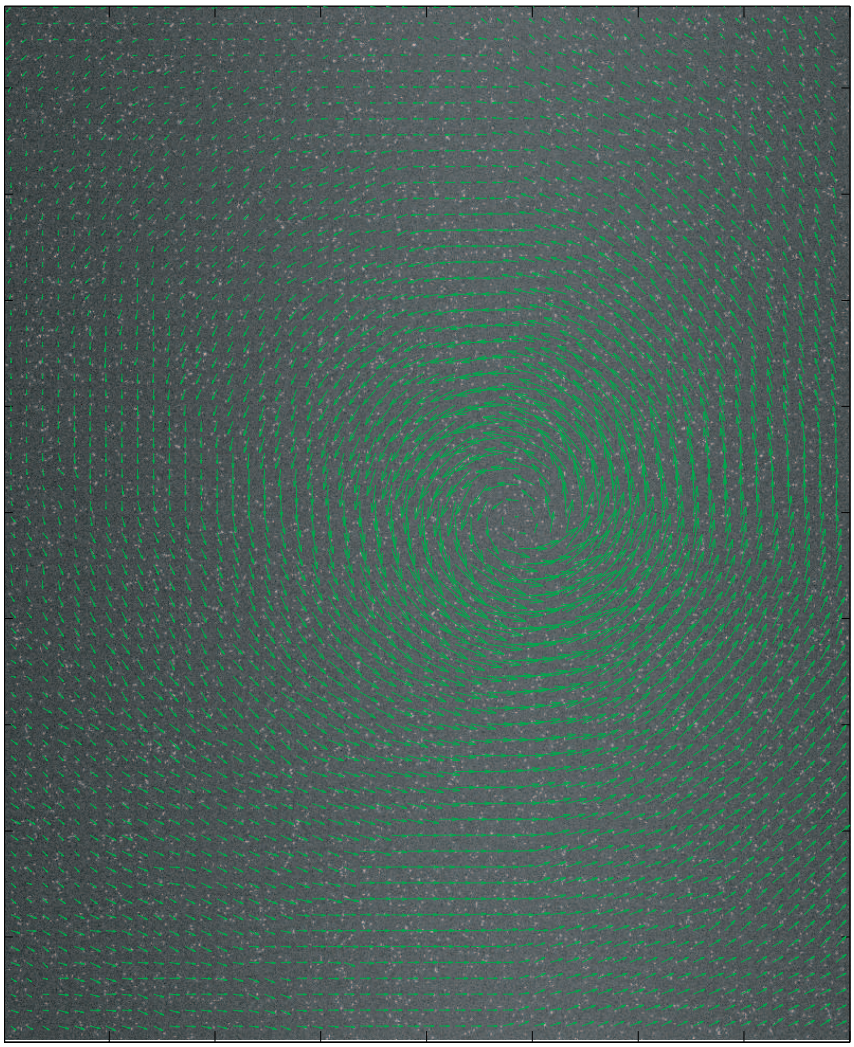

Figure G.3. Single vortex flow field computed by optical flow. This is a zoom-in version of the vortex on the left side of the jet, and therefore of higher resolution than the PIV image featuring double vortices. Multi-resolution optical flow with the same specifications was applied to produce this vector flow field.

Bibliography

ABDEL-MASSIH-T., DULAC-Y., TAKTAK-A., AGGOUN-Y., MASSABUAU-P., ELBAZ-M., CARRIÉ-D., AND ACAR-P. (2005). Assessment of atrial septal defect size with 3D-transesophageal echocardiography: Comparison with balloon method, *Echocardiography*, **22**(2), pp. 121–127.

ACHENBACH-S., ULZHEIMER-S., BAUM-U., KACHELRIESS-M., ROPERS-D., GIESLER-T., BAUTZ-W., DANIEL-W. G., KALENDER-W. A., AND MOSHAGE-W. (2000). Noninvasive coronary angiography by retrospectively ECG-gated multislice spiral CT, *Circulation*, **102**, p. 2823.

ADRIAN-R. J. (2005). Twenty years of particle image velocimetry, *Experiments in Fluids*, **39**, pp. 159–169.

AHLBERG-J. (1996). *Active Contours in Three Dimensions*, PhD thesis, Linköping University.

AKPA-B. S., HOLLAND-D. J., SEDERMAN-A. J., JOHNS-M. L., AND GLADDEN-L. F. (2007a). Enhanced (13)C PFG NMR for the study of hydrodynamic dispersion in porous media, *Journal of Magnetic Resonance Imaging*, **186**(1), pp. 160–165.

AKPA-B. S., MATTHEWS-S. M., SEDERMAN-A. J., YUNUS-K., FISHER-A. C., JOHNS-M. L., AND GLADDEN-L. F. (2007b). Study of miscible and immiscible flows in a microchannel using magnetic resonance imaging, *Analytical Chemistry*, **79**(16), pp. 6128–6134.

ALAHYARI-A., AND LONGMIRE-E. (1994). Particle image velocimetry in a variable density flow: Application to a dynamically evolving microburst, *Experiments in Fluids*, **17**, pp. 434–440.

ALSBERG-E., TRAHEY-G., BOHS-L., FRIEMEL-B., NIGHTINGALE-K., AND WALKER-W. (1994). Three-dimensional flow visualization via reconstruction from successive two-dimensional vector velocity maps, *Proceedings of the 16th Annual International Conference of the IEEE*, **1**, pp. 598–599.

ALSOP-D. (2007). Arterial spin labeling with pulsed radio frequency sequences, *United States Patent Application*, US 2007/0132452 A1.

AMIAZ-T., LUBETZKY-E., AND KIRYATI-N. (2007). Coarse to over-fine optical flow estimation, *Pattern Recognition*, **40**(9), pp. 2496–2503.

ANANDAN-P. (1989). A computational framework and an algorithm for the measurement of visual motion, *International Journal of Computer Vision*, **2**(3), pp. 283–310.

ANDERSON-J. D. (1995). *Computational Fluid Dynamics: The Basics with Applications*, McGraw Hill.

ARVAND-A., HAHN-N., HORMES-M., AKDIS-M., MARTIN-M., AND REUL-H. (2004). Comparison of hydraulic and hemolytic properties of different impeller designs of an implantable rotary blood pump by computational fluid dynamics, *Artificial Organs*, **28**(10), pp. 892–898.

BALTES-C., KOZERKE-S., HANSEN-M. S., PRUESSMANN-K. P., TSAO-J., AND BOESIGER-P. (2005). Accelerating cine phase-contrast flow measurements using k-t BLAST and k-t SENSE, *Magnetic Resonance in Medicine*, **54**(6), pp. 1430–1438.

BALZER-J., KÜHL-H., AND FRANKE-A. (2008). Real-time three-dimensional transoesophageal echocardiography for guidance of atrial septal defect closures, *European Heart Journal*, **29**(18), p. 2226.

BANKS-D. C. (1995). A predictor-corrector technique for visualizing unsteady flow, *IEEE Transactions on Visualization and Computer Graphics*, **1**(2), pp. 151–163.

BARRON-J. L., AND THACKER-N. A. (2005). Tutorial: Computing 2D and 3D optical flow, *Tina Memo No. 2004-012*.

BARRON-J. L., FLEET-D., AND BEAUCHEMIN-S. (1994). Performance of optical flow techniques, *International Journal of Computer Vision*, **12**(1), pp. 43–77.

BARTEL-T., KONORZA-T., BARBIERI-V., ERBEL-R., PACHINGER-O., AND MÜLLER-S. (2008). Single-plane balloon sizing of atrial septal defects with intracardiac echocardiography: An advantageous alternative to fluoroscopy, *Journal of the American Society of Echocardiography*, **21**(6), pp. 737–740.

BEERBAUM-P., PARISH-V., BELL-A., GIESEKE-J., KÖRPERICH-H., AND SARIKOUCH-S. (2008). Atypical atrial septal defects in children: noninvasive evaluation by cardiac MRI, *Pediatric Radiology*, **38**(11), pp. 1188–1194.

BEHAR-V., ADAM-D., AND LYSYANSKY-P. (2004). Improving motion estimation by accounting for local image distortion, *Ultrasonics*, **43**(1), pp. 57–65.

BELLHOUSE-B. J., AND BELLHOUSE-F. H. (1969). Fluid mechanics of the mitral valve, *Nature Medicine*, **224**, pp. 615–616.

BERGEN-J. R., AN-P., HANNA-T. J., AND HINGORANI-R. (1992). Hierarchical model-based motion estimation, *Proceedings of the European Conference on Computer Vision*, pp. 237–252.

BISWAS-G., WEINBERG-J. B., AND FISHER-D. H. (1998). ITERATE: a conceptual clustering algorithm for data mining, *IEEE Transactions on Systems, Man, and Cybernetics, Part C: Applications and Reviews*, **28**(2), pp. 219–230.

BLOOMER-T. N., PLEIN-S., RADJENOVIC-A., HIGGINS-D. M., JONES-T. R., RIDGWAY-J. P., AND SIVANANTHAN-M. U. (2001). Cine MRI using steady state free precession in the radial long axis orientation is a fast accurate method for obtaining volumetric data of the left ventricle, *Journal of Magnetic Resonance Imaging*, **14**(6), pp. 685–692.

BOGREN-H. G., AND BUONOCORE-M. H. (1999). 4D magnetic resonance velocity mapping of blood flow patterns in the aorta in young vs. elderly normal subjects, *Journal of Magnetic Resonance Imaging*, **10**(5), pp. 861–869.

BOGREN-H. G., BUONOCORE-M. H., AND VALENTE-R. J. (2004). Four-dimensional magnetic resonance velocity mapping of blood flow patterns in the aorta in patients with atherosclerotic coronary artery disease compared to age-matched normal subjects, *Journal of Magnetic Resonance Imaging*, **19**, pp. 417–427.

BOHRNSTEDT-G. (1983). Measurement, *Handbook of Survey Research*, Academic Press, New York.

BOHS-L. N., FRIEMEL-B. H., KISSLO-J., HARFE-D. T., NIGHTINGALE-K. R., AND TRAHEY-G. E. (1995). Three-dimensional flow images by reconstruction from two-dimensional vector velocity maps, *Journal of the American Society of Echocardiography*, **8**(6), pp. 915–923.

BOUGUET-J. Y. (2000). Pyramidal implementation of the Lucas Kanade feature tracker, *Technical report*, OpenCV documentation, Microprocessor Research Labs, Intel Corp.

BRANDS-P. J., HOEKS-A. P. G., AND RENEMAN-R. S. (1995). The effect of echo suppression on the mean velocity estimation range of the RF cross-correlation model estimator, *Ultrasound in Medicine & Biology*, **21**, pp. 945–959.

BRANDT-E., EBBERS-T., WIGSTRÖM-L., ENGVALL-J., AND KARLSSON-M. (2001). Automatic detection of vortical flow patterns from three-dimensional phase contrast MRI, *Proceedings of the International Society for Magnetic Resonance in Medicine*, **9**, p. 1838.

CALVERT-P. A., AND KLEIN-A. A. (2008). Anaesthesia for percutaneous closure of atrial septal defects, *Continuing Education in Anaesthesia, Critical Care & Pain 2008*, **8**(1), pp. 16–20.

CARITEAU-B., AND FLÓR-J. B. (2006). An experimental investigation on elliptical instability of a strongly asymmetric vortex pair in a stable density stratification, *Nonlinear Processes in Geophysics*, **13**(6), pp. 641–649.

CARR-J. C., SIMONETTI-O., BUNDY-J., LI-D., PERELES-S., AND FINN-J. P. (2001). Cine MR angiography of the heart with segmented True Fast imaging with steady-state precession, *Radiology*, **219**, pp. 828–834.

CHANDRAN-K. B. (1992). *Cardiovascular Biomechanics*, New York University Biomedical Engineering Series, New York University Press.

CHANDRAN-K. B. (1993). Flow dynamics in the human aorta, *Journal of Biomechanical Engineering*, **115**(4B), pp. 611–616.

CHANDRAN-K. B., CABELL-G. N., KHALIGHI-B., AND CHEN-C. J. (1983). Laser anemometry measurements of pulsatile flow past aortic valve prostheses, *Journal of Biomechanics*, pp. 865–873.

CHANDRAN-K. B., WAHLE-A., VIGMOSTAD-S. C., OLSZEWSKI-M. E., ROSSEN-J. D., AND SONKA-M. (2006a). Coronary arteries: Imaging, reconstruction, and fluid dynamic analysis, *Critical Reviews in Biomedical Engineering*, **34**(1), pp. 23–103.

CHANDRAN-K. B., YOGANATHAN-A. P., AND RITTGERS-S. E. (2006b). *Biofluid Mechanics: The Human Circulation*, CRC Press, Taylor & Francis Group.

CHAOUI-R., TADDEI-F., RIZZO-G., BAST-C., LENZ-F., AND BOLLMANN-R. (2002). Doppler echocardiography of the main stems of the pulmonary arteries in the normal human fetus, *Ultrasound in Obstetrics and Gynecology*, **11**(3), pp. 173–179.

CHENG-R., LAI-Y. G., AND CHANDRAN-K. B. (2004). Three-dimensional fluid-structure interaction simulation of bileaflet mechanical heart valve flow dynamics, *Annals of Biomedical Engineering*, **32**(11), pp. 1471–1483.

CHENG-R., LAI-Y. G., AND CHANDRAN-K. B. (2006). Three-dimensional fluid-structure interaction simulation of bileaflet mechanical heart valve flow dynamics, *Annals of Biomedical Engineering*, **32**(11), pp. 1471–1483.

CHEN-M.-C., WU-C.-J., YIP-H.-K., CHANG-H.-W., FANG-C.-Y., YU-T.-H., AND FU-M. (2003). Left atrial platelet activity with rheumatic mitral stenosis: Correlation study of severity and platelet P-Selectin expression by flow cytometry, *Chest*, **124**, pp. 1663–1669.

CHEN-Q., STOREY-P., LEVINE-D., LI-W., AND EDELMAN-R. (2001). A breath-hold three dimensional True FISP sequence for abdominal MRI, *Proceedings of the International Society for Magnetic Resonance in Medicine*, **9**, p. 232.

CHOA-J., AND BENKESER-P. J. (2006). Cardiac segmentation by a velocity-aided active contour model, *Computerized Medical Imaging and Graphics*, **30**(1), pp. 31–41.

CLOUGH-A. V., MANUEL-A. J., HAWORTH-S. T., AND DAWSON-C. A. (2000). Application of indicator dilution theory to time-density curves obtained from dynamic contrast images, *Proceedings of SPIE, Medical Imaging 2000: Physiology and Function from Multidimensional Images*, **3978**, pp. 457–465.

COHEN-L. D. (1991). On active contour models and balloons, *Computer Vision, Graphics, and Image Processing*, **53**(2), pp. 211–218.

CORPETTI-T., HEITZ-D., ARROYO-G., MËMIN-E., AND SANTA-CRUZ-A. (2006). Fluid experimental flow estimation based on an optical-flow scheme, *Experiments in Fluids*, **40**, pp. 80–97.

CROSS-R. R., SABLE-C. A., SLACK-M. C., AND MARTIN-G. R. (2001). Three-dimensional imaging of atrial septal occlusion device, *Pediatric Cardiology*, **22**(5), pp. 427–428.

CURFMAN-G. D., AND HILLIS-L. D. (2003). A new look at cardiac exercise testing, *New England Journal of Medicine*, **348**, pp. 775–776.

CUZOL-A., HELLIER-P., AND MÉMIN-E. (2007). A low dimensional fluid motion estimator, *International Journal of Computer Vision*, **75**(3), pp. 329–349.

DALL'ARMELLINA-E., HAMILTON-C. A., AND HUNDLEY-W. G. (2007). Assessment of blood flow and valvular heart disease using phase-contrast cardiovascular magnetic resonance, *Echocardiography*, **24**(2), pp. 207–216.

DEUTSCH-H. J., SECHTEM-U., MEYER-H., THEISSEN-P., SCHICHA-H., AND ERDMANN-E. (1994). Chronic aortic dissection: comparison of MR imaging and transesophageal echocardiography, *Radiology*, **192**, pp. 645–650.

DINSMORE-R. E., LIBERTHSON-R. R., WISMER-G. L., MILLER-S. W., LIU-P., THOMPSON-R., MCLOUD-T. C., MARSHALL-J., SAINI-S., STRATEMEIER-E. J., OKADA-R. D., AND BRADY-T. J. (1986). Magnetic resonance imaging of thoracic aortic aneurysms: comparison with other imaging methods, *American Journal of Roentgenology*, **146**(2), pp. 309–314.

DUAN-L., JIN-J. S., TIAN-Q., AND XU-C. S. (2006a). Nonparametric motion characterization for robust classification of camera motion patterns, *IEEE Transactions on Multimedia*, **8**(2), pp. 323–340.

DUAN-L., WANG-J., ZHENG-Y., JIN-J. S., LU-H., AND XU-C. (2006b). Segmentation, categorization, and identification of commercial clips from TV streams using multimodal, *Proceedings of the 14th annual ACM international conference on Multimedia, Santa Barbara, California*, pp. 201–210.

DUNCAN-R. F., TEO-K. S. L., AND WORTHLEY-S. G. (2008). Cardiac magnetic resonance documentation of a double atrial septal defect before and after percutaneous closure with an amplatzer septal occluder, *International Journal of Cardiology*, **130**(1), pp. e42–e43.

DURONGPISITKUL-K., TANG-N. L., SOONGSWANG-J., LAOHAPRASITIPORN-D., AND NANAL-A. (2004). Predictors of successful transcatheter closure of atrial septal defect by cardiac magnetic resonance imaging, *Pediatric Cardiology*, **25**(2), pp. 124–130.

DU-Y. P., MCVEIGH-E. R., BLUEMKE-D. A., SILBER-H. A., AND FOO-T. K. (2001). A comparison of prospective and retrospective respiratory navigator gating in 3D MR coronary angiography, *International Journal of Cardiovascular Imaging*, **17**(4), pp. 287–294.

EBBERS-T., WIGSTRÖM-L., BOLGER-A. F., WRANNE-B., AND KARLSSON-M. (2002). Noninvasive measurement of time-varying three-dimensional relative pressure fields within the human heart, *Journal of Biomechanical Engineering*, **124**(3), pp. 288–293.

EDELMAN-R. R. (2004). Contrast-enhanced MR imaging of the heart: Overview of the literature, *Radiology*, **232**, pp. 653–668.

EFROS-A. A., AND LEUNG-T. K. (1999). Texture synthesis by non-parametric sampling, *Proceedings of the 7th International Conference on Computer Vision (ICCV'99)*, **2**, pp. 1033–1038.

EGEBLAD-H., BERNING-J., EFSEN-F., AND WENNEVOLD-A. (1980). Non-invasive diagnosis in clinically suspected atrial septal defect of secundum or sinus venosus type. value of combining chest x-ray, phonocardiography, and M-mode echocardiography, *British Heart Journal*, **44**(3), pp. 317–321.

EGGERS-J., ROLFS-A., AND BENECKE-R. (1999). Monitoring the effectiveness of anticoagulative therapy in left atrial spontaneous echo contrast by cerebral microemboli detection, *Stroke*, **30**, pp. 1974–1981.

EICH-R. H., STAIB-I., AND ENERSON-D. (1959). An experimental evaluation of the indicator dilution technique for the measurement of mitral regurgitation, *Journal of Clinical Investigation*, **38**(11), pp. 2035–2043.

ELKINS-C. J., MARKL-M., IYENGAR-A., WICKER-R., AND EATON-J. (2004). Full field velocity and temperature measurements using magnetic resonance imaging in turbulent complex internal flows, *International Journal of Heat and Fluid Flow*, **25**, pp. 702–710.

ENGELMAYR-G. C. J., SOLETTI-L., VIGMOSTAD-S. C., BUDILARTO-S. G., FEDERSPIEL-W. J., CHANDRAN-K. B., VORP-D. A., AND SACKS-M. S. (2008). A novel flex-stretch-flow bioreactor for the study of engineered heart valve tissue mechanobiology, *Annals of Biomedical Engineering*, **36**(5), pp. 700–712.

ENGLISH-P. T., AND MOORE-C. (1995). *MRI for Radiographers*, Springer-Verlag London, Great Britain.

ETEBARI-A., AND VLACHOS-P. P. (2005). Improvements on the accuracy of derivative estimation from DPIV velocity measurements, *Experiments in Fluids*, **39**(6), pp. 1040–1050.

EUSEMANNA-C. D., BELLEMANNB-M. E., AND ROBBA-R. A. (2000). Quantitative analysis and parametric display of regional myocardial mechanics, *Proceedings of SPIE, Medical Imaging 2000: Image Display and Visualization*, **3976**, pp. 238–246.

FERZIGER-J. H., AND PERIC-M. (2001). *Computational Methods for Fluid Dynamics*, number ISBN: 3540420746, 3rd edn, Springer.

FISHMAN-A. P. (2000). The Fick principle and the steady state, *American Journal of Respiratory and Critical Care Medicine*, **161**(3), pp. 692–693.

FOUCAUT-J. M., AND STANISLAS-M. (2002). Some considerations on the accuracy and frequency response of some derivative filters applied to particle image velocimetry vector fields, *Measurement Science and Technolology*, **13**, pp. 1058–1071.

FOURAS-A., AND SORIA-J. (1998). Accuracy of out-of-plane vorticity measurements derived from in-plane velocity field data, *Experiments in Fluids*, **25**, pp. 409–430.

FREEDOM-R. M., YOO-S.-J., MIKAILIAN-H., AND WILLIAMS-W. (2003). *The Natural and Modified History of Congenital Heart Disease*, Blackwell Publishing.

FRIESEN-G. M., JAQNNETT-T. C., JADALLAH-M. A., YATES-S. L., QUINT-S. R., AND NAGLE-H. T. (1990). A comparison of the noise sensitivity of nine QRS detection algorithms, *IEEE Transactions on Bio-Medical Engineering*, **37**, p. 85.

FRISCH-R. E., SNOW-R. C., JOHNSON-L. A., GERARD-B., BARBIERI-R., AND ROSEN-B. (1998). Magnetic resonance imaging of overall and regional body fat, estrogen metabolism, and ovulation of athletes compared to controls, *Journal of Clinical Endocrinology and Metabolism*, **77**(2), pp. 471–477.

FRITSCHER-K. D., PILGRAM-R., AND SCHUBERT-R. (2005). *Lecture Notes in Computer Science, Functional Imaging and Modeling of the Heart*, Springer, Berlin, Heidelberg, chapter on Automatic Cardiac 4D Segmentation Using Level Sets, pp. 113–122.

FRITTS-H. W., AND COURNAND-A. (1958). The application of the fick principle to the measurement of pulmonary blood flow, *Proceedings of the National Academy of Sciences of the United States of America*, **44**(10), pp. 1079–1087.

FRYDRYCHOWICZA-A., WEIGANGC-E., LANGERA-M., AND MARKLB-M. (2006). Flow-sensitive 3D magnetic resonance imaging reveals complex blood flow alterations in aortic Dacron graft repair, *Interactive CardioVascular and Thoracic Surgery*, **5**, pp. 340–342.

FRYDRYCHOWICZ-A., WINTERER-J. T., ZAITSEV-M., JUNG-B., HENNIG-J., LANGER-M., AND MARKL-M. (2007). Visualization of iliac and proximal femoral artery hemodynamics using time-resolved 3D phase contrast MRI at 3T, *Journal of Magnetic Resonance Imaging*, **25**, p. 10851092.

FUA-P., AND BRECHBÜHLER-C. (1997). Imposing hard constraints on deformable models through optimization in orthogonal subspaces, *Computer Vision and Image Understanding*, **65**(2), pp. 148–162.

FUCHSA-F., LAUBB-G., AND OTHOMOC-K. (2003). TrueFISP—technical considerations and cardiovascular applications, *European Journal of Radiology*, **46**(1), p. 28.

FUJIO-K., GOTANDA-M., YAMAGUCHI-T., TAKAYAMA-S., TSUKAYA-T., MATSUI-K., HIBINO-H., HIYAMA-K., SHIMIZU-K., YOSHINO-K., AND HAYASHI-M. (1995a). MRI apparatus for receiving nuclear-magnetic resonance signals of a living body, *United States Patent Application,* US Patent 5427103.

FUJIO-K., GOTANDA-M., YAMAGUCHI-T., TAKAYAMA-S., TSUKAYA-T., MATSUI-K., HIBINO-H., HIYAMA-K., SHIMIZU-K., YOSHINO-K., AND HAYASHI-M. (1995b). MRI apparatus for receiving nuclear-magnetic resonance signals of a living body, *Magnetic Resonance Imaging*, **13**(7), pp. XII–XII(1).

FYRENIUS-A., EBBERS-T., WIGSTRÖM-L., KARLSSON-M., WRANNE-B., BOLGER-A. F., AND ENGVALL-J. (1999). Left atrial vortices studied with 3D phase contrast MRI, *Clinical Physiology and Functional Imaging*, **19**(3), p. 195.

FYRENIUS-A., WIGSTRÖM-L., EBBERS-T., KARLSSON-M., ENGVALL-J., AND BOLGER-A. F. (2001). Three dimensional flow in the human left atrium, *Heart*, **86**, pp. 448–455.

GALDERISI-M., CATTANEO-F., AND MONDILLO-S. (2007). Doppler echocardiography and myocardial dyssynchrony: a practical update of old and new ultrasound technologies, *Cardiovascular Ultrasound*, **5**, p. 28.

GARDIN-J. M., SUNG-H. W., YOGANATHAN-A. P., BALL-J., MCMILLAN-S., AND HENRY-W. L. (1988). Doppler flow velocity mapping in an in vitro model of the normal pulmonary artery, *Journal of the American College of Cardiology*, **12**, pp. 1366–1376.

GATEHOUSE-P. D., KEEGAN-J., CROWE-L. A., MASOOD-S., MOHIADDIN-R. H., KREITNER-K. F., AND FIRMIN-D. N. (2005). Applications of phase-contrast flow and velocity imaging in cardiovascular MRI, *European Radiology*, **15**, pp. 2172–2184.

GEOGIEV-G., SHISHENKOV-M., NINOV-B., AND DOSHEVA-I. (2006). Clinical signification of a modified dilution method (mdm) for blood loss assessment in the cases of nonvariceal upper gastrointestinal bleeding, *Khirurgiia*, **1**, pp. 21–23.

GEROSA-G., F.-M., D.-C., AND T.-B. (2004). Searching for a correct method of evaluation for valve prosthesis performance, *Journal of Heart Valve Disease*, **13**(1), pp. S1–S3.

GERTSCH-M., AND CANNON-C. P. (2003). *The ECG: A Two-Step Approach to Diagnosis*, Springer.

GHARIB-M., RAMBOD-E., KHERADVAR-A., SAHN-D. J., AND DABIRI-J. O. (2006). A global index for heart failure based on optimal vortex formation in the left ventricle, *Proceedings of the National Academy of Sciences USA (PNAS)*, **103**(16), pp. 6305–6308.

GHISTA-D. N., CHANDRAN-K. B., RAY-G., AND REUL-H. (1978). Optimal design of aortic leaflet prosthesis, *Journal of the Engineering Mechanics Division*, **104**(1), pp. 97–117.

GHISTA-N. D. (2008). *Applied Biomedical Engineering Mechanics*, CRC Press.

GHISTA-N. D., AND NG-E. Y.-K. (2007). *Cardiac Perfusion and Pumping Engineering (Clinically-Oriented Biomedical Engineering)*, World Scientific Publishing Company.

GIACHETTI-A., AND TORRE-V. (1995). Optical flow and deformable objects, *Proceedings of the 5th International Conference on Computer Vision*, p. 706.

GIACHETTI-A., AND TORRE-V. (1996). The use of optical flow for the analysis of non-rigid motions, *International Journal of Computer Vision archive*, **18**(3), pp. 255–279.

GLADDEN-L. F. (1994). Nuclear magnetic resonance in chemical engineering: principles and applications, *Chemical Engineering Science*, **49**(20), pp. 3339–3408.

GLADDEN-L. F., AND ALEXANDER-P. (1996). Applications of nuclear magnetic resonance imaging in process engineering, *Measurement Science and Technology*, **7**, pp. 423–435.

GLEESON-F. V. (2006). The chest radiograph in heart disease, *Medicine*, **34**(4), pp. 136–141.

GLEESON-T. G., MWANGI-I., HORGAN-S. J., CRADOCK-A., FITZPATRICK-P., AND MURRAY-J. G. (2008). Steady-state free-precession (SSFP) cine MRI in distinguishing normal and bicuspid aortic valves, *Journal of Magnetic Resonance Imaging*, **28**, pp. 873–878.

GLOBITS-S., AND HIGGINS-C. B. (1995). Assessment of valvular heart disease by magnetic resonance imaging, *American Heart Journal*, **129**(2), pp. 369–81.

GLOR-F. P., WESTENBERG-J. J. M., VIERENDEELS-J., DANILOUCHKINE-M., AND VERDONCK-P. (2008). Validation of the coupling of magnetic resonance imaging velocity measurements with computational fluid dynamics in a U bend, *Artificial Organs*, **26**(7), pp. 622–635.

GOETZ-W. A., LANSAC-E., LIM-H.-S., WEBER-P. A., AND DURAN-C. M. G. (2005). Left ventricular endocardial longitudinal and transverse changes during isovolumic contraction and relaxation: a challenge, *American Journal of Physiology - Heart and Circulatory Physiology*, **289**, pp. 196–201.

GONZALEZ-R. C., AND WOODS-R. E. (2002). *Digital Image Processing, 2nd edition*, Prentice-Hall, Inc., New Jersey, USA.

GOSHTASBY-A., AND TURNER-D. A. (1995). Segmentation of cardiac cine MR images for extraction of right and left ventricular chambers, *IEEE Transactions on Medical Imaging*, **14**(1), pp. 56–64.

GOUBERGRITS-L., KERTZSCHER-U., SCHÖNEBERG-B., WELLNHOFER-E., PETZ-C., AND HEGE-H.-C. (2008). CFD analysis in an anatomically realistic coronary artery model based on non-invasive 3D imaging: comparison of magnetic resonance imaging with computed tomography, *International Journal of Cardiovascular Imaging*, **24**(4), pp. 411–421.

GOVINDARAJAN-V., UDAYKUMAR-H. S., AND CHANDRAN-K. B. (2009). Two-dimensional simulation of flow and platelet dynamics in the hinge region of a mechanical heart valve, *Journal of Biomechanical Engineering*, **131**(3), p. 031002.

GRIN-Y. T. (1975). Gyromagnetic ratio and a nature of the backbending of the moment of inertia, *Physics Letters B*, **59**(5), pp. 419–420.

GUITERREZ-M. A., REBELO-M., FURUIE-S. S., MELO-C. P., MOURA-L., AVILA-L., AND PARGA-J. R. (1997). Myocardial motion estimation in gated-MRI using optical flow refined with scale-space, *Computers on Cardiology*, **24**, pp. 153–156.

GUYTON-A. C., AND HALL-J. E. (2006). *Textbook of Medical Physiology*, 11 edn, Elsevier Saunders.

HAMBRECHT-R., NIEBAUER-J., FIEHN-E., KÄLBERER-B., OFFNER-B., HAUER-K., RIEDE-U., SCHLIERF-G., KÜBLER-W., AND SCHULER-G. (1995). Physical training in patients with stable chronic heart failure: Effects on cardiorespiratory fitness and ultrastructural abnormalities of leg muscles, *Journal of the American College of Cardiology*, **25**(6), pp. 1239–1249.

HAO-X., BRUCE-C., PISLARU-C., AND GREENLEAF-J. F. (2000). A novel region growing method for segmenting ultrasound images, *Ultrasonics Symposium, 2000 IEEE*, **2**, pp. 1717–1720.

HARRISON-M. R., SMITH-M. D., GRAYBURN-P. A., KWAN-O. I. L., AND DEMARIA-A. N. (2007). Normal blood flow patterns by color doppler flow imaging, *Echocardiography*, **4**(6), pp. 485–493.

HARTIALA-J. J., MOSTBECK-G. H., FOSTER-E., FUJITA-N., DULCE-M. C., CHAZOUILLERES-A. F., AND HIGGINS-C. B. (1993). Velocity-encoded cine MRI in the evaluation of left ventricular diastolic function: measurement of mitral valve and pulmonary vein flow velocities and flow volume across the mitral valve, *American Heart Journal*, **125**, pp. 1054–1066.

HASEGAWA-H., LITTLE-W. C., OHNO-M., BRUCKS-S., MORIMOTO-A., CHENG-H.-J., AND CHENG-C.-P. (2003). Diastolic mitral annular velocity during the development of heart failure, *Journal of the American College of Cardiology*, **41**, pp. 1590–1597.

HASE-H., YONEDA-M., TOKAI-S., KATO-J., AND SUEN-C. Y. (2003). Color segmentation for text extraction, *International Journal on Document Analysis and Recognition*, **6**(4), pp. 271–284.

HATLE-L., AND ANGELSEN-B. (1982). *Doppler ultrasound in cardiology: Physical Principles and Clinical Applications, 2nd Edition*, Philadelphia, Lea and Febiger.

HELFT-G., WORTHLEY-S. G., BEYGUI-F., ZAMAN-A. G., FEUVRE-C. L., VACHERON-A., METZGER-J. P., BADIMON-J. J., AND FUSTER-V. (2001). Identification of unstable coronary atherosclerotic plaques, *Arch Mal Coeur Vaiss*, **94**, pp. 583–590.

HERBORN-C. U., VOGT-F., LAUENSTEIN-T. C., GOYEN-M., DEBATIN-J. F., AND RUEHM-S. G. (2003). MRI of the liver: Can true FISP replace HASTE?, *Journal of Magnetic Resonance Imaging*, **17**(2), pp. 190–196.

HEROLD-V., MÖRCHEL-P., FABER-C., ROMMEL-E., HAASE-A., AND JAKOB-P. M. (2006). In vivo quantitative three-dimensional motion mapping of the murine myocardium with PC-MRI at 17.6 T, *Magnetic Resonance in Medicine*, **55**, pp. 1058–1064.

HIGGINS-C. B., SAEED-M., WENDLAND-M., BOURNE-M., STEFFANS-J., AND SAKUMA-H. (1994). Evaluation of myocardial function and perfusion in ischemic heart disease, *Magnetic Resonance Materials in Physics, Biology and Medicine*, **2**(3), pp. 177–184.

HIRSCH-R., KILNER-P. J., CONNELLY-M. S., A. N. REDINGTON-M. G. S. J. S., AND SOMERVILLE-J. (1994). Diagnosis in adolescents and adults with congenital heart disease. prospective assessment of individual and combined roles of magnetic resonance imaging and transesophageal echocardiography, *Circulation*, **90**, pp. 2937–2951.

HOPPE-U. C., DEDERICHS-B., DEUTSCH-H. J., THEISSEN-P., SCHICHA-H., AND SECHTEM-U. (1996). Congenital heart disease in adults and adolescents: comparative value of transthoracic and transesophageal echocardiography and MR imaging, *Radiology*, **199**(3), pp. 669–677.

HORN-B. K. P., AND SCHUNCK-B. G. (1981). Determining optical flow, *Artificial Intelligence*, **17**, pp. 185–203.

HOROWITZ-A. L. (1994). *MRI Physics for Radiologists - A Visual Approach, 3rd edition*, Springer-Verlag, New York, USA.

IKBALA-M., CHAKRAVARTYA-S., WONG-K. K. L., MAZUMDAR-J., AND MANDAL-P. K. (2008). Unsteady response of non-Newtonian blood flow through a stenosed artery in magnetic field, *Journal of Computational and Applied Mathematics, doi:10.1016/j.cam.2008.11.010*.

JASJIT-S. S. (2000). Computer vision, pattern recognition and image processing in left ventricle segmentation: The last 50 years, *Pattern Analysis and Applications*, **3**(3), pp. 209–242.

JIMINEZ-J., WRAY-A. A., SAFFMAN-P. G., AND ROGALLO-R. S. (1993). Intense vorticity in isotropic turbulence, *Journal of Fluid Mechanics*, **255**, pp. 65–90.

JOHN-B., STILES-M. K., KUKLIK-P., CHANDY-S. T., YOUNG-G. D., MACKENZIE-L., SZUMOWSKI-L., JOSEPH-G., JOSE-J., WORTHLEY-S. G., KALMAN-J. M., AND SANDERS-P. (2008). Electrical remodelling of the left and right atria due to rheumatic mitral stenosis, *European Heart Journal*, **29**, pp. 2234–2243.

JONASSON-L., HAGMANN-P., BRESSON-X., MEULI-R., CUISENAIRE-O., AND THIRAN-J.-P. (2003). White matter mapping in DT-MRI using geometric flows, *Proceedings of the 9th International Workshop on Computer Aided Systems Theory, Las Palmas de Gran Canaria*, pp. 80–82.

JONASSON-L., HAGMANN-P., POLLO-C., BRESSON-X., WILSON-C. R., MEULI-R., AND THIRAN-J.-P. (2007). A level set method for segmentation of the thalamus and its nuclei in DT-MRI, *Signal Processing*, **87**(2), pp. 309–321.

JUNG-B., SCHNEIDER-B., MARKL-M., SAURBIER-B., GEIBEL-A., AND HENNIG-J. (2004). Measurement of left ventricular velocities: phase contrast MRI velocity mapping versus tissue-Doppler-ultrasound in healthy volunteers, *Journal of Cardiovascular Magnetic Resonance*, **6**(4), pp. 777–783.

KANUNGO-T., MOUNT-D. M., NETANYAHU-N. S., PIATKO-C. D., SILVERMAN-R., AND WU-A. Y. (2002). An efficient k-means clustering algorithm: Analysis and implementation, *IEEE Transactions on Pattern Analysis and Machine Intelligence*, **24**(7), pp. 881–892.

KASAI-C., NAMEKAWA-K., KOYANO-A., AND OMOTO-R. (1985). Real-time two-dimensional blood flow imaging using an autocorrelation technique, *IEEE Transactions on Sonics and Ultrasonics*, **32**(3), pp. 458–464.

KASLIWAL-R. R., CHOUHAN-N. S., SINHA-A., GUPTA-P., TANDON-S., AND TREHAN-N. (2005). Real-time three-dimensional transthoracic echocardiography, *Indian Heart Journal*, **57**(2), pp. 128–137.

KASS-M., WITKIN-A., AND TERZOPOULOS-D. (1988). Snakes: Active contour models, *International Journal of Computer Vision*, **1**(4), pp. 321–331.

KAUFMAN-L., AND ROUSSEEUW-P. (1990). *Finding Groups in Data: An Introduction to Cluster Analysis*, John Wiley and Sons.

KELLMAN-P., ZHANG-Q., LARSON-A. C., SIMONETTI-O. P., MCVEIGH-E. R., AND ARAI-A. E. (2004). Cardiac first-pass perfusion MRI using 3D trueFISP parallel imaging using TSENSE, *Proceedings of the International Society for Magnetic Resonance in Medicine*, **11**, p. 310.

KERWIN-W., HERTZBERG-J., COOKE-J., CHLUDA-H., SHANDAS-R., AND GILL-E. (2004). Vorticity imaging of diastolic cardiac inflow by phase-contrast MRI, *Proceedings of the 2004 IEEE International Symposium on Biomedical Imaging: From Nano to Macro, Arlington, VA, USA*, **1**, pp. 300–303.

KILNER-P. J. (1998). *Morphodynamics of Flow Through the Heart*, PhD thesis, University of London.

KILNER-P. J., YANG-G.-Z., WILKES-A. J., MOHIADDIN-R. H., FIRMIN-D. N., AND YACOUB-M. H. (2000). Asymmetric redirection of flow through the heart, *Nature Medicine*, **404**, pp. 759–761.

KIM-H., LU-J., SACKS-M. S., AND CHANDRAN-K. B. (2008). Dynamic simulation of bioprosthetic heart valves using a stress resultant shell model, *Annals of Biomedical Engineering*, **36**(2), pp. 262–275.

KIM-M. S., KLEIN-A. J., AND CARROLL-J. D. (2007). Transcatheter closure of intracardiac defects in adults, *Journal of Interventional Cardiology*, **20**(6), pp. 524–545.

KINI-V., BACHMANN-C., FONTAINE-A., DEUTSCH-S., AND TARBELL-J. M. (2000). Flow visualization in mechanical heart valves: Occluder rebound and cavitation potential, *Annals of Biomedical Engineering*, **28**(4), pp. 431–441.

KIRIS-C., KWAK-D., ROGERS-S., AND CHANG-I.-D. (1997). Computational approach for probing the flow through artificial heart devices, *Journal of Biomechanical Engineering*, **119**(4), pp. 452–460.

KLAUSNER-S. C., BOTVINICK-E. H., SHAMES-D., ULLYOT-D. J., FISHMAN-N. H., ROE-B. B., EBERT-P. A., CHATTERJEE-K., AND PARMLEY-W. W. (1977). The application of radionuclide infarct scintigraphy to diagnose perioperative myocardial infarction following revascularization, *Circulation*, **56**, pp. 173–181.

KOKTZOGLOU-I., KIRPALANI-A., CARROLL-T. J., LI-D., AND CARR-J. C. (2007). Dark-blood MRI of the thoracic aorta with 3D diffusion-prepared steady-state free precession: Initial clinical evaluation, *American Roentgen Ray Society*, **189**, pp. 966–972.

KORTSMIT-J., DRIESSEN-N. J. B., RUTTEN-M. C. M., AND BAAIJENS-F. P. T. (2009). Real time, non-invasive assessment of leaflet deformation in heart valve tissue engineering, *Annals of Biomedical Engineering*, **37**(3), pp. 532–541.

KUETHE-D. O. (1989). Measuring distributions of diffusivity in turbulent fluids with magnetic-resonance imaging, *Physical Review A*, **40**, pp. 4542–4551.

KUKLIK-P., SZUMOWSKI-L., ŻEBROWSKI-J., AND WALCZAK-F. (2004). The reconstruction, from a set of points, and analysis of the interior surface of the heart chamber, *Physiological Measurement*, **25**, pp. 617–627.

LAGERSTRAND-K. M., VIKHOFF-BAAZ-B., STARCK-G., AND FORSSELL-ARONSSON-E. (2006). Quantitative phase-contrast flow MRI measurements in the presence of a second vessel closely positioned to the examined vessel, *Journal of Magnetic Resonance Imaging*, **23**(2), pp. 156–162.

LAISSY-J. P., BLANC-F., SOYER-P., ASSAYAG-P., SIBERT-A., TEBBOUNE-D., ARRIVE-L., BROCHET-E., HVASS-U., AND LANGLOIS-J. (1995). Thoracic aortic dissection: diagnosis with transesophageal echocardiography versus MR imaging, *Radiology*, **194**, pp. 331–336.

LANGE-A., WRIGHT-R. A., AL-NAFUSI-A., SANG-C., PALKA-P., AND SUTHERLAND-G. R. (1996). Doppler myocardial imaging: A new method of data acquisition for three-dimensional echocardiography, *Journal of the American Society of Echocardiography*, **9**(6), pp. 918–921.

LARSON-A. C., WHITE-R. D., LAUB-G., MCVEIGH-E. R., LI-D., AND SIMONETTI-O. P. (2004). Self-gated cardiac cine MRI, *Magnetic Resonance in Medicine*, **51**(1), pp. 93–102.

LAUERMA-K., NIEMI-P., HÄNNINEN-H., JANATUINEN-T., VOIPIO-PULKKI-L.-M., KNUUTI-J., TOIVONEN-L., MÄKELÄ-T., MÄKIJÄRVI-M. A., AND ARONEN-H. J. (2000). Multimodality MR imaging assessment of myocardial viability: combination of first-pass and late contrast enhancement to wall motion dynamics and comparison with FDG PET-initial experience, *Radiology*, **217**, pp. 729–736.

LAWSON-M. A. (1999). Cardiovascular imaging in the new millennium, *Proceedings of the Baylor University Medical Center (BUMC)*, **12**, pp. 115–120.

LEE-V. S. (2005). *Cardiovascular MRI: Physical Principles to Practical Protocols*, Lippincott Williams & Wilkins.

LEMMON-J. D., AND YOGANATHAN-A. P. (2000). Computational modeling of left heart diastolic function: examination of ventricular dysfunction, *Journal of Biomechanical Engineering*, **122**(4), pp. 297–303.

LEYMARIE-F., AND LEVINE-M. D. (1993). Tracking deformable objects in the plane using an active contour model, *Pattern Analysis and Machine Intelligence*, **15**(6), pp. 617–634.

LEY-S., LEY-ZAPOROZHAN-J., KREITNER-K., ILIYUSHENKO-S., PUDERBACH-M., HOSCH-W., WENZ-H., SCHENK-J., AND KAUCZOR-H. (2007). MR flow measurements for assessment of the pulmonary, systemic and bronchosystemic circulation: Impact of different ECG gating methods and breathing schema, *European Journal of Radiology*, **61**(1), pp. 124–129.

LINGURARU-M. G., VASILYEV-N. V., MARX-G. R., TWORETZKY-W., NIDO-P. J. D., AND HOWE-R. D. (2008). Fast block flow tracking of atrial septal defects in 4D echocardiography, *Medical Image Analysis*, **12**(4), pp. 397–412.

LIN-W., AND ROBB-R. A. (2000). Visualization of cardiac dynamics using physics-based deformable model, *Proceedings of the SPIE, Medical Imaging 2000: Image Display and Visualization*, **3976**, pp. 210–217.

LIU-Q., MIRC-D., AND FU-B. (2008). Mechanical mechanisms of thrombosis in intact bent microvessels of rat mesentery, *Journal of Biomechanics*, **41**(12), pp. 2726–2734.

LI-W., STOREY-P., CHEN-Q., LI-B. S. Y., PRASAD-P. V., AND EDELMAN-R. R. (2004). Dark flow artifacts with steady-state free precession cine MR technique: Causes and implications for cardiac MR imaging, *Radiology*, **230**, pp. 569–575.

LODHA-S. K., PANG-A., SHEEHAN-R. E., AND WITTENBRINK-C. M. (1996). UFLOW: Visualizing uncertainty in fluid flow, *Seventh IEEE Visualization 1996 (VIS '96)*, pp. 249–254.

LOEVSTAKKEN-L., BJAERUM-S., MARTENS-D., AND TORP-H. (2004). Real-time blood motion imaging a 2D blood flow visualization technique, *IEEE Ultrasonics Symposium*, **1**, pp. 602–605.

LONG-Q., XU-X. Y., KÖHLER-U., ROBERTSON-M. B., MARSHALL-I., AND HOSKINS-P. (2002). Quantitative comparison of CFD predicted and MRI measured velocity fields in a carotid bifurcation phantom, *Biorheology*, **39**(3-4), pp. 467–474.

LORENZO-VALDÉS-M., SANCHEZ-ORTIZ-G. I., MOHIADDIN-R., AND RUECKERT-D. (2002). *Lecture Notes in Computer Science, Medical Image Computing and Computer-Assisted Intervention - MICCAI 2002*, Springer Berlin, Heidelberg, chapter on Atlas-Based Segmentation and Tracking of 3D Cardiac MR Images Using Non-rigid Registration, pp. 642–650.

LOTZ-J., MEIER-C., LEPPERT-A., AND GALANSKI-M. (2002). Cardiovascular flow measurement with phase-contrast MR imaging: Basic facts and implementation, *Radiographics*, **22**, pp. 651–671.

LUCAS-B., AND KANADE-T. (1981). An iterative image registration technique with an application to stereo vision, *Proceedings of the DARPA Image Understanding Workshop*, pp. 121–130.

LUO-S., AND JIN-J. S. (2005). Recent progresses on cerebral vasculature segmentation for 3D quantification and visualization of MRA, *Proceedings of the 3rd International Conference on Information Technology and Applications (ICITA 2005)*, **1**, pp. 656–661.

MAIER-S. E., MEIER-D., BOESIGER-P., MOSER-U. T., AND VIELI-A. (1989). Human abdominal aorta: comparative measurements of blood flow with MR imaging and multigated Doppler US, *Radiology*, **171**, pp. 487–492.

MALIK-M., AND CAMM-A. J. (2004). *Dynamic Electrocardiography*, Blackwell publishing.

MANNA-A. L., SUTARIA-N., AND PRASAD-S. K. (2007). MRI in ischemic heart disease: From coronaries to myocardium, *Indian Journal of Radiology and Imaging*, **17**(2), pp. 98–108.

MARKL-M., AND PELC-N. J. (2004). On flow effects in balanced steady-state free precession imaging: pictorial description, parameter dependence, and clinical implications, *Journal of Magnetic Resonance Imaging*, **20**(4), pp. 697–705.

MARKL-M., CHAN-F. P., ALLEY-M. T., WEDDING-K. L., DRANEY-M. T., ELKINS-C. J., PARKER-D. W., R-R. W., TAYLOR-C. A., HERFKENS-R. J., AND PELC-N. J. (2003). Time-resolved three-dimensional phase-contrast MRI, *Journal of Magnetic Resonance Imaging*, **17**, pp. 499–506.

MARKL-M., DRANEY-M. T., HOPE-M. D., LEVIN-J. M., CHAN-F. P., ALLEY-M. T., PELC-N. J., AND HERFKENS-R. J. (2004). Time-resolved 3-dimensional velocity mapping in the thoracic aorta: visualization of 3-directional blood flow patterns in healthy volunteers and patients, *Journal of Computer Assisted Tomography*, **28**, pp. 459–468.

MARK-M., HARLOFF-A., BLEY-T. A., ZAITSEV-M., JUNG-B., WEIGANG-E., LANGER-M., HENNIG-J., AND FRYDRYCHOWICZ-A. (2007). Time-resolved 3D MR velocity mapping at 3T: Improved navigator-gated assessment of vascular anatomy and blood flow, *Journal of Magnetic Resonance Imaging*, **25**, pp. 824–831.

MARTIN-E. T., AND SANDLER-D. A. (2007). MRI in patients with cardiac devices, *Current Cardiology Reports*, **9**(1), pp. 63–71.

MCINERNEY-T., AND TERZOPOULOS-D. (2000). T-snakes: Topology adaptive snakes, *Medical Image Analysis*, **4**(2), pp. 73–91.

MCMAHON-C. J., FELTES-T. F., FRALEY-J. K., BRICKER-J. T., GRIFKA-R. G., TORTORIELLO-T. A., BLAKE-R., AND BEZOLD-L. I. (2002). Natural history of growth of secundum atrial septal defects and implications for transcatheter closure, *Heart*, **87**(3), pp. 256–259.

MERRIFIELD-R., KEEGAN-J., FIRMIN-D., AND YANG-G.-Z. (2001). Dual contrast TrueFISP imaging for left ventricular segmentation, *Magnetic Resonance in Medicine*, **46**(5), pp. 939–945.

MERRIFIELD-R., LONG-Q., XU-X. Y., KILNER-P. J., FIRMIN-D. N., AND YANG-G.-Z. (2004). Combined CFD/MRI analysis of left ventricular flow, *MIAR 2003*, pp. 229–236.

MEUNIER-P., DIZES-S. L., AND LEWEKE-T. (2005). Physics of vortex merging, *Comptes Rendus Physique*, **6**(4-5), pp. 431–450.

MIELKE-G., AND BENDA-N. (2002). Blood flow velocity waveforms of the fetal pulmonary artery and the ductus arteriosus: reference ranges from 13 weeks to term, *Ultrasound in Obstetrics and Gynecology*, **15**(3), pp. 213–218.

MILLE-J., BONE-R., MAKRIS-P., AND CARDOT-H. (2007). Segmentation and tracking of the left ventricle in 3D MRI sequences using an active surface model, *Proceedings of the 12th IEEE International Symposium on Computer-Based Medical Systems*, pp. 257–262.

MOORE-E. H., WEBB-W. R., VERRIER-E. D., BROADDUS-C., GAMSU-G., AMPARO-E., AND HIGGINS-C. B. (1984). MRI of chronic posttraumatic false aneurysms of the thoracic aorta, *American Journal of Roentgenology*, **143**(6), pp. 1195–1196.

MORBIDUCCI-U., PONZINI-R., GRIGIONI-M., AND REDAELLI-A. (2007). Helical flow as fluid dynamic signature for atherogenesis risk in aortocoronary bypass. a numeric study, *Journal of Biomechanics*, **40**(3), pp. 519–534.

MORBIDUCCI-U., PONZINI-R., RIZZO-G., CADIOLI-M., ESPOSITO-A., COBELLI-F. D., MASCHIO-A. D., MONTEVECCHI-F. M., AND REDAELLI-A. (2009). In vivo quantification of helical blood flow in human aorta by time-resolved three-dimensional cine phase contrast magnetic resonance imaging, *Annals of Biomedical Engineering*, **37**(3), pp. 516–531.

MORGAN-HUGHES-G. J., MARSHALL-A. J., AND ROOBOTTOM-C. (2003). Morphologic assessment of patent ductus arteriosus in adults using retrospectively ECG-gated multidetector CT, *American Journal of Roentgenology*, **181**, pp. 749–754.

MORISE-A. P. (2004). Heart rate recovery: Predictor of risk today and target of therapy tomorrow?, *Circulation*, **110**, pp. 2778–2780.

MOSER-K. W., GEORGIADIS-J. G., AND BUCKIUS-R. O. (2001). On the use of optical flow methods with spin-tagging magnetic resonance imaging, *Annals of Biomedical Engineering*, **29**, p. 9.

MUDRY-K. M., PLONSEY-R., AND BRONZINO-J. D. (2003). *Biomedical Imaging*, number ISBN 0-8493-1810-6, CRC Press.

MULLINGERA-K., DEBENERB-S., COXONA-R., AND BOWTELLA-R. (2008). Effects of simultaneous EEG recording on MRI data quality at 1.5, 3 and 7 tesla, *International Journal of Psychophysiology*, **67**(3), pp. 178–188.

NARULA-J., VANNAN-M. A., AND DEMARIA-A. N. (2007). Of that waltz in my heart, *Journal of the American College of Cardiology*, **49**, pp. 917–920.

NEUENSCHWANDER-W., FUA-P., IVERSON-L., SZÉKELY-G., AND KUBLER-O. (1997). Ziplock snakes, *International Journal of Computer Vision*, **25**(3), pp. 191–201.

NG-E. Y.-K., AND ZHOU-W. (1999). Numerical simulation of mixed-flow 'blood pump' with computational fluid dynamics, *Proceedings of the 3rd ASME/JSME Joint Fluids Engineering Conference, San Francisco, California*, pp. FEDSM99–6851.

NG-E. Y.-K., AND ZHOU-W. (2000). Application of CFD techniques to a scaled rotary blood pump, *International Journal of Computational Fluid Dynamics*, **8**(4), pp. 561–569.

NIENABER-C. A., VON KODOLITSCH-Y., V. NICOLAS-V. S., PIEPHO-A., BROCKHOFF-C., KOSCHYK-D. H., AND SPIELMANN-R. P. (1993). The diagnosis of thoracic aortic dissection by noninvasive imaging procedures, *New England Journal of Medicine*, **328**(22), p. 1637.

NIJM-G. M., SAHAKIAN-A. V., SWIRYN-S., CARR-J. C., SHEEHAN-J. J., AND LARSON-A. C. (2008). Comparison of self-gated cine MRI retrospective cardiac synchronization algorithms, *Journal of Magnetic Resonance Imaging*, **28**(3), pp. 767–772.

OTSUKI-T., MAEDA-S., IEMITSU-M., SAITO-Y., TANIMURA-Y., SUGAWARA-J., AJISAKA-R., AND MIYAUCHI-T. (2007). Postexercise heart rate recovery accelerates in strength-trained athletes, *Medicine & Science in Sports & Exercise*, **39**(2), pp. 365–370.

OVERELL-J. R., BONE-I., AND LEES-K. R. (2000). Interatrial septal abnormalities and stroke: A meta-analysis of case-control studies, *Neurology*, **55**, pp. 1172–1179.

OYRE-S., PEDERSEN-E. M., RINGGAARD-S., BOESIGER-P., AND PAASKE-W. P. (1997). In vivo wall shear stress measured by magnetic resonance velocity mapping in the normal human abdominal aorta, *European Journal of Vascular and Endovascular Surgery*, **13**, pp. 263–271.

OYRE-S., RINGGAARD-S., KOZERKE-S., PAASKE-W. P., ERLANDSEN-M., BOESIGER-P., AND PEDERSEN-E. M. (1998). Accurate noninvasive quantitation of blood flow, cross-sectional lumen vessel area and wall shear stress by three-dimensional paraboloid modeling of magnetic resonance imaging velocity data, *Journal of the American College of Cardiology*, **32**, pp. 128–134.

PALANIAPPAN-K., KAMBHAMETTU-C., HASLER-A., AND GOLDGOF-D. (1995). Structure and semi-fluid motion analysis of stereoscopic satellite images for cloud tracking, *Proceedings of the 5th International Conference on Computer Vision*, pp. 659–665.

PAN-J., AND TOMPKINS-W. J. (1985). A real-time QRS detection algorithm, *IEEE Transactions on Bio-Medical Engineering*, **32**(3), pp. 230–236.

PARAGIOS-N. (2003). A level set approach for shape-driven segmentation and tracking of the left ventricle, *IEEE Transactions On Medical Imaging*, **22(6)**, pp. 773–776.

PARK-M., JIN-J. S., AND LUO-S. (2007). A novel approach for enhancing the visual perception of ribs in chest radiography, *Proceedings of the IEEE/ICME International Conference on Complex Medical Engineering (ICME 2007)*, Beijing, China.

PAULIS-R. D., SCHMITZ-C., SCAFFA-R., NARDI-P., CHIARIELLO-L., AND REUL-H. (2005). In vitro evaluation of aortic valve prosthesis in a novel valved conduit with pseudosinuses of valsalva, *Journal of Thoracic and Cardiovascular Surgery*, **130**, pp. 1016–1021.

PHILLIPS. (1984). *Philips Medical Systems Clinical Education, Basic principles of MR imaging,*, 1st edn, Philips Medical Systems.

PIATKOWSKI-R., SCISLO-P., AND KOCHANOWSKI-J. (2009). Transoesophageal real-time three-dimensional echocardiography in assessing large multiperforated atrial septal aneurysm, *European Heart Journal*.

PIERRAKOS-O., AND VLACHOS-P. P. (2006). The effect of vortex formation on left ventricular filling and mitral valve efficiency, *Journal of Biomechanical Engineering-Transactions of ASME*, **128**(4), pp. 527–539.

PLEHN-G., VORMBROCK-J., BUTZ-T., CHRIST-M., TRAPPE-H.-J., AND MEISSNER-A. (2008). Different effect of exercise on left ventricular diastolic time and interventricular dyssynchrony in heart failure patients with and without left bundle branch block, *International Journal of Medical Science*, **5**, pp. 333–340.

PLEIN-S., BLOOMER-T. N., RIDGWAY-J. P., JONES-T. R., BAINBRIDGE-G. J., AND SIVANANTHAN-M. U. (2001). Steady-state free precession magnetic resonance imaging of the heart: Comparison with segmented k-space gradient-echo imaging, *Journal of Magnetic Resonance Imaging*, **14**(3), pp. 230–236.

PODRID-P. J., AND KOWEY-P. R. (2001). *Cardiac Arrhythmia: Mechanisms, Diagnosis and Management, 2nd Edition*, LippincottWilliams and Wilkins Publication.

POTTER-M. C., AND WIGGERT-D. C. (1997). *Mechanics of Fluids, Second Edition*, Prentice-Hall International, Inc.

POWELL-A. J., MAIER-S. E., CHUNG-T., AND GEVA-T. (2000). Phase-velocity cine magnetic resonance imaging measurement of pulsatile blood flow in children and young adults: In vitro and in vivo validation, *Pediatric Cardiology*, **21**, pp. 104–110.

PUVANESWARY-M., SINGHAM-T., AND BASTIAN-B. (2003). Atrial septal aneurysm: MRI and echocardiography correlation, *Australasian Radiology*, **47**(4), pp. 468–471.

RAFFEL-M., WILLERT-C., AND KOMPENHANS-J. (1998). *Particle Image Velocimetry*, Springer-Verlag, Berlin Heidelberg, Germany.

RAGUIN-L. G., HONECKER-S. L., AND GEORGIADIS-J. G. (2005). MRI velocimetry in microchannel networks, *3rd IEEE/EMBS Special Topic Conference on Microtechnology in Medicine and Biology*, pp. 319–322.

RASMUSSEN-F., AND LINZELL-J. L. (1963). The accuracy of the indicator absorption method of measuring mammary blood flow by the Fick principle, *Quarterly Journal of Experimental Physiology and Cognate Medical Sciences*, **49**(2), pp. 219–225.

REDPATH-T. W. (1998). Signal-to-noise ratio in MRI, *British Journal of Radiology*, **71**, pp. 704–707.

REHWALD-W. G., CHEN-E.-L., KIM-R. J., AND JUDD-R. M. (2004). Noninvasive cineangiography by magnetic resonance global coherent free precession, *Nature Medicine*, **10**, pp. 545–549.

ROBINSON-S. K. (1989). A review of vortex structures and associated coherent motions in turbulent boundary layers, *Proceedings of the Second IUTAM Symposium on Structure of Turbulence and Drag Reduction,* Zurich, Switzerland, pp. 25–28.

ROBINSON-S. K. (1991). Coherent motions in the turbulent boundary layer, *Annual Review of Fluid Mechanics*, **23**, p. 601.

ROBINSON-S. K., KLINE-S. J., AND SPALART-P. R. (1989). A review of quasi-coherent structures in a numerically simulated boundary layer, *NASA Technical Memorandum 102191.*

ROLDÁN-F.-J., VARGAS-BARRÓN-J., VÁZQUEZ-ANTONA-C., CASTELLANOS-L. M., ERDMENGER-ORELLANA-J., ROMERO-CÁRDENAS-A., AND MARTÍNEZ-RÍOS-M.-A. (2008). Three-dimensional transesophageal echocardiography of the atrial septal defects, *Cardiovascular Ultrasound*, **6**(1), p. 38.

ROSAMOND-W., FLEGAL-K., FURIE-K., GO-A., GREENLUND-K., HAASE-N., HAILPERN-S. M., HO-M., HOWARD-V., KISSELA-B., KITTNER-S., LLOYD-JONES-D., MCDERMOTT-M., MEIGS-J., MOY-C., NICHOL-G., ODONNELL-C. J., ROGER-V., RUMSFELD-J., SORLIE-P., STEINBERGER-J., THOM-T., WASSERTHIEL-SMOLLER-S., AND HONG-Y. (2007). Heart disease and stroke statistics–2007 update. a report from the american heart association statistics committee and stroke statistics subcommittee, *Circulation*, **115**, pp. e69–e171.

ROSAMOND-W., FLEGAL-K., FURIE-K., GO-A., GREENLUND-K., HAASE-N., HAILPERN-S. M., HO-M., HOWARD-V., KISSELA-B., KITTNER-S., LLOYD-JONES-D., MCDERMOTT-M., MEIGS-J., MOY-C., NICHOL-G., ODONNELL-C. J., ROGER-V., RUMSFELD-J., SORLIE-P., STEINBERGER-J., THOM-T., WASSERTHIEL-SMOLLER-S., AND HONG-Y. (2008). Heart disease and stroke statistics–2008 update. a report from the american heart association statistics committee and stroke statistics subcommittee, *Circulation*, **117**, pp. e25–e146.

RUHNAU-P., KOHLBERGER-T., NOBACH-H., AND SCHNORR-C. (2005). Variational optical flow estimation for particle image velocimetry, *Experiments in Fluids*, **38**(1), pp. 21–32.

SABER-N. R., GOSMAN-A. D., WOOD-N. B., KILNER-P. J., CHARRIER-C. L., AND FIRMIN-D. N. (2001). Computational flow mdeling of the left ventricle based on in vivo MRI data, *Annals of Biomedical Engineering*, **29**, pp. 275–283.

SADLO-F., PEIKERT-R., AND SICK-M. (2006). Visualization tools for vorticity transport analysis in incompressible flow, *IEEE Transactions on Visualization and Computer Graphics*, **12**(5), pp. 949–956.

SAFFMAN-P. (1992). *Vortex Dynamics, 1st edition*, Cambridge University Press.

SANCHEZ-R. J., AND KHALIL-L. (2005). Badger heart program: health screenings targeted to increase cardiovascular awareness in women at four northern sites in wisconsin, *2005*, **104**(6), pp. 24–29.

SCHENKEL-T., MALVE-M., REIK-M., MARKL-M., JUNG-B., AND OERTEL-H. (2009). MRI-based CFD analysis of flow in a human left ventricle: methodology and application to a healthy heart, *Annals of Biomedical Engineering*, **37**(3), pp. 503–515.

SEITZ-J., STROTZER-M., SCHLAIER-J., NITZ-W. R., VÖLK-M., AND FEUERBACH-S. (2006). Comparison between magnetic resonance phase contrast imaging and transcranial doppler ultrasound with regard to blood flow velocity in intracranial arteries: Work in progress, *Journal of Neuroimaging*, **11**(2), pp. 121–128.

SHAN-K., CONSTANTINE-G., SIVANANTHAN-M., AND FLAMM-S. D. (2004). Role of cardiac magnetic resonance imaging in the assessment of myocardial viability, *Circulation*, **109**, pp. 1328–1334.

SHAPIRO-L. G., AND STOCKMAN-G. C. (2001). *Computer Vision*, number ISBN 0-13-030796-3, New Jersey, Prentice-Hall.

SHAW-G. R., AND SAVARD-P. (1995). On the detection of QRS variations in the ECG, *IEEE Transactions on Bio-Medical Engineering*, **42**(7), pp. 736–741.

SHI-Y. (2001). *Numerical and Experimental Study of Pulsatile Flow in Bileaflet Mechanical Heart Valves*, PhD thesis, Nanyang Technological University.

SHI-Y., ZHAO-Y., YEO-T. J., AND HWANG-N. H. (2003). Numerical simulation of opening process in a bileaflet mechanical heart valve under pulsatile flow condition, *Journal of Heart Valve Disease*, **12**(2), pp. 245–255.

SIEMENS. (2007). *syngo MultiModality Workplace Operator Manual, Siemens Medical, München Germany*, Siemens Medical, München Germany.

SILVER-D., AND WANG-X. (1996). Volume tracking, *Proceedings of the 7th Conference on Visualization '96*, p. 157.

SINGH-R. P., AND LI-Z. (2007). A mass conservative streamline tracking method for three-dimensional CFD velocity fields, *Journal of Flow Visualization and Image Processing*, **14**(1), pp. 107–120.

SKOLNICK-A., VAVAS-E., AND KRONZON-I. (2009). Optimization of ASD assessment using real time three-dimensional transesophageal echocardiography, *Echocardiography*, **26**(2), pp. 233–235.

SMITH-R. L., BLICK-E. F., COALSON-J., AND STEIN-P. D. (1972). Thrombus production by turbulence, *Journal of Applied Physiology*, **32**, pp. 261–264.

SPIEKER-L. E., RUSCHITZKA-F., BADIMON-J. J., NOLL-G., AND CORTI-R. (2004). Shear stress-dependent platelet function after LDL cholesterol apheresis, *Thrombosis Research*, **113**(6), pp. 395–398.

SPRECHER-D. L., ADAMICK-R., ADAMS-D., AND KISSLO-J. (1987). In vitro color flow, pulsed and continuous wave doppler ultrasound masking of flow by prosthetic valves, *American College of Cardiology*, **9**, pp. 1306–1310.

STAHLBERG-F., SONDERGAARD-L., AND THOMSEN-C. (1995). MR flow quantification with cardiovascular applications: a short review, *Acta Paediatrica Supplement*, **410**, pp. 49–56.

STALLMANN-F. W., AND PIPBERGER-H. V. (1961). Automatic recognition of electrocardiographic waves by digital computer, *Circulation Research*, **9**, pp. 1138–1143.

STAUDER-N. I., MILLER-S., SCHEULE-A. M., ZIEMER-G., AND CLAUSSEN-C. D. (2001). MRI diagnosis of a previously undiagnosed large trabecular ventricular septal defect in an adult after multiple catheterizations and angiocardiograms, *British Journal of Radiology*, **74**, pp. 280–282.

STAVENS-D. (2008). Lecture notes on optical flow and OpenCV., *Guest Lecture, Computer Science 223b, Stanford University*.

STEIN-P. D., AND SABBAH-H. N. (1974). Measured turbulence and its effect on thrombus formation, *Circulation Ressearch*, **35**, pp. 608–614.

SÜHLING-M., ARIGOVINDAN-M., JANSEN-C., HUNZIKER-P., AND UNSER-M. (2003). Myocardial motion analysis and visualization from echocardiograms, *Proccedings of the SPIE International Symposium on Medical Imaging MI'03*, pp. 306–313.

SVENSSON-J. (2003). Contrast-enhanced magnetic resonance angiography: Development and optimization of techniques for paramagnetic and hyperpolarized contrast media, *Acta radiologica.*, **429**, pp. 1–30.

TAKAHASHI-T., AND MIYAMOTO-Y. (1998). Influence of light physical activity on cardiac responses during recovery from exercise in humans, *European Journal of Applied Physiology and Occupational Physiology*, **77**(4), pp. 305–311.

TAMAI-J., NAGATA-S., AKAIKE-M., ISHIKURA-F., KIMURA-K., TAKAMIYA-M., MIYATAKE-K., AND NIMURA-Y. (1990). Improvement in mitral flow dynamics during exercise after percutaneous transvenous mitral commissurotomy. noninvasive evaluation using continuous wave Doppler technique, *Circulation*, **81**, pp. 46–51.

TANG-A., KACHER-D., LAM-E., BRODSKY-M., JOLESZ-F., AND YANG-E. (2007). Multi-modal imaging: Simultaneous MRI and ultrasound imaging for carotid arteries visualization, *Proceedings of the 29th Annual International Conference of the IEEE (EMBS 2007), Lyon, France*, pp. 2603–2606.

TANGELDER-G. J., SLAAF-D. W., MUIJTJENS-A. M., ARTS-T., OUDE EGBRINK-M. G., AND RENEMAN-R. S. (1986). Velocity profiles of blood platelets and red blood cells flowing in arterioles of the rabbit mesentery, *Circulation Research*, **59**, pp. 505–514.

TEO-K. S. L., DUNDON-B. K., MOLAEE-P., WILLIAMS-K. F., CARBONE-A., BROWN-M. A., WORTHLEY-M. I., DISNEY-P. J., SANDERS-P., AND WORTHLEY-S. G. (2008). Percutaneous closure of atrial septal defects leads to normalisation of atrial and ventricular volumes, *Journal of Magnetic Resonance Imaging*, **10**(1), p. 55.

TEO-K. S. L., ROBERTS-THOMSON-K., AND WORTHLEY-S. G. (2004). Utility of intravascular ultrasound in the diagnosis of ambiguous calcific left main stenoses, *Journal of Invasive Cardiology*, **16**, p. 385.

TERZOPOULOS-D., AND METAXAS-D. (1991). Dynamic 3D models with local and global deformations: Deformable superquadrics, *IEEE Transactions on Pattern Analysis and Machine Intelligence*, **13**(7), pp. 703–714.

TERZOPOULOS-D., WITKIN-A., AND KASS-M. (1987). Symmetry-seeking models for 3D object recognition, *International Journal of Computer Vision*, **1**(3), pp. 211–221.

TETSUYA-M. (2003). ECG gating in cardiac MRI, *Japanese Journal of Magnetic Resonance in Medicine*, **23**(4), pp. 120–130.

THOMAS-E. J., KUMAR-R., DASAN-J. B., CHANDRASHEKAR-N., AGARWALA-S., TRIPATHI-M., AND BAL-C. S. (2003). Radionuclide scintigraphy in the evaluation of gastro-oesophageal reflux in post-operative oesophageal atresia and tracheo-oesophageal fistula patients, *Nuclear medicine communications*, **24**(3), pp. 317–320.

THOMPSON-R. B., AND MCVEIGH-E. R. (2004). Flow-gated phase-contrast MRI using radial acquisitions, *Magnetic Resonance in Medicine*, **52**(3), pp. 598–604.

TRAHANIAS-P. E. (1993). An approach to QRS complex detection using mathematical morphology, *IEEE Transactions on Bio-Medical Engineering*, **40**(2), pp. 201–205.

UTERHINNINGHOFEN-R., LEY-S., ZAPOROZHAN-J., SZABÖ-G., AND DILLMANN-R. (2006). A versatile tool for flow analysis in 3D-phase-contrast magnetic resonance imaging, *International Journal of Computer Assisted Radiology and Surgery*, **1**(1), pp. 107–117.

VANDENBERG-B. F., DELLSPERGER-K. C., CHANDRAN-K. B., AND KERBER-R. E. (1988). Detection, localization, and quantitation of bioprosthetic mitral valve regurgitation: An in vitro two-dimensional color-Doppler flow-mapping study, *Circulation*, **78**, pp. 529–538.

VANYUSHIN-Y. S., SITDIKOV-F. G., AND ISKHAKOVA-A. T. (2000). Characteristics of cardiac activity in 5- to 7-year-old children during graded exercise, *Human Physiology*, **26**(3), pp. 345–348.

VARAPRASATHAN-G. A., ARAOZ-P. A., HIGGINS-C. B., AND REDDY-G. P. (2002). Quantification of flow dynamics in congenital heart disease: Applications of velocity-encoded cine MR imaging, *Radiographics*, **22**, pp. 895–905.

VASAN-R. S., LARSON-M. G., BENJAMIN-E. J., EVANS-J. C., REISS-C. K., AND LEVY-D. (1999). Congestive heart failure in subjects with normal versus reduced left ventricular ejection fraction, *Journal of the American College of Cardiology*, **33**, pp. 1948–1955.

VON DER SCHULENBURG-D. A. G., AKPA-B. S., GLADDEN-L. F., AND JOHNS-M. L. (2008). Non-invasive mass transfer measurements in complex biofilm-coated structures, *Biotechnology and Bioengineering*, **101**(3), pp. 602–608.

WAHLE-A., LOPEZD-J. J., OLSZEWSKIA-M. E., VIGMOSTADB-S. C., CHANDRAN-K. B., ROSSENC-J. D., AND SONKAA-M. (2006). Plaque development, vessel curvature, and wall shear stress in coronary arteries assessed by X-ray angiography and intravascular ultrasound, *Medical Image Analysis*, **10**(4), pp. 615–631.

WALKER-A., OLSSON-E., WRANNE-B., RINGQVIST-I., AND ASK-P. (2004). Accuracy of spectral doppler flow and tissue velocity measurements in ultrasound systems, *Ultrasound in Medicine & Biology*, **30**(1), pp. 127–132.

WATANABE-H., SUGIURA-S., KAFUKU-H., AND HISADA-T. (2004). Multiphysics simulation of left ventricular filling dynamics using fluid-structure interaction finite element method, *Biophysics Journal*, **87**(3), pp. 2074–2085.

WEBB-G., AND GATZOULIS-M. A. (2006). Atrial septal defects in the adult - recent progess and overview, *Circulation*, **114**, pp. 1645–1653.

WENG-N., YANG-Y.-H., AND PIERSON-R. (1997). Three-dimensional surface reconstruction using optical flow for medical imaging, *IEEE Transactions on Medical Imaging*, **16**, p. 630.

WENG-W., FAN-W., LIAO-G., AND QIN-J. (2001). An improved cross-correlation method for (digital) particle image velocimetry, *Acta Mechanica Sinica*, **17**(4), pp. 332–339.

WIGSTROM-L., SJOQVIST-L., AND WRANNE-B. (1996). Temporally resolved 3D phase contrast imaging, *Magnetic Resonance In Medicine*, **36**, pp. 800–803.

WINTER-M., BERNINK-F., GROENINK-M., BOUMA-B., VAN DIJK-A., HELBING-W., TIJSSEN-J., AND MULDER-B. (2008). Evaluating the systemic right ventricle by cmr: the importance of consistent and reproducible delineation of the cavity, *Journal of Cardiovascular Magnetic Resonance*, **10**, p. 40.

WOLBARST-A. B. (1999). *Looking Within How X-ray, CT, MRI, Ultrasound, and Other Medical Images are Created, and How They Help Physicians Save Lives*, University of California Press, USA.

WONG-K. K. L., KELSO-R. M., WORTHLEY-S. G., SANDERS-P., MAZUMDAR-J., AND ABBOTT-D. (2009a). Cardiac flow analysis applied to phase contrast magnetic resonance imaging of the heart, *Annals of Biomedical Engineering*.

WONG-K. K. L., KELSO-R. M., WORTHLEY-S. G., SANDERS-P., MAZUMDAR-J., AND ABBOTT-D. (2009b). Medical imaging and processing methods for cardiac flow reconstruction, *Journal of Mechanics in Medicine and Biology*, **9**(1), pp. 1–20.

WONG-K. K. L., KELSO-R. M., WORTHLEY-S. G., SANDERS-P., MAZUMDAR-J., AND ABBOTT-D. (2009c). Noninvasive cardiac flow assessment using high speed magnetic resonance fluid motion tracking, *PLoS ONE*, **4**(5), p. e5688.

WONG-K. K. L., KELSO-R. M., WORTHLEY-S. G., SANDERS-P., MAZUMDAR-J., AND ABBOTT-D. (2009d). A novel technique for cardiac flow component analysis applied to the human atrium, *Medical Engineering & Physics*.

WONG-K. K. L., KELSO-R. M., WORTHLEY-S. G., SANDERS-P., MAZUMDAR-J., AND ABBOTT-D. (2009e). Theory and validation of magnetic resonance fluid motion estimation using intensity flow data, *PLoS ONE*, **4**(3), p. e4747.

WONG-K. K. L., MAZUMDAR-J., PINCOMBE-B., WORTHLEY-S. G., SANDERS-P., AND ABBOTT-D. (2006). Theoretical modeling of micro-scale biological phenomena in human coronary arteries, *Medical & Biological Engineering & Computing*, **44**(11), pp. 971–982.

WORTHLEY-S. G. (2001). *Magnetic Resonance Imaging of Atherosclerotic Plaque*, PhD thesis, University of Adelaide.

WORTHLEY-S. G., AND FAYAD-Z. A. (2002). Utility of cardiovascular magnetic resonance imaging, *Heart, Lung and Circulation*, **11**, p. 63.

WORTHLEY-S. G., FAROUQUE-H. M. O., HELFT-G., AND MEREDITH-I. T. (2002). Coronary artery imaging in the new millennium, *Heart, Lung and Circulation*, **11**(1), pp. 19–25.

WU-M.-N., LIN-C.-C., AND CHANG-C.-C. (2007). Brain tumor detection using color-based k-means clustering segmentation, *Proceedings of the Third International Conference on Intelligent Information Hiding and Multimedia Signal Processing*, **2**, pp. 245–250.

XIA-G. H., ZHAO-Y., AND YEO-J. H. (2005). Numerical simulation of 3D fluid-structure interaction using an immersed membrane method, *Modern Physics Letters B*, **19**(28-29), pp. 1447–1450.

XIONG-F. L., AND CHONG-C. K. (2007). PIV-validated numerical modeling of pulsatile flows in distal coronary end-to-side anastomoses, *Journal of Biomechanics*, **40**, pp. 2872–2881.

XIONG-F. L., AND CHONG-C. K. (2008). A parametric numerical investigation on haemodynamics in distal coronary anastomoses, *Medical Engineering & Physics*, **30**(3), pp. 311–320.

XIONG-F., YEO-J. H., CHONG-C. K., CHUA-Y. L., LIM-K. H., OOI-E. T., AND GOETZ-W. A. (2008). Transection of anterior mitral basal stay chords alters left ventricular outflow dynamics and wall shear stress, *Journal of Heart Valve Disease*, **17**(1), pp. 54–61.

XU-C., AND PRINCE-J. L. (1998). Snakes, shapes, and gradient vector flow, *IEEE Transactions on Image Processing*, **7**(3), pp. 359–369.

YAMASHITA-S., ISODA-H., HIRANO-M., TAKEDA-H., INAGAWA-S., TAKEHARA-Y., ALLEY-M. T., MARKL-M., PELC-N. J., AND SAKAHARA-H. (2007). Visualization of hemodynamics in intracranial arteries using time-resolved three-dimensional phase-contrast MRI, *Journal of Magnetic Resonance Imaging*, **25**, pp. 473–478.

YANG-G. Z., MOHIADDIN-R. H., KILNER-P. J., AND FIRMIN-D. N. (1998). Vortical flow feature recognition: A topological study of in-vivo flow patterns using MR velocity mapping, *Journal of Computer Assisted Tomography*, **22**, pp. 577–586.

YATES-L. A., AND CHAPMAN-G. T. (1991). Streamlines, vorticity lines, and vortices, *AIAA Paper 91-0731*.

YAU-D., LAWRENCE-B., AND CROZIER-S. (2001). A method for the design of MRI radiofrequency coils based on triangular and pulse basis functions, *Magnetic Resonance Materials in Physics, Biology and Medicine*, **13**(3), pp. 145–151.

YEARWOOD-T. L., AND CHANDRAN-K. B. (1982). Physiological pulsatile flow experiments in a model of the human aortic arch, *Journal of biomechanics*, **15**(9), pp. 683–704.

YOSHINO-H., AND TAKEUCHI-H. (1994). Signal receiving coil device for MRI apparatus, *United States Patent Application*, US Patent 5327898.

YU-Q., KONG-X., AND LIU-D. (2003). Differential diagnosis of arachnoid cyst from subarachnoid space enlargement by phase-contrast cine MRI, *Chinese Medical Journal*, **116**(1), pp. 116–120.

ZHAO-S. Z., PAPATHANASOPOULOU-P., LONG-Q., MARSHALL-I., AND XU-X. Y. (2003). Comparative study of magnetic resonance imaging and image-based computational fluid dynamics for quantification of pulsatile flow in a carotid bifurcation phantom, *Annals of Biomedical Engineering*, **31**(8), pp. 962–971.

ZHUKOV-L., BAO-Z., GUSKOV-I., WOOD-J., AND BREEN-D. (2002). Dynamic deformable models for 3D MRI heart segmentation, *Proceedings of the SPIE Medical Imaging 2002: Image Processing*, **4684**, pp. 1398–1405.

ZILE-M. R., AND BRUTSAERT-D. L. (2002). New concepts in diastolic dysfunction and diastolic heart failure: Part I, *Circulation*, **105**, pp. 1387–1393.

ZOBKOV-V. V. (2002). Improved method of cardiac activity monitoring during physical exercises, *Human Physiology*, **28**(1), pp. 134–136.

Index

Résumé

Kelvin Wong graduated from Nanyang Technological University (NTU), Singapore, with a Bachelor of Mechanical and Production Engineering (with Honours) in 2001. He then obtained a Masters of Applied Information Technology, at the University of Sydney in 2003. He worked for Kruger Ventilation Industries in Singapore as a research specialist and commenced his PhD in biomedical engineering at The University of Adelaide in 2006. He completed his PhD in 2009.

Kelvin's research interests include medical imaging, flow visualisation, biofluid mechanics and computational fluid dynamics. He has authored more than ten peer-reviewed journal and conference publications, including papers in *Public Library of Science (PLoS)*, *Annals of Biomedical Engineering (ABME)* and *Medical & Biological Engineering & Computing (MBEC)* journals. He has given ten conference presentations, and received a Young Investigator Award at the *15th International Conference on Mechanics in Medicine and Biology (ICMMB)* and an Outstanding Paper Award at the *13th International Conference on Biomedical Engineering (ICBME)* in 2006 and 2008 respectively. He is also the recipient of the Heart Foundation Travel Grant in 2009. Kelvin has developed the *Magnetic Resonance Fluid Motion Tracking* technique and created the *Medflovan* medical image processing software to analyse cardiac blood flow.

Scientific Genealogy

My scientific genealogy via my supervisors are as follows:

Kelvin K. L. Wong's Scientific Genealogy via Jagannath Mazumdar			
1934	DSc	Moscow State University	A. A. Ilyushin
1958	DSc	Moscow State University	Vladimir Dimitrievich Klyushnikov
1966	PhD	Moscow State University	Jagannath Mazumdar
2009	PhD submitted	University of Adelaide	Kelvin K. L. Wong

Kelvin K. L. Wong's Scientific Genealogy via Derek Abbott			
1668	MA	University of Cambridge	Isaac Newton
1706	MA	University of Cambridge	Roger Cotes
1715	MA	University of Cambridge	Robert Smith
1723	MA	University of Cambridge	Walter Taylor
1742	MA	University of Cambridge	Stephen Whisson
1756	MA	University of Cambridge	Thomas Postlethwaite
1782	MA	University of Cambridge	Thomas Jones
1811	MA	University of Cambridge	Adam Sedgwick
1830	MA	University of Cambridge	William Hopkins
1857	MA	University of Cambridge	Edward John Routh
1868	MA	University of Cambridge	John William Strutt (Lord Rayleigh)
1883	MA	University of Cambridge	Joseph John Thomson
1903	MA	University of Cambridge	John Sealy Townsend
1923	DPhil	University of Oxford	Victor Albert Bailey
1948	MSc	University of Sydney	Ronald Ernest Aitchison
1964	PhD	University of Sydney	Peter Harold Cole
1980	PhD	University of Adelaide	Kamran Eshraghian
1995	PhD	University of Adelaide	Derek Abbott
2009	PhD submitted	University of Adelaide	Kelvin K. L. Wong